

https://dspace.org/

A stable high temperature gold nano-catalyst: synthesis, characterization and application

Barrett, Dean Howard

2013-01-31
https://hdl.handle.net/10539/12346

Downloaded from a DSpace repository. https://dspace.org/

A Stable High Temperature Gold Nano-Catalyst: Synthesis, Characterization and Application

Submitted by Dean H. Barrett

University of the Witwatersrand

Department of Chemistry

Supervised by Dr P.J Franklyn and Emeritus Professor M.S Scurrell

A thesis submitted in fulfullment of the requirements for the degree of

Doctor of Philosophy

Declarations

I declare that this thesis is my own unaided work. It is being submitted for the Degree of Doctor of Philosophy in the University of the Witwatersrand, Johannesburg. It has not been submitted before for any degree or examination in any other University

_____

Signature of Candidate on the _____day of _____ 2012

Abstract

A stable high temperature gold nano-catalyst: synthesis, characterization and application

The ability of supported gold nanoparticles to catalyse many reactions even at very low temperatures has spurred a great deal of research into the field. Reactions such as CO oxidation and NOx reduction have many industrial applications as well as uses in the motor industry for catalytic converters. The interest is both for scientific as well as economic reasons as gold supplies far exceed all PGM supplies. Scientifically gold catalysts are able to catalyze reactions from below 0°C, a feat that no PGM catalyst can achieve. The low temperature activity of gold catalysts will reduce the emission of pollutants during start up. Since the discovery and development of gold catalysts one of the most researched topics has been finding ways to stabilise the gold nanoparticles on the support surface. The importance of gold nanoparticle stability is crucial as the catalysts are only highly active if the gold nanoparticles are less than 5 nm in size. A number of companies have worked to develop gold catalysts that are stable for long durations at temperatures over 450°C with no significant progress made over the last two decades other than a catalyst produced by Toyota.

In this thesis, literature reviews of current support materials as well as synthesis methods are investigated in order to determine reasons for the instability of current gold catalysts. Further, the Mintek Aurolite catalyst is tested and its deactivation mechanisms probed using in-situ VT-PXRD, Rietveld refinement, TEM, HR-TEM, as well as CO oxidation tests. Testing revealed flaws in the support structure of the catalyst which resulted in dramatic deactivation. As titania is such a common support material for many reactions in industry as well as being known to be one of the best supports for gold it was chosen as a support material. However, as is revealed, in its current forms and morphologies it is unable to provide the thermodynamically stable and high surface areas that are required for a stable catalyst After the development of a robust and reproducible synthesis method for the deposition of gold and other PGM's a number of supports were tested. These include silica and zirconia as

well as titania derivatives such as Degussa P25 and commercial anatase. Initially these supports offer high usable surface areas but after a relatively small amount of time complete deactivation occurs. Reasons for this deactivation are determined and the information gained is used to develop supports that can combat these deactivation processes. Phase pure nano anatase is synthesised which produced a support with an incredibly large surface area compared to the aforementioned supports. The catalyst was able to withstand temperatures over 450°C for longer durations compared to other catalysts exposed to the same conditions. However, the phase conversion of the anatase to its thermodynamically stable form rutile once again deactivated the catalyst with time. Finally a rutile nanosupport is developed with the desired morphology and thermodynamic stability needed for high temperature applications. The catalyst is able to withstand temperatures over 550°C for more than 200 hours as well as still being active after exposure to 810°C. The industrial Aurolite catalyst showed complete deactivation after just 12 hours at 500°C. The catalyst produced in this thesis has been shown to be one of the most stable and thermally resistant gold catalysts in the world.

Acknowledgments

To my father, the greatest man I have ever known. I hope that one day I can be like you. To my mother, the kindest person I know who always puts everyone before of herself. You have sacrificed so much for me.

I would like to thank Dr Paul Franklyn and Professor Mike Scurrell for all their help and guidance, without your help I would never have been the scientist I am today. I have learnt so much from you.

To Basil Chassoulous for all of his help with and time spent laughing together while working.

To Professor Neil Coville who always has a wise word when required.

To Professor Dave Billing for allowing me access to the diffraction instruments as well as teaching me to challenge conventional wisdom.

To all of my friends, thanks for the encouragement over the years.

To my friend Dr Roy Forbes, for all his help and guidance.

I would like to thank the Wits Department of Chemistry for the opportunity that they have afforded me.

Finally to the NRF and Mintek for financial support that made this work possible.

Jehovah Jireh, my provider.

"Chemists are a strange class of mortals, impelled by an almost maniacal impulse to seek their pleasures amongst smoke and vapour, soot and flames, poisons and poverty, yet amongst all these evils I seem to live so sweetly that I would rather die than change places with the King of Persia." - Johann Joachim Becher, Physica subterranea (1667)

Contents

Declarations i

Abstract ii

Acknowledgments iv

Summary v

Table of Contents vi

1 Introduction 2

1.1 Supply and demand of gold 2

1.2 Chemical and physical properties of gold 7

1.3 Gold and the CO oxidation reaction 10

1.3.1 Interaction of oxygen with gold nanoparticles 13

1.3.2 Chemisorption of oxygen on gold surfaces 15

1.3.3 Interaction of CO with gold clusters 17

1.3.4 CO oxidation using gold nanoparticles 17

1.4 Kinetic behavior and the reaction mechanism 21

1.5 Producing active nanogold catalysts 22

1.5.1 Strong contact of the gold nanoparticles with the support 23
1.5.2 Size control of the gold nanoparticles 23
1.5.3 Selection of the correct support 26
1.5.4 A note on catalyst deactivation 26

2 Techniques of Characterization 29

2.1 BET 29
2.2 X-ray Diffraction 31
2.2.1 Lab instruments 32
2.2.2 NIST LaB_6 reference material 34
2.2.3 The Anton Paar variable temperature chamber 35
2.2.4 Software used for interpretation of diffraction data 36
2.3 Rietveld Refinement 40
2.3.1 Parameters in the Rietveld method 41
2.3.2 The final Rietveld equation. 48
2.3.3 Refinement methods used on the data in this thesis . . . 50
2.3.4 Input Files and Refinement Parameters. 51
2.4 Electron Microscopy 53
2.4.1 The concept of resolution 54
2.4.2 Electron diffraction (ED and SAD) 56
2.4.3 Scanning transmission electron microscopy (STEM) . . . 57
2.4.4 Energy Dispersive Spectroscopy (EDS) 61
2.5 Tomography 61
2.6 Catalytic testing 63

3 Aims **65**

4 Au and Au-Pt on amorphous silica and zirconia **67**

4.1 Introduction 67

4.2 Synthesis 71

4.2.1 Deposition of Au and Au-Pt onto amorphous silica and zirconia using the DP method 71

4.2.2 Theoretical mass loading 72

4.2.3 Discussion of the synthesis method 73

4.2.4 PXRD 73

4.3 Addition of platinum to the Au-silica and Au-zirconia system . . 82

4.4 Electron microscopy 91

4.4.1 SEM 91

4.4.2 TEM 92

4.5 Conclusions 94

5 The use of titania as a catalyst support **102**

5.1 Introduction 102

5.2 Au and Au-Pt supported on commercial anatase phase TiO_2 . . 103

5.3 Experimental 105

5.4 In-situ PXRD of commercial anatase 106

5.5 TEM 116

5.5.1 TEM analysis of 5% Au supported on commercial anatase 116

5.5.2 TEM analysis of 5% Au-1% Pt supported on commercial anatase 118

5.5.3 TEM analysis of 5% Au-2% Pt supported on commercial anatase . . . 125

5.5.4 EDS analysis . . . 136

5.6 5% Au-3% Pt supported on commercial anatase . . . 137

5.6.1 Particle size distributions for three different Au : Pt ratios 143

5.7 Conclusions . . . 143

6 The Mintek Aurolite^{TM} catalyst and the use of Degussa P25 as a support 145

6.1 Introduction to the use of Degussa P25 as a support . . . 145

6.2 In-situ PXRD of Degussa P25 . . . 146

6.3 Introduction to the Mintek Aurolite catalyst . . . 149

6.4 In-situ PXRD . . . 149

6.4.1 Rietveld refinement . . . 150

6.5 TEM . . . 160

6.6 Conclusions . . . 160

7 Titania nanostructures 165

7.1 The importance of titania nanostructures . . . 166

7.2 The structure of nanomaterials . . . 167

7.3 Synthesis of titania nanostructures . . . 168

8 Nano anatase as a support for Au and Au-Pt nanoparticles 170

8.1 Introduction . . . 170

8.2 Synthesis . . . 171

8.3 In-situ PXRD . . . 172

8.4 Rietveld refinements . . . 172
8.4.1 Comparison of commercial anatase to nano anatase . . . 175
8.5 TEM . . . 179
8.6 CO oxidation testing . . . 186
8.7 Conclusions . . . 187

9 In search of a catalyst stable for temperatures exceeding 400°C 189

9.1 Introduction to high temperature gold catalysis . . . 189
9.2 Synthesis of thermodynamically stable, high surface area, nano rutile as a support structure . . . 193
9.3 BET . . . 194
9.4 In-situ PXRD . . . 195
9.4.1 In-situ PXRD of pure NRS . . . 196
9.4.2 5% Au on NRS . . . 198
9.4.3 8% Au on NRS . . . 199
9.4.4 Rietveld refinements . . . 202
9.5 A note on preparation of the NRS . . . 208
9.6 TEM . . . 214
9.6.1 Electron diffraction . . . 214
9.6.2 TEM . . . 214
9.6.3 EDS . . . 221
9.7 Tomography . . . 226
9.8 Catalysis Data . . . 226
9.9 Conclusions . . . 231

10 Conclusions **234**

11 Future work **241**

12 Testing for use in Bombardier (Rotax) race engines **243**

12.1 Exhaust gas temperature testing 243

12.2 Conclusions 246

List of Figures

1.1 1 kilogram gold bars in the vault at vendor Proaurum in Germany. 3

1.2 Averaged annual gold price in USD and GBP since 1900. With the steadily increasing demand and price of gold over the last few years dehedging on a net basis has been occurring. The dehedging is caused by an almost constant averaged increase in the gold price. When this occurs it is in the producers interest to hold onto the gold for as long as possible and not to sell the gold prior to it being mined. 5

1.3 Price per ounce of gold from 1900. A constant averaged increase in the gold price has resulted in dehedging by gold producers. . 5

1.4 Fractional contraction of the 6s orbitals due to relativistic effects[8]. 8

1.5 Potential energy curves representing the interaction of molecular oxygen with a gold cluster or a gold surface[25]. 16

1.6 There are multiple ways that CO can chemisorb onto a gold surface: (A) linear, (B) bridged (C) dissociated and (D) sideways on[25]. 18

1.7 The CO oxidation mechanism that was first proposed by Haruta and co workers[33]. 19

1.8 The early stages of the CO oxidation process where the CO is chemisorbed at the periphery of the active gold particle[40]. . . . 20

1.9 FT-IR spectra for CO absorbed on Au-TiO_2 calcined at 200°C, 300°C and 600°C for various sizes of gold nanoparticle[21]. 21

1.10 TOF's of gold and platinum showing the difference in TOF's when the gold and platinum are bound either as a sphere or hemispherically[41]. Hemispherically bound particles far out perform particles that are not bound in this fashion. Platinum however only shows a small difference in TOF's as a function of bonding[41]. 24

1.11 Reaction rates of CO oxidation over fresh and deactivated Au-TiO_2 as well as unsupported gold as a function of particle size[41]. 25

1.12 Operating condition of a catalyst and processes that can occur on the surface leading to deactivation[25]. 27

1.13 Mechanisms of deactivation of a catalyst[25]. 28

2.1 The 6 most common physical adsorption isotherms[48]. 30

2.2 The powder diffractometers used to collect data in this thesis are set up in Bragg-Brentano geometry as shown, this geometry is used for preferentially and randomly oriented samples. 33

2.3 Internal structure of the Bruker D2 Phaser. 34

2.4 Intensity dependance on slit selection. 36

2.5 Changes in peak shape and intensity are dependent on counting time. Further, the reduction in the Cu$k\alpha_1/k\alpha_2$ can also be seen as counting time is increased. As the data collections were limited by the large amount of time that the catalysts spend at high temperatures it was viable to use a long counting time of 0.75 seconds per step. 37

2.6 The Bruker D8 with the XRK attachment in Bragg-Brentano geometry. 38

2.7 The XRK chamber with all gas lines attached. 38

2.8 macor sample holder prior to insertion into the chamber 39

2.9 Macor sample holder. 39

2.10 Macor holder with central opening (2) and frit (3) that fits into (2). 40

2.11 Multiple scattering considerations must be taken into consideration when an incident beam of X-rays strikes a sample[52]. . . . 42

2.12 Polarization of the incident beam. 44

2.13 Change in the LP factor vs Bragg angle[51]. 44

2.14 Diffraction pattern collected at room temperature[51]. 45

2.15 Diffraction pattern collected at non-ambient temperature showing deviations[51]. 46

2.16 The incident beam may penetrate deeply into the sample and be deflected internally by the crystal planes resulting in lower peak intensities at the detector[52]. 47

2.17 The Scherrer equation is derived from the full width at half maximum (FWHM)[51]. 48

2.18 An example of the input file used for the refinement of Degussa P25 support. Rietveld refinement input files such as this were used throughout the thesis where in-situ PXRD data was collected. Over 1100 Rietveld refinements were conducted on in-situ data in this thesis. 52

2.19 A number of different types of signals that are produced when an electron beam contacts a specimen. Most of these signals can be detected using different types of TEM. When a number of these techniques are combines the TEM becomes a very powerful instrument in materials characterization[53]. 56

2.20 The two basic imaging modes in a TEM are illustrated above a) Diffraction mode and b) Image model[53]. 58

2.21 Ray diagram showing the formation of a diffraction pattern[53]. The insertion of an aperture in the image plane results in the creation of a virtual aperture in the plane of the specimen which is demonstrated here slightly above the specimen plane. Electrons that find themselves inside the area of the virtual aperture at the entrance surface of the specimen will be allowed through into the imaging system to contribute to the selected area diffraction pattern. All other electrons which are represented by the dotted lines will hit the selected area diffraction diaphragm. 59

2.22 Scanning the convergent probe for STEM image formation using two pairs of scan coils between the C2 lens, which is usually switched off, and the upper-objective polepiece. The double-deflection process ensures that the probe remains parallel to the optic axis as it scans across the specimen surface[53]. 60

2.23 The principal of EDS[53]. 62

2.24 CO oxidation catalytic testing unit setup. 64

4.1 Gold loading and yield of DP versus solution pH for Au-TiO_2 supported on Degussa P-25. The catalysts were prepared by DP with NaOH used as the base and preparation at 75°C with a nominal gold loading of 13 wt.%[57]. 68

4.2 Gold loading and yield of the DP method versus solution pH for Au-TiO_2 on Degussa P-25. The catalysts were prepared by DP with NaOH used as the base. Preparation was at 75°C with a nominal gold loading of 1 wt%[58]. 69

4.3 Various samples supported on silica prepared and heated under different conditions. Unheated sample (left), 200°C, 300°C and finally 400°C (far right). All samples are 5% Au on silica. 74

4.4 Unheated sample (left), 200°C, 300°C and finally 400°C (far right) The samples shown are 5% Au-1% Pt on silica. In all cases the different colours can be attributed to the samples optical absorption in the visible region of the spectrum which is due to the relativistic lowering of the gap between the 5d band and the Fermi level, without this effect the gold nanoparticles would be a white/silver colour and have the same propensity to tarnish and corrode[8]. 74

4.5 5% Au on silica (*pH 2.85, 1.0 M urea, 120˚C, 1hr*). 75

4.6 5% Au on silica (*pH 2.85, 1.0 M urea, 300˚C, 1hr*). 76

4.7 Zoomed view of 5% Au on silica (*pH 2.85, 1.0 M urea, 300˚C, 1hr*). The pattern showed the increased intensity of the gold diffraction peaks due to higher thermal exposure. 76

4.8 5% Au on silica (*pH 9 at start of synthesis, pH 4 at end of synthesis, 1.0 M urea, 0.1 M NH_4OH, 120˚C, 1hr*). The pattern showed the amorphous nature of the support. 77

4.9 Zoomed view of 5% Au on silica (*pH 9 at start, pH 4 at end of synthesis, 1.0 M urea, 0.1 M NH_4OH, 300˚C, 1hr*). The two broad peaks result from metallic gold. 78

4.10 5% Au on silica (*pH 7, 1.0 M urea, 0.25 M NH_4OH, 120˚C, 1 hr).* 79

4.11 5% Au on silica (*pH 7, 1.0 M urea, 0.25 M NH_4OH, 300˚C, 1 hr*). 79

4.12 5% Au on silica (*pH 9, 1.0 M urea, 0.25 M NH_4OH, 120˚C, 1hr*) 80

4.13 5% Au on silica (*pH 9, 1.0 M urea, 0.25 M NH_4OH, 300˚C, 1hr*). 80

4.14 Averaged crystallite size VS synthesis pH of 5% Au on silica and zirconia supports heated to 300°C for 1 hour. Corresponding sample designations are given in Table 4.2. Zirconia PXRD patterns are discussed later. 81

4.15 Zoomed region between 35° and 50° 2θ highlighting the two gold diffraction peaks. 5% Au-1% Pt on silica (*pH 9, 1.0 M urea, 0.25 M NH_4OH, 300˚C, 1hr*). 83

4.16 5% Au-1% Pt on silica (*pH 9, 1.0 M urea, 0.25 M NH_4OH, 400˚C, 1hr*) 84

4.17 5% Au-2% Pt on silica, (*pH 9, 1.0 M urea, 0.25 M NH_4OH, 400˚C, 1hr*). 84

4.18 5% Au-1% Pt on silica with a NaCl spike in red. (*pH 9, 1.0 M urea, 0.25 M NH_4OH, 300˚C, 1hr*). 85

4.19 5% Au-1% Pt on silica (*pH 8, 1.0 M urea, 0.25 M NH_4OH, 400˚C, 1hr*). The diffraction pattern shows the two principal gold diffraction peaks. For all samples it was these two principal peaks at 38.2° and 44.4° 2θ, corresponding to the (111) and (011) respectively, that were analyzed for gold crystallite size. 86

4.20 Zoomed diffraction pattern of 5% Au-1% Pt on zirconia, (*pH 9, 1.0 M urea, 0.25 M NH_4OH, 300^{o}C, 1 hr*). 86

4.21 Zoomed diffraction pattern of 5% Au-2% Pt on zirconia, (*pH 9, 1.0 M urea, 0.25 M NH_4OH, 300^{o}C, 1 hr)*. 87

4.22 Gold particle sizes after samples were exposed to 300°C for one hour, all synthesis parameters were held constant at (*pH 9, 1.0 M urea, 0.25 M NH_4OH, 300^{o}C, 1 hr*). The gold crystallite size changes with respect to the support and metal composition are shown. Au-Pt on zirconia was not investigated as the pH range used was not in zirconia's isoelectric range. 87

4.23 5% Au on silica (*pH 9, 1.0 M urea, 0.25 M NH_4OH, 400^{o}C, 1 hr*). 88

4.24 5% Au-1% Pt on silica (*pH 9, 1.0 M urea, 0.25M NH_4OH, 400^{o}C, 1 hr*). 89

4.25 Gold crystallite size Vs temperature showing the effect of the addition of 2% platinum compared to pure gold samples. Silica was used as the support with each set of samples exposed to 300°C and 400°C for 1 hour. 89

4.26 The combination of 9 (3 sets of 3 repeat samples) powder diffraction patterns illustrated the reproducibility of the results as well as the synthesis method. The most intense peaks in blue are a combination of three diffraction patterns from the samples that made up 5% Au. One step down towards the green region is the three samples of 5% Au-1% Pt. Finally, the least intense peaks are from the 5% Au-2% Pt samples. Each of the samples consistently fitted into their grouping as the diffraction patterns at each interval are uniform with no outlying patterns. Thus, the reproducibility of the synthesis method was reproducible within experimental error. 90

4.27 SEM image of 5% Au supported on silica. The resolution was not sufficient to see any gold particles on the surface. 91

4.28 SEM image collected in back scattered mode of 5% Au on silica. The small bright flashes showed gold nanoparticles on the surface. 92

4.29 TEM image of 5% Au-1% Pt nanoparticles supported on silica after heating to 200°C for 1 hour. The image reveals the amorphous nature of the support as no crystalline structure could be seen. The dark spots are gold-platinum nanoparticles on the surface of the amorphous silica. 93

4.30 Sintering effects noted in the TEM. 95

4.31 HR-TEM image of 5% Au on amorphous silica after heating to 200°C for 1 hour clearly showing the lattice planes of the gold nanoparticle. 96

4.32 HR-TEM of 5% Au on amorphous silica after heating to 300°C for 1 hour. 97

4.33 HR-TEM image of 5% Au on amorphous silica after heating to 300°C for 1 hour. Some nanoparticles were observed to be bound epitaxially to the surface that has been shown to be an important aspect in the oxidation of carbon monoxide when pertaining to gold based catalysts[41]. However, the bond formed between the nanoparticle and the support is not strong as many of the gold nanoparticles were not associated with the support after heating. 98

4.34 HR-TEM image of a gold nanoparticle prepared on amorphous silica after heating to 300°C for 1 hour. The image shows lattice fringes corresponding to (110) orientation twinning. This effect may be from the combination of a number of small gold crystallites sintering to form larger particles such as the one shown here. This Figure provided further evidence of the sintering process occurring when the samples are exposed to non-ambient temperatures with the ability of the gold nanoparticles to move over the surface to combine with other nanoparticles. 99

4.35 5% Au-1% Pt on amorphous silica after thermal treatment at 400°C for 1 hour. At 400°C the thermal energy imparted to the catalyst resulted in a large increase in particle size. Both silica and zirconia were found to be insufficient support materials. . . 100

5.1 Crystallographic representations of anatase on the left of the Figure (tetragonal, I41/*amds*) and rutile on the right (tetragonal, P42/*mnm*) generated using DIAMOND 3.2f [69]. Brookite is the third polymorph of titania which occurs at very high temperatures far in excess of temperatures that will be reached by catalysts in this thesis. Thus it is not discussed. 103

5.2 In-situ PXRD of commercial anatase (Sigma). A total of 52 diffraction patterns were collected over a temperature range of 30°C to 900°C. The data collection took a total of 36 hours to collect. 107

5.3 Rietveld refinements of commercial anatase at low to medium temperatures in the collection range were relatively straight forward as the only major phase present being anatase with only a very small amount of rutile. At low temperatures the rutile phase is almost indistinguishable from the background. Refinements on all the supports were necessary to monitor the support structure as temperature was increased to draw comparisons between unloaded and loaded supports. The grey difference line at the bottom of the image shows that the difference between the calculated and observed data is minimal as thus the refinement is good. 107

5.4 In-situ PXRD of commercial anatase (Sigma). 108

5.5 Rietveld refinement results of average crystallite size of the commercial anatase support. Large crystallite sizes resulted in lower a surface area, however the support stability at high temperature is good. 109

5.6 In-situ PXRD of 5% Pt supported on commercial anatase. In-situ diffraction studies showed that using the modified DP method it was possible to deposit platinum onto the anatase support as broad diffraction peaks corresponding to the Pt (111) reflection can be seen at high temperatures although the peak is very broad. 110

5.7 In-situ PXRD of 5% Pt supported on commercial anatase. . . . 110

5.8 In-situ PXRD of 5% Au on commercial anatase. 111

5.9 In-situ PXRD of 5% Au on commercial anatase. 111

5.10 Rietveld refinement of one of the 53 collected patterns from the in-situ PXRD data set of 5% Au on commercial anatase. The diffraction pattern shown was collected at high temperature over 800°C with an increase in the evolution of the rutile phase seen as the anatase begins to convert to rutile. The (110) rutile reflection is shown in the yellow box to indicate the phase. Again the difference pattern in grey shows the good fit of the calculated pattern. The evolution of the gold phase can also be seen and is discussed in Figure 5.11. Rietveld refinements were conducted on all the 52 collected diffraction patterns for quantitative analysis. 112

5.11 A zoomed image taken from TOPAS (34.5° - 47.5° 2θ) of the three phases under investigation after the 5% Au on commercial anatase catalyst was exposed to high temperature for a number of hours in the XRK chamber. The usefulness of the Rietveld method is demonstrated as even phases that were overlapping could be accurately resolved. Here, anatase, rutile and gold phases are all overlapping in the 37.5° - 39.0° 2θ range. The use of the Rietveld method allowed for the gold diffraction peaks to be accurately resolved and analyzed. This is shown in the green calculated diffraction peaks in the image. On completion of the refinement gold crystallite size could be accurately attained as well as quantitative phase information. An R_{DW} value of 1.86 confirmed the high quality data fit. 113

5.12 In-situ PXRD of 5% Au-2% Pt supported on commercial anatase.113

5.13 In-situ PXRD of 5% Au-2% Pt supported on commercial anatase.114

5.14 5% Au and 5% Au-2% Pt on commercial anatase showing particle sizes and support phase dependence on temperature. Refinements commenced at 200°C to ensure that reduction of the catalysts had taken place. The small increase in the crystallite sizes at 400°C-500°C is due to the metal particles rearranging themselves on the surface as seen in the TEM study in Section 5.5 The rearrangement results in more stable nanoparticles with slightly larger sizes. The rapid growth of the metal nanoparticles at 690°C is a result of the support undergoing a phase transition from anatase to rutile. 114

5.15 TEM image of gold nanoparticles supported on commercial anatase heated to 300°C for 2 hours. 117

5.16 High magnification image of gold on anatase heated to 300°C. . 118

5.17 HR-TEM image of gold on anatase heated to 400°C. Epitaxial contact between the gold nanoparticles and the support was noted.119

5.18 HR-TEM of 5% Au-1% Pt heated to 300°C for 2 hours on anatase.120

5.19 HR-TEM image taken at high magnification of 5% Au-1% Pt on anatase showed the interesting shapes of the nanoparticles after heating to 300°C. Many of the nanoparticles exhibited a hexagonal structure. The geometry of the nanoparticles is dependent on a number of factors. Rearrangements of the nanoparticles were seen to occur as temperature varied. These rearrangements of the nanoparticles structure can be either positive or detrimental depending on how the rearrangement takes place and what structure is taken. It was noted that in general the rearrangements that took place using the method described in this text resulted in epitaxially bound hemispherically shaped nanoparticles which are ideal for carbon monoxide oxidation reactions as shown in Figure 5.19-5.21. 121

5.20 5% Au-1% Pt on anatase heated to 400°C. With the use of HR-TEM particles of less than 1.5 nm can be seen. The massive size of the support material can also be seen from the image. . . 122

5.21 High magnification image of 5% Au- 1% Pt on anatase heated to 400°C. 123

5.22 5% Au-1% Pt on anatase after exposure to 400°C for 2 hours. The image showed that many of the particles had increased in size while some of the more isolated particles had remained small. This gave some information on the process of sintering as the process did not appear top be uniform when the change in size of the particles was considered. 124

5.23 Low magnification image of 5% Au-2% Pt nanoparticles supported on commercial anatase after exposure to 400°C for 2 hours showing homogeneous dispersion and smaller particle sizes compared to the 5% Au sample heated to the same temperature. The images showed a distribution of particle sizes with a number of particles smaller than 5 nm and some particles even smaller than 2 nm. The very small particles are only clearly visible at higher magnifications. These distributions are graphed in section 5.6.1. 126

5.24 High magnification HR-TEM of Au-Pt nanoparticles on the anatase-rutile phase boundary catalyzing the phase transformation from anatase to rutile after heating to 400°C. The reason for the later onset of the emergence of the rutile phase in the PXRD is due to the heating rates that were selected for the data collections. If the heating rate was slower and data collections took longer the rutile phase would emerge at lower temperatures. This was seen in the in-situ PXRD data collections on the Aurolite catalyst where data collections are significantly longer (Chapter 6). 127

5.25 HR-TEM image of 5% Au-2% Pt on anatase after heating to 400°C. 129

5.26 HR-TEM image of 5% Au-2% Pt on anatase after heating to 400°C. HR-TEM showed many of the smaller nanoparticles that were not visible at lower magnification. This image also shows the beautiful orientation and arrangement of the crystal planes that make up the commercial anatase support. 130

5.27 HR-TEM image of 5% Au-2% Pt heated to 300°C. 131

5.28 HR-TEM image of 5% Au-2% Pt heated to 300°C. 132

5.29 High magnification HR-TEM image of of 5% Au-2% Pt on anatase heated to 300°C 133

5.30 High magnification HR-TEM image of 5% Au-2% Pt on anatase heated to 400°C. The image demonstrated how the nanoparticles are epitaxially bound to the support. This type of bonding is crucial for an active catalyst as the manner in which the gold nanoparticles are bound to the surface plays an important role in CO oxidation [41]. 134

5.31 HR-TEM image of 5% Au-2% Pt on anatase heated to 400°C . . 135

5.32 EDS of the 5% Au-2% Pt on anatase. 136

5.33 5% Au-3% Pt on anatase after heating to 300°C. 137

5.34 High magnification HR-TEM image of 5% Au-3% Pt on anatase heated to 300°C showing a number of very large particles in and amongst a number of smaller particles. 138

5.35 5% Au-3% Pt heated to 400°C showing even larger particles after exposure to 400°C for 2 hours. After exposure to 400°C the separation between very large and small particles was even more apparent. This trend is continued throughout all the samples that were analyzed with this Au : Pt ratio. 139

5.36 5% Au-3% Pt on anatase heated to 400°C. 140

5.37 High magnification HR-TEM image of 5% Au-3% Pt on anatase heated to 400°C. 141

5.38 High magnification HR-TEM image of 5% Au-3% Pt on anatase heated to 400°C. 142

5.39 Particle size distribution of Au and Au-Pt nanoparticles determined from TEM images. Over 450 nanoparticles were analyzed for each distribution[86]. (D.H Barrett, P.J Franklyn and M.S Scurrell (2010). Variable Temperature Study of Au and Au-Pt Nanoparticles on Selected Oxide Supports. MRS Proceedings, 1279, 40) 143

6.1 In-situ PXRD of pure Degussa P25. The data collection was undertaken using 30°C intervals from 300°C to 900°C. Data collections were started at 300°C as no change in the P25 will occurred below these temperatures. 146

6.2 In-situ PXRD of P25. The higher temperature portion of the data collection is highlighted in the blue region of the diagram. This portion shows the rapid growth of the rutile phase while the demise of the anatase phase can also be noted as anatase was converted to rutile. Once the onset of the phase transition began it was only a few hours before the rate of conversion became exponential. At low to moderate temperatures <400°C the P25 was relatively stable. 147

6.3 Rietveld refinement results of the in-situ PXRD data collections of pure Degussa P25. 148

6.4 Temperature Vs data collection time for the Aurolite catalyst. From 350°C to 700°C, three one hour long scans were collected at each temperature. It was not deemed necessary to heat the catalyst to 900°C as was done in the pure P25 data collection as the phase transition would most certainly have occurred by this stage. 150

6.5 In-situ PXRD of the Mintek Aurolite catalyst. Other than the very small diffraction peaks associated with metallic gold at higher temperatures, the data collection resembled that of the P25 patterns as the same support material is used. However, quantitative Rietveld analysis revealed a number of differences. . 151

6.6 Rietveld refinement image taken from TOPAS refinement software. The observed diffraction pattern is shown in blue. Overlayed onto the observed pattern is the calculated pattern in red resulting from the Rietveld refinement. The almost perfect overlap of the observed and calculated patterns demonstrated a very successful refinement. Refinements were conducted on all collected diffraction patterns. 151

6.7 The anatase phase is highlighted in blue from the resulting calculated diffraction pattern. Once the refinement is completed it is possible to examine each phase independently. 152

6.8 Calculated rutile diffraction pattern shown in black. 152

6.9 Calculated gold pattern shown in green. The low gold loading of 1% as well as relatively small gold crystallite sizes result in low intensity diffraction peaks being produced by the gold. In the case of the Aurolite catalyst the low intensity gold peaks were more a factor of the low gold loading (1%) as opposed to small crystallite sizes. As will be shown in Figure 6.14 the gold crystallite sizes only remained small below 400°C before large increases were noted 153

6.10 Finally at high temperature all the anatase had completely converted to rutile with only rutile and gold phases are now present.153

6.11 Zoomed view of the refinement fit between 33° to 45.5° 2θ. As can be seen an exceptionally good fit is attained with an almost completely linear difference pattern. The small broad gold diffraction peak can also be clearly seen at 38.2° 2θ. 154

6.12 In-situ PXRD of the Mintek Aurolite catalyst. 154

6.13 Results of the Rietveld refinements from the in-situ data collection of the Aurolite catalyst. The graph displays the anatase and rutile phase transformations with respect to temperature. The final data collection occurs once the XRK chamber cools down to room temperature with a scan also being undertaken at 400°C as the chamber cools. Thus, the two data points at 400°C and 30°C are from the scans collected after the maximum temperature had been reached and a scan collected. Then as the chamber cools the final two scans at 400°C and 30°C were collected. Hence, the final data point corresponding to 100% rutile and 0% anatase was collected last at 30°C. The phase percentages showed that a complete transformation had already occurred. All Rietveld refinement data is graphed in this manner. 155

6.14 Rietveld refinement results of gold crystallite sizes vs temperature of the Aurolite catalyst. The maximum error for the refinements was 0.4 nm for gold crystallite sizes calculated using TOPAS. The two data points corresponding to crystallite sizes of approximately 18 nm were collected as the chamber cools down after reaching the maximum assigned temperature and are the final data collection points. This method of data collection and graphing is used throughout the text. 156

6.15 Rietveld refinement results of the in-situ PXRD data collection on the Aurolite catalyst. 158

6.16 Aurolite catalyst after heating to 500°C for 12 hours with the rutile phase highlighted in red and the gold phase in blue. . . . 159

6.17 Low magnification image of the fresh Aurolite catalyst. The P25 support material had a relatively small particle size around 25 nm which confirmed the Rietveld results. The small particle sizes of the gold nanoparticles also confirmed the in-situ PXRD results at 300°C. The image shows homogeneous dispersion of the gold nanoparticles over the surface of the support. 161

6.18 HR-TEM image of the Aurolite catalyst after heating to 300°C as is standard during the manufacturing process of the catalyst. 162

6.19 Aurolite catalyst after heating to 300°C taken at an intermediate magnification. Many smaller gold nanoparticles are only visible under higher magnification. 163

7.1 Number of papers published from 1998 to 2008 on titania nanostructures[123]. 167

7.2 Titanate nanofibres a (left) and b (right)[120, 123]. 168

8.1 In-situ PXRD of nano anatase support. Data collections were conducted from 15° to 120° 2θ with temperature ranges from 30°C to 720°C in 15°C increments. Temperatures higher than 720°C were not investigated for the pure support initially but were analyzed when Au and Au-Pt were deposited. 172

8.2 Temperature Vs time plot for data collections showing the catalysts being tested for almost 60 hours at temperatures from 30°C to 800°C. 173

8.3 Rietveld refinement of pure nano anatase support at low temperature taken from TOPAS. The difference pattern shows the quality of the fit for the pattern. The steep gradient of the pattern at low angles was due to air scattering of the beam. Further, the low intensity of the diffraction peaks was attributed to the nano support as the crystallite sizes of the support material were very small at less than 10 nm. This could also be seen from the broadness of the diffraction peaks. Phase purity of the product was also noted with 100% nano anatase produced. . . . 173

8.4 In-situ PXRD of pure nano anatase support. The increase in the intensity of the diffraction peaks at high temperatures showed the growth of the support material from low to high temperatures. 174

8.5 Rietveld refinement results from the in-situ PXRD data collections of the crystallite sizes of nano anatase. 175

8.6 In-situ PXRD of 5% Au on nano anatase. 175

8.7 Rietveld refinements showing the support crystallite size of 5% Au on nano anatase. The support showed good stability at low to medium temperatures with the ability to maintain a high surface area. However, at high temperatures the crystallite size increased quite dramatically. Initial conclusions were that the support may be very useful at low to medium temperatures as it had a very high surface area at these temperatures as well as being phase pure. For low temperature CO oxidation the nano anatase support was found to be superior to both commercial anatase and Degussa P25 due to its small crystallite sizes and high usable surface area. However, the thermodynamic phase transformation of anatase to rutile is unavoidable at higher temperatures. 176

8.8 Rietveld refinement results of the gold crystallite sizes from the data collection of the 5% Au on nano anatase. The gold crystallite sizes are indeed smaller when compared to the Aurolite catalyst at high temperatures. However, the gold crystallite sizes in this range are still too large to facilitate the oxidation of carbon monoxide at low temperatures once the catalyst had been exposed to high temperatures. The profile of the graphs shape is different when compared to gold supported on the commercial anatase as well as P25 where a dramatic exponential growth of the gold crystallites was observed. This was not observed because the catalyst did not undergo a phase transition. Thus the phase pure nano anatase managed to deter the onset of the anatase to rutile phase transition, the curve of the graph, or more simply put, the increase in the gold crystallite size is much flatter with a more gradual, gentler slope. This provided more evidence of the detrimental effect phase changes had on gold nanoparticle stability. It must also be noted that the data collections for nano anatase were almost three times as long when compared to the commercial anatase samples. This highlighted the nano anatase's superior thermal stability as well as the increased stability of the supported nanoparticles. 177

8.9 In-situ PXRD of 5% Au-5% Pt supported on nano anatase. Even after exposure to 810°C the nano anatase still remained phase pure with the onset of the conversion of anatase to rutile delayed. Small diffraction peaks can be noted for gold and platinum, however most of the peaks are lost in the very broad anatase peaks. At 810°C the nano anatase is still 100% phase pure even after the catalyst was exposed to high temperatures for 3 times longer than the commercial anatase based catalysts. Further, even higher metal loadings of platinum were used to try and overload the support and force the phase change to occur earlier than it may happen if less supported nanoparticles were present. Neither of these factors affected the catalyst thus the addition of gold and platinum nanoparticles as well as increased exposure to high temperatures did not result in a phase transformation of anatase to rutile. 178

8.10 In-situ PXRD of 5% Au-5% Pt supported on nano anatase. The aim was to determine if the addition of platinum or gold effects the phase transition from anatase to rutile as was the case when commercial anatase was used. The diffraction data revealed that no rutile is present even at high temperatures due to the phase purity of the synthesised product. 179

8.11 5% Au on nano anatase support after heating to 400°C for 2 hours. Small homogeneously dispersed nanoparticles were observed as well as small support sizes. 180

8.12 5% Au on nano anatase heated to 400°C for 2 hours. The image shows the gold nanoparticles were homogeneously dispersed over the surface. 181

8.13 5% Au on nano anatase heated to 400°C for 2 hours. The image showed how small the gold nanoparticles were, being far smaller than the scale bar of 5 nm. 182

8.14 5% Au on nano anatase heated to 400°C. 183

8.15 High magnifications image of 5% Au on nano anatase heated to 600°C for 2 hours. An increase in both the support and gold nanoparticle size was evident. However, the gold nanoparticle size is still small with most of the gold nanoparticles less than 5 nm in size. 184

8.16 5% Au on nano anatase heated to 600°C for 2 hours. The in-situ PXRD and TEM results concurred as both techniques showed an increase in the particle sizes of both the support and gold nanoparticles from 400°C to 600°C, albeit that the increase was not dramatic as the support still maintained its nano characteristics with large usable surface area. 185

8.17 Graph of CO conversion vs temperature. **Sample A** corresponded to the nano anatase support which was heated to 400°C for 1 hour prior to the addition of gold to remove the residual citric acid remaining from the synthesis of the support. The citric acid acted as a capping agent in the synthesis. **Sample B** is the unheated support and thus still contained citric acid on the surface of the catalyst. 186

9.1 Precious metal loadings of the Nanostellar NSgold^{TM} catalyst. As the graph demonstrates, the NSgold catalyst is not a true "gold" catalyst. (www.nanostellar.com) 191

9.2 Aurolite in-situ PXRD collection time vs NRS data collection times. 196

9.3 In-situ PXRD of the NRS. The diffraction patterns showed the support was phase pure as well as giving information on the morphology of the nanostructure. 197

9.4 In-situ PXRD of the NRS. 197

9.5 Rietveld refinement results of pure NRS crystallite sizes of the (011) and (110) orientation with respect to temperature. 198

9.6 In-situ PXRD of 5% Au on NRS. 199

9.7 In-situ PXRD of 5% Au on NRS. The intensity of the diffracted peaks at higher temperatures is lower as well as the peaks being broader when gold was added to the NRS compared to the pure NRS in-situ data collection shown in Figures 9.6 and 9.7. 200

9.8 Rietveld refinements of 5% Au on NRS. Results showed the crystallite sizes of both the (011) and (110) orientations were much smaller when small amounts of gold nanoparticles were added to the structure. After heating to over 800°C, the support was only approximately 30 and 40 nm respectively for the (110) and (011) orientations. Thus, after 200 hours at high temperature the support was still very stable with a high usable surface area, this was confirmed by BET studies where a surface area of $74.81 m^2/g$ was attained. The initial surface area of the NRS support was $97.28 m^2/g$ prior to the variable temperature data collection. The refinements gave a gold loading of 3.91% confirming that not all the gold was deposited during the modified DP method. The sample will still be referred to as 5% Au-NRS even though the true loading was 3.91% Au. 201

9.9 In-situ PXRD of 8% Au on NRS. The increased gold loading gave more intense gold diffraction peaks making it possible to study the change in the gold crystallite size as a function of temperature. 202

9.10 Rietveld refinement example of a diffraction pattern collected at 540°C taken from the in-situ data collection. The intensity can be seen to be quite low for both the support and the supported nanoparticles with a maximum count of only 1800. This was due to the nanostructure of the support with the size of the nanorods being well within the 'nanoscale' region at less than 15 nm as shown in Figure 9.9. The overlap of the gold and rutile peaks was clearly evident at 38.8° and 44.4° 2θ. The small black strikes under the difference pattern indicates the hkl reflections for gold in black and in blue for rutile. The difference pattern showed a good fit of the calculated pattern. Rietveld analysis gave an actual gold loading of 6.45% from the initial theoretical loading of 8%. The increase in the percentage loading of gold nanoparticles to the catalyst had the desired effect, as more gold nanoparticles present on the surface resulted in a greater number of diffraction centers. The increase in the number of diffraction centers in turn increased the intensity of the gold peaks while Rietveld refinement showed that the gold nanoparticles were still very small as well as stable throughout the temperature range as shown in Figure 9.14. 203

9.11 Rietveld refinement of the diffraction pattern collected at 810°C resulting from the in-situ data collection after exposure of the catalyst to temperatures exceeding 450°C for more than 200 hours. The higher gold loading used in this sample had the desired effect of increasing the intensity of the gold diffraction peaks when compared to the 5% loaded samples (actual loading of 3.91% Au). After being exposed to such high temperatures the intensity of the diffraction peaks increased over time. However, the increase was not dramatic. The gold diffraction intensity only increased by 150 counts when compared to samples at 500°C showing the stability of the catalyst. The broadness of the gold peaks also decreased slightly pointing toward a small growth in the crystallite size of the nanoparticles. These results were quantified using the Rietveld method and shown in Figure 9.17. 203

9.12 In-situ PXRD of 8% Au on NRS showing the increase in intensity of the gold diffraction peaks. 204

9.13 8% Au on NRS showing the crystallite sizes of the (110) and (011) directions. The addition of more gold to the surface (6.45% compared to 3.91%) resulted in a decrease in support size of both the (110) and (011) directions over the measured temperature range. 205

9.14 Comparison of the (011) direction of rutile nanorods for the pure NRS, 5% Au and 8% Au-NRS samples. 205

9.15 Zoomed view of the gold peaks at 38.2° and 44.4° 2θ for the 8% Au on NRS sample. 206

9.16 Rietveld refinement results of the gold-NRS catalyst particle sizes vs temperature. Even after exposure to temperatures over 450°C for nearly 200 hours and over 600°C for over 100 hours, the gold crystallite size remained small with only a gentle upward trend. 207

9.17 Rietveld refinements comparing the gold NRS catalyst with the Aurolite catalyst. Even at 8% Au loading the support was not adversely affected by overloading of supported nanoparticles. The high surface area of the catalyst resulted in enough usable surface area for the gold nanoparticles to remain homogeneously and sparsely positioned over the support. This feature was also observable using TEM and will be discussed further in the TEM section. 207

9.18 1% Au-NRS catalyst. This catalyst, along with all others produced using a certain batch of synthesised NRS proved to be inactive once they had been exposed to temperatures over 500°C for 12 hours. From in-situ diffraction studies the support appeared to be completely standard. 208

9.19 1% Au-NRS catalyst. The NRS had not completely converted to rutile during the synthesis resulting in a monolayer of anatase on the ends of the structure. The monolayer was so thin that the effect could only be seen using TEM. 209

9.20 TEM image of the NRS support after heating to 500°C for 12 hours. Closer inspection revealed anatase on the nanorods that, after heating, resulted in the formation of rutile that encapsulated the nanorods as well as the active gold nanoparticles. Further, the voids between the nanorod structures that allow the gas to easily flow though the catalyst were also blocked. 210

9.21 The highlighted section shows the ends of the rods covered by the unconverted anatase. As the structures were held at high temperatures the anatase converted to rutile further deactivating the catalyst. 211

9.22 Thin layers of anatase can be seen covering the nanorod structures. 212

9.23 Large amounts of anatase covering the nanorods. Even the pore structures between the nanorods were blocked. 213

9.24 Electron diffraction images showed anisotropic growth of the rutile nanorods. This was demonstrated by the bright spots on the diffraction rings. If there were no anisotropic growth the rings would be consistent circles of uniform intensity. The bright spots indicated diffraction is more prevalent in certain directions due to the morphology of the nanorod structures. This confirmed what was observed in the PXRD diffractograms with respect to anisotropic growth of the nanorods. 215

9.25 TEM image of the 5% Au-NRS catalyst. The images showed dandelion type structures with gold on the tips of the nanorods after heating to 550°C for 24 hours. 216

9.26 STEM image of the 5% Au-NRS catalyst after exposure to 550°C for 24 hours. 217

9.27 HR-TEM of gold nanoparticles on the catalyst after heating to 450°C for 24 hours. 218

9.28 HR-TEM of gold nanoparticle after heating the catalyst to 450°C for 24 hours 219

9.29 HR-TEM of gold nanoparticles the 5% Au-NRS catalyst. Many of the gold nanoparticles could be seen to be isolated on the tips of the nanorods after heating to 450°C for 24 hours. 220

9.30 8% Au-NRS catalyst heated to 810°C in the in-situ PXRD data collection. On completion of the in-situ PXRD data collection the sample was removed from the XRK chamber. It was almost assumed that the catalyst would not be active after exposure to such high temperatures for such a long duration (over 200 hours). However, when the catalyst was removed and examined, a deep purple/blue colour was noted. From almost hundreds of previously produced catalysts using some form titania as a support one becomes able to empirically correlate the colour of the catalyst to its potential ability to oxidize CO. There is a correlation between gold nanoparticle size and colour of the catalyst. Thus, by the law of trichotomy there is a correlation between the catalysts colour and the catalysts ability to oxidize CO. A deep purple/blue colour is usually indicative of a highly active reduced catalyst. This was difficult to believe after the catalyst had been exposed to such high temperatures for so long. The catalyst was almost immediately taken for both TEM and CO oxidation testing. The TEM results showed a catalyst that while having some large particles in the size range of 5 to 10 nm there were also many particles less than 5 nm in size. Rietveld refinements as well as CO oxidation tests confirmed this finding. This result placed the catalyst in the same operating temperature range as that of the Toyota catalyst with the Au-NRS catalyst being exposed to higher temperatures for a longer duration when compared to the Toyota catalyst. The image also showed how the nanorods had increased in size compared to the samples that have been exposed to 550°C. However, the increase was not dramatic resulting in a support that was still stable and a catalyst that although not as active as the fresh unheated sample, still had a large number of active gold nanoparticles on the surface to facilitate the CO oxidation reaction as shown in Figure 9.35. 222

9.31 EDS of 1% Au-0.2% Pt-NRS catalyst showing the presence of both gold and platinum nanoparticles. 223

9.32 HR-TEM image of gold on NRS. 224

9.33 Difference in contact surface area between a flat cubic type morphology, such as commercial anatase and Degussa P25, compared to that of a rod type structure in the case of the NRS. Higher contact surface area's of the NRS support further aided in nanoparticle stability. 224

9.34 HR-TEM image of the 5% Au-NRS catalyst showing only a few gold nanoparticles per rod after the catalyst was exposed to 550°C for 24 hours. 225

9.35 Images extracted from tomographic tilt series at regular intervals. The circled regions track groups of gold nanoparticles indicating the progression of the particles at the end of the rods. The tilt series confirms that the gold is located only at the tips of the rods and not inside the structure. Tracking of all gold particles in eTomo confirmed this observation. 227

9.36 CO oxidation testing of various catalysts. The catalysts tested were 1% Au-NRS as well as 1% Au-x% Pt-NRS catalysts, where x=0.1 or 1. The Aurolite catalyst was used as a benchmark with the 8% Au-NRS catalyst also tested after the in-situ PXRD data collection after exposure to 810°C. A number of the catalysts were heated to 550°C for 120 hours to test their CO oxidation ability after exposure to prolonged high temperatures. The Aurolite catalyst was tested fresh, as well as after exposure to 550°C for 12 hours. 228

12.1 7 times Formula 1 World champion Micheal Schumacher still drives for the Italian Kart manufacturer Tony Kart and helps with the development of new chassis and engines. His presence as well as other high profile drivers shows the massive interest and large amount of capital investment of teams and manufacturers in the sport. 244

12.2 Design of the current karting exhaust system (Bombardier). The silencer mat, identified by number 2 on the schematic, is made of the same material that is used in laboratories to support powder catalysts during testing. 245

12.3 Telemetry data from a test session. The ambient atmospheric temperature was 26°C with a track temperature of 37°C. The left hand column shows the data collection parameters. The bottom graphs are of each completed lap and finally the large central graph is of the two exhaust gas temperatures (EGT) labeled as EGT_under and EGT_over. One temperature is collected before the silencer (EGT_over) and one temperature after the silencer (EGT_under). All other parameters have been omitted for simplicity. 247

12.4 Exhaust temperatures of the fastest lap of the session. This corresponded to the highest temperatures attained by the exhaust gases showing the catalyst should be able to withstand the maximum exhaust temperatures according to the in-situ PXRD data. 248

12.5 Exhaust gas temperatures of the first lap showing how the exhaust gas temperatures rapidly increase from ambient up to over 600°C for the EGT_over. 249

12.6 Exhaust gas temperatures (EGT's) of the 7th and fastest lap. The bar graph shows the percentage time that the gases are within a given temperature range. For EGT_over (before silencer) the temperatures reach a maximum of 622°C while for EGT_under (after silencer) the gasses reach a maximum temperature of 559°C. Current gold based catalysts would not survive gas temperatures produced by the engines. However, the Au-NRS catalyst should be able to withstand this temperature range based on in-situ PXRD and CO oxidation tests. 250

12.7 5% Au, 0.1 M urea, pH 2.85 263

12.8 5% Au, 0.1 M urea, pH 2.85, 120°C, 1hr 263

12.9 5% Au, 0.1 M urea, pH 2.85, 300°C, 1hr 264

12.105% Au, 0.1 M urea, pH 2.85, 300°C, 1hr, repeat 264

12.115% Au, 0.1 M urea, pH 2.85, 300°C, 1hr, repeat 265

12.125% Au, 1.0 M urea, pH 2.85, 120°C, 1hr 265

12.135% Au, 1.0 M urea, pH 2.85, 120°C, 1hr 266

12.145% Au, 0.1 M urea, pH 2.85, 120°C, 1hr, repeat 266

12.155% Au, 0.1 M urea, pH 2.85 267

12.165% Au, 0.1 M urea, pH 2.85, 120°C, 1hr 267

12.175% Au, 0.1 M urea, pH 2.85, 120°C, 1hr, repeat 268

12.185% Au, 0.1 M urea, pH 2.85, 120°C, 1hr, repeat 268

12.195% Au, 1.0 M urea, pH 2.85, 300°C, 1hr 269

12.205% Au, 1.0 M urea, pH 2.85, 300°C, 1hr 269

12.215% Au, 1.0 M urea, 0.1 M NH_4OH, pH 9 start, pH 4 end 270

12.225% Au, 1.0 M Urea, 0.1 M NH_4OH, 120°C, 1hr 270

12.235% Au, 1.0 M Urea, 0.25 M NH_4OH, pH 9. then pH 4, 300°C, 1hr271

12.245% Au, 1.0 M Urea, 0.25 M NH_4OH, pH 9 271

12.265% Au, 1.0 M Urea, 0.25 M NH_4OH, pH 9, 300°C, 1hr 272

12.255% Au, 1.0 M Urea, 0.25 M NH_4OH, pH 9, 120°C, 1hr 272

12.275% Au, 1.0 M Urea, 0.25 M NH_4OH, pH 7 273

12.285% Au, 0.1 M Urea, 0.25 M NH_4OH, pH 7, 120°C, 1hr 273

12.295% Au, 1% Pt, 1.0 M Urea, 0.25 M NH_4OH, pH 7 274

12.305% Au, 1.0 M Urea, 0.25 M NH_4OH, pH 7, 200°C, 1hr 274

12.315% Au, 1% Pt, 1.0 M Urea, 0.25 M NH_4OH., pH 7, 200°C, 1hr . 275

12.325% Au, 1% Pt, 1.0 M Urea, 0.25 M NH_4OH, pH 7, 200°C, 1hr . 275

12.335% Au, 1% Pt, 1.0 M Urea, 0.1 M NH_4OH., ph 7, 300°C, 1hr . . 276

12.345% Au, 2% Pt, 1.0 M Urea, 0.25 M NH_4OH, pH 7, 200°C, 1hr . 276

12.355% Au, 2% Pt, 1.0 M Urea, 0.25 M NH_4OH, pH 7, 300°C, 1hr . 277

12.365% Au, 2% Pt, 1.0 M Urea, 0.25 M NH_4OH, pH 7, 200°C, 1hr . 277

12.375% Au, 2% Pt, 1.0 M Urea, 0.25 M NH_4OH, pH 7, 300°C, 1hr . 278

12.385% Au, 1.0 M Urea, 0.25 M NH_4OH, pH 7, 300°C, std NaCl . . 278

12.395% Au, 1% Pt, 1.0 M Urea, 0.25 M NH_4OH, pH 7, 300°C, 1hr, std 279

12.405% Au, 1% Pt, 1.0 M Urea, 0.25M NH_4OH, pH 7, 300°C, 1hr, std 279

12.415% Au, 2% Pt, 1.0 M Urea, 0.25 NH_4OH., pH 7, 300°C, 1hr, std 280

12.425% Au, 1% Pt, 0.25 M Urea, 0.1 M NH_4OH, pH 7, silica, 400°C, 1hr 280

12.435% Au, 1% Pt, 0.25 M Urea, 0.1 M NH_4OH, pH 7, silica, 400°C, 1hr 281

List of Tables

2.1 Instrument details of the Bruker D8 Advance. 34

2.2 Bruker D2 phaser instrumental parameters. 35

4.1 Reaction conditions for the preparation of samples. An important parameter is the final pH of the solution after completion of the DP synthesis as this effected gold loadings as well as particle size of the supported metal. 73

4.2 Synthesis parameters of samples prepared for Figure 4.14. 81

List of abbreviations

PGM's –Platinum group metals

EFT –Electronically traded fund

FCC –Face centered cubic

AEM - Analytical electron microscopy

HR-TEM – High resolution transmission electron microscopy

Au-NP's – Gold nanoparticles

XRD –X-ray diffraction

EELS- Electron energy loss spectroscopy

PXRD – Powder X-ray diffraction

VT-PXRD – Variable temperature powder X-ray diffraction

HOMO – Highest occupied molecular orbital

DFT – Density functional theory

FT-IR - Fourier transform Infrared spectroscopy

IMP – Impregnation technique

DP – Deposition precipitation

TOF – Turn over frequencies

BET - Brunauer, Emmett and Teller

ASTM - The American Society for Testing and Materials

NIST - National Institute for Standards and Technology

FWHM – Full width at half maximum

SH –Spherical harmonics

FEG – Field emission gun

AEM – Analytical electron microscopy

EDS – Energy dispersive spectroscopy

EELS - Electron energy loss spectroscopy

HAADF - High angle annular dark field

STEM -Scanning transmission electron microscopy

ED – Electron diffraction

XAS – X-ray adsorption spectroscopy

CCD – Charged coupled device

SAD – Selected area diffraction

SEM – Scanning electron microscopy

TCD – Thermal conductivity detector

GC – Gas chromatography

GOF - Goodness of fit

NRS – Nano rutile support

ICSD - Inorganic crystal structure database

CIF - Crystallographic information file

TOPAS - total pattern analysis software

PJF-XRD - Paul John Franklyn X-ray diffraction analyzer

EVA - Evaluation software

Patents, publications and presentations

- Patent (SA Provisional Patent Application 2011/06802) The patent includes the nanostructured support material for gold and all platinum group metals placed onto the novel support. The patent resulted in no publications from the work due to IP constraints.
- D.H Barrett, P.J Franklyn and M.S Scurrell (2010). Variable Temperature Study of Au and Au-Pt Nanoparticles on Selected Oxide Supports. MRS Proceedings, 1279, 40.
- Materials Research Society (MRS) . "High temperature resistant Au catalysts supported on radially aligned rutile nanorods". November 2011, Boston Massachusetts, USA.
- International Materials Research Congress (IMRC) "Stabilisation of Au nanoparticles using Platinum group metals on silica and titania". November 2010, Cancun, Mexico.
- ESPCA Advanced school "New developments in the field of synchrotron radiation". January 2011, LNLS, Campinas, Sao Paulo, Brazil.
- Bruker Topas Rietveld refinement users meeting. Indaba hotel Johannesburg ,Gauteng, June 2009.
- Science at Synchrotrons – February 2008, DST Pretoria.
- CATSA (Catalysis society of South Africa) – October 2008, Rawsonville, Western Cape. Oral presentation "The use of Pt for the stabilisation of supported Au nanoparticles".
- SANI (South African Nano Initiative), March 2009, CSIR Pretoria, oral presentation "Quantitative Rietveld refinement of Au and Pt nanoparticles supported on titania" –Winner of best presentation.
- SANI (South African Nano Initiative), March 2010, University of Johannesburg. Oral presentation "Titania nanostructures as supports for Au and PGM's".

Chapter 1

Introduction

1.1 Supply and demand of gold

Gold is a unique metal, as well as being one of the most interesting elements that appears on the periodic table. This is demonstrated by the fact that it is one of only two metals that is coloured as well as being the most malleable of all metals. It is properties such as these that have given gold significant value over and above many other metals from as far back as ancient Egypt thousand of years ago. Only recently have some other platinum group metals (PGM's) been able to catch up to gold in value per ounce. This is primarily due to the relatively new discoveries of scientifically valuable properties of the platinum group metals (PGM's) as well as for economic investment due to their remarkable stability in the bulk.

The scientific value of gold has almost been entirely overlooked for a long period of time as focus was placed on the metal for purposes such as jewelry, a monetary asset held by central banks and for use in the electronics industry. As will be discussed later, the discovery of golds remarkable catalytic activity, starting with the oxidation of carbon dioxide, has opened up an entirely new and ever expanding field of scientific research into gold. However, long before Haruta discovered gold's ability to catalyze the CO oxidation reaction, Micheal Faraday noted the incredible colours that different sized gold colloids produced. These colloids are still in existence and are stored in the Royal Institution of Great Britain in London.



Figure 1.1: 1 kilogram gold bars in the vault at vendor Proaurum in Germany.

Hundreds of years since Faraday's observation to present day more than $13 billion worth of gold has been used in various industrial and medical applications alone[1]. Further, when compared to the platinum group metals, there is more gold reserves in the world than all the other PGM's combined. The total amount of gold is estimated at 170 000 metric tonnes that would correspond to a cube of 20.72 meters per side[1]. Current prices result in the production of gold being a $160 billion per annum industry[1].

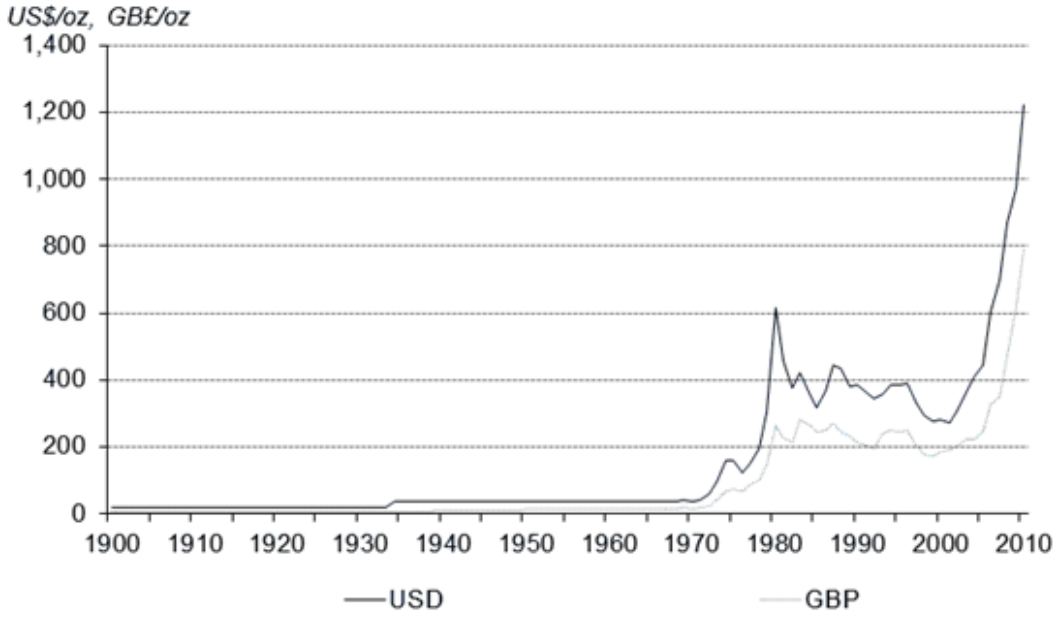
There are currently a number of uses for gold that carry much of the current demand for gold around the world. The sources that provide supply to these multi-billion dollar industries are important to consider if a new gold catalyst was discovered that, for instance, could be used in the motor industry as demand would be raised, resulting in an increase in the gold price due to high demand. There are two major sources of gold: firstly gold that is mined each year and secondly gold that is presently in circulation above ground. Examples of above ground gold consist of gold that has been recycled from industry and the jewelry industries as well as central banks and private holdings as in Figure 1.1. A very significant contribution to the gold supply each year is made by central banks[2]. They provide over 500 tonnes of gold to the supply stream. This supply is crucial to the world circulation and also has an effect on the gold price as demand can be met with the additional supply from the central banks.

Mining still contributes the major component of supply with a peak of 2650 tonnes in 2001[3]. The process whereby gold is attained by central banks is an interesting one. Gold is not directly purchased by the central banks and investment companies, what is done is known as hedging. Hedging entails a process whereby the gold producers sell their future mined gold at today's current prices. Thus, what occurs is that investment companies will own the

gold that has not yet been mined. In return the mining companies can rely on steady cash flows in the future as the gold is bought before it is even removed from the ground. Thus, gold is borrowed and sold in today's markets with the producers then delivering the gold at a later date to the central banks. Variations in the market may cause gold prices to change drastically over short periods of time as shown in Figure 1.2. This effect has led gold producers to hedge their transactions in favour of company stability in a move to manage the risk of adverse price movements in the gold price. There may be a number of reasons that producers may want to consider the use of hedging contracts with investment companies or central banks. The three main reasons are that the producers may want to protect their income against falling gold prices. Secondly is to secure a future premium price with the last reason being a financing package for the producer. Hedging of gold gives producers the advantage of being able to forecast revenues and ensure future returns even if the gold price drops from when the contract is signed. However, the drawback is if the gold price rises sharply for any reason after the contract is signed the producers cannot to share in the profits that result from the higher prices as shown in Figure 1.3.

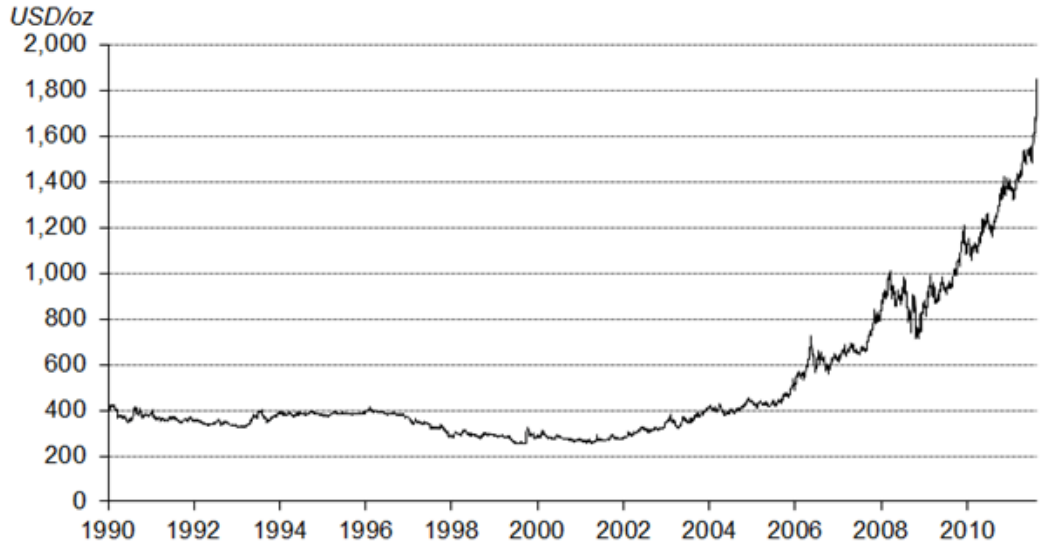
The investment into gold can be split into two main divisions. One is made up of people purchasing bars and coins, these are so called physical products. The second is people buying futures, options, and electronically traded funds known as ETF's, referred to as paper products. Mining is the largest supplier of gold and is a one of the most important industrial sectors in the South African economy. South Africa is one of the largest producers of gold in the world, but before new mines can be established they have to face tough scrutiny to ensure that it is indeed economically viable to mine the gold. Once this has been established the gold is removed from the ore by a process called heap leaching. Heap leaching uses sodium cyanide to extract the gold from lower grade ore, it is far more cost effective than using traditional methods such as milling the ore.

Traditionally the "big four" countries that mined gold were South Africa, America, Canada and Australia. South Africa produced the most gold for over a century with the height of production reaching over 1000 tonnes in 1970. By



Source: Reuters Datastream, World Gold Council

Figure 1.2: Averaged annual gold price in USD and GBP since 1900. With the steadily increasing demand and price of gold over the last few years dehedging on a net basis has been occurring. The dehedging is caused by an almost constant averaged increase in the gold price. When this occurs it is in the producers interest to hold onto the gold for as long as possible and not to sell the gold prior to it being mined.



Source: Reuters Datastream, LBMA, World Gold Council

Figure 1.3: Price per ounce of gold from 1900. A constant averaged increase in the gold price has resulted in dehedging by gold producers.

2007 this Figure had dropped to 270 tonnes[4]. This is due to much of the surface gold having been extracted over the last 100 years and now mining companies are finding it necessary to go to much deeper levels in order to find gold deposits as this is far more labour and energy intensive. This is the general trend with all the countries that make up the "big four"[3].

There is a substantial amount of gold that is above ground. Estimates put this above ground amount at over 170 000 tonnes and is the combination of over 60 years of mine production[1]. This large amount of gold separates it from other precious metals such as the PGM's. A reason for this is that almost all gold that has ever been mined is still in circulation in some form or another as it is impervious to corrosion. Ironically its indestructible nature also implies that it is chemically inert in the bulk. Nearly 58000 tonnes of gold in the world are held by central banks as bullion, which is usually in bar form, as well as being held by private investors and institutions. Half of this total is made up of jewelry items. Another 19000 tonnes of the world's gold is in the form of electronics and 4000 tonnes is thought to be in unaccounted forms such as trading ships that were lost at sea over the past centuries carrying large payloads of gold.

Gold was once the most valuable asset in central banks and it was against gold that all paper currencies were backed. In 1932 the gold standard was disbanded and this was later followed in the early 1970's by the removal of the Bretten Woods system. The new system allowed the price of gold to be market determined and thus more easily traded. However that is not to imply that gold is any less important now than it was 100 years ago. In fact as can be seen in the period of August 2011, during the United State's debt ceiling and euro zone crisis, gold prices rocketed as investors and central bank scrambled to attain gold for security amidst turbulent markets[3-5].

In times similar to those highlighted above when the price of gold increases dramatically it becomes far more profitable for recycling of gold to occur. In 1998, 1100 tonnes of gold was recovered from scrap following the east Asian economic crisis. Interestingly the next year, following a decrease in the gold price, the retrieval of gold from recycling slumped to 600 tonnes. Recycled of gold originates from the electronics and jewelry industry. India consumes on average 500-600 tonnes of gold per year as jewelry depending on price in that year. General consensus is that Indian's hold around 15000 tonnes of the world supply of gold. The manufacturing, industrial and scientific (including

medical) sectors use 15% of the supply of gold.

There is far more gold available for use in the world compared to all platinum group metals combined, making gold a viable choice for scientific applications even if gold remains one of the most expensive metals on the periodic table[3].

1.2 Chemical and physical properties of gold

Gold is the 79th element on the periodic table and was first discovered and used by humans as a pure metal, before other metals thousands of years ago. A number of wars have been waged over the last millenia to attain it. There is no doubt that the reasons for this were gold's beautiful colour, malleability, high density along with its complete aversion to corrosion which made it incredibly sought after. Another very important reason was that it was found as a pure metal and as alluvial deposits.

When one asks a chemist what is it that chemists do the response may entail an answer involving moving electrons, or perhaps the answer will be something along the lines of "we study the movement and change in electrons and electronic states". When the electronic configuration of gold is studied, it revealed some very interesting facts that in turn start to reveal some of the many interesting properties of gold. It is the electronic configuration that controls many of the scientifically relevant parameters such as chemical reactivity, optical properties, and the crystal structure of the element. The beautiful colours produced by gold nanoparticles, first noted by Faraday, are caused by localized surface plasmon resonance[6].

Gold's electronic structure is [Xe] $4f^{14}5d^{10}6s^{1}$. This configuration ensures that the 4f electrons under screen the 5d, 6s and p electrons from the nuclear charge results in a lanthanide contraction[6]. The contraction in turn results in the 5d metal series having similar lattice constants to that of the 4d metals. In heavier elements such as gold, there is also a relativistic factor that must be taken into account as the velocity of the 1s electrons begin to approach the speed of light. The mass of the electrons therefore increases relativistically resulting in a contraction of their orbitals around the nucleus. Due to this the higher s and p orbitals also contract, including the higher 6s and 6p orbitals that results in these orbitals being smaller than they usually would have been[6]. The final

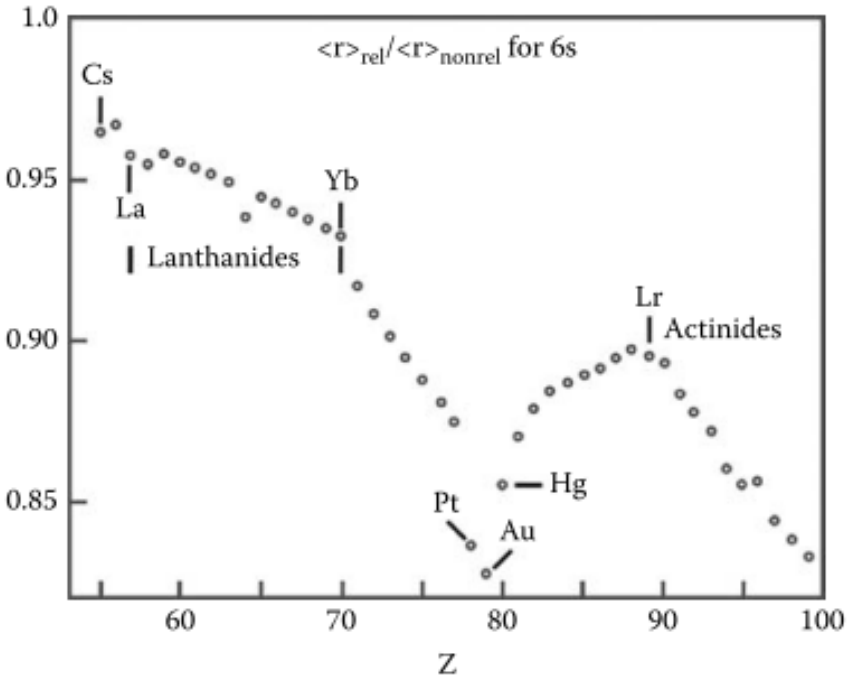


Figure 1.4: Fractional contraction of the 6s orbitals due to relativistic effects[8].

result of all these effects are that the 5d and 5f orbitals expand outwards and are thus destabilised, which in turn, has an associated increase in energy[7,8]. This effect is demonstrated in Figure 1.4.

The average radial velocity of the 1s electron has been estimated by Pyykkö and Desclaux[8]. The speed of light in atomic units is 137.036. This implies that for gold $v_r = 79$au, $v_r = Z$, where Z is the atomic number, which is 58% of the speed of light. We can approximate the actual electron mass of a 1s electron as :

$$M*_e = M_e\sqrt{1-(v/c)^2}$$

where v and c are the speeds of the electron and light respectively. Here v_r =79au, which is approximately 58% of the speed of light. Finally $M_e$is the rest mass of the electron. Thus the mass of the electron becomes $1.224M_e$ from which the Bohr radius can be calculated using

$$a_0 = \frac{4\Pi\epsilon\hbar^2}{m_e^2}$$

where e is the electron charge, ϵ is the absolute permittivity and $\hbar$ is Planck's constant. The result shows that the radius is approximately 20% smaller than

would have been the case if relativistic effects were not at play.

The excellent resistance of gold to corrosion can be attributed to the stabilisation of the 6s orbital, as gold has a high first ionization potential. However gold has oxidation states available to it that are not accessible to either copper or silver, with the +I and +II and +III states being readily accessible and even the +V state in fluoride compounds[9, 10].

Another useful attribute is gold's "aurophillicity" that describes gold's electron-electron interaction between non-valence orbitals. This effect can be seen in the manner in which gold atoms arrange themselves[11]. This effect is even demonstrated in this work where with the use of HR-TEM different arrangements of gold atoms forming various shapes depending on how many atoms form the metal cluster can be observed. The effect results in the gold atoms being packed closer, due to the proximity of the energy of the 5d electrons to the 6s electrons and thus the s-d orbital hybridization is easier. This results in the breaking of the usual $5d^{10}$configuration and allows for unusual bonding to occur[11].

Relativistic effects play an important role on the crystal structure of gold. Gold crystallizes in a face-centered cubic structure (FCC). In most metals that are similar to gold, the two high symmetry phases, namely the (110) and the (100) surfaces reconstruct, while the (111) surface does not undergo reconstruction. However in gold this is not the case, all three of the high symmetry phases reconstruct[12]. This can once again be attributed to relativistic effects. When gold nanoparticles are considered, surface tension is an important parameter to consider as liquid gold has a high surface tension between 1.1 and 1.2 J/m^2[13]. This value is increased to 1.3 to $1.5 J/m^2$in the solid state. When the nano state is considered and the gold nanoparticles are less than 10 nm, the FCC structure is no longer the most stable configuration. The system prefers icosahedral, decahedral and defective FCC structures[14].

Melting points are a very important factor to consider when working with nanoparticles and is even more important when gold is considered due to the fact that the catalytic activity is directly related to gold nanoparticle size[41]. As the size of gold decreases from bulk down into the nano scale of less than 100 nm the melting point decreases due to an increase in the surface to volume ratio. The effect can be mathematically determined by

$$\frac{T_m}{T_r} = 1 - \frac{4}{\rho_{sl}} \left\{ \gamma_s - \gamma_l \left(\frac{\rho_s}{\rho_l} \right) \right\} \frac{1}{d}$$

where $T_m(r)$ and $T_{(m)}(\infty)$ are the melting points of the particles of radius r and the bulk material respectively, $\rho_s$and ρ_l are the density of the solid and the liquid respectively and finally γ_s and γ_l are the free energy of the solid and the liquid respectively[15].

There are various reports of melting points for different size gold nanoparticles. These range from 430°C for nanoparticles in the naked form and even down to 380°C for particles coated in a silica casing[15,16]. When the gold nanoparticles are placed onto a substrate this temperature has been seen to be lowered even further down to 104°C[17]. This is an extremely important factor when considering catalysts based on gold nanoparticles that are to be used at elevated temperatures, especially over 400°C where many CO oxidation catalysts operate. It may prove difficult to try and catalyze reactions at elevated temperatures when the nanoparticles are turning into a liquid phase. However, there is now evidence showing that when gold nanoparticles are extremely small, particles consisting of only tens of atoms, that the melting points can increase as the thermodynamic model being used above breaks down at these very small size ranges[18,19]. This result bodes well for the type of high temperature applications that the catalysts in this text are designed for.

1.3 Gold and the CO oxidation reaction

Of the entire periodic table only twelve of the metallic elements show usable catalytic activity[20]. Further some metals such as osmium cannot be used as a catalyst as it forms dangerous tetroxides under certain conditions. The excellent catalytic properties of the group VIII elements can be attributed to their optimum degree of d-band valency[21]. Gold has fully occupied d-bands combined with a relatively high ionization potential when compared to similar metals such as copper and silver that readily lose electrons out of the d-band and give them their catalytic activity.

Studies into the adsorption of H_2 and O_2 onto smooth gold surfaces have shown that no adsorption occurs at temperatures below 200°C[22]. Gold also possesses

a lower melting point than both palladium and platinum. When the particle size of the gold is decreased to less than 2 nm, quantum-size effects further lower the melting point down to 300°C[23].

However, there is still dispute as to the effects of particle size on the melting point of gold nanoparticles. The result of this lowered melting point is that the gold nanoparticles (Au-NP's) coagulate far more readily when compared to platinum and palladium when calcined at temperatures above 300°C. However when gold nanoparticles were prepared and placed onto a TiO_2 support in the early 1980's by Bond and Sermon and calcined at 110-278°C it was found that it possible to develop a relatively active catalyst. Although these catalysts were active it is likely that the catalysts were poisoned by chlorine and sodium ions present due to the synthesis methods used.

A later discovery made in 1983 by Haruta et al.. proposed that if gold was deposited as hemispherical nanoparticles its activity is greatly increased[24]. It was this finding by Haruta et al.. that began the rebirth into gold catalysis research. The importance of this discovery is that unlike other metals, nanogold has the ability to catalyze the CO oxidation reaction from very low temperatures. Thus, in auto-catalysts where it takes time for the exhaust gasses to be converted due to cold engine temperatures, nanogold catalysts are able to convert the gasses as soon as the engine is started.

Bulk gold is chemically inert and does not posses any significant catalytic properties. However when gold particles are small enough, usually 10 nm or smaller depending on the reaction to be catalyzed, the catalytic properties of gold change to produce a material able to catalyze many important reactions such as CO oxidation and propylene oxidation[20]. For many years research into the catalytic properties of gold dwindled until recently when gold nanoparticles showed very good stability and high catalytic activity at ambient temperatures[21]. The paper by Haruta et al.. in 1989 showed that Au-NP's supported on Co_3O_4, Fe_2O_3 and TiO_2 were highly active catalysts for both CO oxidation and H_2 oxidation, NO reduction, water-gas shift reaction, CO_2 hydrogenation and the catalytic combustion of methanol[21].

Gold catalysts have three characteristic properties: they are active at low temperatures, activated by moisture and are very selective. For an expensive metal of such value, beauty and nobility gold had quite a humble beginning in the catalysis field when it was mixed with iron oxide in order to remove

odours in toilets. Since the initial use in toilets it has taken on more elegant roles such as, but certainly not limited to :

- decomposing dioxin at low temperatures when deposited on Fe_2O_3 or La_2O_3
- use in CO_2 lasers[34]
- high selectivity in hydrogenation reactions and partial oxidation
- Contributed to green chemical processes
- Methanol synthesis

Most of the recent research into catalysis using Au-NP's has focused on CO oxidation reactions[20]. Research has been conducted in order to determine the mechanism of the catalytic process along with particle size, metal support interactions and their effect on the activity of the catalyst. For the study of high temperature gold catalysts, the CO oxidation reaction is ideal because of all the reactions that gold catalyses the CO oxidation reaction is very susceptible to changes in the gold nanoparticle size. Thus small increases in the size of the gold nanoparticles on the surface of the catalyst results in a direct decrease in the conversion of CO to CO_2 [20].

Even though there is currently much research into nanogold catalysts, research into Au-based bimetallic catalysts remains elusive. Synergism in bimetallic Au-Pd catalysts were reported in hydrogenation reactions and hydrocarbon reactions[36,37]. In hydrodechlorination reactions, improved activity and selectivity could be reached by alloyed or core/shell type Au-Pd bimetallic nanoparticles in supported form or as a colloid in liquid phase reactions when compared to the mono-metallic palladium analogues[23]. Synergistic cooperation of gold and palladium was shown also in oxidation reactions, such as H_2O_2 formation from H_2 and O_2 and selective alcohol oxidation[39].

Since Langmuir presented a theory describing the oxidation of CO it has been one of the most studied catalytic reactions[25]. This 'simple' reaction is involved in many important industrial and environmental applications such as cleaning exhaust emissions, production of hydrogen by steam, reforming of methanol and also has applications in fuel-cells.

"The promotional effect of Au on Pd in bimetallic systems were assigned in some cases to electronic (or ligand) effect lowering somewhat the electron density on Pd and/or to geometric (ensemble) effect. In CO oxidation a combination of gold and palladium seemed to be an interesting possibility to achieve a catalyst with higher activity and to better understand the nature of the outstanding activity of gold containing catalysts"[40].

Au-NP's have been shown to exhibit single phase alloy characteristics in the nano-crystal and also bimetallic alloy properties on the surface. The nano-crystal and surface alloy properties can be directly correlated with the bimetallic composition[37]. Further, binding sites have been shown to be dependent on the bimetallic composition of the alloy. The inclusion of Pt with Au in a nanoparticle results in a d-band shift of Pt in the nano-crystals[37]. With the use of PXRD, the presence of unique alloy properties has been revealed for the nano-crystal core that are in sharp contrast to the miscibility gap known for the bulk alloy counterpart[37]. There are a number of important parameters that need to be considered during the reduction of the gold nanoparticles as this is an important step in producing active catalysts. These include, the reducing ability of the metal components, the reducing agent, rate of reduction, the quality of precursors, temperature and the atmosphere of the treatments[40].

1.3.1 Interaction of oxygen with gold nanoparticles

Even though it is quite remarkable how fast the catalytic process occurs, what is even more remarkable is that it does not simply involve a single step but is a combination of multiple complex steps that make up a full catalytic cycle. The initial step in the process is chemisorption of the reactant molecules. In this step the molecules have their first interaction with the surface of the catalyst. In the second step the molecules are bound to the surface of the catalyst in such a manner as to not be bound too strongly to the surface as that would result in poisoning of the catalyst, but at the same time the bond has to be strong enough to facilitate the reaction and interaction of the catalyst and the molecules that are significant in the reaction.

The first question that must be addressed is the ability of gold to chemisorb oxygen. At first glance this would seem impossible due to gold not being corroded in nature as well as being known as one of the most noble of all metals. The chemisorption of oxygen is possible under certain conditions.

It is best to start this discussion by looking at simple gold clusters and the interaction of oxygen. The term cluster is generally applied to small assemblies of atoms that are formed in the vapour phase or in matrix isolation. This distinguishes them from particles, which are formed by chemical or physical means. Particles are often formed in conjunction with a support.

There are a large number of papers published on the subject of the interaction and the complexes formed between gold clusters and molecular oxygen[20-24]. The research agrees that complex formation requires the cluster to have an odd number of electrons, and that the one having the highest energy, in the HOMO, is passed to the oxygen molecule thereby acquires a negative charge as O_2^{2-}. It is not certain if the oxygen molecule is dissociated or not. If however, the oxygen however does dissociate then this must imply that there is a charge transfer from the cluster to the oxygen molecule. The molecule is made weaker by the electron transfer and the valence band structure is also completely changed by the addition of the oxygen molecule to the gold surface. This type of reaction has been viewed as a radical-radical type as the anionic cluster interacts with the oxygen. This ties in nicely with the findings that neutral, cationic clusters and anionic clusters having an odd number of atoms, are all either unreactive or of low reactivity since all of them have even electron counts[20-24].

As cluster size grows, the electron in the gold cluster become increasingly delocalised, and efficient radical-radical reaction requires a high charge concentration. There is evidence for the disappearance of band structure in small gold particles and this effect also applies to clusters, those with $n < 20$, where n is the number of gold atoms, having no d-band. When n exceeds 70, the valence band region is almost the same as that of bulk metal. The typical lack of reactivity towards oxygen therefore also correlates with the appearance of overlapping electron energy levels and metallic character. The trend is also shown by the gradual increase in the gap between the top of the valence band and the Fermi level E_p[25]. This conclusion implies that the need for small gold nanoparticles is absolutely critical for a reaction such as the CO oxidation reaction that is investigated in this thesis. It also explains why the CO oxidation reaction is known to be one of the most sensitive reactions to gold particle size when compared to many other reactions involving nanogold in which the ability of the catalyst to maintain high conversion and activity is not as dependent on the size of the gold.

The coordination number of the atom at the reaction site also plays an important role in the adsorption of oxygen[26,27]. This is due to the fact that the charge concentrates on the atom of lower coordination number on the gold clusters. This effect can be linked to the energy gap between the E_f and E_p the decrease in the top of the valence band as the coordination number decreases[28,29]. Local density of states calculations predict the way that electrons may be found at a point. These as well as DFT calculations are in agreement that, as particle size decreases, so does the coordination number. Thus the picture that emerges is that even more important than quantum effects, catalytic oxidations are primarily governed by chemisorption of oxygen as $O^{2-}$and that this is the key species in the reaction. For this to take place however, the gold needs to be sufficiently small with sizes less than 5 nm being optimal.

1.3.2 Chemisorption of oxygen on gold surfaces

It has been found that under ambient temperatures and pressures the adsorption of oxygen onto bulk gold surfaces does not take place[30]. The only time that adsorption was noted was when impurities such as silicon, sulfur and calcium were present[29-31].

Section A of the curve shown in Figure 1.5 represents the approach of an oxygen molecule towards the surface of the catalyst. The approaching molecule initially experiences a weak attraction caused from physical adsorption. At this point, unless there are orbitals emerging from the gold surface with which the approaching molecule can interact, with the resulting force is repulsion and no further interaction occurs. At low temperatures this is generally the case. At higher temperatures the incoming molecule experiences a very large potential energy barrier before it can meet with section B of the curve. Section B of the curve shows the energy barrier of the dissociated molecule. This is normally an activation energy E_{ads} that is usually too high for the molecule to overcome. However, if electron transfer to the molecule is carried out this process becomes possible. Section C of the curve is then also accessible and the adsorbed molecule can change into a $O_2^-$with a very small activation energy. The position of section C is dependent on the availability of electrons at the time of the meeting of the molecule and the surface.

The activation energy that needs to be overcome in passing from A to C will increase with cluster size due to the increase in (E_d-E_p), where E_d is the

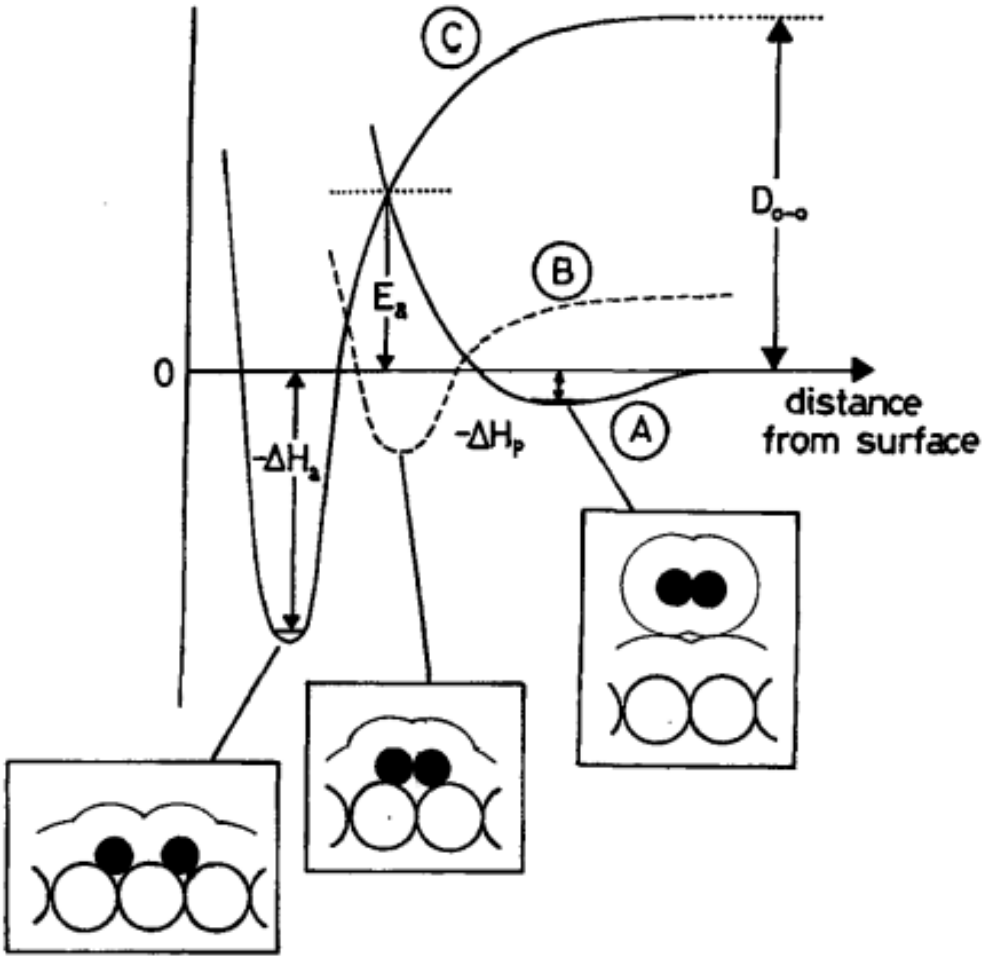


Figure 1.5: Potential energy curves representing the interaction of molecular oxygen with a gold cluster or a gold surface[25].

energy of the top of the valence band. For the same reason, with particles and extended surfaces, it will rise as the coordination number of the gold atom increases. In summary molecular oxygen may interact in four ways[25].

1. Oxygen may become adsorbed onto the support in an activated form that is adjacent to the gold particle to which the other reactant molecule is also attached.

2. Oxygen may react through a type of Rideal-Eley mechanism. This type of mechanism proposes that only one of the molecules adsorbs while the other molecule reacts with it directly from the gas phase, without adsorbing first.

3. The incoming oxygen molecule may extract charge from the gold atoms that have a high number of low coordination number surface sites.

4. Dissociative chemisorption of the oxygen into atoms on the same type of surface sites may occur.

1.3.3 Interaction of CO with gold clusters

When mixtures of CO and O_2 were passed over a gold surface it was found that the CO absorbed 10 times faster than the oxygen[20,32]. It was revealed that one possible mechanism is through the adsorption of the two molecules in a synergic process with electron density being donated from the CO to the O_2. This allows for oxygen chemisorption as O_2^{2-} at a neighboring site. Much like the chemisorption of oxygen on gold surfaces CO prefers to adsorb at site defects at which atoms are found in a low coordination number, as was shown previously. A review of the literature shows that CO does indeed absorb onto gold surfaces, however the adsorption is quite weak. CO prefers atoms of low coordination number and the desorption process can occur at even below 25°C. This is shown in Figure 1.6.

1.3.4 CO oxidation using gold nanoparticles

The metals of groups 8 to 10 bind CO very strongly leading to low catalytic activity especially at lower temperatures (<250°C) where gold continues to

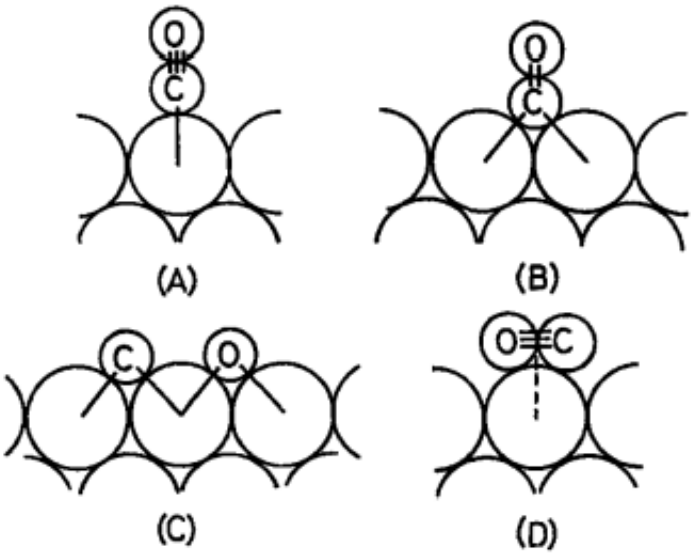


Figure 1.6: There are multiple ways that CO can chemisorb onto a gold surface: (A) linear, (B) bridged (C) dissociated and (D) sideways on[25].

catalyze the CO oxidation reaction readily. As this thesis involves the use of a support, focus will be placed on the CO oxidation reaction when gold nanoparticles are bound to a substrate.

The use of the substrate provides sites for oxygen chemisorption as the support provides a mechanism for the activation of the oxygen. Meanwhile the CO is chemisorbed onto the metallic gold particles on the surface of the support. The result is an interaction between the support and supported gold particles where both perform a role in the oxidation of CO[33]. When reaction temperatures are kept below -73°C, the TiO_2 perimeter around the gold particles are saturated with carbonate species formed by surface reactions of CO. This can hinder the reaction under certain conditions. The reaction of CO with O_2 takes place on the edges, steps and corner sites of the gold particles as shown in Figure

1.7. The corresponding activation energies are almost 0 kJ/mol that allows for catalytic activity to be tested at any temperature, provided that the particle sizes of the gold are small enough[33].

When temperatures are above 25°C the reactions begin to take place on the perimeter interfaces between the CO and the gold particles and oxygen absorbed on the support surfaces. Once again it is the gold particle size that determine how many of the edge, step and corner sites exist as the frequency of their occurrence is determined by mean particle size. A mechanism for this reaction has been proposed by Haruta et al.. in Figures 1.7 and 1.8.

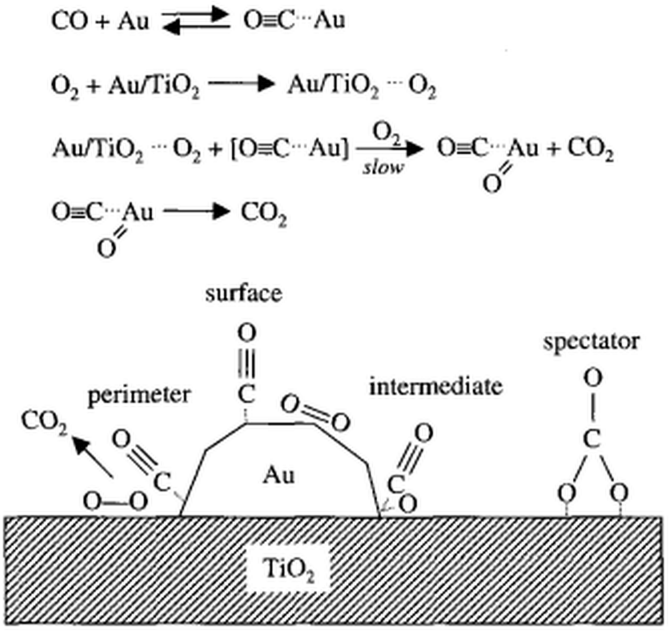


Figure 1.7: The CO oxidation mechanism that was first proposed by Haruta and co workers[33].

It is still unclear how the support activates the oxygen molecule[33]. However it has been shown that for gold supported on TiO_2, a Langmuir-Hinselwood mechanism is proposed. This mechanism states that the rate of a heterogeneous reaction is controlled by the reaction of the adsorbed molecules and that all adsorption and desorption pressure are in equilibrium. This type of mechanism involving noncompetitive adsorption fits the model best[34]. Another important feature that has been realized from the study of the mechanism is the importance of how the gold particle is bound. The gold nanoparticle needs to be bound hemispherically to the support surface for highest reactivity.

The calcination step is often undertaken at higher temperatures between 130°C and 250°C. Hydrogen or other reducing gasses are flowed over the catalyst during this process. Reduction can take place at high temperature or with the use of the reducing gas. When the reaction to be catalyzed is the CO oxidation reaction, then the CO itself may act as the reducing agent. It is often useful to use hydrogen as the reducing gas prior to the reaction as it helps to remove residual chlorine that may still be present from the synthesis of the catalyst.

Removal of residual chlorine is important as it has been shown to be a factor in the sintering process and should be avoided once the catalyst is to be used. The calcination step results in a change in the oxidation state of gold from Au(III)

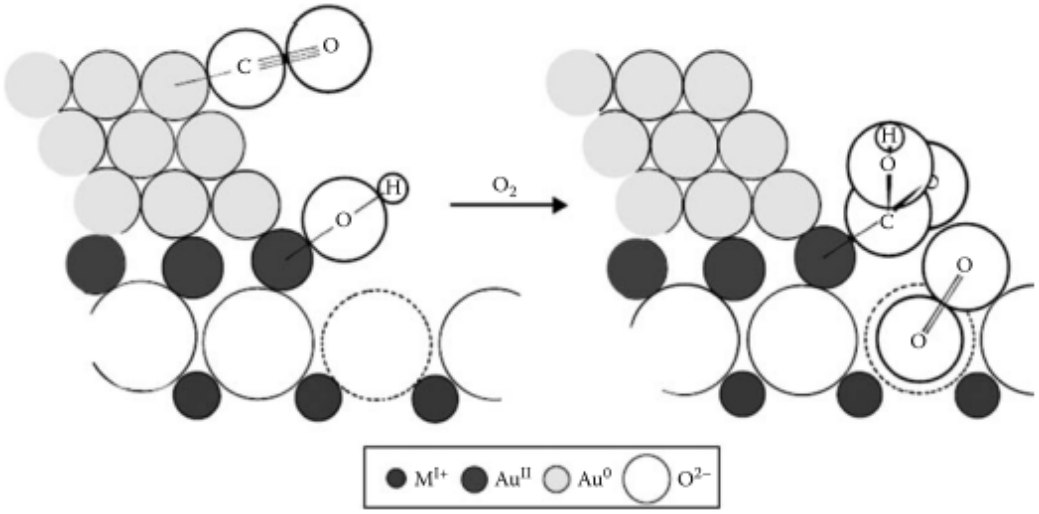


Figure 1.8: The early stages of the CO oxidation process where the CO is chemisorbed at the periphery of the active gold particle[40].

to Au(0). There may be some unreduced gold left over from the reduction step, as proposed by Bond and Thompson (Figure 1.8). This small amount of residual unreduced gold may also be crucial in the CO oxidation process.

Chemisorption as shown in Figure 1.8 occurs at gold particles of low coordination number. A hydroxyl ion is also moved in from the support to a Au(III) ion that then creates an anionic vacancy. This results in the formation of a carboxylate group, followed by an oxygen molecule occupying an anion vacancy O^{2-}. This oxidizes the carboxylate group by extracting a hydrogen atom, forming carbon dioxide, and the resulting hydroperoxide ion (HO^{2-}) then oxidizes a further carboxylate species forming another carbon dioxide and restoring two hydroxide ions to the support surface. This completes the catalytic cycle for the oxidation process.

DFT calculations provide evidence that the oxygen molecules adsorp on the edge of the particle with the oxygen-oxygen bond being stretched by electron transfer from the gold. This is first initiated by the Ti cations and the oxygen vacancies at the interface[35-39]. One of the most important aspects for the development of new catalysts is the ability of the catalyst to remain active for long periods of time, as deactivation is one of the most important factors that hold back the commercialization of gold catalysts for large scale application. This deactivation is more prevalent when gold catalyst are used for CO oxidation as this reaction is very sensitive to changes in the catalyst, especially when changes in gold particle size are concerned.

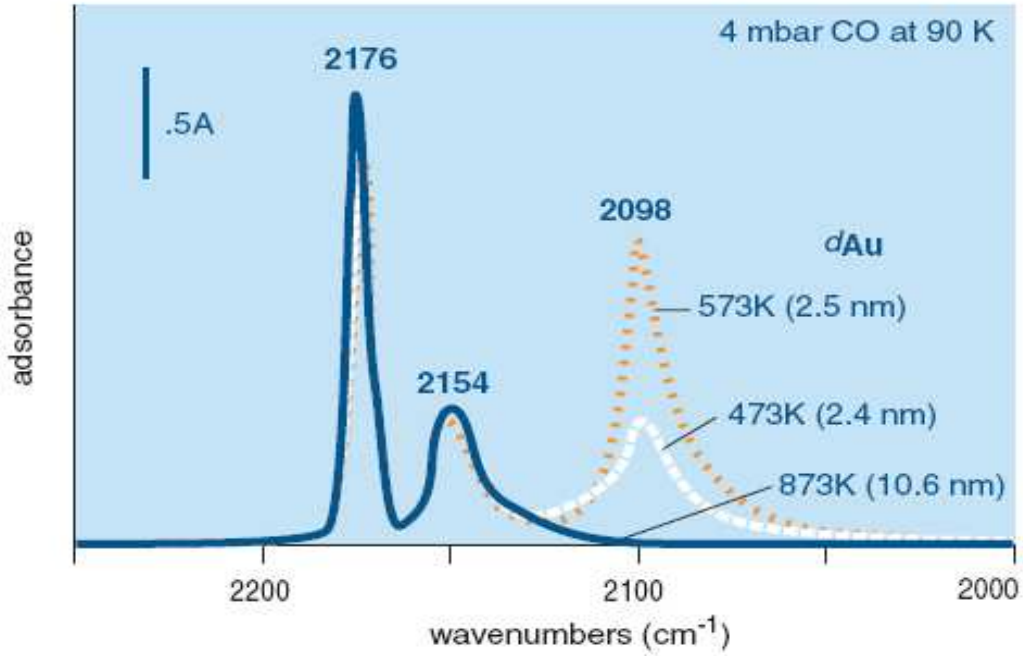


Figure 1.9: FT-IR spectra for CO absorbed on Au-TiO_2 calcined at 200°C, 300°C and 600°C for various sizes of gold nanoparticle[21].

1.4 Kinetic behavior and the reaction mechanism

The rate of CO oxidation has been shown to be independent of CO concentration down to 0.1% CO volume and is only slightly dependent on the concentration of oxygen[13]. It is believed that CO and O_2 are absorbed onto the catalyst surfaces nearly to saturation point with the reaction of CO being the rate determining step[41].

The FT-IR in Figure 1.9 shows the oxidation of CO at -183°C over Au-TiO_2 that had been calcined at various temperatures[31]. The most active catalyst resulted from the calcinations at 300°C. The peak at 2110-2120 cm^{-1} can be assigned to the CO that has been linearly adsorbed on the metallic gold sites. When the catalyst is calcined at 600°C the gold particles grow to over 10 nm in diameter and the peak can be seen to have a reduced area. This infers that only the steps, edges, corners and not the smooth surfaces of the gold particles are responsible for the catalytic activity as the number of steps, edges and corners are reduced as the particle sizes increase. This is consistent with density functional theory calculations showing how the CO interacts with these sites[32]. However with that said, there has been no direct experimental evidence where

oxygen has been activated for reacting with CO absorbed on the gold surfaces and whether the oxygen is dissociatively or non-dissociatively absorbed[25].

1.5 Producing active nanogold catalysts

The preparation of highly dispersed gold catalysts was, for many years, by impregnation techniques (IMP). This technique involves immersing a metal oxide support in an aqueous solution of $HAuCl_4$. This is followed by evaporation of water to disperse the $HAuCl_4$ over the metal oxide support. Calcination in air at temperatures exceeding 200°C then follows. This technique generally results in the formation of Au-NP's larger than 30 nm in size. Further, the remaining chloride ions on the surface lead to sintering of the Au-NP's, further reducing their catalytic activity[25]. The reason for the large particle size of the gold nanoparticles was due to the inability of the gold to bind strongly to the support material[8]. The result was that the gold was highly mobile over the surface and rapid sintering occurs when the catalyst was heated to temperatures as low as 200°C. Other methods have been developed for the deposition of gold onto support surfaces. Each of the methods offer different advantages and disadvantages when compared.

There are four techniques that are accepted as the best known methods of preparation for Au-NP's on various reducible oxide supports. These are co-precipitation, co-sputtering, deposition-precipitation (DP) and gas phase grafting. Essentially the main requirement of the preparation technique is that a strong bond between the gold and the support is formed, a parameter that is not met by the impregnation technique resulting in the a synthesis of an inactive catalyst after reduction. It is not possible to deposit gold hydroxide on silica, silica-alumina or WO_3[41], however other gold precursors exist that do allow for the deposition albeit with limited success, on these supports. Fortunately, it is possible to deposit gold onto certain supports and the gold remains as nanoparticles at temperatures up to around 400°C due to the epitaxial contact of the Au-NP's with the metal oxide support. However at temperatures above 400°C current gold catalysts deactivate rapidly. There are a number of important properties that need to be considered when designing a catalyst using nanogold as the active agent. Some of these factors are highlighted in the sections that follow.

1.5.1 Strong contact of the gold nanoparticles with the support

For applications where the catalyst will be used at temperatures above ambient, it is very important that the gold nanoparticles have strong contact with the support structure. This strong contact acts as a stabilizing effect to the energetic gold nanoparticles and binds them to the surface. This reduces the ability of the nanoparticles to sinter by limiting their migration on the surface and therefore helps to maintain the activity of the catalyst. There are various choices of supports available for Au-NP's. Specifically for the oxidation of CO the most common supports are TiO_2, Fe_2O_3, Co_3O_4 and NiO. Interestingly all of these support materials have semi-conducting properties[25]. Some Alkali-earth metals have also been used, for example $Mg(OH)_2$ and $Ba(OH)_2$, however these metal supports result in a catalyst that is active for only 3-4 months after synthesis, if stored correctly, as the gold particles still sinter slowly over long periods of time[10].

Turn over frequencies (TOF) depend strongly on the contact structure of how the Au-NP's are attached to the support, while this is not important in platinum catalysts and is one of the striking differences between catalysts comprised of platinum group metals and gold. Depending on how the Au-NP's are bound to the surface the TOF's can change by a factor of four when compared to platinum based catalysts as shown in Figure 1.10[43].

1.5.2 Size control of the gold nanoparticles

For CO oxidation activity is primarily, but not solely, governed by the size of the gold nanoparticles[40]. Thus control of the nanoparticle size is one of the critical parameters in the determination of how active a gold catalyst may be. If the Au-NP's are kept down to a size of 2-4 nm as well as being epitaxially bound to the surface, it has been shown that the activity of gold is similar to that of platinum[25]. This size corresponds to a layer of 3-4 gold atoms provided once again that the Au-NP's form hemispherical contacts with the surface. Figure 1.10 compares turn over frequencies of platinum and gold and further compares the TOF's of the metal particles when attached as either spheres or hemispheres[41].

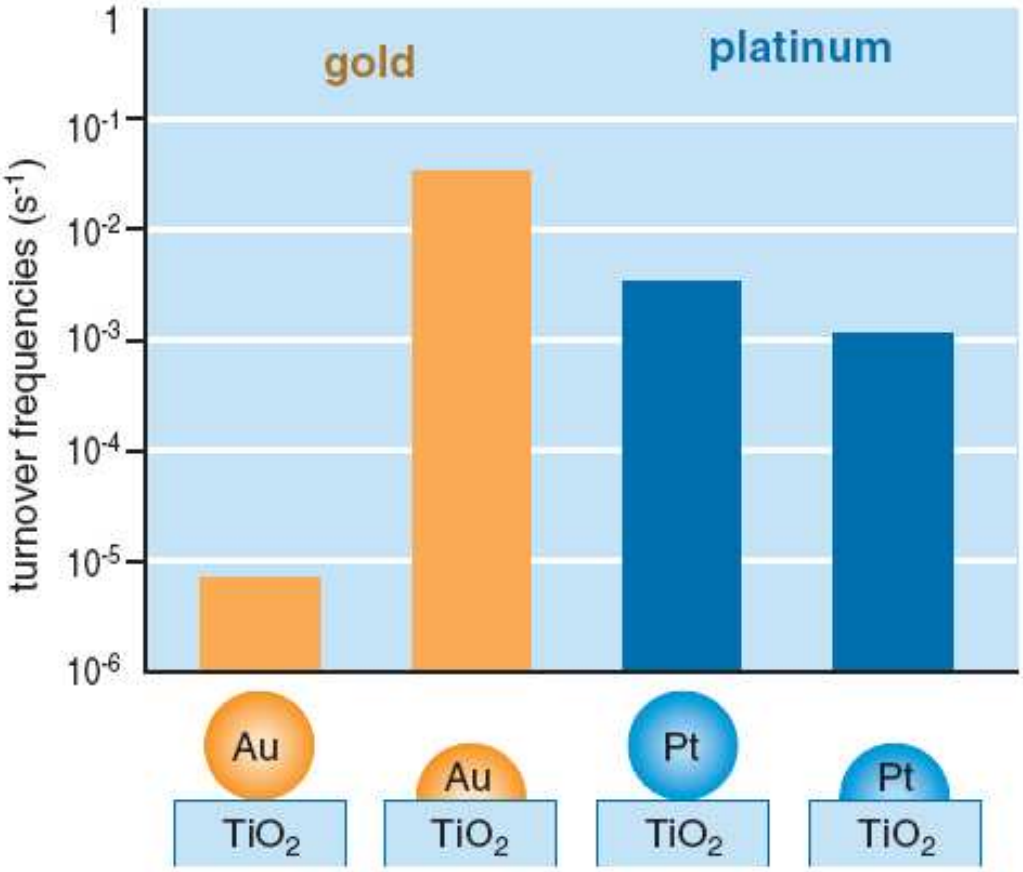


Figure 1.10: TOF's of gold and platinum showing the difference in TOF's when the gold and platinum are bound either as a sphere or hemispherically[41]. Hemispherically bound particles far out perform particles that are not bound in this fashion. Platinum however only shows a small difference in TOF's as a function of bonding[41].

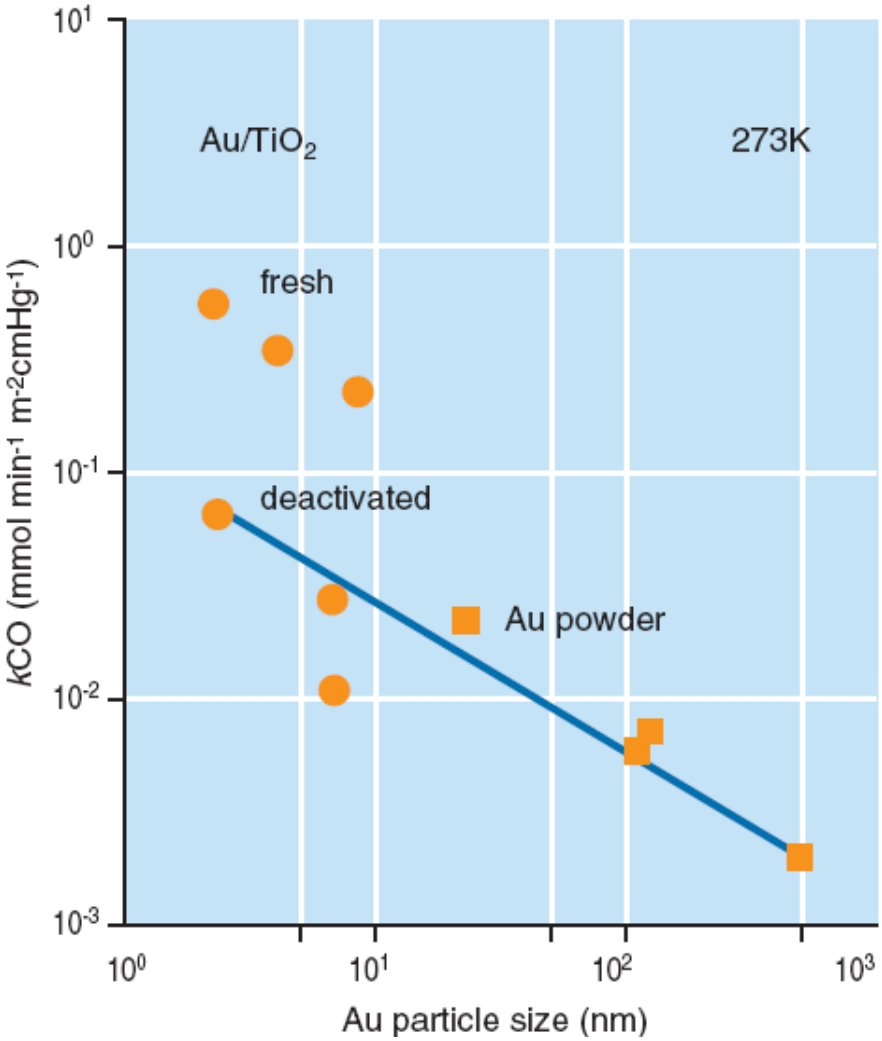


Figure 1.11: Reaction rates of CO oxidation over fresh and deactivated Au-TiO_2 as well as unsupported gold as a function of particle size[41].

If the temperature is lowered from 80°C to -70°C the rates of conversion differed by around an order of magnitude compared to when the temperature was raised from -70°C to 80°C. It is thought that this occurs from the accumulation of carbonate species on the surface of the support at low temperatures thus resulting in the loss of activating power of the perimeter interfaces of the O_2.

1.5.3 Selection of the correct support

From investigations using TEM it was determined that when titania, found in one of two crystalline phases at room temperature (anatase and rutile) is used as a support, the gold nanoparticles on anatase contact the surface in a more epitaxial manner when compared to rutile. From these studies researchers were able to conclude that the Ti^{4+} cations around the surface of the gold particles are more uniform on anatase than for rutile[44]. Therefore, rutile has not been extensively researched as a support.

While a support such as anatase may be very useful. As it has a relatively high surface area, it also has draw backs such as not being thermodynamically stable over 450°C. Further, the kinetics of thermodynamic changes of the support material change dramatically when metallic nanoparticles are placed on the surface. For alumina, silica and titania the TOF's are nearly equal implying that the contribution of these support metals is similar. What does contribute is water content, as alumina and silica need a higher water concentration in their surface than TiO_2[45]. Only highly acidic supports such as mixtures of SiO_2-Al_2O_3 do not make appropriate supports.

Gold supported on $Mg(OH)_2$ has been shown to be extremely active for CO oxidation at -77°C, giving 100% conversion at 20000h^{-1}mg/g-cat. However the catalyst deactivated suddenly after three months when activity even at 200°C was lost[46]. This is likely attributed to sintering effects.

1.5.4 A note on catalyst deactivation

Catalysts may deactivate through a number of mechanisms. The routes for deactivation of existing catalyst must always be considered when designing a new catalyst. As shown in Figure 1.12, the processes that may be occurring on a surface are numerous.

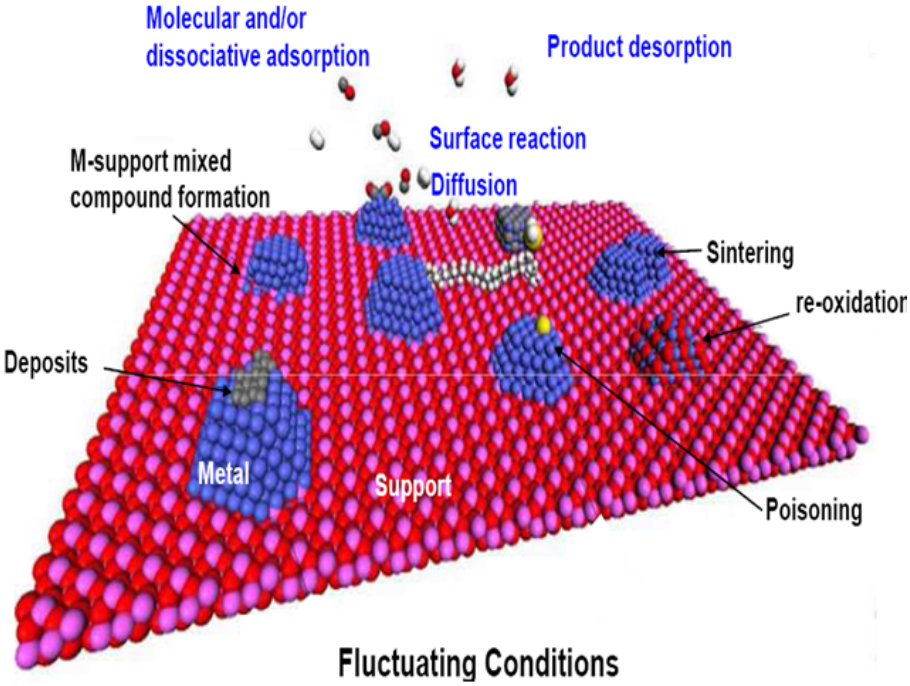


Figure 1.12: Operating condition of a catalyst and processes that can occur on the surface leading to deactivation[25].

The four most prevalent deactivation routes for catalysts are highlighted below.

- Coke formation - carbon deposits begin to clog the pores of the catalyst and may also block active sites reducing activity.
- Poisoning - certain elements such as heavy metals or sulfur bind so strongly to the active site that there is not sufficient energy to remove them. Thus the active site is blocked from further reactions in the catalytic cycle.
- Sintering - active metal particles move around the surface and thus combine with other particles to reduce their surface energy, leading to a decrease in active surface area.
- Encapsulation - sintering of the support material results in loss of surface area and massive reduction in pore volumes trapping the active sites within the catalyst support where no reactant gasses can penetrate.

These deactivation mechanisms are illustrated below in Figure 1.13

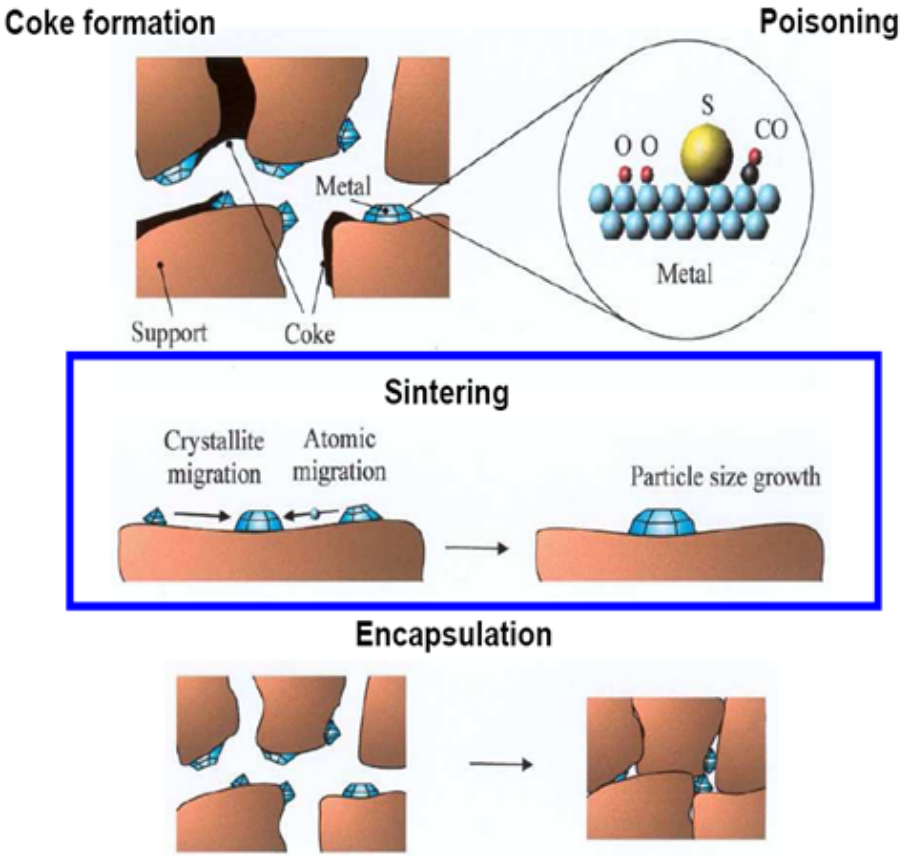


Figure 1.13: Mechanisms of deactivation of a catalyst[25].

Chapter 2

Techniques of Characterization

2.1 BET

The BET method was first developed by three scientists (Brunauer, Emmett and Teller) while were working on ammonia catalysts[48]. Monolayer adsorption can be described by a Langmuir isotherm while multilayer adsorption requires the use of the BET method. Physisorption is determined by a number of factors such as temperature, gas pressure, interaction between the surface and the gas along with the surface area. Adsorption is the process whereby a gas is brought into contact with a surface and under certain temperature and pressure conditions[47]. The concentration of the gas is greater near the surface, referred to as the absorbant, than in the bulk of the gas phase referred to as the absorbate. This adsorption process is accompanied by a decrease in the free energy of the system. Thus a decrease in entropy occurs which implies that the adsorption process is always exothermic as it is a spontaneous process[47].

When chemisorption (chemical adsorption) occurs, a chemical bond is formed between the surface atoms or ions and the gas molecule, which is accompanied by a transfer of electrons between the gas and the surface that is being studied. Thus a monolayer is formed between the absorbate and the surface[47]. It is rare that gases that have been chemisorped can be removed isothermally in vacuum only, especially on metal surfaces, where heating well above the adsorption temperature is usually required for complete desorption of the gas. Physically adsorbed gases can be removed readily from the adsorbent by evacuation at the same temperature at which adsorption took place.

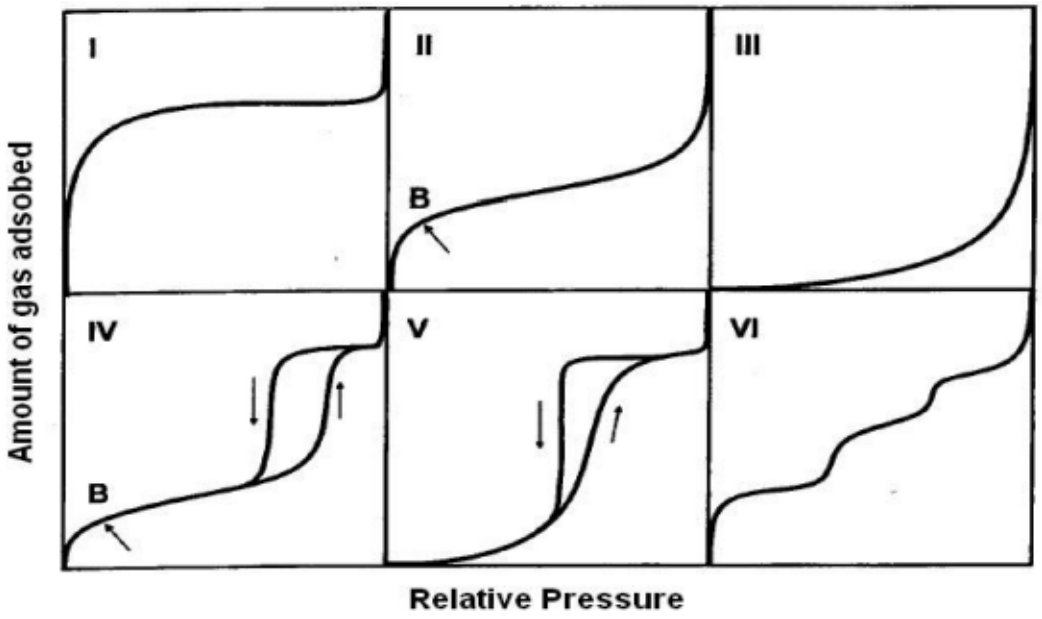


Figure 2.1: The 6 most common physical adsorption isotherms[48].

The study of surface areas is an important parameter when considering the supports used for gold catalysts. The BET method is useful in determining the surface areas of new supports that are produced, further it is also important in order to examine how the support structures of the catalysts change as the catalyst is cycled through various temperature treatments. Finally, when the thermodynamic changes such as the phase change from anatase to rutile occurs, it is important to correlate the phase change with a change in the surface area as this parameter has a direct influence on catalytic activity.

The amount of gas absorped is measured by the quantity ν, which is a volume (measured in cm^3) of gas adsorbed per gram of adsorbent. It is measured as a function of pressure, P , as temperature is held constant. In theory there are a number of possible isotherms that may exist but there are 6 principal isotherms shown in Figure 2.1[48].

When adsorption does not occur past the monolayer the isotherm takes on a type I shape as are found in porous systems such as zeolites.

Multilayer adsorption on highly porous adsorbants are characteristic of types IV and V. The flattening of isotherms near the saturation vapour pressure is due to the filling of the capillaries within the sample. Type II isotherms are observed very commonly, being essentially the same as type IV isotherms with the only difference being a lack of capillary filling. Type III isotherms are very rare and are usually attributed to a non-wetting system.

The BET equation given by

$$\frac{1}{v[(\frac{P_0}{P}-1)]} = \frac{c-1}{v_m c}(\frac{P}{P_0}) + \frac{1}{v_m c}$$

where P and P_0 are the equilibrium and the saturation pressure of adsorbates at the temperature of adsorption, v is the adsorbed gas quantity, v_m is the monolayer adsorbed gas quantity and finally c is the BET constant. There are a number of assumptions made when the BET method is applied. These are, a homogeneous surface, no lateral interactions between molecules and the uppermost layer must be in equilibrium with vapour phase. The first layer assumes heat of adsorption while higher layers heat of condensation and finally at saturation pressure.

When BET is to be conducted on a material it is important to use a standardized technique. The American Society for Testing and Materials (ASTM) has an approved method for adsorption as well as a full description of the method can be accessed[49].

The BET setup for the data collections in this thesis were as follows : The N_2 adsorption-desorption experiment was conducted at -193°C using a Micrometrics TriStar surface area and porosity analyzer. Prior to the experiment, the sample was out gassed at 200°C for 6 h. The BET surface areas were obtained in a relative pressure range from 0.05 to 0.30. The total pore volume was calculated from the amount of N_2 vapor adsorbed at a relative pressure of 0.99.

2.2 X-ray Diffraction

One of the most versatile ways to measure structural properties such as strain state, grain size, epitaxy, phase composition, preferred orientation, and defect structure is using X-ray diffraction (XRD). XRD offers a method for measuring atomic spacing and as it is a non-destructive technique it can also be used to conduct in-situ studies (gas, temperature and pressure) on materials. In this thesis the terms in-situ PXRD (in-situ powder X-ray diffraction) and VT-PXRD (variable temperature powder X-ray diffraction) are used interchangeably.

Within the wide variety of materials where XRD finds use, are catalysis and not only can in-situ work be conducted, but more recently in-operando where catalysts can be tested under operating conditions. Further the catalyst can be tested to beyond its usual operating limits and structural changes in the catalyst relating to its activity can be analyzed. Materials with any elemental composition can be studied with XRD however, the heavier elements are preferred because greater diffraction intensities are observed.

Like all techniques used for characterization, XRD also has its drawbacks. The X-rays that are diffracted are of low intensity when compared to diffraction from electrons. This is particularly prominent when low weight elements are analyzed. When XRD is applied to nano materials the technique information is more difficult to attain as the particle and crystallite sizes become smaller. With the decrease in crystallite sizes the number of diffraction centers decrease and so does the intensity of the diffracted beam.

When metal nanoparticles are loaded on supports for use in catalysis, it is often found that the crystallite sizes of the nano particles are less than 10 nm. This is further complicated by the fact that most catalysts that consist of supported nanoparticles have very low metal loadings, typically less than 5%, often to as low as 1%. For particle sizes less than 5 nm coupled with low metal loadings the spread and number of diffraction centers becomes very small and the intensity observed by the detector is often lost in the background noise. Thus XRD of nanomaterials poses its own complexities, however there are ways to overcome these.

When both the supported metal particles are very small (in the region of 5 nm) and the support is also nanoscale, the problem of resolving and interpreting the diffraction peaks becomes even more difficult. However, XRD is still one of the most important methods for characterizing nanomaterials as crucial information about the support is attained. The support is undoubtedly one of the most important factors in attaining an active and very importantly a stable catalyst under varying conditions.

2.2.1 Lab instruments

Both structural and quantitative X-ray data in this thesis were collected using powder X-ray diffraction. Two diffractometers were used for data collection in

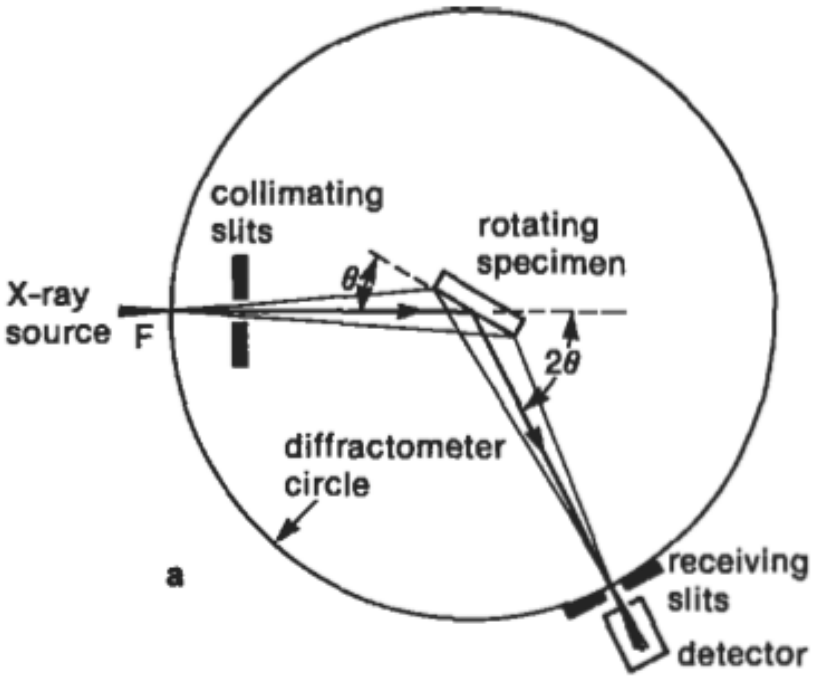


Figure 2.2: The powder diffractometers used to collect data in this thesis are set up in Bragg-Brentano geometry as shown, this geometry is used for preferentially and randomly oriented samples.

this work. The primary instrument was a Bruker D8 Advance X-ray Diffractometer that is equipped with an Anton Paar XRK 900 reaction chamber. This diffractometer was used in performing all of the in-situ variable temperature diffraction experiments (in-situ PXRD). Additionally, a Bruker D2 Phaser was also used for routine diffraction work. The powder X-ray diffractometers specifications used in this thesis are listed in Table 2.1.

The Bruker D8 advance uses a sealed tube Cu X-ray source and is equipped with a primary beam Göbel mirror and a Bruker VÅNTEC-1 PSD detector using a radial Söller slit and a secondary beam nickel filter. The diffractometers were both in Bragg-Brentano geometry as shown in Figure 2.2 The in-situ PXRD data was collected with the Anton Paar XRK 900 heating stage which operates under inert or ambient atmospheric conditions in the temperature range between 30°C and 900°C.

A Bruker D2 Phaser desktop diffractometer was used for room temperature data collections as shown in Figure 2.3. The diffractometer used a sealed tube Cu X-ray source and is equipped with a Bruker Lynxeye PSD detector using

	Parameter	Value
Goniometer radii	Primary radius (mm)	250
Detector	Secondary radius (mm)	250
	2theta angular range (°)	12
Geometry	Parallel beam optics	-
Slits	Primary soller slit (°)	2.5
	Secondary soller slit (°)	2.5
X-ray generator	Cu-radiation-voltage	40 KV
	Cu-radiation- current	40 mA

Table 2.1: Instrument details of the Bruker D8 Advance.

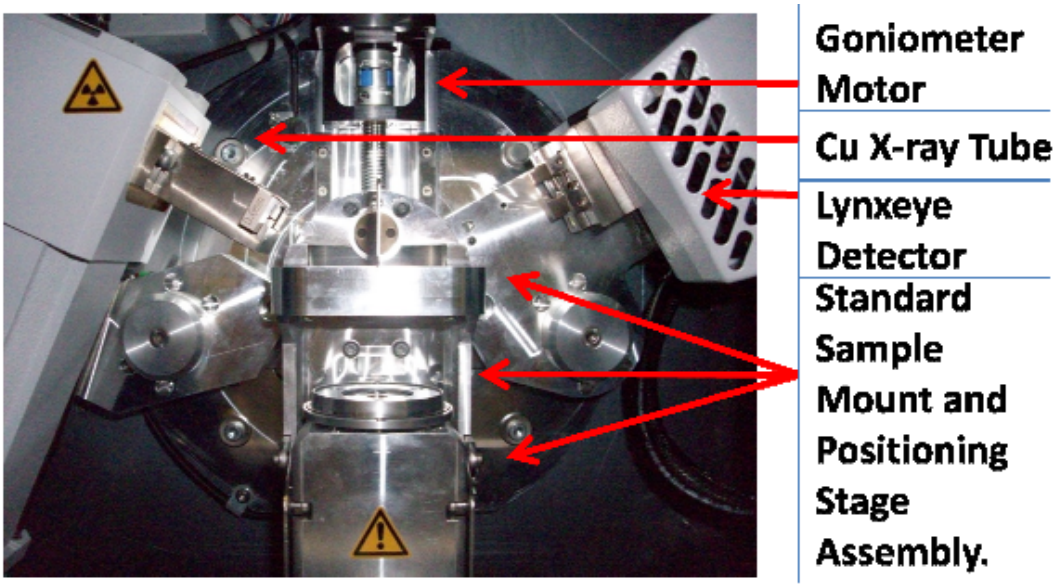


Figure 2.3: Internal structure of the Bruker D2 Phaser.

secondary beam Söller slits and a secondary beam Ni filter.

Instrument parameters for the Bruker D2 Phaser are given in Table 2.2.

2.2.2 NIST LaB_6 reference material

The need to use a NIST (National Institute for Standards and Technology) standard for the D8 Diffractometer is to determine a standard instrument configuration. The Bruker D8 is able to collect data from 1° to 12° 2θ simultaneously with the use of the VANTEC detector. This detector has an angular opening that could be controlled, affecting the rate at which the data collection

	Parameter	Value
Goniometer radii	Primary radius (mm)	70.7
	Secondary radius (mm)	70.7
Detector	2theta angular range detector (°)	5
Slits	Primary soller slit (°)	2.5
	Secondary soller slit (°)	2.5
X-ray generator	Cu radiation - voltage	30 KV
	Cu radiation - current	10 mA

Table 2.2: Bruker D2 phaser instrumental parameters.

could be performed due to the increased counting rate. However, a slit was used and faster collecting times resulted in broader diffraction peaks due to axial divergence resulting from collecting data over multiple ranges simultaneously. The result was a compromise between being able to collect data rapidly and good resolution as shown in Figure 2.4. For this work the detector was set at 3° 2θ that provided the best compromise between collection speed and resolution as shown in Figure 2.5. Selection of the count time per step and step size was achieved using a certified standard reference material, LaB_6, manufactured by the National Institute of Standards and Technology (NIST). This was supplied with certification detailing its preparation and describing the careful determination of the cubic lattice parameter of 4.1569162 Å ± 9.7x10^{-7} Å using a Cu incident X-ray beam of λ = 1.54059Å. The effects of the slit opening as well as counting time are shown in Figures 2.4 and 2.5 respectively.

A 0.6 mm fixed diversion slit was chosen due to the fact that most of the samples are nanoscale materials and thus would not diffract very strongly. The 0.6 mm slit allows for a higher intensity beam to penetrate the sample as shown in Figure 2.4. However, it also results in a loss of resolution as can be seen in Figure 2.4 when compared to narrower slits.

2.2.3 The Anton Paar variable temperature chamber

All in-situ PXRD measurements were conducted using the variable temperature chamber (Anton Paar XRK 900). The XRK 900 has a maximum heating rate of 30°C/min and is capable of experiments from ambient up to 900°C. Further, the XRK was able to support a number of gasses that could be pumped though the chamber at pressures up to 10 bar.

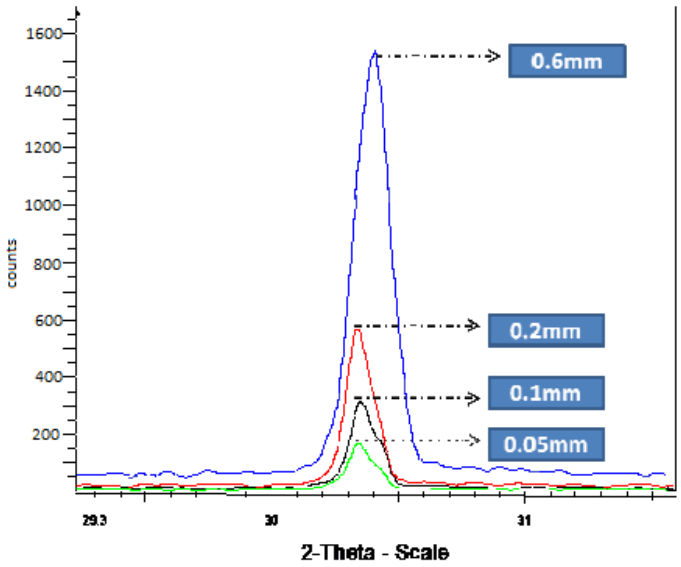


Figure 2.4: Intensity dependance on slit selection.

There were two sample holders used for data collection. The first was a macor ceramic type holder that is 0.5 mm deep with an internal diameter of approximately 11 mm and is produced by Bruker AXS shown in Figure 2.9. This sample holder was used when there was no need to flow gasses through the sample. The fritted sample holder is also made from macor as shown in Figure 2.10, but is designed to allow gasses to pass though the sample. A new macor sample holder was purchased for the collection of data as macor is a form of ceramic material that under certain conditions can absorb impurities from other experiments into its crystal matrix. Two data collections were spoilt using older sample holders that contained impurities which embedded themselves into the macor ceramic at high temperatures. The impurities were absorbed by the titania catalyst support. Following this a new sample holder was purchased and was exclusively used for the work conducted in this thesis to avoid cross contamination.

Due to the shallowness of the sample holder the signal to noise ratio was poorer when compared to other, deeper, sample holders.

2.2.4 Software used for interpretation of diffraction data

Bruker AXS evaluation package (EVA) All fingerprint phase identification and drawing of both 2D and 3D images was done using EVA.

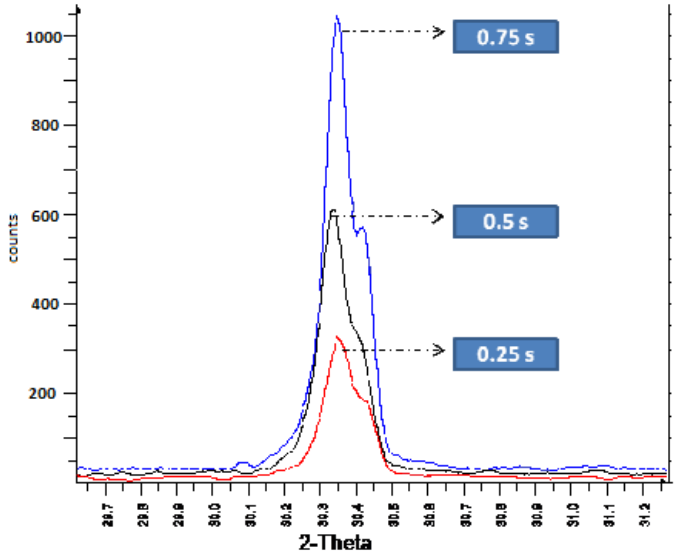


Figure 2.5: Changes in peak shape and intensity are dependent on counting time. Further, the reduction in the Cu$k\alpha_1/k\alpha_2$ can also be seen as counting time is increased. As the data collections were limited by the large amount of time that the catalysts spend at high temperatures it was viable to use a long counting time of 0.75 seconds per step.

Bruker AXS total pattern analysis software (TOPAS) Rietveld refinements were carried out using TOPAS Version 4.2, all refinements were conducted using the graphical interface as opposed to the launch mode application.

Diamond Structure viewer Structural diagrams were generated using diamond version 3.2c (crystal impact, 1999).

Structural databases Structural data used in this work was obtained from the Inorganic Crystal Structure Database (ICSD) (2010, Release 2). Structural data were output as crystallographic information files (CIF) and converted to structure files for use in TOPAS V4.2.

PJF-XRD Analyzer (diffraction analysis software written by Paul Franklyn) In some cases particle sizes obtained from the Rietveld refinements were compared to those obtained using PJF-XRD analyzer as well as TEM images.

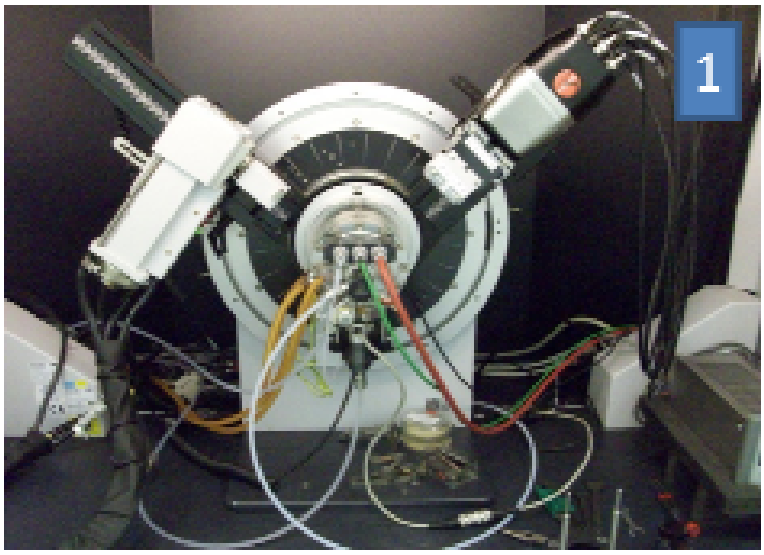


Figure 2.6: The Bruker D8 with the XRK attachment in Bragg-Brentano geometry.

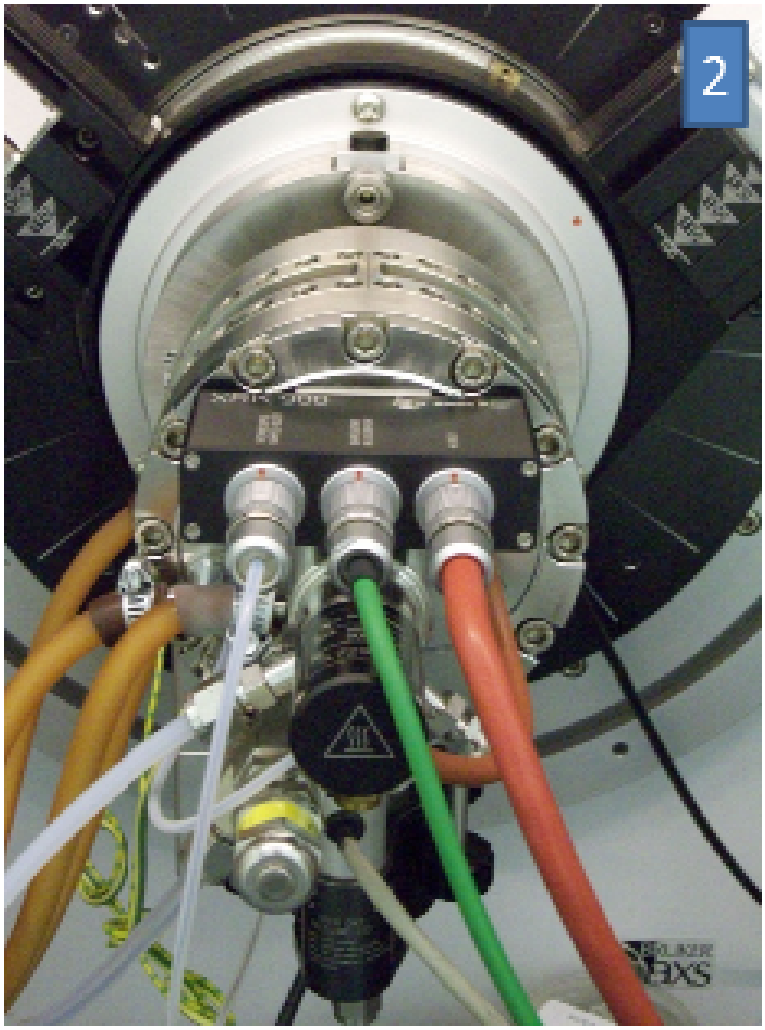


Figure 2.7: The XRK chamber with all gas lines attached.

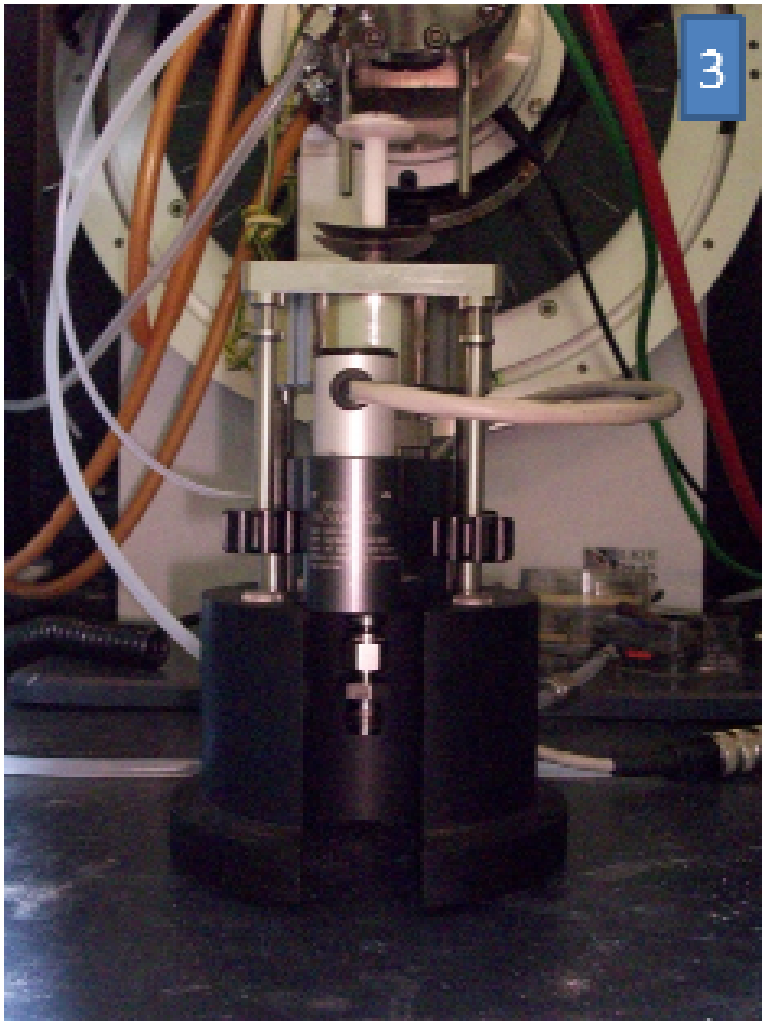


Figure 2.8: macor sample holder prior to insertion into the chamber

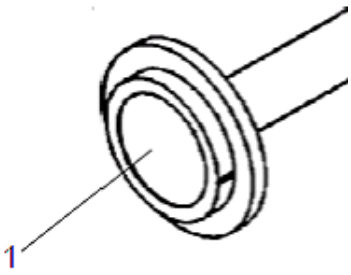


Figure 2.9: Macor sample holder.

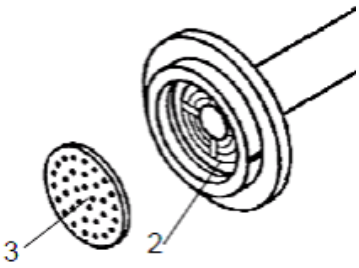


Figure 2.10: Macor holder with central opening (2) and frit (3) that fits into (2).

2.3 Rietveld Refinement

Much of this section on the Rietveld method was derived from the definitive text namely, The Rietveld method by R.A. Young. Oxford press, 1969[51]. The Rietveld method involves using experimentally collected powder diffraction data and applying a least squares refinement procedure to find a calculated pattern that best fits the experimental data through variation of critical structural constants[51,52]. The calculated pattern is derived from various models and descriptions of the crystal structures, instrumental factors, corrections for instrumental and sample aberrations as well as the diffraction optics. The process is iterative, whereby the objective is to minimize the difference between the observed and calculated patterns while still ensuring that the final result makes physical as well as chemical sense.

Rietveld refinement may be used for a number of reasons, listed below

- Solving an unknown crystal structure
- Calculating the amount of disorder or mixing on a Wyckoff site
- Quantitatively determining the percentages of different phases in a sample
- Determining the size of crystallites in various phases

In this work the last two points were the parameters that were most of interest and both the quantification of the phases present along with the crystallite sizes were very important to the activity of the catalyst. Rietveld refinement fits the entire pattern at once and simultaneously refines

- atomic positions

- disorder or mixing between atomic sites
- lattice parameters
- profile parameters, or more simply put, the peak shape, and
- background parameters.

There were a number of factors affecting peak intensities and a short summary of each of these factors will now be considered as shown in Figure 2.11. Firstly it must be noted that the observed diffraction peak intensity is a product of the structure factor given by F_{hkl} and a number of additional terms. F_{hkl} determines the fraction of amplitude $\frac{A}{A_0}$ that is reflected when an X-ray wave of amplitude A_0 crosses a single sheet of plane (hkl). The diffraction peak intensity is calculated using F_{hkl} and additional terms to calculate how these waves, coming from successive crystal planes, combine together with interference to form the resultant diffracted wave. Any change in F_{hkl} will produce an observable change in the diffraction peak intensity. For instance this can occur by replacing all or a fraction of N_j with another atom (alloying or substitutional doping) or moving the position(xyz) of an atom.

Anomalous scattering of X-rays with energies near the absorption edge of the atom may also result in changes to the scattering factor. However this occurrence only matters when the energy of the incident X-ray approaches the ionization energy of atom i.e. when the wavelength of the incident X-ray is near the absorption edge of an atom in the structure. Anomalous scattering describes how some photons with energy approaching the ionization energy will be scattered out of phase with the majority of photons, thus varying the expected intensity.

2.3.1 Parameters in the Rietveld method

1. Structure factors (form factors)

The structure factor, $|F_{hkl}|$ is defined as the amplitude of the wave scattered by all the atoms in a unit cell over the amplitude of the wave scattered by one electron and is given by

$$F_{hkl} = \sum f_n exp[2\pi i(hu + kv + lw)]$$

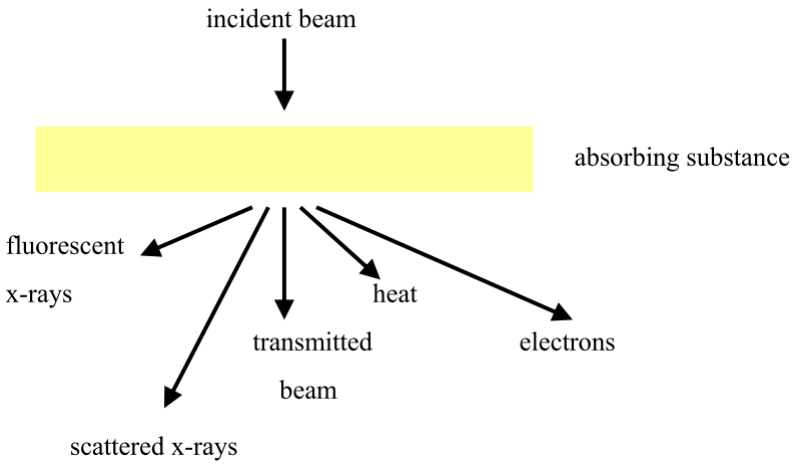


Figure 2.11: Multiple scattering considerations must be taken into consideration when an incident beam of X-rays strikes a sample[52].

where f_n is the atomic scattering factor, u, v, w describe the atomic arrangement. $|F|^2$ is proportional to the intensity of the diffracted beam. Note that $exp(\pi i) = -1$, $exp(2\pi i) = +1$ and $exp(n\pi i) = exp(-n\pi i)$ and thus the final equation can be given by

$$F_{hkl} = \sum N_j f_j exp[2\pi i(hx_j + ky_j + lz_j)]$$

The amplitude of X-rays scattered by a crystal is determined by the arrangement of atoms in the diffracting planes. The structure factor quantifies the amplitude of the X-rays scattered by a crystal. The pattern of atoms in the unit cell scatters strongly in some directions and weakly in others owing to interference of the wavelets scattered by the atoms. F_{hkl} sums the result of scattering from all of the atoms in the unit cell to form a diffraction peak from the (hkl) planes of atoms. The amplitude of the scattered X-rays is determined by where the atoms are on the atomic planes. This is expressed by the fractional coordinates $x_j y_j z_j$ and what atoms are on the atomic planes. The scattering factor f_j quantifies the relative efficiency of scattering at any angle by the group of electrons in each atom while N_j is the fraction of every equivalent position that is occupied by atom j.

X-rays are electromagnetic radiation that are able to interact with an electron, the results of this interaction emits the X-ray as a spherical wave. The number of electrons around an atom defines how strongly it will scatter the incident X-ray beam. The X-ray beam does not interact with atoms, but rather interacts with electrons that happen to be clustered around the atomic nuclei. The

initial strength of the atomic scattering factor is equal to the number of electrons around the atom. The scattering factor, f, is a product of several terms describing the interaction of the X-ray with the electrons around an atom.

2. Multiplicity

This parameter is dependent on the space group that the structure is found in and is proportional to the intensity of the diffracted beam depending on thehkl values of the reflection. Multiplicity is also affected by any distortions in the system.

3. Lorentz factor

The Lorentz factor is a measure of the amount of time that a point of reciprocal lattice remains on the sphere of reflection during the measuring process and is given by the equation

$$LF = \frac{1}{4sin2\theta.cos\theta}$$

A number of factors can influence the Lorentz factor as shown in Figure 2.13. Including small deviations from Bragg's Law that depends on $\frac{1}{sin2\theta}$, the orientation of the crystals that is dependent on $cos\theta$ and finally the portion of the diffraction cone that intercepts the detector that also depends on $\frac{1}{sin\theta}$.

4. Polarization factor and LP factor

The polarization factor (Figure 2.12) is given by the equation

$$LP = \frac{1}{2}(1 + cos^2 2\theta)$$

If however a monochromator is used then the equation above is changed to

$$\frac{1}{2}(1 + cos^2 2\theta.cos^2 2\theta_m)$$

where $\theta_m$is the Bragg angle for the monochromator.

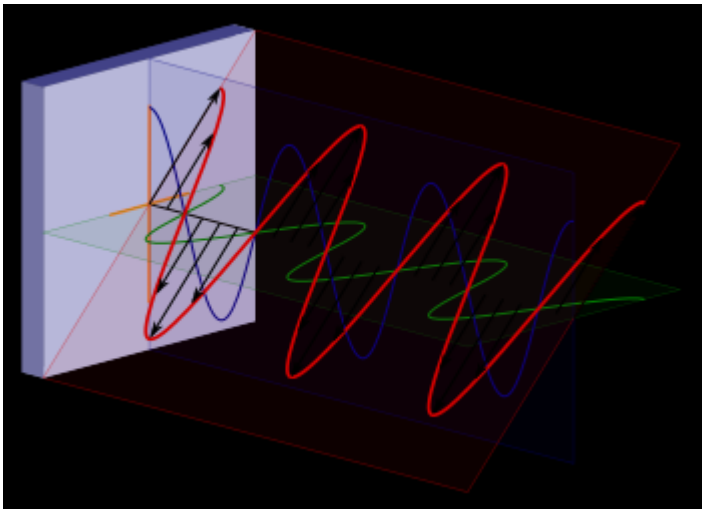


Figure 2.12: Polarization of the incident beam.

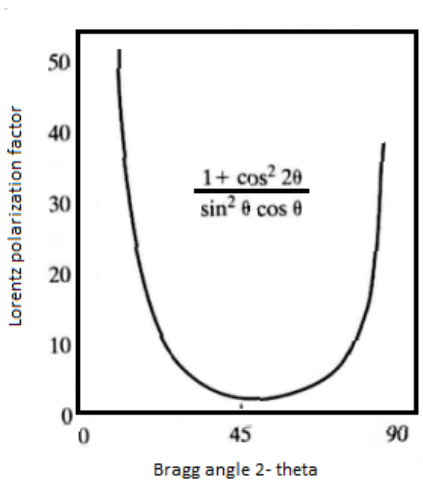


Figure 2.13: Change in the LP factor vs Bragg angle[51].

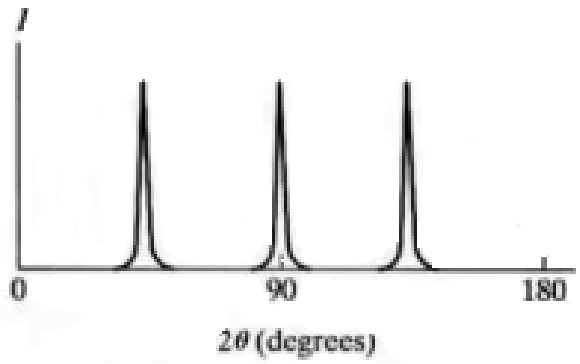


Figure 2.14: Diffraction pattern collected at room temperature[51].

Thus, Polarization factor is given by

$$PF = \frac{1}{2}(1 + cos^2 2\theta)$$

and the LP factor by

$$LP = \frac{(1 + cos^2 2\theta)}{(sin^2\theta.cos\theta)}$$

Note that if a monochromator is used, then the polarization factor is :

$$PF = \frac{1}{2}(1 + cos^2 2\theta.cos^2 2\theta M)$$

where θM is the Bragg angle for the monochromator. For neutron diffraction, polarization is a constant.

5. Temperature factor or atomic displacement.

Thermal motion of the atom changes the scattering factor and thus thermal vibrations that occur when the material being studied is heated results in the unit cell changing dimension and thus a change in the 2θ positions occurs as shown in Figures 2.14 and 2.15. Further a decrease in the intensities of the diffracted beam occurs along with an increase in the intensity of the background scattering is observed.

The efficiency of scattering by an atom is reduced because the atom and its electrons are not stationary. The atom is vibrating about its equilibrium lattice site. This effect is exaggerated during heating of the material and the amount

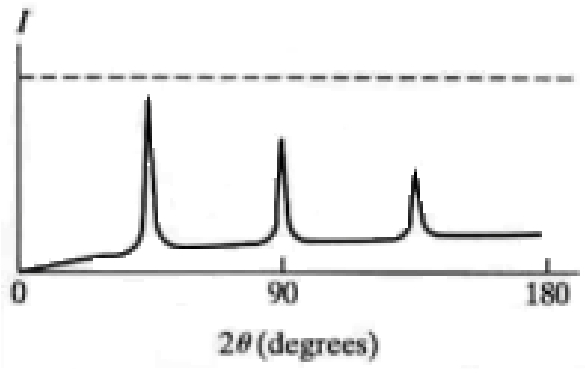


Figure 2.15: Diffraction pattern collected at non-ambient temperature showing deviations[51].

of vibration is quantified by the Debye-Waller temperature factor:

$$B = 8\pi^2 U^2$$

where U^2 is the mean-square amplitude of the vibration. This is for isotropic vibration. Occasionally B is broken down into six B_{ij} anisotropic terms if the amplitude of vibration is not the same in all directions.

6. Absorption

$$I_{diffracted} = I_{diffracted} exp^{-\mu t} t$$

Where, μ is the linear absorption coefficient and t is the thickness of the sample.

7. Preferred orientation

Due to the fact that crystals are not completely randomly oriented diffraction may be preferred in certain orientations. Examples where this may occur is in plate-like crystals or needle-shaped crystals.

There are two functions that allow compensation for this effect. First is the March-Dollase function given by

$$P(\alpha) = (r^2 cos2\alpha + sin^2 \frac{\alpha}{r})^{\frac{-3}{2}}$$

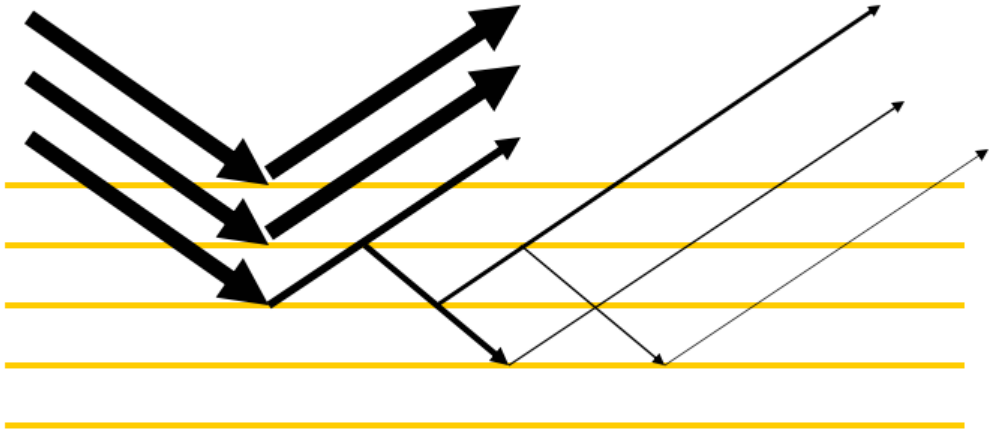


Figure 2.16: The incident beam may penetrate deeply into the sample and be deflected internally by the crystal planes resulting in lower peak intensities at the detector[52].

where $P(\alpha)$ is the pole distribution, α the angle between hkl and the PO vector and r an adjustable parameter. Secondly is the spherical harmonic function which is a measurement of the pole density distributions of a number of diffraction planes. This function is more complex and thus more powerful than the March-Dollase function.

8. Extinction coefficients

This factor compensates for the destructive interference caused by internal re-reflections within the crystals as shown in Figure 2.16. The effect of this makes the strong peaks appear weaker. This is why it is very important to ensure that the sample is very finely ground.

Crystallite size

The accurate determination of crystallite size is very important for catalysts. Here the crystallite size is determined in the following way using the Scherrer equation that is built into the TOPAS software. However, using TOPAS the Scherrer equation (Figure 2.17) is adjustable depending on the type of sample being analyzed such as if the crystallites are present as cubes, spheres or rods.

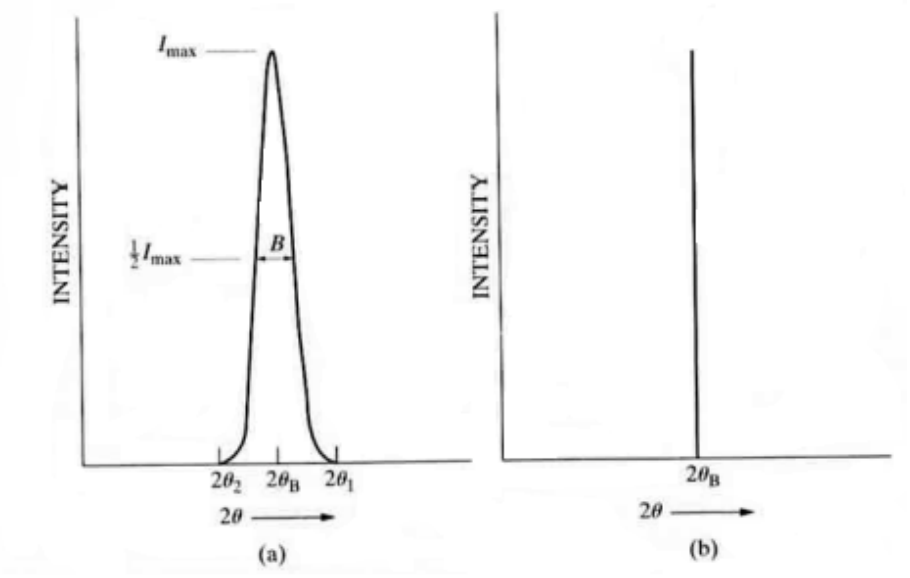


Figure 2.17: The Scherrer equation is derived from the full width at half maximum (FWHM)[51].

The Scherrer equation is given by

$$\tau = \frac{k\lambda}{Bcos\theta}$$

where k is the shape function that is dependent on the morphology of the crystallites being studied

If Lorentzian $B_{exp} = B_{size} + B_{inst}$

If Gaussian $B^2_{exp} = B^2_{size} + B^2_{inst}$

2.3.2 The final Rietveld equation.

Putting all the parameters together the calculated diffraction pattern to attain the final Rietveld equation given by

$$y_{ci} = s \sum L_k \left\| F_k \right\|^2 \phi(2\theta_i - \theta_k) P_k A + y_{bi}$$

where y_{ci} is the calculated intensity at the i_{th} step, s scale factor, k the Miller indices, hkl for a Bragg reflection, L_k multiplicity, Lorentz and polarization

factor F_k structure factor for the k_{th} Bragg reflection, ϕ reflection profile function, P_k Preferred orientation, A absorption factor and y_{bi} for the background intensity at the i_{th} step.

There are some basic requirements for a good Rietveld refinement. These include :

1. accurate diffraction data
2. a reasonable starting structural model
   (a) space group symmetry
   (b) approximate atomic positions
   (c) the model may be from : isostructural materials, theoretical simulations or high-resolution atomic imaging.

There are a number of factors that are produced when a refinement is completed, these factors allow one to determine the goodness of fit of the calculated pattern. These factors are

R-structure factor given by

$$R_f = \frac{\sum \left\| I_k('obs')^{\frac{1}{2}} - I_k('calc')^{\frac{1}{2}} \right\|}{\sum I_k('obs')^{\frac{1}{2}}}$$

R-Bragg factor by

$$R_B = \frac{\sum \|I_k('obs') - I_k('calc')\|}{\sum I_k('obs')}$$

R-pattern

$$R_p = \frac{\sum \|y_i(obs) - y_i(calc)\|}{\sum y_i(obs)}$$

R-weighted pattern

$$R_{wp} = \left\{ \frac{\sum w_i(y_i(obs) - y_i(calc))^2}{\sum w_i(y_i(obs))^2} \right\}^{\frac{1}{2}}$$

Reduced Chi-squared

$$\chi^2 = \left(\frac{R_{wp}}{R_{exp}} \right)^2$$

The most commonly used equation is the R_{wp}. This is the equation that will be used in this text to determine the goodness of fit of the calculated patterns.

In summary the parameters in the refinement are changed for the crystal structure and an observation of how they change the calculated diffraction pattern is noted. The unit cell lattice parameters determine where the diffraction peaks are observed and the peak intensity is determined by a number of factors including what atoms are in the crystal and their positions xyz, the site occupancy of the atom, the relative scattering strength of the atom and the scattering factor, a product of the number of electrons around the atom and finally the thermal parameter of the atom.

2.3.3 Refinement methods used on the data in this thesis

Rietveld refinements were performed using TOPAS V4.2. Structure solution and parametric Rietveld refinement data was obtained using the launch mode interface. All other reported refinements were performed using the graphical user interface.

Quantitative Rietveld refinement was conducted in order to determine the relative phase abundance and average crystallite sizes of the crystalline phases present in the sample. Several variables employed in a refinement should vary smoothly with temperature or remain constant over the entire temperature range. Therefore, for these refinements several variables were described using overall descriptions. These include an overall simple axial model to describe axial divergence and an overall parameter to describe the zero point off set of the diffractometer. These variables were averaged over all diffractograms in the data set thus lowering the error in the minimization procedure. Furthermore, several variables which vary independently with temperature were refined. These include lattice parameters of all phases present in the sample as well as the general position of the oxygen atoms within the rutile (monoclinic-TiO_2) structure. Since the morphology of sample can be well defined as rod-like it was also deemed necessary to refine several spherical harmonics vectors so as to account for preferred orientation within the sample.

2.3.4 Input Files and Refinement Parameters.

A refined TOPAS input file for the first diffraction pattern collected at 30°C during the heat treatment of the Degussa P25 support is given as an example with accompanying explanations as shown in Figure 2.18. Green text is used for names, such as file names, structure names as well as space group names. The text in light blue represents parameters that were not refined as only selected parameters were chosen for refinement depending on the sample and instrument setup. The Figures of merit are not refinable parameters but were rather measures of the accuracy of the refinement and thus were able to change. Red text represents parameters that were to be refined, where @ corresponds to the refine operator in TOPAS. The example shown here contained 19 independent parameters. All other input files were merely variations of this example with minor differences in the number of parameters that were refined. This was due to the different types and number of structures as well as preferred orientation parameters that were often required for certain phases due to their morphology such as a nanorod type structure. The number of refinable parameters was kept as low as possible for every refinement. The errors associated with each parameter (also calculated by TOPAS) were monitored in order to ensure that the standard deviation was always less than 8 %, ensuring the precision of the refinement. A silicon spike is also present in the input file to determine the peak positions for calibration.

Refinements were completed using the graphical user interface (GUI) in TOPAS as opposed to launch mode. The refinements were parametrized with refined parameters being a global zero error, absorption correction and simple axial model. Therefore, the instrument profile remained constant over all data in the data set as the in-situ variable temperature data collections consist, in some cases, of over 90 diffraction patterns in a single data set. Since the background was a convolution of both sample and instrument specific aberrations i.e. incoherent scattering and destructive interference which is likely considering that many of the the samples are nano sized. This is further perpetuated by air scattering due to the lack of an incident beam anti-scatter slit and thus the noise was picked up by the detector. The defined independent variables for each of the two oxygen general positions within the rutile structure are denoted oxyXX where XX was a number corresponding to the diffraction pattern number within the data set. Separately defined variables for each spherical harmonic function over all the data for the rutile structure were imputted.



Figure 2.18: An example of the input file used for the refinement of Degussa P25 support. Rietveld refinement input files such as this were used throughout the thesis where in-situ PXRD data was collected. Over 1100 Rietveld refinements were conducted on in-situ data in this thesis.

In the case of the rutile nanorods to account for the direction of propagation of the nanorod structure, the use of the spherical harmonic algorithm was valid. Furthermore, due to the morphology of the nanorods, the (110) peak was over estimated in intensity while the (011) and (111) were under estimated in intensity. While increasing the order of magnitude of the spherical harmonic (SH) function does remedied the situation the result was unfortunately, physically meaningless. A possible way of using a higher order SH function would be to limit the minimum values to "Zero" since negative SH values were not permissible. In some refinements the range of the refinement was limited in order to determine the morphology of the nanorods (Chapter 9).

This process occurred over all data. Given the fact that the diffracted intensity is so low due to the nanostructure of the material it is possible that one may over parametrize the data by adding further convolutions and complex descriptions to the consequent refinement. Furthermore, low intensity data runs the risk of data over parametrization since counting errors are significant, all necessary steps were taken to avoid this. This can be seen from the raised background which is not uncommon for nano systems.

2.4 Electron Microscopy

Much of this section was derived from D. B. Williams and C. B. Carter, Transmission Electron Microscopy for Materials Science[53]. With the growth of research interest into nanotechnology a method for studying these materials at the nanoscale was needed. TEM allowed for the atomic resolution study of the materials as well as being able to analyze the materials defects and crystallography. Further, this was coupled to the instruments ability to collect spectroscopic as well as diffraction data from sub-nanometer sections of the sample. For these reasons and many more TEM is an indispensable technique in the characterization of nanomaterials.

In TEM a sample, that must be less than 200 nm in thickness, is placed into a high vacuum and is then bombarded with a highly focused, near to single energy electron beam. The beam has enough energy such that the electrons are able to pass all the way through the sample. A series of electromagnetic lenses focuses the transmitted electrons. These transmitted electrons then form an image from the region that the beam was focused on provided the

material has sufficient contrast. Like all techniques TEM has both advantages and disadvantages.

Unlike XRD, TEM is not a bulk technique and so analysis must be conducted on a large number of randomly selected portions of the same sample in order to attain good sampling statistics. However the resolution limit is what gives TEM a major advantage when compared to many other techniques. When applied to the characterization of nanomaterials TEM is invaluable as it is able to image metallic nanoparticles on various oxide supports even when then nanoparticles are less than 2 nm in size! This is a feat that no XRD instrument has attained. Further TEM also gives information on how the nanoparticles are distributed over the catalyst. Homogenous distribution of nanoparticles is crucial for good activity and is another piece of information that cannot be gained from using XRD. However, better characterization of a material is when both of these techniques were used in tandem.

Electrons are very strongly scattered when compared to X-rays, this is because electrons are charged particles and thus they interact with both the electron cloud and the nucleus of the atom, whereas X-rays only interact with the nucleus.

2.4.1 The concept of resolution

Resolution is defined as the smallest point to point distance that can accurately be resolved. The classical Rayleigh description of the visible light microscope is given by the equation

$$\delta = \frac{0.61\lambda}{\mu sin\beta}$$

Where λ is the wavelength of the radiation, μ is the refractive index of the viewing medium and β is the semi-angle of collection of the magnifying lens. The term $\mu sin\beta$ is often referred to as the numerical aperture and is approximated to unity, thus the only variable that affects the resolution in the above equation is the wavelength of the electron beam. In an electron microscope, the equation can be simplified further, finally resulting in a approximation for resolution being $\approx 1.22\frac{\lambda}{\beta}$

De Broglie then showed that the wavelength of the elections is related to their

energy, E, and can be approximated to

$$\lambda = \frac{1.22}{E^{\frac{1}{2}}}$$

where E is in eV and λ is in nm. This result implies that the resolution of the microscope can be bettered if the energy of the electrons is increased. In applications it is crucial that good resolution is obtained. Very small nanoparticles (2 nm or smaller) are highly active for the CO oxidation reaction. Even the best XRD instruments cannot accurately characterize particles of this size, so the HR-TEM becomes an invaluable tool to determine how the particles are deposited over the surface, their coordination to the surface, their size distribution, ie, if the particles are monodisperse over the surface of the support, as well as the morphology and crystallinity can be investigated.

Electrons are a form of ionizing radiation that is capable of removing a tightly bound electron from deep within the inner shells of the atom. This is done by the incoming electron transferring some of its energy to individual atoms in the sample. The result of this effect allows for a number of techniques collectively known as AEM or analytical electron microscopy as shown in Figure 2.19. These methods allow chemical information as well as other details about the sample to be known. One such technique known as EDS (energy dispersive spectroscopy) is used in this thesis and is covered in Section 2.4.4.

Data in this thesis was collected on a Tecnai F20 X-Twin TEM with C_s of 1.0 mm and a point to point resolution limit of 1.9 Å operated at 200 kV. The machine was equipped with a high angle annular dark field (HAADF) detector for scanning transmission electron microscopy, a Gatan electron energy-loss spectroscopy (EELS) filter and GIF imaging system. The standard bright field imaging system is a 4 k chip (2048 x 2048 pixels). Images were collected in spot-size 1 with beam spread to ensure low-dose conditions at 200 kV. Images were collected at, or as close to, the Sherzer defocus setting of the microscope. Samples were loaded onto holey carbon films for analysis. The energy dispersive spectroscopy (EDS) system is an Oxford EDAX system. An FEI Tecnai G2 Spirit electron microscope operating at 120 kV was also used.

ImageJ software was used to examine the collected TEM images. TomoJ was used to produce a 3D tomogram of 134 TEM images in Section 9.7

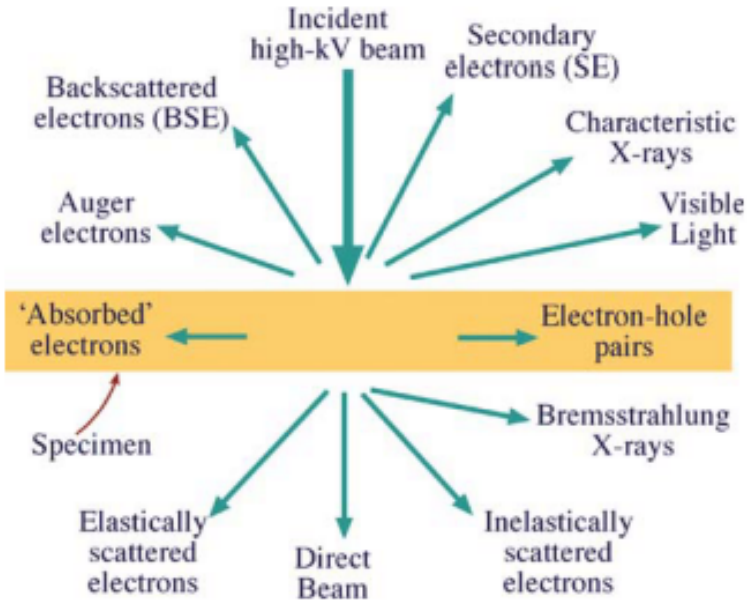


Figure 2.19: A number of different types of signals that are produced when an electron beam contacts a specimen. Most of these signals can be detected using different types of TEM. When a number of these techniques are combines the TEM becomes a very powerful instrument in materials characterization[53].

2.4.2 Electron diffraction (ED and SAD)

In a TEM the electron beam is treated in two different ways. When the electron is scattered it is treated as a particle, but when the electron is diffracted it is treated as a wave. Diffraction forms a subset of elastic scattering. Scattering may be applied to both particles and to diffraction of waves, however both of these terms apply to electrons. In a TEM diffraction is not limited to Bragg diffraction but encompasses all types of diffraction occurring from any interaction from a wave. In 1927 Thompson, Reid, Davisson, and Germer independently showed that it was possible for electrons, when being passed through thin crystals of nickel to be diffracted. However it was not until 1939 that Kossel and M Ollenstedt first observed diffraction inside a TEM[53]. For the TEM electron beam probe, magnetic lenses, now aberration corrected, are extremely difficult for X-ray and neutron competitors to produce equivalent systems, even with much more limited performance. Perhaps most important of all, energy-loss spectroscopy (EELS) provides unrivaled spatial resolution combined with parallel detection that is not possible with X-ray absorption spectroscopy (XAS) where absorbed X-rays disappear, rather than losing some energy and continuing to the detector. Today electron diffraction is one of the most useful aspects of a TEM when applied to nanotechnology. One of the

reasons for this usefulness of the diffraction pattern is that it can always be related to the crystallographic and analytical image of the specimen. At all times the crystallographic information in the diffraction pattern and all the analytical information can be related to the image of the specimen.

The objective lens in a TEM takes the beam of electrons emerging from the back of the sample and disperses them in the back focal plane to create a diffraction pattern and then finally recombines them to form an image in the image plane. Figure 2.20 shows how the electrons travel through the TEM to produce a diffraction image. The intensity of the direct beam needs to be accounted for as a very intense direct beam can damage both the sample and the viewing screen and saturate the CCD camera. To compensate for this an aperture can be inserted above the specimen which will control how much of the beam is able to reach the sample and hence the CCD camera.

Diffraction mode involves projecting the diffraction pattern onto the imaging screen and the lens selects the back focal plane, whereas image mode involves projecting the image onto the screen and in this case the lens selects the image plane of the objective lens as its object. Thus, in summary, the basic principle of TEM operation when you want to look at a diffraction pattern is the back focal point of the objective lens involving the insertion of a SAD aperture into the image plane of the objective lens as shown in Figure 2.21.

2.4.3 Scanning transmission electron microscopy (STEM)

With the use of a fine probe one is able to produce STEM images. STEM differs from SEM due to the fact that the scanning beam must not change direction as the beam is scanned, in a SEM the scanning beam simply pivots about a point above the specimen. If the beam does change the electron diffraction and scattering of the electron beam will change resulting in a very difficult image to try and interpret. Thus the beam must scan parallel to the optical axis at all times such that it copies the parallel beam in a TEM even though it is in scanning mode.

A very useful fact of STEM mode is that lenses are not used to form images. This is useful because lenses in the TEM contribute to many types of aberrations that contribute to lower resolutions than what are theoretical possible. Thus the defects that occur in the lenses do not affect the STEM images the

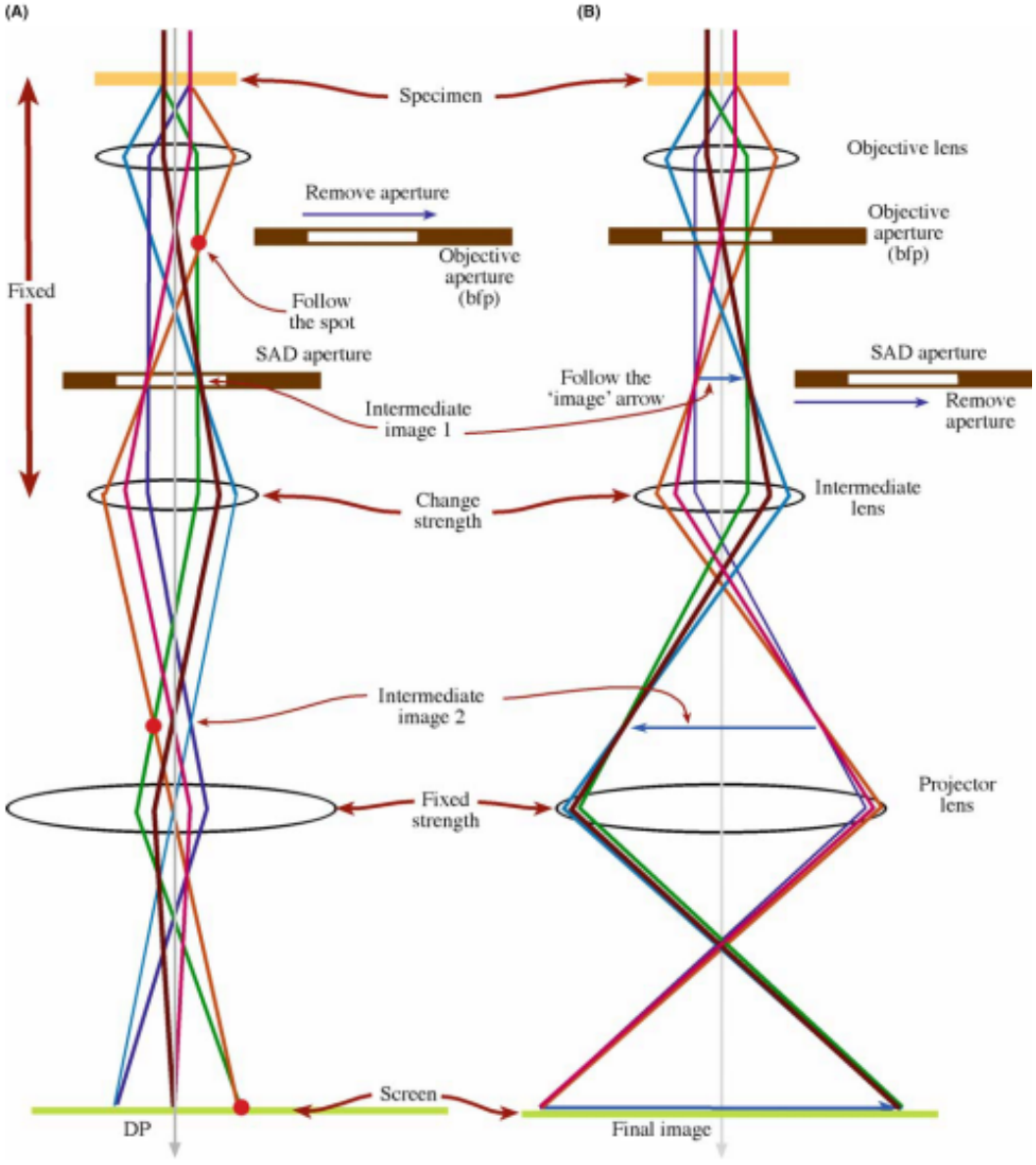


Figure 2.20: The two basic imaging modes in a TEM are illustrated above a) Diffraction mode and b) Image model[53].

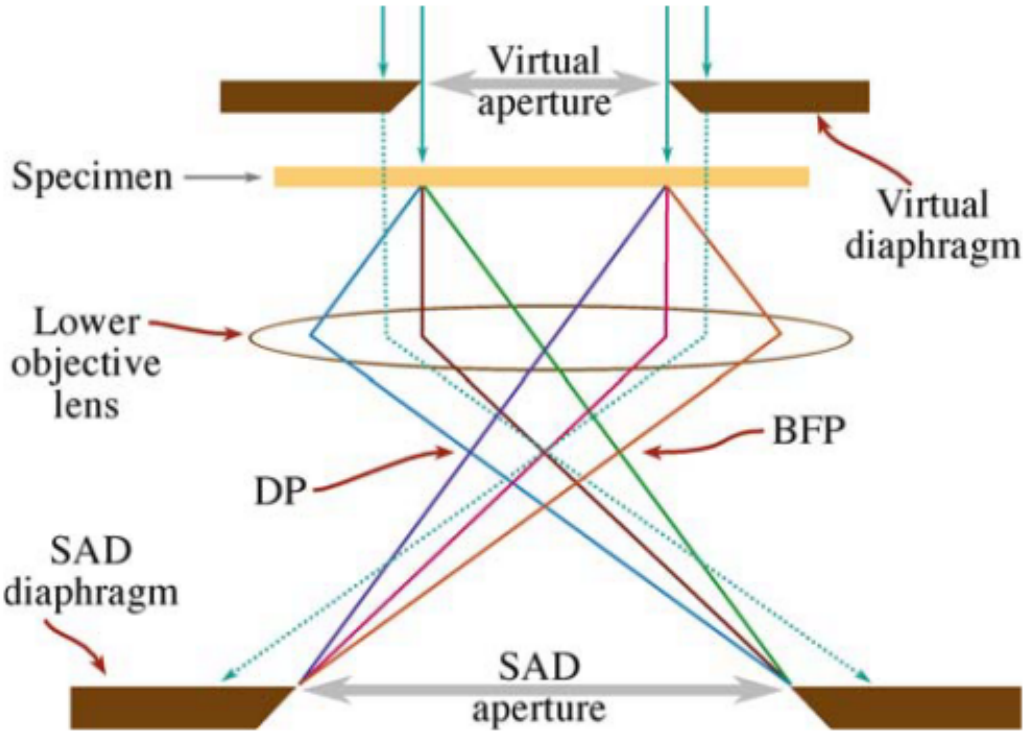


Figure 2.21: Ray diagram showing the formation of a diffraction pattern[53]. The insertion of an aperture in the image plane results in the creation of a virtual aperture in the plane of the specimen which is demonstrated here slightly above the specimen plane. Electrons that find themselves inside the area of the virtual aperture at the entrance surface of the specimen will be allowed through into the imaging system to contribute to the selected area diffraction pattern. All other electrons which are represented by the dotted lines will hit the selected area diffraction diaphragm.

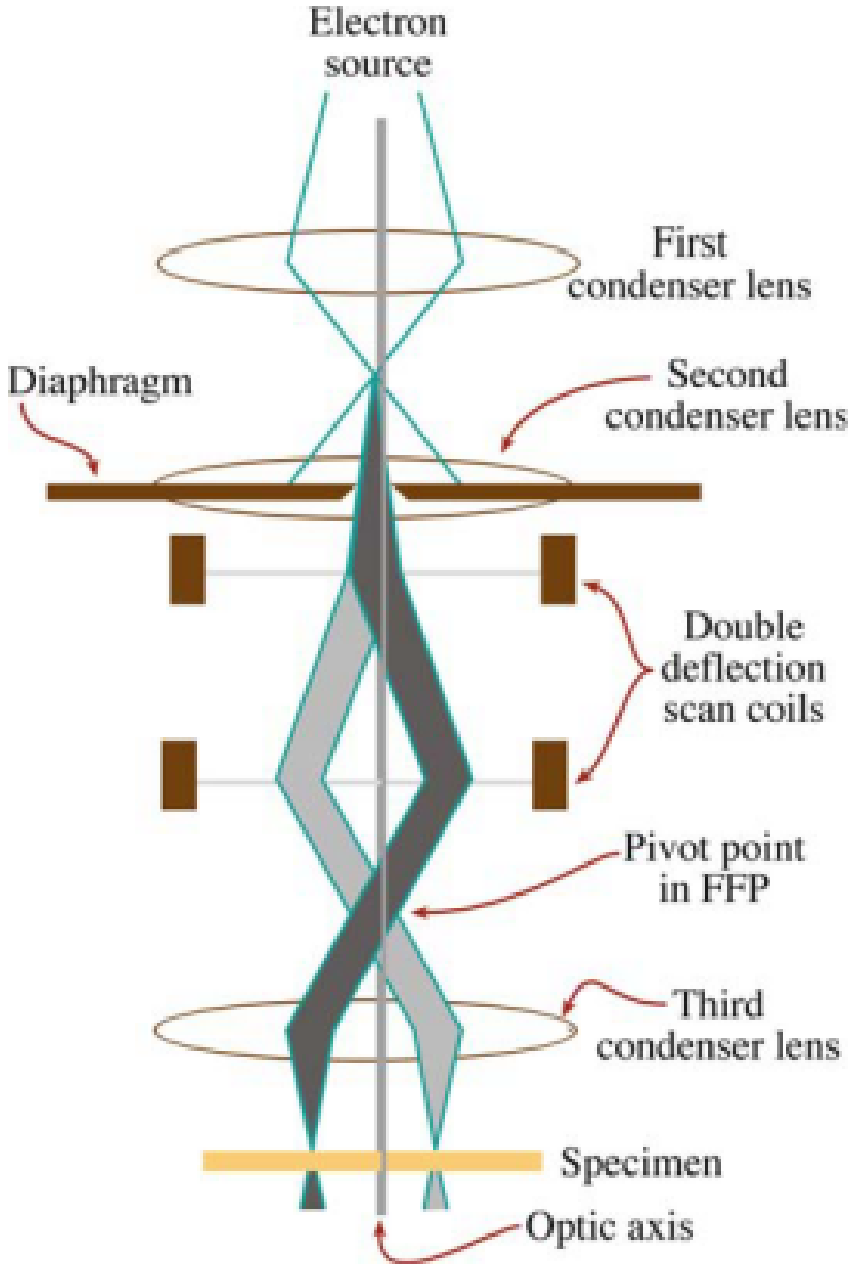


Figure 2.22: Scanning the convergent probe for STEM image formation using two pairs of scan coils between the C2 lens, which is usually switched off, and the upper-objective polepiece. The double-deflection process ensures that the probe remains parallel to the optic axis as it scans across the specimen surface[53].

way they affect normal TEM images. An image is formed over several seconds as a STEM signal is generated at a single point over a sample that is detected and amplified then transferred to a computer. The signal is collected by the insertion of a bright field detector which intercepts the direct beam electrons which varies in intensity depending on a specific point on the specimen that is illuminated by the probe at that specific time.

2.4.4 Energy Dispersive Spectroscopy (EDS)

When the electron beam produced in a TEM strikes the specimen electrons in the inner core of the atom can be ejected. As a result outer electrons then drop down to replace the electrons that have been ejected. When the outer electrons move in to replace the ejected ones there is a change in energy of the electron as it moves from the outer to inner shell. Thus an X-ray with an energy that is characteristic to the element is released. It is this X-ray that is detected by the EDS detector which uses a silicon or germanium detector as shown in Figure 2.23. This is made possible by the fast processing speeds from modern semiconductors. The detector in turn produces a voltage pulse that is proportional to the X-ray energy. This pulse is then converted into a signal and is then counted in energy channels that are displayed as spectrum and even a compositional map. One of the most important aspects for EDS is to maximize the number of X-ray counts in order to attain a strong signal.

The method to form EDS spectra is an extension of a TEM or STEM image. Once a TEM or STEM image is collected of the area one wants to analyze the beam is condensed. It is easier in STEM mode to compensate for drift and also easier to form compositional images. Thus in STEM mode an image is created and then the scanning probe is simply stopped in the position where analysis is wanted and then the EDS is switched on.

2.5 Tomography

I would like to express my gratitude to Dr P.J Franklyn for his help with the collection and reconstruction of the TEM images used to produce the tomogram in this thesis.

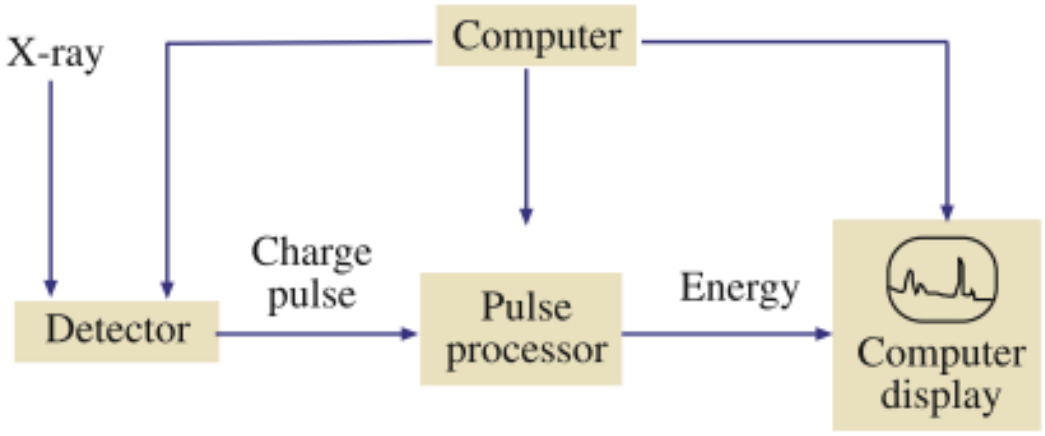


Figure 2.23: The principal of EDS[53].

Traditional electron microscopy suffers from a compression of the depth information into a single dimension, leading to the so-called "two-headed rhinoceros problem". In brief, this states that if you were to view one rhinoceros standing facing left, with another standing facing right such that the front legs of the one lined up with the back legs of the other (and vice-versa), the result, if you were to view the scene in projection, would be that it would be impossible to tell if there were two rhinoceros or one with a head on its front and back. The same is true in TEM, where, in a standard image, it is impossible to determine from a single image the relative positioning of various particles.

This problem can be overcome by tilting the sample to a different angle and recording additional images of the same region of the sample. In this manner, the relative separation of two particles can be determined. Tomography extends this further by rotating the sample over a whole range of tilting angles, with images collected at regular tilt angles. The details of each image can then be back-projected in order to assemble a full three dimensional representation of the sample.

The FEI Tecnai F20 microscope housed at University of the Western Cape has proprietary FEI software that automates the process. The software assists in the alignment of the sample (as the tilt axis of the sample holder must co-incide with the eucentric height of the microscope to ensure minimal drift over the tilt-range). Once the initial and final tilt angle are then given, as well as the tilt series spacing, the software then automatically proceeds through the tilt series, ensuring the alignment of the sample and the microscope holds approximately constant over entire tilt series.

Software (such as eTomo) was then used to reconstruct the tilt series. Due to the thickness of the samples used in this work, it was found that reconstructions were not sensible, or rather were not the best means of analysing the data. Instead, the tilt series itself was examined and individual gold nanoparticles were tracked to determine their relative positions on the support.

2.6 Catalytic testing

The following instrumentation and setup was used for CO oxidation testing of all the catalysts. 150 mg of catalyst was used in each case at NTP with a gas hourly space velocity of 24000ml.h^{-1}.g^{-1}. The gasses were a combination of 5% CO in He and 10% O_2 in He. Prior to all data collections the catalysts were exposed to H_2 for one hour at 150°C to ensure that all the tested catalysts were fully reduced. Analysis was undertaken at a minimum temperature of 50°C as the thermocontroller errors increase as the temperature is lowered further. The Mintek Aurolite catalyst was used as a standard for comparison. The system is highlighted below in Figure 2.24 and consists of the following

- a TCD-GC
- 6 way sample valve inlet system
- a Garmac TCD detector
- a Supelco Carboxon 1000 column
- data acquisition software used is the Clarity data package.

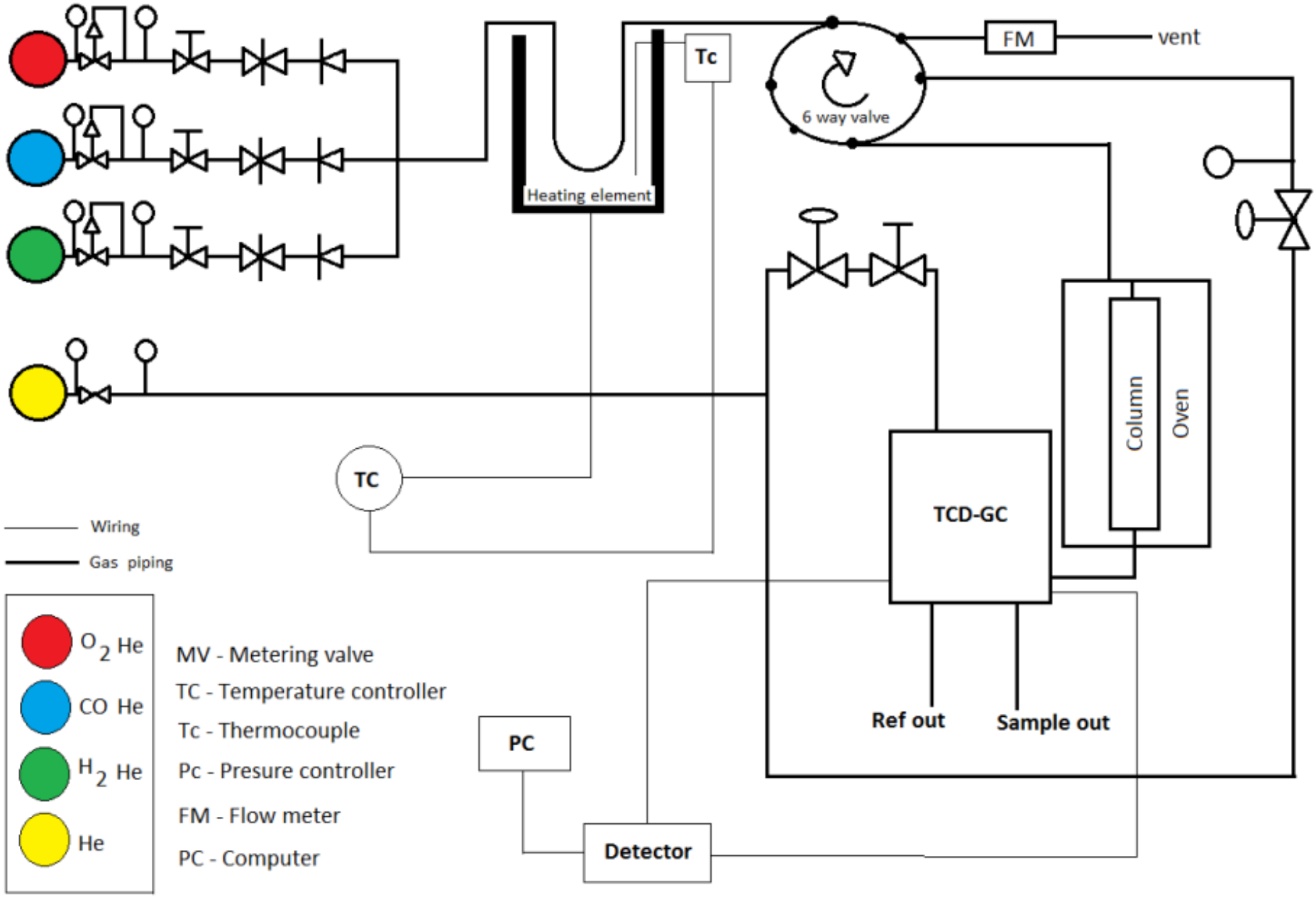


Figure 2.24: CO oxidation catalytic testing unit setup.

Chapter 3

Aims

The aim of this work was to make an incremental improvement in the ongoing search for a means of producing a thermally stable, but highly active, gold catalyst. The intention was to work on the theoretical view that if the gold nanoparticles could be stabilised and if the interaction between the gold and the surface of the support material could be enhanced, then the stability of the catalyst would improve. The initial work aimed to use platinum as a bimetallic alloy to enhance the stability of gold. In order to measure the effect of platinum the synthesis was to be carried out on a support hostile to gold deposition, but also one that would not interfere in the PXRD analysis of the catalysts. This work resulted in the development of a robust and reproducible synthesis method whereby gold nanoparticles were stabilised via the addition of small amounts of platinum.

A number of commercial as well as laboratory synthesised catalyst supports consisting of various forms of titania were chosen so as to see the supports effect on the stabilisation of gold nanoparticles. From the information gained from studying a current industrial gold catalyst, the reasons for its deactivation could be used to develop a catalyst that is able to resist these deactivation pathways. Based on the results of this work, a novel morphology of titanium dioxide was to be found and the deposition precipitation method developed was varied to optimize conditions to create the target catalyst. The aim was to then completely characterize the synthesised catalyst using a variety of analytical techniques and so to carry out the first in-situ variable temperature study of the growth of gold nanoparticles on a support using in-situ PXRD. The Rietveld method would be applied to both current industrial gold based catalysts to

quantitatively determine deactivation mechanisms as well as to the synthesised novel catalyst produced to determine the properties for its thermal stability under non-ambient conditions With the characterization complete, the aim was to test the catalytic activity of the novel catalyst and to compare this to existing commercial catalysts. Finally, the aim was to develop a hypothesis around the reasons for the observed behavior of the catalyst in terms of the structural chemistry of the nano-particles and the support.

Chapter 4

Au and Au-Pt on amorphous silica and zirconia

4.1 Introduction

Deposition of gold and platinum on amorphous silica and zirconia using the standard Deposition-Precipitation method (DP)

The DP method involves an incremental increase in the pH of a solution in which a support material was suspended together with a metallic precursor. An hydroxide or hydrated oxide is then deposited onto the surface of the support as the pH was raised. The process was first used by Geus and co-workers to produce supported nickel and copper catalysts[54,55]. The precursors used in preparing the supported gold catalysts were complexes or salts where gold is usually in the +III oxidation state, however a few available gold salts are in the +I oxidation state. This state is however more unstable. The gold precursor most frequently used is chloroauric acid ($HAuCl_4.3H_20$), which is a commercially available solid with an orange colour. In aqueous solution it is a strong acid and is capable of dissolving alumina and magnesia. When being transfered during experiments it was was observed to dissolve the metallic surface of spatulas used to transfer the crystals! The speciation of the gold ions in solution depends strongly on the concentration, pH and temperature of the solution. When chloroauric acid is dissolved in water it forms anionic

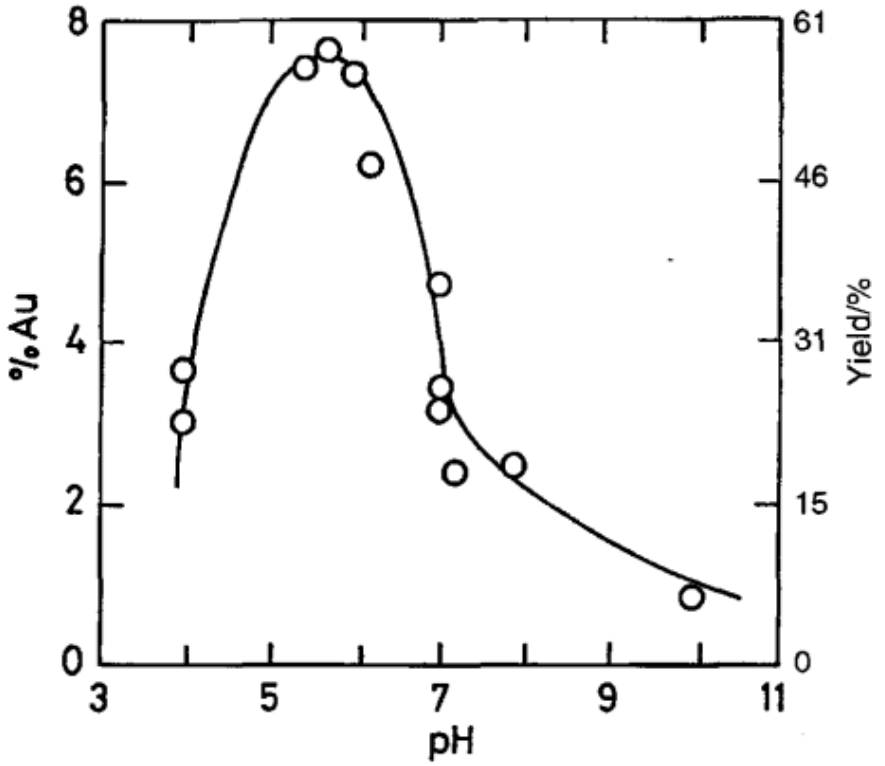


Figure 4.1: Gold loading and yield of DP versus solution pH for Au-TiO_2 supported on Degussa P-25. The catalysts were prepared by DP with NaOH used as the base and preparation at 75°C with a nominal gold loading of 13 wt.%[57].

hydrochlorogold(III) complexes of the form $[Au(OH)_xCl_{4-x}]^-$. Thermodynamic calculations have shown there are three types of gold speciation as pH was increased[56]. These were

1. Hydrolysis by replacement of the chloride ion by an hydroxyl ion.
2. Displacement of the chloride ion from a complex anion by water, giving a neutral species.
3. Loss of a proton from a neutral hydrated ion.

Figure 4.1 shows the maximum loading attained was just under 8% after a nominal gold loading of 13 wt %. The gold loading was shown to be dependent on pH and care had to be taken during the synthesis to monitor any pH changes as shown in Figure 4.2. It was possible to increase the gold loading by using urea as opposed to other forms of bases. The dependance of gold loading on pH was due to the isoelectric point of the support material[25,41]. The isoelectric

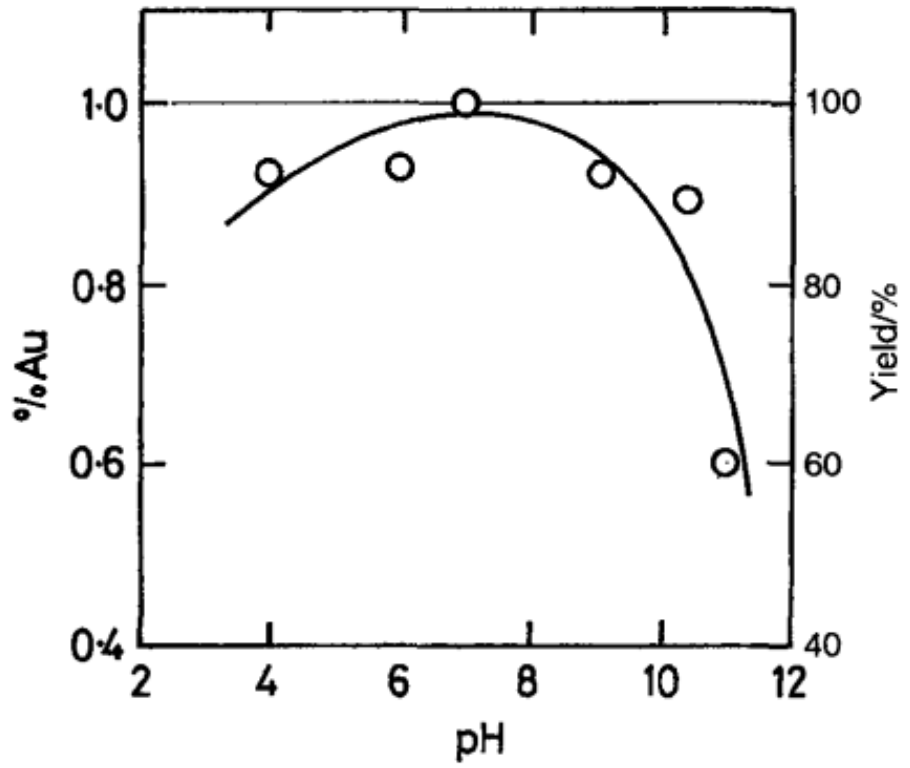


Figure 4.2: Gold loading and yield of the DP method versus solution pH for Au-TiO_2 on Degussa P-25. The catalysts were prepared by DP with NaOH used as the base. Preparation was at 75°C with a nominal gold loading of 1 wt%[58].

point of a material is the pH at which a particular molecule or surface carries no net electrical charge. Thus at certain pH values the gold nanoparticles are either attracted or repelled by the support. For this reason some supports such as silica and alumina are not considered good supports for gold nanoparticles as the isoelectric range of these materials is not ideal for strong binding between the gold nanoparticles and the support surface[25,41].

The isoelectric point determined how strongly the gold will bind to the support surface at different pH's[25,41]. This is a very important parameter in gold catalysis as strong contact with the support is crucial for the stability of the catalyst at non-ambient temperatures[41]. Isoelectric ranges are the reason that the impregnation technique for preparing catalysts does not work well as no bond is formed during the process between the support and the metal nanoparticle.

With the use of a base such as ammonium hydroxide, sodium hydroxide or calcium carbonate the control of pH of the entire solution is possible. A highly basic solution first contacted the acidic solution in very small pockets as it was added dropwise. This resulted in highly basic regions which were created

within the solution albeit only for a very short period of time. This may affect the metal loadings as the support may find itself in the incorrect isoelectric range as the pH of the solution surrounding the support is too high due to the high concentration of base in the vicinity of the support particle. As the pH drops due to more acidic solution surrounding the small region of high alkalinity the gold is able to once again start loading onto the support efficiently.

Following these conclusions it was decided to try and use urea alone as it acts as a delay base by the equation :

$$CO(NH_2)_2 + 3H_2O \rightarrow CO_2 + 2NH_4^+ + 2OH^-$$

A problem that was only discovered after a number of reactions and searching through the literature was that urea needed a significant amount of time to hydrolyze. Thus the use of a standard DP method was not sufficient. Further, for the production of large amounts of catalyst such as in an industrial environment, the standard DP method does not suffice.

In summary, the initial syntheses were undertaken using urea. However, unwittingly insufficient time was allocated for the hydrolysis to occur and thus the pH of the solution was too low after the synthesis was completed as the addition of the chloroauric acid caused the pH of the solution to decline. To compensate for this effect this ammonium hydroxide was added to increase the strength of the base.

Only in the final stages of the synthesis development was a complete change to the method instituted. This change resulted in using urea alone without ammonium hydroxide. The entire solution was heated for 24 hours to allow for the full hydrolysis of base to occur. This resulted in the correct pH being achieved for the duration of the synthesis. The method development will be discussed further in the upcoming sections.

Hydrolysis of urea occurred when the solution temperature rose above 75°C. Once this happens there was a gradual and homogeneous release of hydroxyl ions and an increase in the solution pH. Thus the base was gradually released and in so doing, the solution pH slowly increased, which inhibited the build up of small pockets of high alkalinity found when using other types of bases.

Small gold particle sizes could be attained using a number of supports including silica and titania provided that the deposition time is significantly long enough[41]. With the correct selection of urea concentration both small particle sizes and high metal loadings were achieved. Quantitative Rietveld refinements confirmed the high metal loadings as well as small metal crystallite sizes.

The proposed mechanism was that the deposition starts with hydroxychloro-gold (III) species at pH 2-3 followed by the interaction with the positively charged support oxide surface. Large gold particles are now on the surface and the following step in the process is peptisation. During this process the gold re-disperses itself over the surface and as time passes the gold dispersion becomes better and better with smaller and smaller gold particles resulting[59].

4.2 Synthesis

4.2.1 Deposition of Au and Au-Pt onto amorphous silica and zirconia using the DP method

A 500 mL beaker was placed into a water bath and 200 mL of deionized water was added into the beaker. Amorphous silica (which will just be referred to as silica) or zirconia were used as the catalyst supports, and were added to the water. A stirrer bar was placed into the beaker along with a thermocouple to allow for the solution to be heated to 75°C using a temperature controlled heater stirrer. While the reaction proceeded the temperature was maintained at 75°C. Two burettes were then filled, one with $HAuCl_4.xH_2O$, where x = 3, such that the silica and zirconia would have a theoretical 5% gold loading and the second burette was filled with urea solution. In later experiments ammonium hydroxide of varying concentrations was also used in conjunction with urea. $H_2PtCl_6.xH_2O$, where x = 6 was used in experiments where platinum was added to the 5% gold loading which is shown in Table 4.1. The beaker was covered with parafilm so that no amount of solution could escape due to evaporation, as well as stop the dissolution of CO_2 from the atmosphere. A calibrated pH meter was inserted into the solution to monitor the pH level of the reaction as it progressed.

The $HAuCl_4.3H_2O$ solution was added drop wise over a period of 60 minutes under rapid stirring. As the gold solution was added the pH steadily declined.

The addition of base was needed in order to maintain pH control at a predetermined value. The chosen pH's of the solutions are given in Table 4.1. Once the reaction was completed the solutions were a pale yellow/orange colour depending on the chosen pH of the solution. The beaker was allowed to slowly cool down to room temperature over several hours. Stirring was continued while the solution cooled.

Following the cooling processes the colour of the solution was a dirty golden to light brown colour. The beaker was covered in parafilm and placed into a dark cupboard and left to age for three days. After three days of ageing the solution became clear with a brown/orange precipitate. This was an initial indicator that the gold and platinum had deposited onto the support. The experiment was repeated numerous times with a number of parameters being varied such as change in pH and different loadings of platinum.

The solution was then filtered via vacuum and rinsed through with 500 ml of deionized water heated to 75°C as this aids in the removal of any remaining chloride originating from the gold and platinum precursors. The pH was monitored and washing continued until the eluent reached neutrality. Nine samples were prepared and under varying conditions. Once the samples were prepared they were heated dried in an heating oven overnight at 85°C at and then heated in a furnace to 120°C, 200°C, 300°C and finally selected samples were heated at 400°C for one hour. Some experiments were repeated in triplicate once the reaction conditions were found to be correct. The samples were prepared for characterization using PXRD in order to analyze changes in the gold crystallite sizes. All reaction conditions of all the samples are given in Appendix A1 along with the corresponding PXRD diffractograms.

After completion of experiments 1 and 2 as shown in Table 4.1 the pH of the solution was 2.85. These experiments were completed over 1 hour, later discovered to be insufficient for the urea to hydrolyze and form a basic solution of the required pH. Thus, all the base provided in experiments 3-9 is from ammonium hydroxide and not urea. In later experiments discussed in Chapter 5. Urea was used over a 24 hour synthesis period.

4.2.2 Theoretical mass loading

All metal loadings were calculated via the following equation

Experiment	Au:Pt ratio (%)	Base (M)	Final pH	Support
1	5:0	0.1 urea	2.85	silica
2	5:0	1.0 urea	2.85	silica
3	5:0	1.0 urea , 0.25 NH_4OH	9.0	silica
4	5:0	1.0 urea, 0.25NH_4OH	9.0	silica
5	5:0	1.0 urea, 0.25NH_4OH	7.0	silica
6	5:1	1.0 urea, 0.25 NH_4OH	7.0	silica
7	5:1	1.0 urea, 0.25 NH_4OH	7.0	silica
8	5:2	1.0 urea, 0.25 NH_4OH	7.0	zirconia
9	5:2	1.0 urea, 0.25 NH_4OH	7.0	zirconia

Table 4.1: Reaction conditions for the preparation of samples. An important parameter is the final pH of the solution after completion of the DP synthesis as this effected gold loadings as well as particle size of the supported metal.

$$\text{Theoretical loading} = \frac{mass.Au}{massAu+mass.substrate}$$

4.2.3 Discussion of the synthesis method

The aim of initial experiments was to gain insight into the deposition-precipitation method. The two most important factors influencing the DP method are control of the pH and the correct selection of an appropriate base. The concentration of the base and the final pH of the solution both had a direct impact on the bonding of the gold and platinum nanoparticles onto the surface of the support as shown in Section 4.2.4 as well as the loading that can be achieved. Lower pH levels (approx. pH 7) resulted in high metal loadings. However, the gold nanoparticles, while being small are not as small as they would if the pH of the solution's is adjusted to pH 9. At pH 9 the metal loading then decreases compared to pH 7[41]. The best compromise between metal loading and particle size was attained by careful selection of pH.

4.2.4 PXRD

Once the synthesis was completed an interesting observation was made. When the samples were dried at room temperatures the resulting products were a pale white colour with a hint of golden yellow as shown by the first images in Figures



Figure 4.3: Various samples supported on silica prepared and heated under different conditions. Unheated sample (left), 200°C, 300°C and finally 400°C (far right). All samples are 5% Au on silica.



Figure 4.4: Unheated sample (left), 200°C, 300°C and finally 400°C (far right) The samples shown are 5% Au-1% Pt on silica. In all cases the different colours can be attributed to the samples optical absorption in the visible region of the spectrum which is due to the relativistic lowering of the gap between the 5d band and the Fermi level, without this effect the gold nanoparticles would be a white/silver colour and have the same propensity to tarnish and corrode[8].

4.3 and 4.4. This could be attributed to gold still being in the oxidized Au(I) - Au(III) state. However, once the samples were heated their colour changed to a range of different colours corresponding to reduction to metallic gold. A number of different colours were noted depending on the parameters chosen during the synthesis. This gave some qualitative evidence that the changes being made during the synthesis had a direct influence on the particle size as the colour of the catalysts can be directly related to the particle sizes of the supported metals[8]. Four temperatures were used for calcination, 120°C, 200°C, 300°C and 400°C. At 120°C the temperature was not high enough to reduce the catalysts and form reduced gold crystallites examinable by PXRD. Heating to 300°C for one hour resulted in the evolution of sharper diffraction peaks due to sintering of Au and Au-Pt nanoparticles on the support surface. Finally, selected samples were heated to 400°C for one hour and PXRD analysis was completed.

A number of different pH's were chosen as the target pH to study the effects of pH changes. Isoelectric points would suggest that pH 7-8 would be correct for silica. However, a number of pH's were selected in order to determine the best pH for good surface binding between the gold and the support material. Silica's isoelectric point lies between 1.7 and 3.5. pH's higher than this were

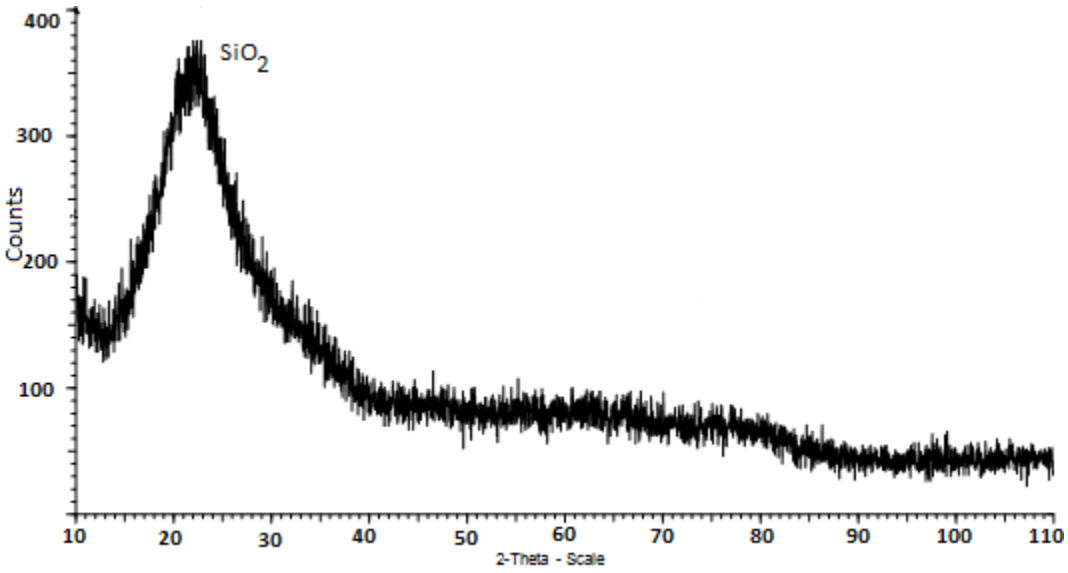


Figure 4.5: 5% Au on silica (*pH 2.85, 1.0 M urea, 120°C, 1hr*).

required for deposition of the metal nanoparticles onto the surface. All samples were repeated in triplicate for reproducibility. The bracketed labeling in the Figures has the following designation

(Final pH of the solution, Concentration of base used, Heating temperature of the prepared catalyst, Duration of heating).

PXRD analysis on the as synthesised samples showed no gold diffraction peaks as seen in Figure 4.5. This was expected, as only once the samples were heated to over 200°C were the Au(III) nanoparticles able to reduce to metallic gold. The characteristic gold peaks at 38.2° and 44.4° 2θ demonstrate the formation of the metallic gold phase along with the support as shown in in Figures 4.6 and 4.7. The large increase in the intensity and sharpness of the gold diffraction peaks showed the rapid increase in the gold crystallite size as the gold was reduced and sintering began to take effect. Scherrer analysis using PJF-XRD Analyzer gave mean particle sizes of 35 nm for the gold crystallites of the 5% Au on silica sample (*pH 2.85, 1.0 M urea, 300°C, 1hr*) shown in Figures 4.6 and 4.7. The very large crystallite sizes could be directly attributed to the low pH of the synthesis. At this low pH the surface of the support had no net surface charge due to the isoelectric range of the silica. The result was that gold particles were unable to form strong bonds with the support surface much like when using the impregnation method. When the catalyst was heated reduction of the gold nanoparticles took place and the sintering of the gold nanoparticles on the surface increases proportionally to the increase

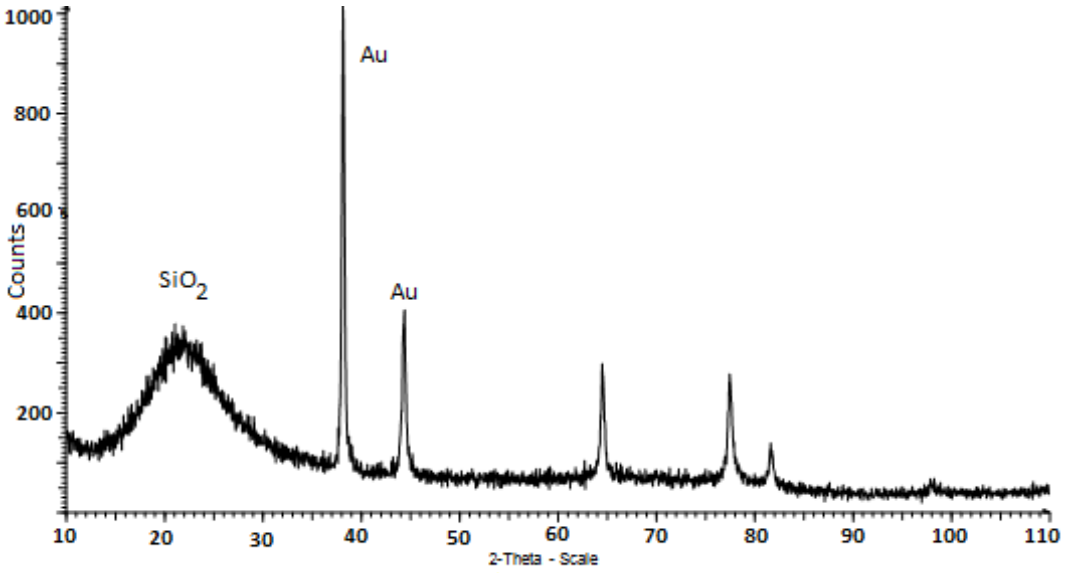


Figure 4.6: 5% Au on silica (*pH 2.85, 1.0 M urea, 300˚C, 1hr*).

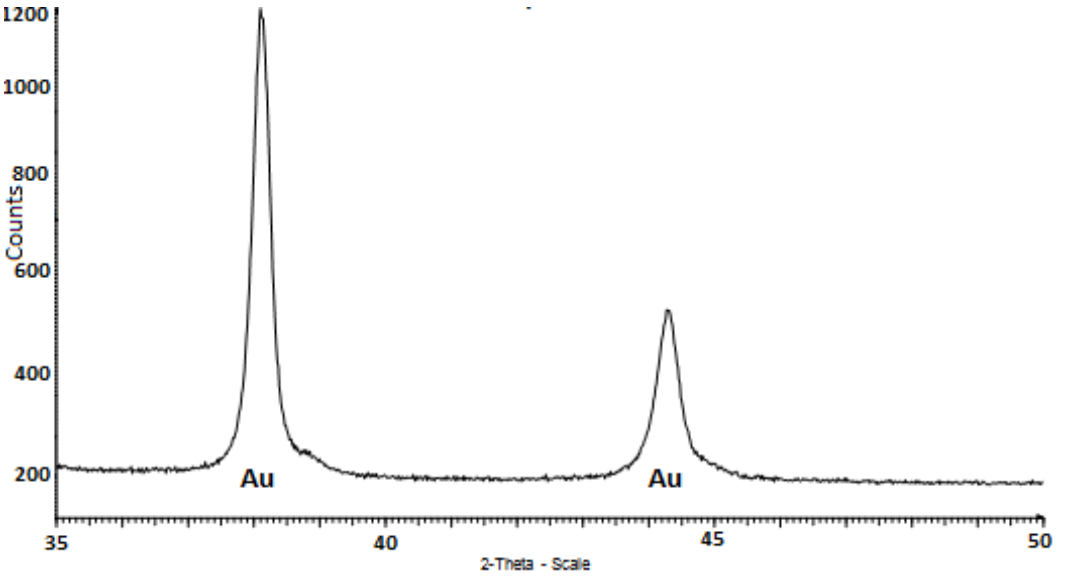


Figure 4.7: Zoomed view of 5% Au on silica (*pH 2.85, 1.0 M urea, 300˚C, 1hr*). The pattern showed the increased intensity of the gold diffraction peaks due to higher thermal exposure.

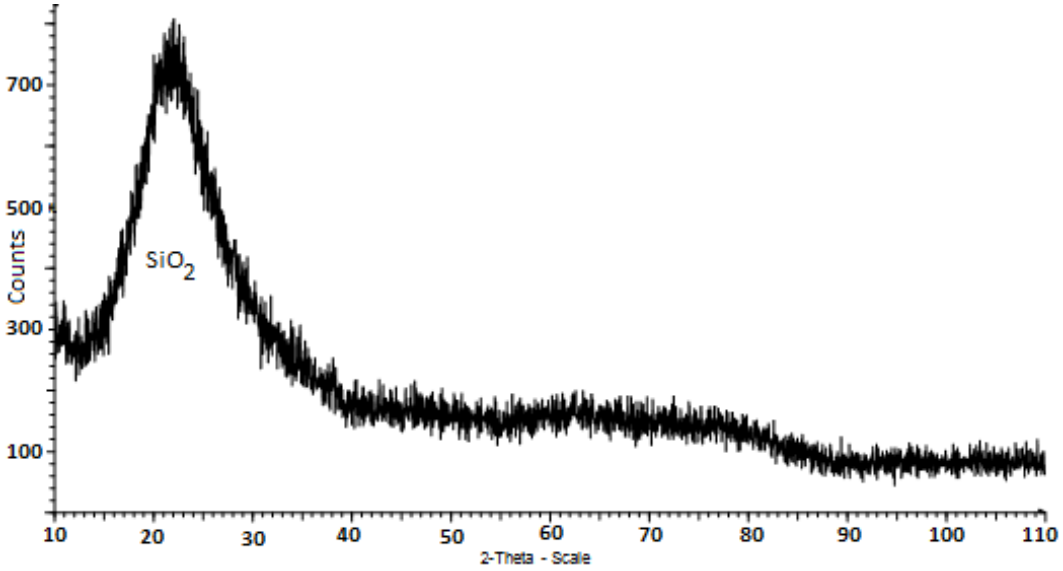


Figure 4.8: 5% Au on silica (*pH 9 at start of synthesis, pH 4 at end of synthesis, 1.0 M urea, 0.1 M NH_4OH, 120˚C, 1hr*). The pattern showed the amorphous nature of the support.

in temperature. As the gold nanoparticles were not bound to the surface they combine with other gold nanoparticles in order to relieve surface energy.

Following the initial findings, the pH value used during the synthesis was raised to between 7 and 9 to work in the appropriate isoelectric range. The addition of a 0.1 M ammonium hydroxide solution to the 1.0 M urea solution allowed the strength of the base solution to be increased such that the pH of the solution could be maintained at 7 for the duration of the synthesis.

Initially the pH of the solution was raised from 2.85 to 9 by the addition of a combination of 1.0 M urea and 0.1 M ammonium hydroxide. However, the concentration of the base was not sufficient to maintain this pH for the duration of the experiment as the chloroauric acid was added. After the synthesis was completed, the pH of the solution had dropped to 4. A further adjustment was needed in order to increase the concentration of the base such that higher pH's could be maintained.

Upon heating, the emergence of the gold diffraction peaks could be seen from the comparison between the PXRD patterns in Figure 4.8 and 4.9. Figure 4.9 is a zoomed in region of the PXRD pattern that shows the two principal gold diffraction peaks. The broadness and somewhat amorphous appearance of the peaks indicated the small crystallite sizes of the gold nanoparticles that were achieved even though the pH during the synthesis was not ideal. Comparison

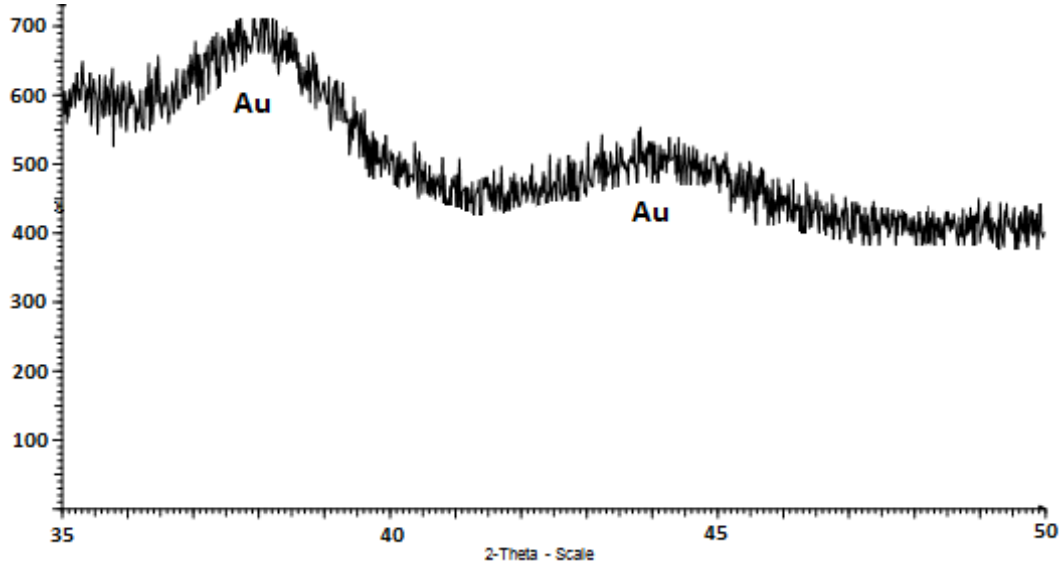


Figure 4.9: Zoomed view of 5% Au on silica (*pH 9 at start, pH 4 at end of synthesis, 1.0 M urea, 0.1 M NH_4OH, 300˚C, 1hr*). The two broad peaks result from metallic gold.

of the PXRD patterns in Figures 4.7 and 4.9 revealed the difference in the gold crystallite size between the samples prepared at pH 2.85 to the samples prepared at pH "9 to 4"(reaction started at pH 9, then ended at pH 4 due to insufficient base). The time spent during the synthesis when the pH of the solution was relatively high, above pH 7, resulted in some amount of bonding between the gold nanoparticles and the silica support. This was noted from increased stability of the gold nanoparticles when the sample was heated to 300°C. PXRD data (Figure 4.9) showed a large decrease in the gold crystallite size as sintering was reduced.

Adjustments to the concentration of the ammonium hydroxide solution was made with the concentration being increased from 0.1 M to 0.25 M. It was found that this adjustment resulted in pH of 7 being maintained for the duration of the reaction.

In this case the only peak in the diffraction pattern shown in Figure 4.10 was that of the silica support (note the support is amorphous), while the two gold peaks manifest themselves only after the catalyst was calcined at 300°C for an hour, as shown in Figure 4.11. The principal gold diffraction peaks at 38.2° and 44.4° 2θ are clearly visible. With the concentration adjustment made to the base, control of the pH throughout the reaction was possible and the pH was kept constant at 7.

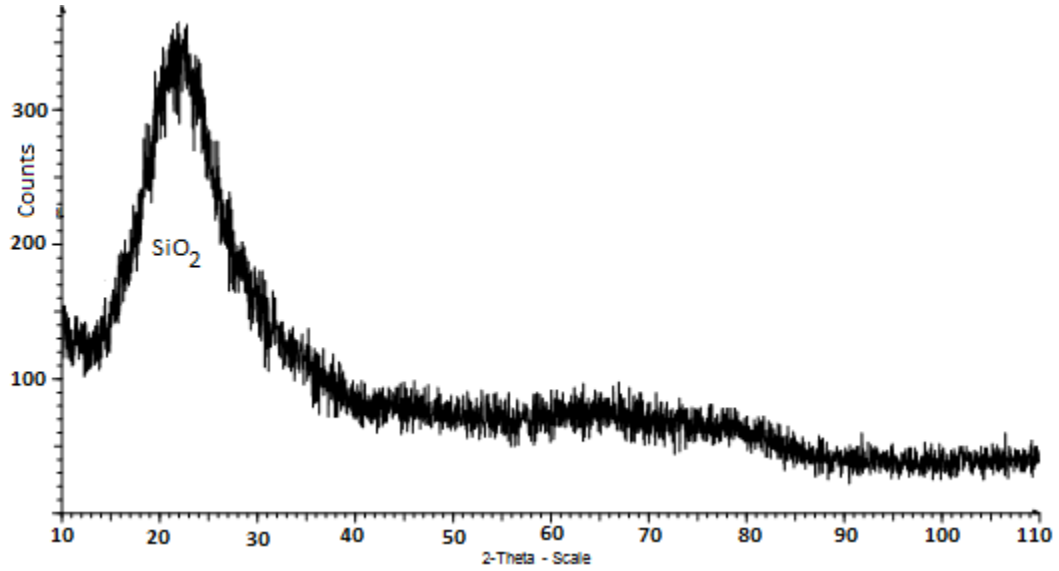


Figure 4.10: 5% Au on silica (*pH 7, 1.0 M urea, 0.25 M NH_4OH, 120°C, 1 hr).*

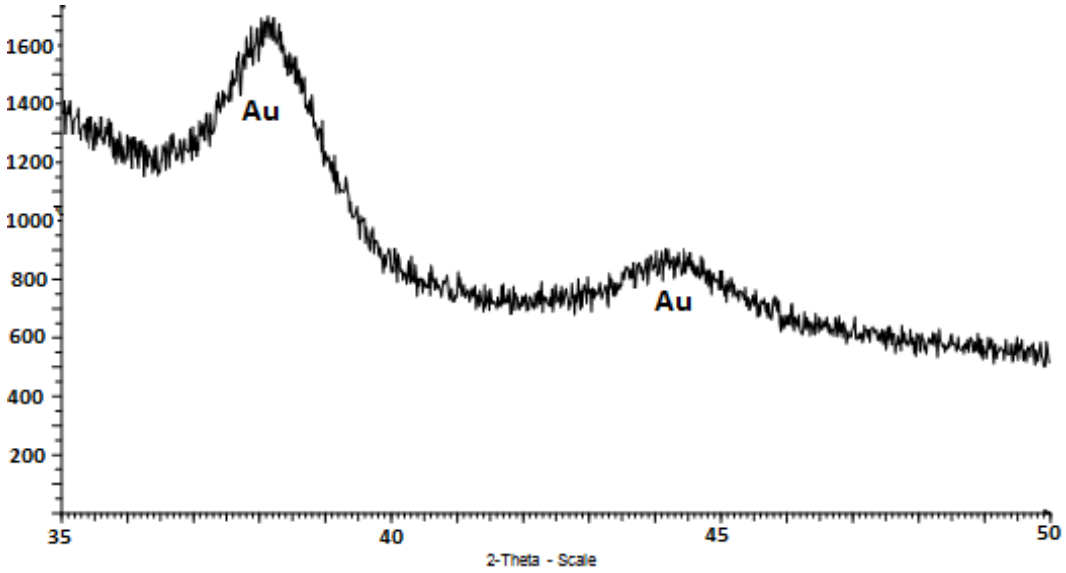


Figure 4.11: 5% Au on silica (*pH 7, 1.0 M urea, 0.25 M NH_4OH, 300°C, 1 hr*).

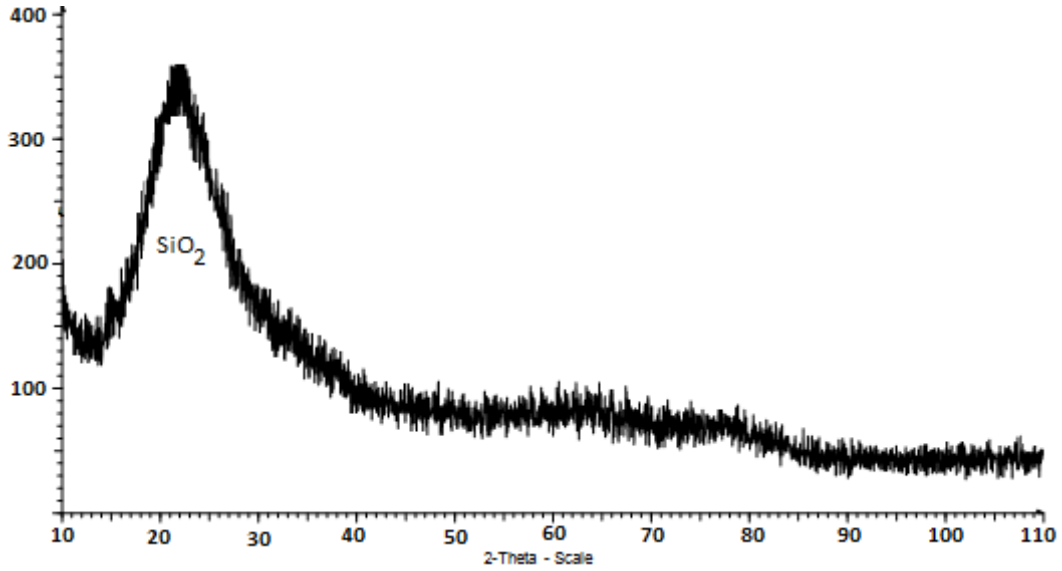


Figure 4.12: 5% Au on silica (*pH 9, 1.0 M urea, 0.25 M NH_4OH, 120˚C, 1hr*)

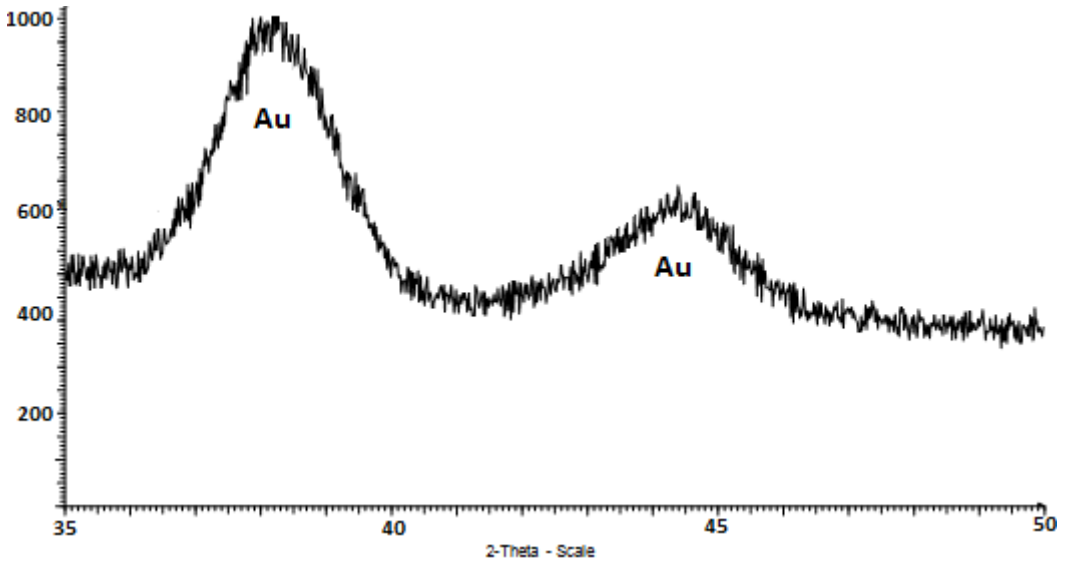


Figure 4.13: 5% Au on silica (*pH 9, 1.0 M urea, 0.25 M NH_4OH, 300˚C, 1hr*).

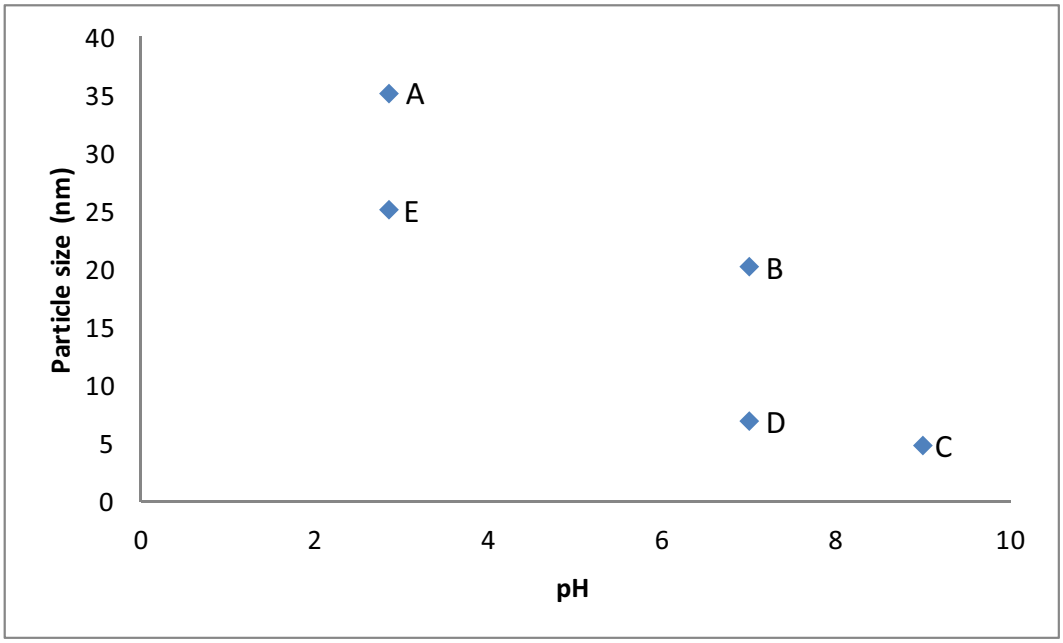


Figure 4.14: Averaged crystallite size VS synthesis pH of 5% Au on silica and zirconia supports heated to 300°C for 1 hour. Corresponding sample designations are given in Table 4.2. Zirconia PXRD patterns are discussed later.

Samples (repeated in triplicate)	**Support**	**Base (M)**
A	Zirconia	0.1 urea
B	Silica	1.0 urea, NH_4OH
C	Silica	1.0 urea, NH_4OH
D	Silica	0.1 urea
E (consisting of 4 repeats)	Silica	1.0 urea, 0.25 NH_4OH

Table 4.2: Synthesis parameters of samples prepared for Figure 4.14.

Comparison between the resulting gold crystallite sizes attained from PXRD with respect to pH and support were plotted as shown in Figure 4.14.

The results of the Scherrer analysis on the collected diffraction patterns are shown in Figure 4.14. The corresponding samples and bases used are given in Table 4.2. Data points are formed from averaged values of three repeat samples, while point E is the average of 4 samples synthesised at pH 7.

From results in Figure 4.14 it was determined that the optimal synthesis conditions were between pH 8-9 using 1.0 M urea and 0.25 M ammonium hydroxide in order to maintain the alkaline pH during the synthesis. Amorphous silica was chosen as the preferred support material over zirconia due to smaller gold crystallites being obtained as shown by the comparison between points A and

D in Figure 4.14. Further, analysis of the gold and platinum diffraction peaks is easier using an amorphous support. The aim of this initial study was to develop a robust and reproducible synthesis method and investigate what parameters influence the crystallite size of the product before being able to study the effect of platinum on the stability of the gold.

When zirconia was used in place of silica the gold crystallite sizes were significantly larger. Thus changing the support from silica to zirconia played a significant role in increasing the gold nanoparticle size under the same preparation conditions. However, the change in the pH of the solution also resulted in a change of the gold nanoparticle size as pH 7, the pH at which the experiment was conducted, was in zirconia's isoelectric range. The pH range for the reaction needed to be in excess of pH 11 to be out of zirconia's isoelectric range resulting in smaller as well as more stable gold nanoparticles.

Scherrer analysis from PXRD data showed that the gold nanoparticle sizes were less than 10 nm and in some cases less than 5 nm when higher pH's were used after thermal treatment with the particle size depending on pH as well as the type of support used. For the first experiment conducted at pH 2.85 and using silica as the support, the particle sizes are large, around 30 nm when heated at 300°C for an hour. The use of zirconia results in even larger gold particle sizes demonstrating silica as being a superior support at the pH's selected due to the isoelectric range.

After a number of experiments the optimal parameters for the preparation of the catalyst could be derived as corresponding to the smallest gold crystallite size of less than 5 nm for the sample prepared at pH 9. Thus, pH's between 8 and 9 using a combination of urea and ammonium hydroxide produced the smallest gold nanoparticles. In later experiments quantitative Rietveld refinement was used to determine the gold loadings of samples prepared using these pH conditions and will be discussed later.

4.3 Addition of platinum to the Au-silica and Au-zirconia system

To determine if platinum had a stabilizing effect on gold nanoparticles triplicate samples were synthesised using the synthesis method developed in the previous

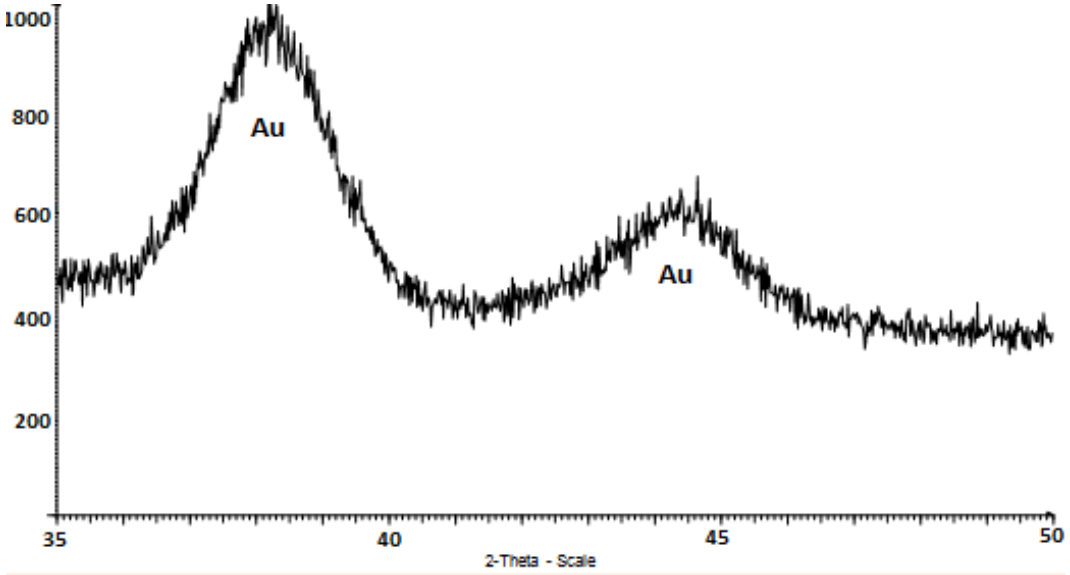


Figure 4.15: Zoomed region between 35° and 50° 2θ highlighting the two gold diffraction peaks. 5% Au-1% Pt on silica (*pH 9, 1.0 M urea, 0.25 M NH_4OH, 300°C, 1hr*).

section. The samples that were produced had a 5% Au- x% Pt loading on amorphous silica and zirconia where x = 1 or 2 such as shown in Figure 4.15. The prepared samples were separated into two batches where one batch was heated for an hour at 300°C and the second batch at 400°C also for one hour. These samples were then compared to ones that did not contain platinum using PXRD.

With an increase in temperature to 400°C as shown in Figures 4.16 and 4.17, the change in the nature of the support material can be seen. The amorphous silica began to develop intense diffraction peaks as the silica formed large crystallites due to the exposure to higher temperatures. This large increase in the crystallinity of the support can be seen from the increased intensity of the silica peaks at 31.5° and 45.5° 2θas shown in Figures 4.16 and 4.17. Further, Pt was also added in addition to Au as shown in Figures 4.19 - 4.21

Figure 4.18 shows the zoomed PXRD pattern of 5% Au-1% Pt on silica. The most intense peak corresponds to a NaCl standard that was used to monitor shifts in the gold peak positions. Shifts of the gold peak may indicate if platinum was being included into the gold lattice, this inclusion is observed through a change in the inter-planar spacing due to the addition of platinum. This can indicate if an alloy is forming between the two metals. However it was not possible to accurately determine any shifts in the lattice parameters of either the gold or the platinum. The difficulty in observing shifts in the

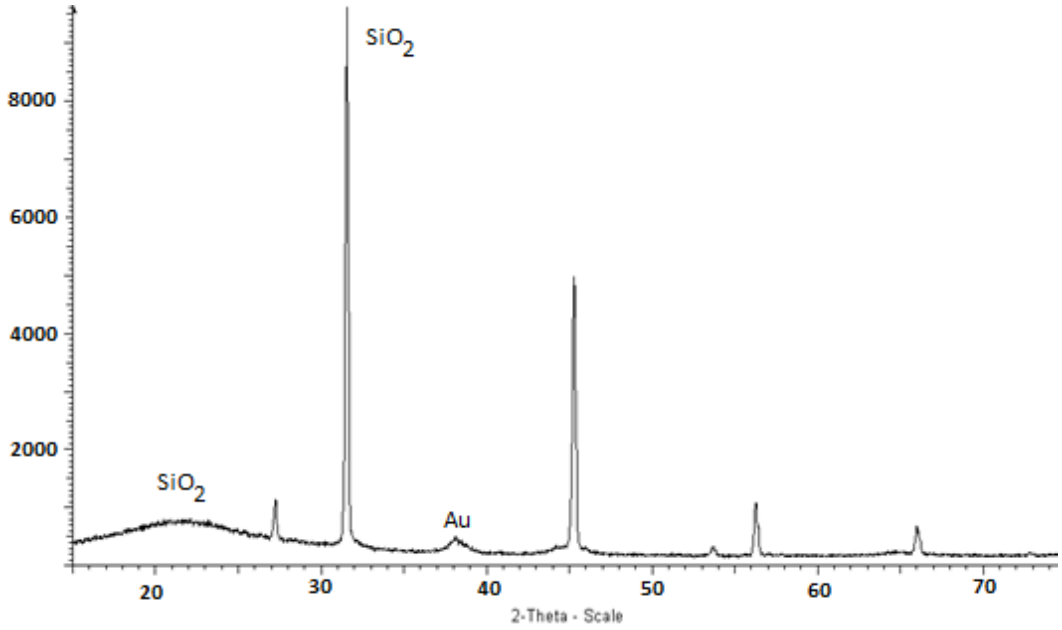


Figure 4.16: 5% Au-1% Pt on silica (*pH 9, 1.0 M urea, 0.25 M NH_4OH, 400˚C, 1hr*)

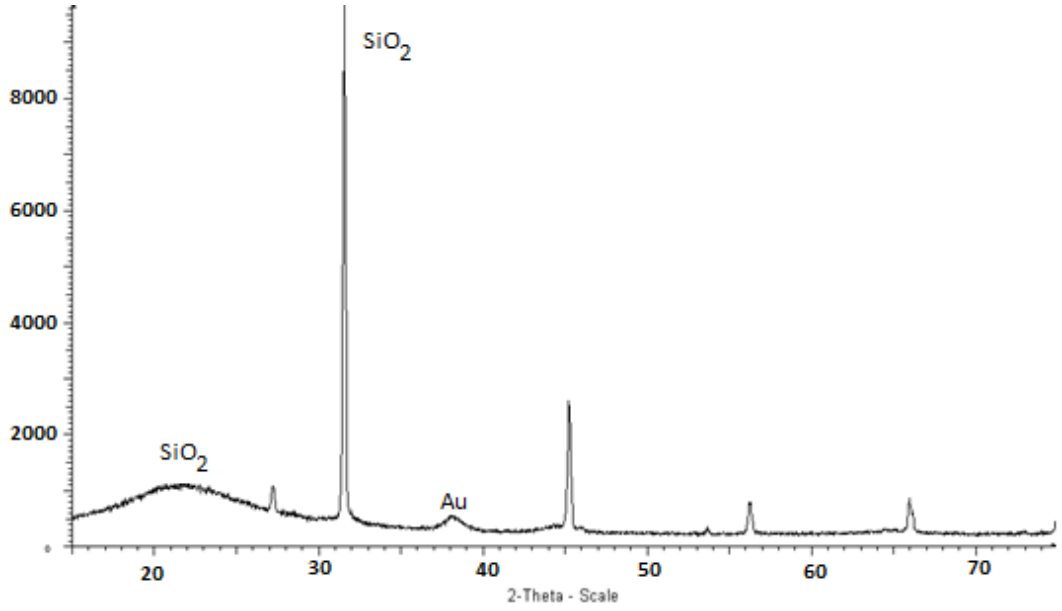


Figure 4.17: 5% Au-2% Pt on silica, (*pH 9, 1.0 M urea, 0.25 M NH_4OH, 400˚C, 1hr*).

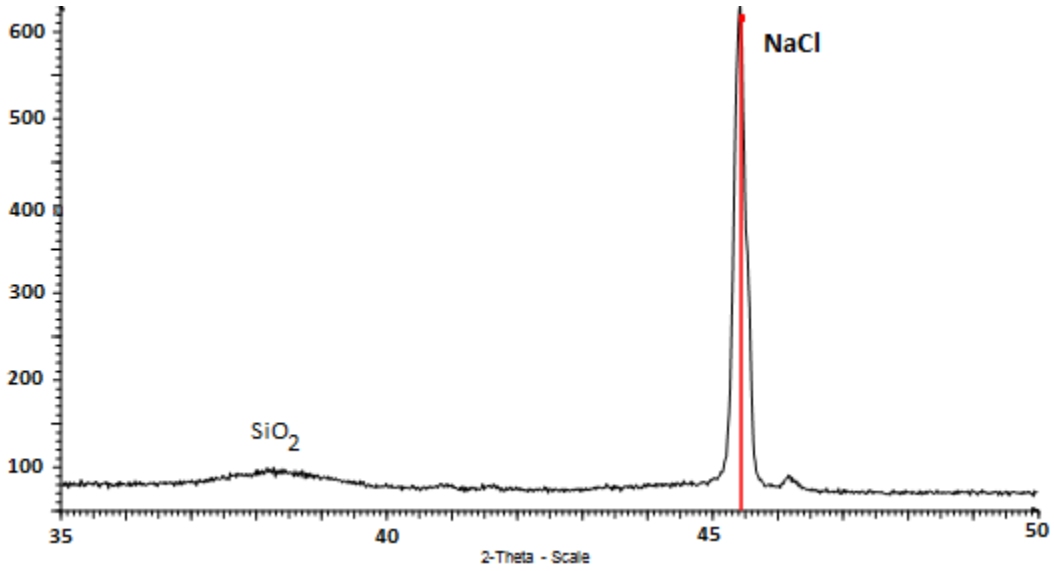


Figure 4.18: 5% Au-1% Pt on silica with a NaCl spike in red. (*pH 9, 1.0 M urea, 0.25 M NH_4OH, 300˚C, 1hr*).

diffraction pattern is increased by the broad nature of the gold peaks. A synchrotron light source would be needed to accurately determine changes in the gold lattice parameter.

Gold crystallite sizes from the all the diffraction patterns were determined using Scherrer analysis and summarized in Figure 4.22. Selected samples were repeated in triplicate and results of the Scherrer analysis averaged to produce Figure 4.22.

Bar 1 in Figure 4.22 shows that the gold crystallites were not stabilised by the zirconia support as the crystallite size is in excess of 9 nm after thermal exposure and was the largest of all the samples. Crystallites sizes in bars 2, 3 and 4 were all prepared using silica as the support, the difference was in the percentage loading of platinum. Bar 2 contains no platinum while the samples in bars 3 and 4 contain 1% and 2% platinum respectively in addition to 5% gold. The addition of platinum aided the stability of the nano-gold particles as the difference in particle size between the 5% Au and 5% Au-2% Pt samples was in excess of 3.5 nm, a value in excess of the determined experimental error. Further, the trend shows, the more platinum that was included, the more stable the nano-gold particles became at non-ambient temperatures when compared to gold nano-particles that contain no platinum. However, this trend did not continue as more platinum was added (Section 5.5). At loadings higher than 3% Pt-5% Au the stabilisation effect is reversed due to the miscibility gap between gold and platinum[77]. This effect is investigated when commercial

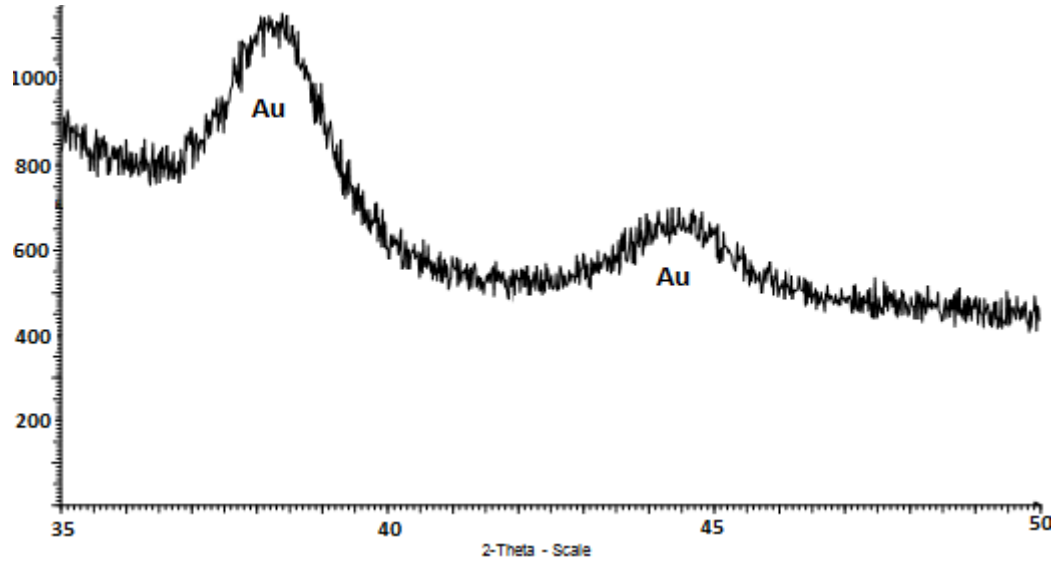


Figure 4.19: 5% Au-1% Pt on silica (*pH 8, 1.0 M urea, 0.25 M NH_4OH, 400°C, 1hr*). The diffraction pattern shows the two principal gold diffraction peaks. For all samples it was these two principal peaks at 38.2° and 44.4° 2θ, corresponding to the (111) and (011) respectively, that were analyzed for gold crystallite size.

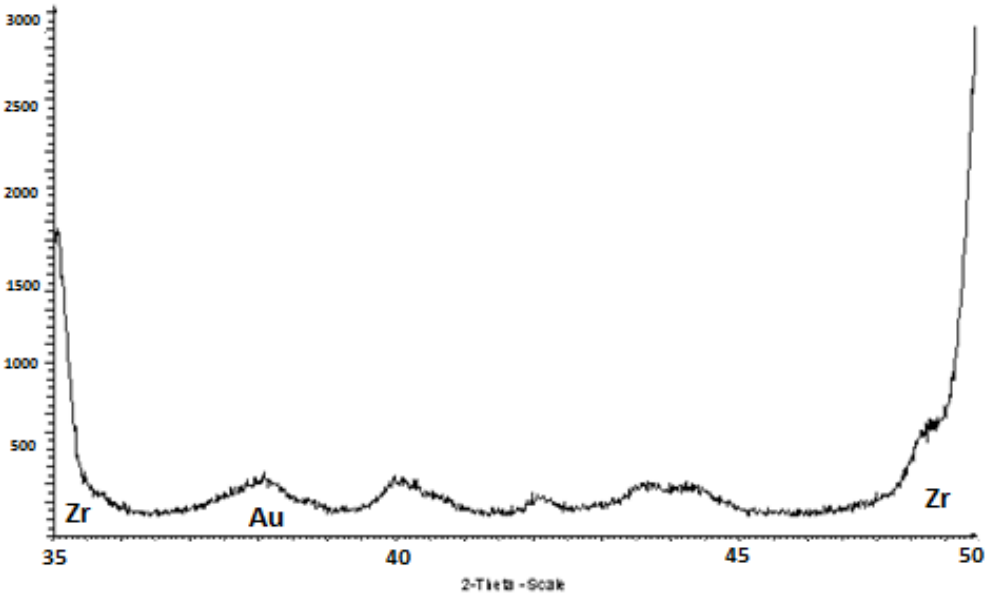


Figure 4.20: Zoomed diffraction pattern of 5% Au-1% Pt on zirconia, (*pH 9, 1.0 M urea, 0.25 M NH_4OH, 300^{o}C, 1 hr*).

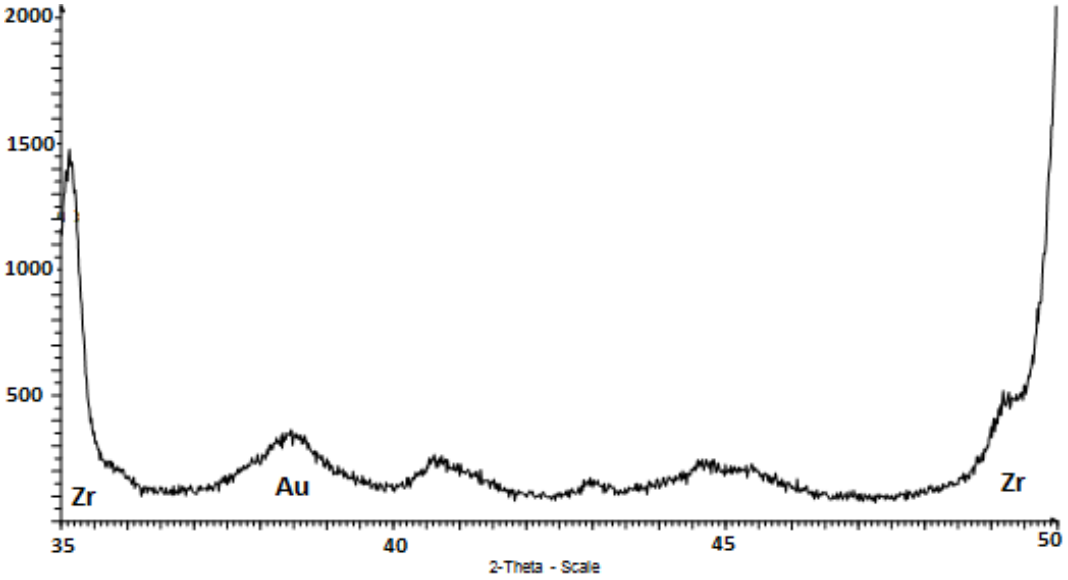


Figure 4.21: Zoomed diffraction pattern of 5% Au-2% Pt on zirconia, (*pH 9, 1.0 M urea, 0.25 M NH_4OH, 300^{o}C, 1 hr)*.

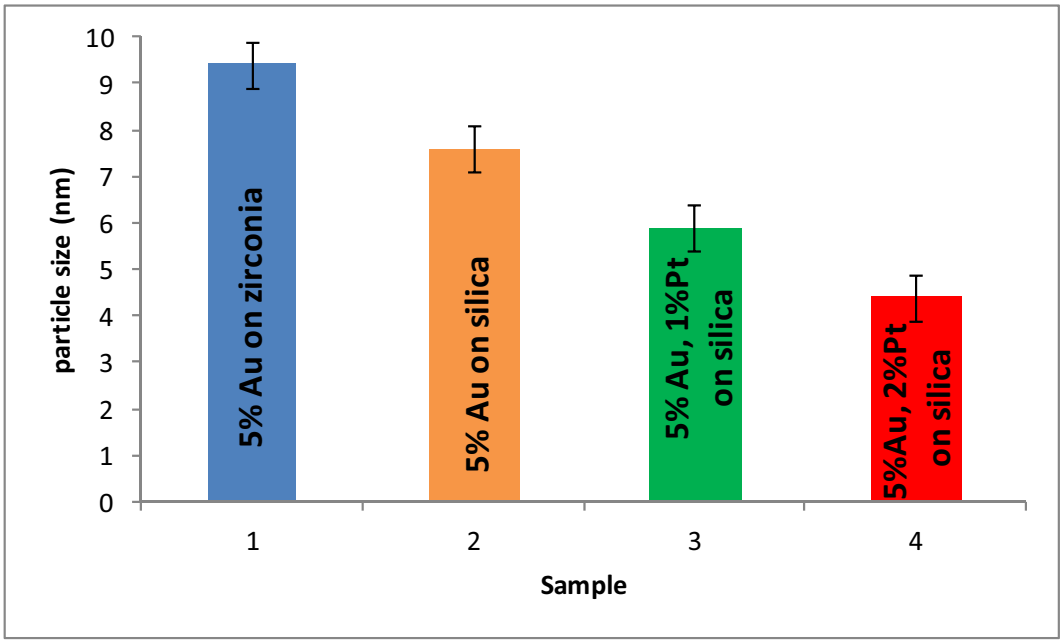


Figure 4.22: Gold particle sizes after samples were exposed to 300°C for one hour, all synthesis parameters were held constant at (*pH 9, 1.0 M urea, 0.25 M NH_4OH, 300^{o}C, 1 hr*). The gold crystallite size changes with respect to the support and metal composition are shown. Au-Pt on zirconia was not investigated as the pH range used was not in zirconia's isoelectric range.

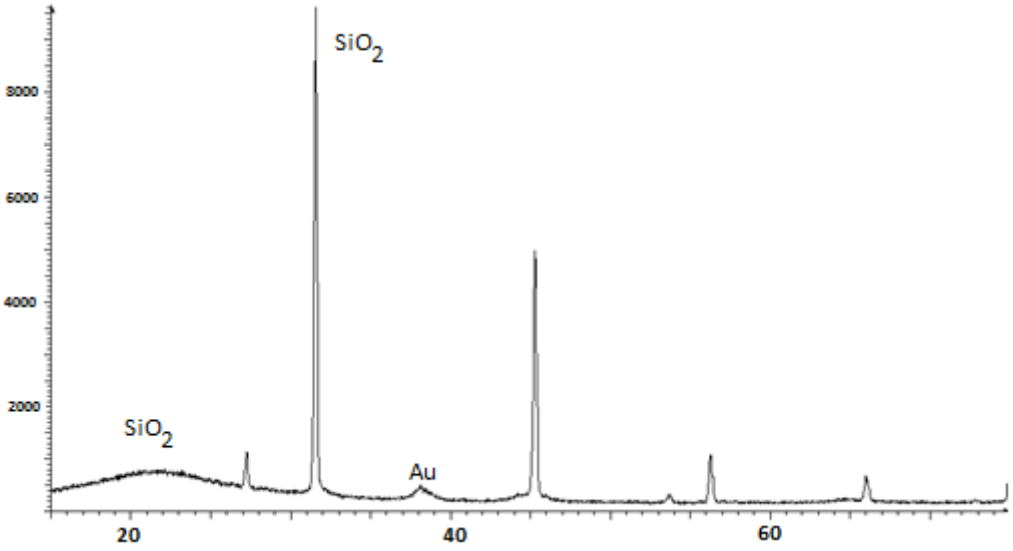


Figure 4.23: 5% Au on silica (*pH 9, 1.0 M urea, 0.25 M NH_4OH, 400^oC, 1 hr*).

anatase was used as the support material with higher platinum loadings as shown in Section 5.6.

Comparing Figures 4.23 and 4.24, the PXRD traces for 5% Au and 5% Au-1% Pt samples after exposure to 400°C for 1 hour show slight differences. The Au diffraction peaks with the 5% Au sample having a slightly more narrow and intense diffraction peak. Comparison between 5% Au and 5% Au-2% Pt samples at 300°C and 400°C are shown in Figure 4.25. PXRD data collections were conducted on the replicate samples and the resulting gold crystallite sizes averaged for each set of repeats to produce Figure 4.25.

The two bars in Figure 4.25 containing the set 5% Au at 300°C and 400°C samples showed how the gold crystallite size increased as the temperature increased from 300°C to 400^{o}C. Smaller gold crystallite sizes, in excess of statistical error, were attained with the addition of 2% platinum. The difference in gold crystallite size between the Au and Au-Pt loaded samples at 400^{o}C was greater than 2 nm. The difference in gold crystallite size is even greater when the 300°C samples were compared. It is evident that the addition of platinum stabilised the gold nano-particles and reduced sintering of the catalyst at higher temperatures when compared to gold catalysts not containing platinum.

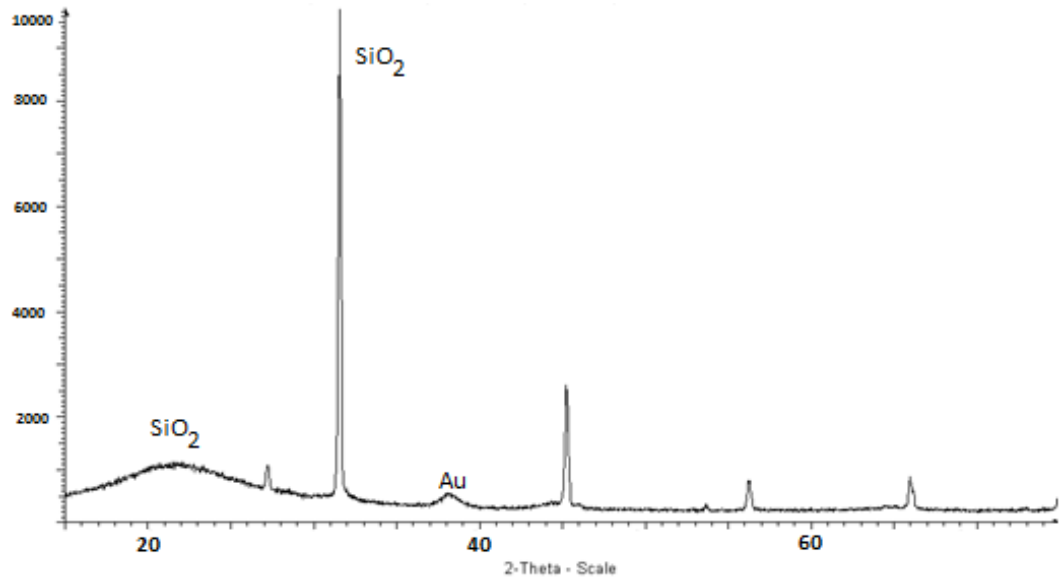


Figure 4.24: 5% Au-1% Pt on silica (*pH 9, 1.0 M urea, 0.25M NH_4OH, 400°C, 1 hr*).

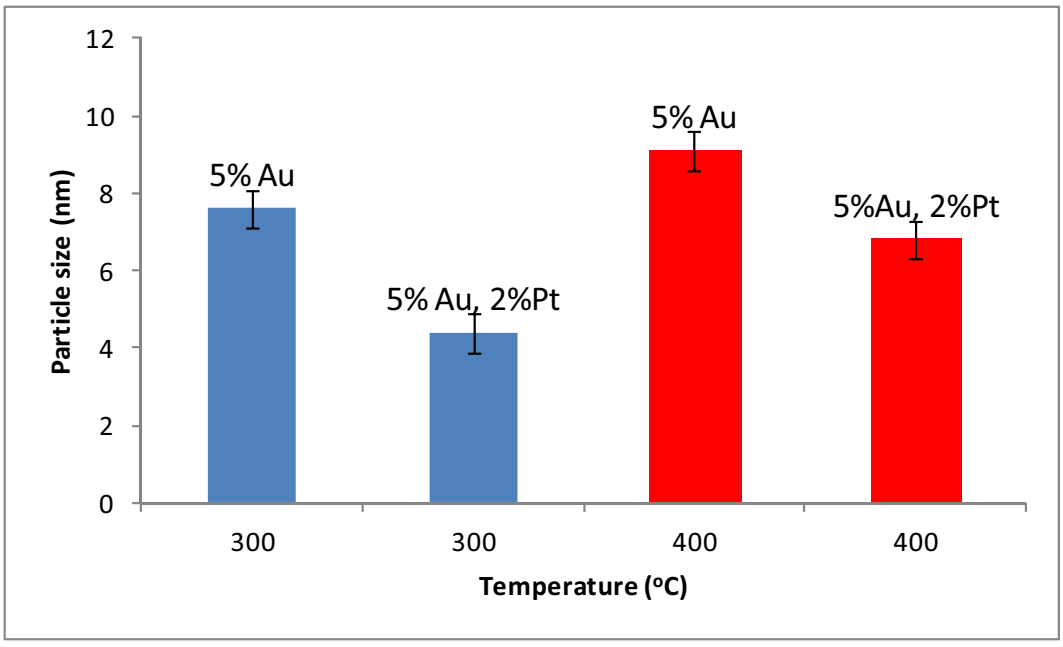


Figure 4.25: Gold crystallite size Vs temperature showing the effect of the addition of 2% platinum compared to pure gold samples. Silica was used as the support with each set of samples exposed to 300°C and 400°C for 1 hour.

Reproducibility

The robustness of the synthetic method was important as it influenced the reproducibility of the procedure. The most important variable that required testing was the gold crystallite size as this is what ultimately determines the catalysts ability to oxidize carbon monoxide[41]. In each case it was necessary to reproduce, within experimental error, the size of the gold nanoparticles. Figure 4.26 is the combination of 3 sets of triplicate samples where one set was comprised of 5% Au, the second set, 5% Au-1% Pt and the third set, 5% Au-2% Pt all supported on silica. The synthesis parameters were held constant at (pH 9, 1.0 M urea, 0.25M NH_4OH, 300^oC, 1 hr). In order to determine if the method was reproducible with respect to gold crystallite size each of the sets of collected diffraction patterns were required to fit closely within a certain grouping. No outlying diffraction patterns occurred between the sets as shown in Figure 4.26, indicating good reproducibility.

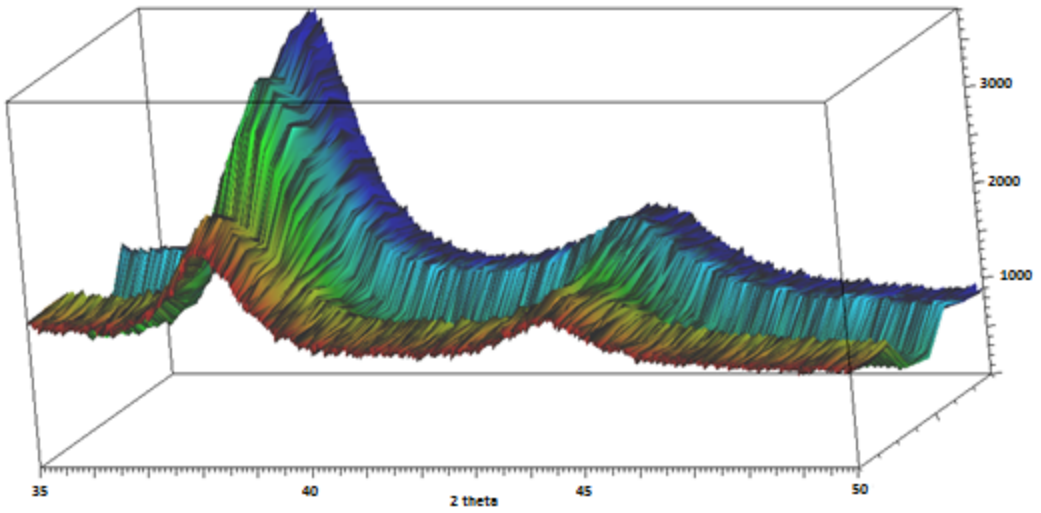


Figure 4.26: The combination of 9 (3 sets of 3 repeat samples) powder diffraction patterns illustrated the reproducibility of the results as well as the synthesis method. The most intense peaks in blue are a combination of three diffraction patterns from the samples that made up 5% Au. One step down towards the green region is the three samples of 5% Au-1% Pt. Finally, the least intense peaks are from the 5% Au-2% Pt samples. Each of the samples consistently fitted into their grouping as the diffraction patterns at each interval are uniform with no outlying patterns. Thus, the reproducibility of the synthesis method was reproducible within experimental error.

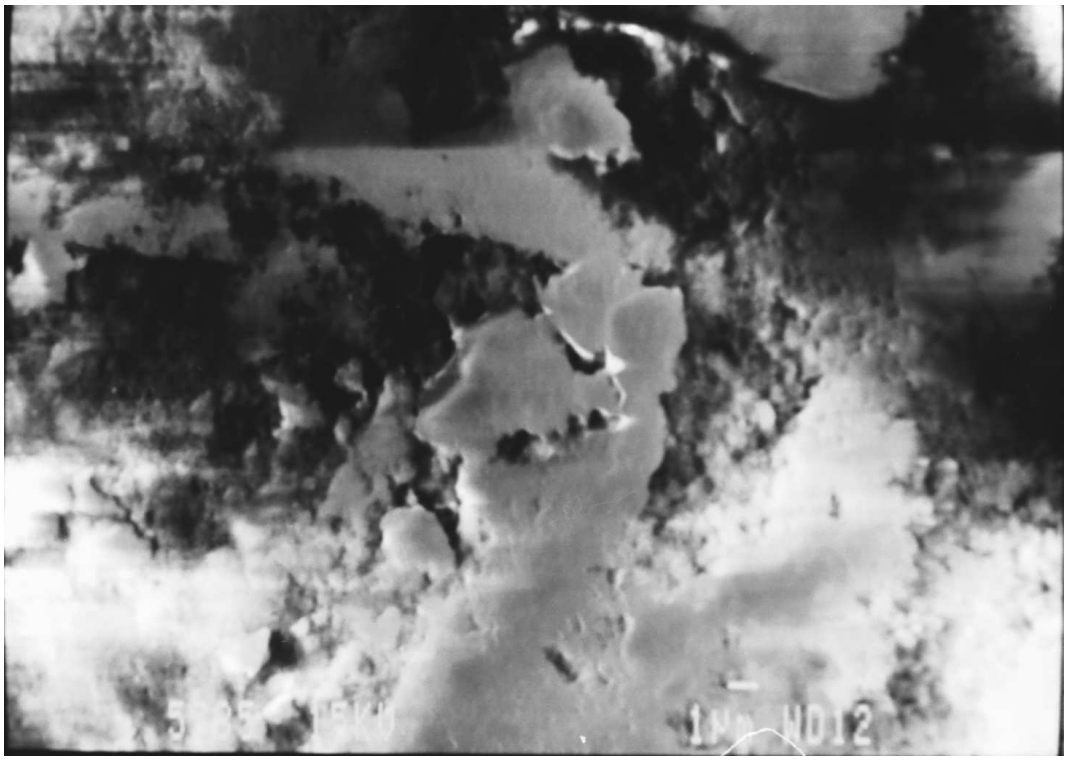


Figure 4.27: SEM image of 5% Au supported on silica. The resolution was not sufficient to see any gold particles on the surface.

4.4 Electron microscopy

4.4.1 SEM

SEM images of various samples were collected in order to determine the dispersion of the nanoparticles over the support surface and to further investigate the particle sizes of the metal nanoparticles. The resolution of the SEM was not sufficient to image the nano-particles as shown in Figure 4.27. However, when the SEM was operated in back scattered mode the images did reveal nanoparticles on the surface as shown in Figure 4.28.

Figures 4.27 and 4.28 showed that the resolution limit of the SEM left much to be desired in terms of viewing the size and morphology of the nanoparticles. Only large nanoparticles could be observed when the SEM was operated in backscattered mode as shown in Figure 4.28. Thus, the result from the SEM analysis was only that gold nanoparticles are present on the surface. No further information could be attained. For more comprehensive analysis TEM was required as the resolution limit of the microscope was far better in comparison to the SEM. However SEM confirmed the presence of well dispersed gold.

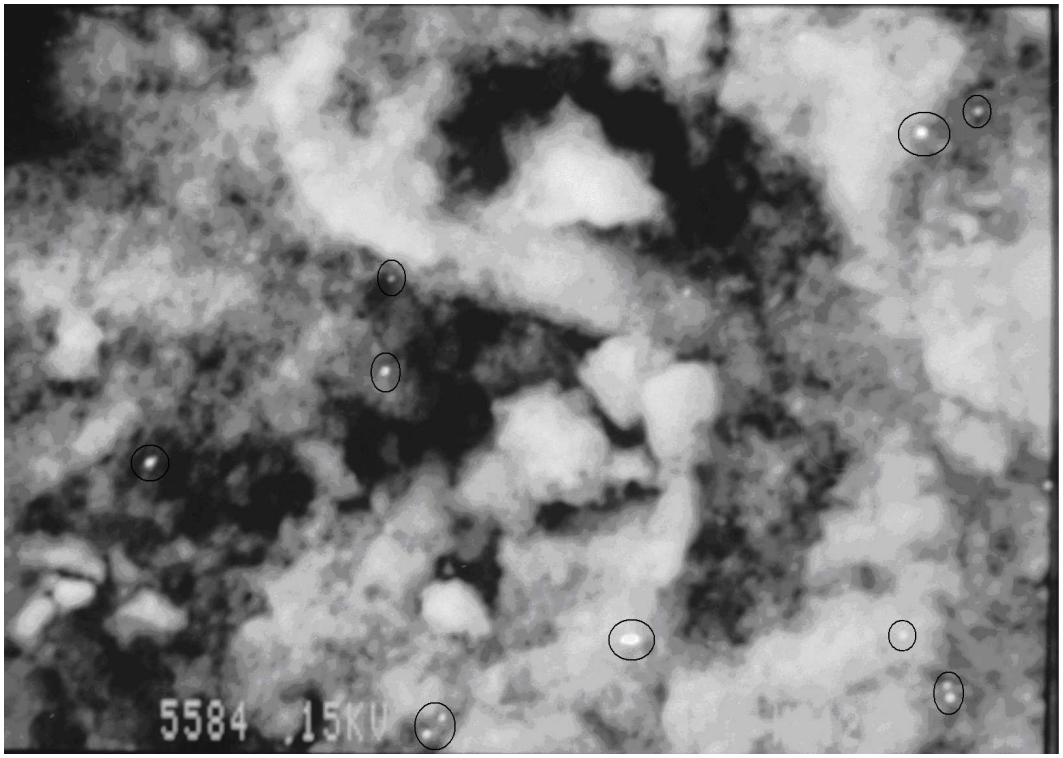


Figure 4.28: SEM image collected in back scattered mode of 5% Au on silica. The small bright flashes showed gold nanoparticles on the surface.

4.4.2 TEM

Initial studies used the Tecnai G2 spirit transmission electron microscope. Later, high resolution images were collected using a Tecnai F20 X-Twin. A number of samples were selected for analysis and were from the same initial batches used for diffraction studies. Samples were heated at several different temperatures for an hour, followed by separation into two portions for analysis using one for X-ray diffraction and one for TEM analysis. This allowed for direct comparison between the data acquired from the two techniques.

The amorphous nature of the support is visible from Figures 4.29 and 4.30 as no defined ordered crystalline form could be seen in the support structure. The darker spots are that of the Au and Au-Pt nanoparticles caused from an enhanced interaction of the electron beam due to the presence of the heavier gold and platinum atoms. Transmission electron microscopy was conducted on Au and Au-Pt samples that were heated to a number of different temperatures. The micrographs showed the nanoparticles are well dispersed over the support with particle size distributions corresponding well with the information attained from the PXRD data. However, the gold nanoparticles were not

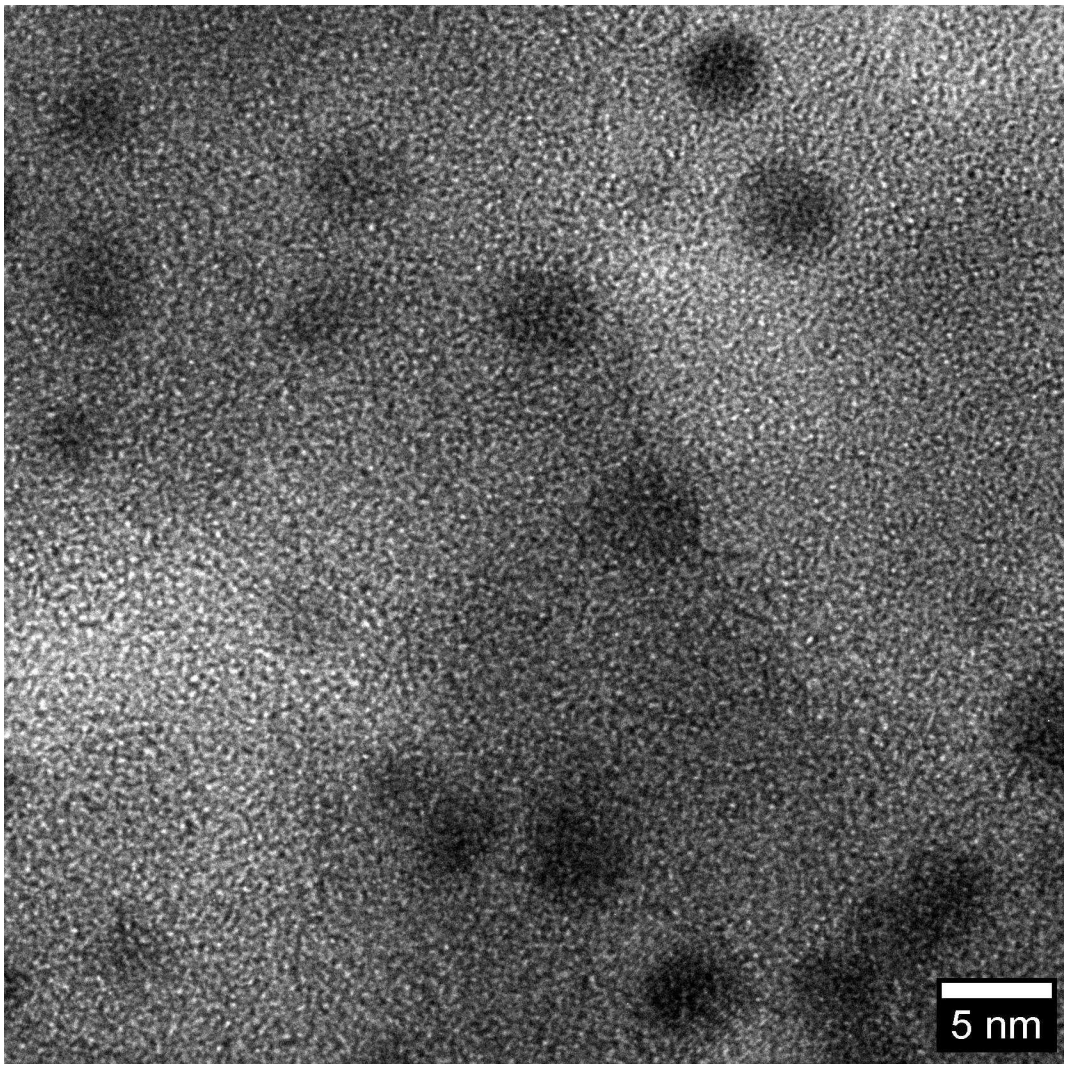


Figure 4.29: TEM image of 5% Au-1% Pt nanoparticles supported on silica after heating to 200°C for 1 hour. The image reveals the amorphous nature of the support as no crystalline structure could be seen. The dark spots are gold-platinum nanoparticles on the surface of the amorphous silica.

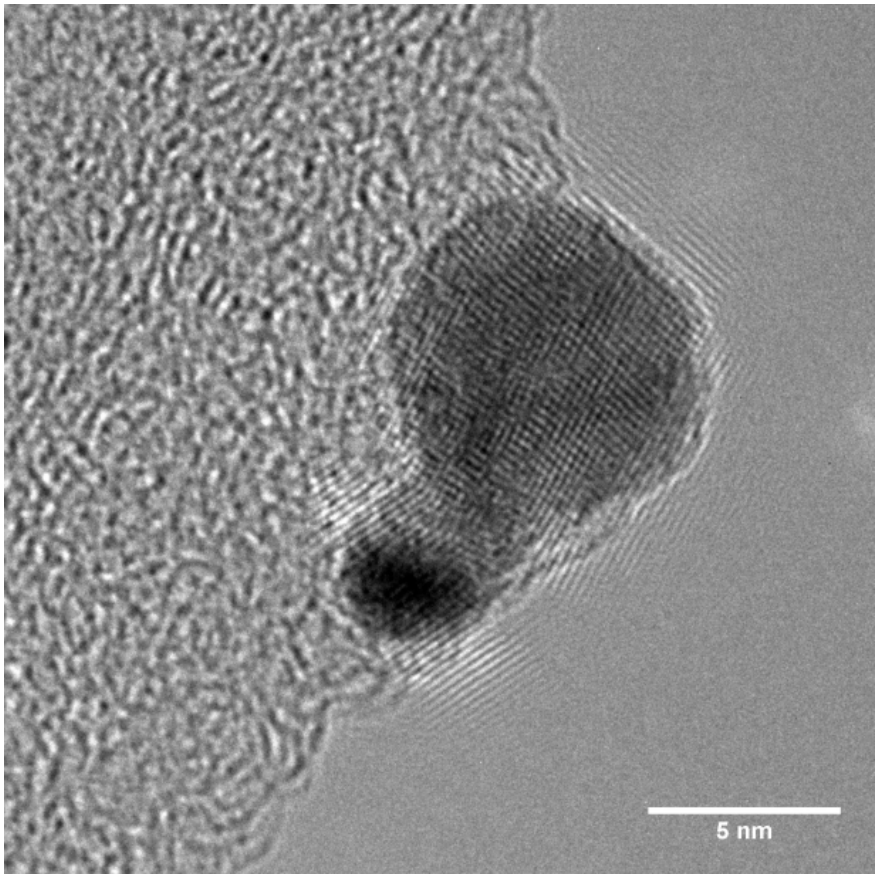
strongly bound to the silica surface as the majority of observed particles were not associated with a support in the TEM images after heating. This effect showed why sintering of the nanoparticles occurred so rapidly when the samples were exposed to non-ambient temperatures as shown in Figure 4.30 a and b. HR-TEM images later indicated the formation of icosahedral nanoparticles as seen in Figure 4.34.

Silica of any type is not regarded as a good support for gold nanoparticles even though a great deal of research has been conducted using it as a support material for gold[25,41]. From Figure 4.31 - 4.35 the observation was that the gold nanoparticles were not strongly associated with the support. This type of weak bonding between the support and the gold nanoparticles will most certainly enhance the amount of sintering observed when compared to a support such as titania as the nanoparticles on the silica support move more freely over the surface and thus coalescence occurs when two or more nanoparticles meet. This sintering of the nanoparticles would result in a decrease in surface energy that would be favorable and enhance the systems stability.

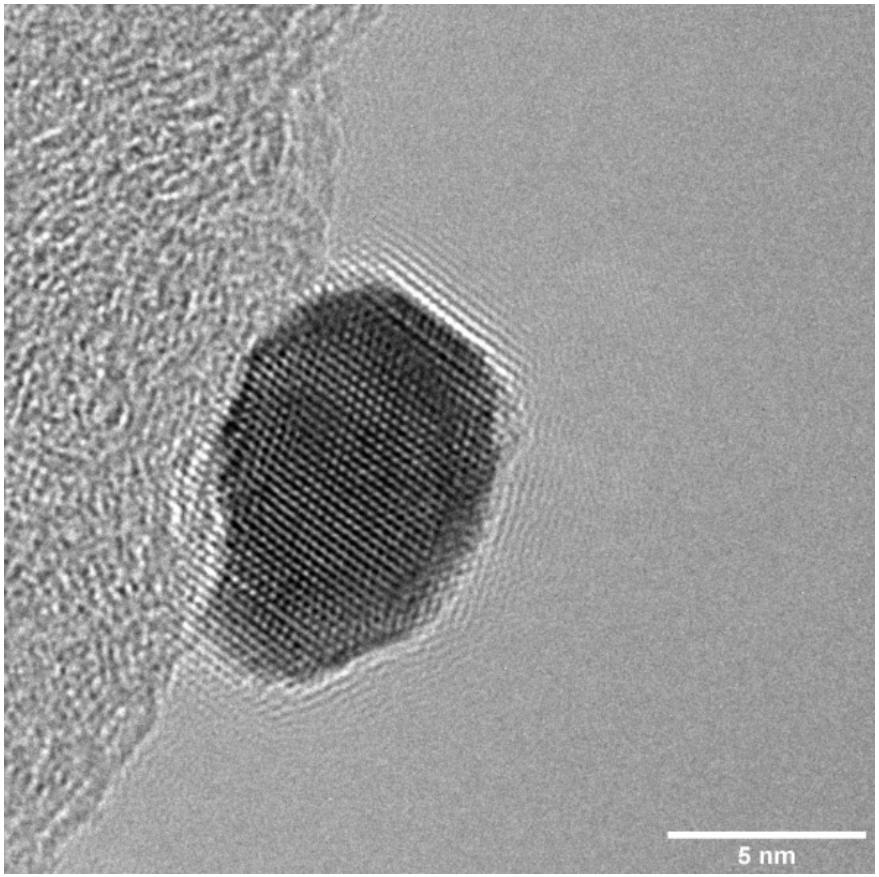
4.5 Conclusions

Development of the synthesis method revealed the pH of the solution must be kept between 7-9 in order to create small nanoparticles with a pH of 8-9 being ideal for silica. The use of urea was negated by the fact that it needed significantly longer synthesis times to hydrolyze effectively and hence the active base in the synthesis was ammonium hydroxide with the role of urea being negligible. Amorphous silica was deemed a better support for the Au and Au-Pt nanoparticles when compared to zirconia under the chosen reaction conditions, however both of these supports were insufficient for any type of high temperature catalysis as the nanoparticles did not bind effectively to the supports. However, addition of platinum to gold aided the gold nanoparticle stability as shown by PXRD analysis.

The use of a better suited support and an even more robust synthesis method was needed. In order to reproduce samples with both small gold nanoparticles as well as high gold loadings the standard DP method, although reasonably efficient, did not suffice. Further changes to the synthesis procedure were necessary when moving to titania based supports as the catalysts produced



(a) High resolution image of 5% Au on amorphous silica after heating to 200°C for one hour. When compared to the silica support the contrast between the crystalline gold nanoparticle and the amorphous support can be clearly seen. The image shows the sintering effect as two gold nanoparticles merge to form a single nanoparticles due to the energy provided from the TEM. Figure 4.30b was taken just 10 seconds after this image once the two nanoparticles had merged together.



(b) High resolution image of 5% Au on amorphous silica after heating to 200°C for one hour. The gold nanoparticle has now merged into a single nanoparticle after exposure to the electron beam heated the support surface of the catalyst resulting in sintering of the gold.

Figure 4.30: Sintering effects noted in the TEM.

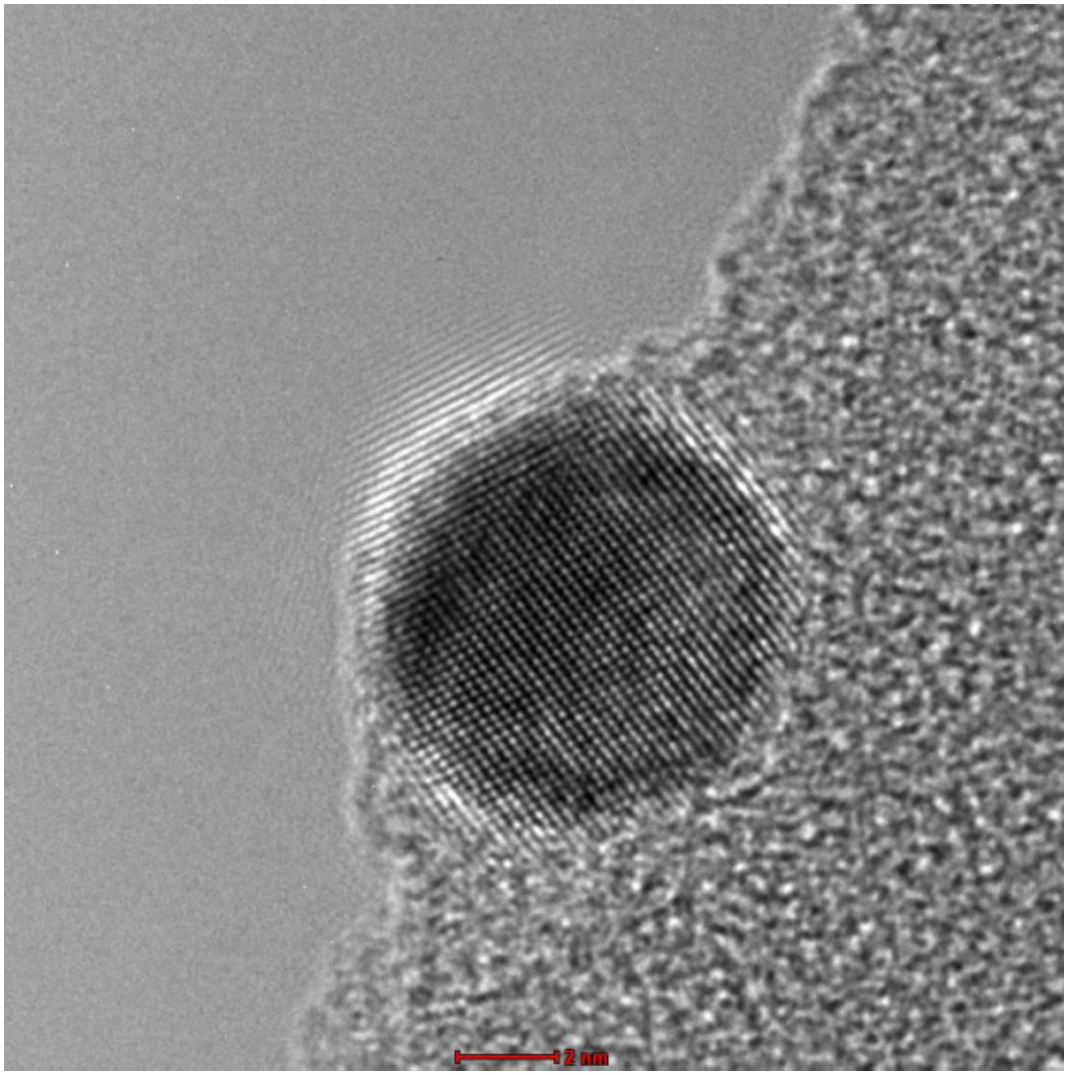


Figure 4.31: HR-TEM image of 5% Au on amorphous silica after heating to 200°C for 1 hour clearly showing the lattice planes of the gold nanoparticle.

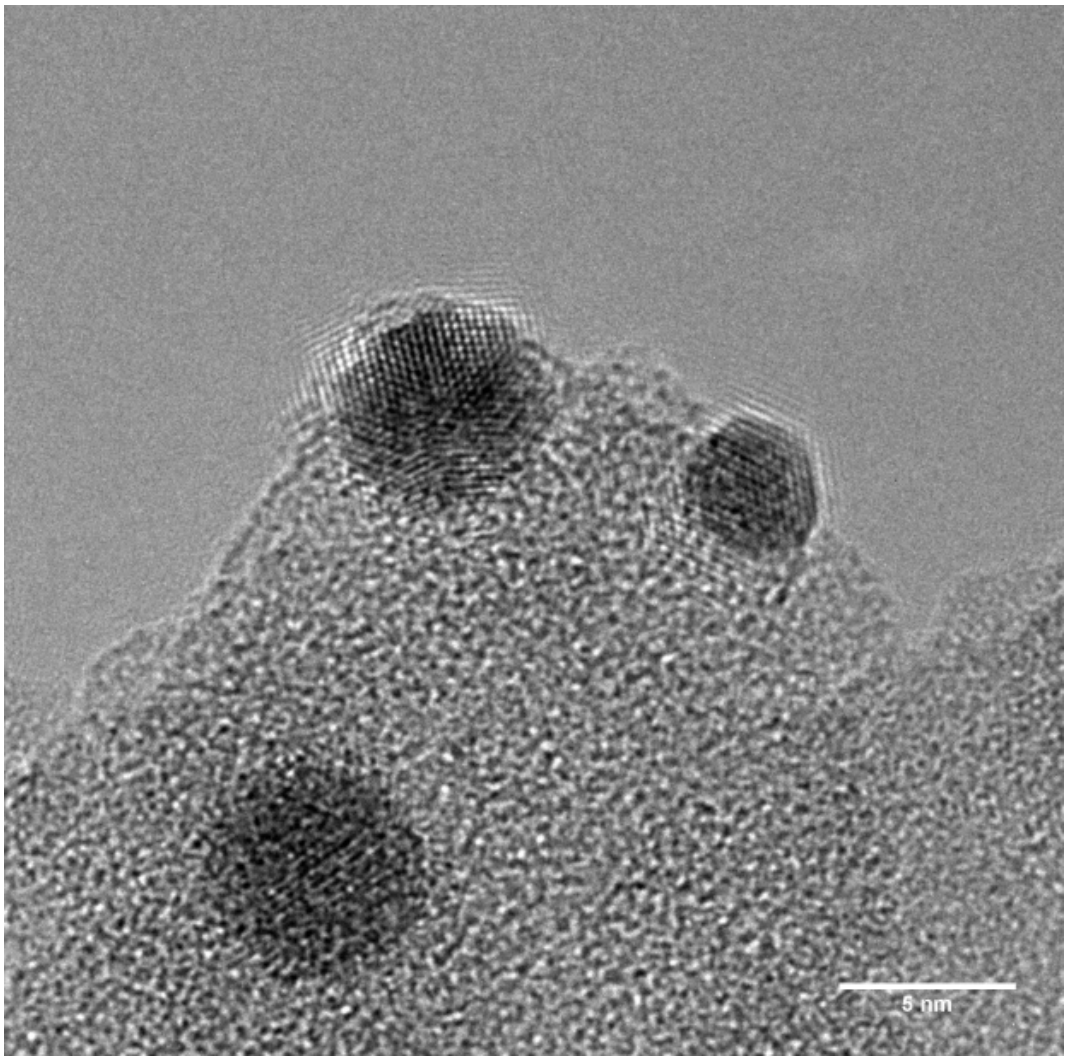


Figure 4.32: HR-TEM of 5% Au on amorphous silica after heating to 300°C for 1 hour.

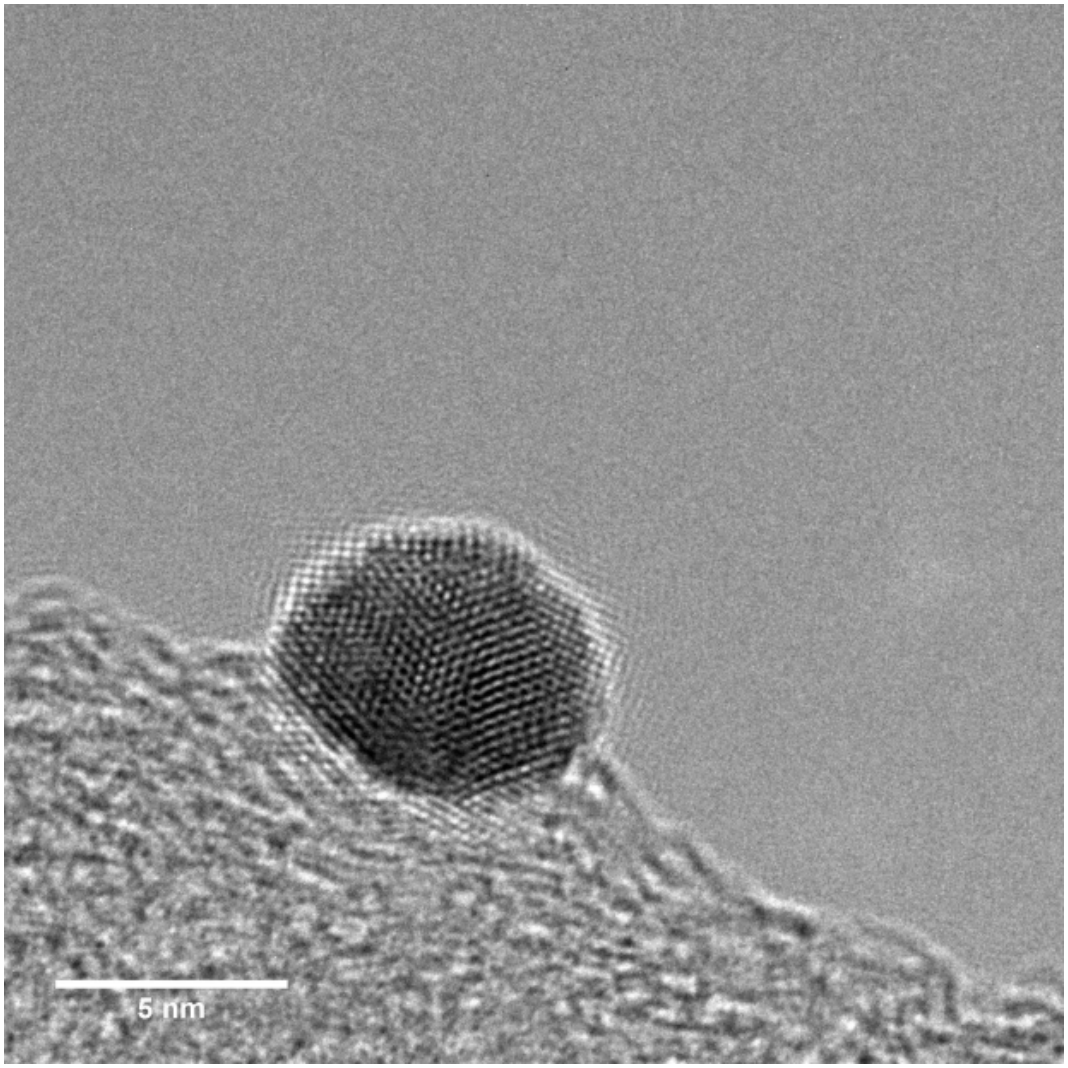


Figure 4.33: HR-TEM image of 5% Au on amorphous silica after heating to 300°C for 1 hour. Some nanoparticles were observed to be bound epitaxially to the surface that has been shown to be an important aspect in the oxidation of carbon monoxide when pertaining to gold based catalysts[41]. However, the bond formed between the nanoparticle and the support is not strong as many of the gold nanoparticles were not associated with the support after heating.

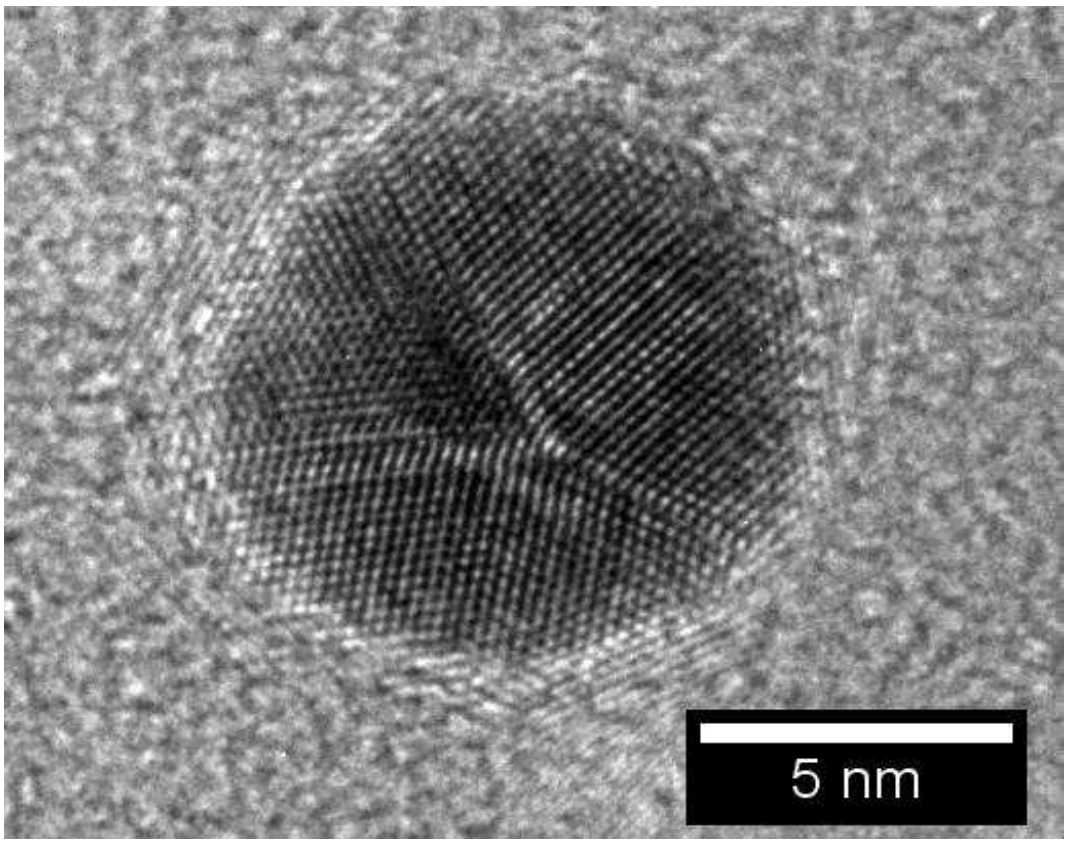


Figure 4.34: HR-TEM image of a gold nanoparticle prepared on amorphous silica after heating to 300°C for 1 hour. The image shows lattice fringes corresponding to (110) orientation twinning. This effect may be from the combination of a number of small gold crystallites sintering to form larger particles such as the one shown here. This Figure provided further evidence of the sintering process occurring when the samples are exposed to non-ambient temperatures with the ability of the gold nanoparticles to move over the surface to combine with other nanoparticles.

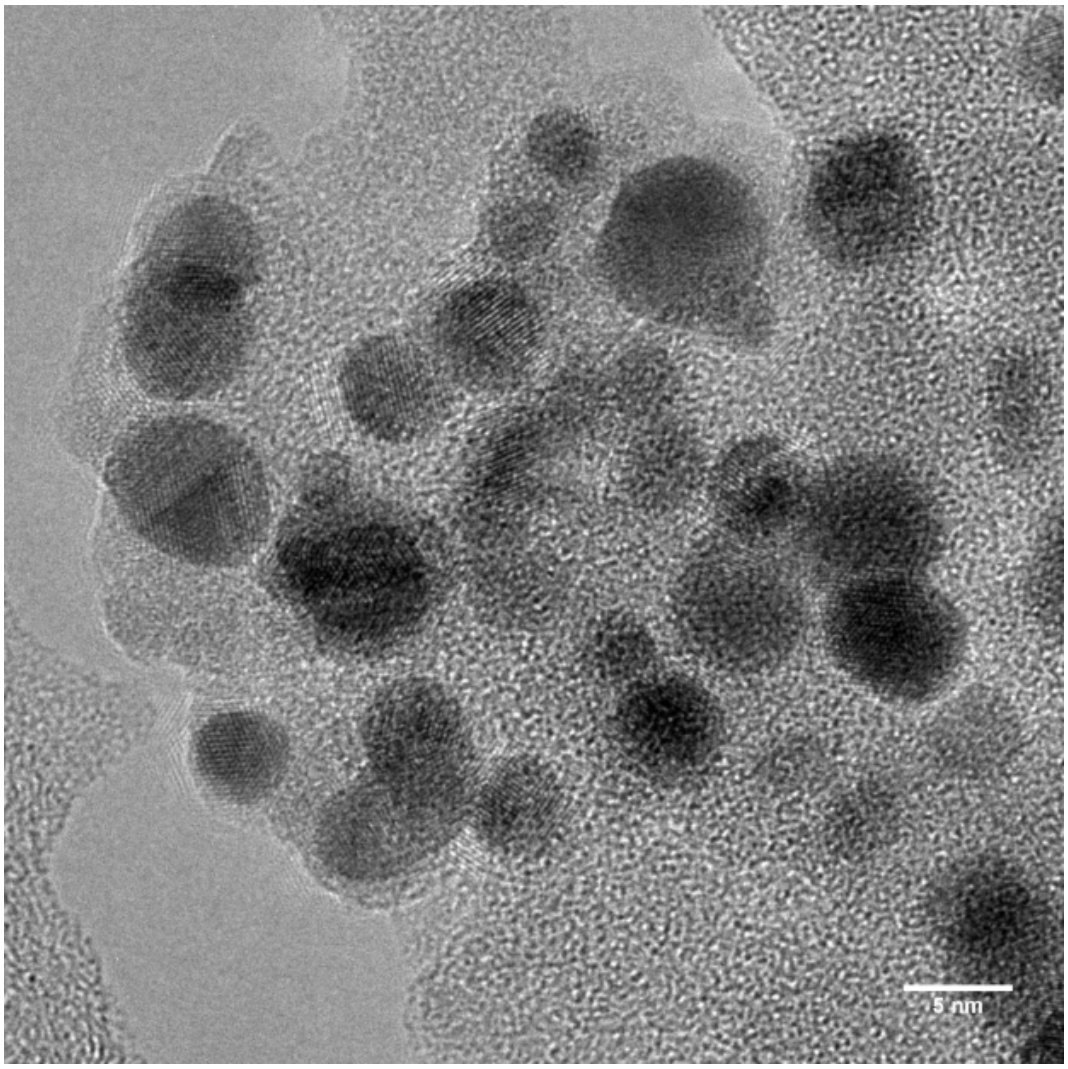


Figure 4.35: 5% Au-1% Pt on amorphous silica after thermal treatment at 400°C for 1 hour. At 400°C the thermal energy imparted to the catalyst resulted in a large increase in particle size. Both silica and zirconia were found to be insufficient support materials.

using these supports would be exposed to higher temperatures compared to the silica and zirconia based catalysts.

Chapter 5

The use of titania as a catalyst support

5.1 Introduction

Titania is one of the most important support materials in the world with Degussa P25 being, by far, the most industrially important form of titania (TiO_2) as it is used as a support for numerous different types of catalysts as well as having various uses in industry. Degussa P25 will be discussed as it contains two of the most stable polymorphs of titania. Further, as it is used as a support material for so many catalysts it is an obvious choice to test as a support for gold catalysts. Current industrially produced gold catalysts such as Mintek's Aurolite^{TM}catalyst use P25 as a support material for gold nanoparticles. There are many different phases of titania that are stable under different conditions, the three most prevalent phases are anatase, rutile and brookite (orthorhombic, P*bca*). Brookite is considered to be the least stable of the three phases, transforming to anatase with little energy input. However, this phase only forms at very high temperatures[74].

Degussa P25 contains a mixture of two TiO_2 phases, namely anatase (tetragonal, I41/*amds*), that is comprised of highly distorted, edge-sharing TiO_2 octahedra[60], and rutile (tetragonal, P42/*mnm*), that is comprised of undistorted, corner and edge-sharing TiO_2 octahedra[61] as shown in Figure 5.1 . The anatase to rutile ratio in Degussa P25 is usually in the region of 4:1, however, heat treatment procedures can affect the ratio. This is due to anatase

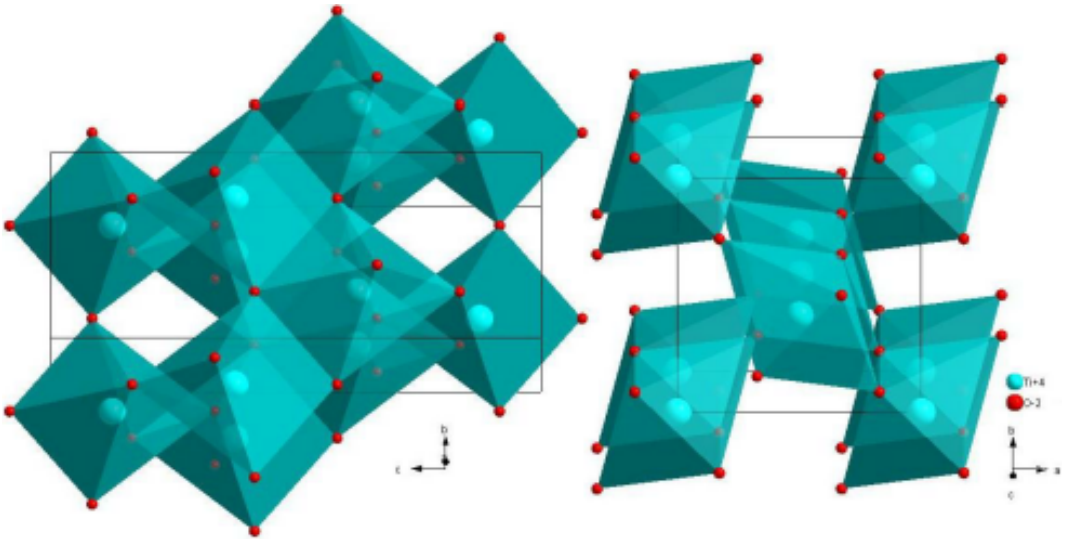


Figure 5.1: Crystallographic representations of anatase on the left of the Figure (tetragonal, I41/*amds*) and rutile on the right (tetragonal, P42/*mnm*) generated using DIAMOND 3.2f [69]. Brookite is the third polymorph of titania which occurs at very high temperatures far in excess of temperatures that will be reached by catalysts in this thesis. Thus it is not discussed.

undergoing a solid-state phase transition to form the thermodynamically stable rutile phase after moderate energy input.

The exact temperature at which the phase transition occurs is sample related since factors such as impurities[62-67], particle size[68-71], pressure[72] and dopants[73] have all been shown to either increase or decrease the temperature of the phase transition to varying degrees.

5.2 Au and Au-Pt supported on commercial anatase phase TiO_2

The need to stabilise gold nanoparticles from the effects of thermal sintering is crucial in controlling the catalytic activity of gold catalysts[25, 41, 59, 75, 76, 77, 78, 80, 82]. Catalytic activity is optimum when the diameters of gold nanoparticle are less than 5 nm[75-78]. In this size range, remarkable activities for a number of reactions can be achieved at temperatures below ambient. When particle sizes exceed 10 nm the catalyst's activity is compromised. Supported nanogold is particularly susceptible to sintering at non-ambient temperatures resulting in the agglomeration of the gold nanoparticles until the catalyst deactivates[79].

Sintering was demonstrated in Chapter 4 where exposure of catalysts to 300°C and 400°C for 1 hour resulted in large increases in gold nanoparticle sizes. The susceptibility of gold catalysts to sintering makes the catalyst very difficult to utilise when reaction temperatures increase and is one of the primary reasons that nanogold catalysts have struggled to find industrial applications where high temperatures are experienced[79]. As with alloys and bimetallics in the bulk state, nano alloys and nano bimetallics have been shown to improve the characteristics of the parent counterparts that make up the nanomaterial[80]. For example, when copper was added to gold, the bimetallic showed an ability to stabilise and limit the growth of the Au-Cu nanoparticles[79]. This stabilising effect has also been shown to exist in Au-Ag systems[81]. As shown in Chapter 4, the addition of platinum to gold caused a stabilizing effect when silica and zirconia supports were used.

The study of such nano alloys and bimetallics is still very much in its infancy. Work by Mott et al.. showed that Au-Pt nanoparticles not only show single phase alloy character in the nano crystal but also bimetallic alloy properties on the surface[82]. Further, they showed that the nanocrystal and surface alloy properties are directly correlated with the bimetallic composition. Further, their findings also showed that these bimetallic alloys can occur in the miscibility gap that is known for the bulk alloy counterparts. This miscibility gap occurs between approximately 20-90% gold (in bulk mixtures), but can vary dramatically depending on the composition and size range if mixtures of nano Au-Pt are considered pointing to the differences between bulk and nano structures[77].

As titania is a more useful support for commercial applications, the particle sizes of supported gold were compared to those of supported gold-platinum systems. The intention was to determine if the platinum added to the gold to stabilised the nanoparticles at non-ambient temperatures. The experimental method was chosen so as to minimize the number of experimental variables and thus allow emphasis to be placed on the effect of addition of platinum to the gold system. As was observed, the preparation method had a significant influence on the metal loading and particle size. Studies have revealed that the preparation method also influences the catalyst's performance[83-85]. The size dependency of the Au and Au-Pt nanoparticles supported on commercial anatase phase TiO_2 was studied as a function of temperature and metal composition via TEM, PXRD and later in-situ PXRD.

5.3 Experimental

Following examination of results in Chapter 4 the need to simplify the synthesis method even further to eliminate as many variables was required. This was done in order to try and achieve the most reproducible and robust method possible to synthesise catalysts. The requirements of the method were that reproducible nanoparticle size and distribution should be obtained, within experimental error, from batch to batch. It was noted in Chapter 4 that the urea was not playing a role due to insufficiently long reaction times to maintain the pH in the alkaline region. Thus, ammonium hydroxide was included as a second base to raise the pH to the desired level between 8-9. After a number of experiments, it was found that the solution required stirring for at least 16 hours at temperatures above 75°C for the desired solution pH to be reached in the absence of ammonium hydroxide and using only urea.

For all samples the modified method for deposition precipitation was used. A 250 mL conical flask was placed onto a temperature controlled heater stirrer and 100 mL of deionized water was added into the conical flask. 1.0 g of commercial anatase (Sigma-Aldrich), the support was added to the water with stirring. $HAuCl_4.3H_2O$ and urea were then also added directly to the flask. In samples that would contain 1, 2 or 3% platinum loading $H_2PtCl_6.6H_2O$ was also added. Various concentrations of urea were tested and the concentration of urea was eventually set at 0.85 M. This concentration was determined to be ideal after consideration of the addition of both the volume of deionized water and concentrations of highly acidic chloroauric acid, as well as the addition of hexachloroplatanic acid. At this concentration of urea, the final pH was found to be between 8 and 8.5 on completion of the synthesis. This pH was optimal for high gold loadings as well as small gold nanoparticles. The theoretical loading of gold was 5%. The conical flask was sealed with parafilm and the reaction was left to occur in a dark fume-hood so that no light entered during the synthesis. Gold and platinum precursors are light sensitive and so this was done to prevent variation from varying light levels. The solution was heated to between 75°C and 80°C to ensure the complete hydrolysis of the urea. The reaction was allowed to take place over 24 hours. Once the reaction was completed, the solution containing the catalyst was washed with hot deionized water and then centrifuged. This process was repeated until the pH of the solution reached neutrality. Finally, the catalyst was placed in a drying oven overnight at 110°C to remove any residual water. Reduction was

only undertaken prior to characterization.

5.4 In-situ PXRD of commercial anatase

Prior to the addition of Au and Au-Pt to commercial anatase it was important to fully characterize the support material without any metallic nanoparticles present. This allowed an analysis of the effect of the metal loading on the support structure to be determined. Thus, comparisons were drawn between the pure support and the catalysts produced with Au and Au-Pt nanoparticles on the support

Phase pure anatase (Sigma-Aldrich) was used to determine the effects when no rutile phase was present. The reduction of the number of phases enhanced the ability to accurately determine the gold loading as well as the gold crystallite size as there was less peak overlap between the phases present. From the in-situ PXRD data collection shown in Figure 5.2, the first notable peak (just to the right of the (110) anatase reflection) is a very low intensity peak of the rutile (110) reflection resulting from a very small amount of rutile that was present. From this it was determined that the purchased anatase was not phase pure as claimed. It was later determined from quantitative Rietveld refinements that rutile constituted less than 2% of the total support, with the bulk of the support being anatase. Compared to other sources of commercial anatase in the lab it was found that this was not an uncommon finding. While 2% rutile may not appear a significant amount, it proved interesting when analysis of the effect of gold on the conversion of anatase to rutile was studied. Firstly the support material was analyzed prior to the addition of any supported material as shown in Figure 5.2.

From the in-situ PXRD data collection (seen in Figures 5.2 and 5.4) it was immediately apparent that the commercial anatase is a thermally stable support. This was demonstrated by the consistency of the diffraction peaks between 30°C and 900°C. Over the entire temperature range there was only a very small change observed in the intensity and peak shape of the diffraction patterns. The final data collection was recorded when the XRK chamber reached 30°C after cooling down. Thus, the final data set at the top of Figures 5.2 and 5.4 shows a slightly more intense set of diffraction peaks compared to the rest of the pattern. The increased intensity occurs due to two reasons.

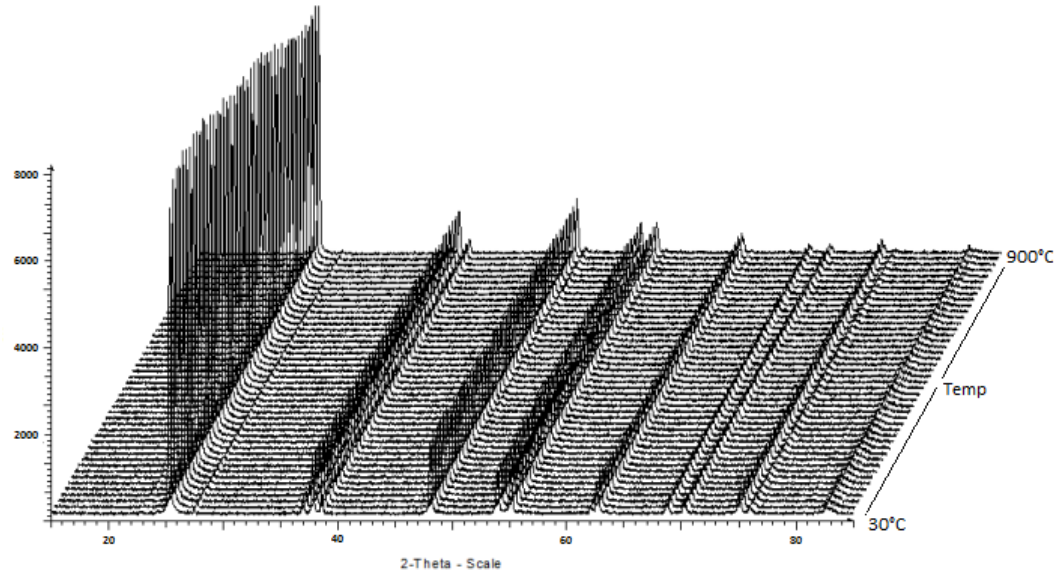


Figure 5.2: In-situ PXRD of commercial anatase (Sigma). A total of 52 diffraction patterns were collected over a temperature range of 30°C to 900°C. The data collection took a total of 36 hours to collect.

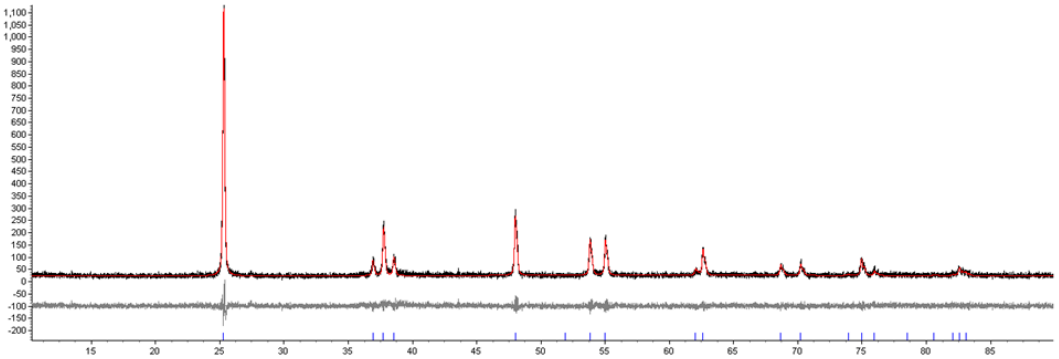


Figure 5.3: Rietveld refinements of commercial anatase at low to medium temperatures in the collection range were relatively straight forward as the only major phase present being anatase with only a very small amount of rutile. At low temperatures the rutile phase is almost indistinguishable from the background. Refinements on all the supports were necessary to monitor the support structure as temperature was increased to draw comparisons between unloaded and loaded supports. The grey difference line at the bottom of the image shows that the difference between the calculated and observed data is minimal as thus the refinement is good.

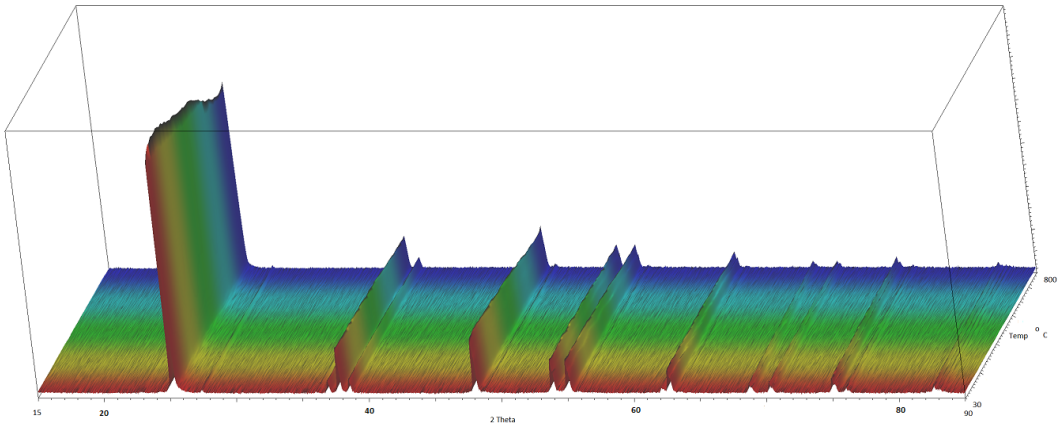


Figure 5.4: In-situ PXRD of commercial anatase (Sigma).

Firstly the time that the support spent at high temperature while the chamber cooled down to ambient and the final scan was then collected. The chamber may take 10 hours to cool down from 900°C and thus the support is exposed to high temperatures for this duration. During this time the support undergoes further changes such as crystallite growth. This crystallite growth will result in an increase in intensity being observed the final diffraction pattern.

The second reason is that the pressure in the chamber may increase at high temperatures. These higher pressures have a direct effect on the beam intensity and thus on the diffraction intensity. Higher pressures resulting from high temperatures can produce lower beam intensities as the X-rays penetrate the gas inside the XRK chamber. Factors such as these were accounted for when Rietveld refinement was undertaken. The results of the Rietveld refinements of the support crystallite size as a function of temperature are shown in Figure 5.5.

The crystallite sizes from quantitative Rietveld refinements of the support revealed why the use of commercial anatase had both advantages and disadvantages. The crystallite sizes were on average around 90 nm, which is very large when compared to a support such as Degussa P25 where the anatase crystallite size is known to be far smaller, around 25 nm and when compared to synthesised nano anatase, where the average support crystallite size was even smaller, being less then 10 nm.

While the large crystallite sizes of commercial anatase offered very good thermal stability, having very large crystallite sizes was offset by a lower surface area, which is a crucial factor for a catalyst support. BET surface area tests revealed that the surface area corresponding to anatase phase with crystallite

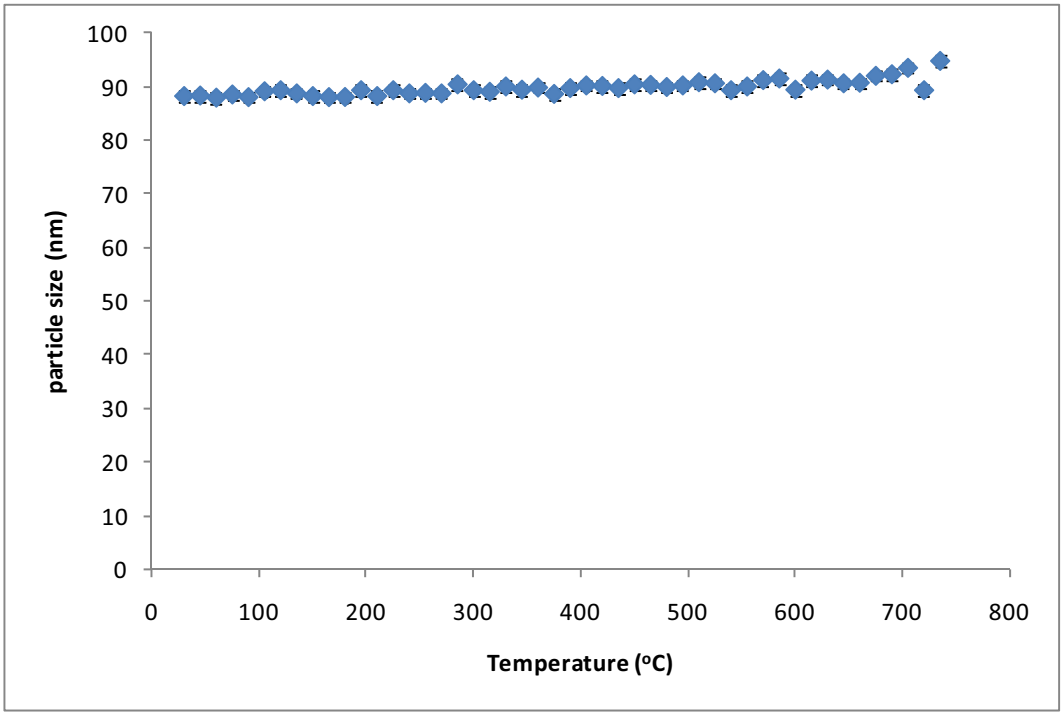


Figure 5.5: Rietveld refinement results of average crystallite size of the commercial anatase support. Large crystallite sizes resulted in lower a surface area, however the support stability at high temperature is good.

sizes between 53-104 nm were 29.7 to 15.0 m^2/g respectively[86]. Thus, compared to Degussa's P25 which had a surface area of $47.1 m^2/g$, the commercial anatase had a significantly lower surface area. The in-situ PXRD results for the commercial anatase support showed that the anatase did not undergo any form of large phase transition from anatase to rutile. However, this was not the case when Au and Au-Pt nanoparticles were placed onto the commercial anatase surface and exposed to the same non-ambient conditions. In-situ PXRD data collections were conducted on samples containing metal loadings of 5% Pt, 5% Au, 5% Au - 1% Pt and 5% Au - 2% Pt samples.

Figure 5.8 and 5.9 show the data collected from the in-situ PXRD of a sample containing 5% Au supported on commercial anatase. A total of 52 patterns were collected over a temperature range of 30^{o} C to 900^{o} C. The diffraction peak of the Au (111) reflection occurred at 38.2^{o} 2θ and was seen to evolve at temperatures around 130^{o}C, although at this temperature the peak was small due to both small gold crystallite size as well as only partial reduction of the gold having occurred. 130° C coincides with the reduction temperature as the oxidized gold nanoparticles were reduced to metallic gold. Above 130° C, the gold peaks gradually began to increase in intensity as the increase in

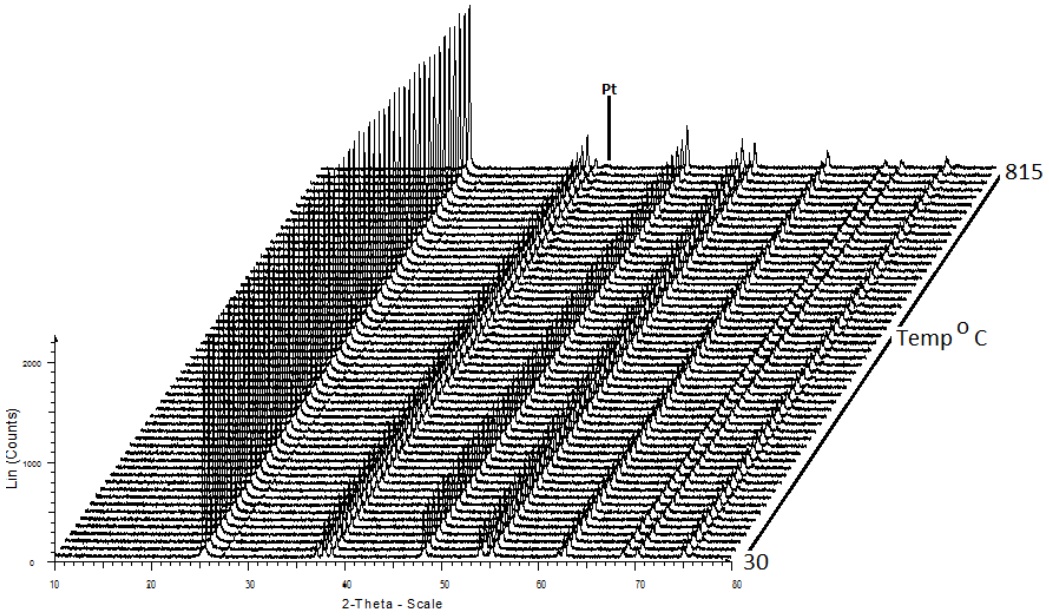


Figure 5.6: In-situ PXRD of 5% Pt supported on commercial anatase. In-situ diffraction studies showed that using the modified DP method it was possible to deposit platinum onto the anatase support as broad diffraction peaks corresponding to the Pt (111) reflection can be seen at high temperatures although the peak is very broad.

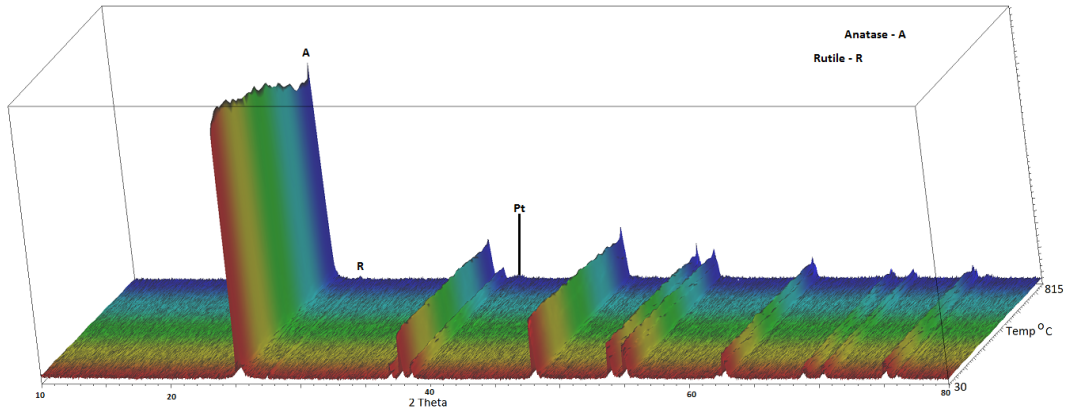


Figure 5.7: In-situ PXRD of 5% Pt supported on commercial anatase.

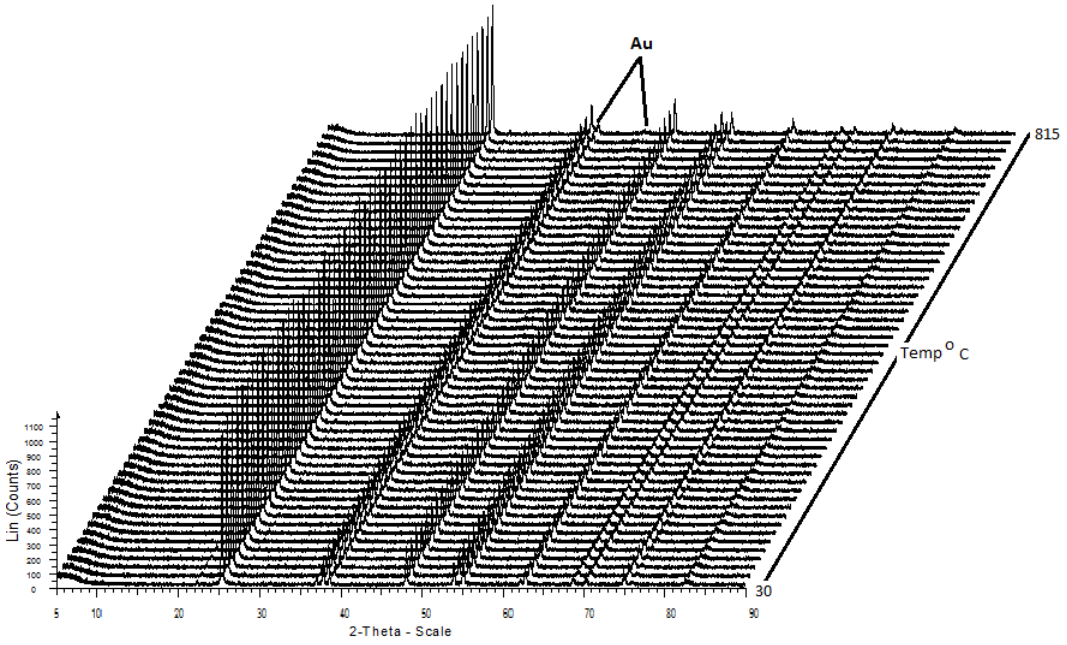


Figure 5.8: In-situ PXRD of 5% Au on commercial anatase.

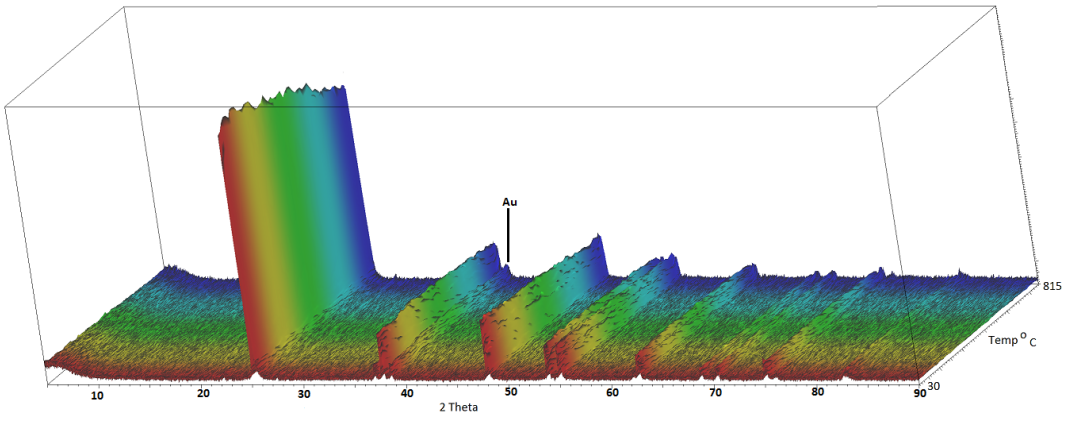


Figure 5.9: In-situ PXRD of 5% Au on commercial anatase.

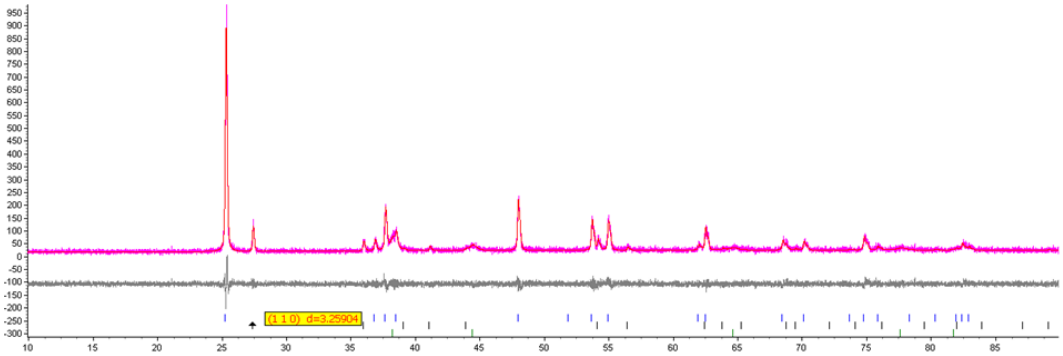


Figure 5.10: Rietveld refinement of one of the 53 collected patterns from the in-situ PXRD data set of 5% Au on commercial anatase. The diffraction pattern shown was collected at high temperature over 800°C with an increase in the evolution of the rutile phase seen as the anatase begins to convert to rutile. The (110) rutile reflection is shown in the yellow box to indicate the phase. Again the difference pattern in grey shows the good fit of the calculated pattern. The evolution of the gold phase can also be seen and is discussed in Figure 5.11. Rietveld refinements were conducted on all the 52 collected diffraction patterns for quantitative analysis.

thermal energy allowed the gold nanoparticles to become more mobile over the surface causing sintering of the gold nanoparticles in order to reduce their surface energy. These observations are confirmed and quantified by Rietveld refinement as shown in Figures 5.10 and 5.11.

Rietveld refinements were conducted on all diffraction patterns from all of the in-situ variable temperature data collections. Figure 5.14 compares the 5% Au sample to the 5% Au-2% Pt sample as well as the evolution of the rutile polymorph of the 5% Au-2% Pt sample.

Figure 5.14 shows the refinement results comparing the 5% Au and 5% Au-2% Pt on commercial anatase catalysts. The plot shows a comparison of gold particle sizes between the 5% Au and 5% Au-2% Pt samples on commercial anatase TiO_2, with each data point corresponding to the data attained from the Rietveld refinement performed on the diffraction data attained at that temperature. The refinements showed consistent and acceptable Figures of merit with averaged GOF = 1.10 ($\pm$ 0.6), D_W = 1.87 ($\pm$ 0.6) and an R_{wp}=16.7 ($\pm$ 1.4). The phase percentage of rutile, also determined during the refinement, is plotted on the second y-axis. The amount of rutile phase titania present increased rapidly in the 5% Au-2% Pt sample at temperatures over 650^{o}C.

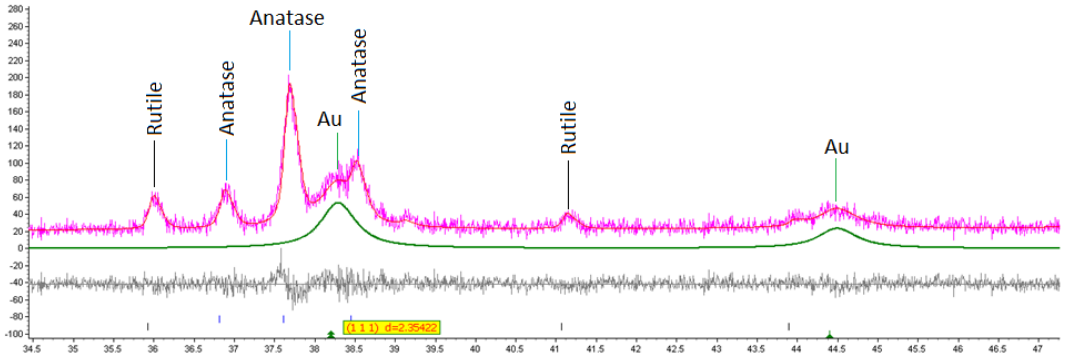


Figure 5.11: A zoomed image taken from TOPAS (34.5° - 47.5° 2θ) of the three phases under investigation after the 5% Au on commercial anatase catalyst was exposed to high temperature for a number of hours in the XRK chamber. The usefulness of the Rietveld method is demonstrated as even phases that were overlapping could be accurately resolved. Here, anatase, rutile and gold phases are all overlapping in the 37.5° - 39.0° 2θ range. The use of the Rietveld method allowed for the gold diffraction peaks to be accurately resolved and analyzed. This is shown in the green calculated diffraction peaks in the image. On completion of the refinement gold crystallite size could be accurately attained as well as quantitative phase information. An R_{DW} value of 1.86 confirmed the high quality data fit.

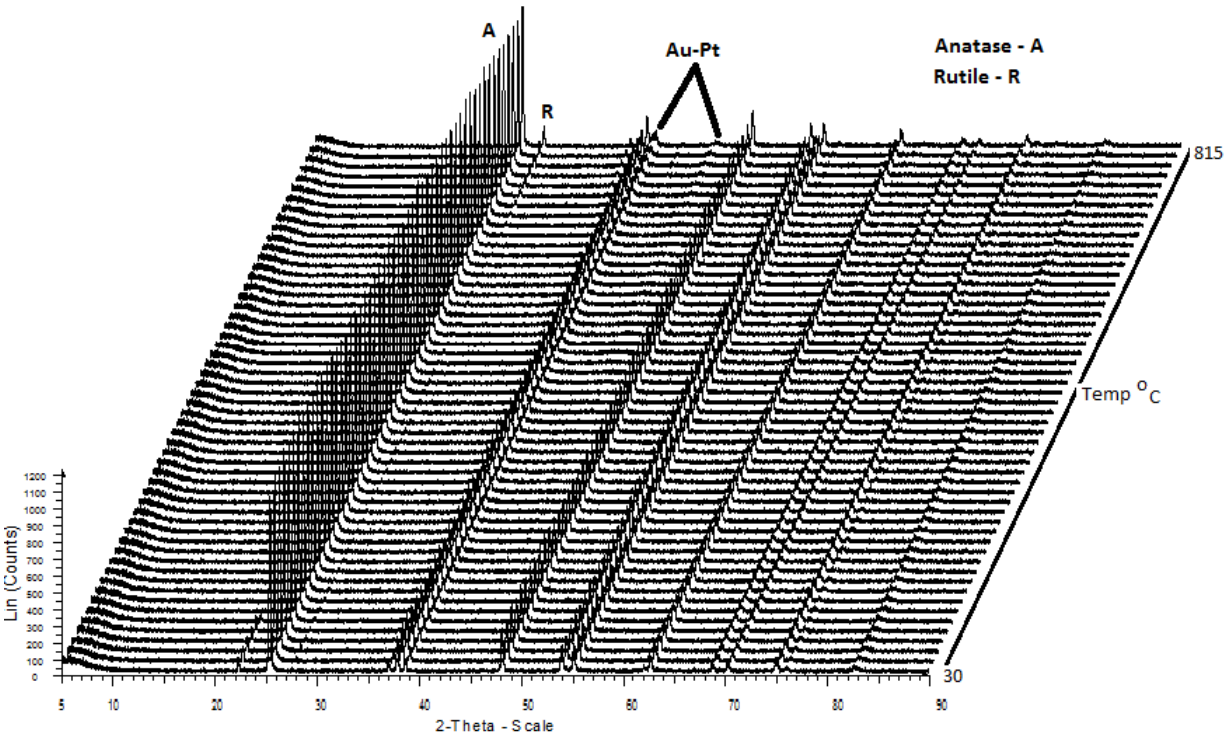


Figure 5.12: In-situ PXRD of 5% Au-2% Pt supported on commercial anatase.

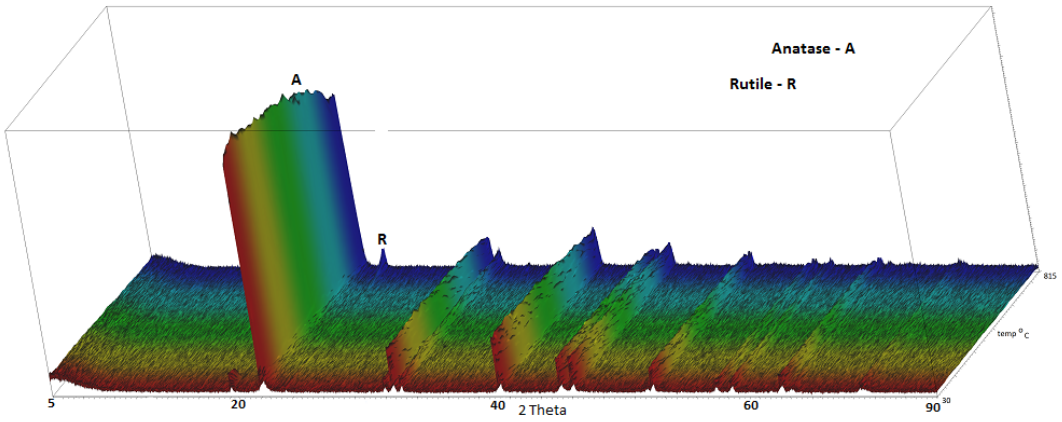


Figure 5.13: In-situ PXRD of 5% Au-2% Pt supported on commercial anatase.

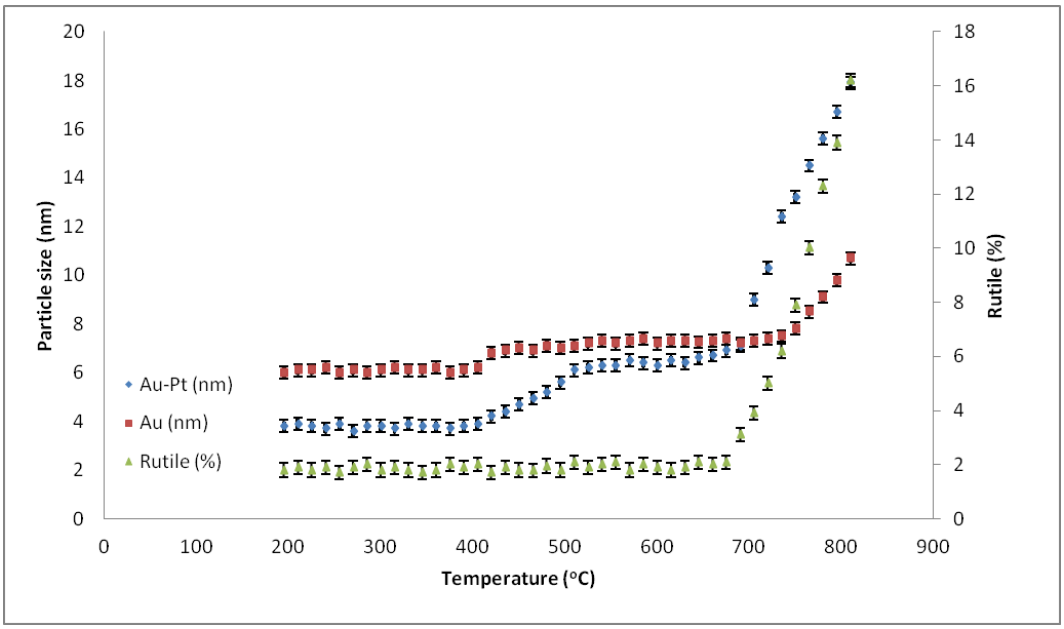


Figure 5.14: 5% Au and 5% Au-2% Pt on commercial anatase showing particle sizes and support phase dependence on temperature. Refinements commenced at 200°C to ensure that reduction of the catalysts had taken place. The small increase in the crystallite sizes at 400°C-500°C is due to the metal particles rearranging themselves on the surface as seen in the TEM study in Section 5.5 The rearrangement results in more stable nanoparticles with slightly larger sizes. The rapid growth of the metal nanoparticles at 690°C is a result of the support undergoing a phase transition from anatase to rutile.

The rapid growth of the supported nanoparticles could be observed to correlate directly with the increase of the amount of rutile phase. After the initial increase of the rutile phase around 650°C, the nanoparticle crystallite size grew in direct proportion to the percentage rutile phase, while the 5% Au sample showed a much more gradual growth with only a small increase in the rutile phase after 810°C. This indicated there may be a catalytic effect of platinum to promote the anatase to rutile phase transformation or, that the combination of gold and platinum provided more sites to catalyse the phase conversion when compared to the sample only containing gold. The metal catalysed phase transition was demonstrated in Section 5.5 when TEM was conducted.

Between 200°C and 400°C, a difference in gold crystallite size of greater than 2 nm was observed between particles with and without platinum. This difference in crystallite size was very similar to the results obtained for the Au and Au-Pt supported on silica samples at the same temperatures. From 500°C the Au-Pt sample crystallite size increased to near that of the pure gold sample. At this point the only feasible explanation was that the metal nanoparticles may have undergone some form of rearrangement, altering any stabilizing effect of the platinum. This hypothesis was confirmed by TEM findings when the samples were analyzed.

The first temperature at which the Au and Au-Pt nanoparticles show a marked increase in size was approximately 450°C. The growth was gradual and did not occur rapidly which was likely due to sintering caused from the increase in temperature. However, the rapid growth that occurred at approximately 690°C showed a direct correlation to the phase percentage of rutile at that temperature. Even at 810°C the 5% Au sample showed a far slower conversion of anatase to rutile that may have been attributed to the metal loadings as the 5% Au sample consisted of 40% less loaded metal when compared to the 5% Au-2% Pt sample.

Use of the DP method for the deposition of nanoparticles onto various supports did not result in 100% of the precursor metal reaching the surface[64]. Quantitative phase analysis from the Rietveld refinements showed that the actual loading of the 5% Au sample was 3.5% ± 0.35%. At low temperatures, before complete reduction had taken place, this value was even lower at 2.2-2.5% (± 0.35%). However this was merely due to some of the gold still being in an oxidized state. The increase from 2.2% to 3.5% gold corresponded to the

complete reduction of the gold.

5.5 TEM

All prepared samples were divided into two, one sample for in-situ PXRD analysis and one for TEM. The TEM samples were then split into a number of smaller batches with the smaller batches being heated to 300°C and 400°C for a period of two hours. This allowed for the observation as to the type of changes the support and the Au as well as the Au-Pt nanoparticles undergo as the samples are exposed to non-ambient temperatures. When compared to the variable temperature diffraction results for the average crystallite size of the commercial anatase support, the TEM images showed that the support material was comprised of large particles (over 85 nm) comparing well to the Rietveld refinement results. While large particle sizes gave a low surface area for the support, this also implied good thermal stability due to the large crystallites. This was seen from the TEM images where, even after heating the samples to 400°C, the support did not show any significant change in particle size. Finally, EDS analysis was undertaken in order to try determine where the platinum was found in relation to gold and if a type of bimetallic or alloy was formed between the two metals. The EDS spectrum can be seen in Figure 5.32.

5.5.1 TEM analysis of 5% Au supported on commercial anatase

Initial low magnification images (such as Figure 5.15) showed good dispersion of the nanoparticles over the surface with a relatively narrow range of gold particle sizes. Particle size analysis was conducted on all images that were collected. ImageJ software was used to measure the average particle diameter of the Au and Au-Pt particles. For each composition of Au and Au-Pt samples, a minimum of 450 particles from numerous micrographs were analyzed to obtain a statistically accurate particle size distributions for the various compositions. For this reason a large number of images were collected at randomly chosen positions around the sample. The results of the particle size analysis are graphed at the in Section 5.6.1 in Figure 5.39. At lower magnification it

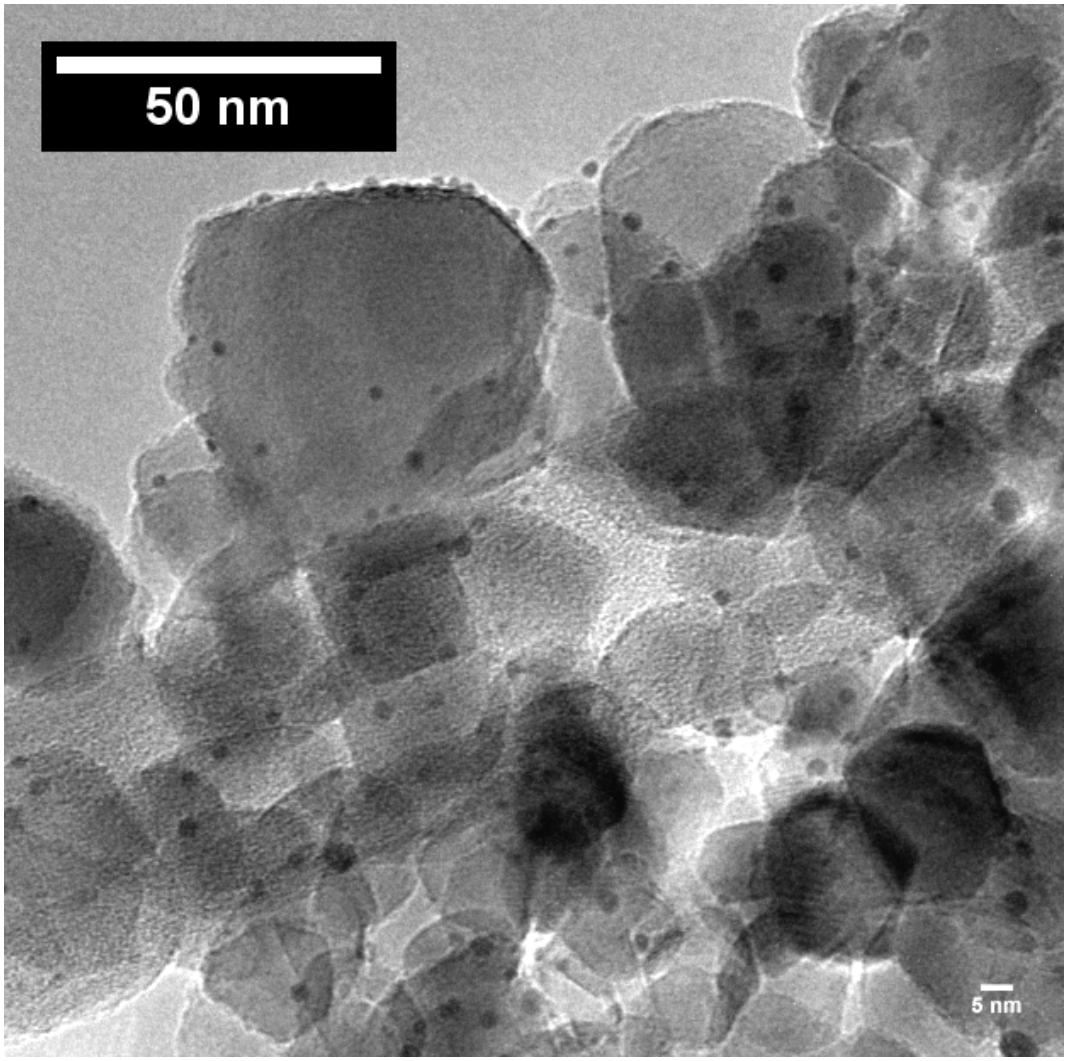


Figure 5.15: TEM image of gold nanoparticles supported on commercial anatase heated to 300°C for 2 hours.

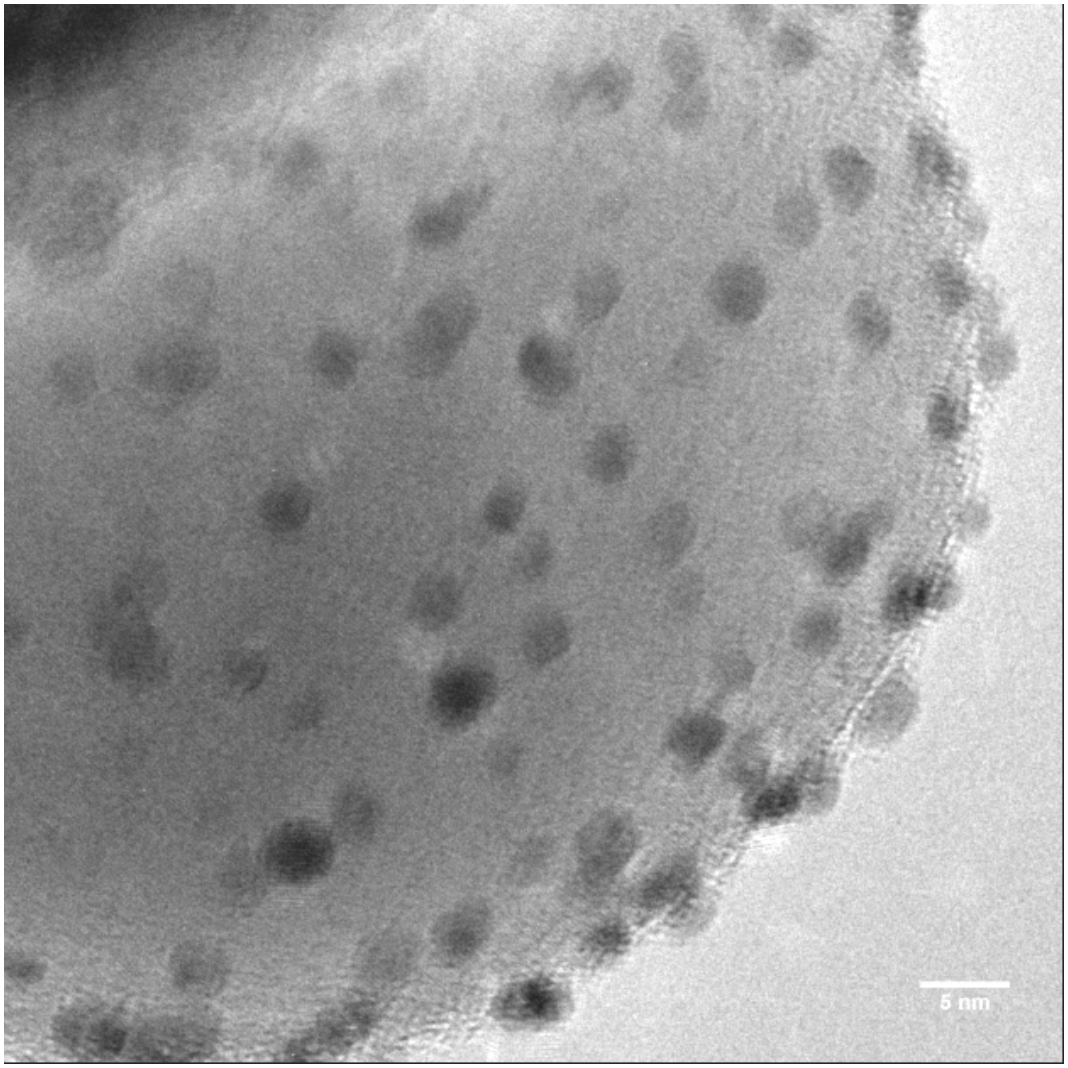


Figure 5.16: High magnification image of gold on anatase heated to 300°C.

was not possible to see very small particles. These particles only became visible under the HR-TEM. With the use of the high resolution TEM, particles of less than 1.5 nm became visible as shown in Figure 5.16.

5.5.2 TEM analysis of 5% Au-1% Pt supported on commercial anatase

Images 5.19 - 5.23 show TEM images collected of 5% Au-1% Pt supported on commercial anatase, some of which have been heated to different temepratures to investigate the effects that these different temperatures have on the support as well as gold-platinum particle sizes.

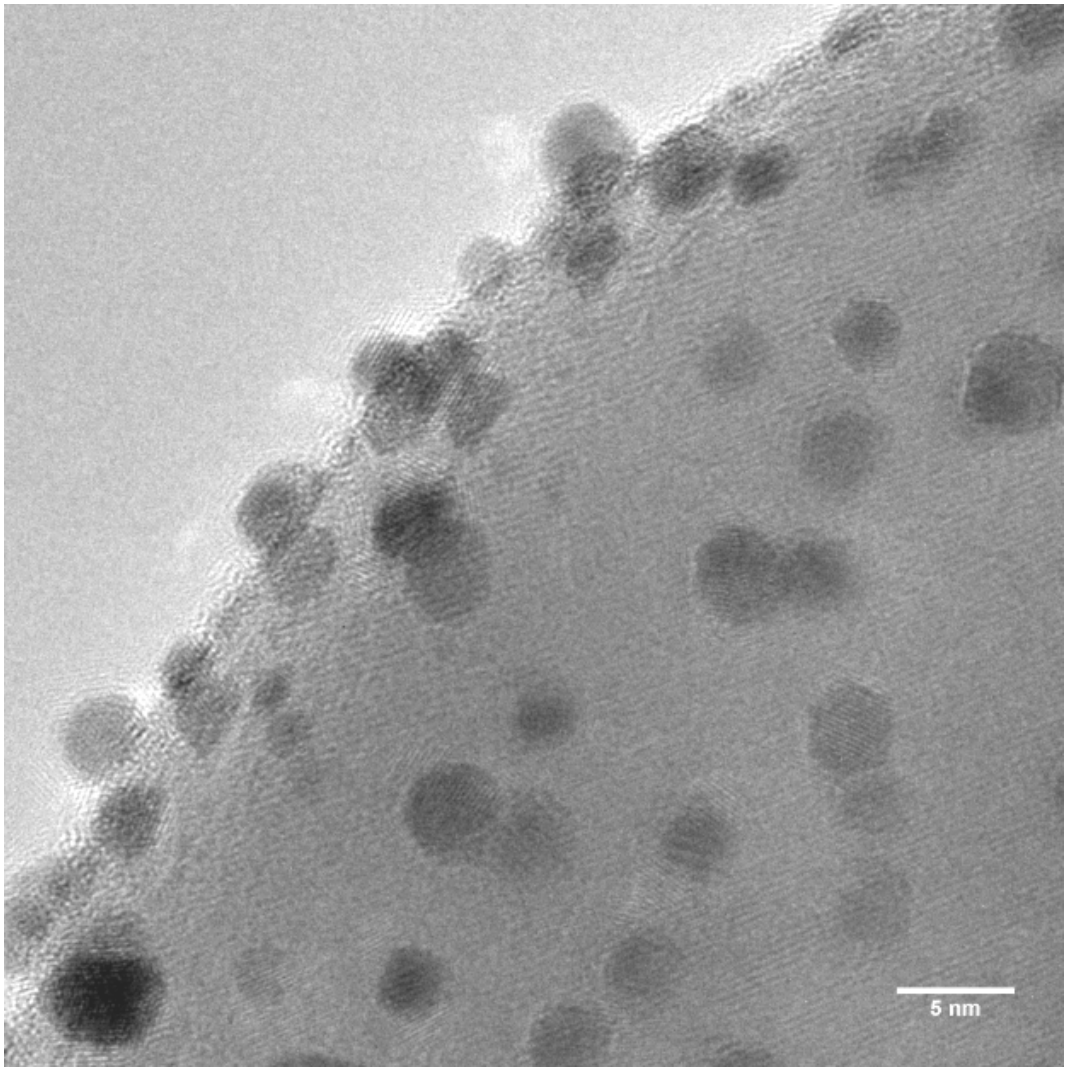


Figure 5.17: HR-TEM image of gold on anatase heated to 400°C. Epitaxial contact between the gold nanoparticles and the support was noted.

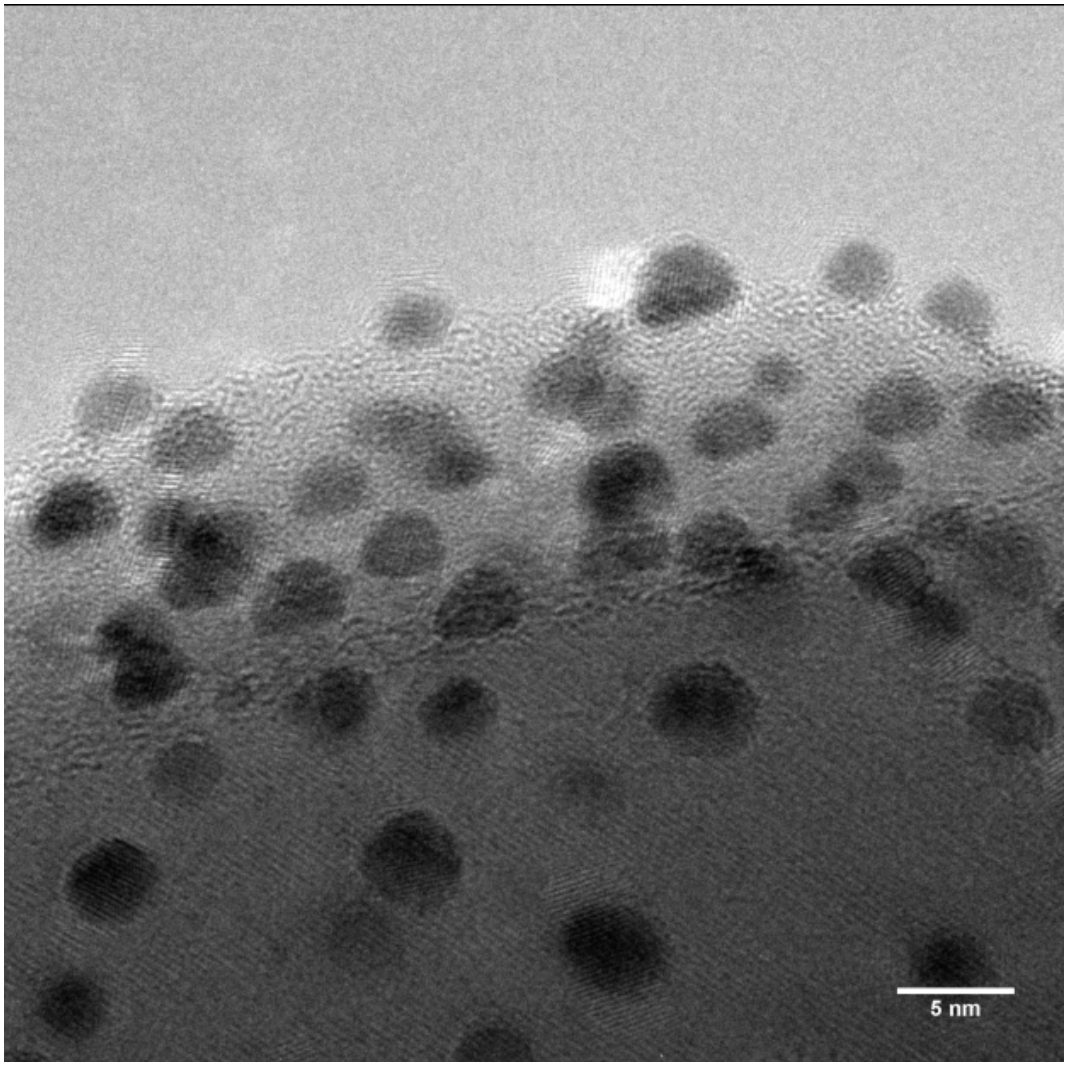


Figure 5.18: HR-TEM of 5% Au-1% Pt heated to 300°C for 2 hours on anatase.

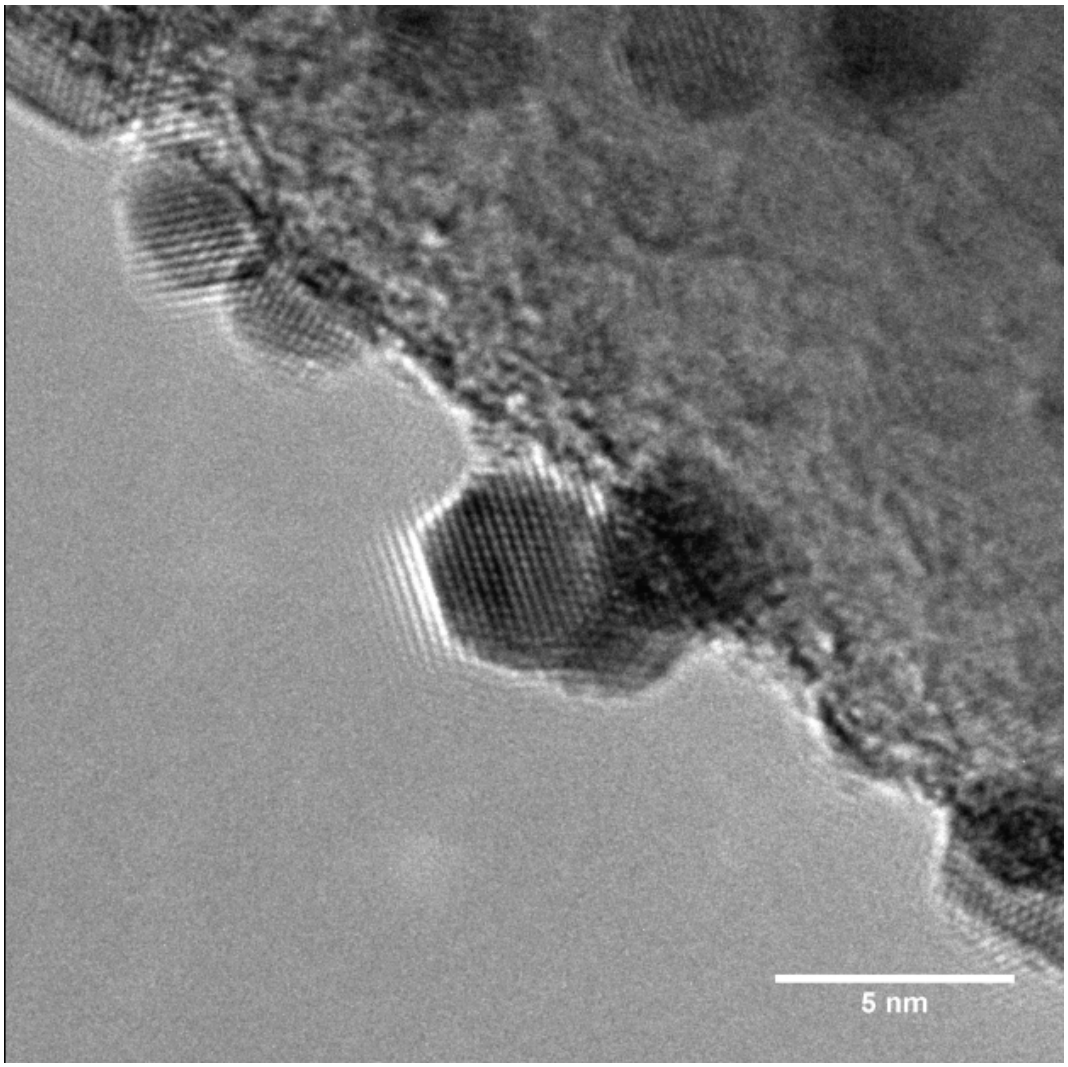


Figure 5.19: HR-TEM image taken at high magnification of 5% Au-1% Pt on anatase showed the interesting shapes of the nanoparticles after heating to 300°C. Many of the nanoparticles exhibited a hexagonal structure. The geometry of the nanoparticles is dependent on a number of factors. Rearrangements of the nanoparticles were seen to occur as temperature varied. These rearrangements of the nanoparticles structure can be either positive or detrimental depending on how the rearrangement takes place and what structure is taken. It was noted that in general the rearrangements that took place using the method described in this text resulted in epitaxially bound hemispherically shaped nanoparticles which are ideal for carbon monoxide oxidation reactions as shown in Figure 5.19-5.21.

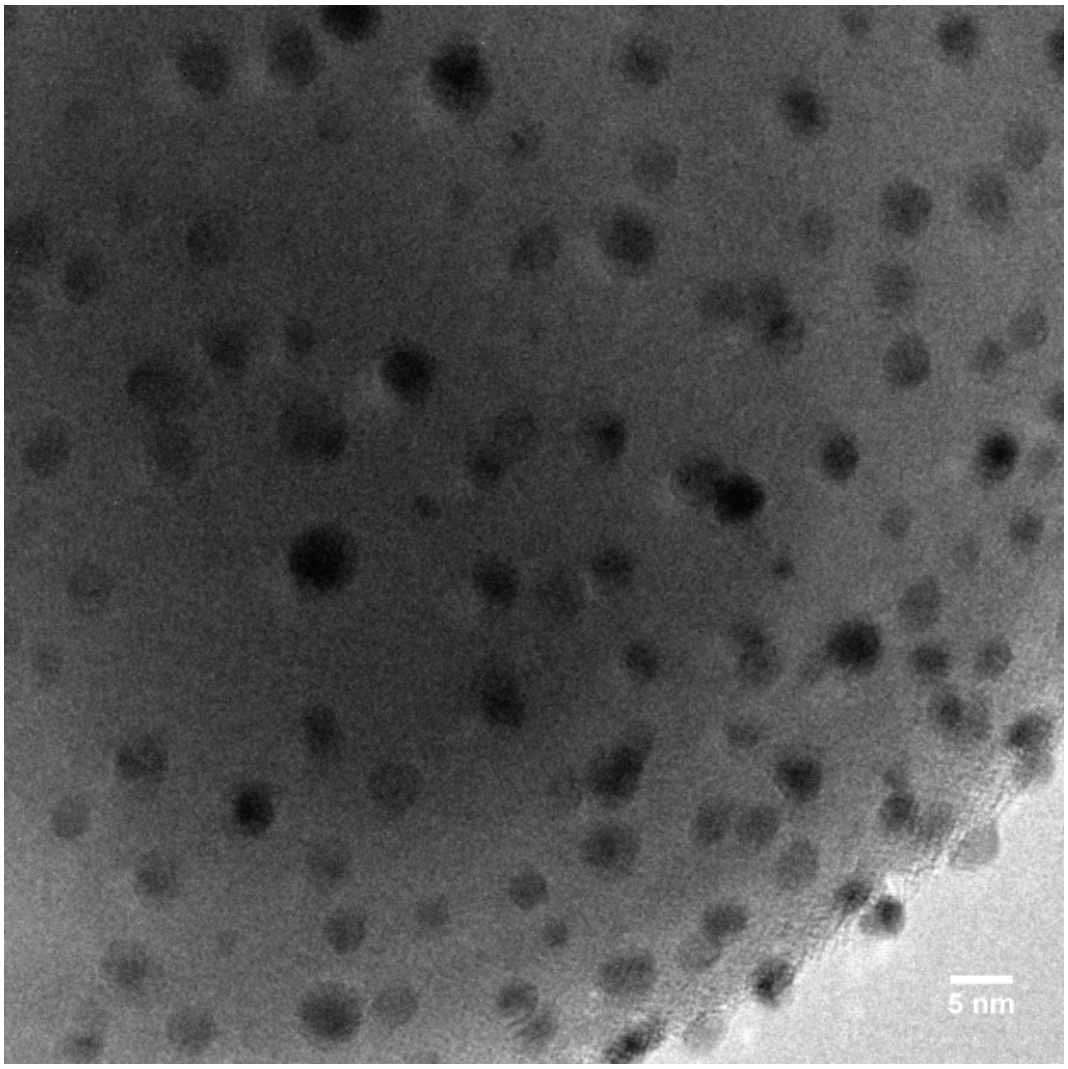


Figure 5.20: 5% Au-1% Pt on anatase heated to 400°C. With the use of HR-TEM particles of less than 1.5 nm can be seen. The massive size of the support material can also be seen from the image.

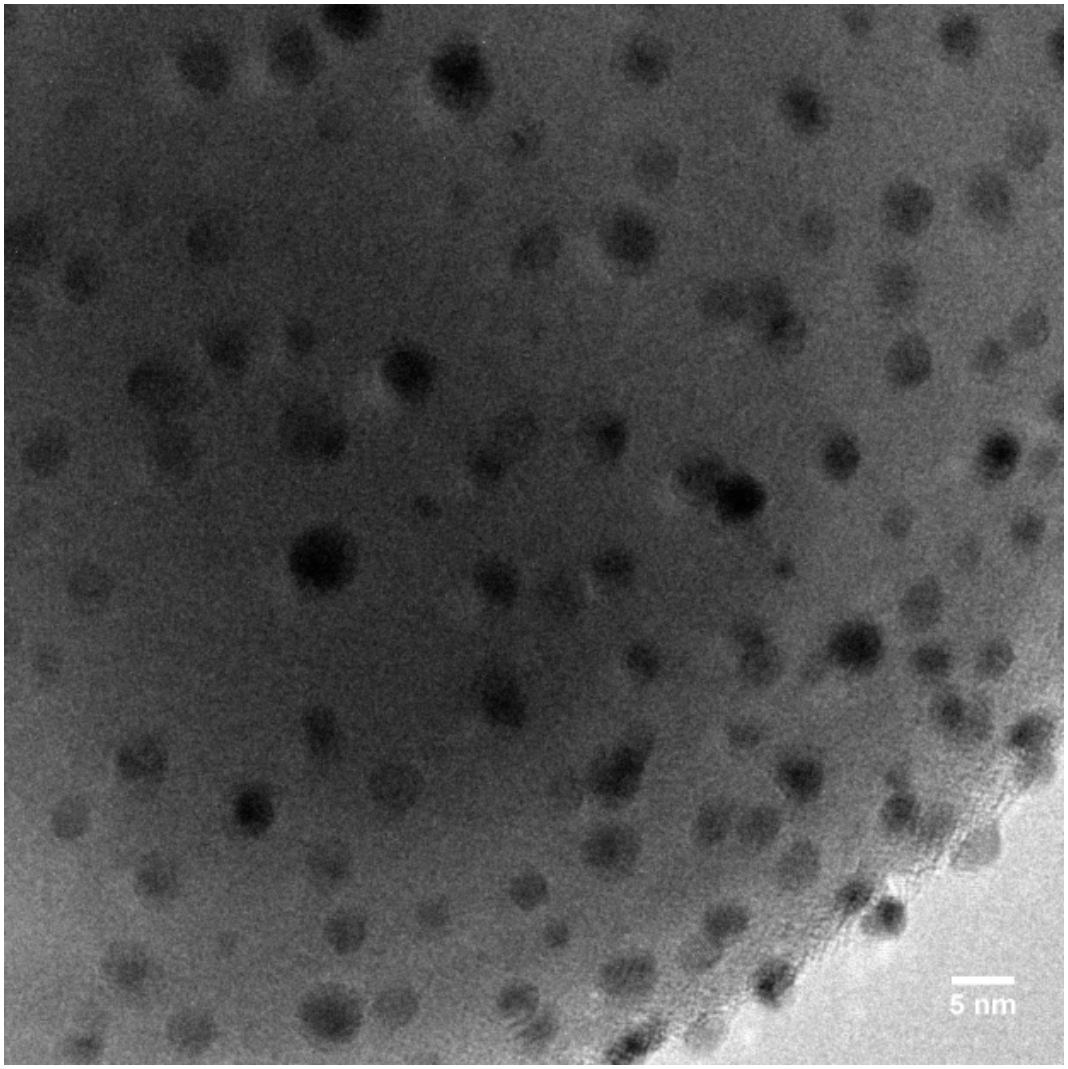


Figure 5.21: High magnification image of 5% Au- 1% Pt on anatase heated to 400°C.

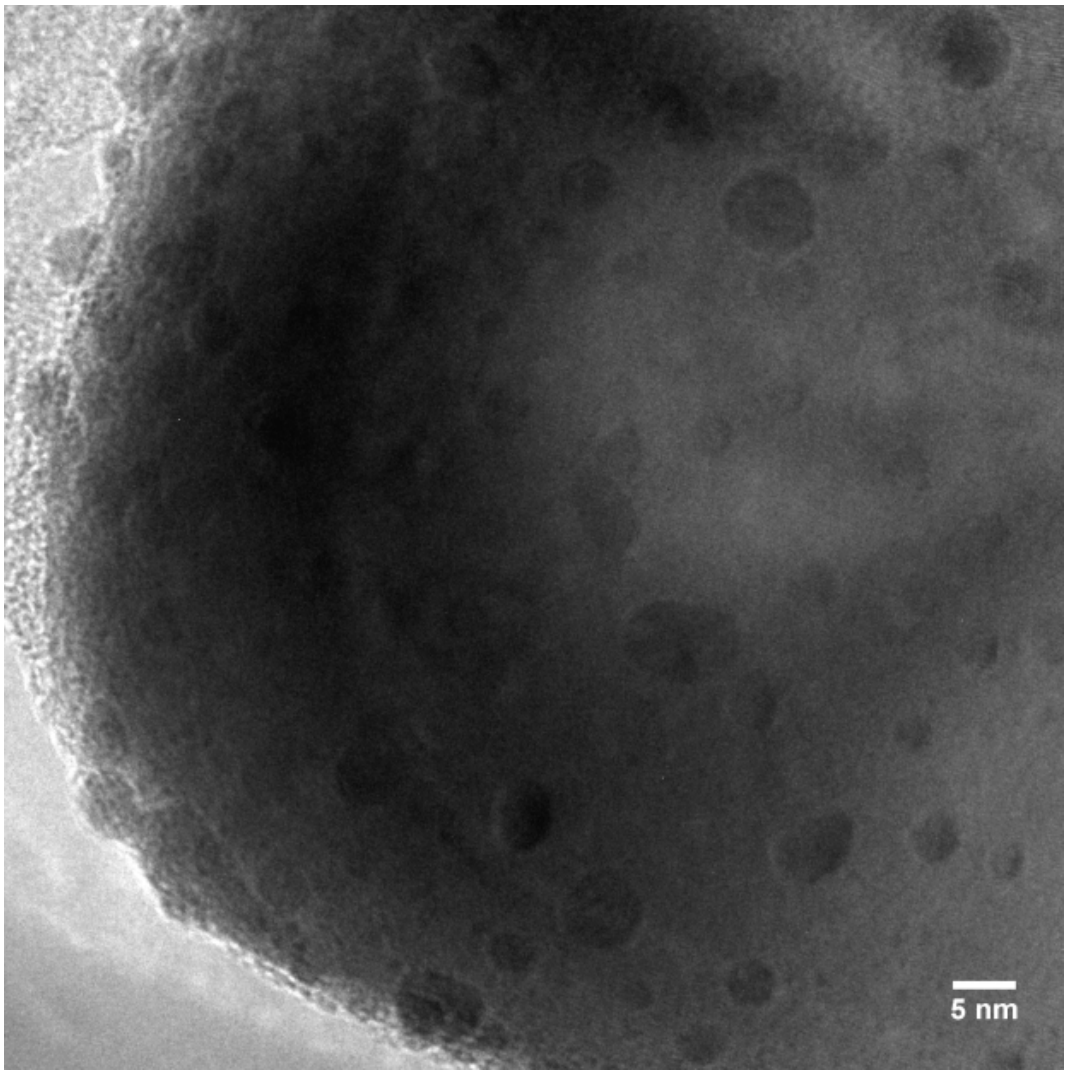


Figure 5.22: 5% Au-1% Pt on anatase after exposure to 400°C for 2 hours. The image showed that many of the particles had increased in size while some of the more isolated particles had remained small. This gave some information on the process of sintering as the process did not appear top be uniform when the change in size of the particles was considered.

5.5.3 TEM analysis of 5% Au-2% Pt supported on commercial anatase

The quantitative phase analysis via Rietveld refinements of the in-situ PXRD data collections revealed the presence of small amounts of rutile phase even though the manufacturer Sigma-Adrich claimed that the anatase was phase pure. Even though the amount of rutile was initially very small (less than 2%), this small amount of the more thermodynamically stable phase resulted in the enhancement of the rate at which phase conversion from anatase to rutile occurred. The conversion rate was further increased when metallic nanoparticles were present on the surface of the support and the catalyst was exposed to non-ambient conditions. Figure 5.24 demonstrated this as a Au- Pt nanoparticle was observed positioned on the phase boundary where the conversion of anatase to rutile was occurring. The metal nanoparticle was seen to be catalyzing the phase transition as the anatase to rutile phase transition should have only occurred over 750°C after a long period of exposure to this temperature[20].

From the PXRD results it was determined that the phase transition was occurring at 670°C for the given heating rate as kinetics also play a role in the conversion rate. The reason for the discrepancy between the in-situ PXRD and TEM data resulted from XRD analysing the catalyst as a bulk. Thus, after heating at moderate temperatures of 400°C, as shown in the TEM analysis, the amount of rutile was still very low and isolated at these temperatures but easily noted using the TEM. Only once the phase transition began to occur more rapidly as more anatase was converted did XRD note its rapid evolution. This was due to the XRK chamber using a heating ramp to slowly heat to 400°C while scans were collected. Once the chamber reached 400°C a scan was started immediately and did not dwell at 400°C for two hours as was the case for the TEM samples heated in the furnace. The TEM analysed samples were placed in a furnace and heated rapidly to 400°C then held at this temperature for 2 hours. For catalysts such as Mintek's Aurolite catalyst, that are supported on P25 TiO_2, the phase transition was seen to be as low as 450 - 500°C and will be discussed further in Chapter 6.

Even after exposure to a relatively low temperature, the onset of the anatase to rutile phase transition could be noted as shown in Figure 5.24. The manner in which the phase transition occurred was postulated. Beginning with a very small amount of rutile being slowly converted to rutile at a metallic site such

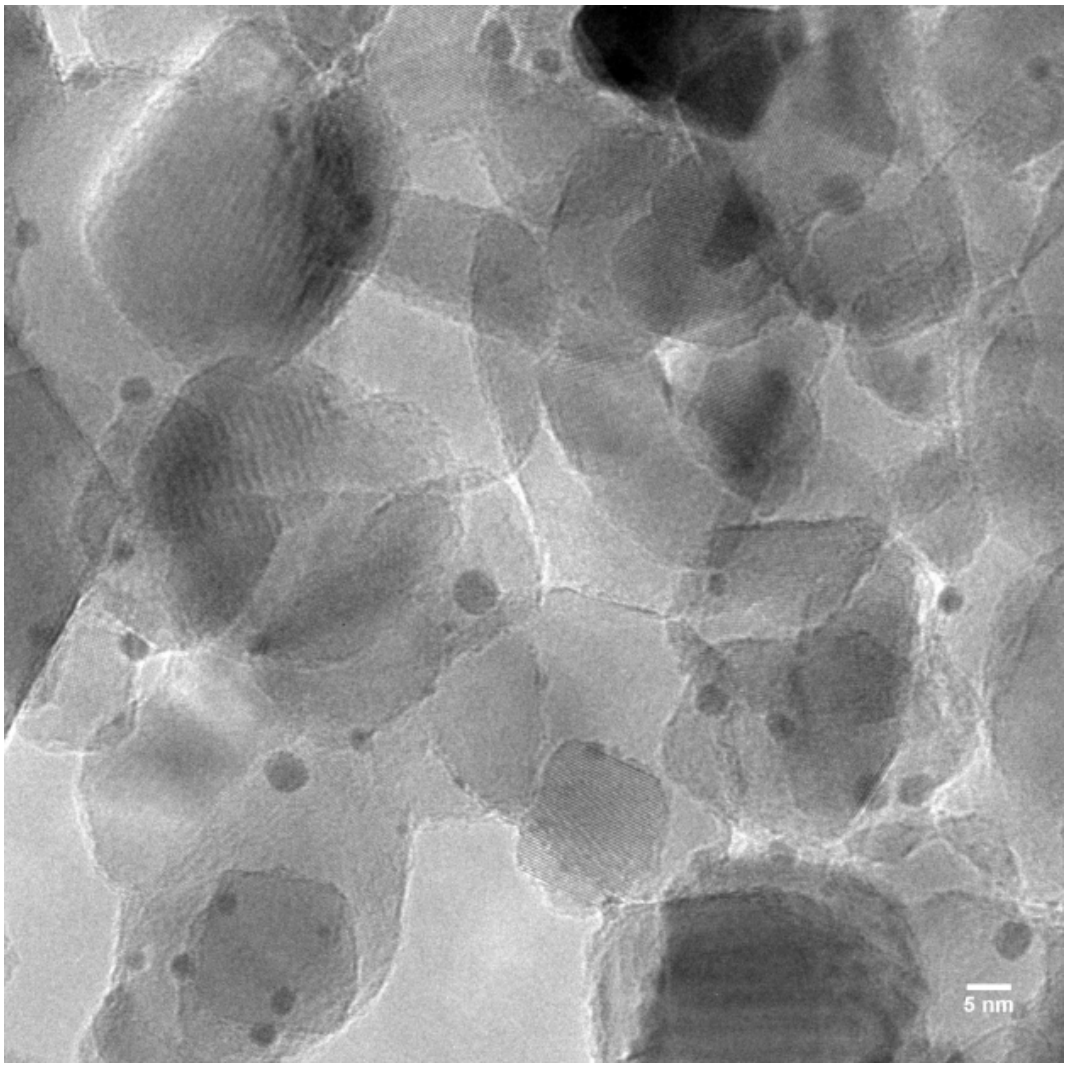


Figure 5.23: Low magnification image of 5% Au-2% Pt nanoparticles supported on commercial anatase after exposure to 400°C for 2 hours showing homogeneous dispersion and smaller particle sizes compared to the 5% Au sample heated to the same temperature. The images showed a distribution of particle sizes with a number of particles smaller than 5 nm and some particles even smaller than 2 nm. The very small particles are only clearly visible at higher magnifications. These distributions are graphed in section 5.6.1.

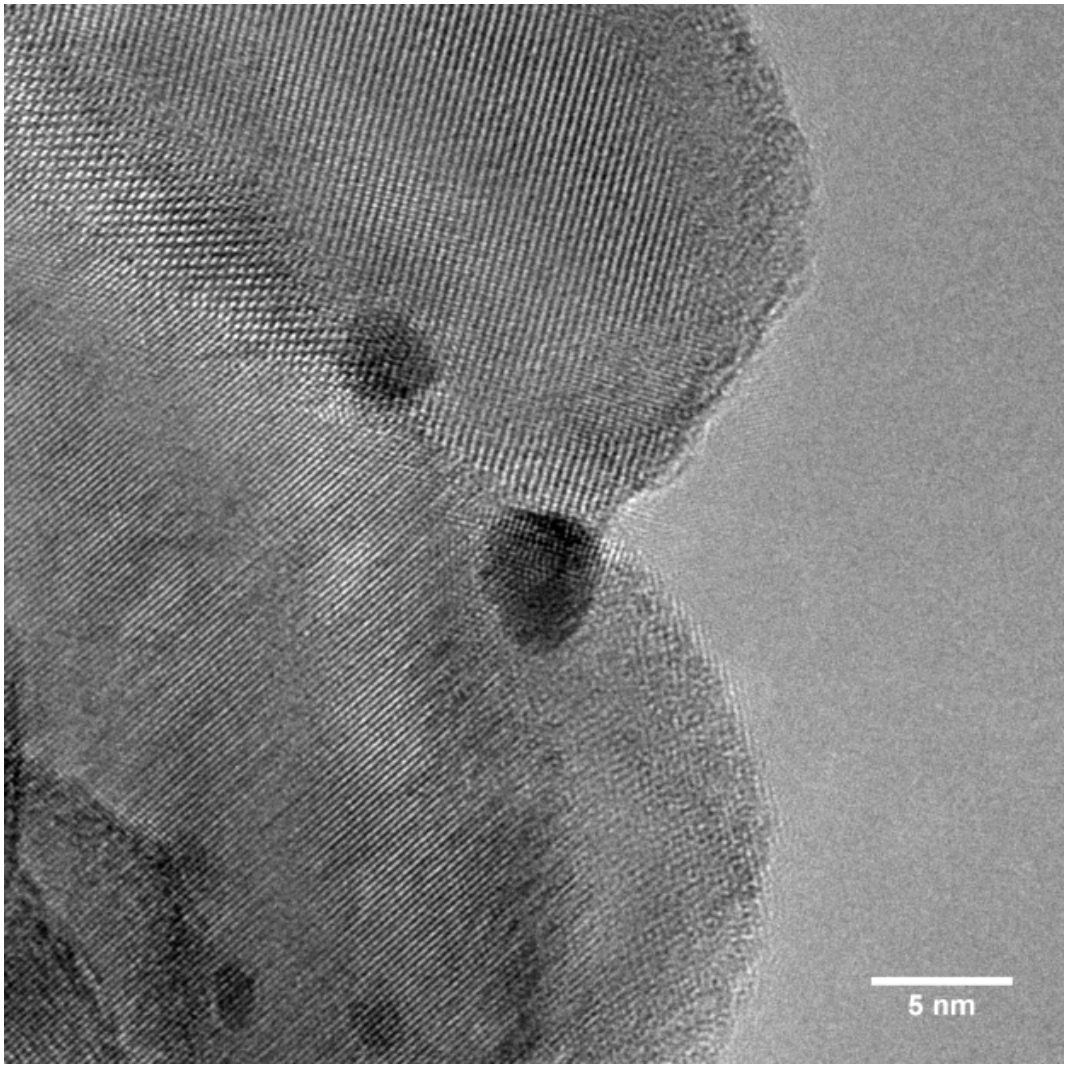


Figure 5.24: High magnification HR-TEM of Au-Pt nanoparticles on the anatase-rutile phase boundary catalyzing the phase transformation from anatase to rutile after heating to 400°C. The reason for the later onset of the emergence of the rutile phase in the PXRD is due to the heating rates that were selected for the data collections. If the heating rate was slower and data collections took longer the rutile phase would emerge at lower temperatures. This was seen in the in-situ PXRD data collections on the Aurolite catalyst where data collections are significantly longer (Chapter 6).

as the gold or gold-platinum nanoparticle-titania interface as shown in Figure 5.24. The conversion reached a critical point where the phase transition rate became exponential. This could be seen from the in-situ PXRD data where the growth of the rutile phase increased exponentially at 690°C.

The range of motion of the nanoparticles over the surface appears to be limited by the energy that is imparted to the system via thermal energy provided to the system. After examination of the TEM images following the catalysts exposure to various temperatures, the change in the distribution of the Au and Au-Pt particles size showed interesting results. What appeared to be happening was that the isolated nanoparticles remained small due to their inability to translate significantly far over the surface in order to merge with other particles. Only the particles that, while still independent, were in close proximity to other nanoparticles were able to merge to form larger particles. This may be an intuitive conclusion but the rationale behind it impacts on the choice of support and the metal loading used for catalysts. For this reason the metal loading must be very carefully chosen with respect to the surface area of the support material. In many instances the surface quickly became overloaded as the amount of supported material increased. Thus an increase in supported material can result in a catalyst that deactivates more rapidly when compared to a catalyst with less supported material. This is due to the close proximity of the supported material on the surface and even a small amount of thermal energy may impart enough energy for the nanoparticles to translate the small distance in order to sinter with a neighboring nanoparticle and relieve surface energy. Further, in many cases, as will be shown in Chapter 6, the surface area can decrease by more than a factor of 10 which leaves the supported material on a very different support structure when compared to the properties that the support had when the catalyst was produced.

Images 5.25 - 5.31 show TEM images collected of 5% Au-2% Pt supported on commercial anatase, some of which have been heated to different temepratures to investigate the effects that these different temperatures have on the support as well as gold-platinum particle sizes. Further, the addition of 1% more Pt is also investigated to determine if the addition of more Pt aids in the catalysts thermal stability.

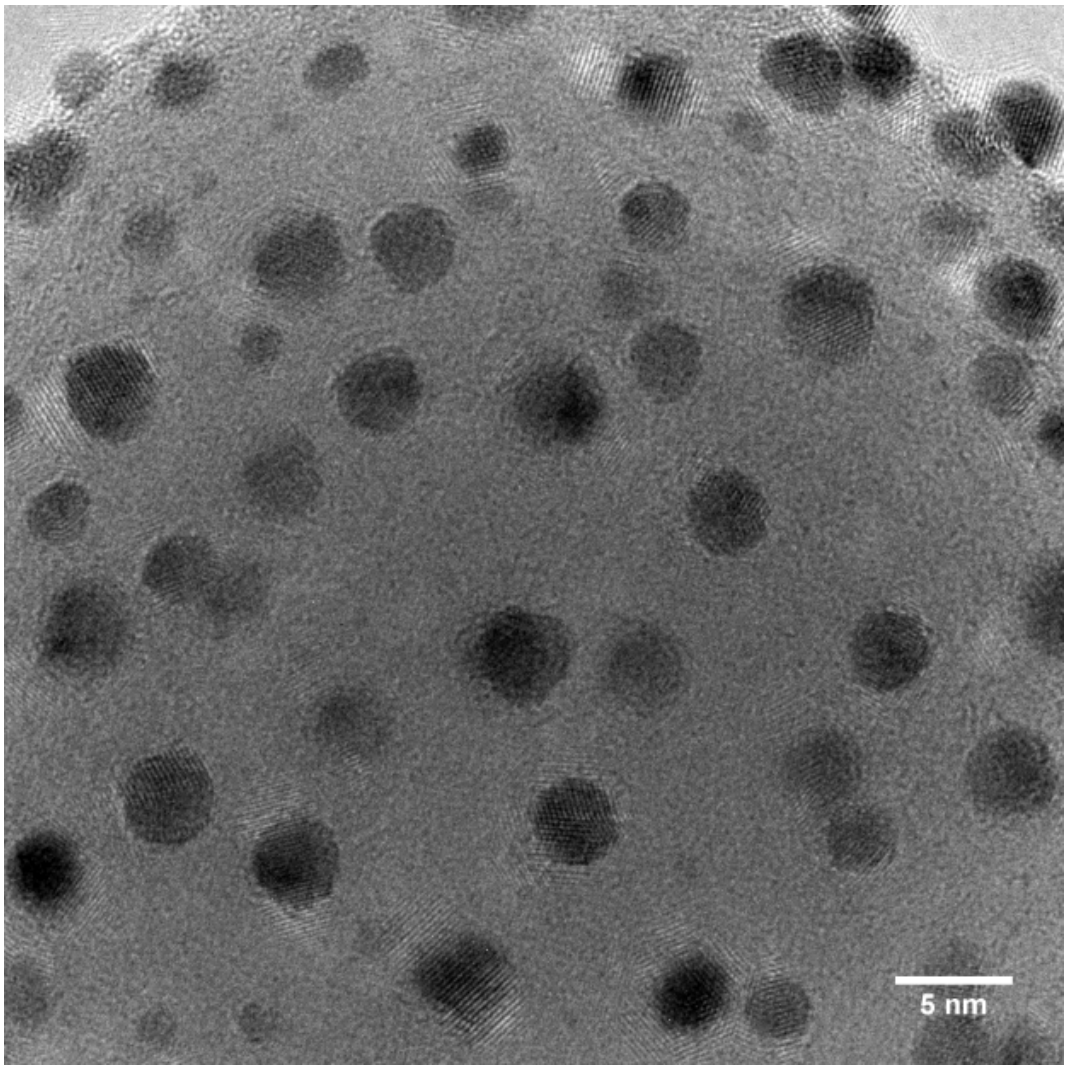


Figure 5.25: HR-TEM image of 5% Au-2% Pt on anatase after heating to 400°C.

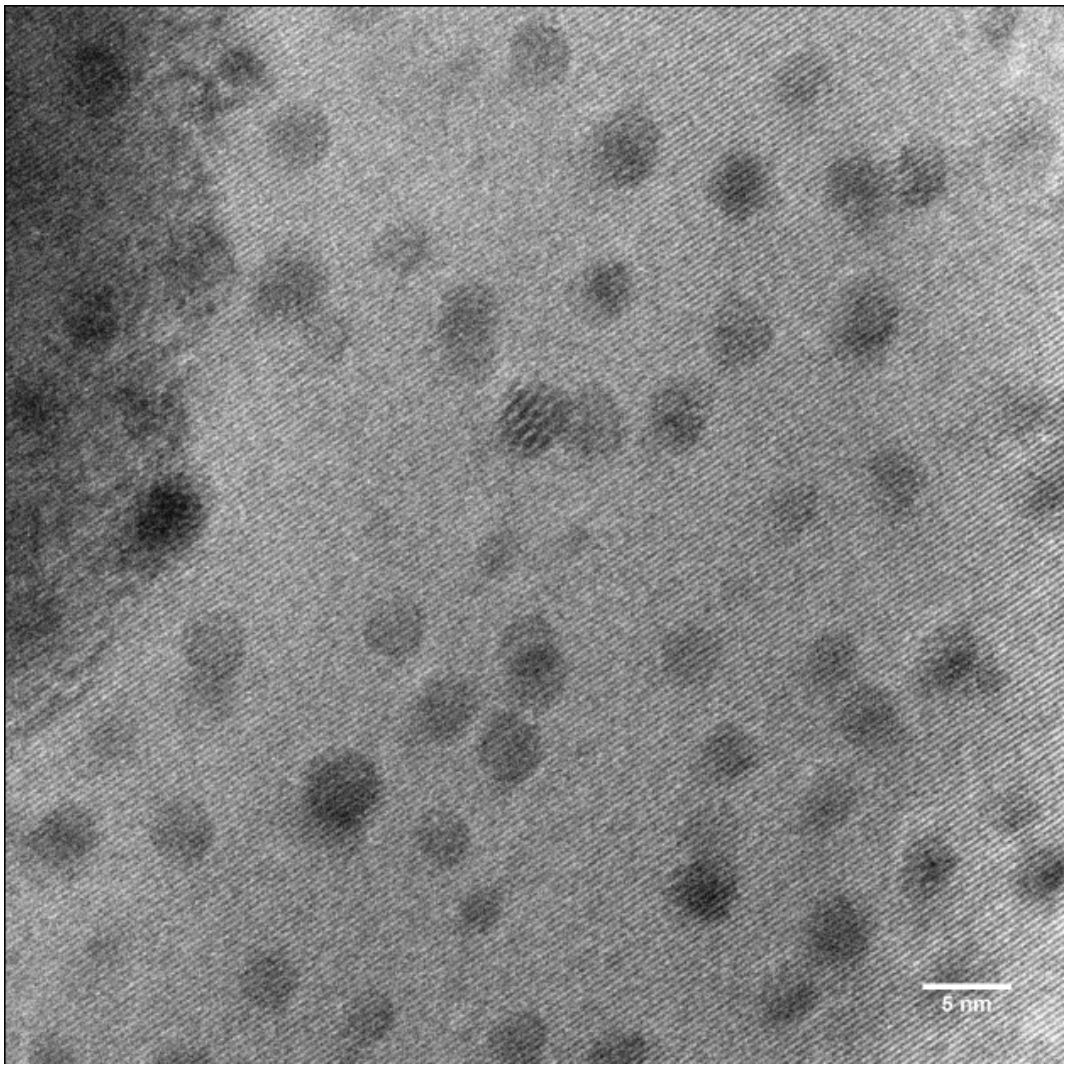


Figure 5.26: HR-TEM image of 5% Au-2% Pt on anatase after heating to 400°C. HR-TEM showed many of the smaller nanoparticles that were not visible at lower magnification. This image also shows the beautiful orientation and arrangement of the crystal planes that make up the commercial anatase support.

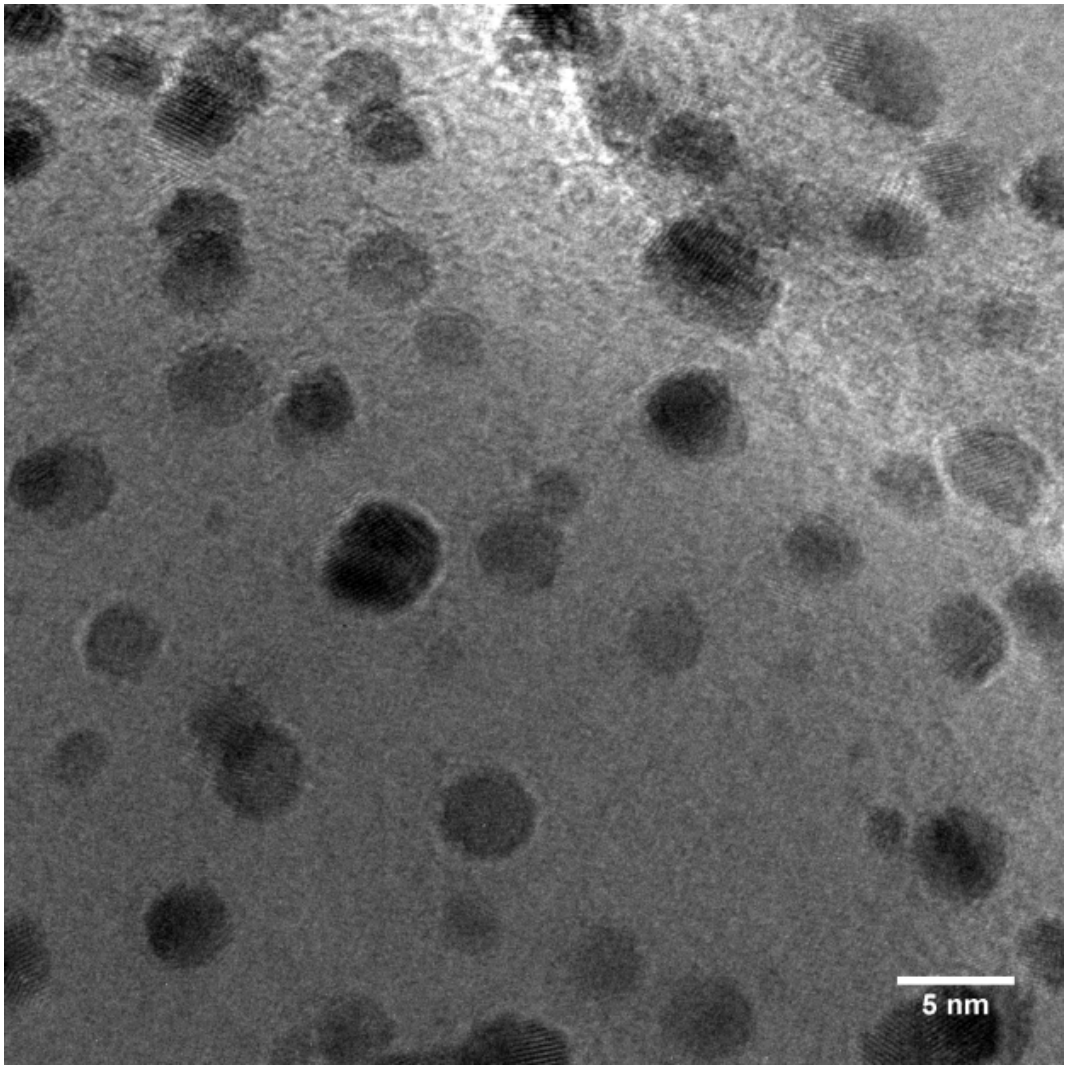


Figure 5.27: HR-TEM image of 5% Au-2% Pt heated to 300°C.

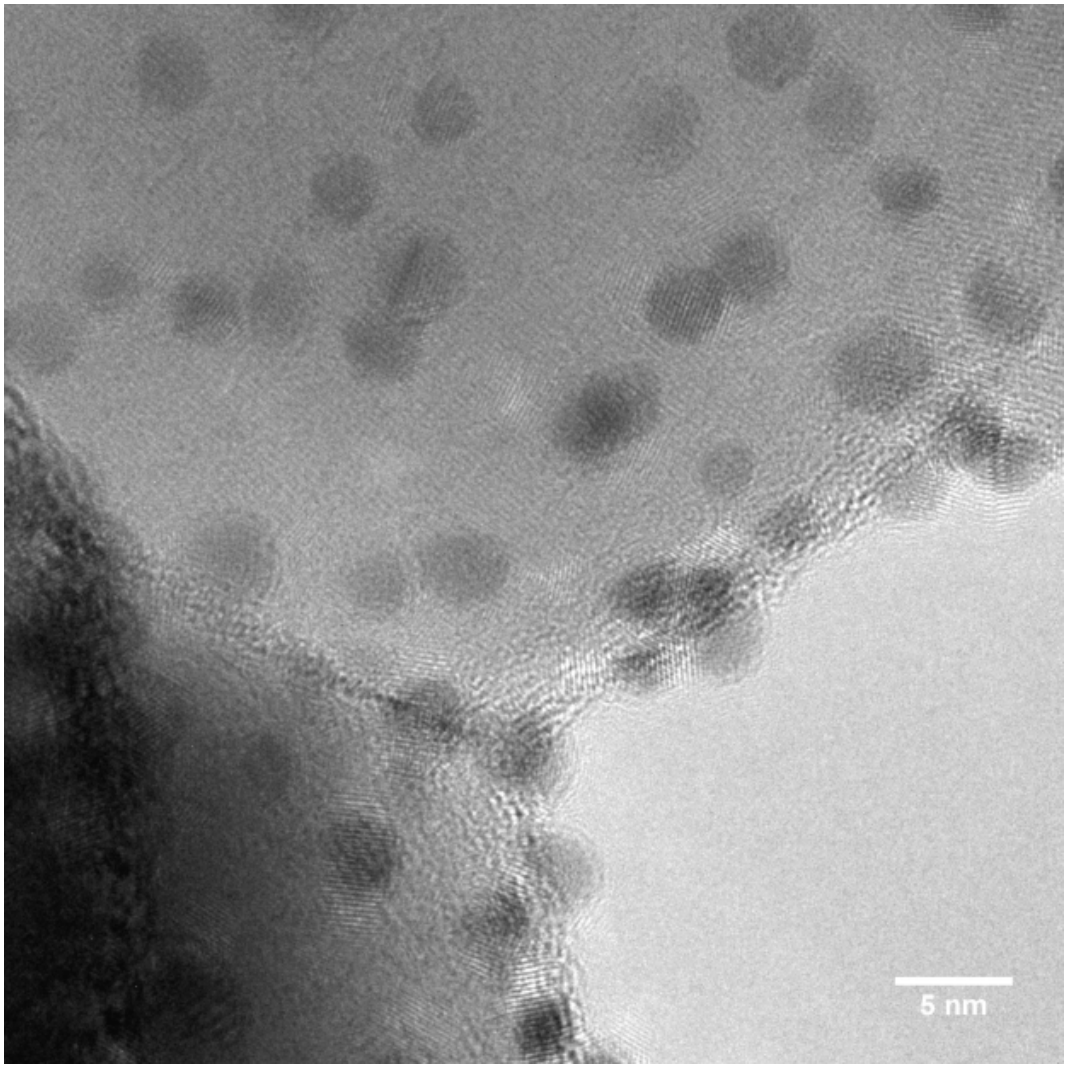


Figure 5.28: HR-TEM image of 5% Au-2% Pt heated to 300°C.

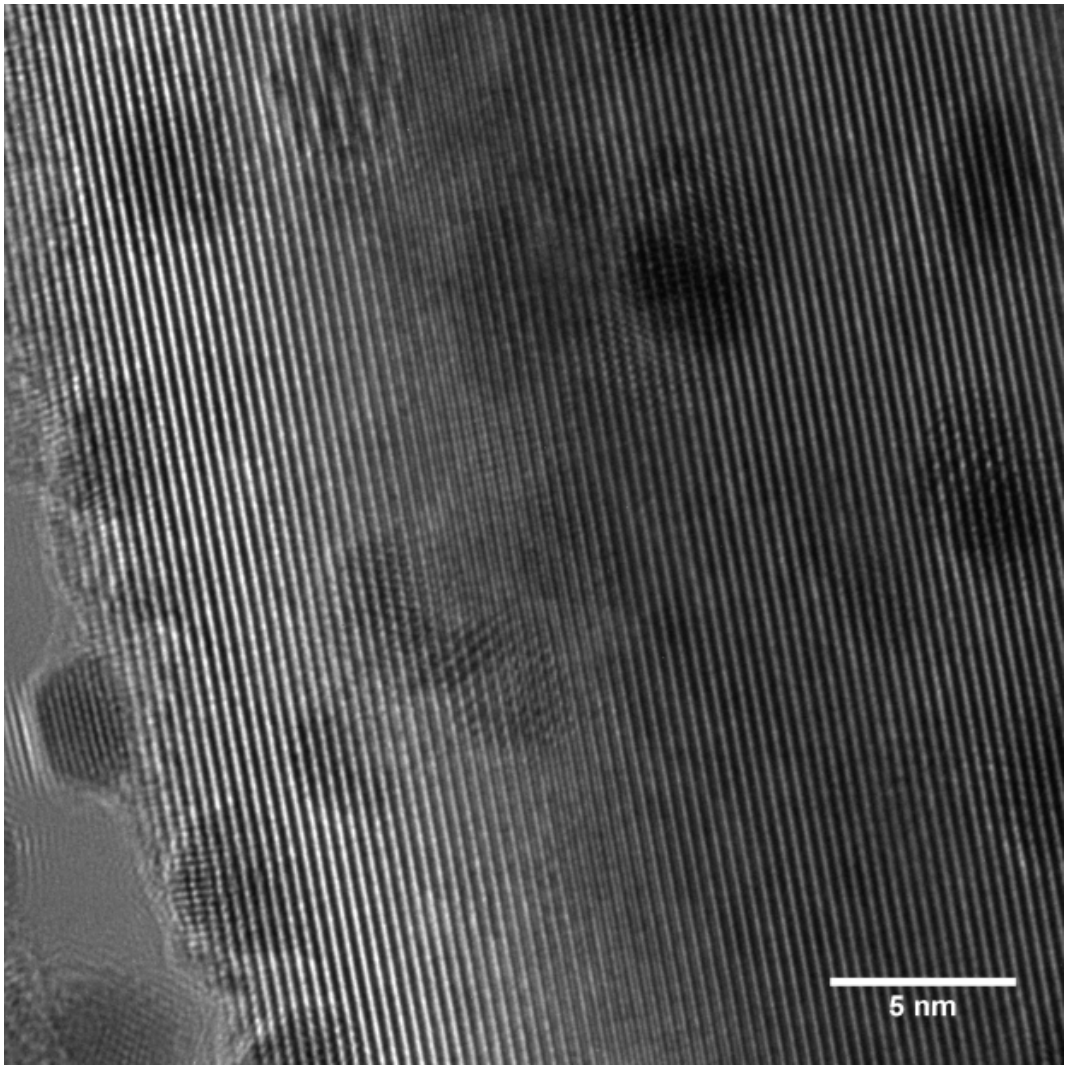


Figure 5.29: High magnification HR-TEM image of of 5% Au-2% Pt on anatase heated to 300°C

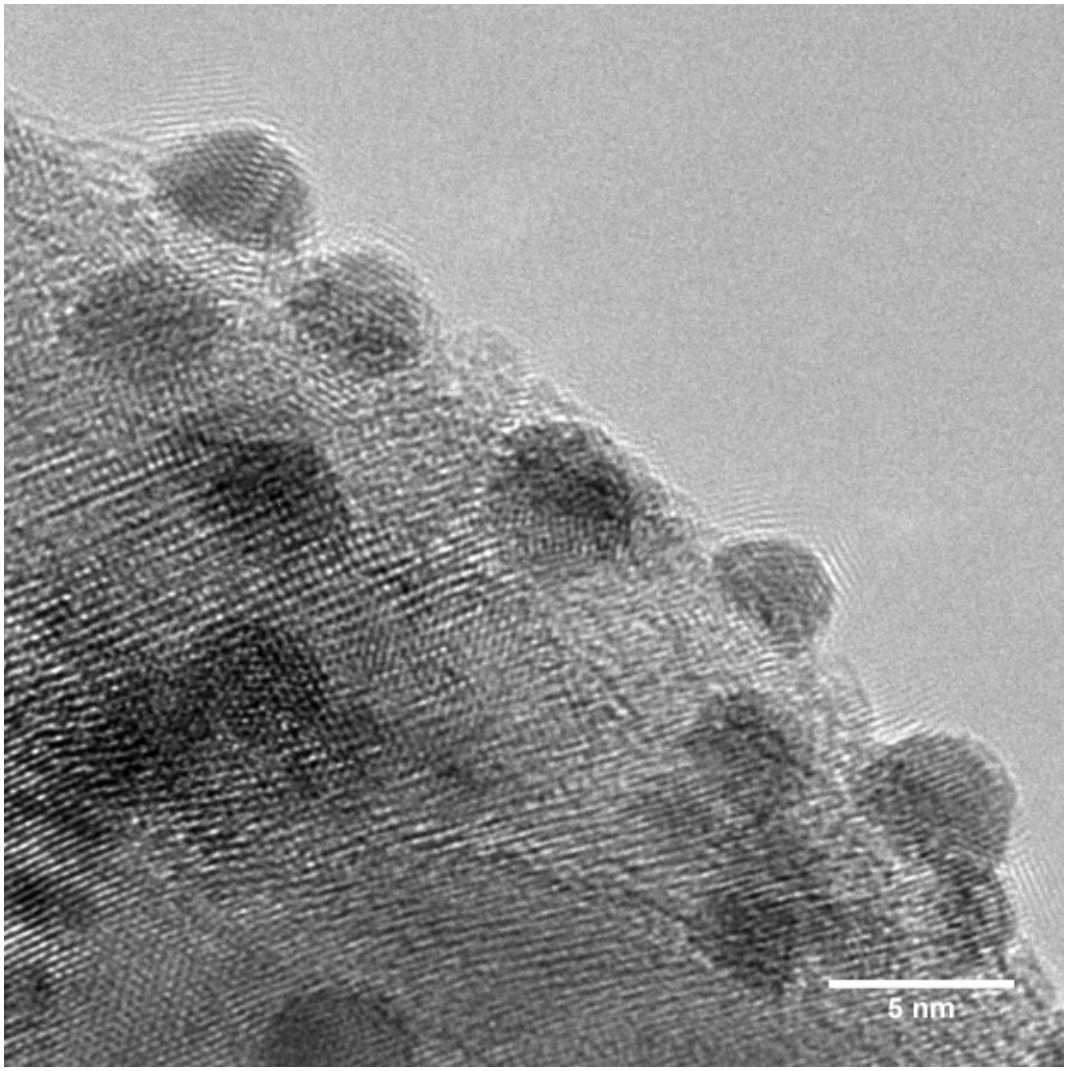


Figure 5.30: High magnification HR-TEM image of 5% Au-2% Pt on anatase heated to 400°C. The image demonstrated how the nanoparticles are epitaxially bound to the support. This type of bonding is crucial for an active catalyst as the manner in which the gold nanoparticles are bound to the surface plays an important role in CO oxidation [41].

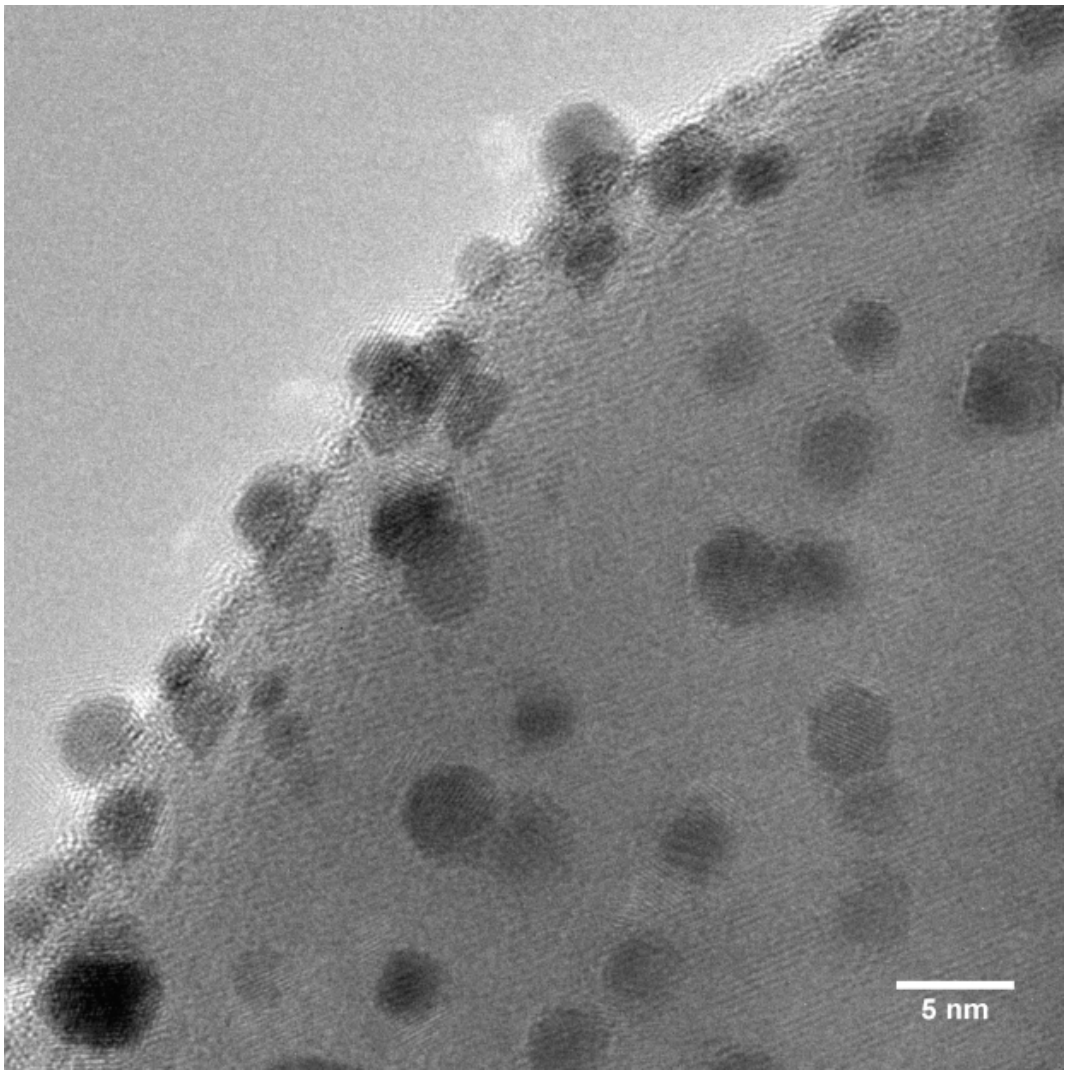


Figure 5.31: HR-TEM image of 5% Au-2% Pt on anatase heated to 400°C

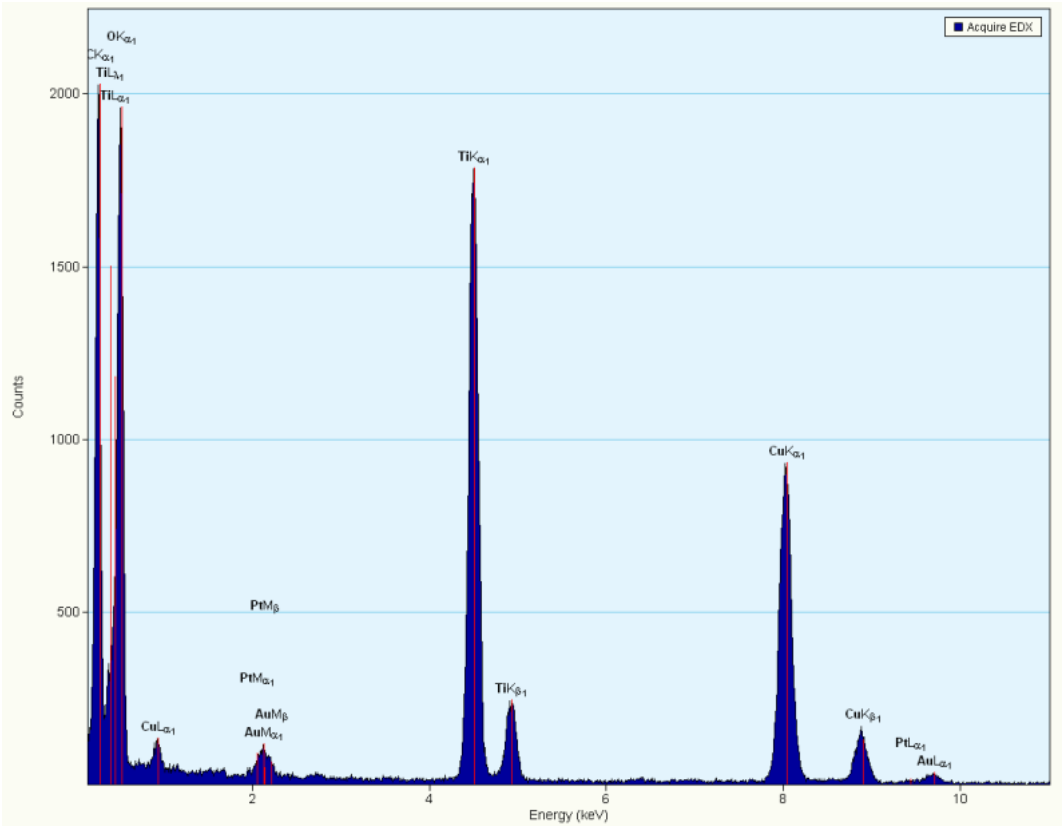


Figure 5.32: EDS of the 5% Au-2% Pt on anatase.

5.5.4 EDS analysis

Signals for both gold and platinum were detected, as seen in Figure 5.32. Conclusive evidence for the position of the platinum relative to gold in the structure could not be attained. This was because the energy resolution of the EDS detector was insufficient to tell the gold and platinum signals apart. It is plausible that gold and platinum may have formed a bimetallic phase[24-29]. This deduction could be drawn according to phase diagrams for gold and platinum. For Au-Pt nanoparticles at this percentage composition, the combination of gold and platinum falls into the miscible region of the phase diagram[77, 82]. As could be seen when the TEM images for 5% Au-3% Pt were examined (Figures 5.33 - 5.38), the composition was no longer in the miscible region and a number of small and very large particles can be observed. Examination of the TEM images revealed a very different picture of the catalyst at this platinum loading when compared to the catalysts of lower platinum percentages and this is discussed in the following section.

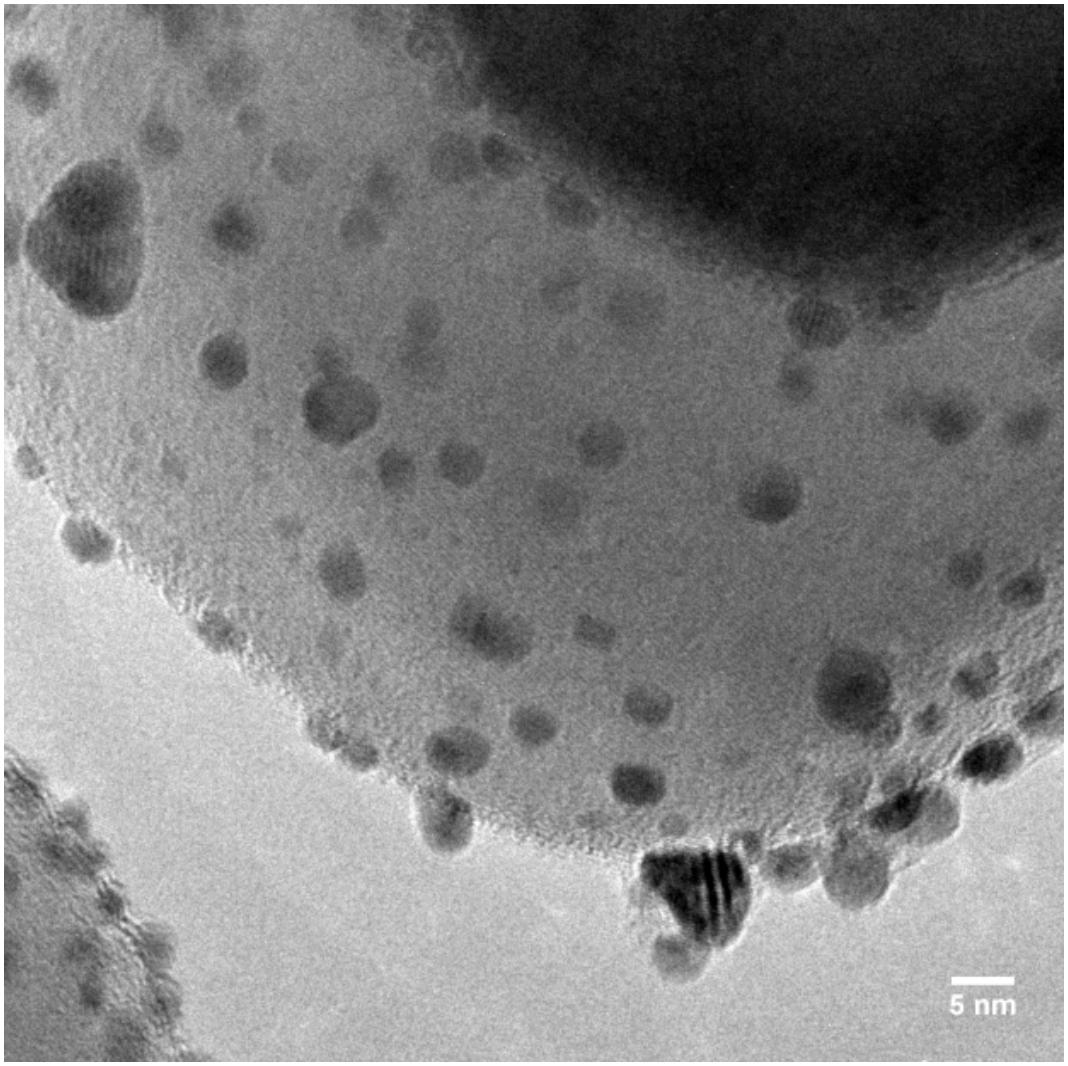


Figure 5.33: 5% Au-3% Pt on anatase after heating to 300°C.

5.6 5% Au-3% Pt supported on commercial anatase

A miscibility gap exists between gold and platinum when the the two metals are alloyed occurring between 20% to 80% mixtures of the two components. The miscibility between gold and platinum has been shown to increase when nanoparticles of the metals are considered[77,82]. When samples of composition 5% Au-3% Pt were produced the resulting catalyst showed interesting particle size distributions as well as interesting particle morphology under the TEM. At first glance of the TEM images (Figures 5.33 and 5.34) a difference was immediately noted when compared to the other combinations of gold and platinum used. Figure 5.33 shows many small nanoparticles, much like the other Au-Pt combinations. There are also a number of very large particles amongst the smaller ones. This was consistent with what what occurs when two metals

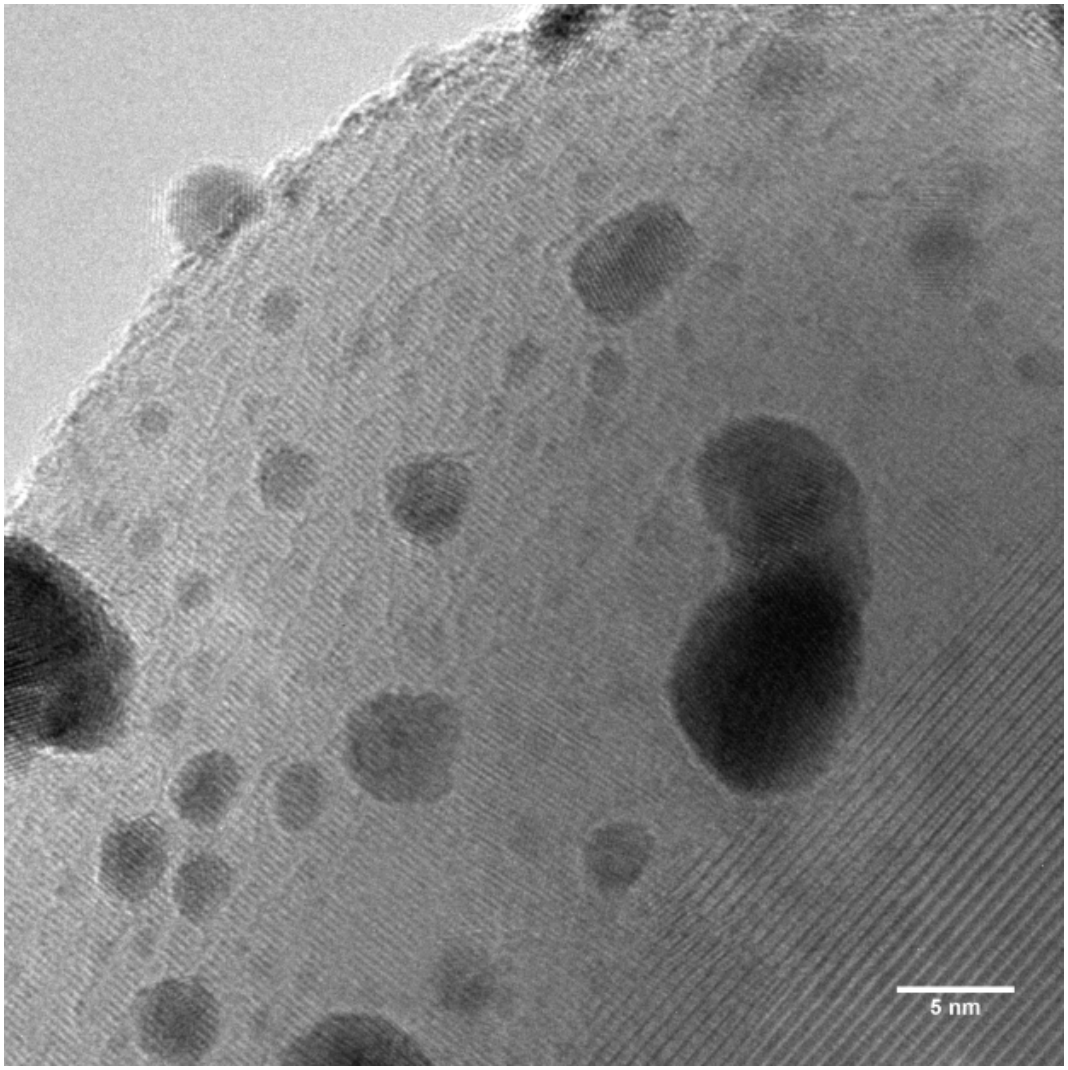


Figure 5.34: High magnification HR-TEM image of 5% Au-3% Pt on anatase heated to 300°C showing a number of very large particles in and amongst a number of smaller particles.

were no longer in ratios that would allow them to be fully miscible within each other. This trend was observed in all the samples studied with this metal combination ratio as can be seen in the following TEM images (Figures 5.33 - 5.38).

For samples containing more than 40% Pt to 60% Au the effect of the immiscibility of the two component metals was observed. Thus, catalysts produced using mixtures of gold and platinum were kept below this value following these findings.

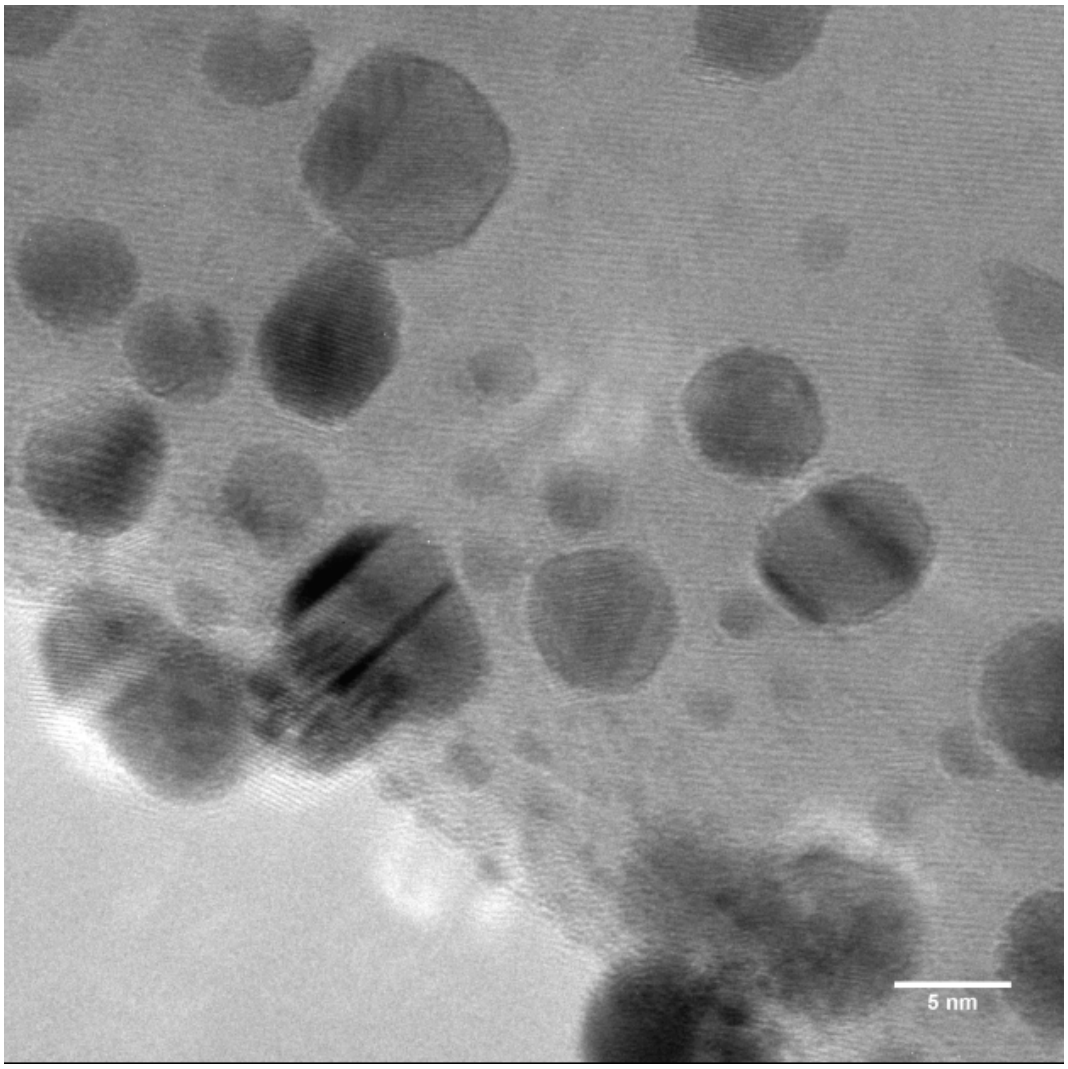


Figure 5.35: 5% Au-3% Pt heated to 400°C showing even larger particles after exposure to 400°C for 2 hours. After exposure to 400°C the separation between very large and small particles was even more apparent. This trend is continued throughout all the samples that were analyzed with this Au : Pt ratio.

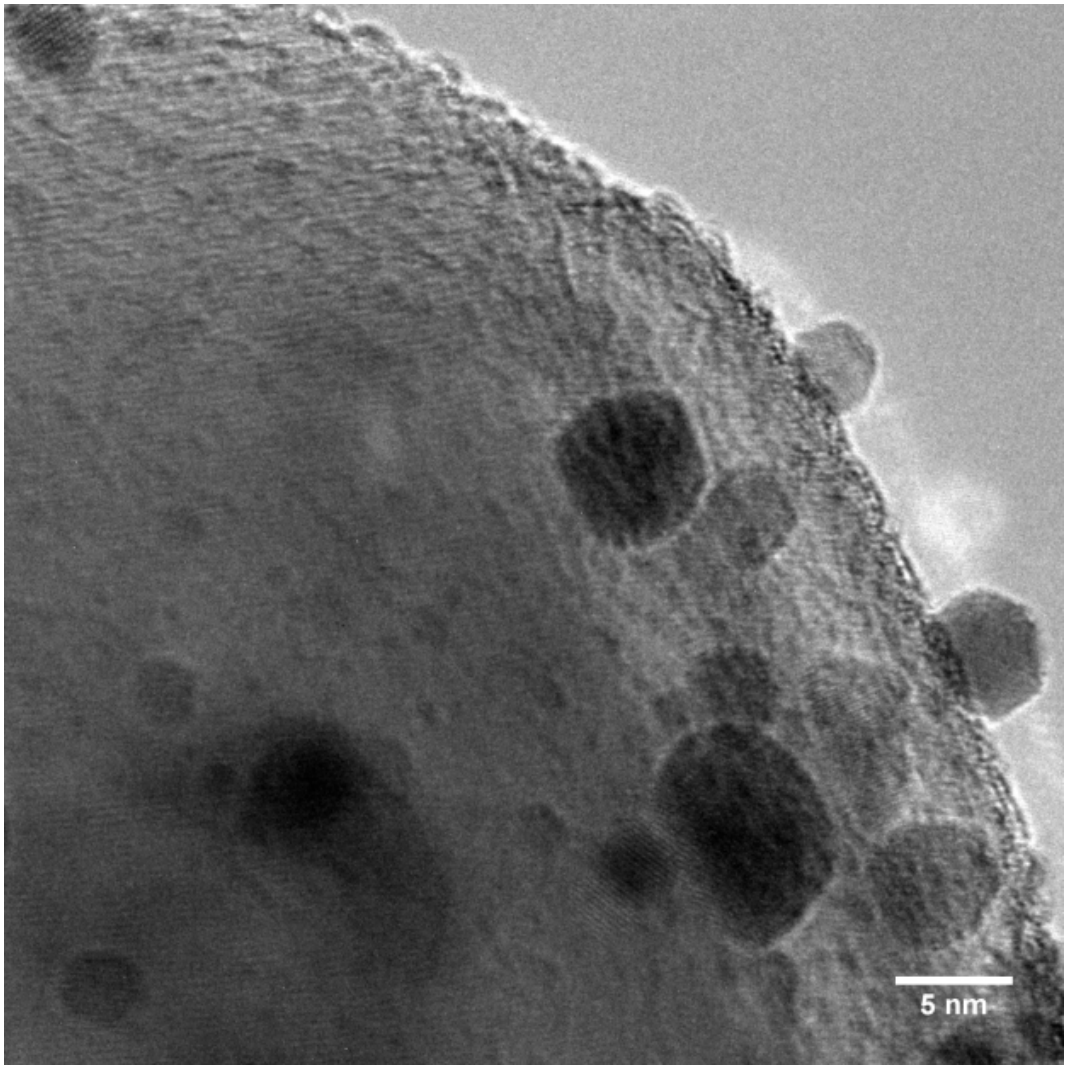


Figure 5.36: 5% Au-3% Pt on anatase heated to 400°C.

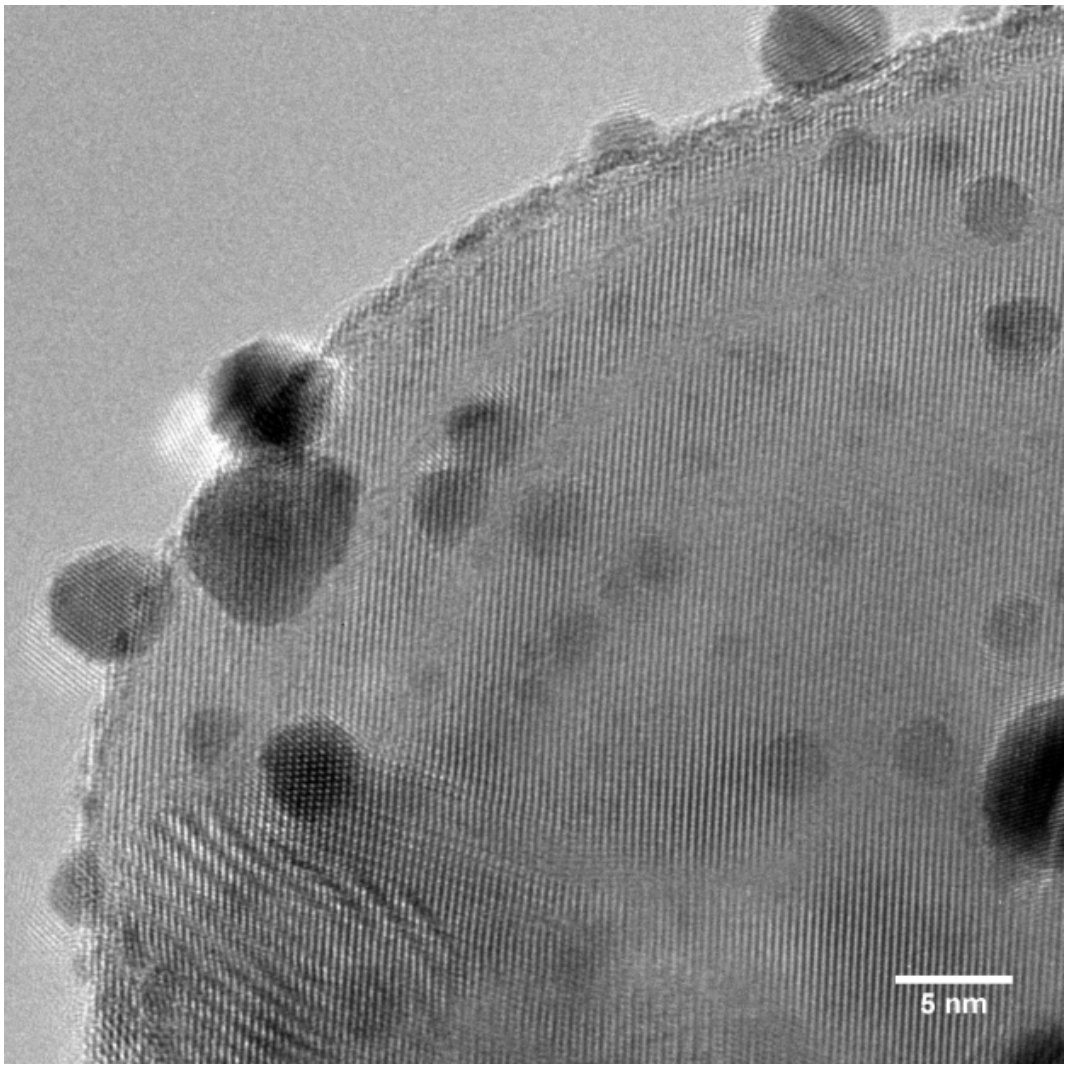


Figure 5.37: High magnification HR-TEM image of 5% Au-3% Pt on anatase heated to 400°C.

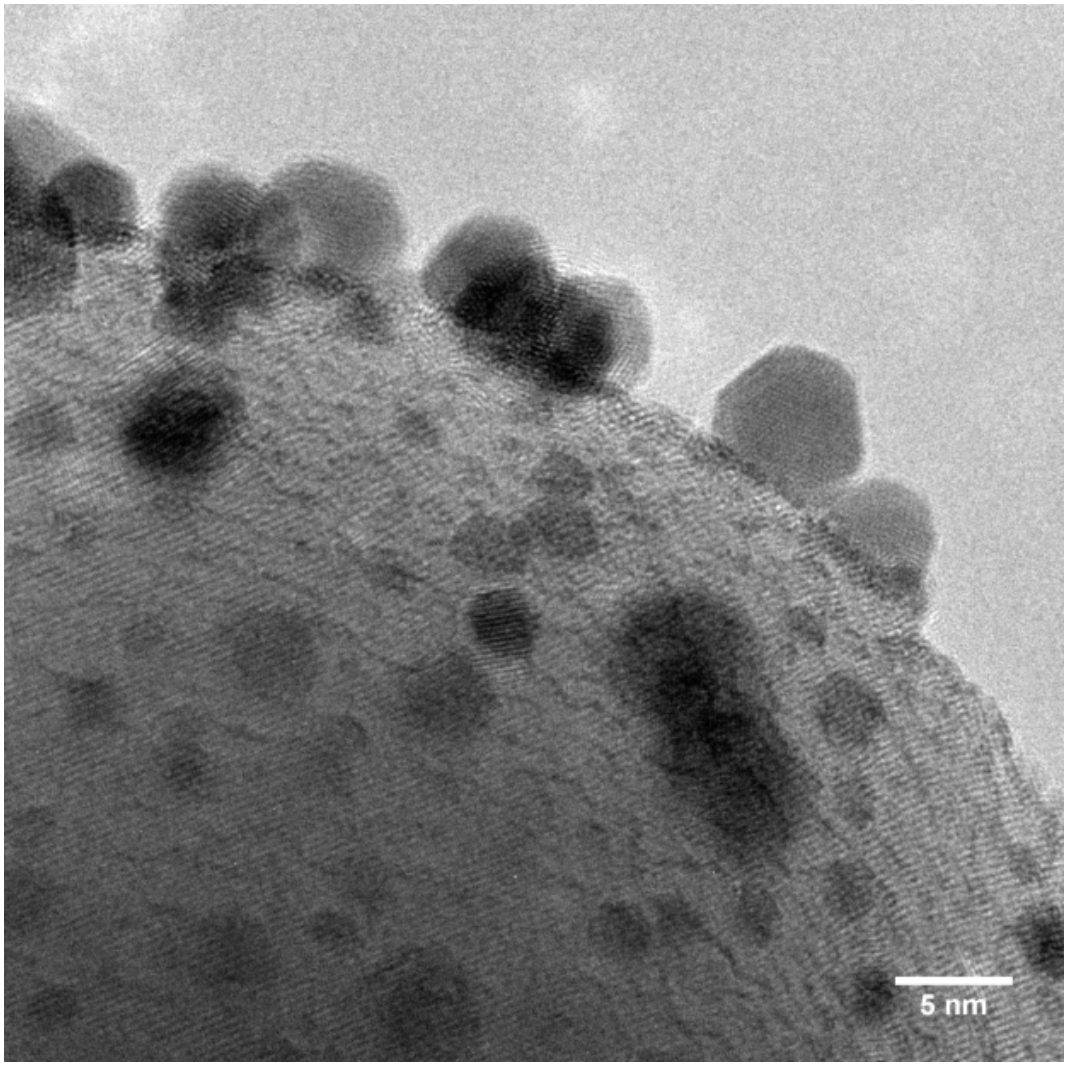


Figure 5.38: High magnification HR-TEM image of 5% Au-3% Pt on anatase heated to 400°C.

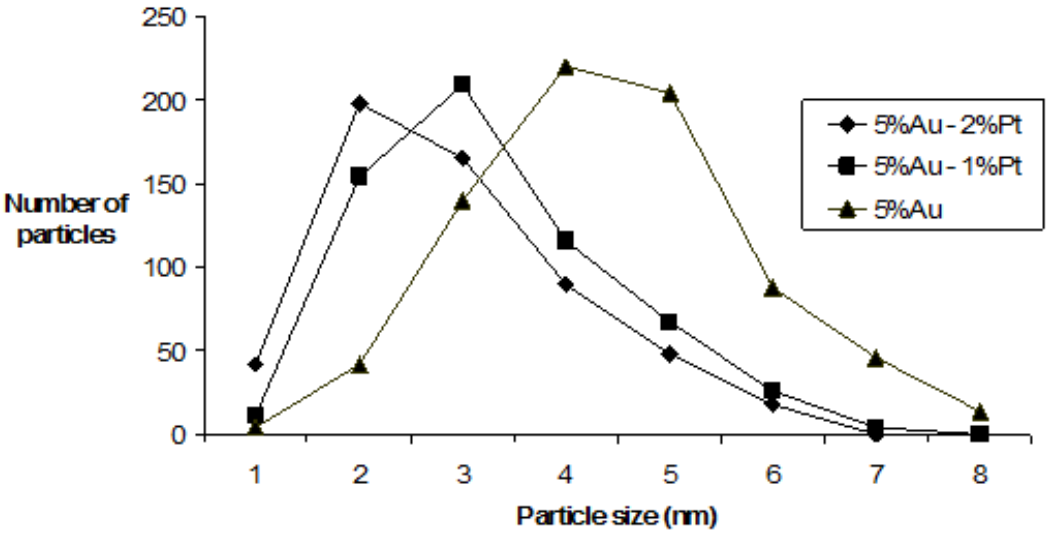


Figure 5.39: Particle size distribution of Au and Au-Pt nanoparticles determined from TEM images. Over 450 nanoparticles were analyzed for each distribution[86]. (D.H Barrett, P.J Franklyn and M.S Scurrell (2010). Variable Temperature Study of Au and Au-Pt Nanoparticles on Selected Oxide Supports. MRS Proceedings, 1279, 40)

5.6.1 Particle size distributions for three different Au : Pt ratios

Particles smaller than 4 nm are the most important due to the associated activity of a catalyst[1-4]. Figure 5.39 shows the results of analyzing the particle sizes of all the TEM micrographs. For pure gold nanoparticles on titania, less than 40% of the particles were smaller than 4 nm after exposure to 300°C for 2 hours. For the 5% Au-1% Pt and 5% Au-2% Pt samples, the percentage of nanoparticles smaller than 4 nm was more than 60% and 70% respectively. This decrease in the Au-Pt particle size distribution showed that the addition of small amounts of platinum to gold nanoparticles aided in the stability of the nanoparticles as a whole when supported on the commercial anatase. This result confirmed what quantitative Rietveld refinements indicated after analysis of the in-situ PXRD data.

5.7 Conclusions

The addition of platinum to gold resulted in a reduction of the overall size of the nanoparticles provided that the composition of the Au:Pt ratio was within

the miscibility gap of the component metals. This was confirmed by in-situ PXRD as well as TEM. When the Au:Pt ratio was 5:1 and 5:2 this was the case. At a Au:Pt ratio of 5:3 the miscibility of the two metals was seen to be compromised when TEM of the samples was undertaken. EDS analysis indicated that gold and platinum may form a bimetallic or alloy structure according to phase diagrams for gold and platinum but this could not be stated with certainty due to the energy resolution of the EDS detector.

The modified synthesis method produced epitaxially bound nanoparticles that are crucial for the conversion of CO. The commercial anatase support, while having good thermal stability at low to medium temperatures resulting from its relatively large mean particle size, contained small amounts of rutile phase. This small amount of rutile was enough to result in an accelerated phase transition when the catalyst was heated to higher temperatures as was seen via in-situ PXRD as well as TEM images. This effect was enhanced further by the addition of metal nanoparticles onto the support surface that were seen to catalyze the phase transition in both in-situ PXRD as well as TEM studies. The large particle sizes (quantitative Rietveld analysis) of the commercial anatase resulted in low surface areas that in turn resulted in the surface quickly becoming overloaded by the gold and platinum nanoparticles, as surface area decreases with an increase in temperature. Finally, when trying to use commercial anatase phase TiO_2 the anatase polymorph was not thermodynamically stable and readily converted to a low surface area rutile structure when exposed to moderate temperatures for a prolonged period of time as shown by the in-situ PXRD results and TEM.

Taking all of the above into consideration, commercial anatase was not a viable support for nanogold catalysts for temperatures over 400°C. Considering that Degussa P25 is used so extensively as a catalyst support this form of titania may offer the type of properties needed for a more stable gold catalyst. Thus, an investigation into the use of P25 as a support for gold nanoparticles followed.

An important result is that the modified deposition precipitation technique proved to be reproducible and reliable across a range of metal loadings and with both gold and platinum. This was therefore the synthetic method adopted for all future gold deposition.

Chapter 6

The Mintek Aurolite^{TM} catalyst and the use of Degussa P25 as a support

6.1 Introduction to the use of Degussa P25 as a support

From the results of the catalysts produced using commercial anatase as a support it was evident that commercial anatase phase titania, while having useful attributes such as a stable support surface resulting from its large particle size, also had drawbacks such as low surface area and a readiness to convert to even lower surface area rutile making it a non-viable support material for gold nanoparticles for use at temperatures over 400°C. At both high and low temperatures it is not a suitable support. At low temperatures it does not have high surface area and at high temperatures the phase transition is prominent. This phase transition is detrimental to the catalysts activity as was discussed in Chapter 5. Degussa's P25 is one of the most widely used support materials in the world. The crystallography of Degussa P25 is examined in Chapter 5. In-situ PXRD was used to analyze Degussa P25 prior to the addition of any metallic nanoparticles. As the industrial Aurolite catalyst produced by Mintek uses P25 as a support material there may be reasons why it is chosen over other supports. The Aurolite catalyst is characterized later in the Chapter, the interaction of the gold nanoparticles with the P25 support as well as

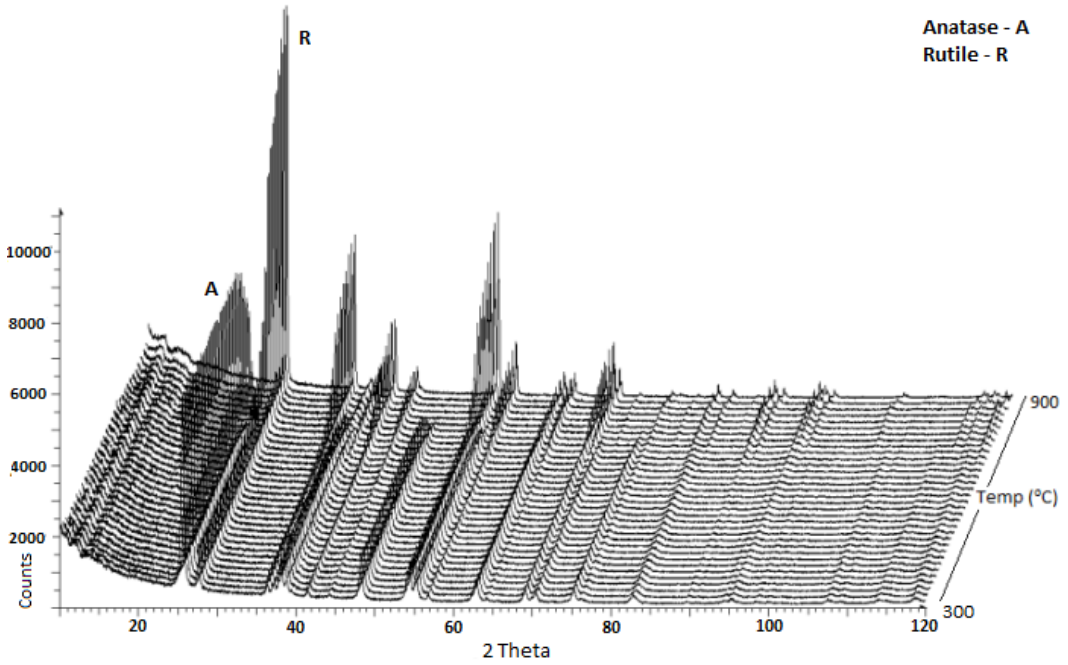


Figure 6.1: In-situ PXRD of pure Degussa P25. The data collection was undertaken using 30°C intervals from 300°C to 900°C. Data collections were started at 300°C as no change in the P25 will occurred below these temperatures.

the thermal stability of the Aurolite catalyst is also investigated.

6.2 In-situ PXRD of Degussa P25

The in-situ PXRD scans showed the two phases present in P25, that of anatase and rutile in Figure 6.1 and 6.2. The most intense peaks at low temperature correspond to the anatase phase while at higher temperatures the phase conversion resulted in the growth of the rutile phase. The evolution of the rutile phase only became prominent at over 700°C when pure P25 is considered. It must be noted that there are both thermodynamics as well as kinetics that need to be considered when phase changes from anatase to rutile are investigated. This is an important aspect to note as the conversion not only resulted in a lower surface area polymorph (rutile : BET surface area of 7.2 m^2/g), however, during the phase change massive encapsulation of the metallic nanoparticles occurred resulting in most of the active sites of the catalyst becoming entrapped within the support. The rate of conversion of anatase to rutile is dependent on both the heating rate and dwell time settings of the XRK chamber. Thus, the phase changes are dependent on how the data collection were set up. At temperatures

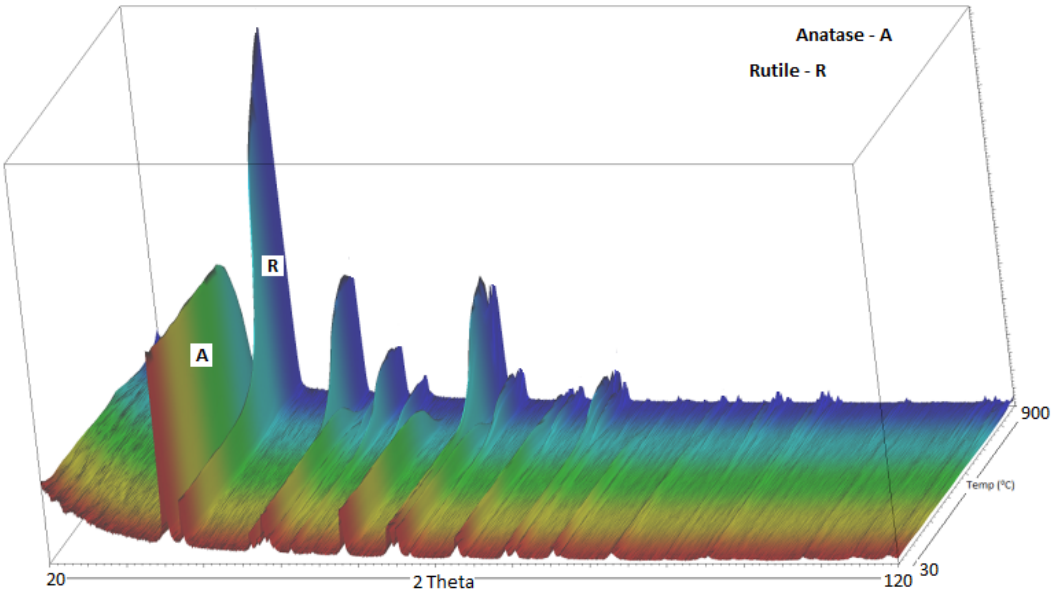


Figure 6.2: In-situ PXRD of P25. The higher temperature portion of the data collection is highlighted in the blue region of the diagram. This portion shows the rapid growth of the rutile phase while the demise of the anatase phase can also be noted as anatase was converted to rutile. Once the onset of the phase transition began it was only a few hours before the rate of conversion became exponential. At low to moderate temperatures <400°C the P25 was relatively stable.

over 450°C the phase change is inevitable as will be discussed when the industrial Aurolite catalyst is studied later in the Chapter. Metallic nanoparticles on the surface of various metal oxide supports have been shown to increase the rate of phase conversion[62-67, 73]. As the phase changes are inevitable as the thermodynamic product is favored in these cases, the only factor is how rapidly the transformation occurs. Throughout the following chapters this rate of conversion will be considered and highlighted when in-situ diffraction data is analyzed.

Rietveld refinements from the in-situ variable temperature diffraction data of Degussa P25, as shown in Figure 6.3, revealed the crystallite size of the anatase phase is approximately 30 nm at low temperatures with the rutile phase being larger than the anatase at an initial value of around 40 nm. Even after exposure to temperatures of 500°C the crystallite size still remained relatively small with only a slight increase in size when compared to the P25 prior to heating. Compared to commercial anatase the P25 was almost four times smaller in size. BET results showed the P25 had a surface area of $46.6 m^2/g$ before heating which compared very well with the quoted value from Degussa of 47.6

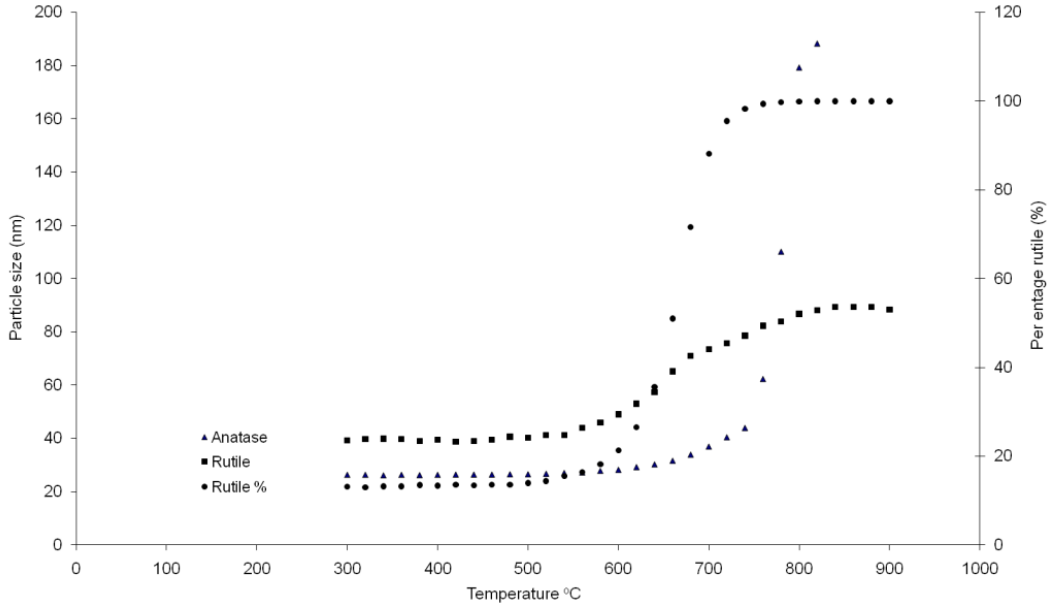


Figure 6.3: Rietveld refinement results of the in-situ PXRD data collections of pure Degussa P25.

m^2/g. The anatase crystallite size only began to increase after 550°C and by the time the temperature had reached 750°C the growth was exponential and the anatase crystallite size reahced a size of ca. 190 nm at ca. 800°C. The rutile phase began to develop around 550°C and continued developing rapidly until all of the anatase had been converted. While the rutile crystallite sizes did not show massive increases the way the anatase did, the rutile reached a size of approximately 90 nm. Again it is important to stress that the temperature and rate at which the phase conversions occurred are dependent on the heating rate and dwell times programmed into the diffractometers variable temperature XRK stage. If the P25 is able to withstand massive phase changes up to 550°C with gold nanoparticles on the surface, then P25 may be a viable support material for gold nanoparticles for reactions that reach 550°C. This is not the case however, as chapter 8 will reveal. The rapidness of the phase change and relatively low maximum temperature of 550°C before the onset of phase transition severely limits P25 as a support as catalyzed reactions such as CO oxidation and NOx reduction, in auto-catalysts for example, are often required to surpass this temperature.

6.3 Introduction to the Mintek Aurolite catalyst

The Aurolite catalyst is an industrial nanogold based catalyst produced by Mintek, South Africa. It has several industrial uses and has undergone extensive testing by the company for potential use as an emission catalyst for diesel engines. The catalysts ineffective long term stability at high temperatures has so far, unfortunately, made the catalyst a non-viable option for auto-catalysts. As a means of understanding current limitations on gold nanocatalysts, the reasons for its limited lifespan at high temperature will be investigated through structural studies. The understanding of the deactivation mechanisms of existing catalysts could aid in the design of a catalyst that is able to resist those deactivation pathways.

Aurolite uses Degussa P25 as a support material with a gold loading of 1%. The catalyst is prepared by a DP method whereby the titania is added to a solution of pH adjusted deionized water containing $Na_2(CO)_3$and $HAuCl_4.3H_2O$. The pH is fixed at 7 for the duration of the deposition followed by filtering, washing, drying and finally calcination at 300°C. The final product after processing is small blue/purple coloured pellets. The Aurolite catalyst is known to be one of the best gold catalysts on the market and has a remarkable ability to facilitate the carbon monoxide oxidation reaction at low temperatures.

6.4 In-situ PXRD

The data collection for the Aurolite catalyst was undertaken for a duration of 64 hours, with a time-temperature profile as shown in Figure 6.4. This temperature versus time profile was chosen so as to spend the bulk of the data collection time at temperatures that are known to stress to the catalyst, hence above 300°C. Gold catalysts such as the Aurolite catalyst are known to be stable up to 400°C. Above this temperature, however, the stability and activity of the catalyst changes dramatically as functions of temperature and time. The exact structural reasons for this rapid deactivation had not been investigated. More than 55 hours of the data collection were spent at temperatures higher than 300°C. The selection of this profile was considered to be more than sufficient, as previous data collected from heat treatments of the Aurolite catalysts at a temperature of 550°C for 12 hours resulted in complete deactivation of the

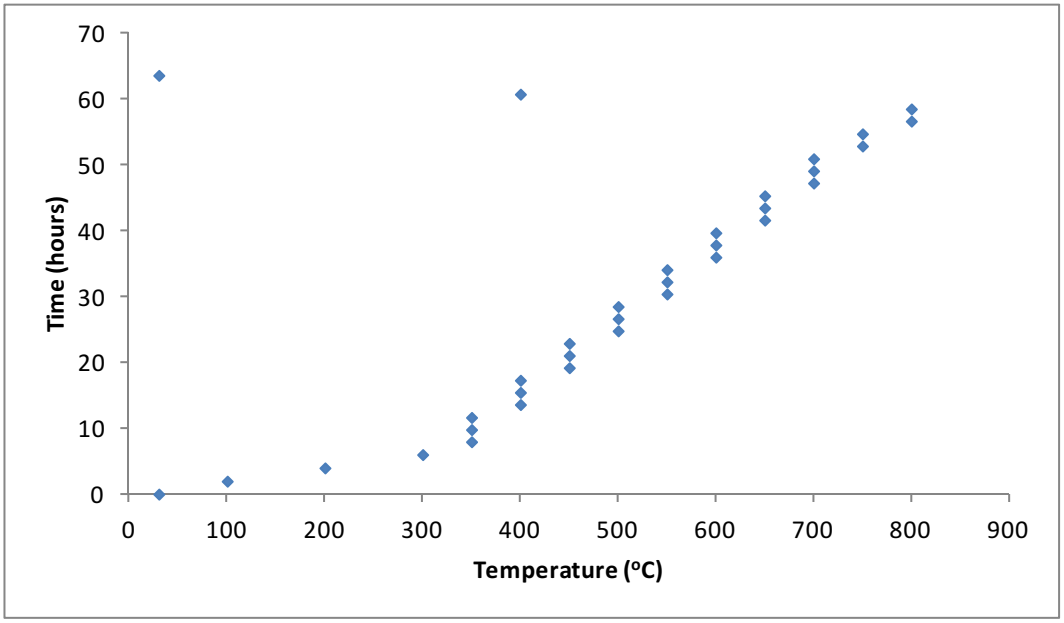


Figure 6.4: Temperature Vs data collection time for the Aurolite catalyst. From 350°C to 700°C, three one hour long scans were collected at each temperature. It was not deemed necessary to heat the catalyst to 900°C as was done in the pure P25 data collection as the phase transition would most certainly have occurred by this stage.

catalyst. These heat treatments will be discussed in Chapter 9. It was further determined that multiple scans at a number of temperature increments would provide the best data set as shown in Figure 6.4. Hence the three dots placed above each other represent scans taken at a stable temperature.

6.4.1 Rietveld refinement

The addition of gold nanoparticles to P25 as is used to produce the Aurolite catalyst added complexity to the refinements as the peak overlap between the three phases present was quite substantial. Examples of the resulting refinements are shown below in Figures 6.6 to 6.11.

The almost linear pattern in grey at the bottom of Figure 6.6 is the difference pattern. The pattern results from the subtraction of the observed from the calculated diffraction pattern. The almost linear nature of the difference pattern indicates a good fit of the data resulting from the refinement. Three crystalline materials could be identified at the example temperature used in plotting Figure 6.6, namely: anatase, rutile and gold. The *hkl* positions of the phases can be seen from the small vertical stripes under the difference pattern.

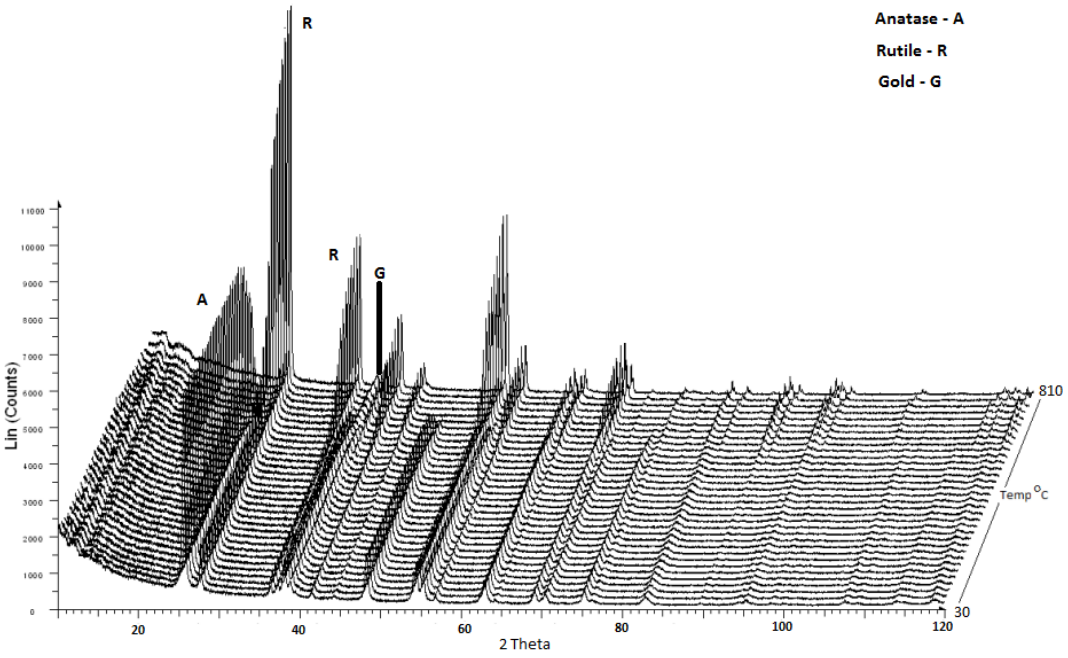


Figure 6.5: In-situ PXRD of the Mintek Aurolite catalyst. Other than the very small diffraction peaks associated with metallic gold at higher temperatures, the data collection resembled that of the P25 patterns as the same support material is used. However, quantitative Rietveld analysis revealed a number of differences.

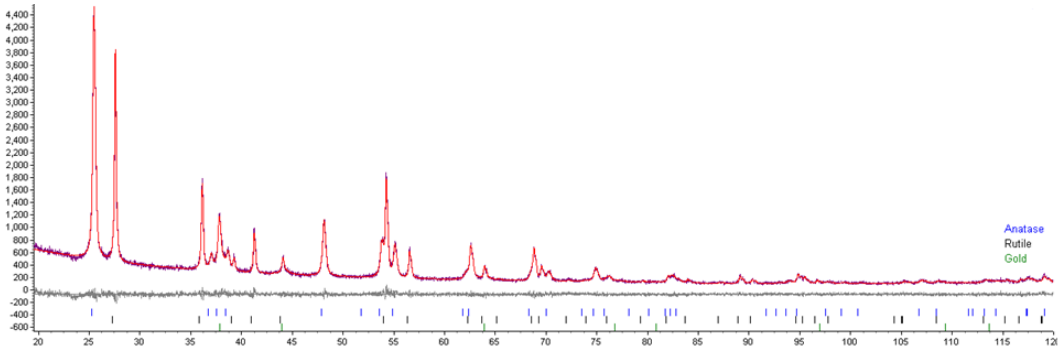


Figure 6.6: Rietveld refinement image taken from TOPAS refinement software. The observed diffraction pattern is shown in blue. Overlayed onto the observed pattern is the calculated pattern in red resulting from the Rietveld refinement. The almost perfect overlap of the observed and calculated patterns demonstrated a very successful refinement. Refinements were conducted on all collected diffraction patterns.

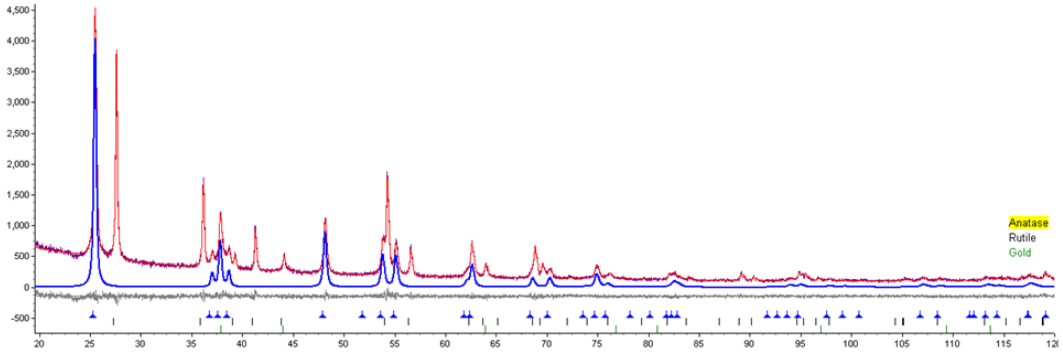


Figure 6.7: The anatase phase is highlighted in blue from the resulting calculated diffraction pattern. Once the refinement is completed it is possible to examine each phase independently.

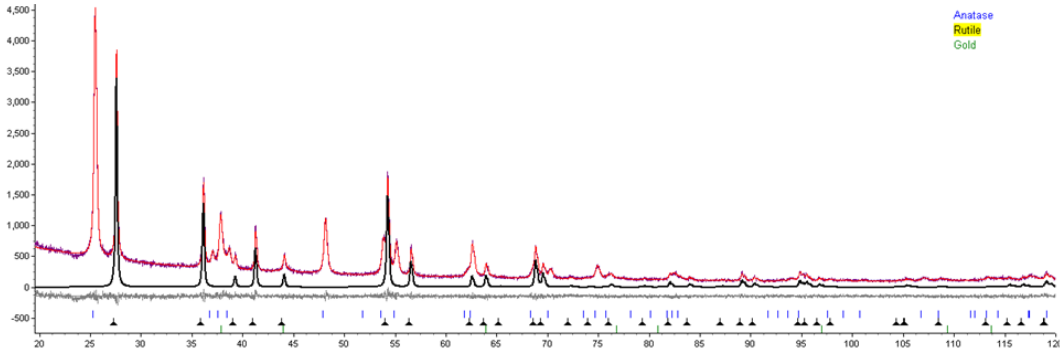


Figure 6.8: Calculated rutile diffraction pattern shown in black.

The blue stripes indicate diffraction peaks for anatase, the black for rutile and the green for gold (as demonstrated in Figures 6.7-6.9) . Each phase could be quantitatively analyzed on completion of the refinement. Rietveld analysis was undertaken on all diffraction patterns that made up the variable temperature data collection.

Mintek claims that the Aurolite catalyst contains 1% gold as determined by a back titration of the solution used to produce the catalyst. Rietveld refinement Figures agreed with their determined value as a value of 1.05% gold loading was attained from the refinements (see Figure 6.11). This accurate determination of the gold phase percentage shows the accuracy and precision that can be attained using the Rietveld method even when the loadings of the supported metal are low and the metal is present as nanoparticles. The small diffraction peak at 38.2° 2θ was the result of gold nanoparticles, as shown in Figure 6.10 and 6.11. The gold peak is small and broad with low intensity for two reasons. One was due to the very low loading of gold at just 1% and the second was due to the relatively small crystallite size. In this experiment, the crystallite size

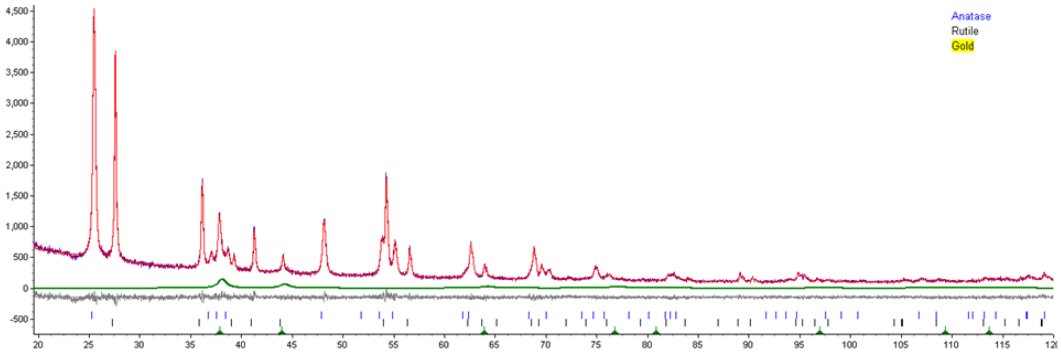


Figure 6.9: Calculated gold pattern shown in green. The low gold loading of 1% as well as relatively small gold crystallite sizes result in low intensity diffraction peaks being produced by the gold. In the case of the Aurolite catalyst the low intensity gold peaks were more a factor of the low gold loading (1%) as opposed to small crystallite sizes. As will be shown in Figure 6.14 the gold crystallite sizes only remained small below 400°C before large increases were noted

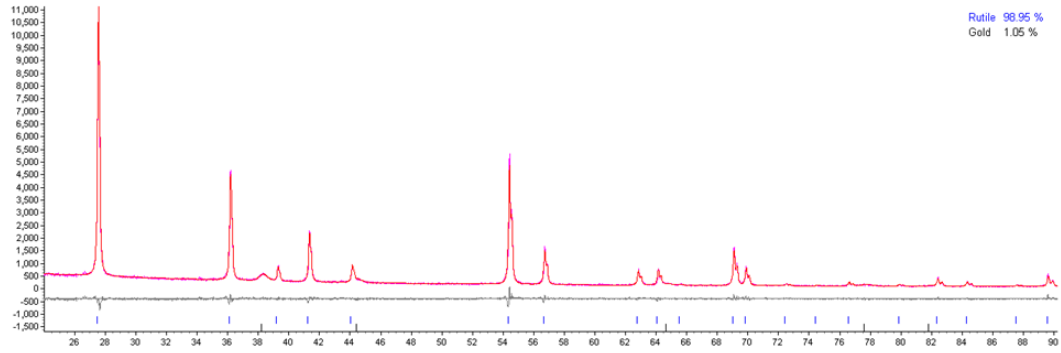


Figure 6.10: Finally at high temperature all the anatase had completely converted to rutile with only rutile and gold phases are now present.

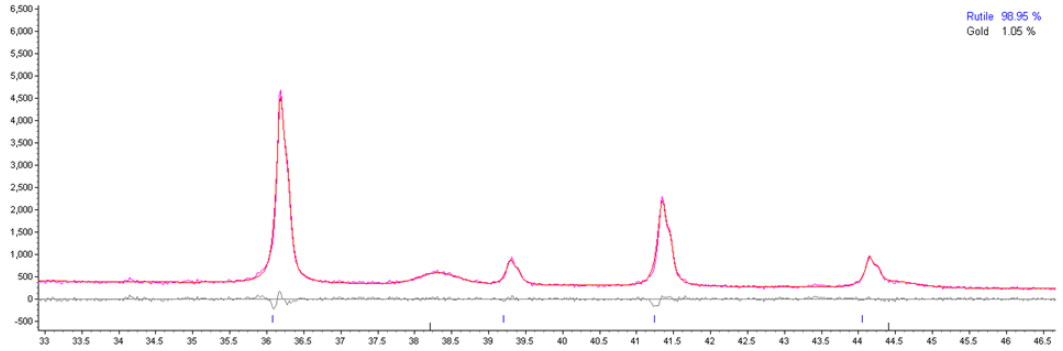


Figure 6.11: Zoomed view of the refinement fit between 33° to 45.5° 2θ. As can be seen an exceptionally good fit is attained with an almost completely linear difference pattern. The small broad gold diffraction peak can also be clearly seen at 38.2° 2θ.

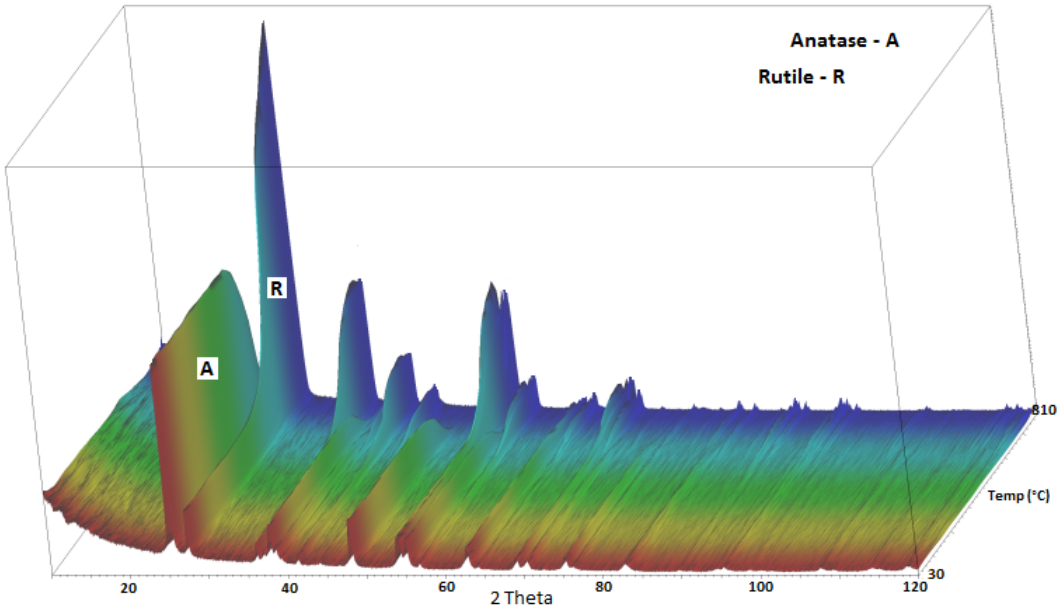


Figure 6.12: In-situ PXRD of the Mintek Aurolite catalyst.

was around 18 nm so the particles did produce reasonable diffraction peaks that could be accurately determined.

At low temperatures, in the red to yellow portion of the diffraction patterns in Figure 6.12, information about the initial state of the support material was observed. While there were very small gold peaks present in the sample at these low temperatures the large, intense diffraction peaks indicate the P25 support with both anatase and rutile peaks was present. This was expected as P25 is used in both cases. The small gold peaks visible at ambient temperature result from the calcination and reduction of the Aurolite catalyst when the catalyst is produced. The catalyst is heated for a number of hours at 300°C before it is packaged. Rietveld refinement revealed more information about the phase

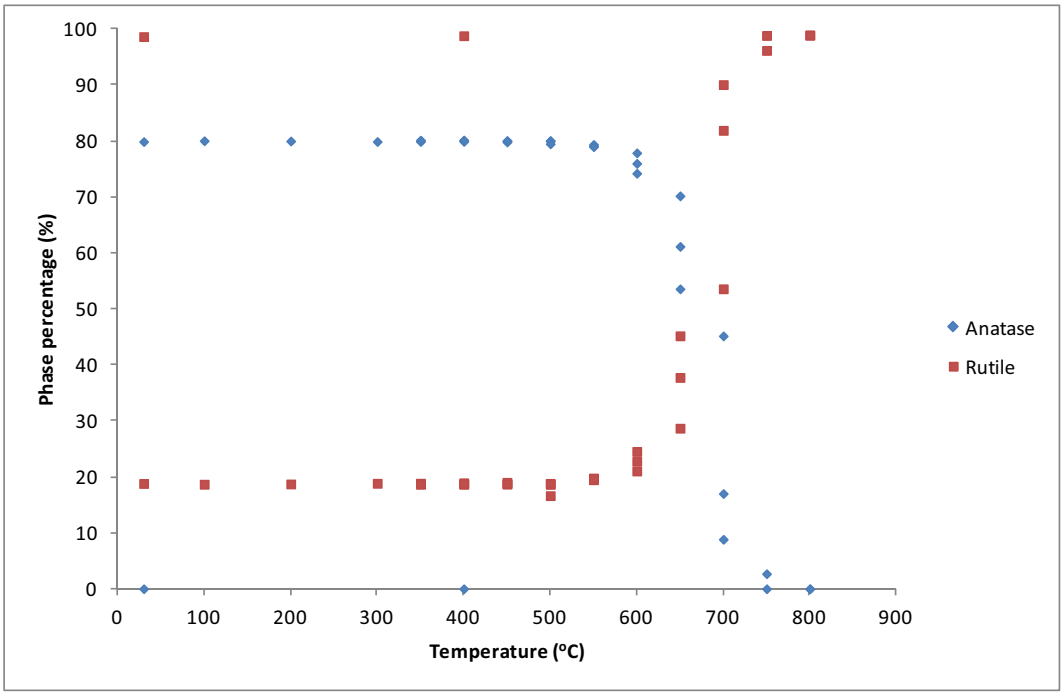


Figure 6.13: Results of the Rietveld refinements from the in-situ data collection of the Aurolite catalyst. The graph displays the anatase and rutile phase transformations with respect to temperature. The final data collection occurs once the XRK chamber cools down to room temperature with a scan also being undertaken at 400°C as the chamber cools. Thus, the two data points at 400°C and 30°C are from the scans collected after the maximum temperature had been reached and a scan collected. Then as the chamber cools the final two scans at 400°C and 30°C were collected. Hence, the final data point corresponding to 100% rutile and 0% anatase was collected last at 30°C. The phase percentages showed that a complete transformation had already occurred. All Rietveld refinement data is graphed in this manner.

transitions that occur at higher temperatures as shown in Figure 6.13.

The refinement results (Figure 6.13) showed very good correlation between the Aurolite and pure P25 when phase percentages at low temperature were examined. Almost identical phase percentages of the anatase and rutile were noted. The exponential manner in which the phase transition occurred can be seen in Figure 6.13 where the onset of the phase transition occurred rapidly after 550°C. The experiment was concluded at 800°C, as from previously attained results, by this temperature complete conversion of the catalyst support from anatase to rutile had taken place.

It was possible to apply Rietveld analysis to the diffraction patterns collected even at low temperatures as the Aurolite catalyst is sold in its reduced form. The crystallite sizes were very stable up to 300°C. This was expected as the catalyst has already been exposed to this temperature in the manufacturing

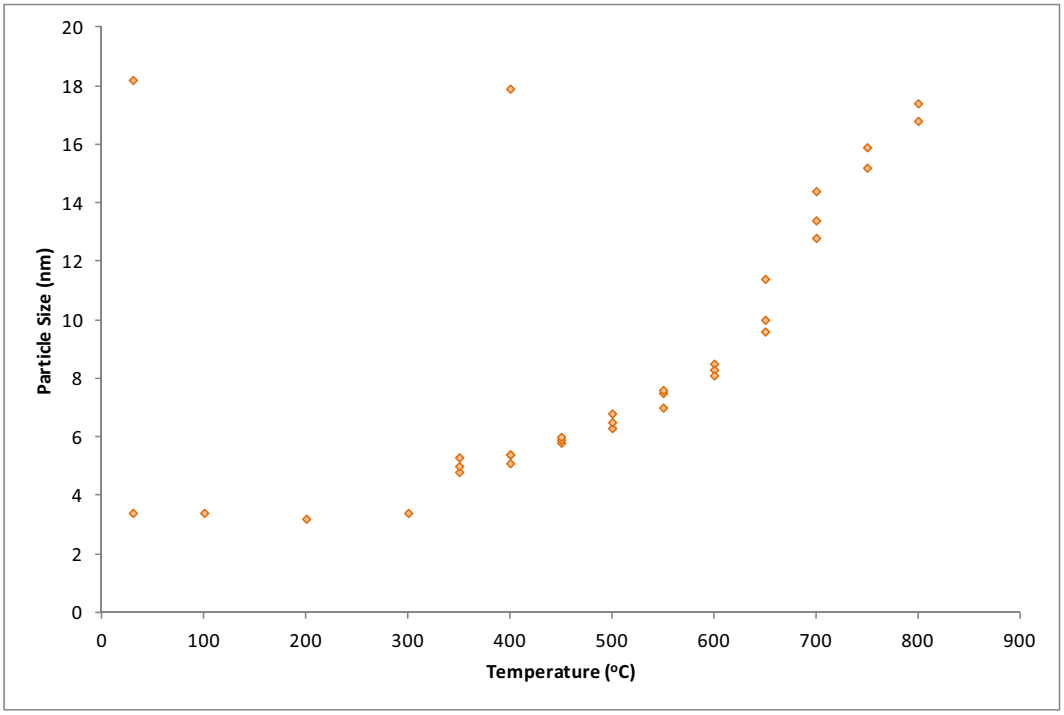


Figure 6.14: Rietveld refinement results of gold crystallite sizes vs temperature of the Aurolite catalyst. The maximum error for the refinements was 0.4 nm for gold crystallite sizes calculated using TOPAS. The two data points corresponding to crystallite sizes of approximately 18 nm were collected as the chamber cools down after reaching the maximum assigned temperature and are the final data collection points. This method of data collection and graphing is used throughout the text.

process. However, the crystallite sizes began to grow steadily as the temperature was increased above 300°C. After consultation with researchers from Mintek the results attained from the in-situ PXRD agreed with their empirical findings. The researchers stated that the catalyst begins to deactivate rapidly after 400°C during CO oxidation testing. If left overnight at temperatures above 450°C the catalyst has been recorded to deactivate completely.

In-situ PXRD and Rietveld refinement had never been applied to the Aurolite catalyst so the information gained shed light on the deactivation mechanism of the catalyst. Much like the Au anatase and Au-Pt anatase samples the growth of the gold nanoparticles occurred more dramatically over 550°C and in the same temperature range as the rapid conversion of anatase to rutile. This can be seen in Figure 6.14 and 6.15. The most rapid increase in the gold crystallite sizes began at 600°C. It is important to stress that the phase conversion occurred at this period in the data collection due to the manner in which the data collection had been set up. If the data collection was slower, i.e. more time was spent at temperatures between 400-600°C, then the phase transition would also have occurred at apparently lower temperatures. This can be seen from Figure 6.16 where the Aurolite catalyst was heated at 500°C for 12 hours resulting in a complete phase transition at this temperature. BET results showed that the Mintek catalyst underwent a massive surface area loss from $48.8 m^2/g$ to only $7.2 m^2/g$ after exposure to 500°C for 12 hours. This massive loss of surface area can be directly correlated to the loss of activity of the Aurolite catalyst. Gold crystallite sizes from Rietveld refinements correlated the phase change with an increase in gold crystallite size. It was not only the phase transition that increased the size of the gold nanoparticles, but also sintering of the particles over the surface. The loss of surface area of the support due to the phase change merely aided in increasing the sintering process as well as encapsulation of the active sites.

The refinement results for the gold crystallite size demonstrated why the Aurolite catalyst is so efficient at low to medium temperature ranges from ambient to 300°C. In this temperature range the gold crystallites were small and hence able to readily facilitate the oxidation of CO. At 350°C the commencement of a large increase in gold crystallite size can be observed in Figure 6.14. More importantly the average size of the gold nanoparticles had now exceeded the 5 nm threshold at which the conversion of CO to CO_2 becomes compromised.

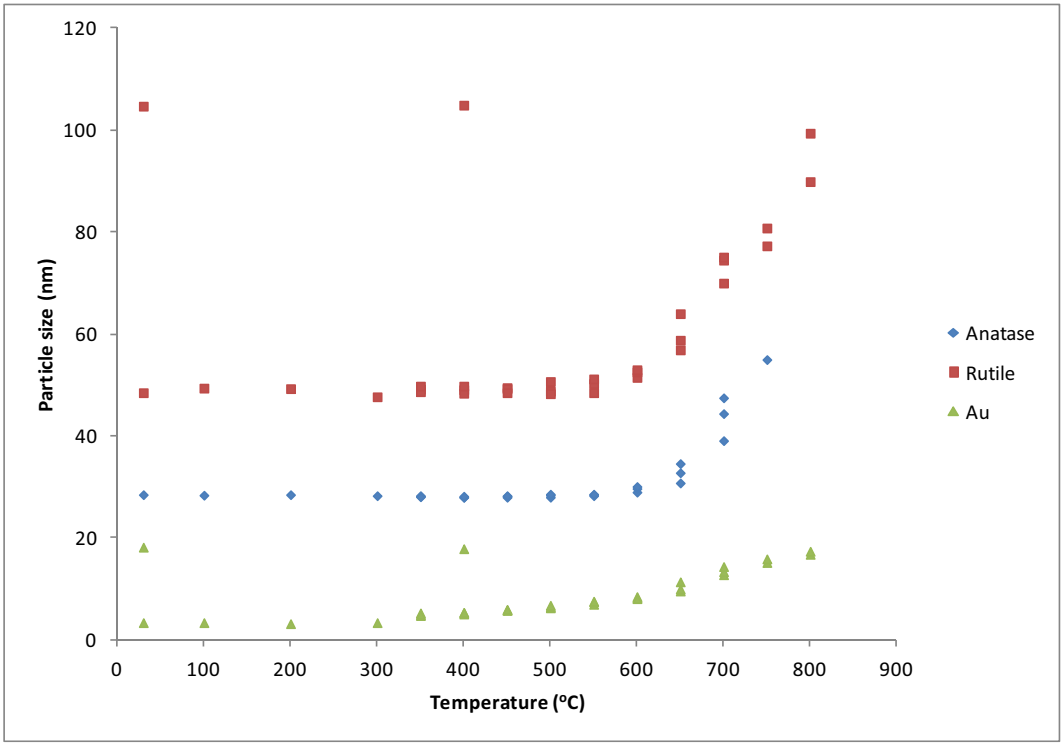


Figure 6.15: Rietveld refinement results of the in-situ PXRD data collection on the Aurolite catalyst.

The addition of gold to P25 to form the Aurolite catalyst showed many similarities to the unloaded P25. The most significant difference however was the much smaller particle size of the anatase during the anatase to rutile conversion in the Aurolite catalyst. This effect may be caused by the addition of the gold. This hypothesis was supported by TEM images of gold and platinum positioned on the anatase-rutile phase boundaries where these nanoparticles appear to be catalyzing the phase transition resulting in a more rapid conversion of the anatase before it can reach the large dimensions observed through sintering of the anatase as in the case of pure P25.

The phase transformation could be correlated to the crystallite size growth of both the anatase and rutile polymorphs. The crystallite sizes remained stable up to 550°C whereafter the growth of the support particles once again took on an exponential function. At the given heating rate with respect to time, the phase transition was complete at 750°C. BET surface area studies gave an average of $47.1 \pm 2.1 m^2/g$ for the 3 replicates of the Aurolite catalyst prior to exposure to non-ambient conditions. When the catalyst was heated to 500°C for 12 hours the surface area decreased dramatically to $7.2 \pm 2.1 m^2/g$. This dramatic decrease in surface area could be attributed to both the sintering

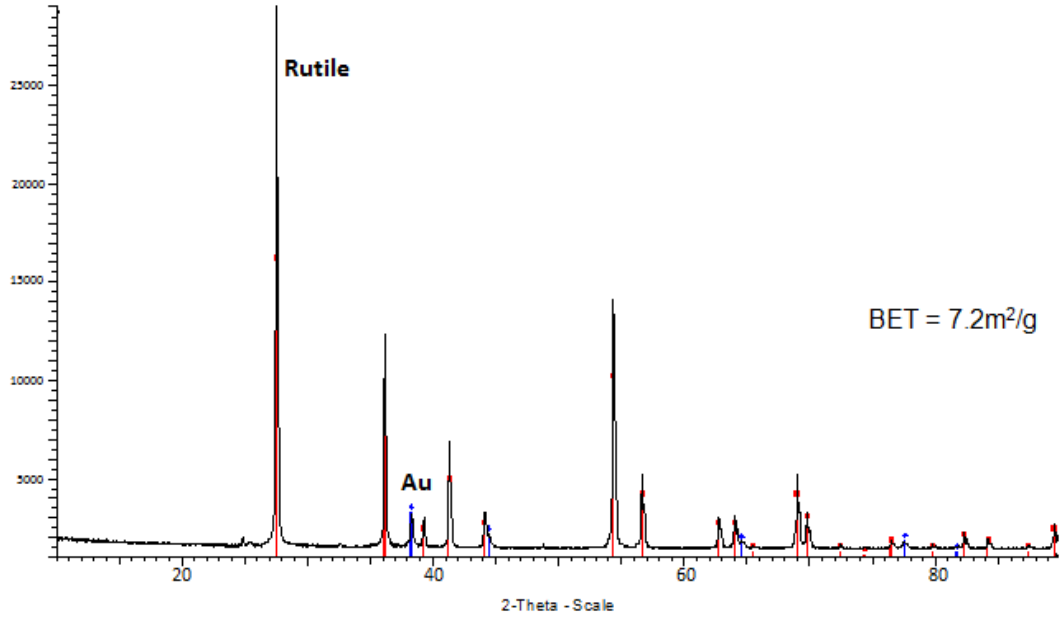


Figure 6.16: Aurolite catalyst after heating to 500°C for 12 hours with the rutile phase highlighted in red and the gold phase in blue.

of the support phase particles, but more importantly to the anatase to rutile phase transformation. As usable surface area is one of the most important parameters for a catalyst support, this massive loss of surface area will most certainly affect the catalysts performance adversely.

Figure 6.16 showed that all the anatase had been converted to rutile after 12 hours and thus surface area had been lost and encapsulation of the catalyst's active sites had occurred along with massive sintering of the gold. Even though the catalyst was only heated at 500°C for 12 hours, complete deactivation occurred with CO oxidation tests showing CO conversion at less than 5% even at high temperatures. BET revealed a surface area of $7.2m^2/g$ (compared to the initial value of $47.1m^2/g$) corresponding to a 7-fold decrease in surface area. Rietveld refinement revealed gold crystallite sizes of over 19 nm, correlating well with the CO oxidation results as gold particles of this size will most definitely not facilitate the CO oxidation reaction. The conversion of anatase to rutile occurs through a wave-front progression in the anatase crystal. Along this front the titanium-oxygen octahedra rearrange through a rotation process. The front extends to the surfaces of the support particles. It is quite possible that gold nanoparticles on the surface of the anatase would be caught by the front migration and be moved along with the wave-front. This would promote sintering of the gold as the nanoparticles would be moved into close proximity.

The conclusion is that current supports used for gold catalysis are insufficient for temperatures exceeding 450°C. What was required was design of a support specifically for gold catalysts to be used at high temperatures. A general purpose support would not suffice. After consultation with researchers at Mintek they confirmed the results and claimed that CO conversion at room temperature drops rapidly once the catalyst has been heated to 400°C for even a short period of time.

In summary, even though P25 is the most extensively used support for gold nanoparticles as well as many other platinum group metals, in-situ PXRD revealed it is not suitable for high temperature applications in gold catalysis. A complete survey of the literature has revealed that no other support offered any better alternative. A completely new support material was required in order to create a stable platform for the gold nanoparticles.

6.5 TEM

A sample of the Aurolite catalyst was analyzed using TEM as shown in Figure 6.17 -6.19. The TEM results revealed the manufacturers claims of a catalyst using P25 with gold particle sizes of between 2.5-5 nm. Image 6.19 is a typical TEM image of the fresh Aurolite catalyst with the gold nanoparticles homogeneously dispersed over the surface.

6.6 Conclusions

Quantitative Rietveld refinements performed on in-situ PXRD data confirmed claims that the Aurolite catalyst is produced with 1% gold loading on Degussa P25. TEM also revealed the gold nanoparticle sizes for the fresh catalyst were in the range of 2-5 nm. A catalyst with gold nanoparticles of this size correlate well with a highly active catalyst at room temperatures. In-situ PXRD revealed the deactivation mechanism of the Aurolite catalyst as phase conversion of the anatase to rutile. This conversion as well as an increase

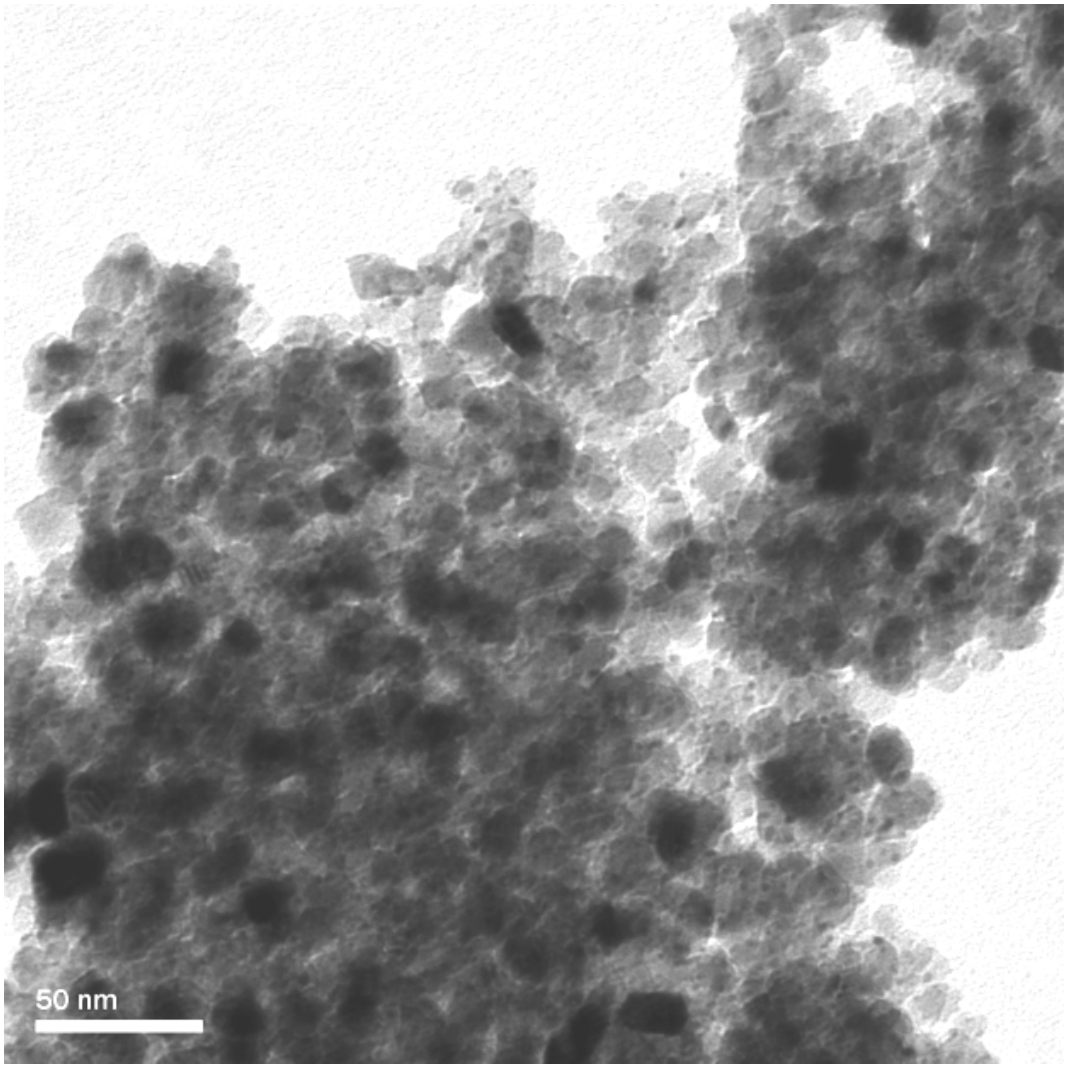


Figure 6.17: Low magnification image of the fresh Aurolite catalyst. The P25 support material had a relatively small particle size around 25 nm which confirmed the Rietveld results. The small particle sizes of the gold nanoparticles also confirmed the in-situ PXRD results at 300°C. The image shows homogeneous dispersion of the gold nanoparticles over the surface of the support.

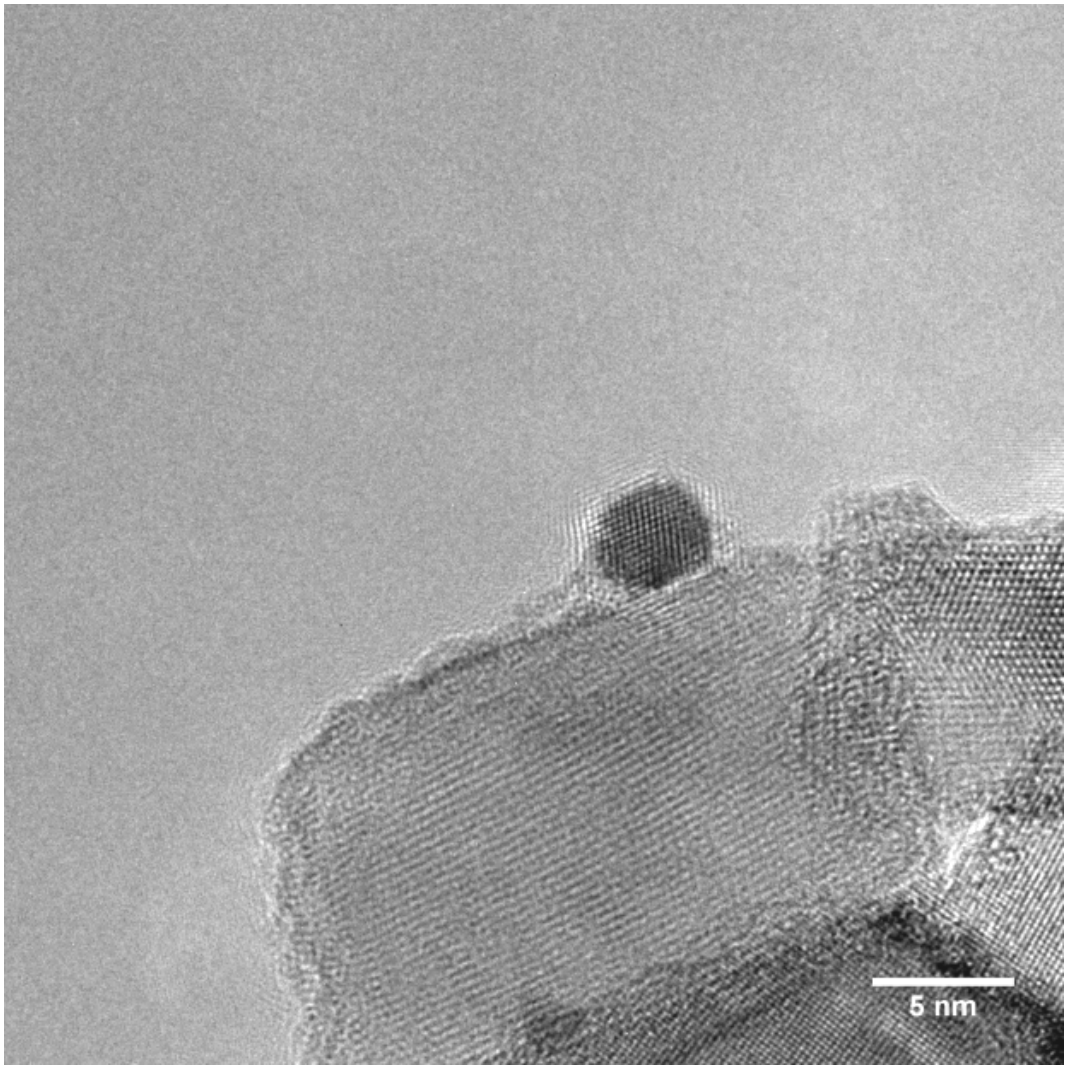


Figure 6.18: HR-TEM image of the Aurolite catalyst after heating to 300°C as is standard during the manufacturing process of the catalyst.

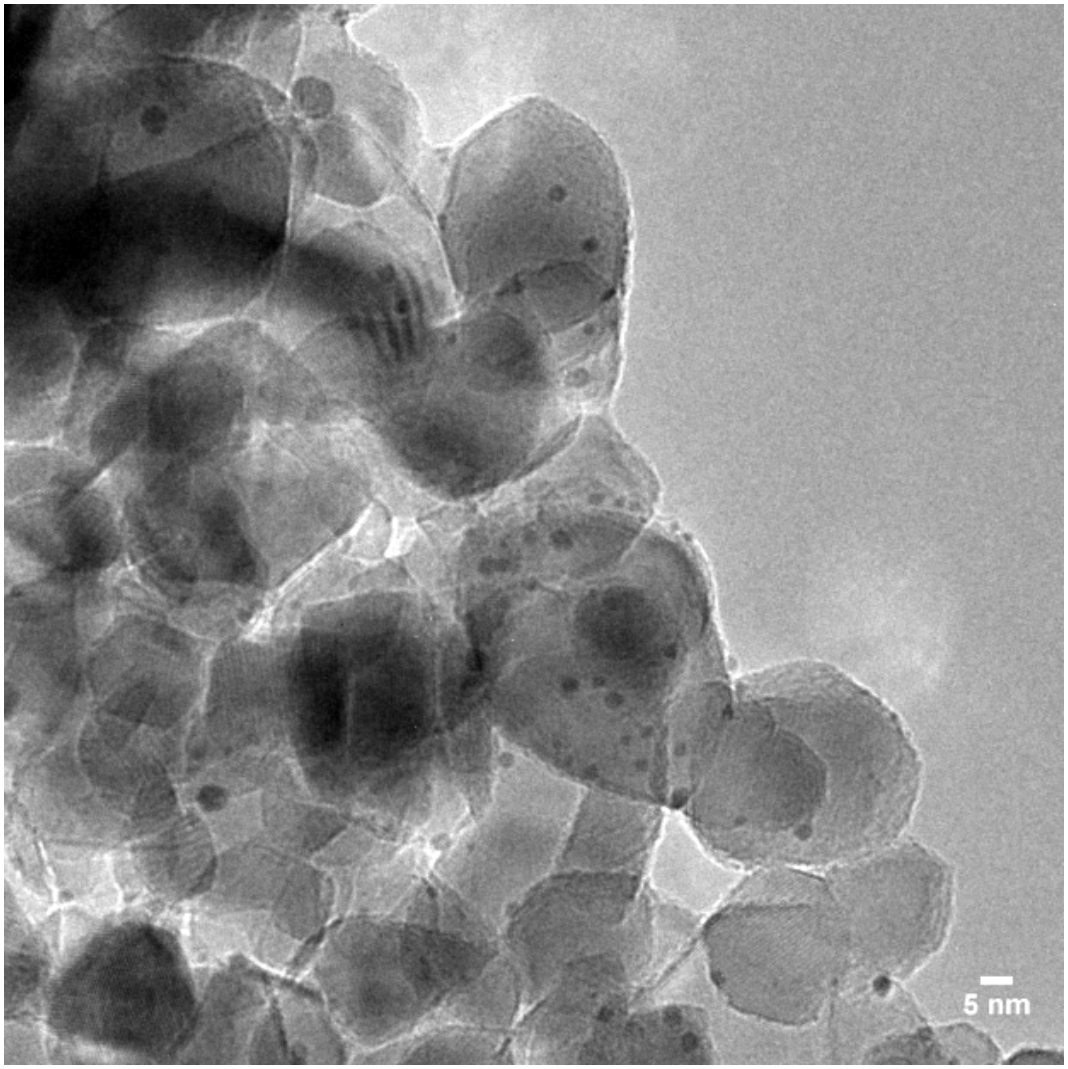


Figure 6.19: Aurolite catalyst after heating to 300°C taken at an intermediate magnification. Many smaller gold nanoparticles are only visible under higher magnification.

in crystallite sizes of the support resulted in massive loss of surface area and perhaps encapsulation of the gold nanoparticles.

An unstable support surface resulted in unstable gold nanoparticles under non-ambient temperatures. Rietveld refinements conducted on the in-situ data showed the rapid growth of the gold nanoparticles which was directly correlated to the phase transformation as well as sintering effects. When the Aurolite catalyst was exposed to 500°C for 12 hours, it was found that a phase change of the support occurred. As the phase transformation was shown to be a major contributing factor to the increase in gold nanoparticle sizes and thus deactivation of the catalyst (Chapter 9) it is likely that the cause of deactivation of current Au-TiO_2 catalysts over periods of months may be attributed to this same reason. As rutile is the thermodynamically favored polymorph of titania the catalyst support may, over a period of months, slowly phase convert towards higher percentages of rutile. When this occurs the catalyst will deactivate slowly with time.

Even though titania is known to be the best support material for gold nanoparticles, in its current form, when loaded with gold nanoparticles it was not able to withstand temperatures over 400°C as would be required for many industrial or emission control type applications. Current forms of titania once again were shown to be insufficient for use as supports for gold nanoparticles at temperatures over 400°C.

Chapter 7

Titania nanostructures

Existing supports have been shown to lack suitability for high temperature gold catalysis. Therefore a support needed to be designed and tailored specifically for this application. From results and insight gained from studying the supports in the previous chapters as well as an understanding into the deactivation mechanisms of the Aurolite catalyst, it was possible to propose supports that may be resilient to the factors that are the cause of deactivation of existing catalysts. Focus moved to nanostructured materials as a possible means to produce the desired catalyst.

A nanostructured material can be described as a material that has an internal or surface structure in the nanoscale region with at least one dimension in the size range of 1-100 nm. For instance, Damascus steel was known for its remarkable strength compared to other swords of the day that were produced from steel from other regions[109]. Centuries later it was discovered that carbon nanotubes along with cementite nanofibres were the cause of the steels remarkable strength. These carbon nanotubes entered the steel matrix during the production of the steel at high temperature and originated from the clays that were found in the region.

In 1991, a paper by Sumio Iijima on carbon nanotubes created a buzz around these newly discovered nanostructures[88]. The synthesis of nanostructured titania is attributed to Kasuga et al.. in 1998[118]. From this initial paper the amount of published papers has increased remarkably from year to year. In 2008 over 800 papers on the subject were published as shown in Figure 7.1. While compared to carbon nanostructures titania based nanostructures are

far less popular, there are benefits when titania nanostructures are concerned. For example they are low cost and synthesis methods are also simpler which allows the synthesis of these materials to be scaled up and used in an industrial environment. It is also relatively simply to obtain phase and elementally pure titania.

Like many other nanostructured materials, titania nanostructures have a very high specific surface area and it is possible to tailor the products for specific applications by controlling the synthesis conditions. Much like in the case of carbon nanostructures, the primary area of focus on titania has been on producing nanotubes and the functionalising of these structures with the intention of maximising surface area. The physio-chemical properties of nanomaterials have been shown to be very different to those of the counterpart bulk materials and this has opened up new branches of research into these new and exciting materials. Nanostructured forms of titania have shown promise in many applications such as catalysis, solar cells and wide band gap materials for gas sensing, amongst others[109, 112]. Hydrothermally synthesised TiO_2 has also been shown to be more stable than commercial P25 TiO_2 powders during the sintering process as a result of the phase purity of the synthesised product[92]. For the CO oxidation reaction titania nanotubes, nanorods and nanopowder have demonstrated superior catalytic properties when compared to polycrystalline rutile and anatase[93]. Finally, nanogold has been shown to catalyze the CO oxidation reaction exceptionally well when supported on TiO_2[114].

7.1 The importance of titania nanostructures

Titania occurs in relatively high abundance and most of its inorganic compounds are low in toxicity. In the 1960's over 80% of all titanium produced was used in the aerospace industry[115, 116]. Since then there have been further improvements in the cost effectiveness of producing titanium and thus the ability to produce titanium compounds. Initially most nanostructured titania compounds were synthesised using sol-gel techniques which produced spheroidal particles of various shapes and dimensions down to a few nanometers. The most interesting and subsequent applications from these nanomaterials have been photocatalysis, dye sensitized photovoltaic cells and sensors[118]. In 1998, Kasuga et al.. discovered an alkaline hydrothermal synthesis route that pro-

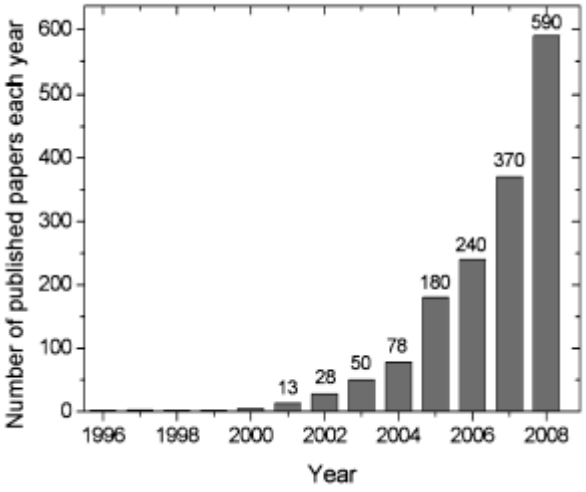


Figure 7.1: Number of papers published from 1998 to 2008 on titania nanostructures[123].

duced titania nanotubes[118]. Following this discovery researchers have made concerted efforts to try understand :

- the mechanism of formation of titania nanotubes,
- how to enhance and improve the synthesis methods, and
- the properties of these new materials.

Many interesting reviews are available on these topics[119, 124].

7.2 The structure of nanomaterials

As is the case with a relatively new field such as nanotechnology, many new terms have appeared and most are used inconsistently. Thus a brief description of morphological forms is necessary.

Nanotubes - nanotubes, also sometimes described as nanoscrolls are long cylindrical shaped objects that contain a hollow cavity in their center that extends through the length of the cylinder. In titanate nanotubes, the walls of the cylinders are always multilayered in a similar fashion to an "onion" type structure. These nanotubes are produced by rolling nanosheets to form the cylinder.

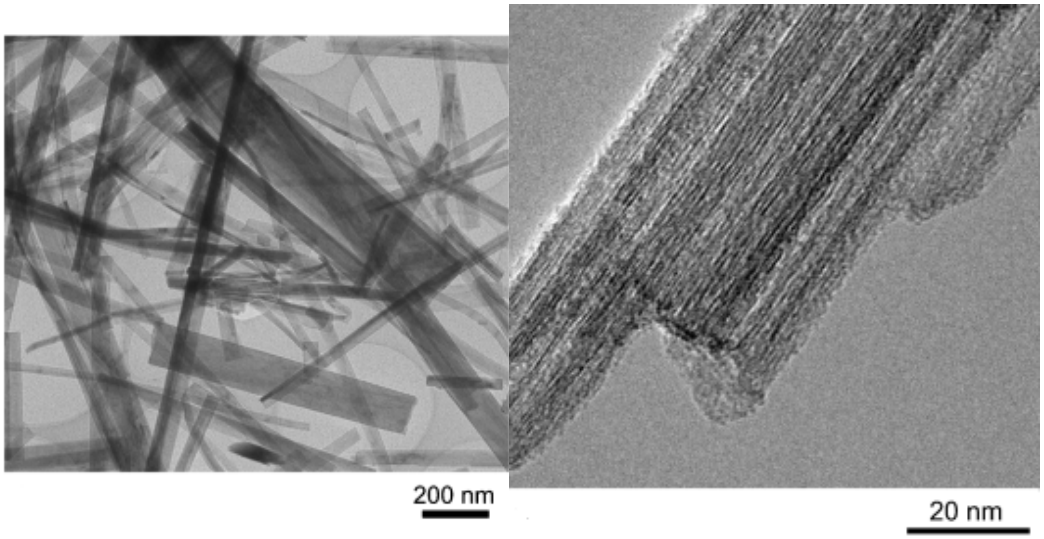


Figure 7.2: Titanate nanofibres a (left) and b (right)[120, 123].

The greater the number of turns in the nanosheet the more concentric circles are formed and thus more layers are added to the cylinder.

Nanowires and Nanorods - These morphologies are long and solid cylinders that have a circular base. The difference between a nanorod and a nanowire is simply that nanowires are longer than nanorods. Contained in the different types of morphologies are a number of different synthesis methods and many different types of nanotubes and nanowires that may have different thickness, roughness and length.

7.3 Synthesis of titania nanostructures

The method used by Kasuga and co-workers for producing titanate nanotubes and nanofibres was via an alkaline hydrothermal route[118]. This method was useful in that it did not require a sacrificial template like many other methods. The method involved the treatment of amorphous TiO_2 with a concentrated solution of NaOH in a PTFA lined batch reactor at temperatures between 100-150°C followed by washing with water and HCl. With this synthesis method it was shown that all three polymorphs of titania could be synthesised as shown in Figures 7.2 a and b[124, 126].

Nanofibres can be produced using a hydrothermal treatment of NaOH at temperatures over 170°C[124, 126]. These structures are characterised by a solid and

elongated morphology in the size range of 20-200 nm, with a length exceeding several microns (Figure 7.2a and b). The problem with using nanotubes as a support for gold nanoparticles is that if gold is deposited onto the nanotubes and exposed to high temperatures, encapsulation of the gold inside the nanotubes occurs readily[120, 123]. Thus, most of the active sites of the nanoparticles are lost as the tube structures collapse at high temperatures. Further, the nanotubes are easily blocked during catalysis resulting in a loss of all the active sites contained within the tube.

Rutile phase titania is rarely even considered as a potential support and over the years has become a support that is almost never studied. Current rutile nanorod synthesis methods create nanorods that are in a bed type structure as all the nanorods orientate in the same direction similar to that as shown in Figure 7.2b. This type of nanorod rutile product is not viable as a support due to the morphology of the structure as the orientation of the nanorods results in a close packing type arrangement of the structure. This type of orientation and morphology shown in Figure 7.2b is not desirable for a number of reasons including: low surface area, inability of reactant gases to permeate the structure as well the potential to encapsulate the active sites of the gold nanoparticles.

Two types of nanophase titania were synthesised with the aim of providing a stable support structure. These two supports and resulting catalysts from the deposition of gold and gold-platinum nanoparticles onto the new supports are investigated in the following chapters.

Chapter 8

Nano anatase as a support for Au and Au-Pt nanoparticles

8.1 Introduction

Following a review of the results from both the commercial anatase and Degussa's P25, conclusions about their suitability as supports for Au and Au-Pt were that neither could produce a thermally stable gold catalyst. Neither of the supports was able to provide high surface area with thermal stability. For use at temperatures less the 450°C, these supports may be viable if great caution is taken to ensure that this temperature is not exceeded. As has been shown, due to thermodynamic considerations it is not possible to use anatase as a support for high temperature applications. However, improvements to the current supports used for gold nanoparticles, such as in the case of the Aurolite catalyst, can be obtained using nano anatase in place of Degussa P25. For a support suitable for low to medium temperatures i.e. from ambient to 450°C, the support requires a high surface area, phase purity and hindered phase transitions.

A potential candidate support was pure nano-anatase. If this could be produced with a very high surface area as well as consisting of small particle sizes. If the anatase was produced 100% phase pure this would aid in inhibiting the onset of the phase transition as no rutile "seeds" would be present to initiate the phase transformation. The premise was that this would result in the support being more stable when compared to both commercial anatase and P25 while providing a higher usable surface area.

8.2 Synthesis

Anatase nanoparticle clusters were synthesised via a hydrothermal reaction. 12.0 mL of $TiCl_4$ was slowly added to 160 mL of deionized water at 0°C containing 0.70 M citric acid in a round bottomed flask. The solution was heated to 180°C for 24 hours under reflux in an oil bath set at 180°C whilst undergoing rapid stirring. The white precipitate was centrifuged and washed with deionized water to remove all the residual chlorides. Washing was continued until the pH of the solution containing the support reached neutrality. This method was designed to be as simple and robust as possible, thus the ability to scale up the process may be achieved.

For the addition of gold nanoparticles a 250 mL conical flask was placed onto a temperature controlled heater stirrer and 100 mL of deionized water was added into the conical flask. 1.0 g of nano anatase, the support, was added to the deionized water. To the deionized water, $HAuCl_4.3H_2O$ and 0.85 M urea were also added in appropriate stoichiometric ratios. The theoretical loading of gold was between 1 and 5% depending on the sample. $H_2PtCl_6.3H_20$ was added when platinum was deposited on the support. A stirrer bar was added to the conical flask and the flask was then sealed.

The reaction was undertaken in a dark fumehood. The solution was heated to between 75°C and 80°C to ensure the complete hydrolysis of the urea. The reaction was allowed to take place over 24 hours. Once the reaction was completed the solution containing the catalyst was washed with hot deionized water and centrifuged. This process was repeated until the pH reached neutrality. Finally, the catalyst was then placed in a drying oven overnight at 110°C to remove any residual water. Reduction was only undertaken just prior to using the catalyst for either CO oxidation reactions on a catalytic testing unit or for characterization. 5% Au on nano anatase was produced for the in-situ PXRD characterization as well as for TEM studies. For catalysis studies 1% Au samples were produced using both heated and unheated nano anatase. The reason for the comparison between heated and unheated support is due to the addition of citric acid during the synthesis of the support. At temperatures over 400°C the citric acid is removed from the support surface. The removal of the citric acid before the deposition of gold nanoparticles onto the support was shown to increase the catalytic activity of the produced catalyst at low temperatures.

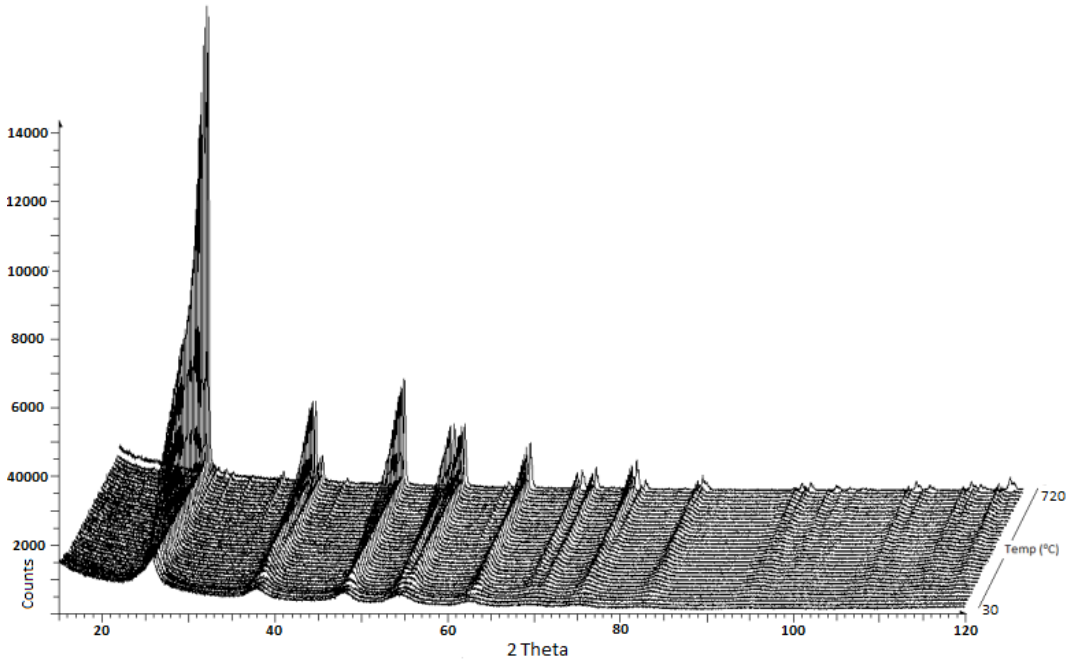


Figure 8.1: In-situ PXRD of nano anatase support. Data collections were conducted from 15° to 120° 2θ with temperature ranges from 30°C to 720°C in 15°C increments. Temperatures higher than 720°C were not investigated for the pure support initially but were analyzed when Au and Au-Pt were deposited.

8.3 In-situ PXRD

Initially the support was studied as shown in Figures 8.1 and 8.4 with a heating profile as shown in Figure 8.2.

8.4 Rietveld refinements

Rietveld refinements such as shown in Figure 8.3 and 8.5 showed that the initial crystallite size of the as synthesised nano anatase was very small, at around 5 nm diameter. Heating of the support prior to the deposition of the metal nanoparticles proved to be useful as this allowed for the initial growth of the support to occur without interfering with the stability of the metal nanoparticles on the surface. A balance between very high surface area and stability of the support was necessary implying a balance between high surface area and crystallite size. On average a BET surface area of 482.3 $\pm$ 7.7 m^2/g was attained across a number of different batches of the synthesised product. Even though much of this surface area was lost upon heating, the nano anatase

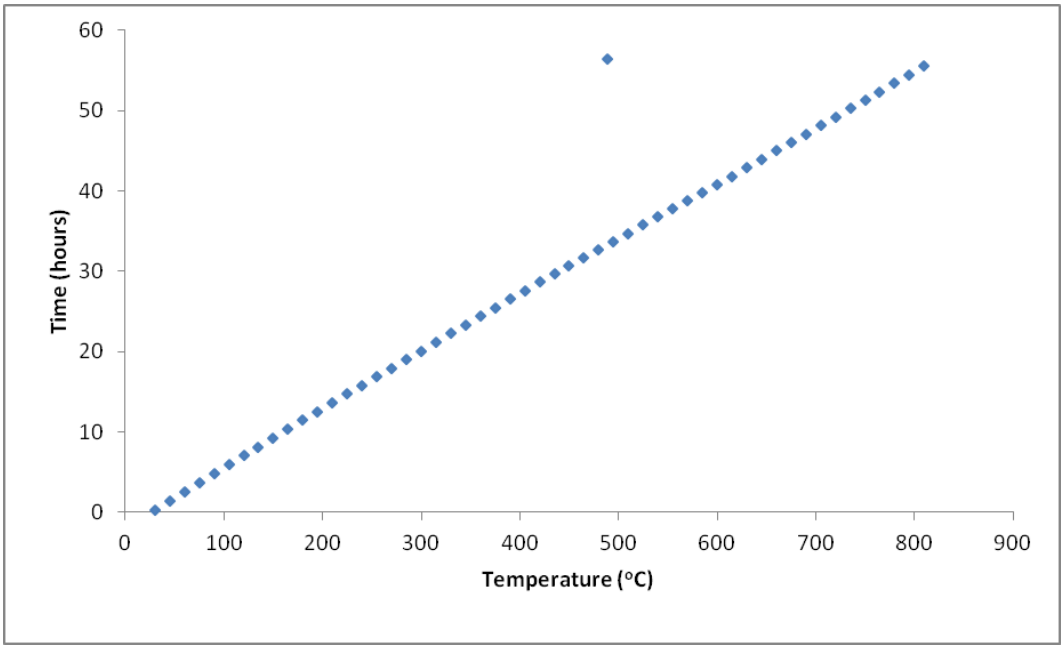


Figure 8.2: Temperature Vs time plot for data collections showing the catalysts being tested for almost 60 hours at temperatures from 30°C to 800°C.

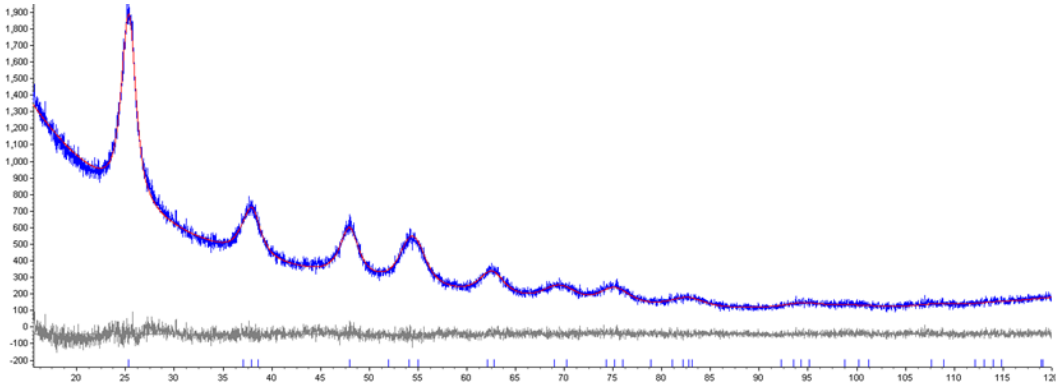


Figure 8.3: Rietveld refinement of pure nano anatase support at low temperature taken from TOPAS. The difference pattern shows the quality of the fit for the pattern. The steep gradient of the pattern at low angles was due to air scattering of the beam. Further, the low intensity of the diffraction peaks was attributed to the nano support as the crystallite sizes of the support material were very small at less than 10 nm. This could also be seen from the broadness of the diffraction peaks. Phase purity of the product was also noted with 100% nano anatase produced.

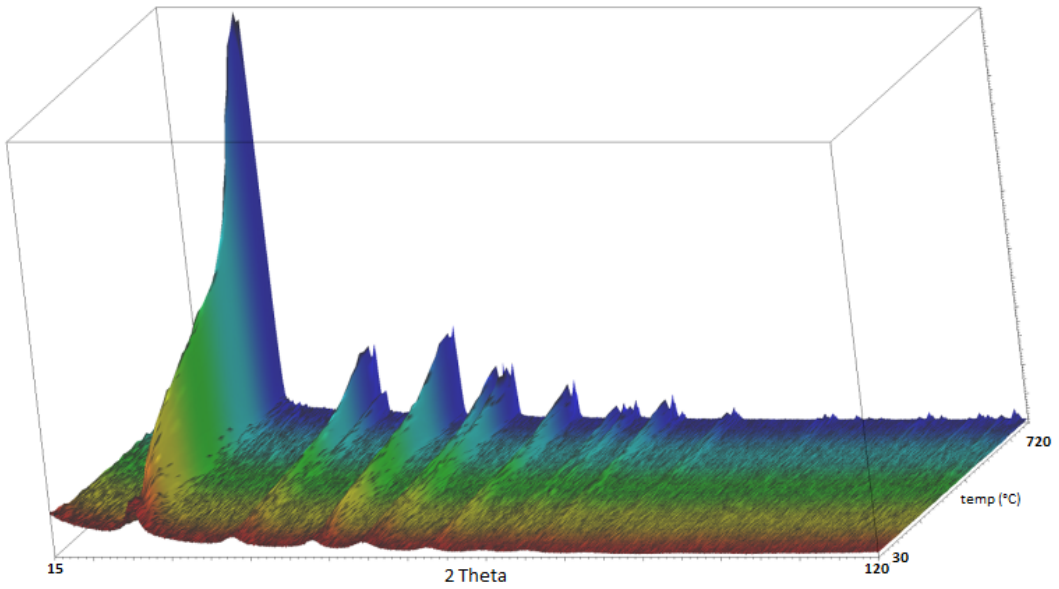


Figure 8.4: In-situ PXRD of pure nano anatase support. The increase in the intensity of the diffraction peaks at high temperatures showed the growth of the support material from low to high temperatures.

still showed surface areas far in excess of both commercial anatase and Degussa P25. Surface areas of over 291.7 m^2/g were attained even after heating the support to 600°C for 12 hours. These results were duplicated in samples that were synthesised at a later time with very high surface areas and small particle sizes being the most common result.

Rietveld refinements (Figure 8.5) gave particle sizes which were very small at the commencement of the data collection. Even at 500°C, the particle sizes were still relatively small (less than 20 nm) when compared to commercial anatase that was greater than 85 nm. BET results showed that the support had a surface area of 487.6 $m^2/g \pm 7.7\ m^2/g$ for the as synthesised product. However, after heating to 500°C for 24 hours this value dropped to just below 310 m^2/g. Even though this is a large loss of surface area, when compared to a support such as P25 that had a surface area of 47.1 m^2/g , the nano anatase still had more than 6 times the usable surface area after quite intense thermal exposure. The in-situ diffraction data also showed that the growth of the particles was not constant. Instead, once the support reached a given temperature, the growth of the crystallites slows down until eventually the growth stops almost completely. Thus, if the support is used at temperatures below 400°C, a very high surface area can be maintained.

Following the data collections on the pure support, Au as well as Pt was de-

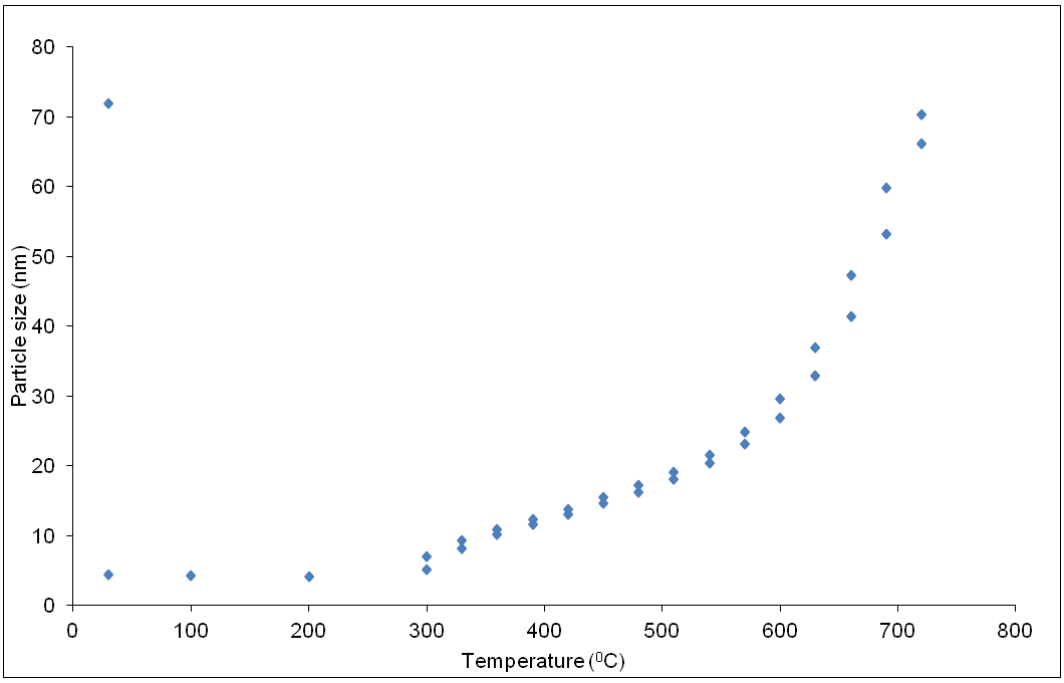


Figure 8.5: Rietveld refinement results from the in-situ PXRD data collections of the crystallite sizes of nano anatase.

posited onto the support and in-situ data collected as shown in Figure 8.6 with the resulting crystallite sizes of the anatase support and the Au nanoparticles shown in Figures 8.7 and 8.8 respectively.

8.4.1 Comparison of commercial anatase to nano anatase

The addition of platinum to commercial anatase with gold resulted in a rapid increase in the evolution of the rutile phase occurring over 690°C, as demon-

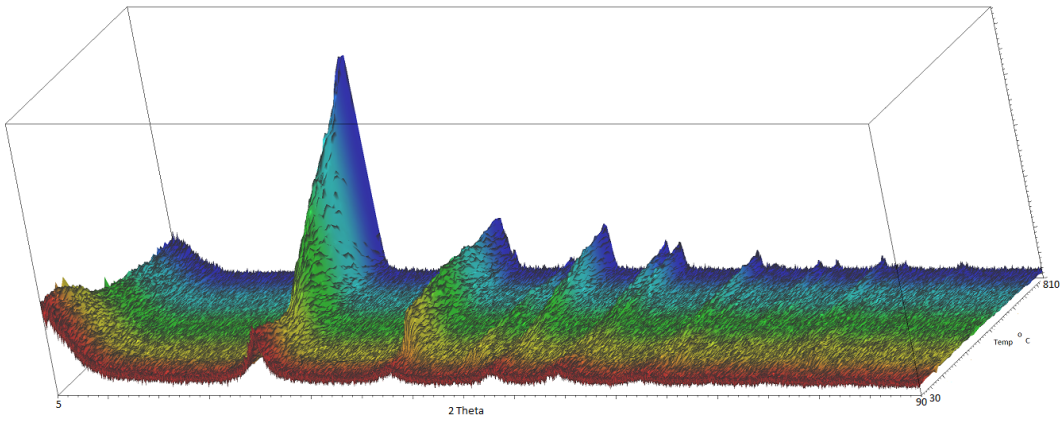


Figure 8.6: In-situ PXRD of 5% Au on nano anatase.

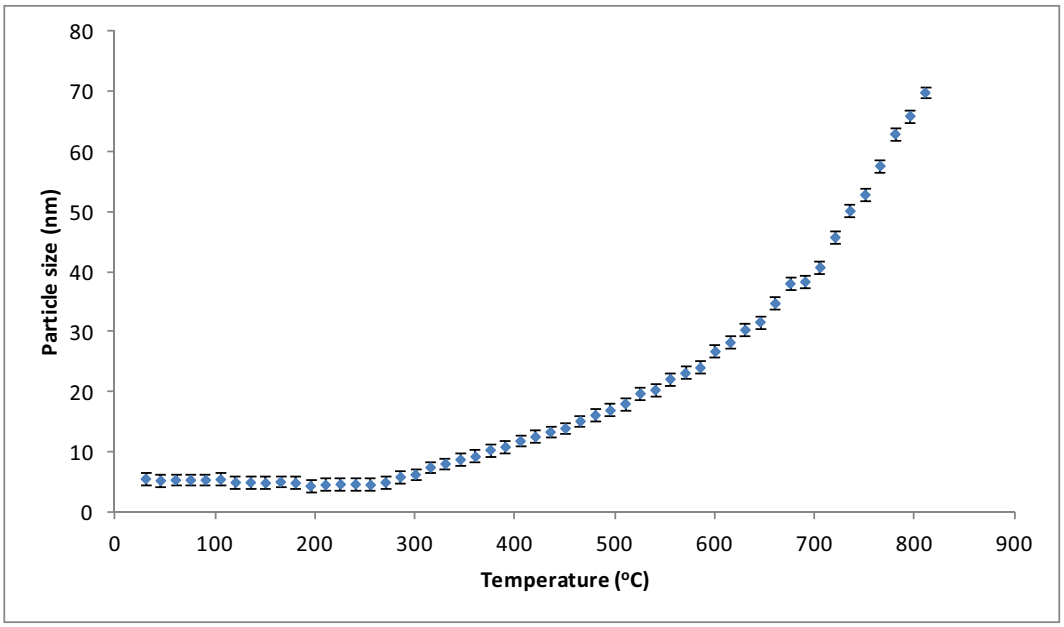


Figure 8.7: Rietveld refinements showing the support crystallite size of 5% Au on nano anatase. The support showed good stability at low to medium temperatures with the ability to maintain a high surface area. However, at high temperatures the crystallite size increased quite dramatically. Initial conclusions were that the support may be very useful at low to medium temperatures as it had a very high surface area at these temperatures as well as being phase pure. For low temperature CO oxidation the nano anatase support was found to be superior to both commercial anatase and Degussa P25 due to its small crystallite sizes and high usable surface area. However, the thermodynamic phase transformation of anatase to rutile is unavoidable at higher temperatures.

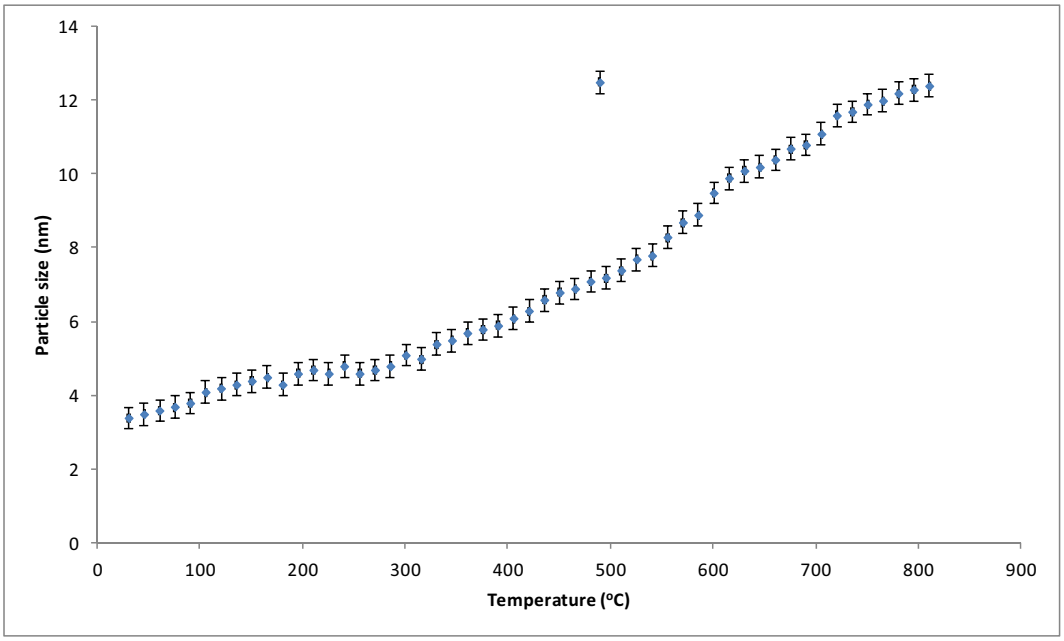


Figure 8.8: Rietveld refinement results of the gold crystallite sizes from the data collection of the 5% Au on nano anatase. The gold crystallite sizes are indeed smaller when compared to the Aurolite catalyst at high temperatures. However, the gold crystallite sizes in this range are still too large to facilitate the oxidation of carbon monoxide at low temperatures once the catalyst had been exposed to high temperatures. The profile of the graphs shape is different when compared to gold supported on the commercial anatase as well as P25 where a dramatic exponential growth of the gold crystallites was observed. This was not observed because the catalyst did not undergo a phase transition. Thus the phase pure nano anatase managed to deter the onset of the anatase to rutile phase transition, the curve of the graph, or more simply put, the increase in the gold crystallite size is much flatter with a more gradual, gentler slope. This provided more evidence of the detrimental effect phase changes had on gold nanoparticle stability. It must also be noted that the data collections for nano anatase were almost three times as long when compared to the commercial anatase samples. This highlighted the nano anatase's superior thermal stability as well as the increased stability of the supported nanoparticles.

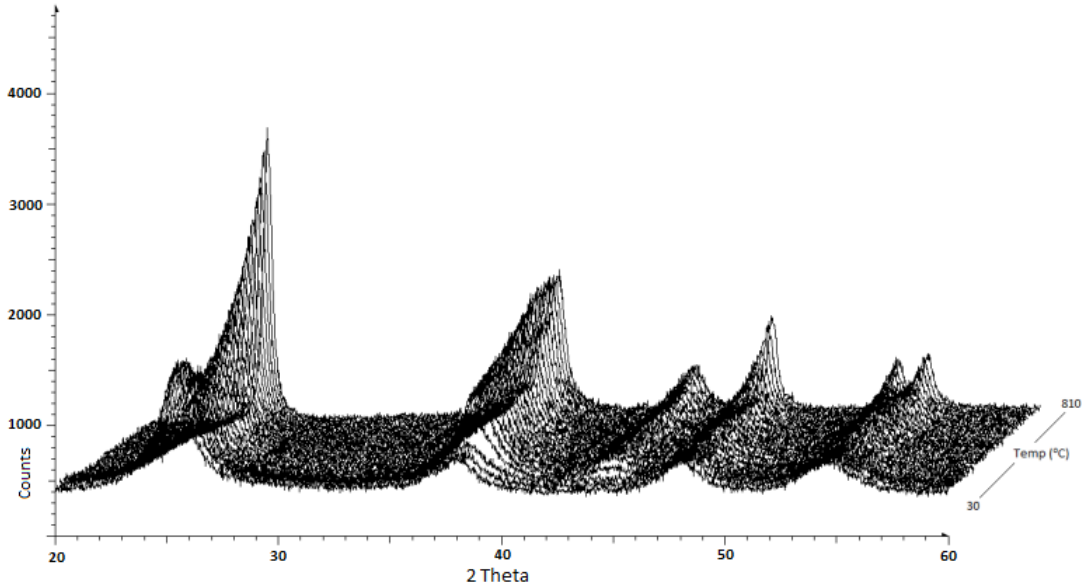


Figure 8.9: In-situ PXRD of 5% Au-5% Pt supported on nano anatase. Even after exposure to 810°C the nano anatase still remained phase pure with the onset of the conversion of anatase to rutile delayed. Small diffraction peaks can be noted for gold and platinum, however most of the peaks are lost in the very broad anatase peaks. At 810°C the nano anatase is still 100% phase pure even after the catalyst was exposed to high temperatures for 3 times longer than the commercial anatase based catalysts. Further, even higher metal loadings of platinum were used to try and overload the support and force the phase change to occur earlier than it may happen if less supported nanoparticles were present. Neither of these factors affected the catalyst thus the addition of gold and platinum nanoparticles as well as increased exposure to high temperatures did not result in a phase transformation of anatase to rutile.

strated in Chapter 5. It was postulated that a phase pure support, such as nano anatase, would provide better phase stability at higher temperatures. This was investigated by the addition of 5% Pt in addition to gold on the nano anatase support. Analysis was undertaken from ambient to 810°C for a similar time duration compared to the Au-Pt commercial anatase sample. The important parameter was the duration spent at a given temperature as well as the heating rate as this affected the kinetics of the phase transition. In this manner the in-situ PXRD data collections were comparable. Longer scan times were used in order to try and enhance the data quality of the nano anatase due to the small crystallite sizes of the support as opposed to a large number of shorter scans of lower resolution as shown in Figure 8.9 and 8.10.

From the variable temperature data it was determined that there was no rutile polymorph formed even at high temperatures. This is in contrast to the

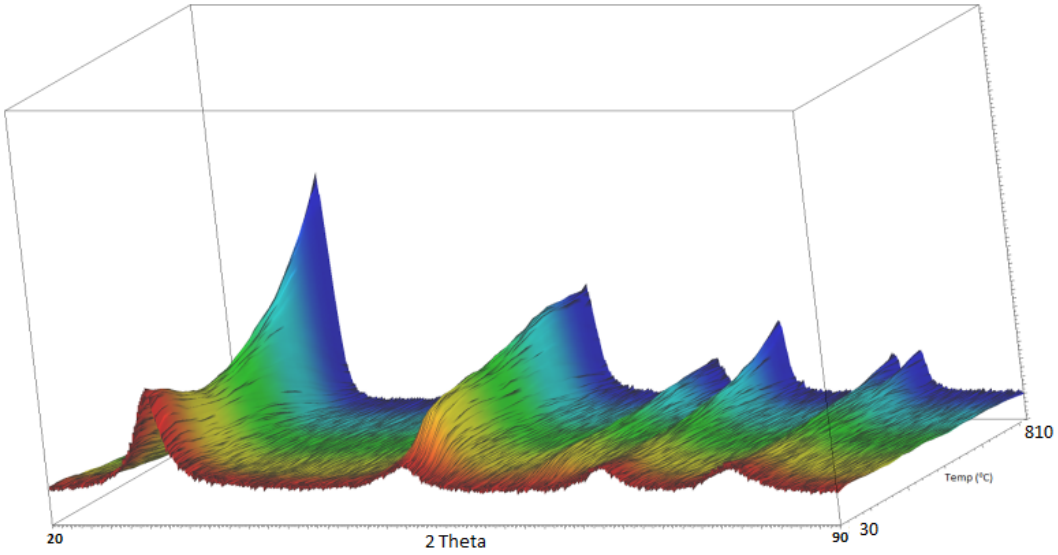


Figure 8.10: In-situ PXRD of 5% Au-5% Pt supported on nano anatase. The aim was to determine if the addition of platinum or gold effects the phase transition from anatase to rutile as was the case when commercial anatase was used. The diffraction data revealed that no rutile is present even at high temperatures due to the phase purity of the synthesised product.

commercial anatase catalysts where the evolution of the rutile phase is rapid and easily noted as the temperature increased with time. The reason for the absence of the rutile phase was due to the phase purity of the synthesised nano product. The hydrothermal method resulted in 100% anatase being produced. While exposure to high temperatures for extended periods of time will undoubtedly result in the conversion of the nano anatase to rutile, as this is a thermodynamic requirement, the nano anatase has a far higher surface area and better phase purity at low to medium temperatures. If one was to consider producing a gold catalyst for use up to 400°C then from a structural perspective, nano anatase would prove a better support material then both Degussa P25 and commercial anatase. This is further highlighted by the oxidation of CO in Section 8.6.

8.5 TEM

Selected samples were heated to 400°C and 600°C for two hours. TEM analysis was then conducted on the heated samples to examine what type of structural changes may have occurred to the catalyst after exposure to these conditions.

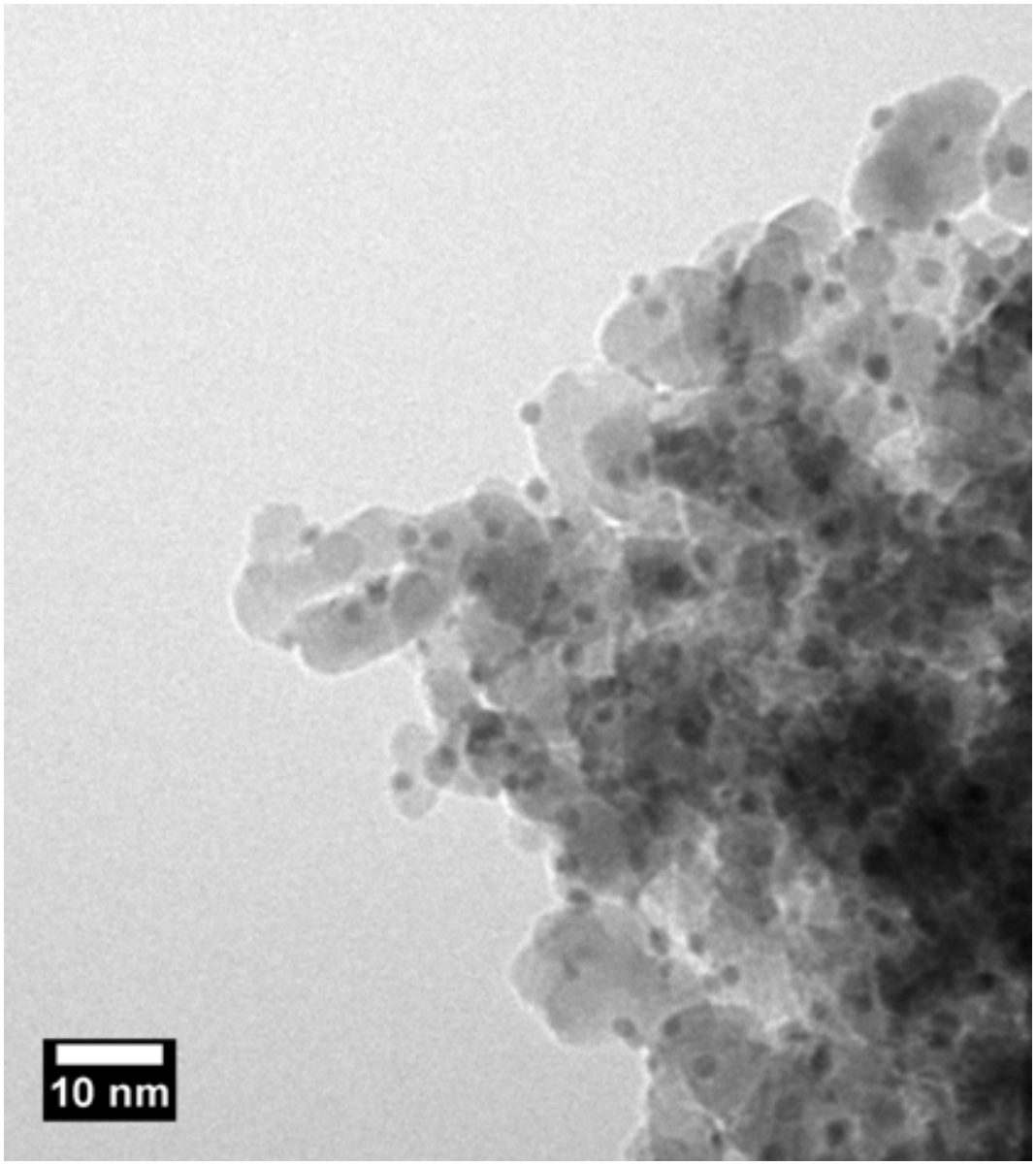


Figure 8.11: 5% Au on nano anatase support after heating to 400°C for 2 hours. Small homogeneously dispersed nanoparticles were observed as well as small support sizes.

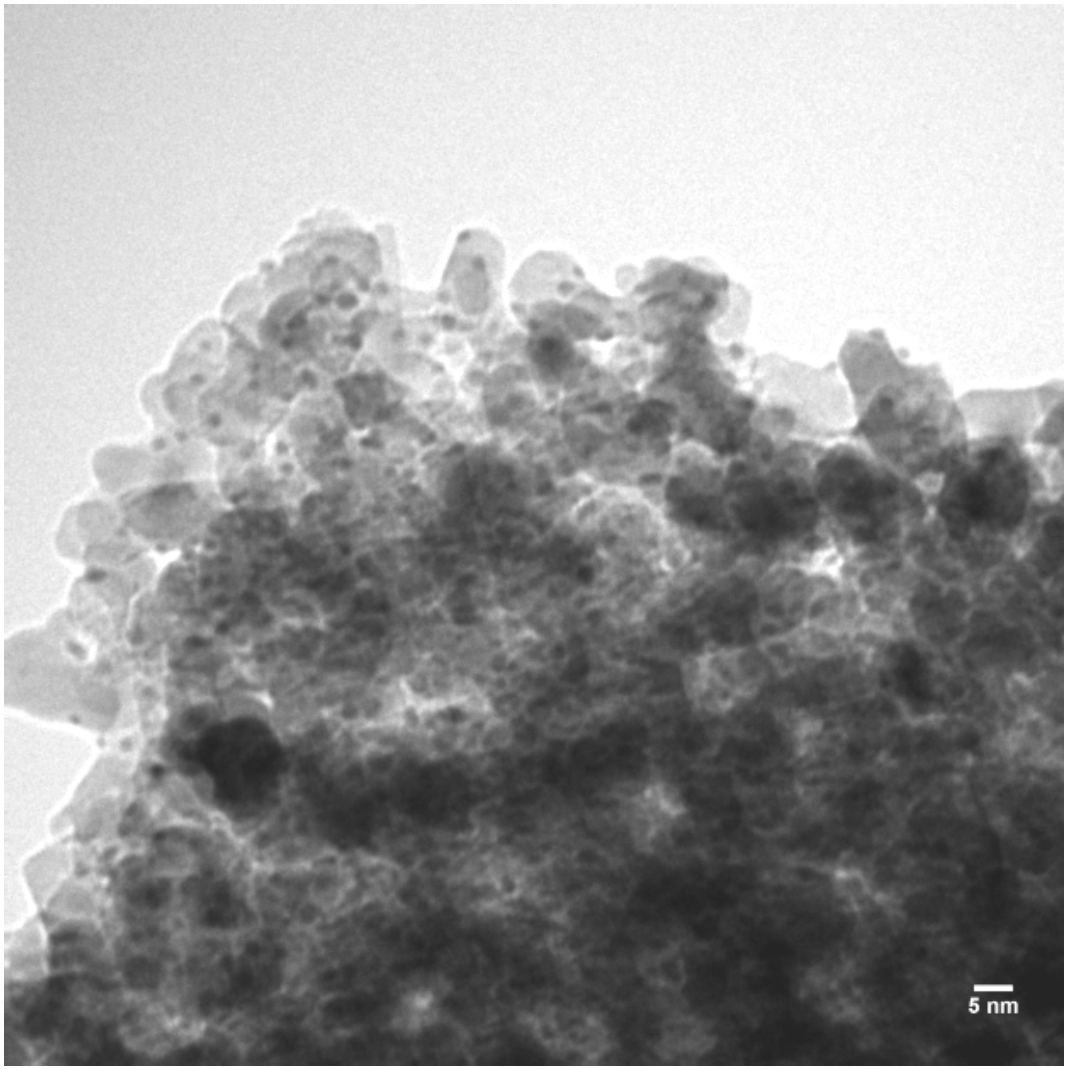


Figure 8.12: 5% Au on nano anatase heated to 400°C for 2 hours. The image shows the gold nanoparticles were homogeneously dispersed over the surface.

The "nanoscale" of the support structure can be seen from the micrographs in Figures 8.11 and 8.14. even after the support has been exposed to 400°C for 2 hours. Both the particle sizes of the support structure and the gold nanoparticles correlate with the variable temperature diffraction data and the resulting Rietveld refinements. Figures 8.15 and 8.16 show an increase in both the support and gold nanoparticle size after exposure to 600°C for 2 hours. However, the gold nanoparticle size is still small with most of the gold nanoparticles less than 5 nm in size.

.

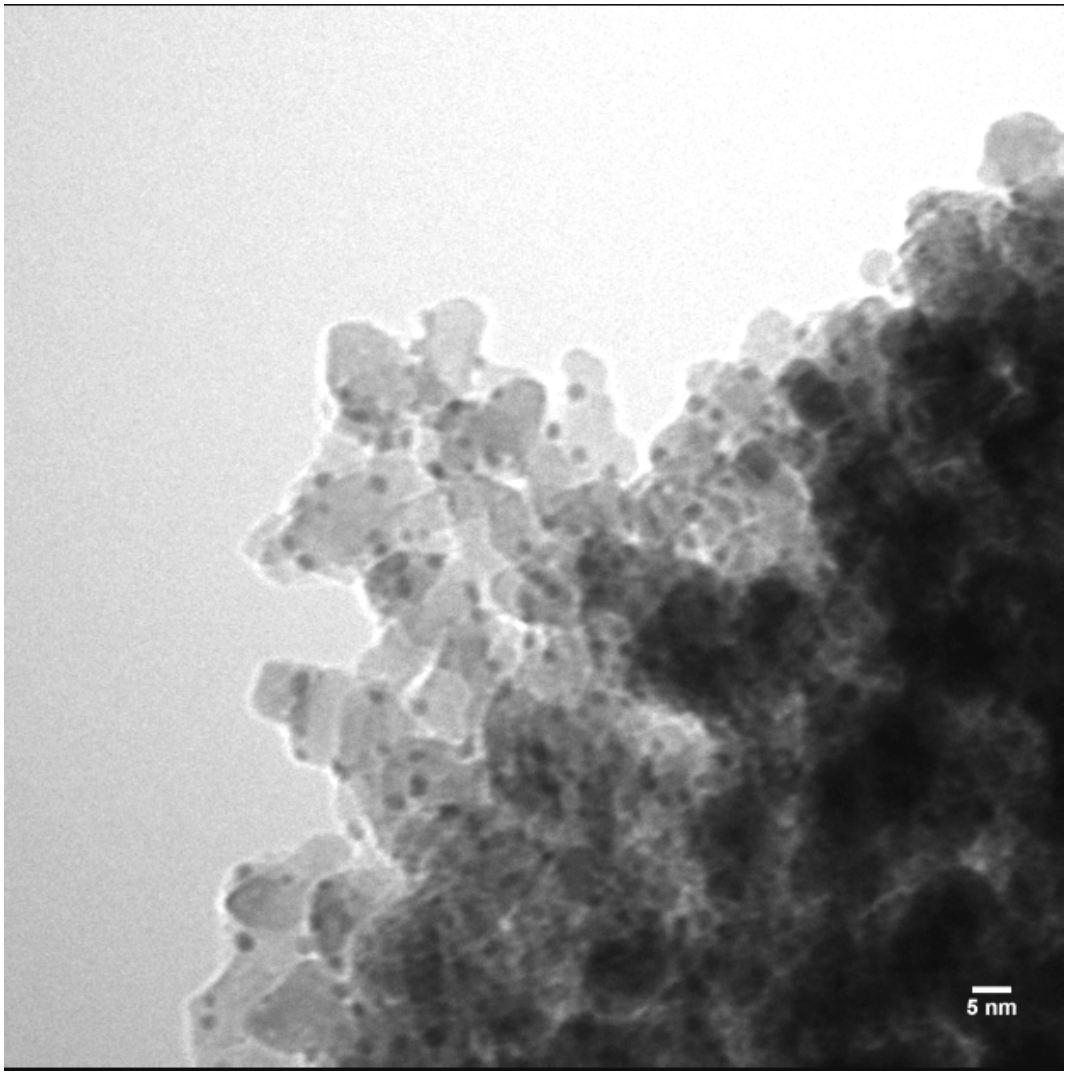


Figure 8.13: 5% Au on nano anatase heated to 400°C for 2 hours. The image showed how small the gold nanoparticles were, being far smaller than the scale bar of 5 nm.

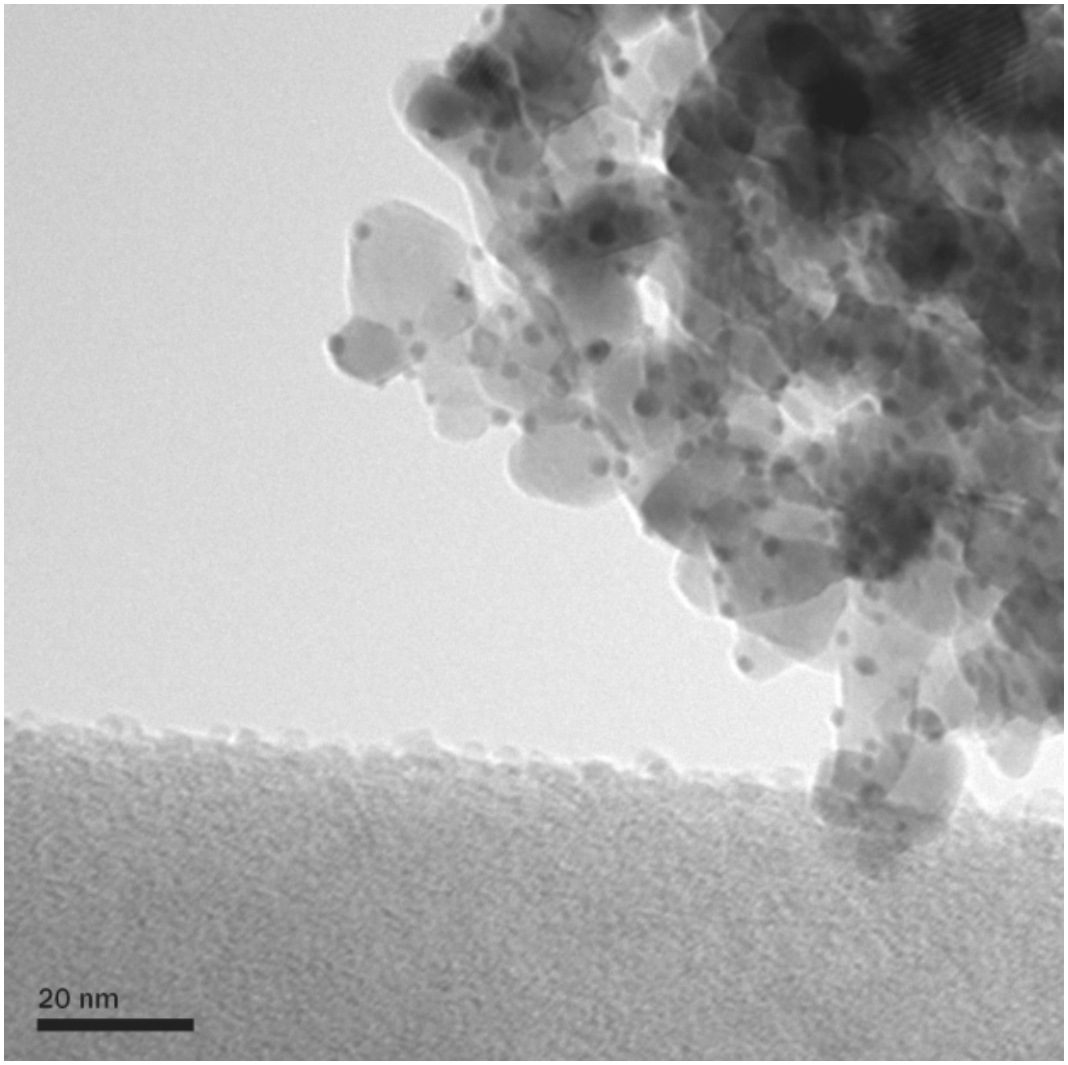


Figure 8.14: 5% Au on nano anatase heated to 400°C.

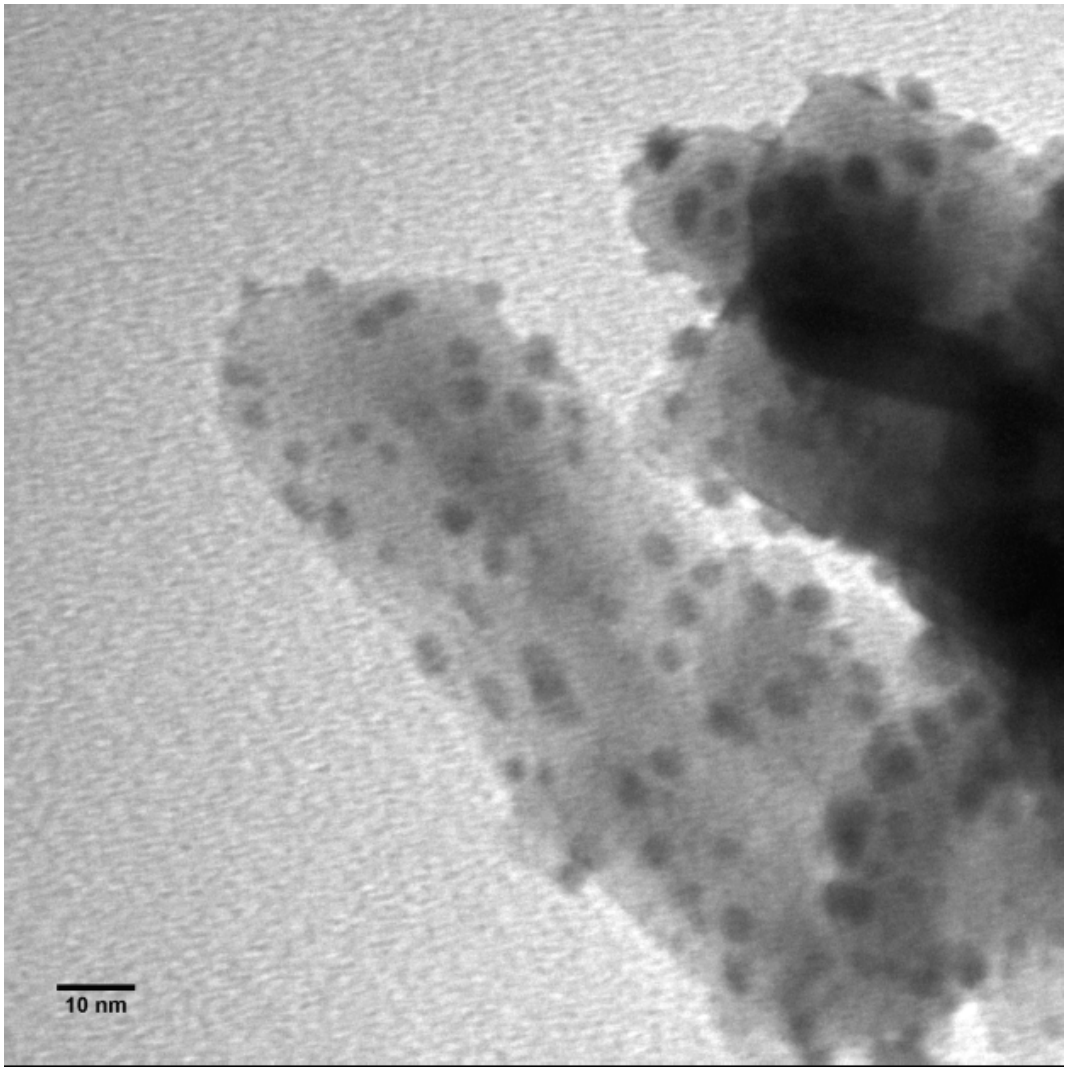


Figure 8.15: High magnifications image of 5% Au on nano anatase heated to 600°C for 2 hours. An increase in both the support and gold nanoparticle size was evident. However, the gold nanoparticle size is still small with most of the gold nanoparticles less than 5 nm in size.

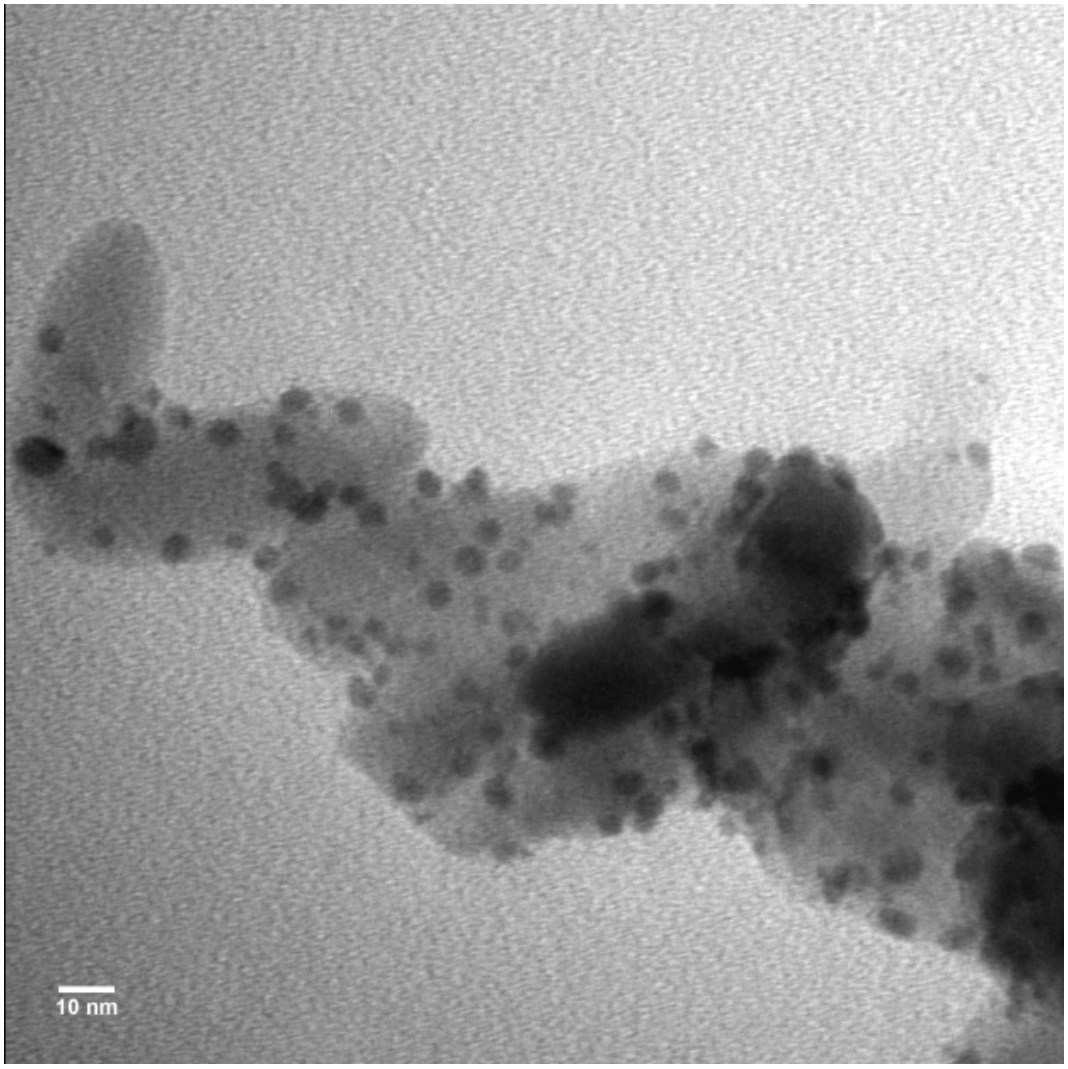


Figure 8.16: 5% Au on nano anatase heated to 600°C for 2 hours. The in-situ PXRD and TEM results concurred as both techniques showed an increase in the particle sizes of both the support and gold nanoparticles from 400°C to 600°C, albeit that the increase was not dramatic as the support still maintained its nano characteristics with large usable surface area.

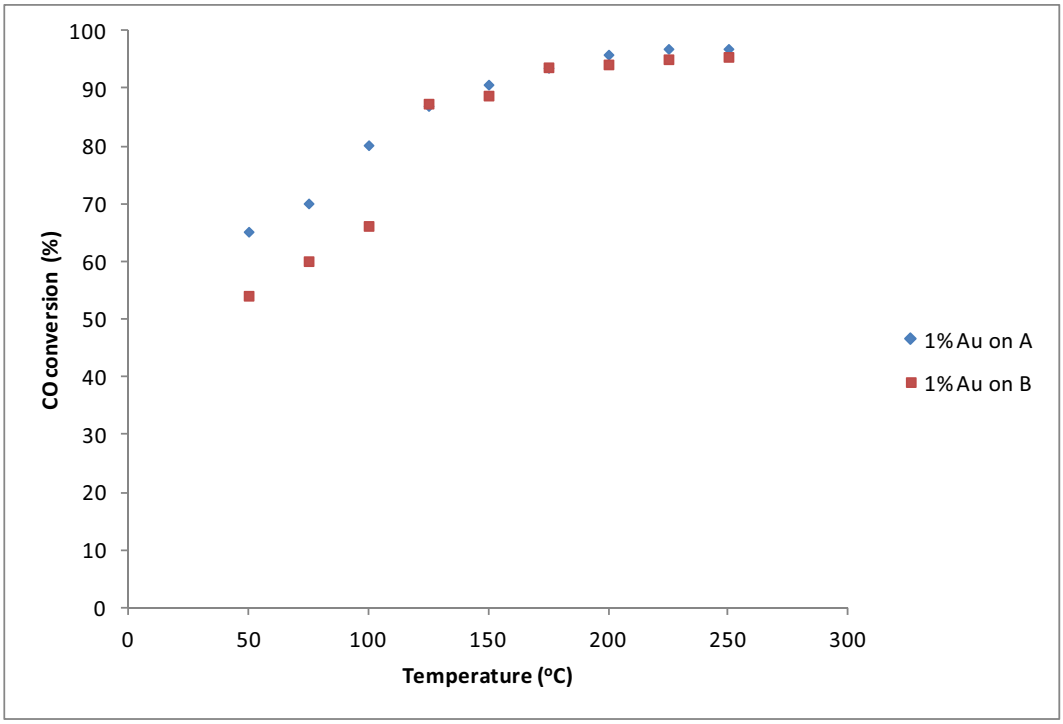


Figure 8.17: Graph of CO conversion vs temperature. **Sample A** corresponded to the nano anatase support which was heated to 400°C for 1 hour prior to the addition of gold to remove the residual citric acid remaining from the synthesis of the support. The citric acid acted as a capping agent in the synthesis. **Sample B** is the unheated support and thus still contained citric acid on the surface of the catalyst.

8.6 CO oxidation testing

Samples of 1% Au on both heated and unheated nano anatase were synthesised. Three repeat samples of both types of catalyst were produced and tested for CO oxidation. The, shown in Figure 8.17, are the averaged CO conversion percentages taken from each of the triplicate sample runs. 1% gold loading was chosen as this is the most common loading used for industrial gold catalysts.

The citric acid affected only the CO oxidation reaction at lower temperatures as seen in Figure 8.17 where a difference of approximately 10% conversion exists between the heated and unheated supports. The results CO conversion percentages compared well with the Aurolite catalyst under the same test conditions are shown in Chapter 9. This catalyst may be able to cope better with higher loadings of gold due to the supports increased surface area when compared to supports such a commercial anatase or P25. This is very useful when very high flow rates are encountered at low temperatures as higher gold loadings will help the catalyst maintain high CO conversion with increased

flow rates.

8.7 Conclusions

The synthesis method resulted in high surface area, 100% phase pure nano anatase TiO_2. The phase purity of the nano anatase was maintained even after exposure to high temperatures where rutile phase formation occurred in both the commercial anatase and Degussa P25 supports. This was shown by in-situ variable temperature powder diffraction. TEM showed the nano type morphology of the nano anatase support as well as small, homogeneously deposited gold nanoparticles on the surface even after exposure to 400°C and 600°C for 2 hours. High surface areas were attained using nano anatase with surface areas greater than 480 m^2/g being achieved over a number of replicate samples. High surface areas were maintained even after the nano anatase was exposed to 500°C for 12 hours, a process that completely deactivated the Aurolite catalyst due to phase conversion to a low surface area rutile. Even the addition of 5% Pt to the 5% Au catalyst did not result in a phase transition after exposure to non-ambient conditions for nearly 60 hours, some 35 hours longer than what commercial anatase catalysts were exposed to. The reason for this stability is attributed to the phase purity of the synthesised product as there was no rutile-nanoparticle phase boundary present where the metal nanoparticles could catalyze the phase transition.

The citric acid, that was used as a capping agent during the synthesis, was easily removed from the support surface with heating. Residual citric acid played a small role when CO oxidation tests were conducted as the citric acid on the support surface may have interfered with the reaction mechanism by inhibiting the active sites of the catalyst. However, this effect was easily counteracted by heating the support to 400°C for 1 hour prior to the deposition of metal nanoparticles thereby removing any residual citric acid.

Rietveld refinements conducted on the in-situ PXRD data showed the gold crystallite sizes were smaller when compared to both gold on commercial anatase and P25 supports as well as that of the Aurolite catalyst even after exposure to non-ambient conditions for a greater time period. This was attributed to the phase purity of the nano anatase, where, under in-situ conditions it was observed that the particles resisted phase conversion and remained

phase pure while maintaining a high usable surface area far greater than that of commercial anatase and P25.

However, the phase transition is inevitable if the catalyst is continually exposed to high temperatures for long periods of time. Thus the support is very suitable for low to medium CO oxidation reactions but unsuitable for prolonged exposure to high temperatures. In order to develop a catalyst that was able to withstand temperatures over 400°C for long periods of time a rationally designed catalyst was needed. A novel catalyst with features such as high surface area with the appropriate support morphology was needed. Further, and crucially important, the support needed to be locked in the thermodynamically most stable polymorph. This implied the use of rutile, a support known to be generally inactive with very low surface area as shown in Figure 6.16.

Chapter 9

In search of a catalyst stable for temperatures exceeding 400°C

9.1 Introduction to high temperature gold catalysis

The stabilisation of gold nanoparticles is extremely important, if not the most important factor when nanogold catalysts are considered, as catalytic activity is directly related to gold particle size[41, 97-103]. For example, catalysts containing nanogold for potential use in the automotive industry must be able to withstand high temperatures from exhaust gases where sintering of the catalysts gold nanoparticles currently results in complete loss of catalytic activity. Further, sintering not only occurs at high temperatures, but occurs slowly over time at ambient temperatures that can result in deactivation of the catalyst over a period of months[25,41].

There are very few gold catalysts having the durability to withstand temperatures over 400°C for extended periods of time without complete loss of activity. Almost all of these catalysts, while showing activity after exposure to moderately high temperatures, are currently not durable enough for long term catalytic applications. An overview of all current high temperature gold catalysts follows.

A catalyst containing gold on cobalt oxide particles supported on a mixture of zirconia-based ceria, zirconia and titania was able to survive 157 hours at

500°C, albeit with some loss of activity along with a large loss of support surface area[104].

In work developed by Seker and Gulari (2005)[105], Au-Al_2O_3 catalysts were able to survive pre-treatments at 600°C in air for 24 hours followed by several cycles of 150-500°C. The catalysts were then kept at 500°C for 12 hours and showed high activities for NO conversion. However, NO conversion is less sensitive to gold particle size changes compared to the CO oxidation reaction implying the catalyst may have undergone deactivation for the CO oxidation reaction while still remaining active for NO conversion.[105]. No information was provided as to the catalyst's ability to oxidize CO. Much like the previous catalyst, the temperatures that the catalysts were exposed to were not significantly high when the duration of exposure was considered.

The most significant discovery over the last decade was made by the Toyota motor company. A patent from Toyota motor company describes a catalyst containing complex gold oxides of the form $Au_2Sr_5O_8$. In this catalyst the gold is entirely ionic and is trapped in the oxide lattice. However, the question that must be posed is how much of the gold is at the surface and available to do catalysis as compared to gold trapped within the oxide support lattice. The case may be that a large percentage of gold is trapped in the interior of the catalyst support. This aside, the Toyota catalyst was tested to 800°C for 5 hours with only a small decrease in its ability to convert C_3H_6 as would be found in a typical exhaust gas stream [106, 107]. One of the most important reasons for the development of a nanogold catalyst is due to its ability, if gold particles remain small enough, to facilitate reactions from ambient temperatures. The Toyota patent claim a T_{50}conversion at 345°C for the fresh catalyst. This high T_{50}value somewhat negates the use of nanogold, as standard PGM based auto-catalysts are also active at this temperature. Thus, the catalyst does not address the light off period at low temperatures. Finally, conversions of C_3H_6 were measured while decreasing the inlet gas temperature from 500 °C to 100 °C by a temperature increment rate of 10 °C/minute. The duration of the testing was not given.

The most recent announcement regarding potential automotive emission catalysts was from Nanostellar, a company based in California, USA. However, the catalyst that has been licensed under the name "NSgold^{TM}" is slightly misleading as the catalyst actually consists of a trimetallic system of Au-Pt-Pd supported on a zeolite such as corderite as shown in Figure 9.1. The catalyst



Figure 9.1: Precious metal loadings of the Nanostellar NSgold^{TM} catalyst. As the graph demonstrates, the NSgold catalyst is not a true "gold" catalyst. (www.nanostellar.com)

is designed to be used in diesel engines. The concerning feature of this catalyst is, when examined closely, that it is merely a standard auto-catalyst with a small amount of gold added to it.

Auto-catalysts are currently produced using a mixture of platinum group metals usually with platinum and one or two other PGM's chosen depending on the cost of the metals at the time. Thus, for example, a standard type auto-catalyst will be a mixture of Pt-Pd supported on corderite along with CeO_2. This type catalyst has been shown to work very efficiently, but with the problem of light off at low temperatures. The addition of gold is claimed to reduce the light off temperature and hence the catalyst is able to catalyze reactions from very low temperatures. However, if the catalyst reaches any significantly high temperature the stability of the gold nanoparticles must be called into question as gold supported on zeolites has been shown to be an unstable combination at high temperatures[25]. No information on the durability of the catalyst after exposure to high temperatures was revealed. However, the catalyst was designed for diesel internal combustion engines where the exhaust gas temperatures are relatively mild when compared to gasoline engines. A full description of the catalyst can be read at patents online[127].

The use of TiO_2 as a support for gold nanoparticles has been extensively used for a number of years as it is known as a highly active support for CO oxidation[102]. A catalyst such as the Mintek Aurolite catalyst uses P25 as a

support as has been demonstrated in previous sections. As research has progressed over the last decades since Haruta first discovered the amazing ability of nanoscale gold to catalyze the CO oxidation reaction at low temperature, research has been conducted on attempting to stabilise gold nanoparticles for higher temperature applications such as automotive catalysts. This has become even more important over the last decade as the prices of PGM's have escalated dramatically as well as the supply of many PGM's now being considered as insufficient. Comparisons of various supports and synthesis methods used for gold catalysis are available in literature[89-96]. Barring a few small improvements over the last couple of decades, the emergence of a true, pure supported nanogold catalyst for high temperature applications such as autocatalysts has not come to fruition.

Titania is in a class of supports known as active supports due its ability to be easily reduced and facilitate the transfer of oxygen between the support and the gold[107]. This is further improved by the effect of its isoelectric point on the deposition of gold nanoparticles to form strong bonds with the TiO_2 support. Anatase has long been the preferred phase of TiO_2 when considering possible supports for various reactions due to its large surface area when compared to rutile's meager 7.2 m^2/g. The limiting factor for both anatase and P25 is the conversion of anatase to the thermodynamically preferred rutile phase (resulting in a massive loss of catalytic activity). As thermodynamics will not favour an increase in surface area of a phase the only option in producing a support was by producing the support already locked into the desired phase.

There are no reports of TiO_2 being used as supports for gold nanoparticles for catalysis at temperatures over 400°C for extended periods of time. Gold on supports such as P25 or phase pure anatase show catalytic activity for only a brief time above such temperatures before deactivation of the catalyst occurs at high temperatures, as shown by the Aurolite catalyst. This was demonstrated in previous chapters. A literature example of this effect was demonstrated when gold catalysts, supported on the three allotropic phases of TiO_2, reduced at 300°C in H_2 and then oxidized at 500°C. Finally, a last reduction step was performed at 150°C. This sequence substantially deactivated the catalysts[108].

Some improvements have been made when titania nanotubes were used as supports. Titania nanotubes have very high surface areas that make for good supports. Due to the high surface energy of the nanotubes they are however, very susceptible to both phase and structural transformations to lower surface

energy. These transformations result in changes to the pore volumes that result in both enhanced sintering and encapsulation of the gold particles within the nanotubes. The most prominent reason for this was the collapse of the tube structure at higher temperatures. This resulted in the encapsulation of all active sites within the nanotube.

If gold catalysts are to be used in applications above 400°C, such as in automotive catalysts, thermal stability of not only the gold nanoparticles but also the stability of the support is crucial for long term activity. In a European driving cycle, temperatures average between 80-450°C while in the extra urban part of the cycle average temperatures of 200-450°C can be expected[107]. Some gold catalysts may cope with these temperatures, however at certain times during the cycle temperatures may reach well over 500°C and enter a thermal region that current gold based catalyst cannot operate in. In gasoline engined vehicles temperatures are even higher. A viable catalyst will have to meet the requirements of both thermal stability and durability to be considered as a potential catalyst for reactions undertaken at temperatures above 500°C for long durations.

9.2 Synthesis of thermodynamically stable, high surface area, nano rutile as a support structure

Radially aligned rutile nanorod dandelion structures, that will be referred to as NRS (nano rutile support), were synthesised via a hydrothermal reaction. 12.0 mL of $TiCl_4$ was slowly added to 160 mL of deionized water at 0°C in a round bottomed flask. The solution was heated to 180°C for 24 hours under reflux whilst undergoing rapid stirring. The white precipitate was centrifuged and washed with deionized water to remove all excess chloride ions. The solution containing the NRS was washed until the pH of the solution reached 7. The NRS was then placed into a heating oven and dried overnight at 110°C. A 250 mL conical flask was placed onto a temperature controlled heater stirrer and 100 mL of deionized water was added to the conical flask. 1.0 g of NRS was added to the deionized water. $HAuCl_4.3H_2O$ and 0.85 M urea was also added. The theoretical loading of gold was between 1 and 8% depending on the sample. Varying amounts of $H_2PtCl_6.xH_20$ was added when platinum was

included. A stirrer bar was added to the conical flask followed by the flask being sealed with the reaction undertaken in a dark fumehood so that no light could enter during the synthesis. The solution was heated to between 75°C and 80°C to ensure the complete hydrolysis of urea. The reaction took place over 24 hours. Once the reaction was complete, the solution containing the catalyst was washed with hot deionized water and then centrifuged. This process was repeated until the pH reached neutrality. Finally, the catalyst was placed in a drying oven overnight at 110°C to remove any residual water. Reduction was only undertaken just prior to using the catalyst for either CO oxidation reactions on a catalytic testing unit or for characterization. 5% and 8% Au on NRS was produced for the in-situ PXRD characterization as well as for TEM studies. For catalysis studies, samples containing 1% Au as well as 1% Au-x% Pt, where x=0.1 or 0.2 were produced in triplicate.

It is important to note, as will be shown using electron diffraction and TEM, the nanorods produced using this synthesis are radially aligned rutile nanorods in a dandelion type structure. This is in contrast to other synthesis methods of nanorutile where the nanorods are lying together and oriented in the same direction in a type of bed structure as shown in Figure 7.2b. The radial alignment of the nanorods resulted in a structure with the desired morphology for a good catalytic support. The simplicity of the synthesis method was very useful as scale up of the method becomes more viable.

9.3 BET

Surface area data was collected for the produced NRS samples. BET results were quite consistent between batches, with a standard deviation of less then 15% between all five batches of support produced. The error may be due to small differences during the synthesis such as temperature of the system over the 24 hour period as the high temperature heater has an inherent error. On average the synthesis method produced a support with the following characteristics :

Surface area. Single point surface area at $\frac{P}{P_o}$ = 0.09854: 95.35 m^2/g +/- 11.05 m^2/g.

BET Surface Area: 101.90m^2/g +/- 13.15 m^2/g.

It is worth noting that the standard deviation within a sample in the surface area measurements encompasses the variaton noted across all the samples for the mean surface area. This implies that that variation across the samples was not statistically significant and was acceptable.

Pore Volume. Single point adsorption total pore volume of pores less than 144.4069 nm diameter at $\frac{P}{P_o} = 0.98641$: 0.08658m^3/g.

Pore Size. Adsorption average pore width ($\frac{4V}{A}$ by BET): 3.398 nm.
BJH Adsorption average pore diameter ($\frac{4V}{A}$): 4.127 nm.
BJH Desorption average pore diameter ($\frac{4V}{A}$): 4.184 nm.

9.4 In-situ PXRD

In-situ diffraction studies were conducted on the unloaded support as well as with various gold loadings. Initial tests, whereby the NRS was heated at a number of temperatures in a furnace followed by PXRD characterization, showed that the NRS was a very stable structure. In order to thoroughly test the support as well as the catalysts produced using the support, data collections needed to be very long. This was necessary to thoroughly stress the catalyst at high temperatures. The time versus temperature profile of the in-situ PXRD data collections is given in Figure 9.2. Figure 9.2 also compares the data collection time for the Aurolite catalyst with the gold loaded NRS catalyst. The data collection for the gold on NRS was undertaken for a significantly longer time. This time vs temperature profile was chosen such that over 90% of the data collections were undertaken at over 450°C, as at these temperatures that the catalyst was stressed. These collection profiles for the gold on NRS samples meant that the catalysts were exposed to temperatures exceeding 450°C for almost 200 hours.

The data collection at temperatures over 450°C was 5 times longer for the catalysts produced using the NRS compared to the Aurolite data collection time. The same data collection times were used for all the NRS catalysts as well as the pure NRS.

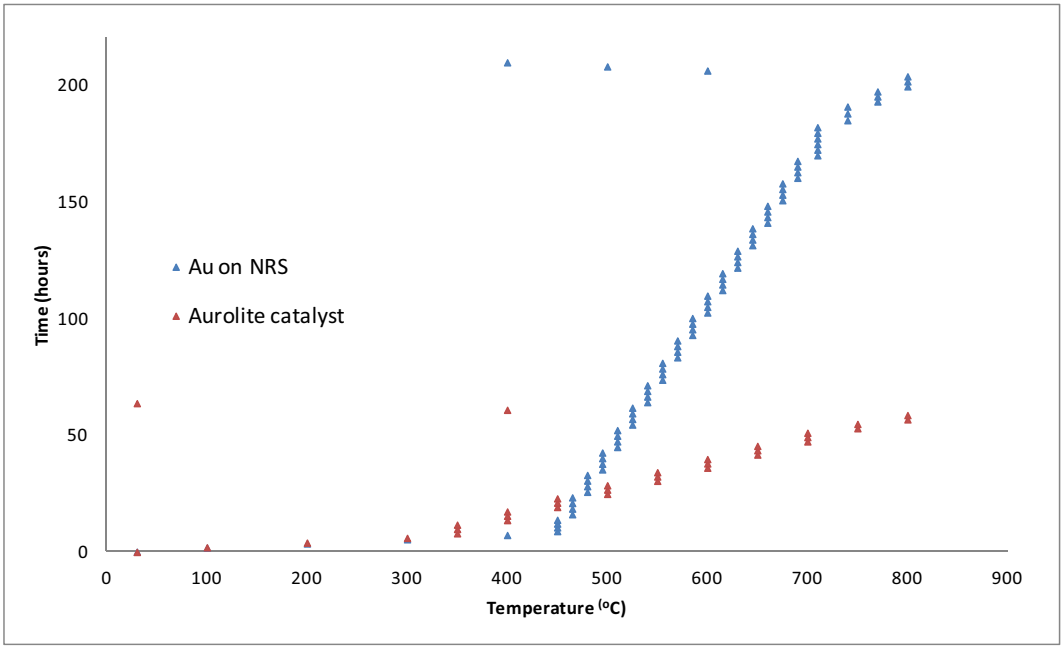


Figure 9.2: Aurolite in-situ PXRD collection time vs NRS data collection times.

9.4.1 In-situ PXRD of pure NRS

At high temperatures the structure was completely phase stable and, as shown in Figures 9.3 and 9.4, 100% of the synthesised product was thermodynamically stable nanorutile. However, in terms of the growth of the structure at high temperatures, an increase in the length of the rod structure and a general increase in the crystallite size was noted. As will be shown when even a very small percentage of gold was added to the NRS, the decrease in the support particle size growth with respect to temperature was dramatic. There were two determining factors when investigating if the synthesised product produced the required support in terms of both the radially aligned nanorod type structure as well as the nano characteristics of the support when using X-ray diffraction. Examination of the (110) and (011) diffraction peaks provided information about the support's morphology as it showed the anisotropic nature of the NRS. This pointed toward a rod type structure as shown in Figure 9.5. Furthermore, the broad and somewhat low intensity of the diffraction peaks also indicated that the anisotropic nanorods were in the desired nanoscale region that confirmed the BET and TEM results of a nano support structure with high surface area. Both of these features are shown in Figure 9.4 as well as quantitatively in Figure 9.5.

The difference in size of the two *hkl* values, as shown in Figure 9.5, from

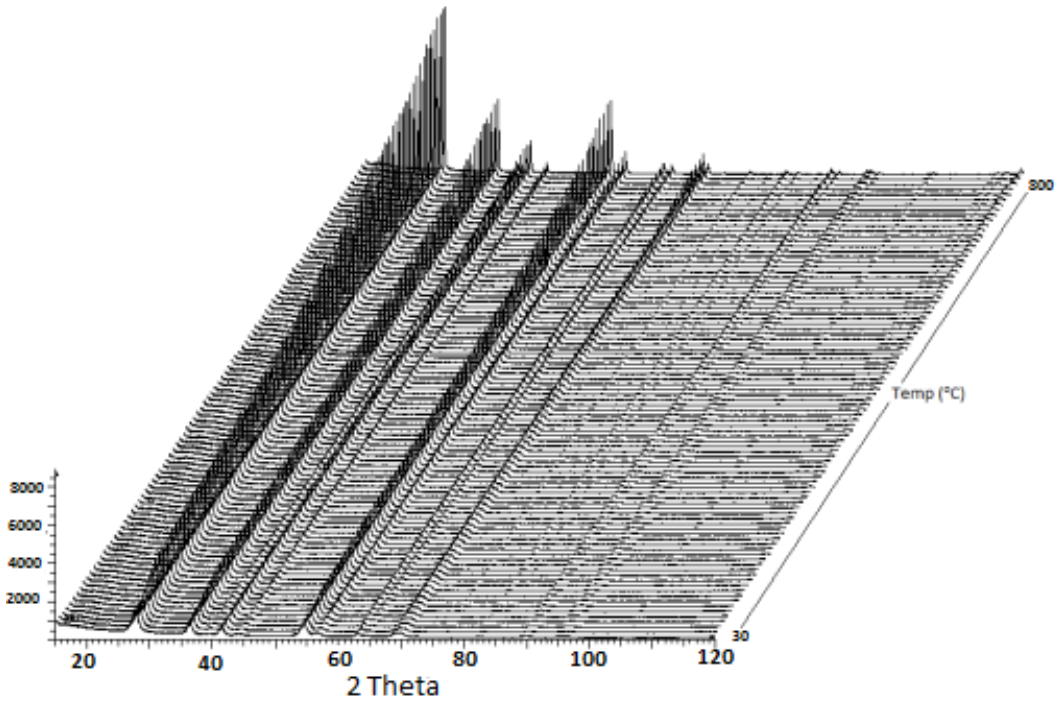


Figure 9.3: In-situ PXRD of the NRS. The diffraction patterns showed the support was phase pure as well as giving information on the morphology of the nanostructure.

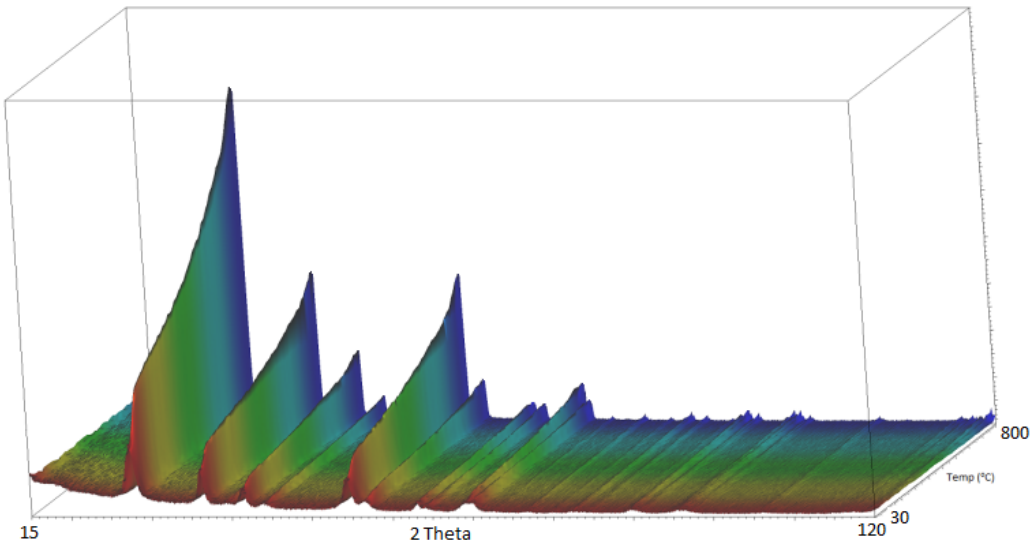


Figure 9.4: In-situ PXRD of the NRS.

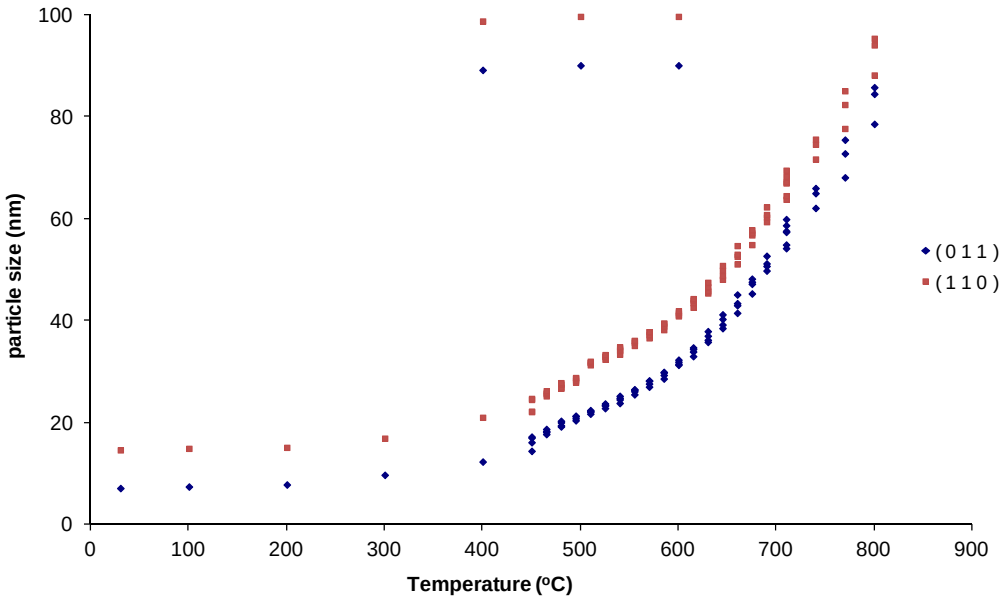


Figure 9.5: Rietveld refinement results of pure NRS crystallite sizes of the (011) and (110) orientation with respect to temperature.

Rietveld analysis applied to the in-situ PXRD data, revealed anisotropic growth along the (110) direction. Initially, the NRS crystallite size was very small, however, as temperatures increased the growth of the nanostructure could be seen. The most rapid growth occurred at temperatures above 500°C. As was shown using TEM and in-situ PXRD, the growth that was observed from the in-situ PXRD was primarily due to propagation and extrusion of the nanorods. Thus, as temperature increased, the nanorods extruded outward.

9.4.2 5% Au on NRS

The most immediate result, when compared to pure NRS, was a decrease in intensity at high temperature of the diffraction peaks originating from the NRS (as shown in Figure 9.6 and 9.7). Rietveld refinements, shown in Figure 9.8, quantitatively confirmed that the size of the nanorods was greatly decreased when 5% gold was present in nanoparticulate form on the support, compared to the pure NRS after the in-situ data collection. Thus, initial conclusions were that gold was acting as a capping agent and inhibiting the growth of the rutile nanorods. This effect increased the stability of the support at non-ambient temperatures. Further, this effect resulted in the NRS being able to retain its

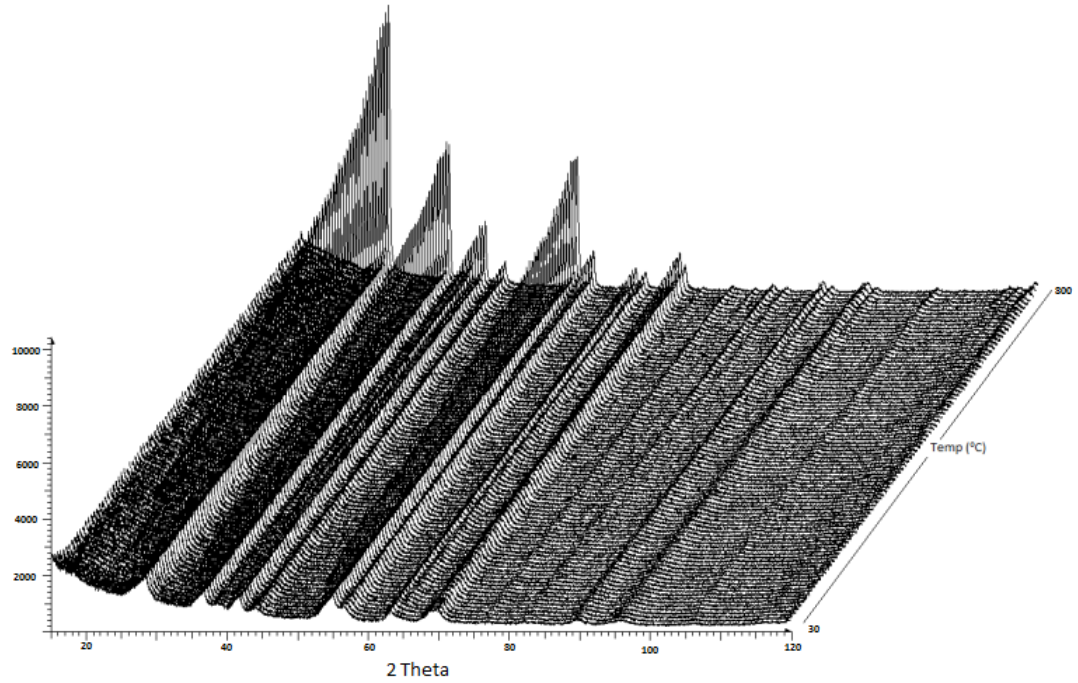


Figure 9.6: In-situ PXRD of 5% Au on NRS.

high surface area, as will be discussed with the BET surface areas.

The diffraction results first indicated that the structure was radially aligned, as electron microscopy studies were only conducted at a later stage. This was deduced from the anisotropy of the peaks, indicating preferential growth along certain planes. Compared to the pure NRS support, the crystallite size of the structure with 1% gold is less than half that of the pure support. The addition of only 3.91% gold (actual loading from Rietveld analysis) was shown to be inhibiting the growth of the rutile nanostructure even further. This was very important as the gold acted to stabilise the support. This was a completely opposite effect compared to other supports such as P25, commercial anatase, as well as nano anatase that were all detrimentally affected by the addition of gold (as well as platinum). The presence of these metals were shown to increase the rate of phase transformation of the support.

9.4.3 8% Au on NRS

Following the results of the catalyst produced with 5% Au loading, catalysts with 8% Au loading on NRS were produced. There were two reasons for this. Firstly, the addition of more gold would allow for a more accurate crystallite

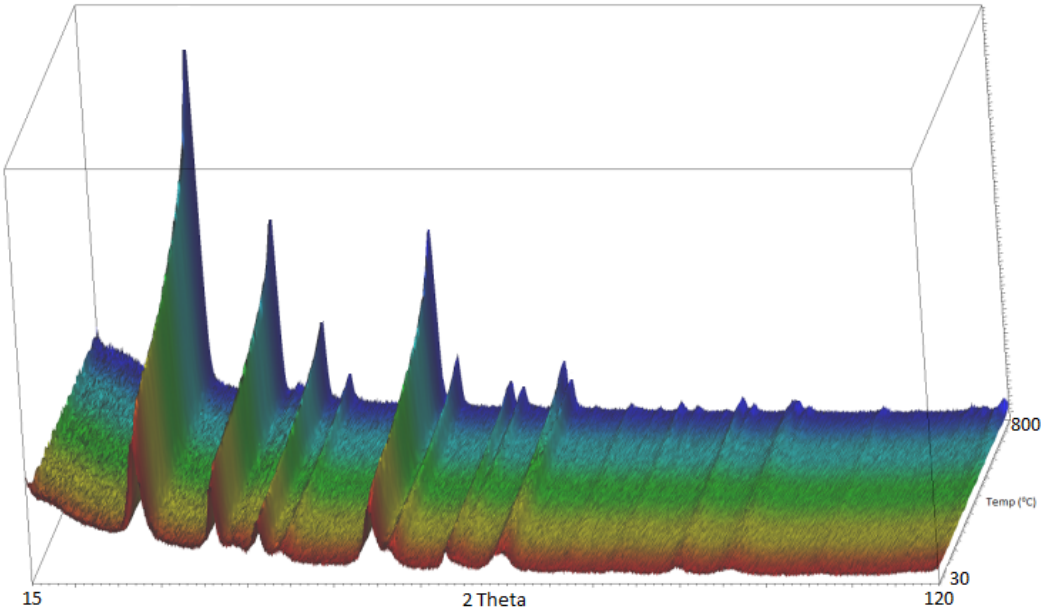


Figure 9.7: In-situ PXRD of 5% Au on NRS. The intensity of the diffracted peaks at higher temperatures is lower as well as the peaks being broader when gold was added to the NRS compared to the pure NRS in-situ data collection shown in Figures 9.6 and 9.7.

size determination from the Rietveld refinements at low to medium temperatures. Due to the remarkable stability of the gold nanoparticles even at very high temperatures when in-situ diffraction studies were conducted on the 5% Au NRS sample, the diffraction peaks for gold were very small and almost lost in the background of the diffraction patterns. This was because of the low gold loading (of 3.91%) as well as very small crystallite sizes The need to quantitatively determine the crystallite sizes of the gold nanoparticles was very important, thus the best method to attain this information was to increase the gold loading. The choice of gold loading was important, as to little would once again result in almost undetectable gold peaks while to much has the ability to overload the sample and dramatically increase the possibility of sintering as so many gold nanoparticles are very closely packed together. Secondly, it was also important to bear in mind that gold catalysts are rarely required to support more than 1% gold. Thus placing large amounts of gold onto the surface may put the NRS support in an unfair position when compared to other gold catalysts loaded with only 1% gold. The addition of more gold did have one advantage as it revealed the effect that extra gold nanoparticles had on the growth mechanism of the structure as shown in Figure 9.9 and 9.12.

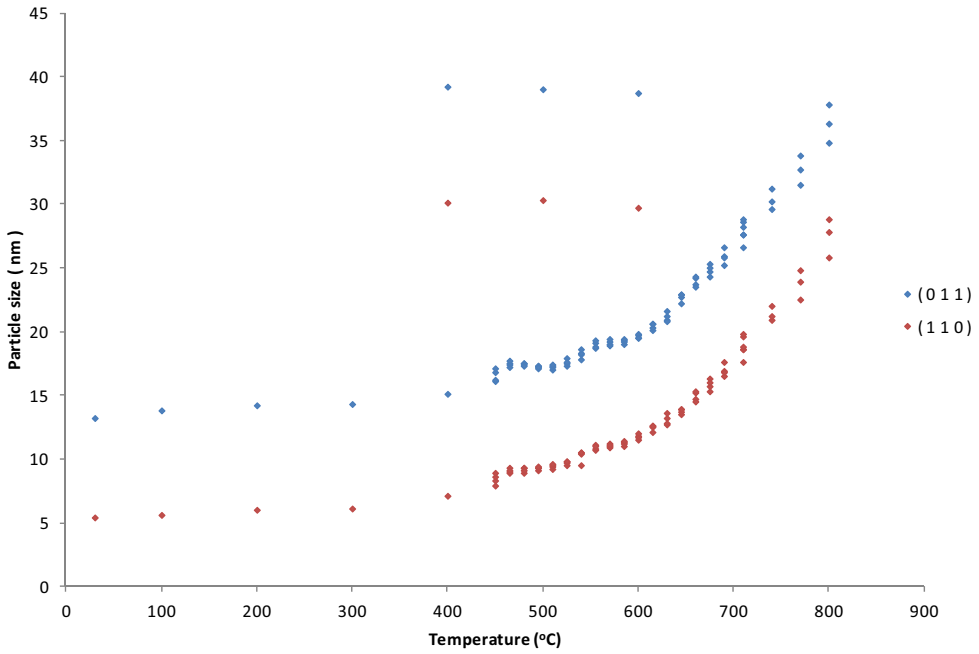


Figure 9.8: Rietveld refinements of 5% Au on NRS. Results showed the crystallite sizes of both the (011) and (110) orientations were much smaller when small amounts of gold nanoparticles were added to the structure. After heating to over 800°C, the support was only approximately 30 and 40 nm respectively for the (110) and (011) orientations. Thus, after 200 hours at high temperature the support was still very stable with a high usable surface area, this was confirmed by BET studies where a surface area of $74.81 m^2/g$ was attained. The initial surface area of the NRS support was $97.28 m^2/g$ prior to the variable temperature data collection. The refinements gave a gold loading of 3.91% confirming that not all the gold was deposited during the modified DP method. The sample will still be referred to as 5% Au-NRS even though the true loading was 3.91% Au.

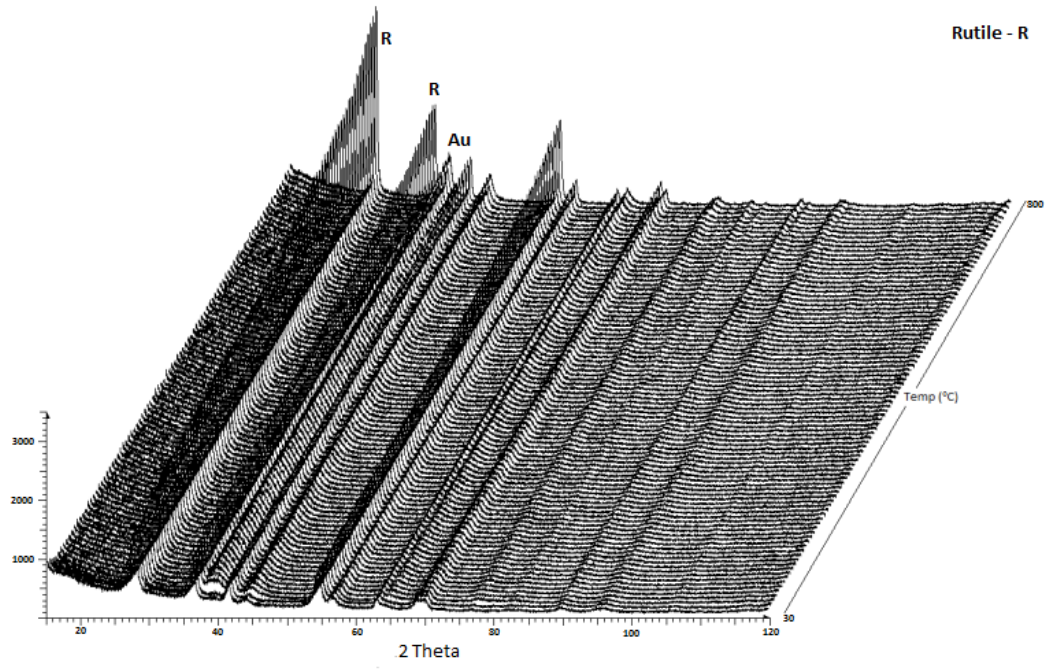


Figure 9.9: In-situ PXRD of 8% Au on NRS. The increased gold loading gave more intense gold diffraction peaks making it possible to study the change in the gold crystallite size as a function of temperature.

9.4.4 Rietveld refinements

Rietveld refinements gave gold loadings of 6.45% as shown in Figures 9.9 - 9.11. Loading below 7% was expected as not all the gold is deposited on the surface during the synthesis. Further, X-ray diffraction only detects crystalline gold. However, this value was high when compared to all the other methods available for depositing gold[83,97]. High metal loadings are not desirable in active catalysts due to high metal costs as well as with traditional catalysts experiencing an overlaoding of the surface leading to and enhacement of the sintering effect of the nanoparticles. The effect of overloading was not observed for NRS however, as Rietveld refinements showed small gold crystallite sizes as well as BET surface area studies giving a surface area of 77.42 m^2/g after the in-situ data collection. After exposure to high temperatures for such a long duration this surface area was still sizeably larger than all of the other commercial supports and by comparison the Aurolite catalyst had a surface area of only 7.2 m^2/g after the in-situ data collection. After in-situ diffraction studies for far shorter time frames all the commercial titania supports and catalysts tested, had surface areas on average less then 7.5 m^2/g. TEM studies further demonstrated the stability of the support after exposure to high temperatures

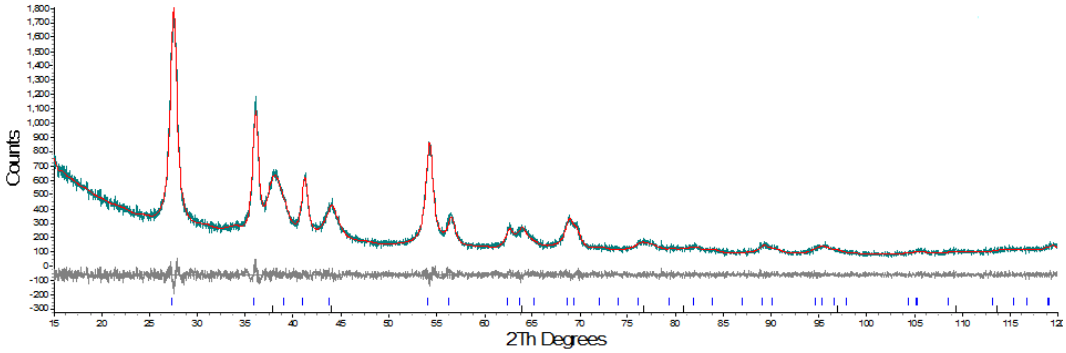


Figure 9.10: Rietveld refinement example of a diffraction pattern collected at 540°C taken from the in-situ data collection. The intensity can be seen to be quite low for both the support and the supported nanoparticles with a maximum count of only 1800. This was due to the nanostructure of the support with the size of the nanorods being well within the 'nanoscale' region at less than 15 nm as shown in Figure 9.9. The overlap of the gold and rutile peaks was clearly evident at 38.8° and 44.4° 2θ. The small black strikes under the difference pattern indicates the hkl reflections for gold in black and in blue for rutile. The difference pattern showed a good fit of the calculated pattern. Rietveld analysis gave an actual gold loading of 6.45% from the initial theoretical loading of 8%. The increase in the percentage loading of gold nanoparticles to the catalyst had the desired effect, as more gold nanoparticles present on the surface resulted in a greater number of diffraction centers. The increase in the number of diffraction centers in turn increased the intensity of the gold peaks while Rietveld refinement showed that the gold nanoparticles were still very small as well as stable throughout the temperature range as shown in Figure 9.14.

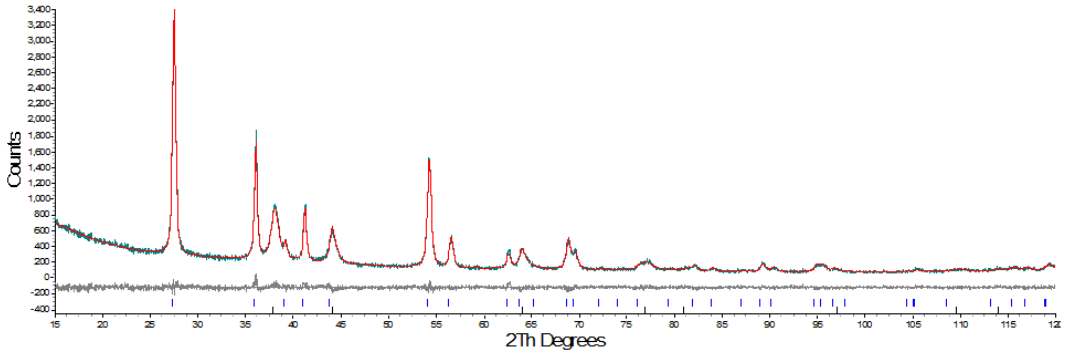


Figure 9.11: Rietveld refinement of the diffraction pattern collected at 810°C resulting from the in-situ data collection after exposure of the catalyst to temperatures exceeding 450°C for more than 200 hours. The higher gold loading used in this sample had the desired effect of increasing the intensity of the gold diffraction peaks when compared to the 5% loaded samples (actual loading of 3.91% Au). After being exposed to such high temperatures the intensity of the diffraction peaks increased over time. However, the increase was not dramatic. The gold diffraction intensity only increased by 150 counts when compared to samples at 500°C showing the stability of the catalyst. The broadness of the gold peaks also decreased slightly pointing toward a small growth in the crystallite size of the nanoparticles. These results were quantified using the Rietveld method and shown in Figure 9.17.

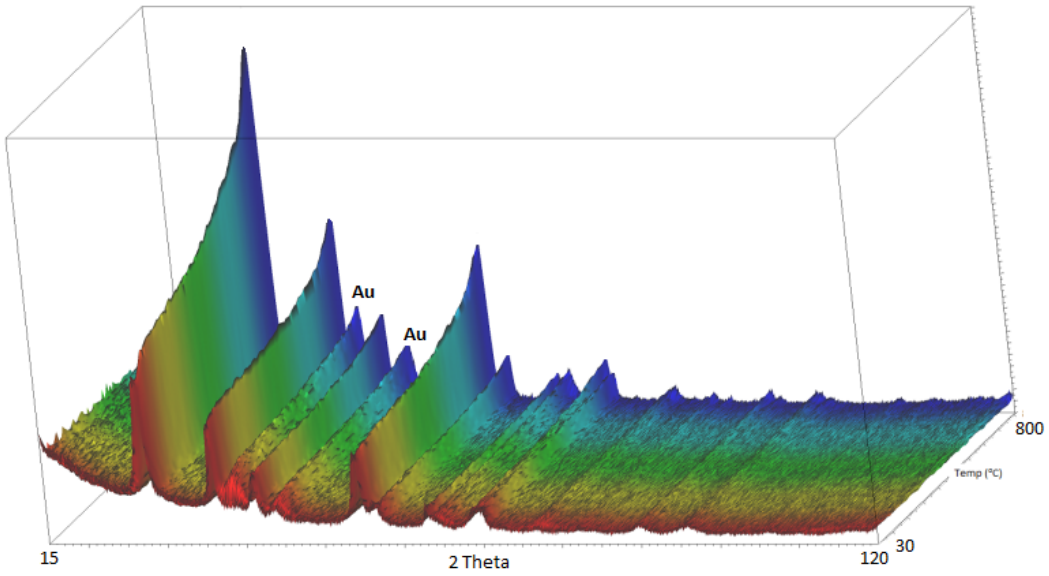


Figure 9.12: In-situ PXRD of 8% Au on NRS showing the increase in intensity of the gold diffraction peaks.

and correlated well with the in-situ data. This is discussed further in Section 9.6.

Refinements showed a maximum crystallite size error of ± 1.9 nm for the support as shown in Figures 9.13 and 9.14. The addition of gold had a direct effect on the growth of the structure at high temperatures.This growth was not thermodynamically phase driven as in the case of P25, commercial anatase as well as nano anatase, as the NRS is already locked into its most stable titania polymorph. Thus, it was possible to slow and even perhaps stop the growth process from occurring and lock the structure in place.

Observations of the rutile nanorods before and after heating cycles indicated that nanoparticles were deposited onto the ends of the rods. This is an expected result as the rods had small diameters (typically around 5-8 nm) and so the tips of the rods were highly strained. Therefore, if the strained environment could be protected by the presence of the metal atoms, the nanorods would become more stable. Also, as the growth direction of the rutile crysallites was along the rod axis, preventing access to the tip of the rod would effectively prevent any growth.

As will be discussed in the TEM section, a small amount of growth was not detrimental to the NRS support. After exposure to temperatures in excess of 450°C for over 200 hours the NRS still remained small enough to provide high

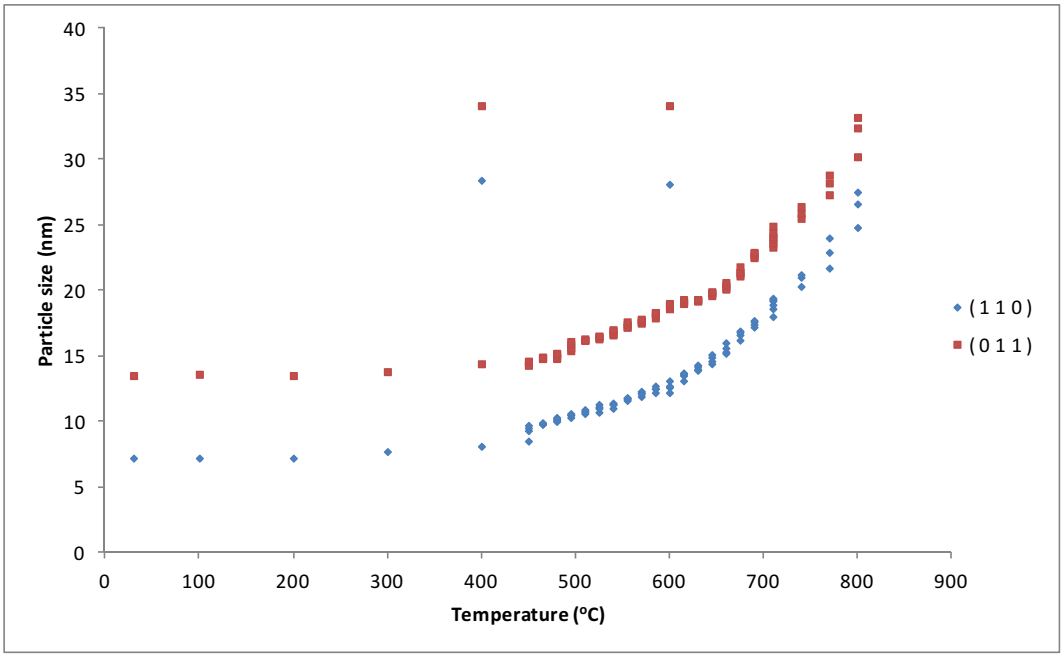


Figure 9.13: 8% Au on NRS showing the crystallite sizes of the (110) and (011) directions. The addition of more gold to the surface (6.45% compared to 3.91%) resulted in a decrease in support size of both the (110) and (011) directions over the measured temperature range.

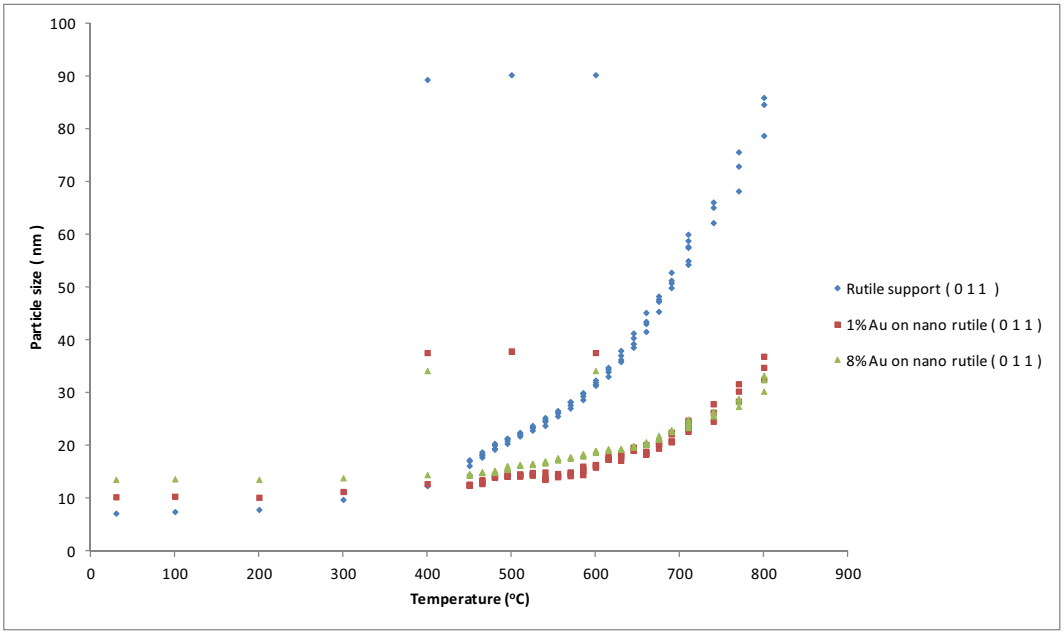


Figure 9.14: Comparison of the (011) direction of rutile nanorods for the pure NRS, 5% Au and 8% Au-NRS samples.

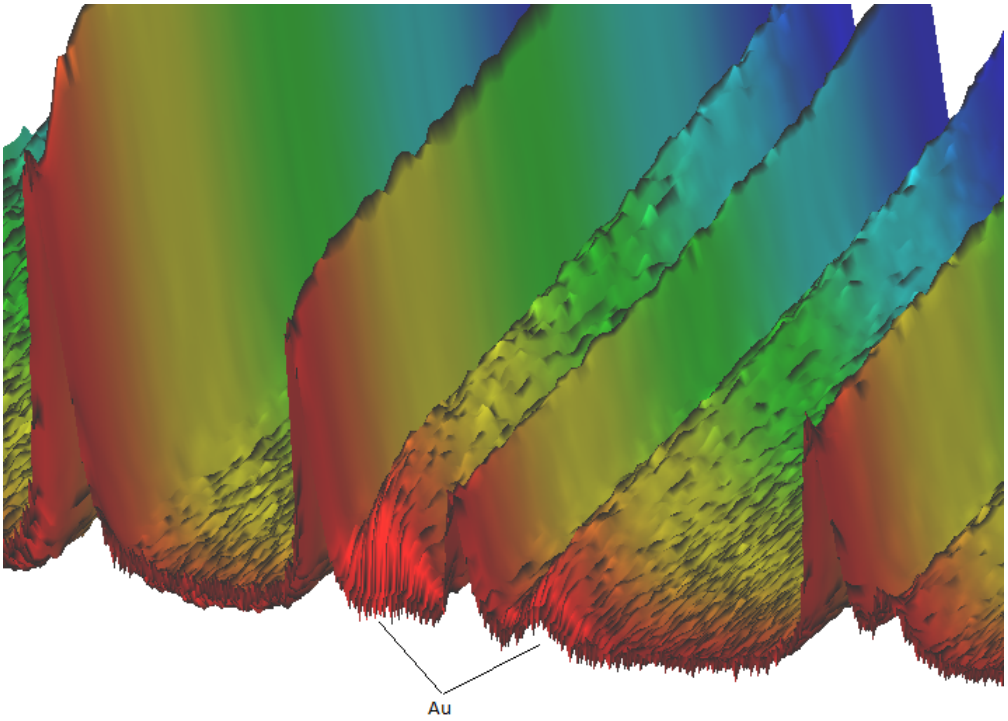


Figure 9.15: Zoomed view of the gold peaks at 38.2° and 44.4° 2θ for the 8% Au on NRS sample.

surface area (BET surface area of 77.41 m^2/g) for the supported metals to remain stable on the surface.

With the use of higher gold loadings, observations were be made on the gold structure at lower temperatures. Figure 9.15 shows the reduction of the gold peaks from Au (I or II) to Au (0). Further, the intensity of the gold peaks increased only slightly as the temperature was increased from ambient to 810°C. The peak shape profile was also consistent throughout the temperature range. This demonstrated the stability of the gold nanoparticles on the surface of the catalyst as well as the resistance of the nanoparticles to sintering even at high temperatures. Even though the gold peaks appeared relatively intense when compared to the rutile peaks, the rutile diffraction peaks were produced from a nanostructure themselves and thus their intensity was also very low when compared to a bulk crystalline phase.

The Rietveld refinement results as shown in Figures 9.16 and 9.17 showed that the Au-NRS catalyst is far more stable and resistant to sintering when compared to the Aurolite catalyst even after the Au-NRS catalyst was exposed to higher temperatures for a significantly longer durations. The morphology, as will be discussed in the TEM section, along with the thermodynamic stability

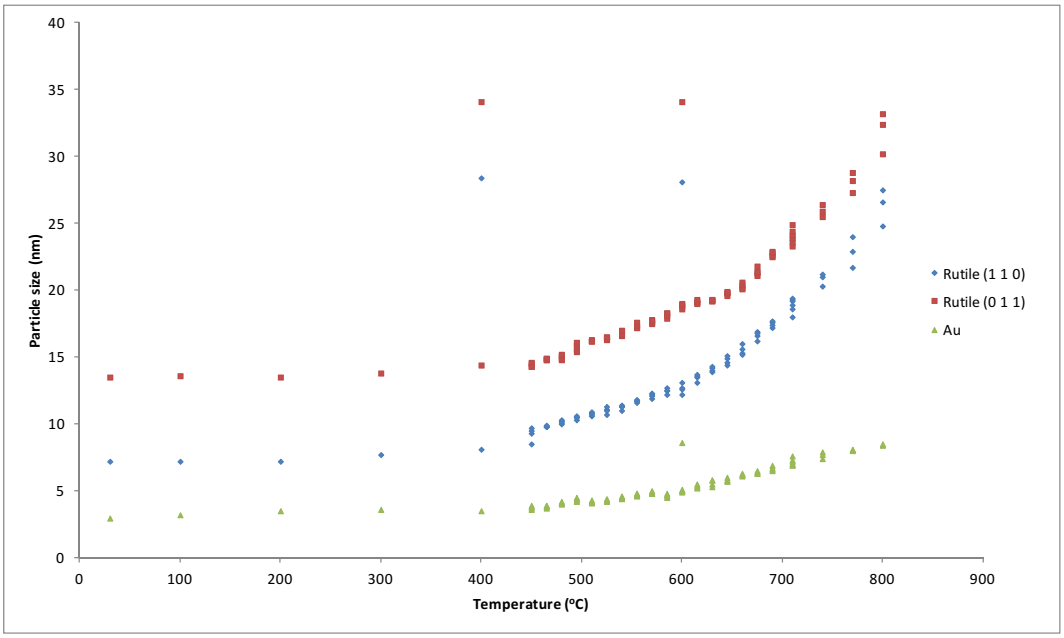


Figure 9.16: Rietveld refinement results of the gold-NRS catalyst particle sizes vs temperature. Even after exposure to temperatures over 450°C for nearly 200 hours and over 600°C for over 100 hours, the gold crystallite size remained small with only a gentle upward trend.

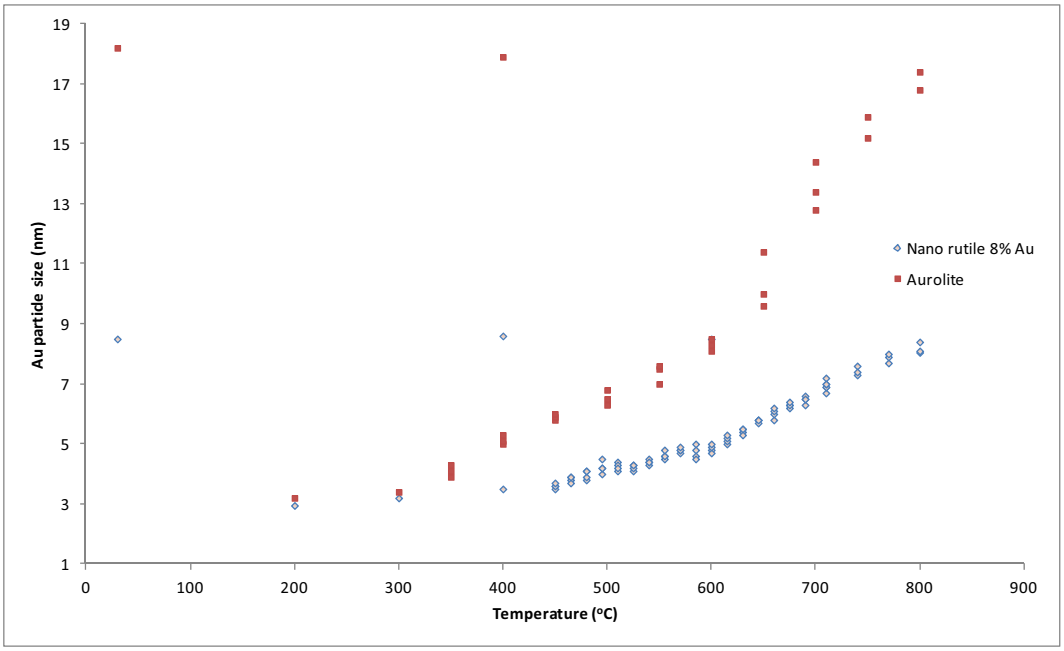


Figure 9.17: Rietveld refinements comparing the gold NRS catalyst with the Aurolite catalyst. Even at 8% Au loading the support was not adversely affected by overloading of supported nanoparticles. The high surface area of the catalyst resulted in enough usable surface area for the gold nanoparticles to remain homogeneously and sparsely positioned over the support. This feature was also observable using TEM and will be discussed further in the TEM section.

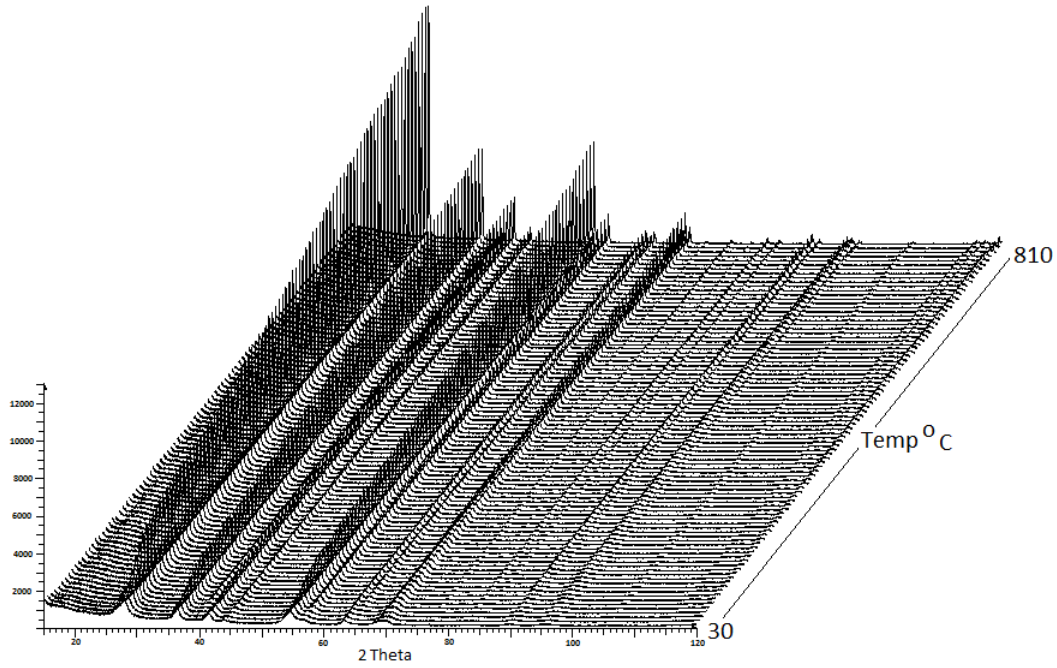


Figure 9.18: 1% Au-NRS catalyst. This catalyst, along with all others produced using a certain batch of synthesised NRS proved to be inactive once they had been exposed to temperatures over 500°C for 12 hours. From in-situ diffraction studies the support appeared to be completely standard.

and high surface area of the catalyst resulted in a structure that is conducive to thermally stable gold nanoparticles even at high temperatures.

9.5 A note on preparation of the NRS

During two of the syntheses of the NRS, a sand bath was used instead of an oil bath. When the resulting support was used for the production of a set of catalysts with various gold loadings, none of the catalysts showed any activity after exposure to temperatures over 500°C for 12 hours. Initially there was confusion as to the reason that this particular batch of catalysts were inactive. Even use of in-situ powder diffraction (Figures 9.18 and 9.19) did not shed any light on the concerning inactiveness of the catalysts as the PXRD patterns matched those previously observed. Only once TEM studies were conducted were the reasons for the catalyst's deactivation determined.

After analysis using HR-TEM it was determined that a very thin layer of anatase phase titania nanoparticles were still present covering the nanorods, as shown in Figures 9.20-9.23. This revealed that an problem had occurred during

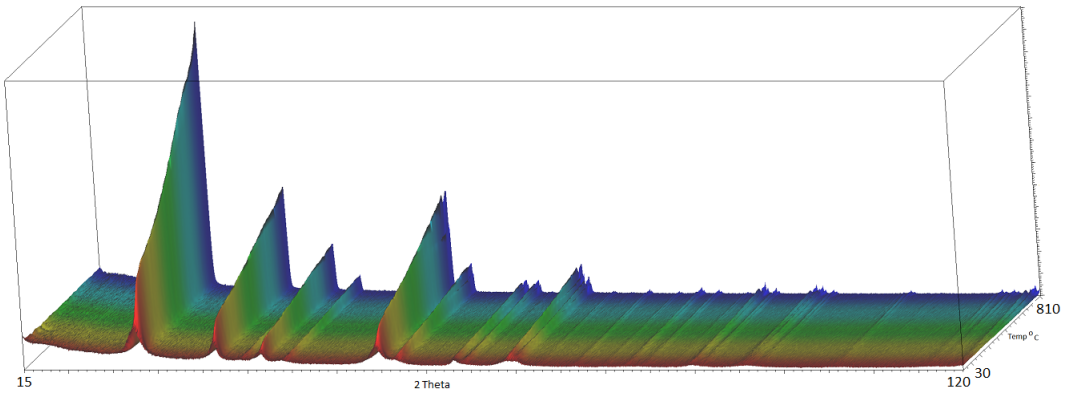


Figure 9.19: 1% Au-NRS catalyst. The NRS had not completely converted to rutile during the synthesis resulting in a monolayer of anatase on the ends of the structure. The monolayer was so thin that the effect could only be seen using TEM.

the synthesis of the NRS. The error was attributed to the use of a sand bath instead of the oil bath. The large thermal gradient through the sand during the synthesis resulted in the reaction vessel not being subjected to the desired temperature for the complete conversion of the anatase to nanorutile. The layer of anatase nanoparticles was enough to result in the complete encapsulation of the rutile nanorod structures when the monolayer of anatase converted to rutile during heating. This encapsulation then trapped all the active sites within the structure resulting in an inactive catalyst.

These results once again proved, although inadvertently, how detrimental an uncontrolled phase change can be to the activity of a catalyst. The deactivation was similar to what occurred to the Aurolite catalyst when the anatase to rutile phase transition resulted in the deactivation of the catalyst (Section 9.8).

Following this discovery only oil baths were used for synthesizing the NRS. The use of a fluid allowed for even heat distribution throughout the oil bath unlike a sand bath where heat ditribution is uneaven through the sand. No further complications in the synthesis of the NRS were encountered once oil baths were used exclusively.

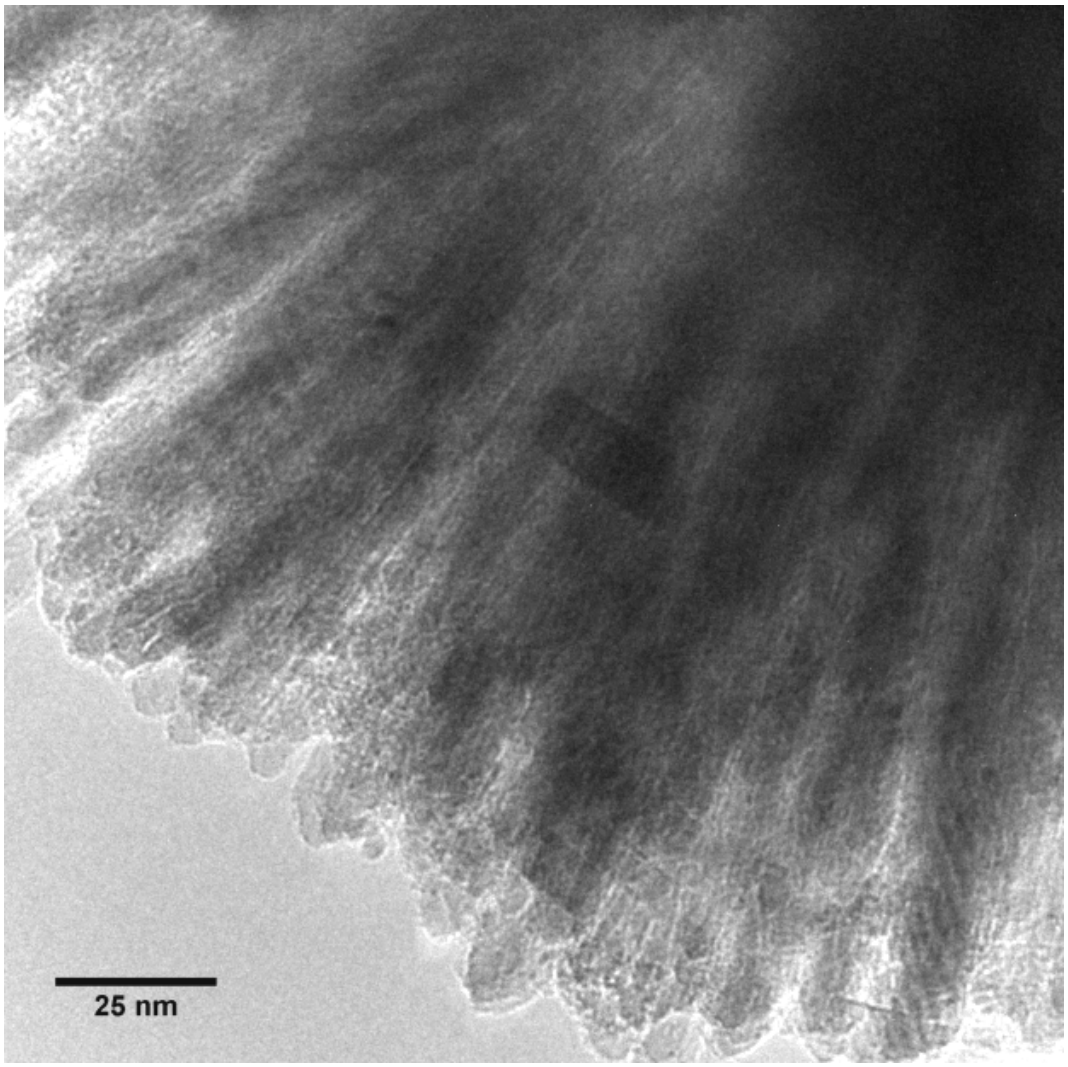


Figure 9.20: TEM image of the NRS support after heating to 500°C for 12 hours. Closer inspection revealed anatase on the nanorods that, after heating, resulted in the formation of rutile that encapsulated the nanorods as well as the active gold nanoparticles. Further, the voids between the nanorod structures that allow the gas to easily flow though the catalyst were also blocked.

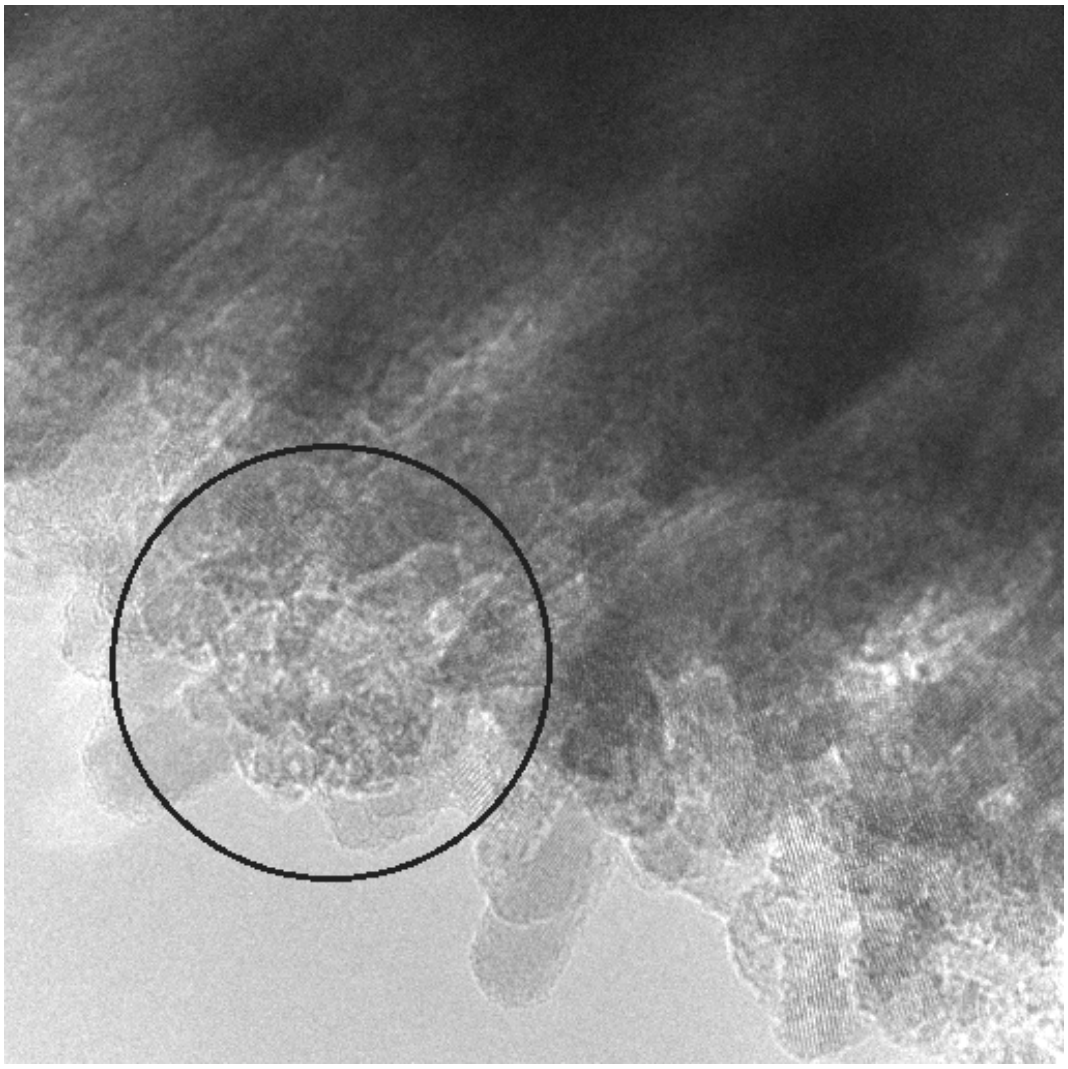


Figure 9.21: The highlighted section shows the ends of the rods covered by the unconverted anatase. As the structures were held at high temperatures the anatase converted to rutile further deactivating the catalyst.

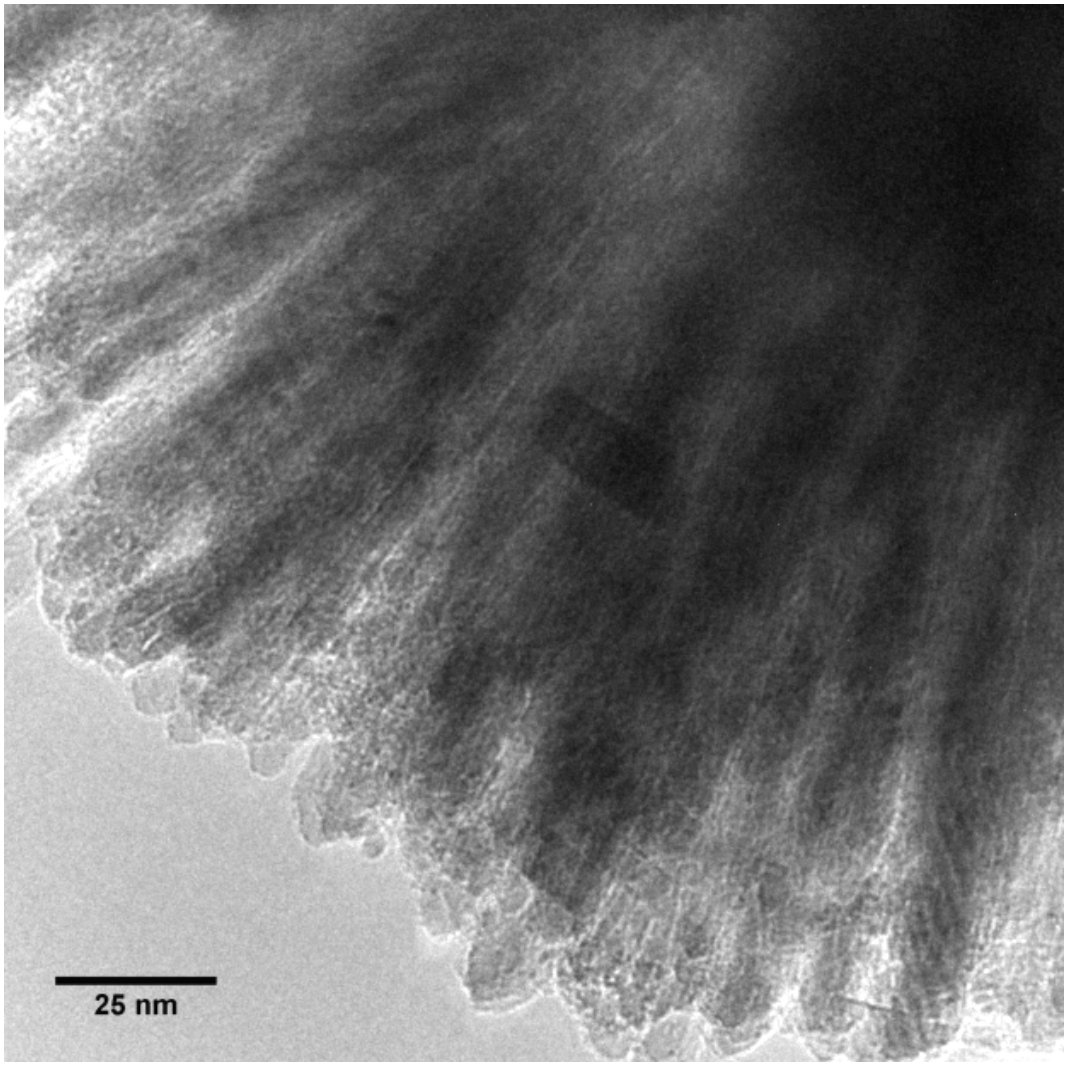


Figure 9.22: Thin layers of anatase can be seen covering the nanorod structures.

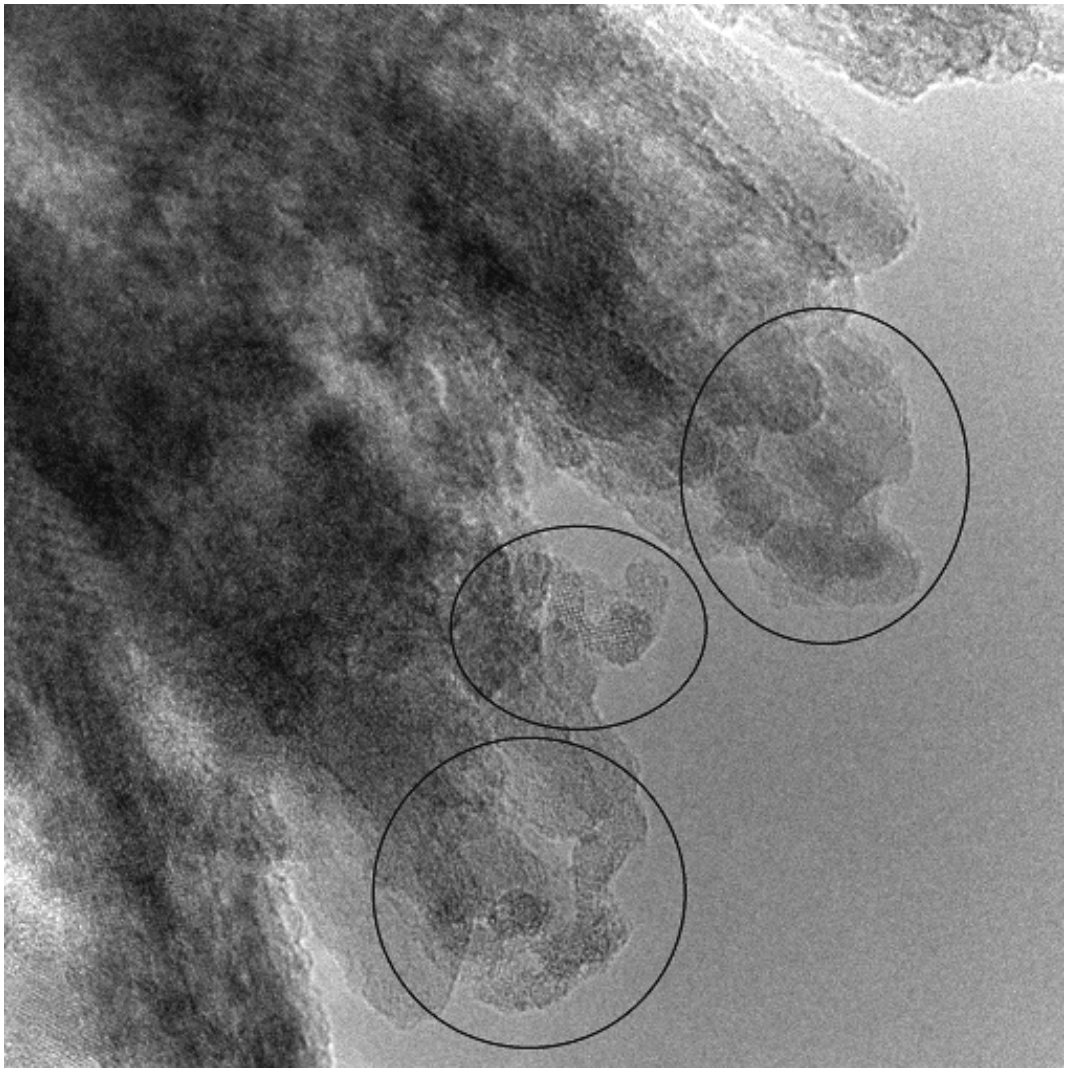


Figure 9.23: Large amounts of anatase covering the nanorods. Even the pore structures between the nanorods were blocked.

9.6 TEM

9.6.1 Electron diffraction

Electron diffraction as shown in Figure 9.24 was undertaken in order to determine the arrangement and orientation of the nanorods and to confirm the in-situ PXRD results. The in-situ PXRD results provided some information about the anisotropic growth of the nanorod structures. Radial alignment of the nanorods was crucial in order to maintain a high surface area as well as the desired morphology such that the nanostructure allowed gas to pass easily through it when catalysis was undertaken. Finally, radially aligned nanorods completely inhibit the transfer of gold across the structure as each nanorod is isolated from the next and for gold migration to occur, the metal would have to "leap" from one rod to another.

TEM analysis as shown in_Figures 9.25-9.27, showed that the nanorods only have a few gold nanoparticles per nanorod. In fact, some nanorods had only a single gold nanoparticle on them, as shown in Figures 9.28 and 9.29. This is an effect of both the morphology and also gives rise to the high surface area. Thus, in these cases it was impossible for sintering to occur as the gold was completely isolated.

9.6.2 TEM

Figure 9.26 revealed the morphology of the Au-NRS catalyst with thousands of radially aligned nanorods as determined in the electron diffraction study. Deactivation of nano gold catalysts has been shown to occur not only at non-ambient temperatures, but also after long periods of time when the catalysts are stored[41]. The 5% Au-NRS was aged for 5 months to determine if a long period of time affected gold particle sizes of the Au-NRS catalyst.

It is worth noting that this aging time was at first unintentional. The catalyst had been taken for TEM analysis and then stored at room temperature in an unsealed vial for several weeks. After this there was an opportunity to take it to an international conference and explore the material on a HRSEM. The catalyst was then returned to the HRTEM for analysis and finally, after this

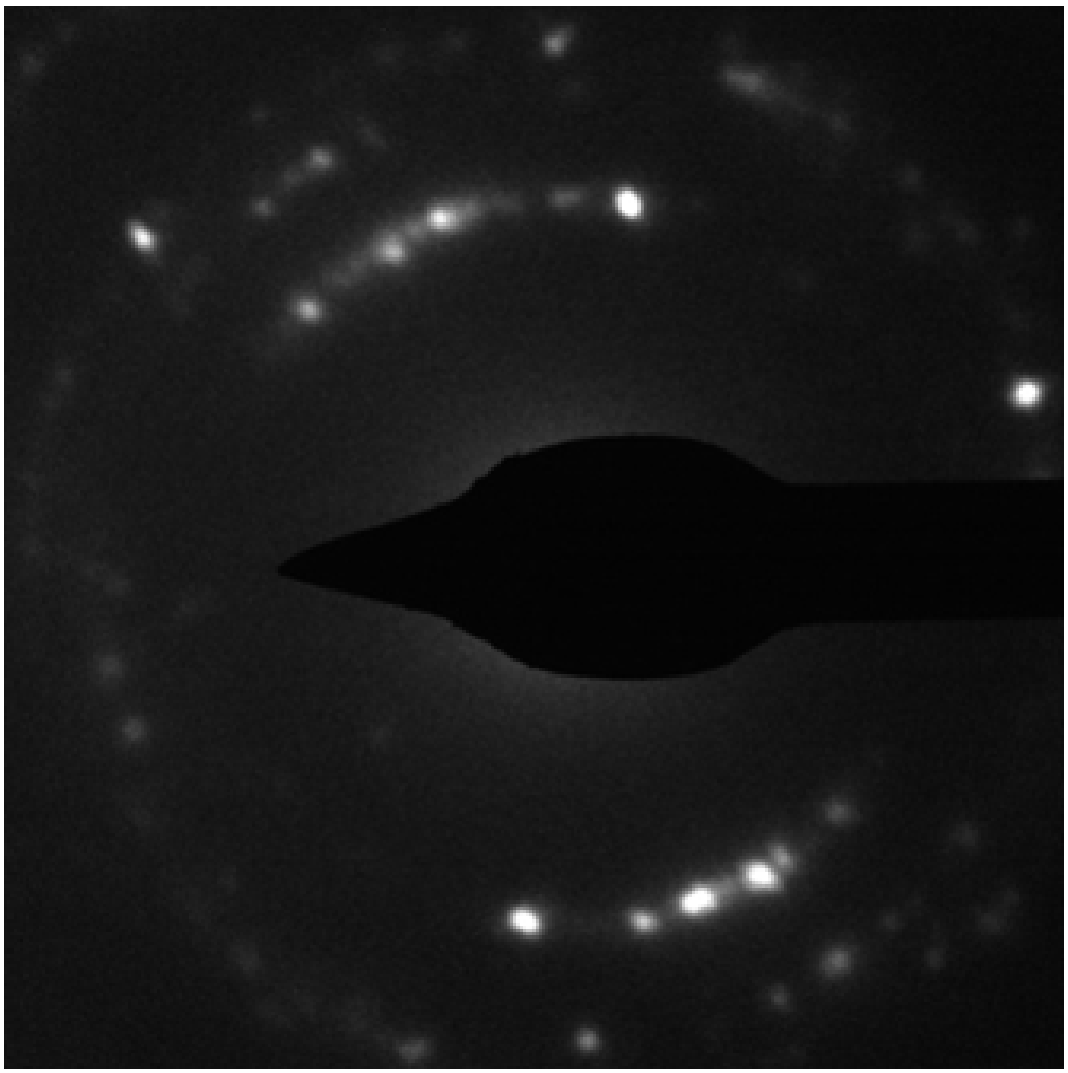


Figure 9.24: Electron diffraction images showed anisotropic growth of the rutile nanorods. This was demonstrated by the bright spots on the diffraction rings. If there were no anisotropic growth the rings would be consistent circles of uniform intensity. The bright spots indicated diffraction is more prevalent in certain directions due to the morphology of the nanorod structures. This confirmed what was observed in the PXRD diffractograms with respect to anisotropic growth of the nanorods.

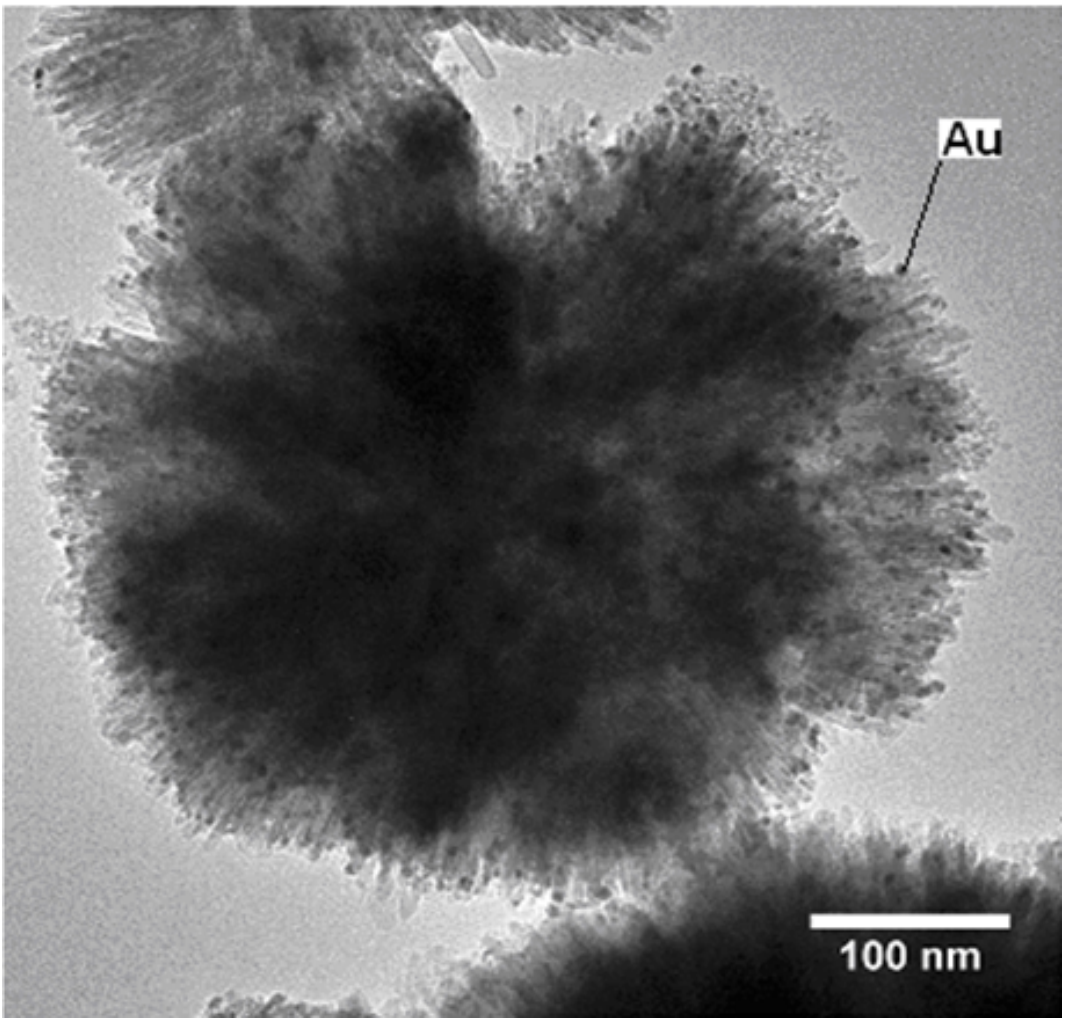


Figure 9.25: TEM image of the 5% Au-NRS catalyst. The images showed dandelion type structures with gold on the tips of the nanorods after heating to 550°C for 24 hours.

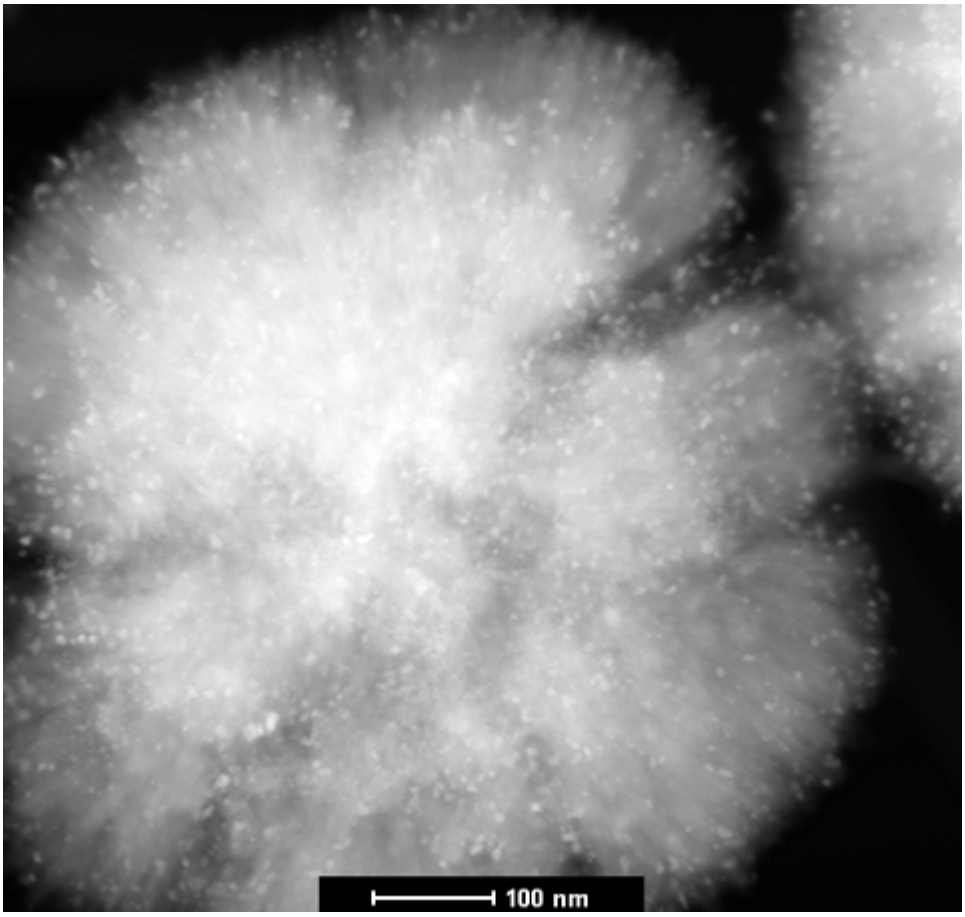


Figure 9.26: STEM image of the 5% Au-NRS catalyst after exposure to 550°C for 24 hours.

cycle, was used on a catalytic testing unit as an initial test-case to practise rig-work. It was over this process that the resistance to growth was noted.

The catalyst, as shown in Figure 9.26 and 9.27, was left in a drawer and stored under atmospheric conditions for 5 months prior to exposure to 550°C for 24 hours followed by TEM analysis. From Figures 9.26 and 9.27 it was determined that this ageing process had no effect on the sample as gold nanoparticle sizes were still very small, further demonstrating the catalyst's remarkable stability.

The bright spots in the STEM image (Figure 9.26)_were caused by the gold nanoparticles, as gold is a heavier element when compared to the elements making up the support. Due to gold's high atomic number and resulting large electron cloud, interaction with the electron beam was far stronger than that of the titania support. The positioning of the gold on the nanorods was a very important factor. From the TEM images it appeared that the gold may be positioned on the tips of the nanorods or possibly inside. STEM

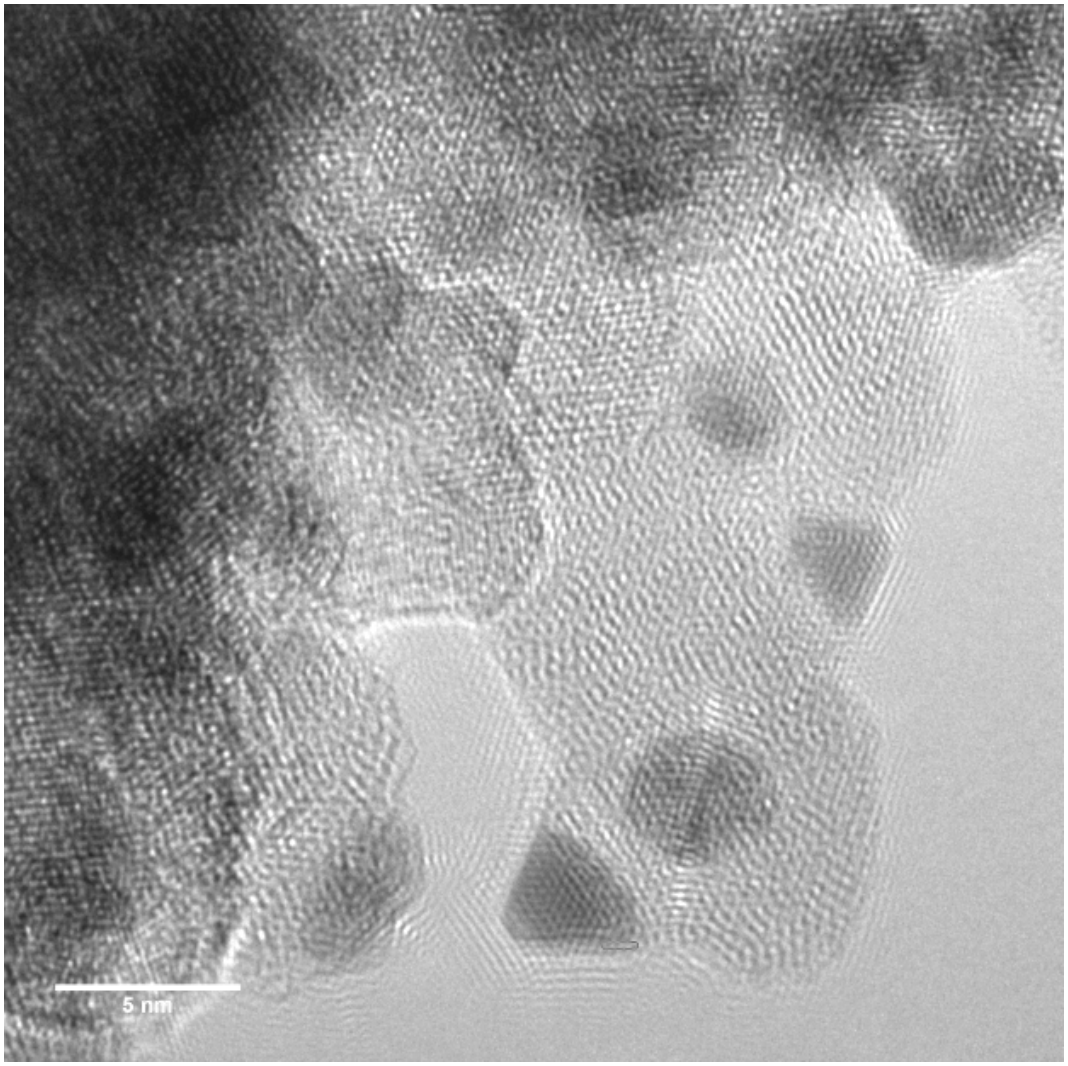


Figure 9.27: HR-TEM of gold nanoparticles on the catalyst after heating to 450°C for 24 hours.

and then 3D tomography were used to confirm that the gold was in fact on the tips of the rods and will be discussed in Section 9.7. As was revealed from the in-situ PXRD data the nanorod structure grew with an increase in temperature whereby the nanorods were extruded from the center of the dandelion outwards. This effect was inhibited when gold was placed on the surface but still occurred to a small extent as was demonstrated by quantitative Rietveld refinements on the in-situ PXRD data. However, this small extrusion of the nanorods did not have a detrimental effect on the catalyst as the gold nanoparticles were transported by the nanorods further outward and further away from other nanorods and thus further away from other gold nanoparticles. This isolation of the gold nanoparticles by the nanorods enhanced the stability of the nanoparticles and the catalyst as a whole.

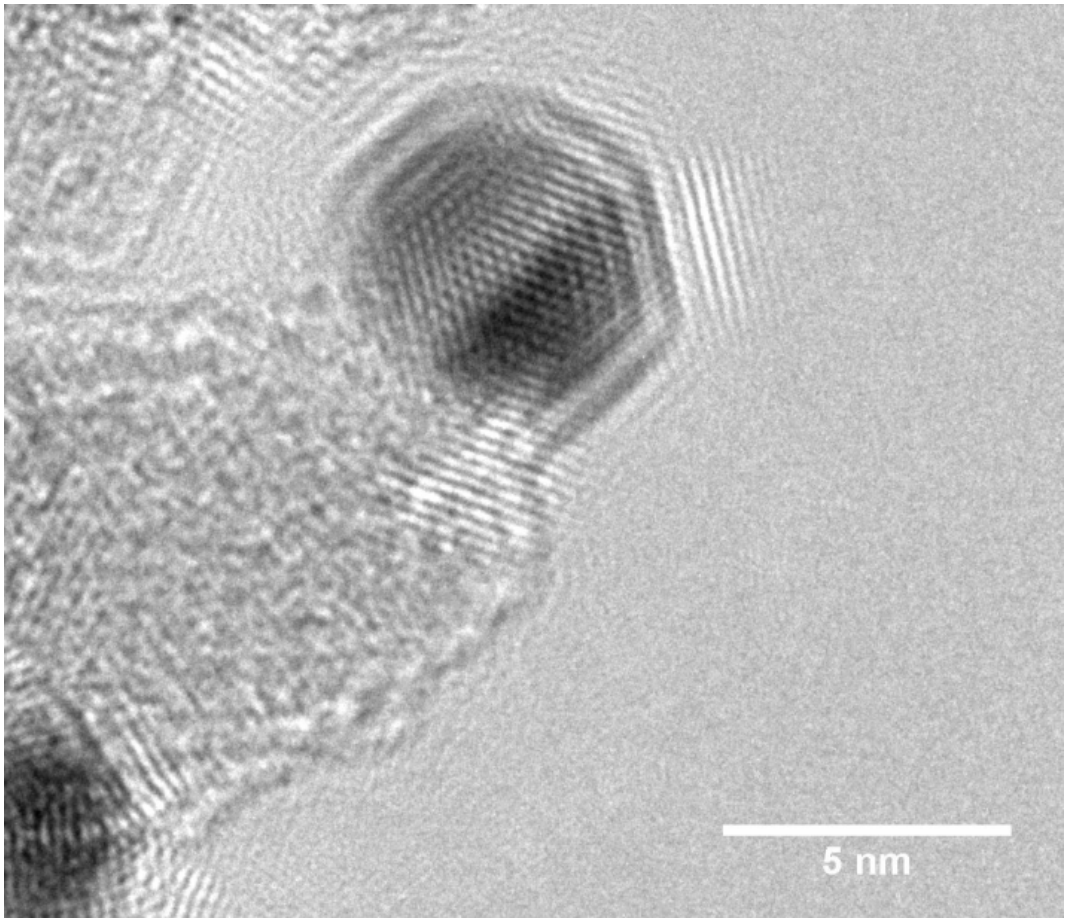


Figure 9.28: HR-TEM of gold nanoparticle after heating the catalyst to 450°C for 24 hours

Many of the TEM images revealed interesting gold morphologies, such as shown in Figures 9.27-9.29, with a number of different crystallographic orientations. Importantly, the gold nanoparticles were epitaxially bound to the surface. The changes from one type of gold morphology to another occurred at relatively low temperatures with the gold crystallites changing shape as the thermal energy of the system increased. The gold crystallites rearranged themselves into the most stable form as temperature was increased. Some of these rearrangements may correlate to small changes in the diffraction patterns as temperature was increased. The arrangement of the crystallites may have an effect on the diffracted beam. However, these small changes would be almost impossible to attribute to changes in the observed patterns as a number of factors are simultaneously at play that may affect the diffracted beam.

The gold particle sizes attained from TEM images were in agreement with the in-situ PXRD results after exposure to comparable temperatures. After thermal exposure, such as that of the catalyst from the in-situ diffraction data

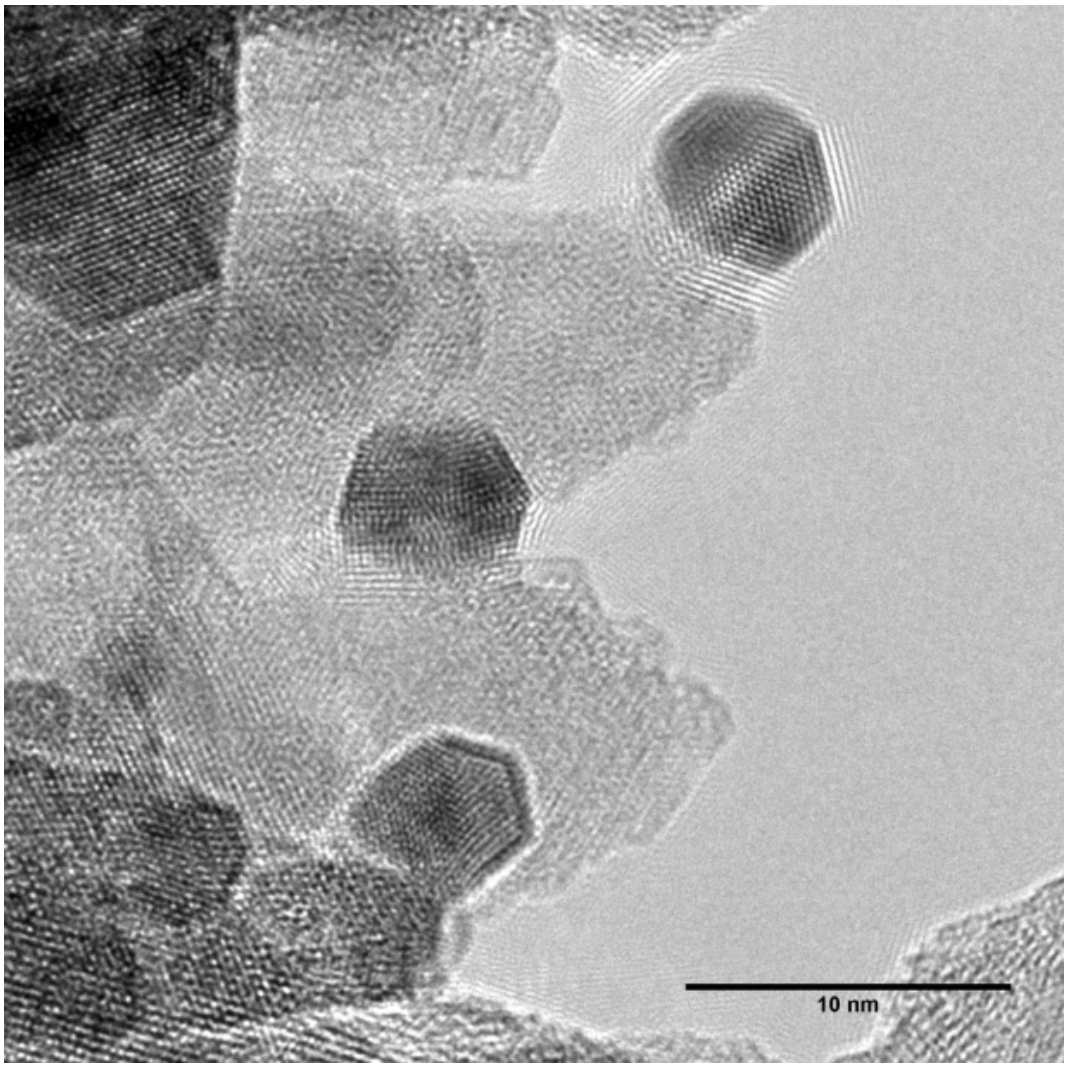


Figure 9.29: HR-TEM of gold nanoparticles the 5% Au-NRS catalyst. Many of the gold nanoparticles could be seen to be isolated on the tips of the nanorods after heating to 450°C for 24 hours.

collection shown in Figure 9.30, the gold nanoparticles were still small, with many in the 4-5 nm size range. However, as shown by quantitative Rietveld refinements, there were also a number of larger gold nanoparticles in the range of 5-9 nm as can be seen in Figure 9.30. Many of the larger nanoparticles could be attributed to the high gold loadings (8% gold in this case) as the probability that two or more gold particles will come into contact on a single rod was increased as the metal loadings were increased.

When the CO oxidation results were considered the TEM results explained what was being observed between the difference in catalytic activity of the fresh catalyst and the heat treated catalysts (Section 9.8). The fresh catalysts only consisted of very small particles less than 5 nm in size. Thus, the activity of the catalyst was very high due to all the gold nanoparticles being involved in CO conversion. Once the catalyst had been heated to temperatures as high as 810°C, as in the case of the 8% Au-NRS catalyst shown in Figure 9.30, a small number of very small gold nanoparticles sintered due to their close proximity to each other. This sintering may also be caused due to small changes in the support structure as could be seen from the in-situ PXRD as the rods grew in size by small amounts corresponding to a small loss in surface area.

Another reason may be the random placement of the gold nanoparticles onto the support during the synthesis. It was shown by the 3D tomography (Section 9.7) that the majority of the gold nanoparticles were deposited on the tips of the support structure. Thus it was likely that some of the gold nanoparticles would be very close to one another especially when the gold loadings were high and thus the probability of contact of two or more gold nanoparticles was quite likely. However, once this initial rearrangement had taken place the support as well as the supported nanoparticles remained very stable and the catalysts could be held at very high temperatures for long periods of time without further deactivation.

9.6.3 EDS

EDS was conducted on a 1% Au-0.2% Pt-NRS sample to try and determine where the platinum was positioned in relation to gold. Again, conclusive evidence of the platinum positioning could not be attained. However, the results did show that platinum was indeed present on the nanorods.

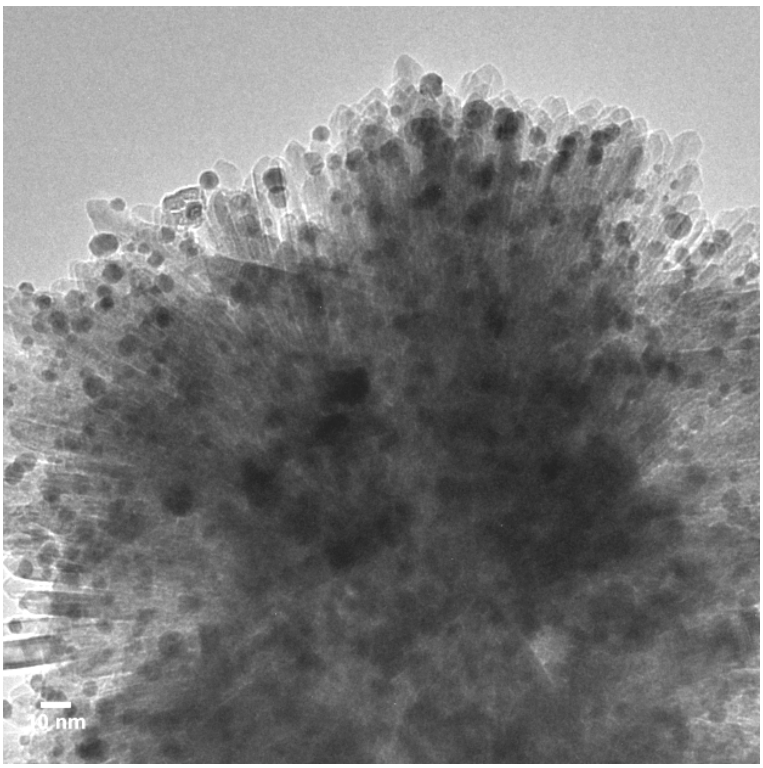


Figure 9.30: 8% Au-NRS catalyst heated to 810°C in the in-situ PXRD data collection. On completion of the in-situ PXRD data collection the sample was removed from the XRK chamber. It was almost assumed that the catalyst would not be active after exposure to such high temperatures for such a long duration (over 200 hours). However, when the catalyst was removed and examined, a deep purple/blue colour was noted. From almost hundreds of previously produced catalysts using some form titania as a support one becomes able to empirically correlate the colour of the catalyst to its potential ability to oxidize CO. There is a correlation between gold nanoparticle size and colour of the catalyst. Thus, by the law of trichotomy there is a correlation between the catalysts colour and the catalysts ability to oxidize CO. A deep purple/blue colour is usually indicative of a highly active reduced catalyst. This was difficult to believe after the catalyst had been exposed to such high temperatures for so long. The catalyst was almost immediately taken for both TEM and CO oxidation testing. The TEM results showed a catalyst that while having some large particles in the size range of 5 to 10 nm there were also many particles less than 5 nm in size. Rietveld refinements as well as CO oxidation tests confirmed this finding. This result placed the catalyst in the same operating temperature range as that of the Toyota catalyst with the Au-NRS catalyst being exposed to higher temperatures for a longer duration when compared to the Toyota catalyst. The image also showed how the nanorods had increased in size compared to the samples that have been exposed to 550°C. However, the increase was not dramatic resulting in a support that was still stable and a catalyst that although not as active as the fresh unheated sample, still had a large number of active gold nanoparticles on the surface to facilitate the CO oxidation reaction as shown in Figure 9.35.

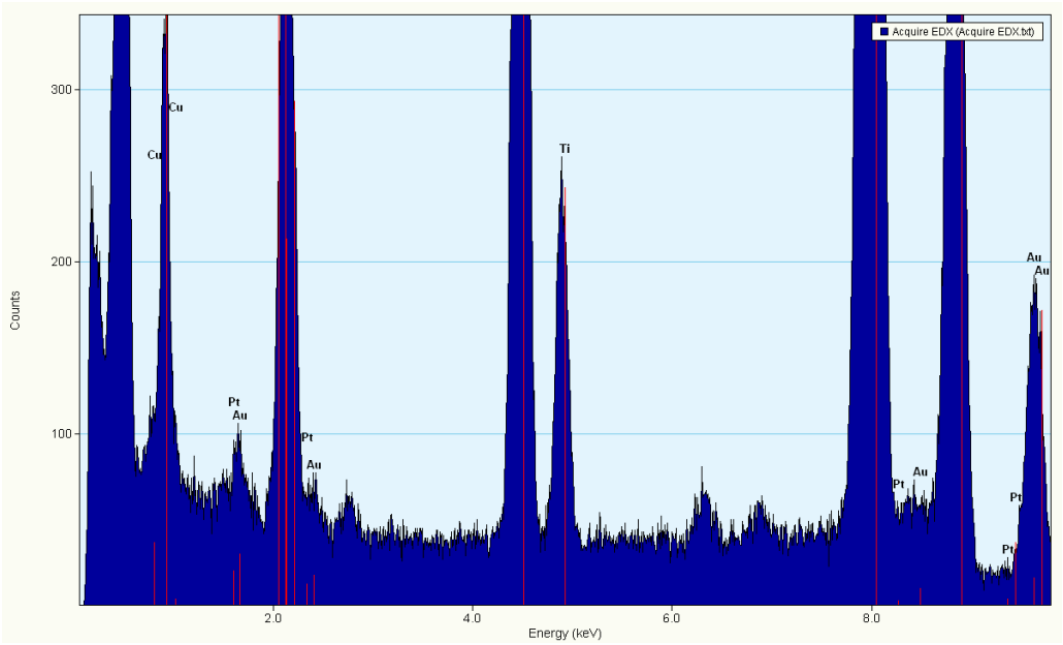


Figure 9.31: EDS of 1% Au-0.2% Pt-NRS catalyst showing the presence of both gold and platinum nanoparticles.

The EDS results suggested that both gold and platinum were present. However, it cannot be stated with certainty where the two metals are positioned with respect to one another due to the close proximity of the molecular weights of gold and platinum, thus making it very difficult to distinguish between the two metals as shown in Figure 9.31.

The morphology and curvature of the nanorod structure results in a larger contact area for the gold nanoparticles to bind onto. When compared to supports such as P25 and commercial anatase, that were seen from the earlier TEM images, these materials consist of cubic type morphologies. This resulted in the gold nanoparticles contacting the faces of the cubes and no curvature was available to enhance the contact area. As shown in Figure 9.33 as well as in the TEM image in Figure 9.32, the nanorods are curved, thus enhancing the contract area. The morphology of the nanorods resulted in a surface that was able to bind gold nanoparticles more strongly when compared to other titania supports (Figure 9.33).

As the nanorod extruded outward from the center of the structure as temperature increased, the gold nanoparticles also moved outwards and away from each other further decreasing the sintering effect as shown in Figure 9.34 where the gold nanoparticles are supported on the nanorod. In-situ PXRD revealed a small amount of anisotropic growth as the catalyst was heated.

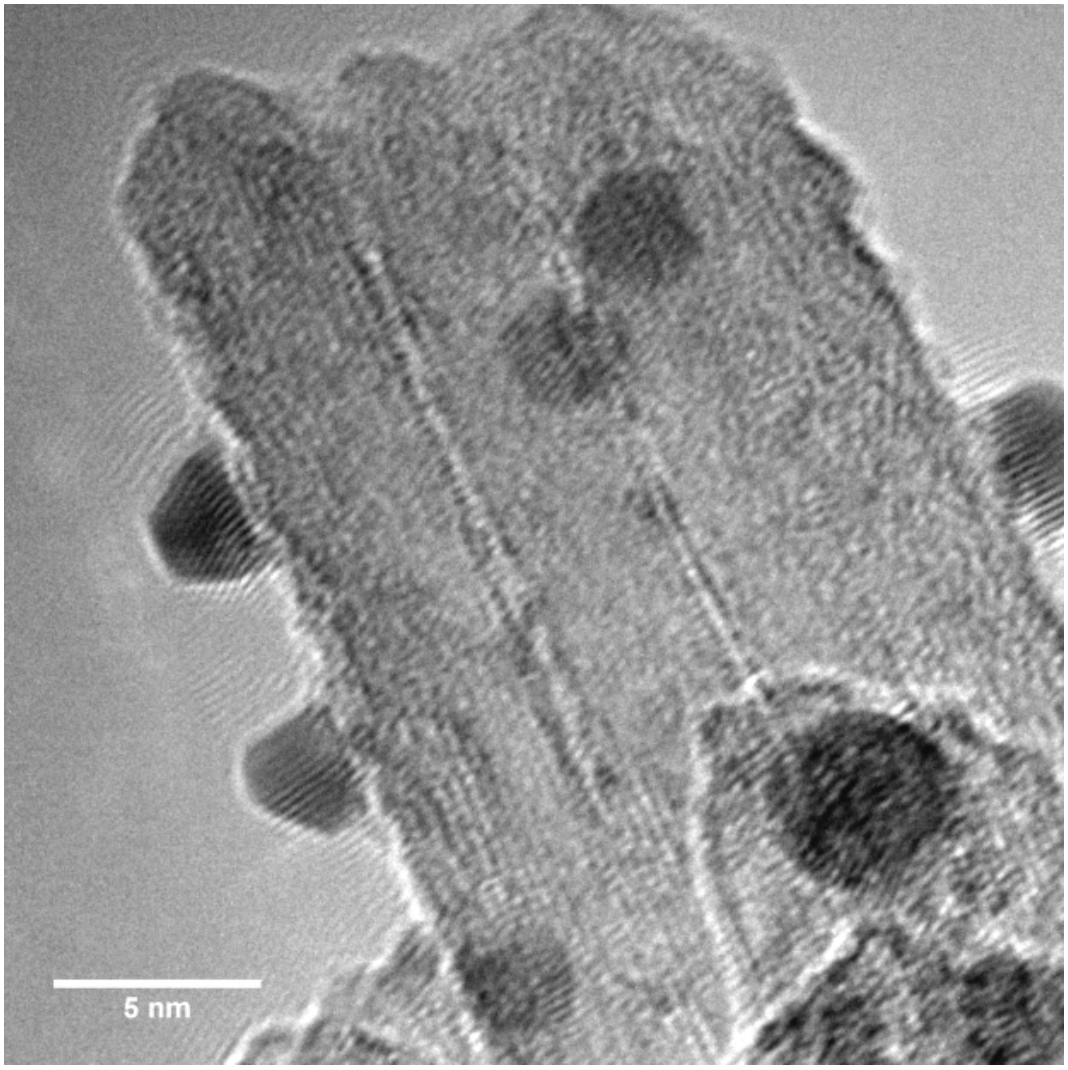


Figure 9.32: HR-TEM image of gold on NRS.

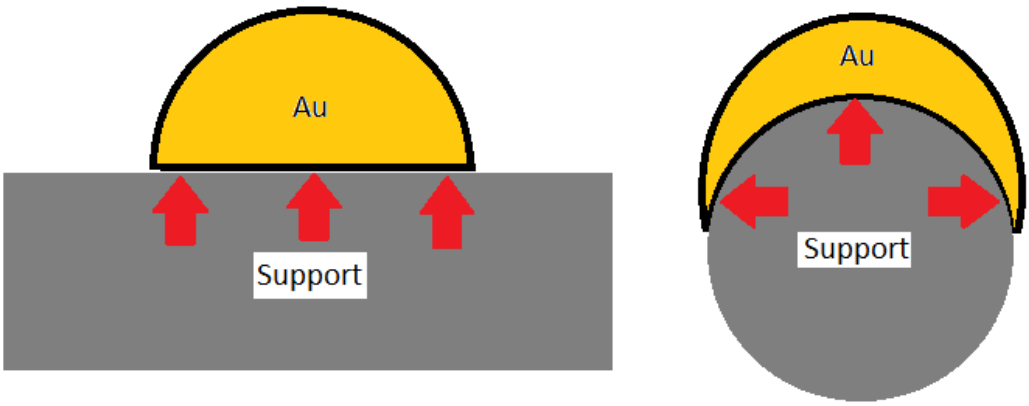


Figure 9.33: Difference in contact surface area between a flat cubic type morphology, such as commercial anatase and Degussa P25, compared to that of a rod type structure in the case of the NRS. Higher contact surface area's of the NRS support further aided in nanoparticle stability.

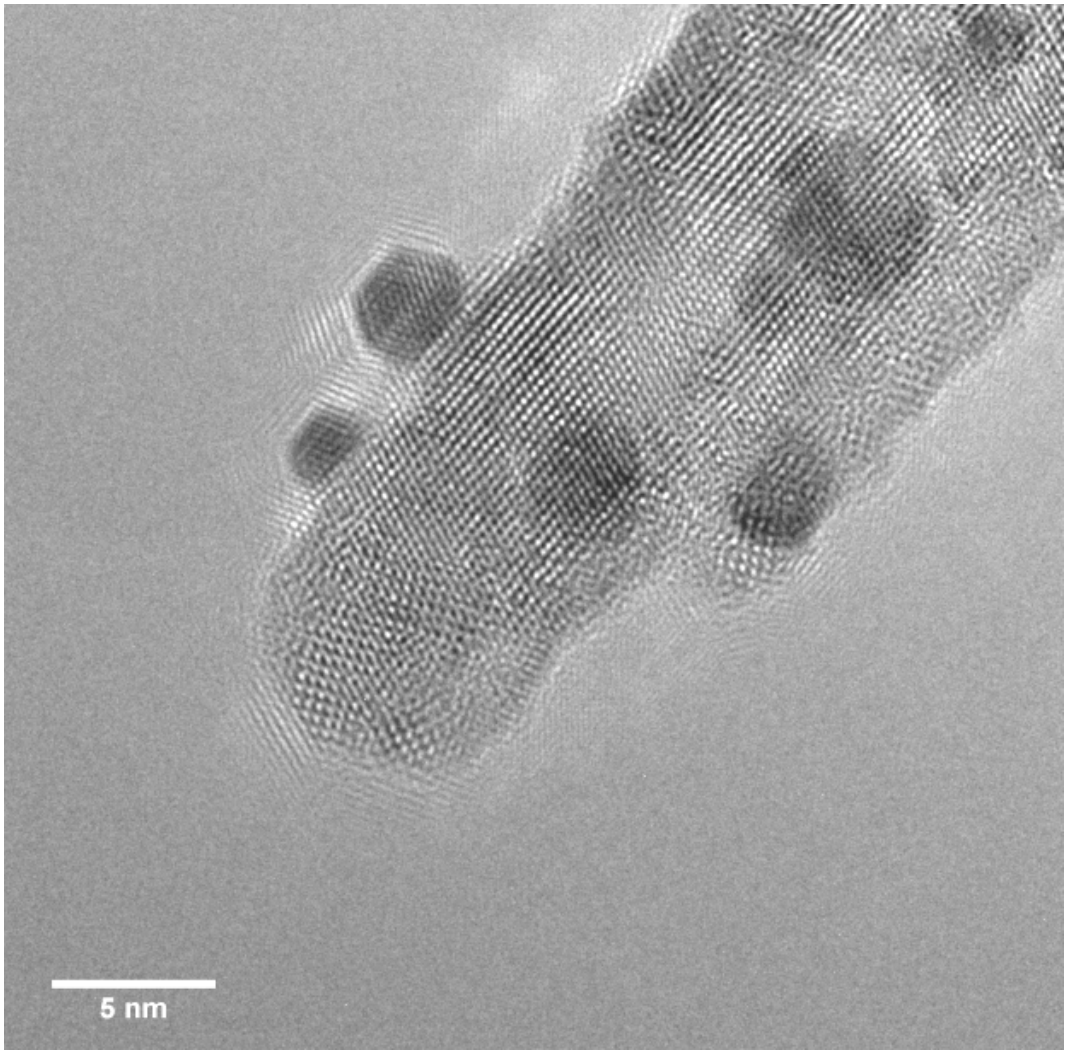


Figure 9.34: HR-TEM image of the 5% Au-NRS catalyst showing only a few gold nanoparticles per rod after the catalyst was exposed to 550°C for 24 hours.

9.7 Tomography

The tomography tilt series was collected that consisted of the combination of 136 TEM images of the 5% Au-NRS catalyst. This revealed that the majority of the gold nanoparticles were at the tips of the nanorods. Some of the collected images are shown in Figure 9.35. eTomo software allowed for individual gold nanoparticles to be tracked as the sample was rotated in the TEM and images collected. When the alignment of the 136 images was completed it was possible to monitor the exact positioning of a large number of gold nanoparticles with respect to one another. The positioning of the gold on the tips of the nanorods further enhanced the thermal stability of the gold nanoparticles.

The primary reason for the tomographic analysis was to be certain regarding the locations of the gold nanoparticles. TEM images were not conclusive as it was possible that some gold could have been located inside the structure. Tomography allowed for confirmation of the gold location. It was initially hoped that a full reconstruction could be completed, however the thickness of the dandelions was too great to allow for this.

9.8 Catalysis Data

There was correlation between the data collected using in-situ PXRD, TEM, ED as well as 3D tomography techniques to the conversion of CO to CO_2. A number of catalysts were tested with all tests being done in triplicate using samples that too were produced in triplicate to test for consistency between the samples. The testing produced data that was both somewhat expected as well as data that revealed more about the catalyst's properties. In some cases the testing of the catalysts also served as a type of characterization technique as the CO conversion could be related directly to the gold particle size. Thus, changes in the conversion could be related to what had occurred to the sample due to exposure to non-ambient conditions.

All catalytic runs were conducted in triplicate and the results averaged to compile Figure 9.36. The chosen gas composition was significantly higher in CO and O_2 compared to the compositions used by Mintek. A 5% CO and 10% O_2 mixture was used while Mintek uses a 1% CO and 2% O_2composition. This composition was chosen as the detector used provided more accurate results

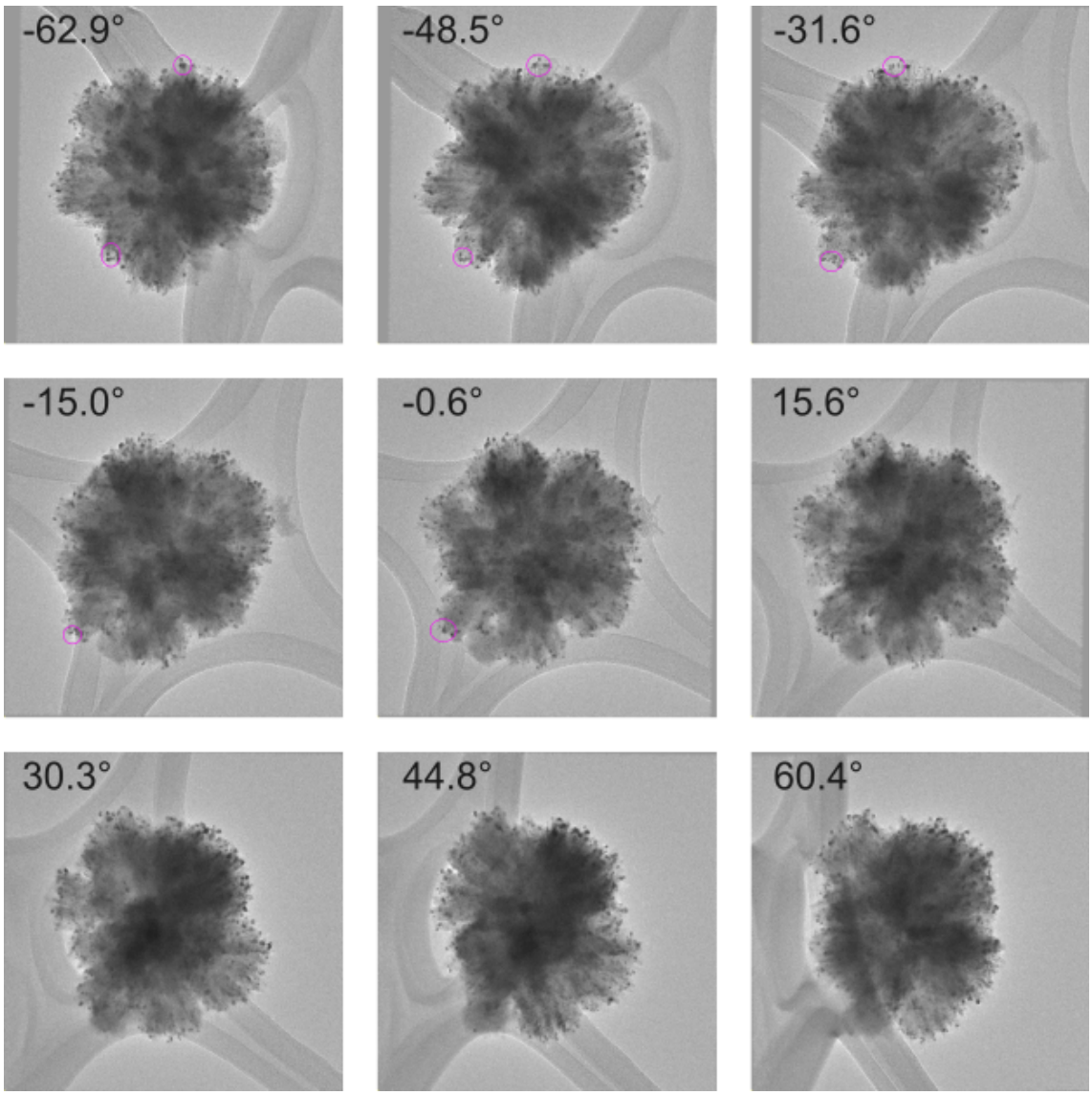


Figure 9.35: Images extracted from tomographic tilt series at regular intervals. The circled regions track groups of gold nanoparticles indicating the progression of the particles at the end of the rods. The tilt series confirms that the gold is located only at the tips of the rods and not inside the structure. Tracking of all gold particles in eTomo confirmed this observation.

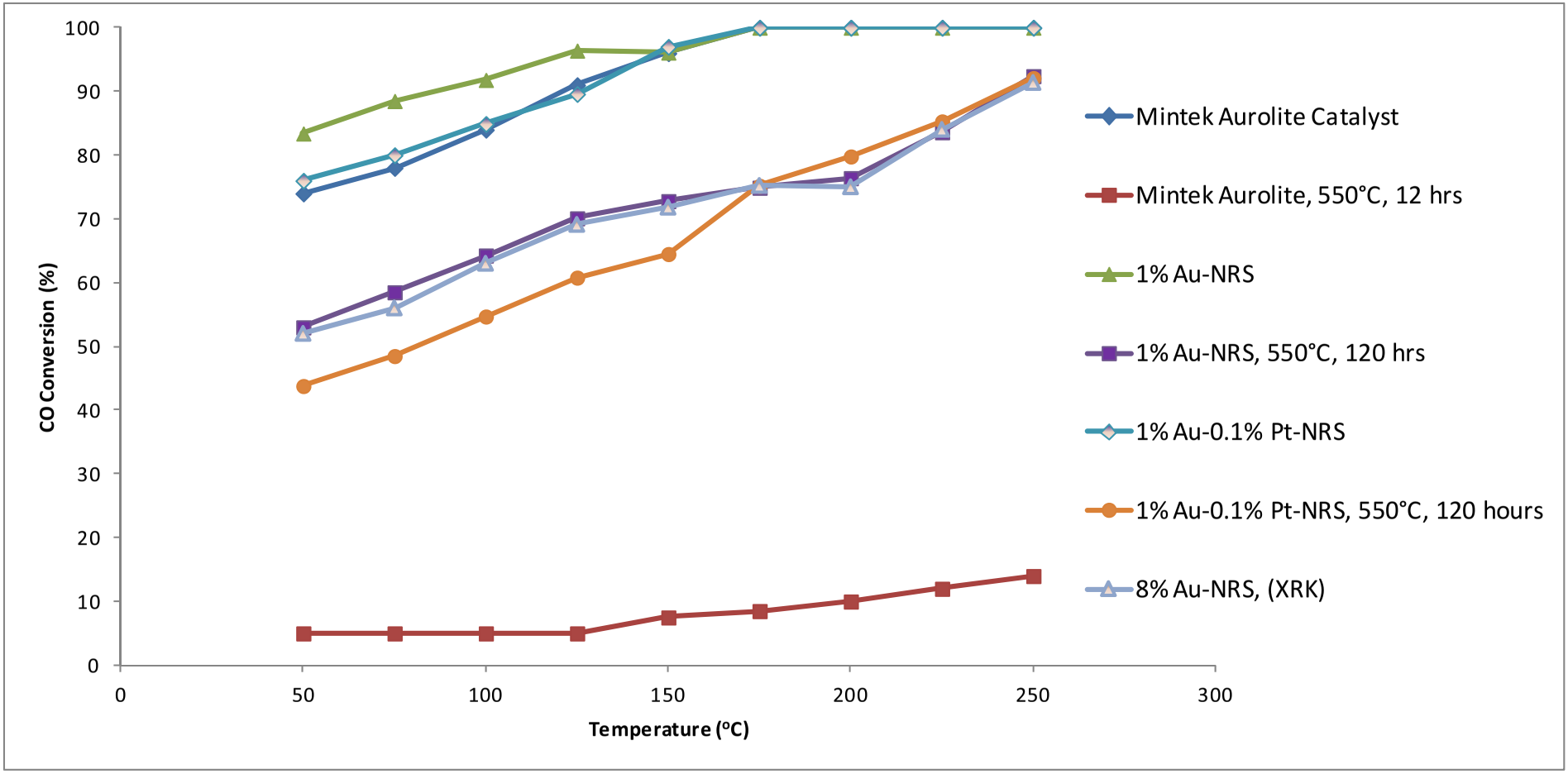


Figure 9.36: CO oxidation testing of various catalysts. The catalysts tested were 1% Au-NRS as well as 1% Au-x% Pt-NRS catalysts, where x=0.1 or 1. The Aurolite catalyst was used as a benchmark with the 8% Au-NRS catalyst also tested after the in-situ PXRD data collection after exposure to 810°C. A number of the catalysts were heated to 550°C for 120 hours to test their CO oxidation ability after exposure to prolonged high temperatures. The Aurolite catalyst was tested fresh, as well as after exposure to 550°C for 12 hours.

at these compositions. Also, the catalysts would be stressed further as higher concentrations of CO and O_2 required the catalyst to use all of its available active sites to convert both the high flow rate as well as the high CO concentrations. Firstly, the triplicate set of Mintek Aurolite catalysts was considered. The catalysts were tested as is, without any exposure to elevated temperatures other than what was experienced during the catalytic test itself. These runs gave very high activity for the flow rate and reaction temperatures used. The fresh catalysts compared very well to the other sets of fresh catalysts and the rates of conversion between the fresh catalysts was similar. However, once the triplicate set of Aurolite catalysts were heated to 550°C for 12 hours the CO conversions decreased massively. The catalysts had now completely deactivated to give CO conversions of less than 5%. The conversion was now almost completely independent of gold and was primarily due to the titania support. This massive deactivation of the set of Aurolite catalysts demonstrated why catalysts of its type have never been applied to auto-catalysts as activity cannot be maintained for long durations after exposure to moderate to high temperatures. In fact, in separate tests the Aurolite catalyst was heated at 450°C for 24 hours and tested. Once again the catalyst completely deactivated showing no oxidation of CO resulting from Au active sites.

Turning attention to the Au-NRS catalysts, the set of 1% Au-NRS catalysts showed very similar activity when compared to the fresh Aurolite catalysts. In fact at low temperatures the Au-NRS catalysts were on average 10 % higher in their ability to oxidize CO. However, this value was close to the experimental error for the data collection thus it was assumed that both of the catalysts were approximately equal with respect to CO conversion prior to exposure to non-ambient temperatures. The NRS based catalysts were then heated at 550°C for 120 hours. Following this heating cycle, CO conversions showed, on average, approximately a 25% decrease in conversion at 50°C compared to unheated NRS. At 150°C the difference had narrowed to less than 20%. Finally, at 250°C the difference was almost negligible at less than 5%. The decrease in CO oxidation was significantly lower when compared to the complete deactivation of the Aurolite catalyst. Even at 250°C the Aurolite catalyst was still only able to achieve meager conversion of 12%. Further, the Au/Au-Pt-NRS catalysts were exposed to 550°C for 120 hours, 96 hours longer than the Aurolite catalyst.

The decrease in the CO conversion of the Au/Au-Pt-NRS catalysts is best explained from TEM and in-situ diffraction results. TEM images revealed

that a small number of the gold nanoparticles sinter forming nanoparticles in a size range dependent on what temperature the catalyst was exposed to as well as the duration of exposure. For example, the Au-NRS catalyst that was exposed to 810°C reached a gold particle size of 9 nm as shown from Rietveld refinements. While a number of these large nanoparticles exist, there were many gold nanoparticles that remained very small and were responsible for the conversion of CO. The 25% loss in CO conversion at 50°C in the samples heated to 550°C for 120 hours was attributed to the sintering of a small number of the gold nanoparticles and the resulting loss of some active sites by the formation of larger particles. The loss of these active sites occurred quite rapidly on comparison between a batch of 1% Au-NRS catalysts where one sample of the catalyst was heated to 550°C for 24 hours and another for 120 hours, no change in activity was noted between the catalysts when they were tested for CO oxidation at 50°C. In both cases the catalysts showed a 25% loss in activity compared to fresh NRS even though one sample was exposed to 550°C for 96 hours longer than the other. This result implied that the Au and Au-Pt-NRS catalyst may be stable indefinitely once the initial loss of activity has taken effect.

This loss of activity compared to the fresh catalysts decreased as CO oxidation temperatures rose in the case of the Au and Au-Pt-NRS catalysts. It is however, not the case when the Aurolite catalyst was considered as even at 250°C the catalysts activity was still only 12% while the Au and Au-Pt-NRS catalysts were at almost 100% conversion.

The addition of platinum to the gold system of the NRS catalyst resulted in some interesting effects when the conversion of CO was considered. After heating to 550°C for 120 hours the 1% Au-0.1% Pt-NRS catalysts gave a lower activity when compared to the 1% Au-NRS catalysts. This occurred for all repeat samples. For supported platinum catalysts, the conversion of CO only occurs at temperatures in excess of 150°C and higher[107]. Thus, at the lower temperatures where the initial CO conversion data was collected the platinum will most certainly have no effect on CO conversion. The platinum may instead be inhibiting CO conversion at these low temperatures. After 150°C the conversion took a small upward movement at 175°C. This may be due to the platinum beginning to aid conversion. However, at these temperatures the effect of the platinum will still be very small. Further, this percentage change in activity is within experimental error and thus may be nothing more

than an anomaly.

The 8% Au-NRS catalyst from the in-situ PXRD data collection taken from the XRK chamber was analyzed. Once the in-situ diffraction data collection was completed the sample chamber was removed from the diffractometer. On inspection, the sample was a purple-blue colour, the same colour of the other active fresh catalysts that had been tested previously. However, the colour may have been more apparent as the sample contained a higher gold loading compared to other Au-NRS catalysts tested. As colour of the catalyst is a qualitative indicator of a gold catalysts potential activity it was decided to test the catalyst for CO oxidation. Samples from previous in-situ data collections were not analyzed for CO oxidation as it was incorrectly assumed that the catalyst would never be able to withstand temperatures over 800°C. However, it was decided to test the final XRK sample and the results are shown in Figure 9.36.

Remarkably the catalyst was still active, albeit with an initial loss of activity similar to the other Au and Au-Pt-NRS catalysts that had been exposed to 550°C for 120 hours. The activity of the catalyst showed that the small initial loss of activity occurs rapidly perhaps from a rearrangement of the gold nanoparticles as seen in the TEM images as a number of different shaped nanoparticles were observed. Once this small initial loss of activity had taken place the catalyst was able to remain stable even after exposure to extremely high temperatures for long periods of time as experienced in the XRK chamber. The catalyst was able to replicate within experimental error the CO conversions achieved by the 1% Au-NRS catalyst that was exposed to 550°C for 120 hours. The result demonstrates the stability of a thermodynamically stable and morphologically designed catalyst. Further, the CO oxidation results are reinforced by the findings of in-situ diffraction, the resulting Rietveld refinements as well as TEM results.

9.9 Conclusions

The synthesis method produced 100% phase pure rutile nanorods in a dandelion type structure as shown by ED, TEM as well as in-situ PXRD. In-situ PXRD as well as electron diffraction and TEM showed the nanorods are radially aligned providing high usable surface areas of approximately $100 m^2/g$ for

the 5 batches produced. The morphology of the Au and Au-Pt-NRS catalysts allows for the easy passage of reactant gasses through the structure aiding in catalysis. The NRS provided a thermodynamically stable, high surface area support structure with the desired morphology to withstand high temperatures as demonstrated using in-situ PXRD, TEM, HR-TEM, as well as 3D tomography. 3D Tomography of the Au-NRS catalyst showed the gold nanoparticles are primarily situated on the tips of the nanorods. This isolation of the gold nanoparticles on the tips of the nanorods further increases the catalysts thermal stability. Unlike all the other tested supports where the addition of metal nanoparticles was found to be detrimental to the stability of the support when exposed to non-ambient temperatures, the addition of metal nanoparticles in the form of both gold and platinum resulted in the NRS supported catalysts being stabilised by these metals. Further, the small amount of growth as the nanorods extrude outward as temperature is increased is not detrimental to the catalyst as the gold nanoparticles on the rods are transported further away from each other. Storage of the Au-NRS catalyst (at ambient temperatures and under air) showed no effect on the gold particle sizes further demonstrating the catalysts long term stability.

The 8% Au-NRS catalyst did not become overloaded by the presence of higher loadings of gold nanoparticles as in-situ PXRD as well as TEM showed the gold nanoparticles still remained small, with only minor changes in the support structure being noted even after exposure to 810°C. The Aurolite catalyst was used as a benchmark and provided very high conversion for the flow rates used when the catalyst was fresh. However, once the Aurolite catalyst was exposed to temperatures of 550°C for 12 hours complete deactivation was noted as CO conversion was less than 5% at 50°C and was only be attributed to the titania support. Even at reaction temperatures over 250°C the Aurolite catalyst only showed a CO conversion of 12% for the three repeats. This result confirmed what was found from in-situ PXRD as studies where large increases in the gold crystallite sizes are noted as temperature is increased. The anatase to rutile phase transition is also a major factor in the deactivation of the Aurolite catalyst.

The Au-NRS and Au-Pt NRS catalysts were able to withstand 550°C for over 120 hours. From results of the 8% Au-NRS catalyst after heating to 810°C when compared to the CO conversion of the catalysts heated to 550°C it was shown that there is no difference in the CO conversion between the two cata-

lysts. It is likely that the catalysts will be able to withstand temperatures in this range indefinitely as the entire system has been shown to be very stable at these temperatures with no change in CO oxidation after exposure to different temperatures for different time periods. The addition of platinum to gold did not show any significant increase in terms of CO conversion as well as any improvement in overall stability of the catalyst. This may be attributed to gold not requiring the stabilisation effect that the platinum provides as with the Au-NRS catalyst is already very stable.

Finally the Au-NRS catalyst was heated to 810°C in the XRK chamber where the catalyst spent almost 200 hours at temperatures above 450°C. Further, the catalyst spent over 100 hours at temperatures exceeding 600°C and still the activity of the catalyst was good with CO conversions at 250°C almost identical to the fresh unheated catalyst as well as the fresh Aurolite catalyst. No gold catalyst has been exposed to such harsh conditions for such long periods of time while still remaining as active as the Au-NRS catalyst.

Chapter 10

Conclusions

From the initial study of gold on amorphous silica and zirconia, the dependence of the catalyst on the synthesis conditions was examined. Experiments revealed that pH control of the solution is critical as well as the selection of the correct support. With the correct selection of pH it was possible to attain both small gold nanoparticles as well as high gold loadings. Further, the selection of the correct pH is crucial as the correct isoelectric range is needed to ensure good binding between the gold nanoparticles and the support.

The synthesis method produced epitaxially bound, monodisperse nanoparticles. With the use of silica and zirconia the binding to the support was not very effective. The use of urea proved to the the best choice of base as it not only negated the need to use other bases, but also acted as a slow release base itself. Thus, the pH of the solution was uniform throughout the solution unlike in the case where the DP is performed drop wise using bases such as ammonium hydroxide. The method resulted in a repeatable, robust synthesis where Au and Au-Pt catalysts can be reproduced within a small margin of error.

While the amorphous silica and zirconia proved useful to study nanoparticles changes resulting from the synthesis technique the supports were found to be insufficient for catalysis due to the poor binding between the nanoparticles and the surface. The addition of platinum to the gold systems did aid in gold nanoparticle stability however, the effects of the platinum were not significant enough for the catalysts to be stable at high temperatures.

After exploring amorphous silica and zirconia, titania was chosen as a support due to its ability to strongly bind gold and platinum nanoparticles to its surface as well as itself being active for the CO oxidation reaction. Commercial anatase phase titania provided by Sigma-Aldrich was used in order to determine if the addition of platinum would have the same effect on gold nanoparticle sizes as was the case in the amorphous silica and zirconia supports. Indeed the addition of small amounts of platinum to the nanogold showed that the overall size of the nanoparticles can be reduced provided that the composition is within the miscibility gap of the component metals. This was confirmed by in-situ PXRD as well as TEM. EDS analysis showed that gold and platinum may form a bimetallic structure according to miscibility gaps in the phase diagrams for gold and platinum but this however cannot be stated with certainty. TEM investigations showed that the synthesis method once again produced epitaxially bound nanoparticles which are crucial for the conversion of CO. The commercial anatase used, while having good thermal stability at low to medium temperatures resulting from its relatively large mean particle size, had small amounts of rutile phase present. This small amount of rutile is enough to result in a complete phase transition when the catalyst was heated to higher temperatures as seen in the in-situ PXRD results and the TEM images. The phase transitions were quantitatively analyzed using Rietveld refinement. The effect was increased with the addition of metal nanoparticles onto the surface as in-situ PXRD data showed the phase transition occurring at lower temperatures compared to the pure support exposed to the same conditions. TEM studies also showed phase conversions occurring at the interface of the metal nanoparticles and the support structure confirming results from the in-situ data collections and Rietveld refinements. The large particle size of the anatase also resulted in a lower surface area which in turn resulted in the surface quickly becoming overloaded by the nanoparticles as surface area was lowered with increasing temperature. Finally, as anatase is not the thermodynamically stable polymorph of TiO_2, it readily converted to a low surface area rutile structure when exposed to moderate to high temperatures for a prolonged period of time. The resulting rutile structure was characterised by massive particle sizes and exceptionally low surface areas. Taking all of the above into consideration commercial anatase was found to not be a viable support for nanogold catalysts for temperatures over 400°C.

As the Mintek Aurolite catalyst uses Degussa P25 as a support as well as the Aurolite catalyst being known to be one of the best industrial nanogold

catalysts available, it was chosen as the benchmark to test synthesised catalysts against. TEM as well as Rietveld refinements performed on in-situ diffraction data confirmed claims that the nanogold catalyst was produced with 1% gold loading on Degussa P25 as well as showing that gold nanoparticle sizes were in the range of 2-5 nm when the catalyst was fresh. While being able to convert CO readily even from ambient temperatures, the Aurolite catalyst deactivated when exposed to temperatures over 400°C.

The first in-situ diffraction and Rietveld refinements of the Aurolite catalyst, and indeed any nanogold based catalyst, revealed the deactivation mechanism of the Aurolite catalyst as being due to the phase conversion of anatase to rutile. The use of the Rietveld method to determine structural information proved crucial in understanding the various catalysts and supports as well as the reasons to the catalysts deactivation. Over 1100 refinements were conducted on in-situ data to elucidate the structural changes of the various catalysts under non-ambient temperatures. The conversion of anatase to rutile in the Aurolite catalyst resulted in massive loss of surface area as well as the possible encapsulation of the gold nanoparticles during the phase transition.

The conversion of anatase to rutile occurred through a wave-front progression in the anatase crystal. Along this front the titanium-oxygen octahedra rearranged through a rotation process. The front extended to the surfaces of the support particles. It is likely that gold nanoparticles on the surface of the anatase are caught by the front migration and are moved along with the wave-front. This promotes sintering of the gold as the nanoparticles are moved into close proximity. An unstable support surface resulted in unstable gold nanoparticles and an inactive catalyst.

Quantitative Rietveld refinement showed the rapid growth of the gold nanoparticles as the catalyst was exposed to non-ambient temperatures. Finally, exposure to 550°C for 12 hours resulted in complete deactivation of the catalyst when CO oxidation tests were conducted with the catalyst only able to reach a CO conversion of 12% at 250°C. The conclusion was that the Aurolite catalyst cannot be used for high temperature applications. These findings revealed that the problem lay in the instability of the support material with loss of active surface area due to thermodynamically driven phase changes being the primary factor causing deactivation due to sintering of the active sites of the gold nanoparticles and possibly also due to encapsulation of active sites.

Due to the low surface area of commercial anatase and the loss of surface area in the case of the Aurolite catalyst from the P25 support, the need for a more stable as well as higher surface area support was needed. Hydrothermal synthesis of phase pure anatase with surface areas approaching $500m^2/g$ resulted in a support which is more resistant to high temperatures when compared to commercial anatase as well as Degussa P25 which was demonstrated by in-situ PXRD and quantitative Rietveld refinements. The citric acid precursor was easily removed with heating resulting in higher CO oxidation rates of the synthesised catalyst. While decreasing the surface area of the support, heating aided in the supports stability. This loss of initial surface area helped to stabilise the support prior to the addition of the gold nanoparticles. Even after some loss of surface area the produced supports still maintained surface areas in excess of $300m^2/g$, some 6 times that of P25. When gold was supported on the nano anatase the gold crystallite sizes were smaller when compared to both gold on commercial anatase and P25 supports as well as that of the Aurolite catalyst when the catalysts were exposed to non-ambient temperatures during in-situ data collections. This can be attributed to the phase purity of the nano anatase where, under the non-ambient conditions, showed an ability to resist phase conversion and remain phase pure as shown by in-situ PXRD and Rietveld refinements. However, the phase transition is inevitable if the catalyst is held at high temperatures for significant periods of time as it is a thermodynamically driven process. Thus the catalyst, due to its very high surface area, is very suitable for low to medium CO oxidation reactions but unsuitable for prolonged exposure to high temperatures.

A hydrothermal synthesis of rutile phase nanorods produced a thermodynamically stable, high surface area support structure with the desired morphology to aid gold nanoparticles to withstand high temperatures. Morphology was a crucial factor in the supports thermal stability with the nanorods being radially aligned as shown by PXRD as well as electron diffraction and TEM. The synthesis method as well as the morphology of the NRS, allowed for gold nanoparticles to be predominately deposited on the tips of the nanorods. This feature was confirmed by 3D tomography as individual nanoparticles could be pinpointed around the dandelion structure and observed as the structure was rotated.

With the relatively high usable surface area of the NRS each of the nanorods that comprise the dandelion structure are only required to support a few

nanoparticles. In fact, TEM revealed that some of the nanorods only supported a single gold nanoparticle. As the morphology of the dandelion structure keeps all of the nanorods independent of one another the transfer or sintering of gold nanoparticles was greatly inhibited. This effect was further enhanced as the nanorods extruded outward as the structure was exposed to high temperatures as characterised by in-situ PXRD and TEM. As the nanorods extruded, gold nanoparticles on the tips of the nanorods were transported outward, further away from other gold nanoparticles. The extrusion of the nanorods did result in a small loss of surface area for the NRS as determined by BET measurements taken before and after heating of the NRS based catalysts. However, this loss of surface area was not large and was shown to be dramatically inhibited by the addition of small amounts of metal nanoparticles. Unlike all the other tested supports where the addition of metal nanoparticles was found to be detrimental to the stability of the support when exposed to non-ambient temperatures, the addition of metal nanoparticles in the form of both gold and platinum resulted in the NRS supported catalysts being stabilised by these metals. The nanorod structure provided better and larger binding surface areas for the gold nanoparticles when compared to the cube type structured supports that are found in anatase and P25. The morphology of the NRS also allowed for improved gas flow through the catalyst when compared to other forms of support The cause of deactivation in the Aurolite catalyst was found to be due to the phase transformation of anatase to rutile. This was not a factor with the Au-NRS catalyst as the structure is already locked into the most thermodynamically stable form. This proved to be one of the most significant features that resulted in a very stable catalyst. Quantitative Rietveld refinements showed that gold crystallite sizes are very small compared to all the other catalysts produced using different types of supports, as well as being more than half the size when compared to the Aurolite catalyst. The stability of the Au-NRS catalyst was highlighted after exposure to high temperatures for a far greater time than all the other tested catalysts as well as exposure to higher temperatures did not deactivate the catalyst as was the case with the Aurolite catalyst.

The Au-NRS and Au-Pt-NRS catalysts were able to withstand 550°C for over 120 hours with only a small loss in activity compared to fresh catalysts. It is likely that the catalysts will be able to withstand temperatures in this range indefinitely as the entire system is very stable at these temperatures. In separate tests, the catalyst was heated to 810°C where it spent almost 200 hours

at temperatures above 450°C during the data collection. Further, the Au-NRS catalyst spent over 100 hours at temperatures exceeding 600°C and still the activity of the catalyst was extremely good compared to fresh catalysts and showed the same propensity to oxidize CO as the Au-NRS catalyst that was heated to 550°C for 120 hours albeit that the two catalysts did have different gold loadings. The 8% Au-NRS catalyst did not become overloaded by the presence of higher gold loadings as in-situ PXRD as well as TEM showed the gold nanoparticles still remained small with only minor changes in the support structure being noted even after exposure to 810°C. CO conversions for the heated Au-NRS catalysts showed, on average, approximately a 25% decrease in conversion at 50°C when compared to the fresh catalyst. At 150°C the difference had decreased to less than 20%. Finally at 250°C the difference is almost negligible at less than 5% when compared to the fresh catalyst. The decrease in CO oxidation is significantly lower when compared to the complete deactivation of the Aurolite catalyst. At 150°C the Au-NRS catalysts showed CO conversions of over 72% at the given flow rates while the Aurolite catalyst showed conversions of less than 5%. By the time the reaction was heated to 200°C the Au-NRS catalyst reached over 80% conversion with the Aurolite catalyst still at only 12% conversion. This, after the Au-NRS catalysts were exposed to 550°C for 96 hours longer than the Aurolite catalyst. No titania based catalyst and indeed any other supported pure gold catalyst has ever reached temperatures near to what the Au-NRS catalyst was exposed to and still remained active as shown by the CO oxidation testing. Very few high temperature nanogold catalysts exist with most of the examples not being able to withstand high temperatures for extended periods of time. The Toyota catalyst is the only gold based catalyst to have ever reached 800°C without complete deactivation occurring. The Au-NRS catalyst has been shown to be able to also achieve this feat and even surpass the Toyota catalyst as the Toyota catalyst was only exposed to 800°C for 5 hours before being cooled to 500°C for the duration of its testing. In-situ PXRD, TEM as well as CO oxidation testing showed that the Au-NRS catalyst that was heated to 600°C-810°C for over 100 hours was able to remain stable and further was able to convert CO just as well as the Au-NRS catalysts that had been exposed to 550°C for 120 hours. This bodes well for the catalyst for applications such as auto-catalysts for diesel internal combustion engines as temperatures as high as 800°C are never reached. However, the ability of a catalyst to be able to still operate well outside designed operating limits is very desirable as this implies that the

catalyst will remain stable at lower temperatures.

Exhaust gas temperatures of Rotax race engines were analyzed as a potential application for the Au-NRS catalyst. The temperatures of the exhaust gases peaked at 622°C with average exhaust gas temperatures not exceeding 600°C, well inside the operating range of the Au-NRS catalyst. The ease of application of the catalyst to the quartz wool mat inside the exhaust system may provide an easy, cost effective way to reduce emissions produced by the race engines. More extensive testing of the catalyst is needed for potential use as an auto-catalyst. However, results presented in this thesis provide strong evidence that the catalyst may have the potential for use in these types of applications.

- On the 20th of September 2011 a Provisional Patent Application was filed, (SA Provisional Patent number 2011/06802). The patent encompasses the Au-NRS catalyst developed in this thesis. Commercialisation of the Au-NRS catalyst is being undertaken by Mintek as well as studies to further enhance the stability. Initial results indicate methods by which complete stabilisation may be achieved.

Chapter 11

Future work

Further stabilisation of the NRS support is likely to be possible. This may be done by the thermal treatment of the NRS prior to the addition of gold nanoparticles. Thus, the NRS is heated for a selected period of time at a predetermined temperature resulting in some growth and a small loss of surface area. This should aid in the stabilisation of the support prior to the addition of the gold nanoparticles. What needs to be determined is the exposure parameters that will be used in terms of temperature, time, as well as heating rates that will give the most favorable product. The balance between a small loss of surface area in return of higher thermal stability must be determined. The effect of pressure and various gasses during this process should also be investigated using in-situ PXRD as well as TEM.

For potential applications in the automotive industry, it would prove useful for the catalyst to be loaded onto corderite. Corderite is the honeycomb structure that current PGM based catalysts are applied to. This is done using a wash coat containing the selected PGM's used for catalysis. A method for the deposition of the Au-NRS catalyst onto this corderite structure will be useful in terms of testing the catalyst as well as potential applications. Only the CO oxidation reaction was tested in this thesis. This was done as the CO oxidation reaction is very sensitive to changes in gold nanoparticle size and thus gives an indication as to what is occurring to the gold nanoparticles as the catalyst is exposed to various conditions. Testing of other reactions such as NOx reduction as well as hydrocarbon oxidation, which are not as dependent on gold particle size, will also prove useful as the combination of these two

reactions with CO oxidation are the type of reactions that take place in three-way automotive catalysts.

It will also be necessary to confirm the cycling activity of the catalyst. To determine this, the catalyst activity will need to be monitored as it is taken from room temperature, to well above 600°C and then back to room temperature, etc. This will confirm whether the growth mechanisms that have been proposed are really completed through the pathways suggested.

Chapter 12

Testing for use in Bombardier (Rotax) race engines

12.1 Exhaust gas temperature testing

For a number of years I have been involved in motorsport of some form or another. For two years I have competed Rotax Max World Challenge, which consists of 49 countries competing in national race championships throughout the world. The Rotax Max Challenge championship has become a highly professional and very scientifically run race series. The telemetry systems on the karts are advanced with the ability to collect data from over 15 inputs every tenth of a second. With the help of one of the premier race teams in South Africa I was interested in collecting data on the exhaust temperatures during a typical race. Karting is a multimillion dollar industry in South Africa alone and engines from Bombardier are used worldwide as they are an FIA (Fédération Internationale de l'Automobile) supplier. The idea came when an exhaust mat was replaced in the kart I race. The design of the exhaust is used on all Rotax kart engines and consists of an internal silencer mat as shown by 2 in Figure 12.2 . The mat is made of the same quartz wool material that is used as the support material for catalysts in the CO oxidation rigs at the university. This allows for easy production and testing of the material by simply adding the Au-NRS onto the existing mat. Thus, in the same manner that CO conversion was undertaken in the lab, it can also be undertaken on a race engine. The engines produced by Rotax are 2-stroke with the ability to freely rev to over 14 000 rpm making them a perfect choice to test the catalyst



Figure 12.1: 7 times Formula 1 World champion Micheal Schumacher still drives for the Italian Kart manufacturer Tony Kart and helps with the development of new chassis and engines. His presence as well as other high profile drivers shows the massive interest and large amount of capital investment of teams and manufacturers in the sport.

under harsh conditions. At this time no catalyst is used for international karting and the governing body, the FIA, is facing much criticism over the fact that while 2 stroke engines are very powerful for their engine capacity , they are also very polluting.

This exhaust design provides a perfect platform to test the Au-NRS catalyst under very hostile conditions. Further, the exhaust mats are replaced regularly and thus new catalyst can be loaded and tested at minimal cost. Two temperature sensors collect temperature data from the exhaust manifold and the exhaust outlet. Thus data can be collected on the gas temperature that passes over the exhaust mat and thus over the potential catalyst. The new Au-NRS catalyst will be able to withstand the temperatures of the exhaust gases as shown in Figures 12.3-12.6. This was tested by collecting data on the exhaust gases during a test session and comparing the temperatures of the gases to the temperatures reached in the in-situ PXRD runs. A comparison of the temperatures gave information on the viability of using the Au-NRS catalyst as a possible treatment for the exhaust gasses of these race engines. Rotax produces thousands of engines per year for teams competing in various championships and most drivers will use a number of engines per year. Two stroke engines have a large expansion box placed after the exhaust manifold outlet from the exhaust valve as shown in Figure 12.2. This expansion box

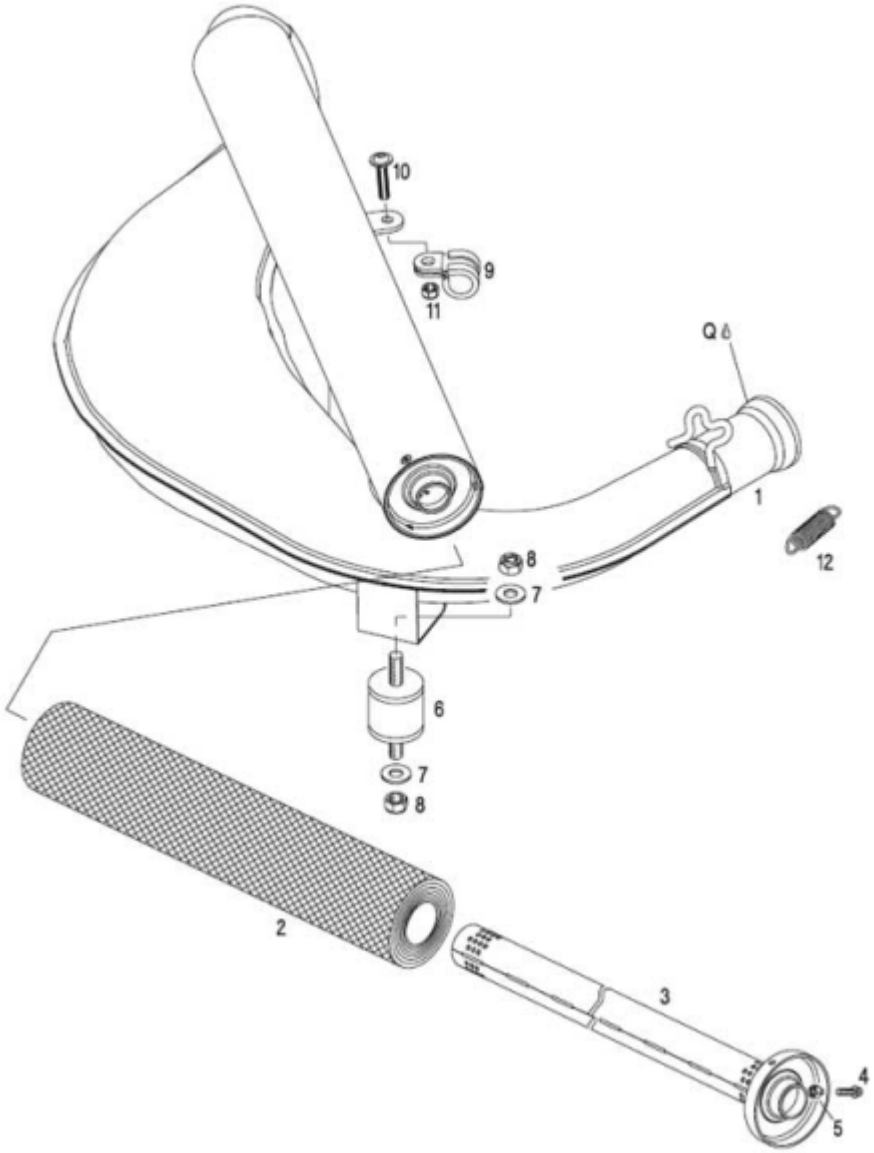


Figure 12.2: Design of the current karting exhaust system (Bombardier). The silencer mat, identified by number 2 on the schematic, is made of the same material that is used in laboratories to support powder catalysts during testing.

rapidly cools the air as it adiabatically expands thus the temperatures of 2-stroke engines are not excessively high when the gasses pass over the silencer. What the actual temperatures were is what was determined using telemetry. Telemetry data was collected using a AIM Micron 4 . Analysis of the data was done using race studio 2 analysis as shown in Figures 12.3-12.6.

12.2 Conclusions

Exhaust gas temperatures never exceeded 622°C for the entire test session with average exhaust gas temperatures being less than 600°C over the entire test. The easy application of the Au-NRS catalyst to the quartz wool silencer mat may be a viable catalyst to help reduce emissions as data from previous experiments indicated that the Au-NRS catalyst will be able to withstand the high temperatures experienced from the exhaust gasses. Further testing of the catalyst under working conditions is needed, this will be done on a full engine test rig. However, initial results are promising.

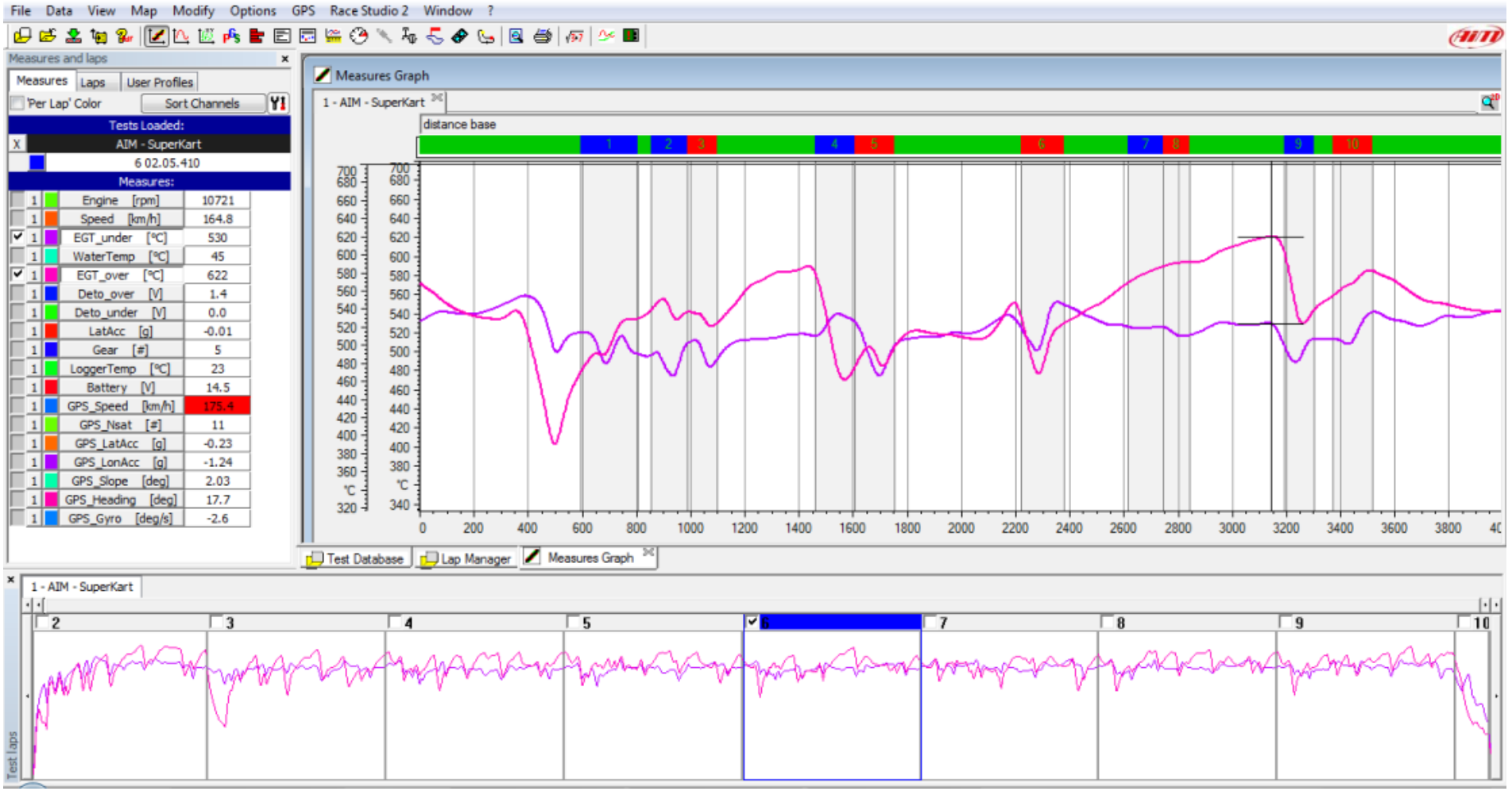


Figure 12.3: Telemetry data from a test session. The ambient atmospheric temperature was 26°C with a track temperature of 37°C. The left hand column shows the data collection parameters. The bottom graphs are of each completed lap and finally the large central graph is of the two exhaust gas temperatures (EGT) labeled as EGT_under and EGT_over. One temperature is collected before the silencer (EGT_over) and one temperature after the silencer (EGT_under). All other parameters have been omitted for simplicity.

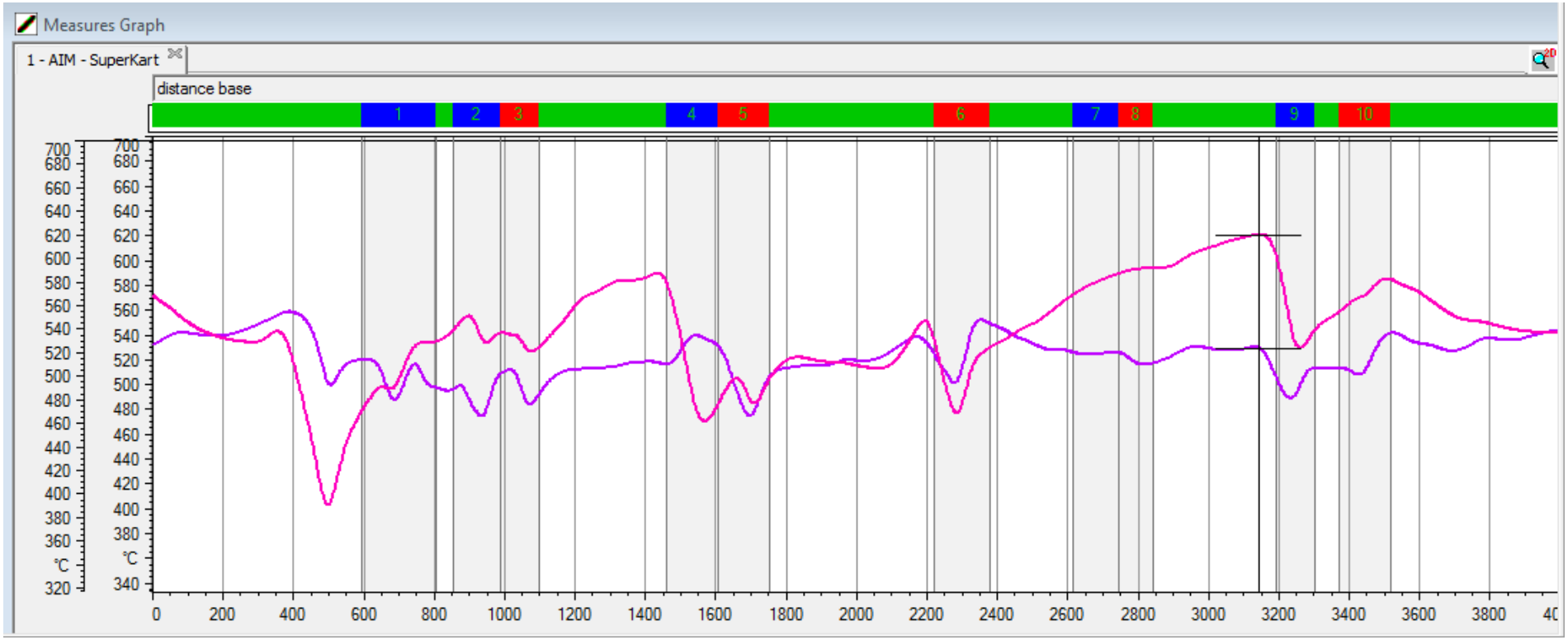


Figure 12.4: Exhaust temperatures of the fastest lap of the session. This corresponded to the highest temperatures attained by the exhaust gases showing the catalyst should be able to withstand the maximum exhaust temperatures according to the in-situ PXRD data.

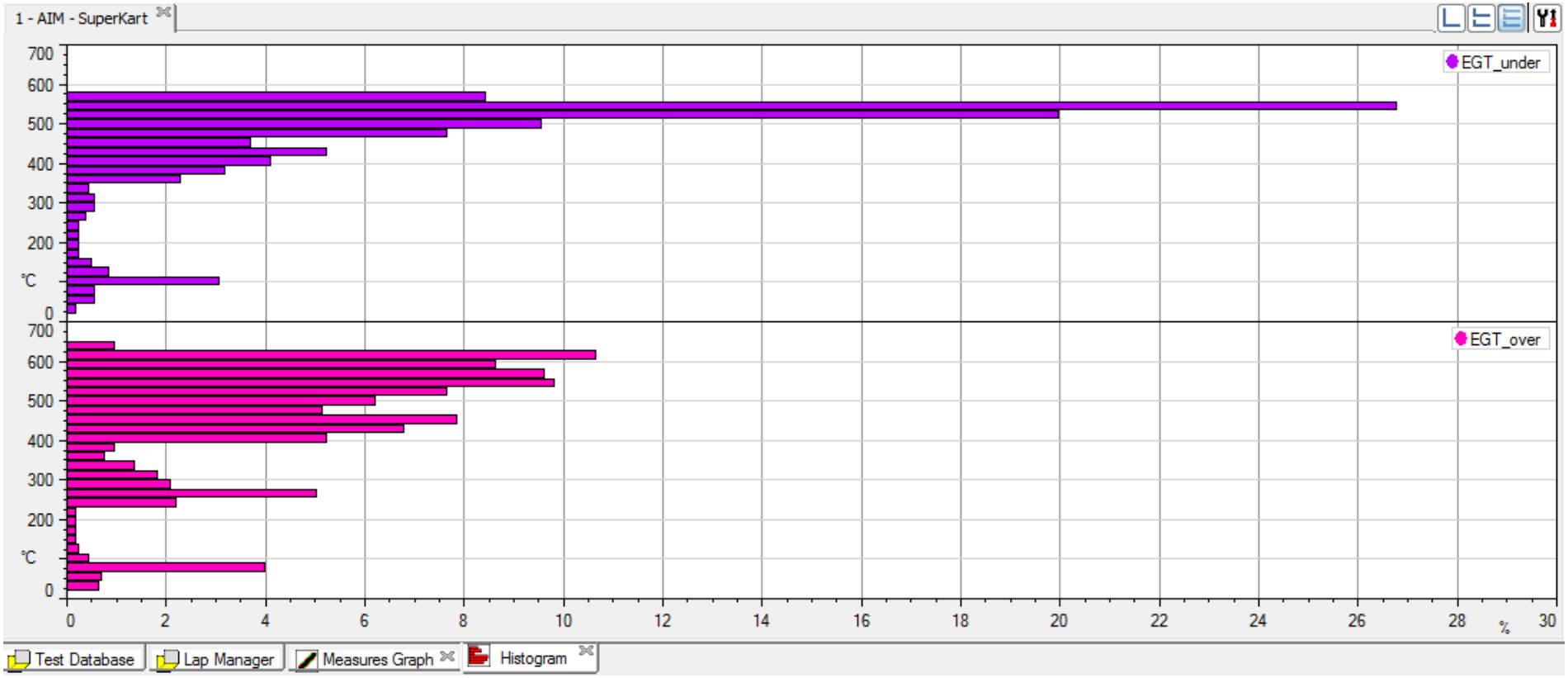


Figure 12.5: Exhaust gas temperatures of the first lap showing how the exhaust gas temperatures rapidly increase from ambient up to over 600°C for the EGT_over.

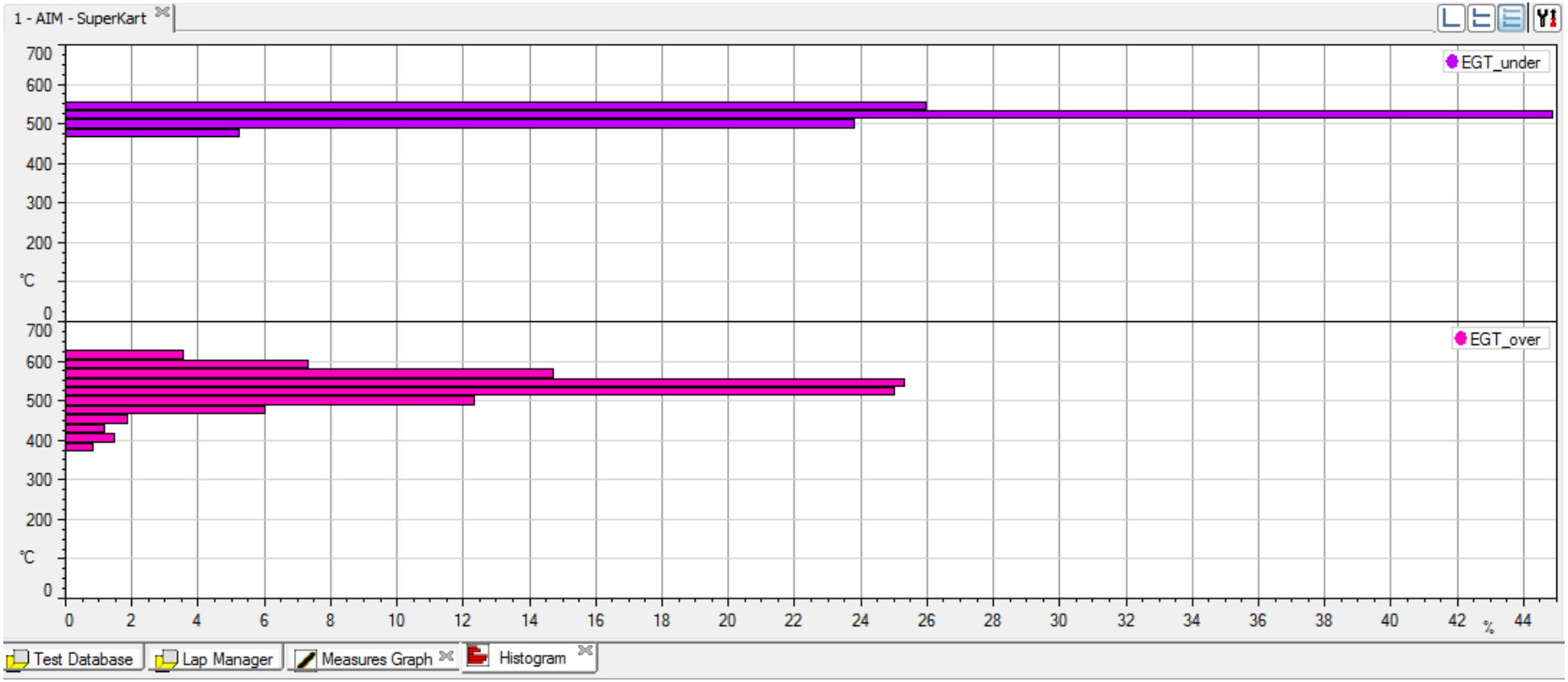


Figure 12.6: Exhaust gas temperatures (EGT's) of the 7th and fastest lap. The bar graph shows the percentage time that the gases are within a given temperature range. For EGT_over (before silencer) the temperatures reach a maximum of 622°C while for EGT_under (after silencer) the gasses reach a maximum temperature of 559°C. Current gold based catalysts would not survive gas temperatures produced by the engines. However, the Au-NRS catalyst should be able to withstand this temperature range based on in-situ PXRD and CO oxidation tests.

References

(1) The World of Gold, Timothy Green, Published by Rosendale Press, London, 1993.

(2) http://www.gold.org/investment/why_how_and_where/why_invest/demand_and_supp

(3) http://topics.bloomberg.com/gold-prices/

(4) http://www.bullion.org/content/?pid=84&pagename=Gold

(5) http://topics.bloomberg.com/gold-prices/

(6) J. Autschbach, S. Siekierski, M. Seth, P. Schwerdtfeger, and W. H. E. Schwarz, J. Comput. Chem., (2002), 2.3., 804., Dependence of relativistic effects on electronic configuration in the neutral atoms of d- and f-block elements.

(7) D. F. Mayers, Proc. R. Soc. London. Ser. A, Math. Phys. Sci. (1934-1990), 1957, 2.4.1., 93. Relativistic self-consistent field calculation for mercury.

(8). P. Pyykkö and J.-P. Desclaux, Acc. Chem. Res., (1979), 1.2., 276. Relativity and the periodic system of elements.

(9) J. Autschbach, S. Siekierski, M. Seth, P. Schwerdtfeger, and W. H. E. Schwarz, J. Comput. Chem., (2002), 2.3., 804. Dependence of relativistic effects on electronic configuration in the neutral atoms of d- and f-block elements.

(10) J. G. Cohn, Gold Bull., (1979), 1.2., 21. Selected properties of gold.

(11) H. Schmidbaur, Gold Bull., (1990), 2.3, 11. The fascinating implications of new results in gold chemistry.

(12) M. J. Ford, C. Masens, and M. B. Cortie, Surf. Rev. Lett., (2006), 1.3., 297. The application of gold surfaces and particles in nanotechnology.

(13) E. Ricci and R. Novakovic, Gold Bull., (2001) 3.4., 41. Wetting and surface tension measurements on gold alloys.

(14) K. Koga, T. Ikeshoji, and K. Sugawara, Phys. Rev. Lett., (2004), 9.2., 115507. Size and temperature dependent structural transitions in gold nanoparticles.

(15) K. Dick, T. Dhanasekaran, Z. Zhang, and D. Meisel, J. Am. Chem. Soc., (2002), 1.2.4. , 2312. Size-dependent melting of silica-encapsulated gold nanoparticles.

(16) R. J. Needs and M. Mansfield, J. Phys: Condensed Matter, (1989), 1., 7555.Calculations of the surface stress tensor and surface energy of the (111) surfaces of iridium, platinum and gold.

(17) A. Plech, R. Cerna, V. Kotaidis, F. Hudert, A. Bartels, and T. Dekorsy, Nano Lett., (2007), 7., 1026. A surface phase transition of supported gold nanoparticles.

(18) B. Soulé de Bas, M. J. Ford, and M. B. Cortie, J. Phys: Condensed Matter, (2006), 1.8., 55. Melting in small gold clusters: a Density Functional molecular dynamics study.

(19). G. S. Shafai, D. G. Kanhere, B. Soulé de Bas, and M. J. Ford, J. Phys. Chem. A, (2007), 1.1.1. , 10769. Ab initio molecular dynamical investigation of finite temperature behavior of the tetrahedral Au 19 and Au 20 clusters S. Krishnamurty.

(20) R. Meyer, C. Lemire, Sh.K. Shaikhutdinov and H.-J. Preund, Gold Bull. 37 (2004) 72.

(21) Q. Sun, P. Jena, Young Dok Kim, M. Fischer and G. Gantefor, J. Chem. Phys. 120 (2004) 6510.

(22) D. Stolcic, M. Fischer, G. Gautefor, Young Dok Kim, Q. Sun and P. Jena, J. Am. Chem. Soc. 125 (2003) 2848

(23) B.E. Salisbury, W.T. Wallace and R.L. Whetten, Chem. Phys. 262 (2000) 131.

(24) M. Okamura, Y. Kitigawa, M. Haruta and Y. Yamaguchi, Appl. Catal. A: Gen. 291 (2005) 37.

(25) G.C. Bond, C. Louis, D.T. Thompson, Catalysis by Gold

(26) N. Lopez, T.V.W. Janssens, B.S. Clausen, Y. Xu, M. Mavrikakis, T. Bligaard and J.K. Norskov, J. Catal. 223 (2004) 232; N. Lopez and J.K. Norskov, J. Am. Chem. Soc. 124 (2002) 11262.

(27) Z.-P. Liu, P. Hu and A. Alavi, J. Amer. Chem. Soc. 124 (2002) 14770.

(28) M.B. Knickelbaum, Ann Rev. Phys. Chem. 50 (1999) 79.

(29) G.C. Bond and D.T. Thompson, Catal. Rev.-Sci. Eng. 41 (1999) 319.

(30) M.E. Schrader, Surf. Sci. 78 (1978).

(31). Y. lizuka, A. Kawamoto, K. Akita, M. Date, S. Tsubota, M. Okumura and M. Haruta, Catal. Lett. 97 (2004) 203.

(32) J. Hagen, L.D. Socaciu, M. Elyazyfer, U. Heiz, T.M. Bernhardt and L. Woste, Phys. Chem. Chem. Phys. 4 (2002) 1707.

(33) M. Haruta, J. New Mater. Electrochem. Systems 7 (2004) 163.

(34) B. Schumacher, V. Plzak, K. Kinne and R.J. Behm, Catal. Lett. 2003 (2003) 109.

(35) Z.-P. Liu, P. Hu and A. Alavi, J. Am. Chem. Soc. VIA (2002) 14770.

(36) Z.-P. Liu, X.-Q. Gong, J. Kohanoff, C. Sanchez and P. Hu, Phys. Rev. Lett. 91 (2003) 266102.

(37) L.M. Molina and B. Hammer, Appl. Catal. A: Gen. 291 (2005) 21.

(38) L.M. Molina, M.D. Rasmussen and B. Hammer, J. Chem. Phys. 120 (2004) 7673.

(39) M. Mavrikakis, P. Stoltze and J.K. Norskov, Catal. Lett. 64 (2000) 101.

(40) G. C. Bond and D. T. Thompson, Gold Bull., (2000), 3.3, 41. Gold-catalysed oxidation of carbon monoxide.

(41) M. Haruta, Catalysis of gold nano-particles deposited on metal oxides. Cattech, (2002), 102-115.

(42) T. Akita, K. Tanaka, S. Tsubota, M. Haruta J. Electron microscopy, 49 (2000) 657

(43) D.A.H Cunningham, W. Vogel, H. Kagayama, S. Tsubota, M. Haruta, Cattal. Lett,.51 (1998) 53.

(44) M. Date, M. Haruta, J. Catal., 178 (2001) 221.

(45) W. Vogel, D. A. H. Cunningham, K. Tanaka, and M. Haruta, Catal. Lett., 40 (1996) 175.

(46) M. Mavrikakis, P. Stoltze, and J. K. Nfrskov, Catal. Lett., 64 (2000) 101.

(47) D. M. Young and A. D. Crowell. Physical Adsorption of Gasses. Butterworths, London, 1962.

(48) S. Brunauer, P. H. Emmett, and E. Teller. J Amer. Chem. Soc. 60 (1968), 309.

(49) Standard Test Method for surface area of catalysts. (D3663-78); Standard Test Methods for Hydrogen Chemisorption on Supported Platinum and Alumina Catalysts. (D3908-5080) American Society for Testing and Materials (ASTM), Philadelphia, PA.

(50) H. P Klug and L. E. Alexander. X-raydiffraction procedures for amorphous and polycrystalline materials. 2nd edition, Wiley.

(51) The Rietveld Method. R. A. Young . Oxford university press, 1969.

(52) N. F. M. Henry, H. Lipson, W. A. Wooster. The Interpretation of X-ray Diffraction Photographs, Macmillan: London, 1951.

(53) D. B. Williams C. B. Carter, Transmission Electron Microscopy for materials science, Springer.

(54) L. A. Hermans and J.W. Geus, Stud. Surf. Sci. Catal. 4 (1979) 113.

(55) J. A. van Dillen, J. W. Geus, L. A. Hermans and J. van der Meijden Proc. 6th Intern. Congr. Catal., London, 1976, G.C. Bond, P.B. Wells, F.C. Tompkins (eds.), The Chemical Society, London (1977) p. 677.

(56) Y. A. Nechayev and G. V. Zvonareva, Geokhimiya 6 (1983) 919.

(57) S. Tsubota, D. A. H. Cunningham, Y. Band and M. Haruta, Stud. Surf. Sci. Catal. 91 (1995) 227.

(58) F. Moreau, G. C. Bond and A. O. Taylor, J. Catal. 231 (2005) 105.

(59) R. Zanella, L. Delannoy and C. Louis, Appl. Catal. A: Gen. 291, (2005) 62.

(60) A. Rubio-Ponce, A. Conde-Gallardo and D. Olguin, Phys. Rev., B78, (1978) 035107-1.

(61) V. I. Khitrova, M. F. Bandule and Z. G. Pinsker, Kristallografiya, 22, (1977), 714 .

(62). A. Suzuki and Y. Kotera, Bull. Chem. Soc. Jpn., 35, (1962) 1353.

(63) R. D. Shannon and J. A. Pask, J. Am. Ceram. Soc., 48, (1965) 391.

(64) E. F. Heald and C. W. Weiss, Am. Mineral., 57, (1972) 10.

(65) K. J. D. MacKenzie, Trans. J. Br. Ceram. Soc., 74, (1975) 77.

(66) S. Hishita, I. Mutoh, K. Koumoto, H. Yanagida, Ceram. Int., 9, (1983) 41 .

(67) J. F. Banfield, B. L. Bischoff and M. A. Anderson, Chem. Geol., 110, (1993) 211.

(68) A. A. Gribb and J. F. Banfield, Am. Mineral., 82, (1997), 717.

(69) H. Zhang and J. F. Banfield, Phase Transformations and Systems Driven Far From Equilibrium, Materials Research Society, Pennsylvania, 619-624. (1998).

(70) H. Zhang and J. F. Banfield, J. Mater. Sci., 8, (1998), 2073.

(71) X. Z. Ding, X. H. Liu and Y. Z. He, J. Mater. Sci. Lett., 15, 1789 (1996). 13. S. C. Liao, K. D. Pae and W. E. Mayo, Nanostruct. Mater., 5, (1995) 319.

(72) X. Z. Ding, L. Liu, X. M. Ma, Z. Z. Qi and Y. Z. He, J. Mater. Sci. Lett., 13, (1994), 462.

(73) Q. Xu, J. Zhang, Z. Feng, Y. Ma, X. Wang and C. Li, Chem. Asian J., 5, (2010) 2158.

(74) W. T. Pennington, J. Appl. Cryst., 32, (1999), 1028.

(75) L.A. Hermans and J.W. Geus, Stud. Surf. Sci. Catal. 4 (1979) 113.

(76) J.A. van Dillen, J.W. Geus, L.A. Hermans and J. van der Meijden Proc. 6th Intern. Congr. Catal., London, 1976, G.C. Bond, P.B. Wells, F.C. Tompkins (eds.), The Chemical Society, London (1977) p. 677.

(77) Y.A. Nechayev and G.V. Zvonareva, Geokhimiya 6 (1983) 919.

(78) S. Tsubota, D.A.H. Cunningham, Y. Band and M. Haruta, Stud. Surf. Sci. Catal. 91 (1995) 227.

(79) F. Moreau, G.C. Bond and A.O. Taylor, J. Catal. 231 (2005) 105.

(80) R. Zanella, L. Delannoy and C. Louis, Appl. Catal. A: Gen. 291 (2005) 62.

(81) D. Mott, J. Luo, A. Smith, P. N. Njoki, L. Wang, C-J. Zhong, Nanoscale Res Lett (2007) 2:12-16

(82) M. Okumura, M. Haruta, Chem. Lett., (1999) CL-991092

(83) M. Haruta, Catal. Surveys Jpn., (1997) 61.

(84) M. Haruta, The abilities and potential of gold as a catalyst, Report of the Osaka National Research Institute 393 (1999) 1-93.

(85) R. Zanella, L. Delannoy, C Louise. Appl Catal A, 291, (2005) 62-72.

(86) K. Suttiponparnit, J. Jaing, M. Sahu, S. Suvchittanont, T Charinpanitkul. Nanoscale Res Lett 6 (2011) 27.

(87) D.H Barrett, P.J Franklyn and M.S Scurrell. Variable Temperature Study of Au and Au-Pt Nanoparticles on Selected Oxide Supports. MRS Proceedings, 1279, (2010), 40.

(88) S. Iijima, Nature, 354, (1991), 56-58.

(89) M. Haruta, S. Tsubota, T. Kobayashi, H. Kageyama, M.J. Genet and B. Delmon., J.Catal. 144 (1993) 175.

(90) M. Haruta, H. Kageyama, N. Kamijo, T. Kobayashi and F. Delannay, Stud. Surf. Sci. Catal. 44 (1988) 33.

(91) Y. Yuan, A.R Kozlova, K. Asakura, H. Wan, K. Tsai and Y. Iwasawa, J. Catal. 170 (1997) 191.

(92) Y. Yuan, K. Asakura, H. Wan, K. Tsai and Y. Iwasawa, Catal. Today 44 (1998) 333.

(93) M.M. Schubert, S. Hackenberg, A.C.v. Veen, M. Muhler, V. Plzak and R.J. Behm, J. Catal. 197 (2001) 113.

(94) S. Arii, F. Mortin, A.J. Renouprez and J.L. Rousset, J. Am. Chem. Soc. 126 (2004) 1199.

(95) M. Okumura, S. Tsubota and M. Haruta, J. Molec. Catal. A: Chem. 199 (2003) 73.

(96) M. Okumura, S. Nakamura, S. Tsubota, T. Nakamura, M. Azuma and M. Haruta, Catal. Lett. 51 (1998) 53.

(97) M. Haruta, Catal. Today 36 (1997) 153. 19.

(98) S.D. Lin, M. Bollinger and M.A. Vannice, Catal. Lett. 17 (1993) 245.

(99) Y. Yuan, K. Asakura, H. Wan, K. Tsai and Y. Iwasawa, Catal. Lett. 42 (1996) 15.

(100) M. M. Schubert, S. Hackenberg, A.C.v. Veen, M. Muhler, V. Plzak and R.J. Behm, J. Catal. 197 (2001) 113.

(101) M. Haruta, N. Yamada, T. Kobayashi and S. Iijima, J. Catal. 115 (1989) 301.

(102) M. Haruta, Stud. Surf. Sci. Catal. 110 (1997) 123.

(103) S.-J. Lee and A. Gavriilidis, J. Catal. 206 (2002) 305.

(104) Mellor J.R, Palazov A.N, Grigorova B.S, Greyling J.F, Reddy K, Letsoalo MP, Marsh JH., Catal. Today., 71, (2002), 145.

(105) (Seker E, Gulari E (2002) Appl. Catal. A 232:203.

(106) Pattrick G, van der Lingen E, Corti CW, Holliday RJ, Thompson DT (2003).

(107) Proc. 6th International Congress on Catalysis and Automotive Pollution Control (CAPOC 6), Brussels, Belgium. European Patent Application, EP1043059 A1.

(108) Wenfu Yan, Bei Chen, S. M. Mahurin, V. Schwartz, D. R. Mullins, Andrew R. Lupini,S. J. Pennycook, Sheng Dai, and S. H. Overbury, J. Phys. Chem. B 2005, 109, 10676-10685.

(109) J. Levec, A. Pintar, Catalytic wet-air oxidation processes: A review. Catal. Today. 124 (3-4) (2007) 172-184.

(110) B. O'Regan, M. Gratzel,"A low-cost, high-efficiency solar cell based on dye-sensitized colloidal TiO_2 films." Nature, 353, (1991) 737-400.

(111) A. Fujishima, T.N. Rao, D.A. Tryk, "TiO_2 Photocatalysts and Diamond Electrodes", Electrochim, Acta, 45, (2000) 4683-4690 .

(112) H. J. Lee, G.M. Kale, Int. J. Appl. Ceram. Technol, 5, 657-665 (2008).

(113) A. V. Grigorieva, et al..., Titania nanotubes, nanorods and nanopowder in the carbon oxidation process, Solid State Sci, (2010).

(114) M. Haruta, Chem. Rec. 3 (2003) 75.

(115) M. Reibold, P. Paufler, A. A. Levin, W. Kochman, N. Patzke, and D. C. Meyer., Nature., (2006), 444, 286.

(116) R. I. Jaffee and N. E Promisel., The science, technology and application of titanium: Proceedings of the 1st conference on titanium, (1968), London , Pergamom press 1970.

(117) A. Fujishima, K. Hashimoto and T. Watanabe, TiO_2 Photocatalysis: Fundamentals and applications, BKC, USA, (1999).

(118) T. Kasuga, M. Hiramatsu, A. Hoson, T. Sekino and K. Niihara, Langmuir, 14, 3160.

(119) X. Chen and S. S. Mao, Chem, Rem., 107, (2007) 2891.

(120) D. V. Bavykin, J. M. Friedrich and F. C. Walsh, Adv. Mater., 18 (2006), 2807.

(121) Q. Chen, L. M. Peng, Int. J. Nanotechnology., 4, (2007) 44.

(122) H. H. Ou and S. L. Lo, Sep. Purif. Technol., 58, (2007), 179.

(123) D. V. Bavykin and F. C. Walsh. Titanate and Titania Nanotubes Synthesis, Properties and Applications.

(124) 23. T. Kasuga, M. Hiramatsu, A. Hoson, T. Sekino and K. Niihara, Adv. Mater.,14, (1999), 1307.

(125). Y. Lan, X. Gao, H. Zhu, Z. Zheng, T. Yan, F. Wu, S. P. Ringer and D. Song, Adv. Funct. Mater., 15 (2005), 1310.

(126). X. D. Meng, D. Z. Wang, J. H. Liu and S. Y. Zhang, Mater. Res. Bull., 39, (2004) 2163.

(127) http://www.freepatentsonline.com/7709407.html.

Appendix

Below are the synthesis conditions and heating temperatures of the 9 prepared samples, all samples were repeated in triplicate using amorphous silica as a support unless otherwise stated :

Samples 1 (5% Au) : (0.1 M urea, pH 2.85, 1hr, 120°C), 2 (0.1 M urea, pH 2.85, 1hr, 300°C), 3 (0.1 M urea, pH 2.85, 1hr, 300°C)

Samples 2 (5% Au) : (0.1 M urea, 45 min at 120°C), (0.1 M urea, 45 min at 200°C), (0.1 M urea, 45 min at 300°C)

Samples 3 (5% Au) : (1.0 M urea, 0.25 M NH_4OH, high-low pH), (1.0 M urea, 0.25 M NH_4OH, high-low pH, 120°C 1hr), (1.0 M urea, 0.25M NH_4OH, high-low pH 300°C, 1hr)

Samples 4 (5% Au) : (1.0 M urea, 0.25 M NH_4OH, pH 9), (1.0 M urea, 0.25 M NH_4OH, pH 9 120°C, 1hr), (1.0 M urea, 0.25 M NH_4OH, pH 9 300°C, 1hr)

Samples 5 (5% Au) : (1.0 M urea, 0.25 M NH_4OH, pH 9), (1.0 M urea, 0.25 M NH_4OH, pH 9, 120°C, 1hr), (1.0 M urea, 0.25 M NH_4OH, pH 9, 200°C, 1hr), (1.0 M urea, 0.25 M NH_4OH , pH 9, 200°C, 1hr), (1.0 M urea, 0.25 M NH_4OH, pH 9, 300°C, 1hr, NaCl std)

Samples 6 (5%Au-1% Pt) : (1.0 M urea, 0.25M NH_4OH, pH 9), (1.0 M urea, 0.25 M NH_4OH, pH 9, 200°C, 1hr), (1.0 M urea, 0.25 M NH_4OH, pH 9, 300°C, 1hr), (1.0 M urea, 0.25 M NH_4OH, pH 9, 300°C, 1hr, NaCl std)

Samples 7 (5% Au-2% Pt) : (1.0 M urea, 0.25 M NH_4OH, pH 9, 200°C, 1hr), (1.0 M urea, 0.25 M NH_4OH, pH 9, 300°C, 1hr)

Samples 8 (5% Au-1% Pt) : (1.0 M urea, 0.25 M NH_4OH, pH 9, 200°C, 1hr), ZrO_2 support (1.0M urea, 0.25M NH_4OH, pH 9, 300°C, 1hr) ZrO_2 support (1.0 M urea, 0.25 M

NH_4OH, pH 9, 300°C, 1hr, NaCl std)

Samples 9 (5% Au-2% Pt) : (1.0 M urea, 0.25 M NH_4OH, pH 9, 200°C, 1hr), ZrO_2support (1.0 M urea, 0.25 M NH_4OH, pH 9, 300°C, 1hr), ZrO_2support (1.0 M urea, 0.25 M NH_4OH, pH 9, 300°C, 1hr, NaCl std)

Powder Diffraction patterns with reaction conditions ;

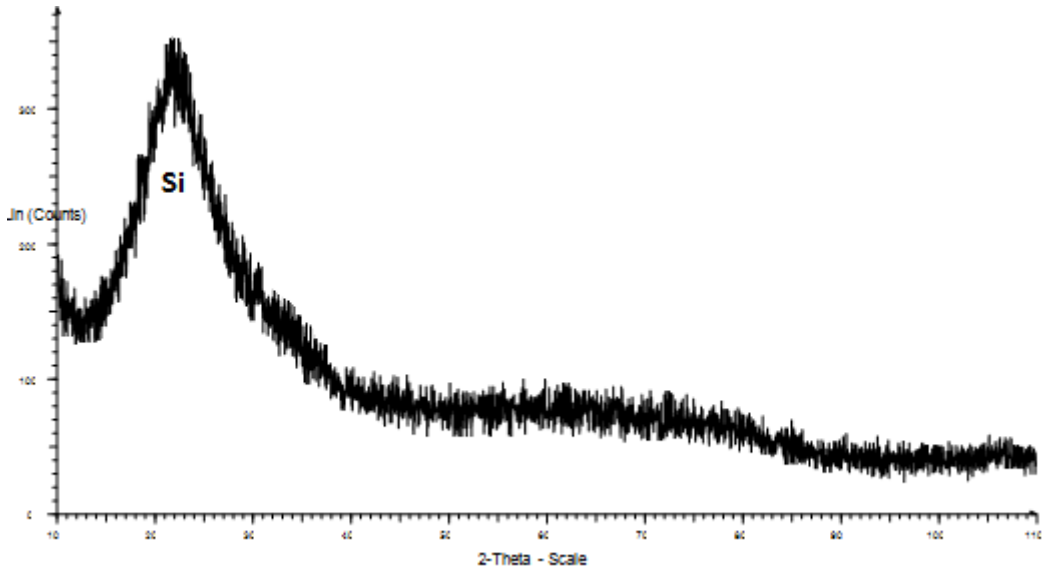


Figure 12.7: 5% Au, 0.1 M urea, pH 2.85

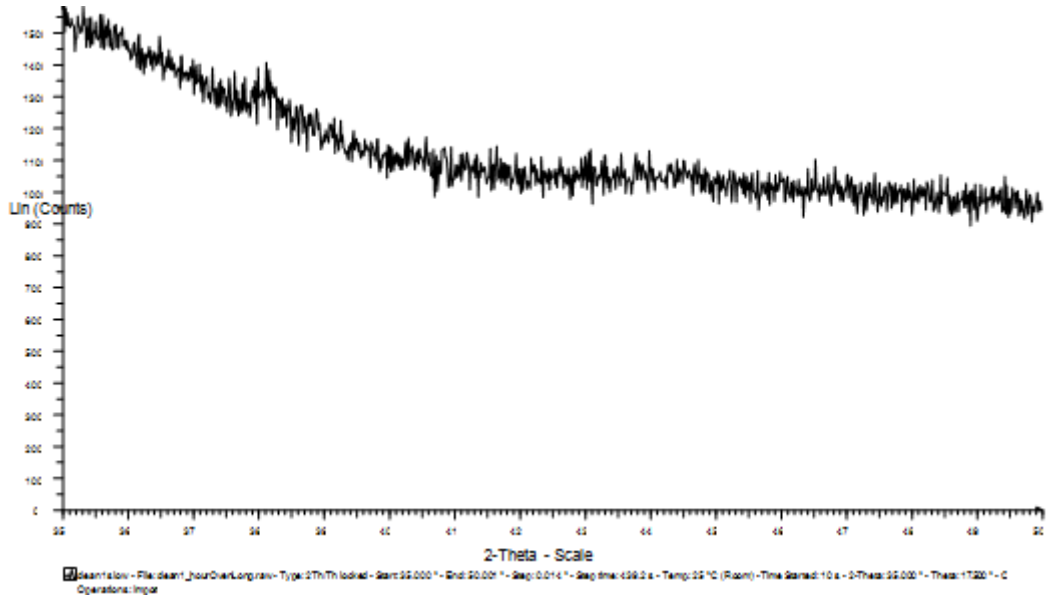


Figure 12.8: 5% Au, 0.1 M urea, pH 2.85, 120°C, 1hr

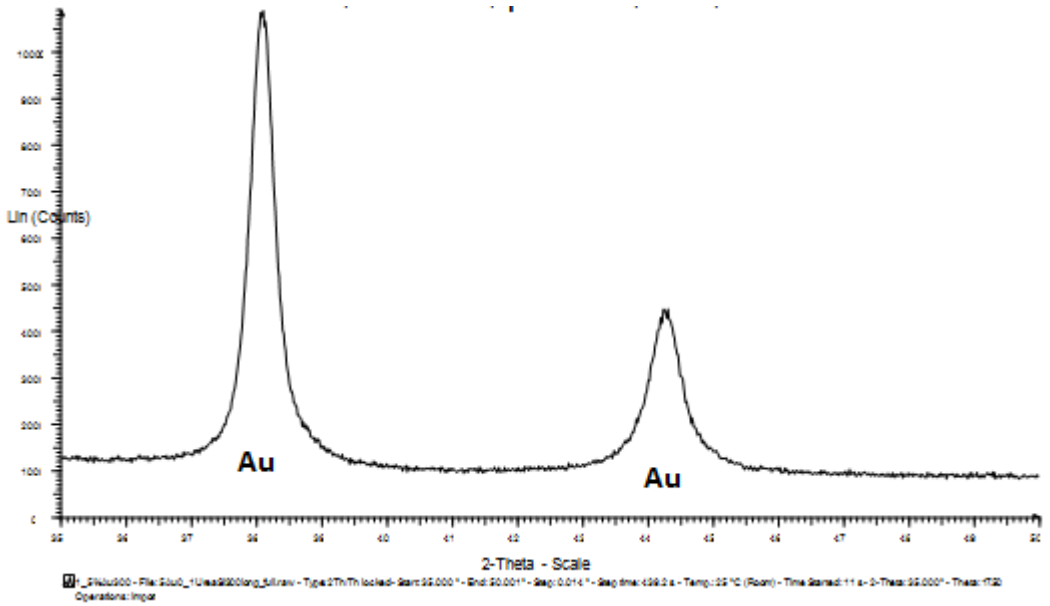


Figure 12.9: 5% Au, 0.1 M urea, pH 2.85, 300°C, 1hr

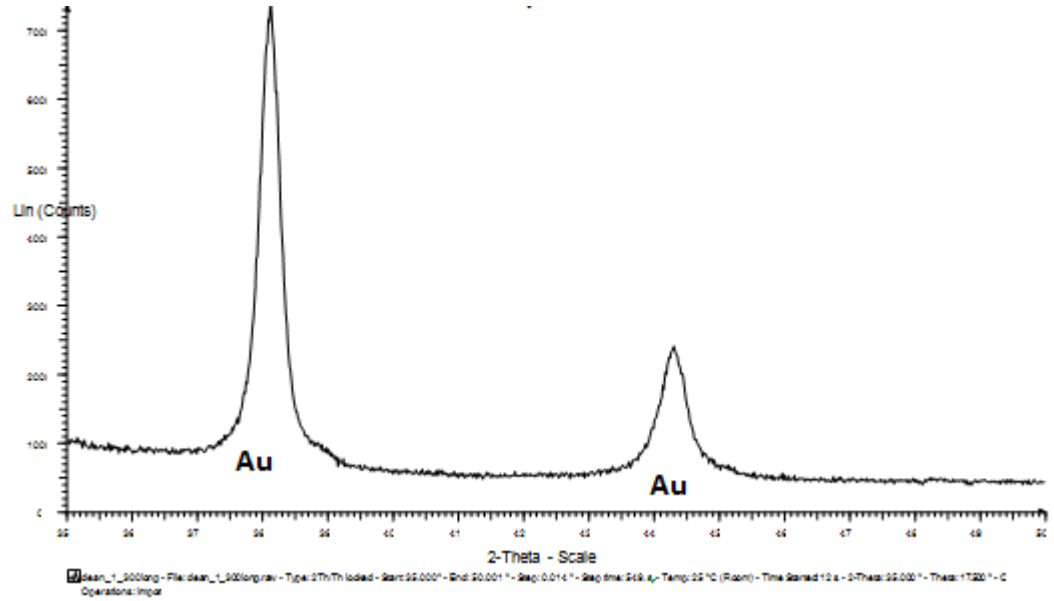


Figure 12.10: 5% Au, 0.1 M urea, pH 2.85, 300°C, 1hr, repeat

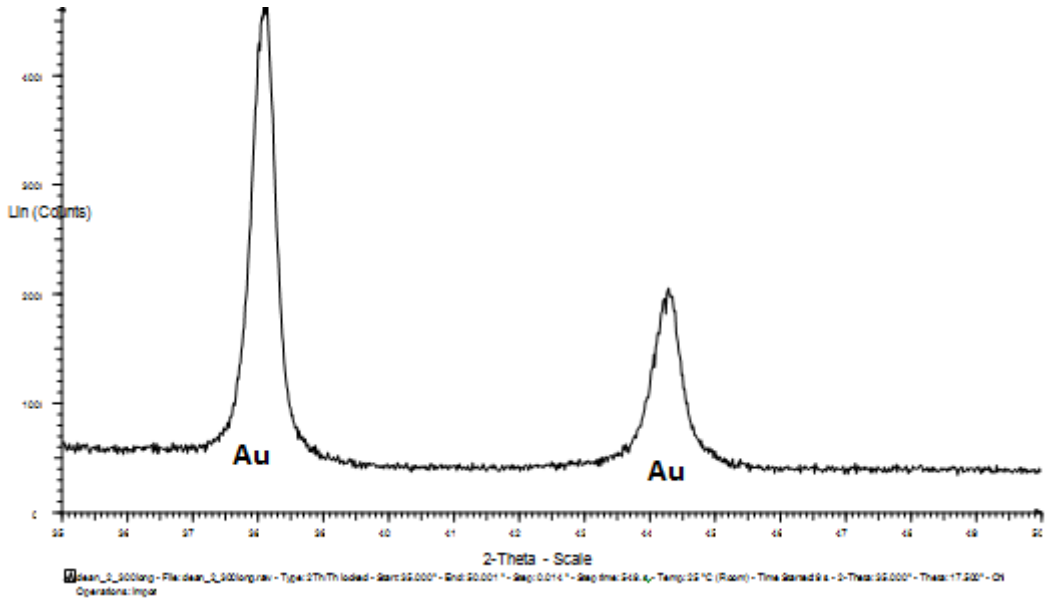


Figure 12.11: 5% Au, 0.1 M urea, pH 2.85, 300°C, 1hr, repeat

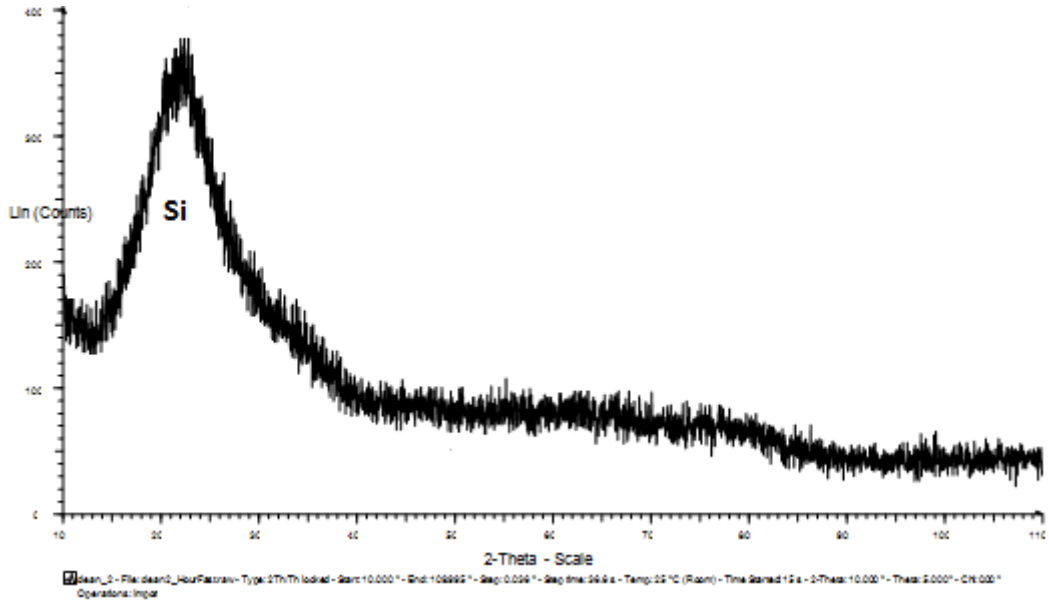


Figure 12.12: 5% Au, 1.0 M urea, pH 2.85, 120°C, 1hr

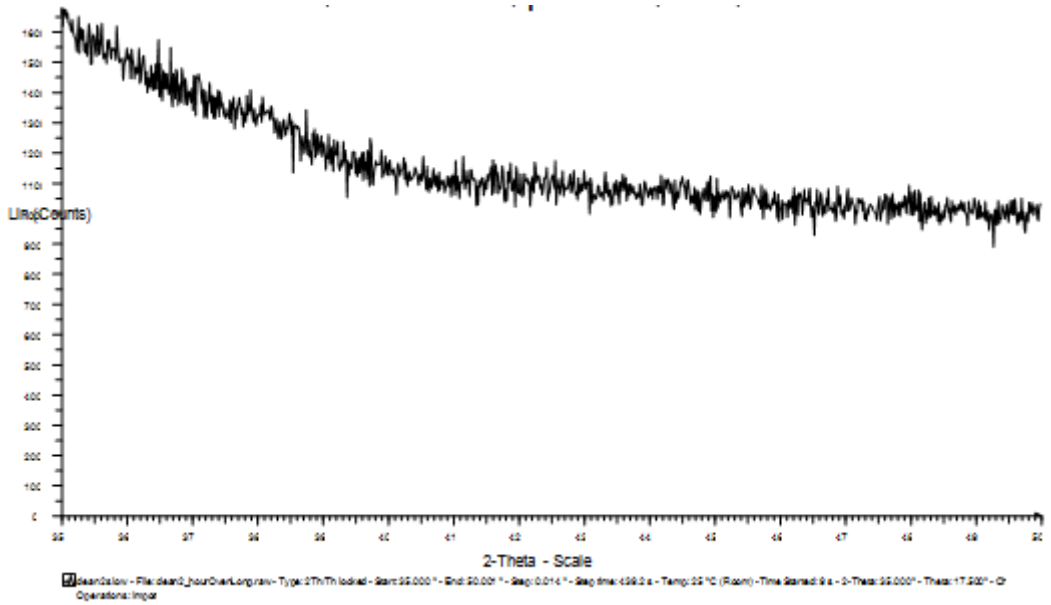


Figure 12.13: 5% Au, 1.0 M urea, pH 2.85, 120°C, 1hr

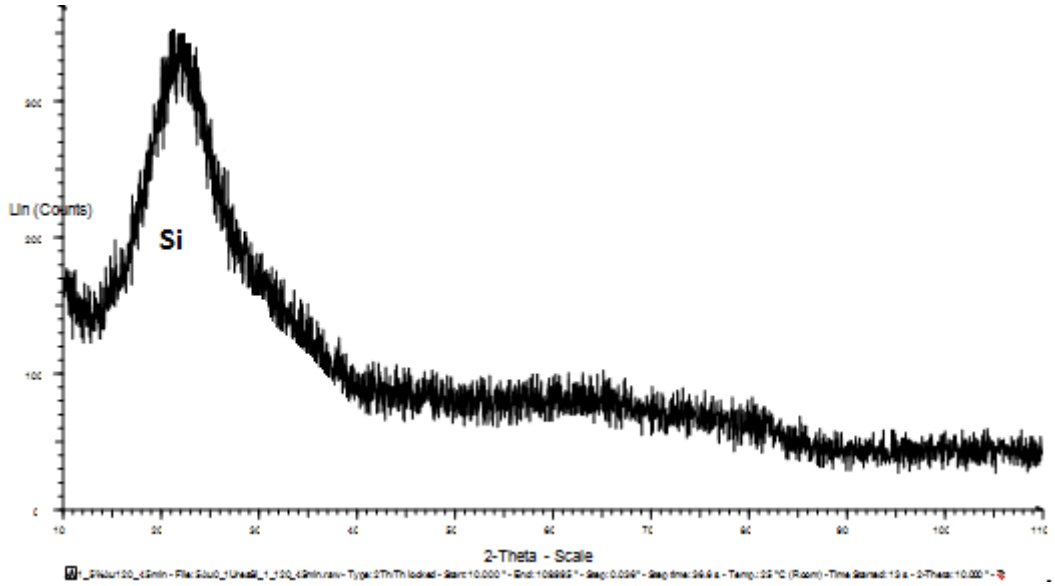


Figure 12.14: 5% Au, 0.1 M urea, pH 2.85, 120°C, 1hr, repeat

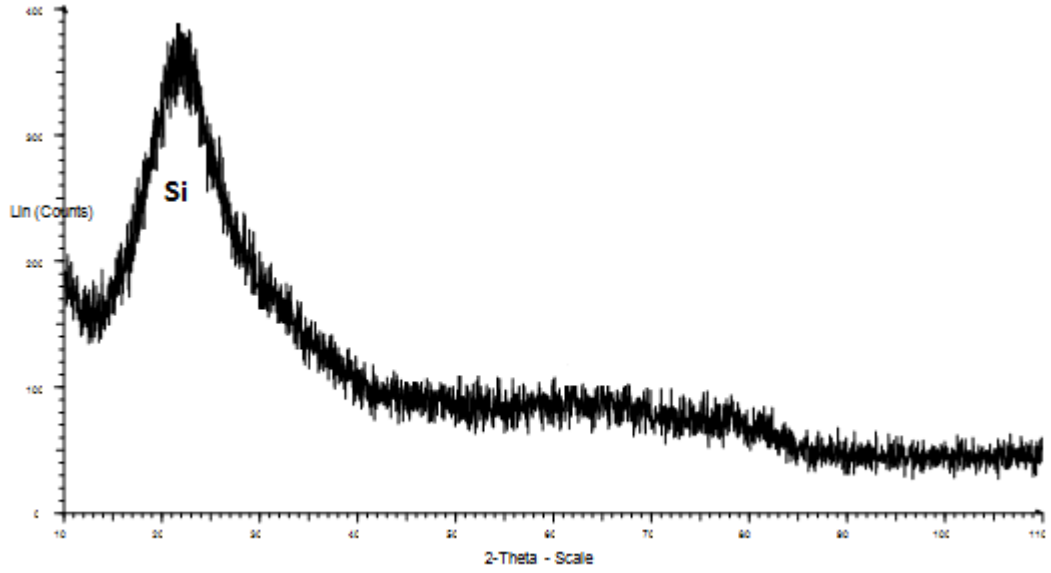


Figure 12.15: 5% Au, 0.1 M urea, pH 2.85

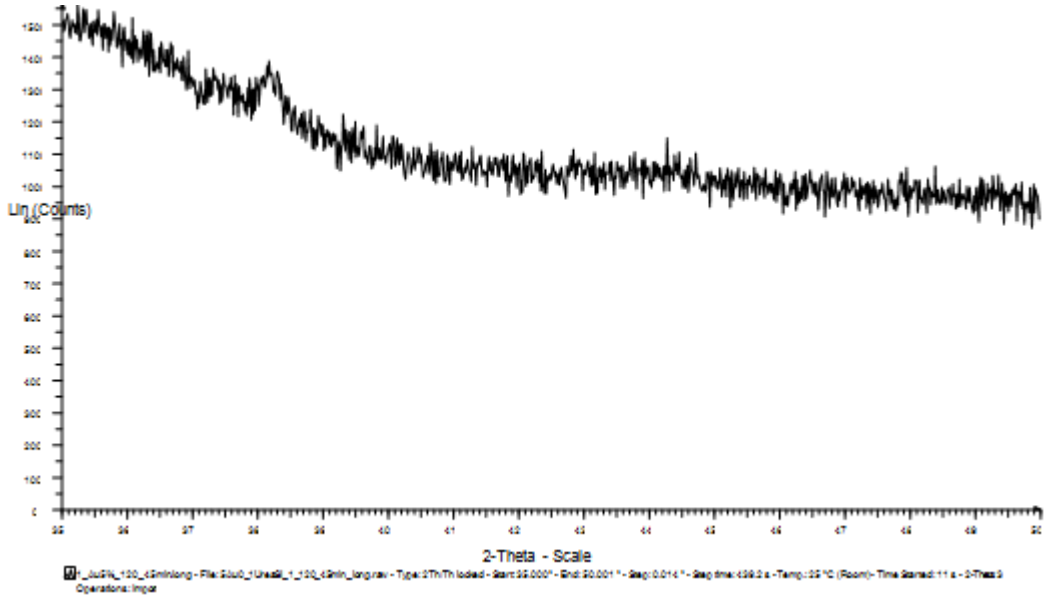


Figure 12.16: 5% Au, 0.1 M urea, pH 2.85, 120°C, 1hr

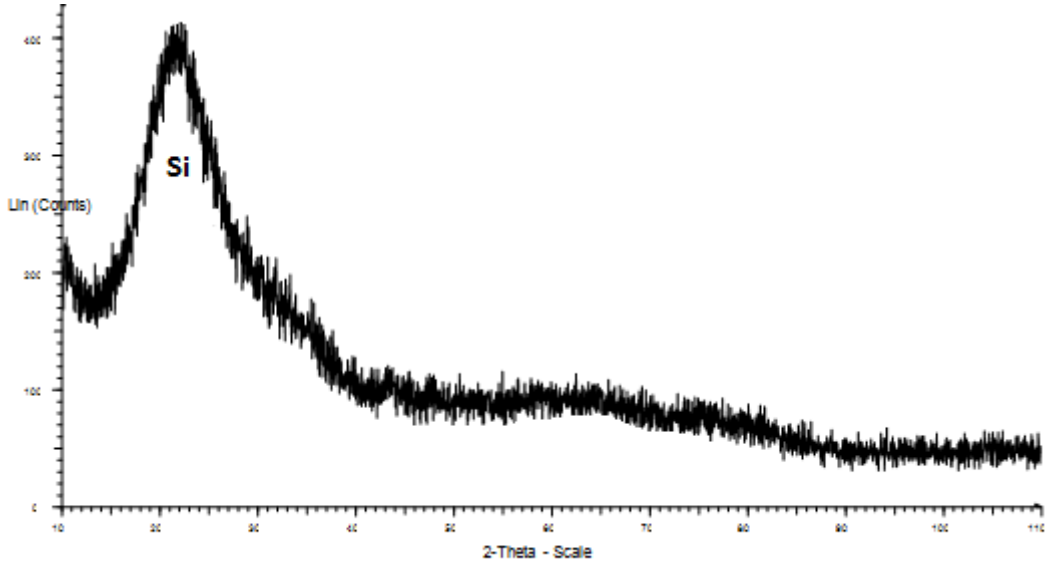


Figure 12.17: 5% Au, 0.1 M urea, pH 2.85, 120°C, 1hr, repeat

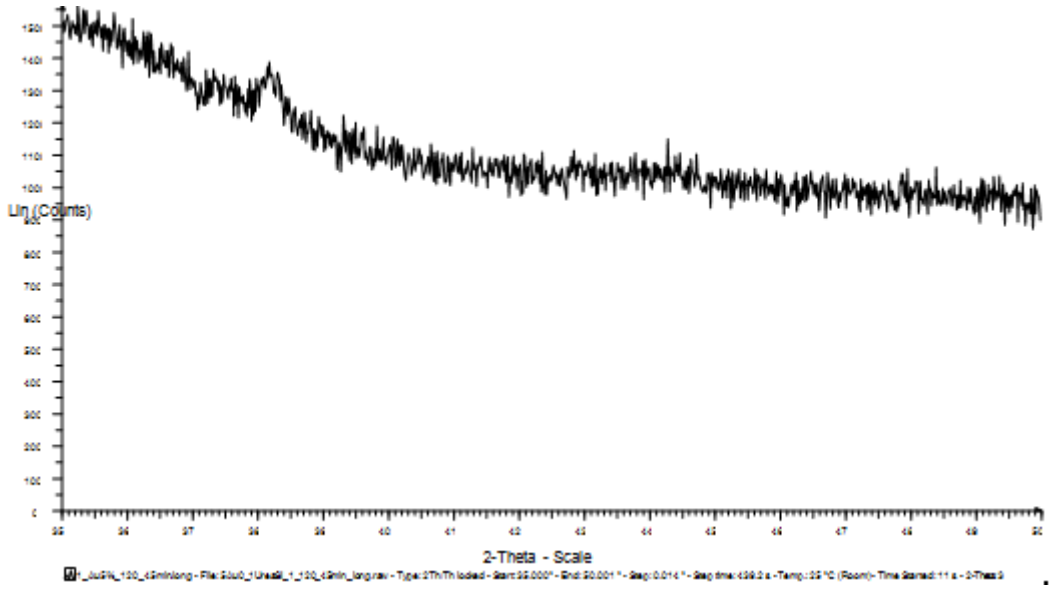


Figure 12.18: 5% Au, 0.1 M urea, pH 2.85, 120°C, 1hr, repeat

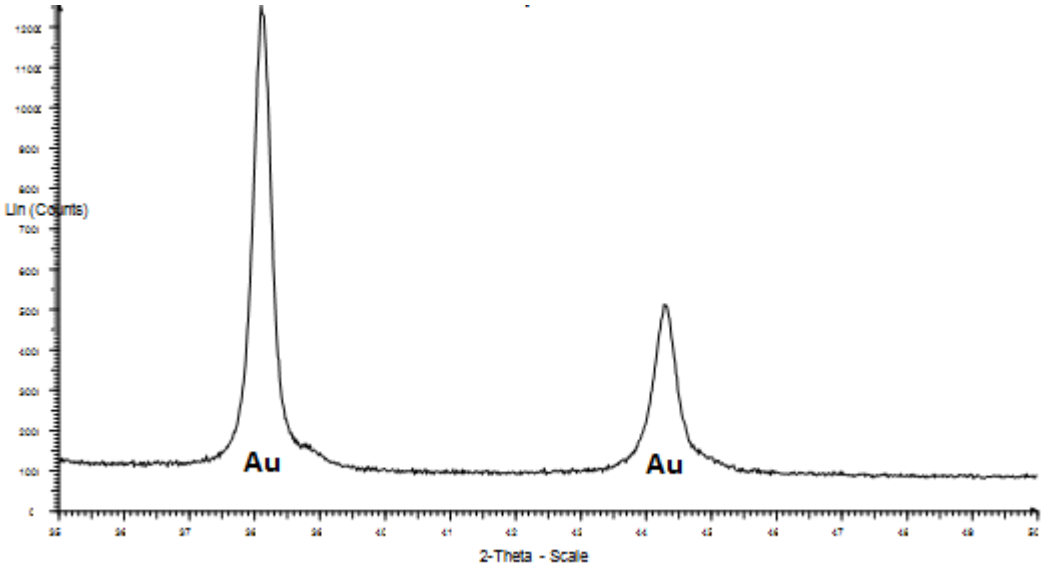


Figure 12.19: 5% Au, 1.0 M urea, pH 2.85, 300°C, 1hr

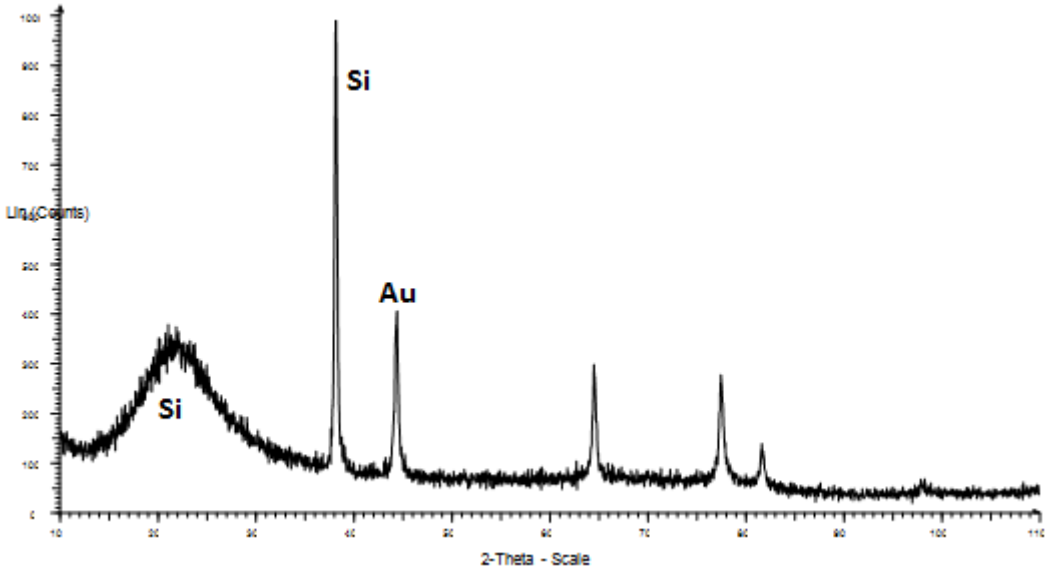


Figure 12.20: 5% Au, 1.0 M urea, pH 2.85, 300°C, 1hr

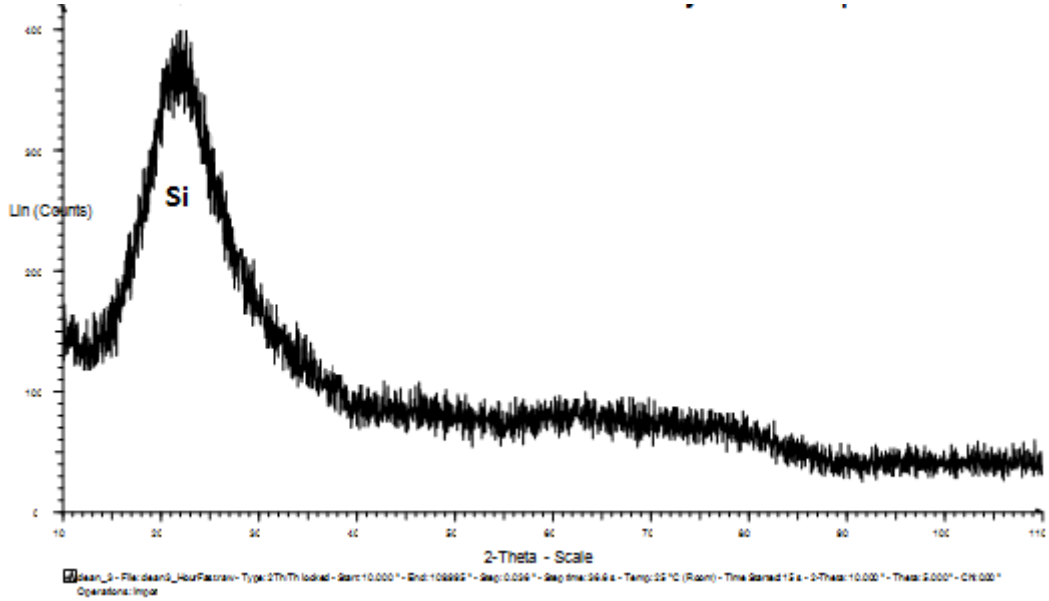


Figure 12.21: 5% Au, 1.0 M urea, 0.1 M NH_4OH, pH 9 start, pH 4 end

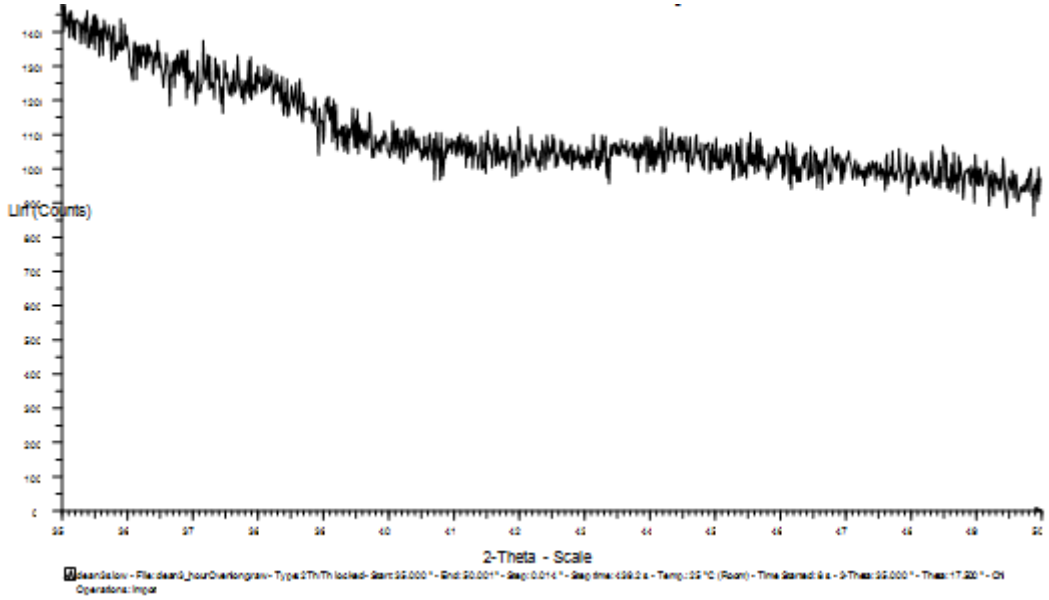


Figure 12.22: 5% Au, 1.0 M Urea, 0.1 M NH_4OH, 120°C, 1hr

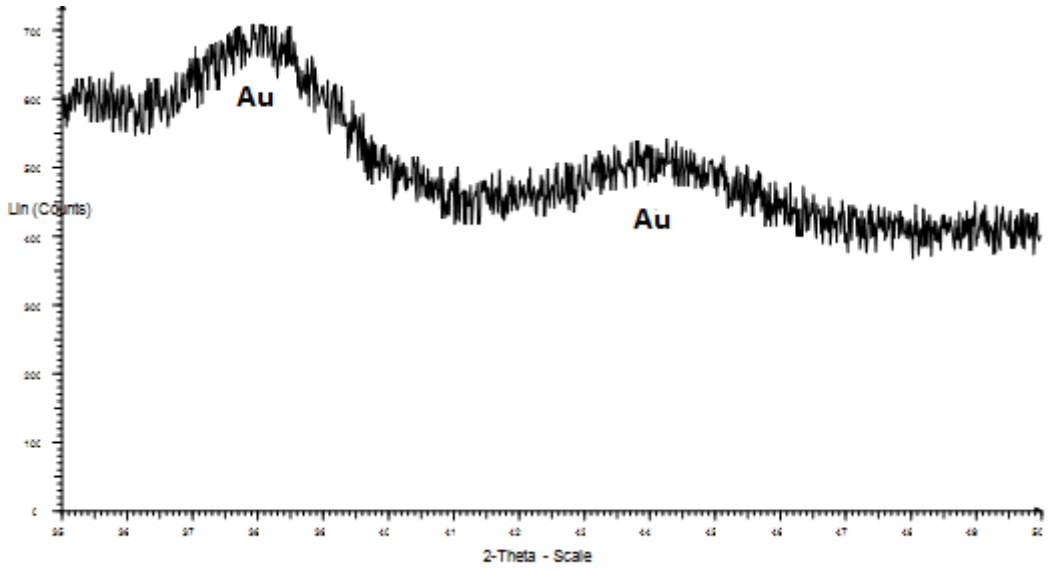


Figure 12.23: 5% Au, 1.0 M Urea, 0.25 M NH_4OH, pH 9. then pH 4, 300°C, 1hr

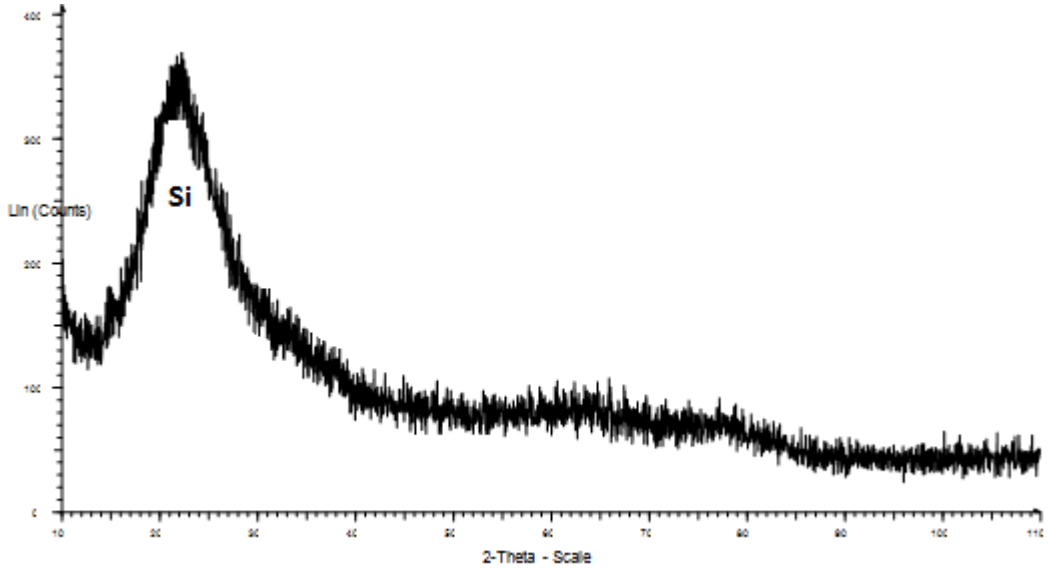


Figure 12.24: 5% Au, 1.0 M Urea, 0.25 M NH_4OH, pH 9

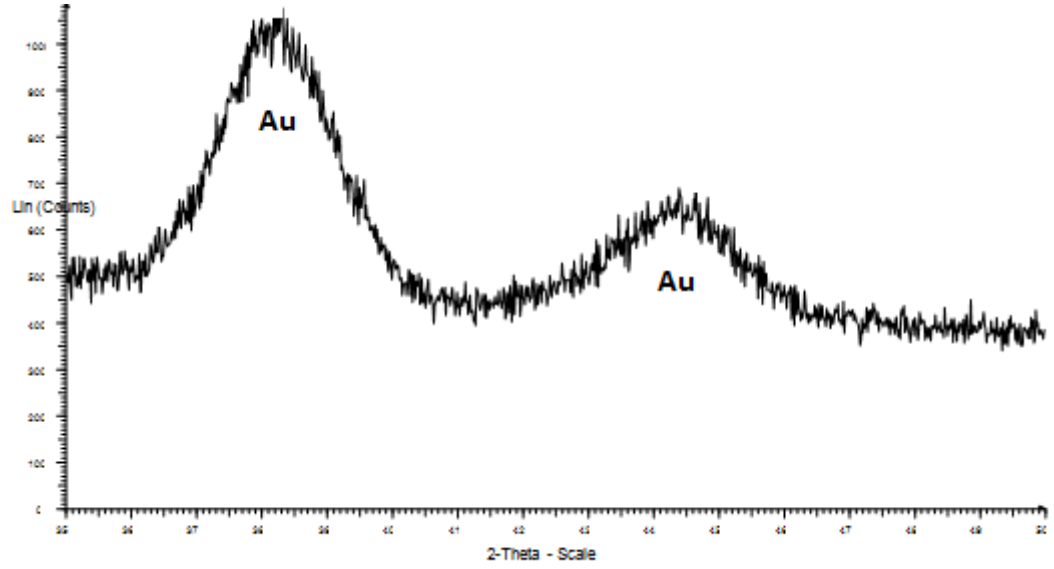


Figure 12.26: 5% Au, 1.0 M Urea, 0.25 M NH_4OH, pH 9, 300°C, 1hr

PXRD patterns.

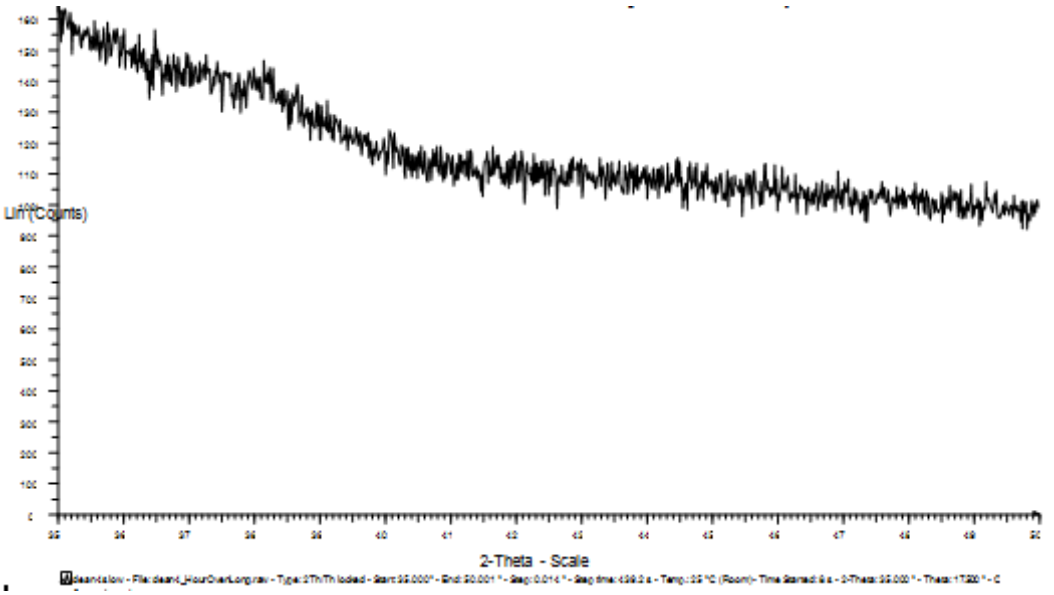


Figure 12.25: 5% Au, 1.0 M Urea, 0.25 M NH_4OH, pH 9, 120°C, 1hr

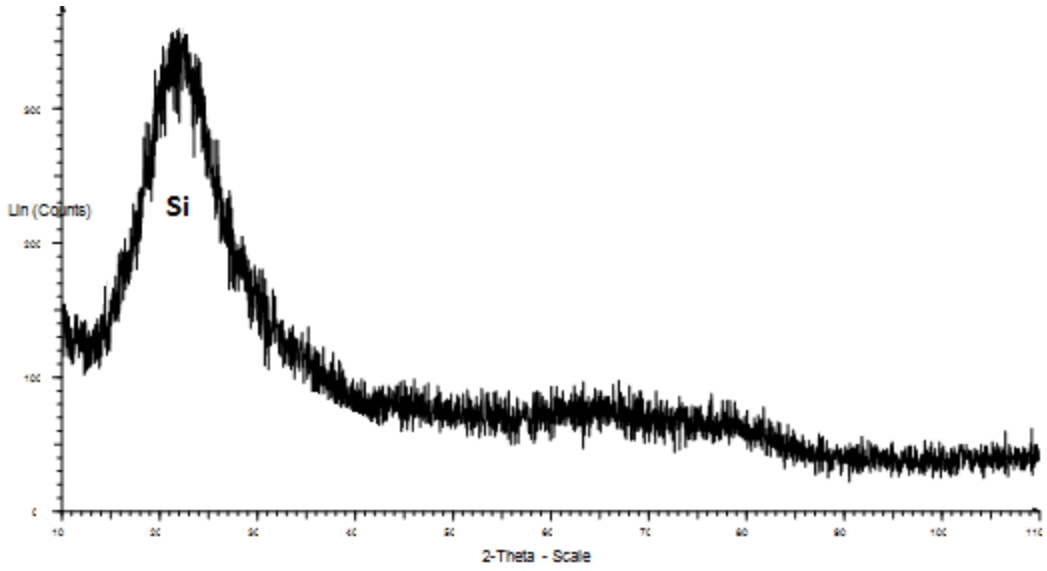


Figure 12.27: 5% Au, 1.0 M Urea, 0.25 M NH_4OH, pH 7

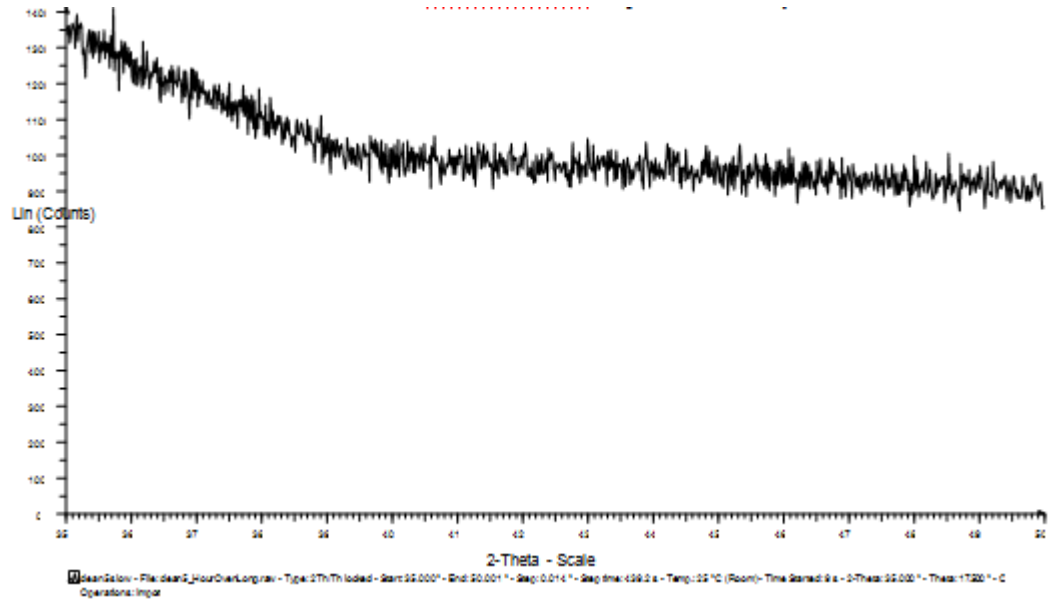


Figure 12.28: 5% Au, 0.1 M Urea, 0.25 M NH_4OH, pH 7, 120°C, 1hr

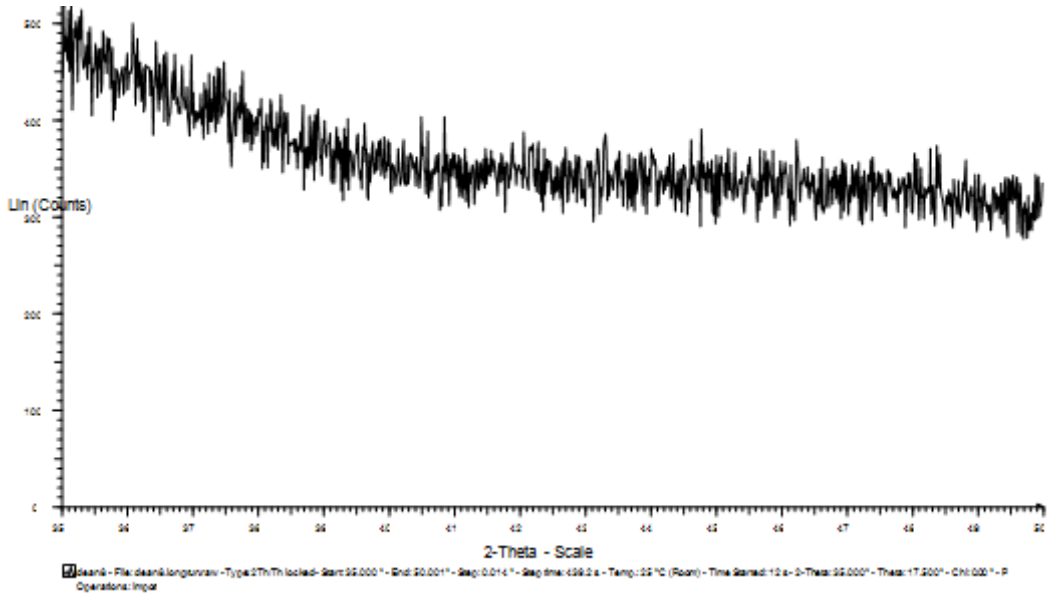


Figure 12.29: 5% Au, 1% Pt, 1.0 M Urea, 0.25 M NH_4OH, pH 7

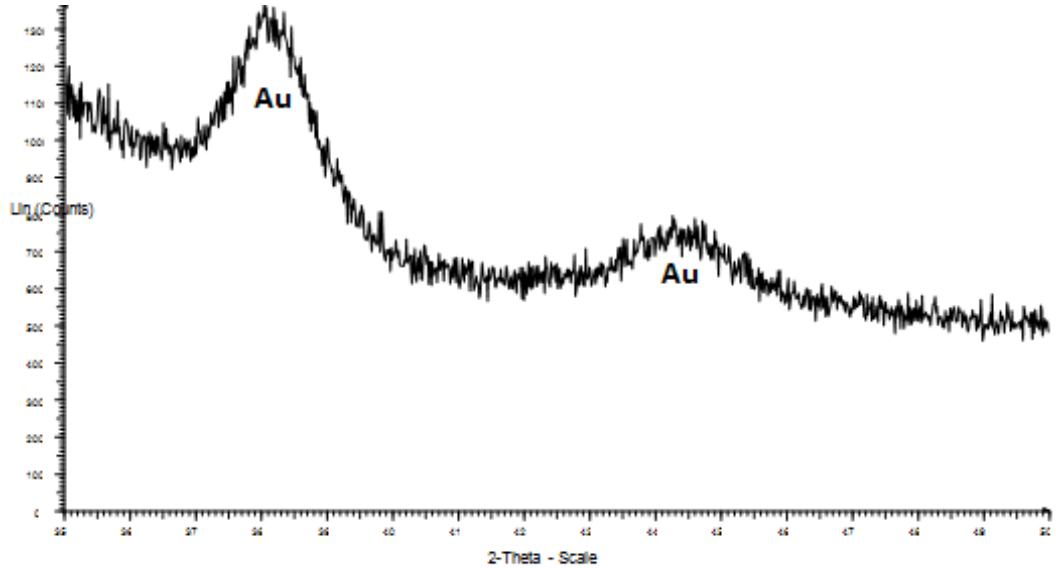


Figure 12.30: 5% Au, 1.0 M Urea, 0.25 M NH_4OH, pH 7, 200°C, 1hr

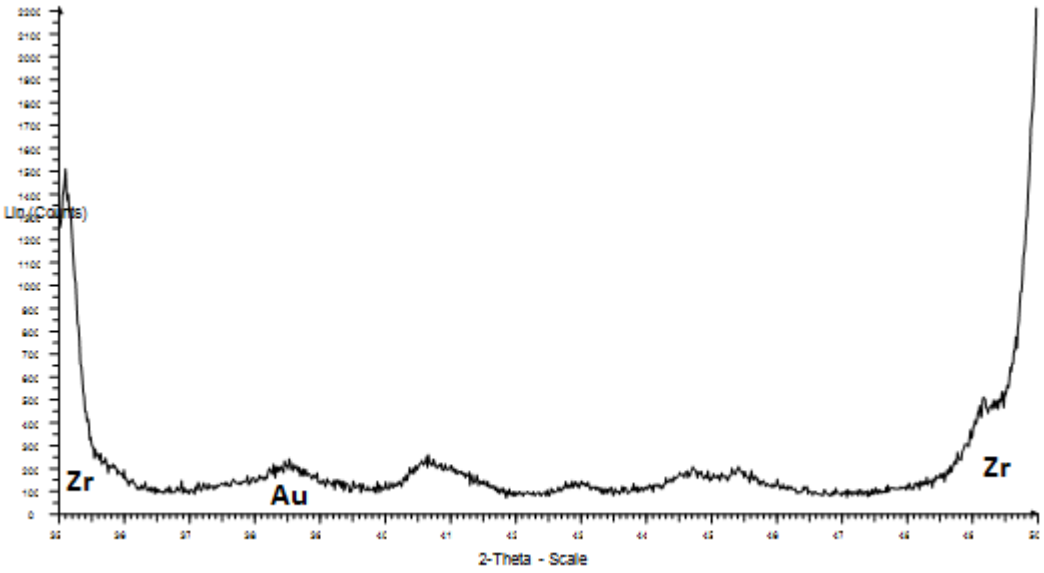


Figure 12.31: 5% Au, 1% Pt, 1.0 M Urea, 0.25 M NH_4OH., pH 7, 200°C, 1hr

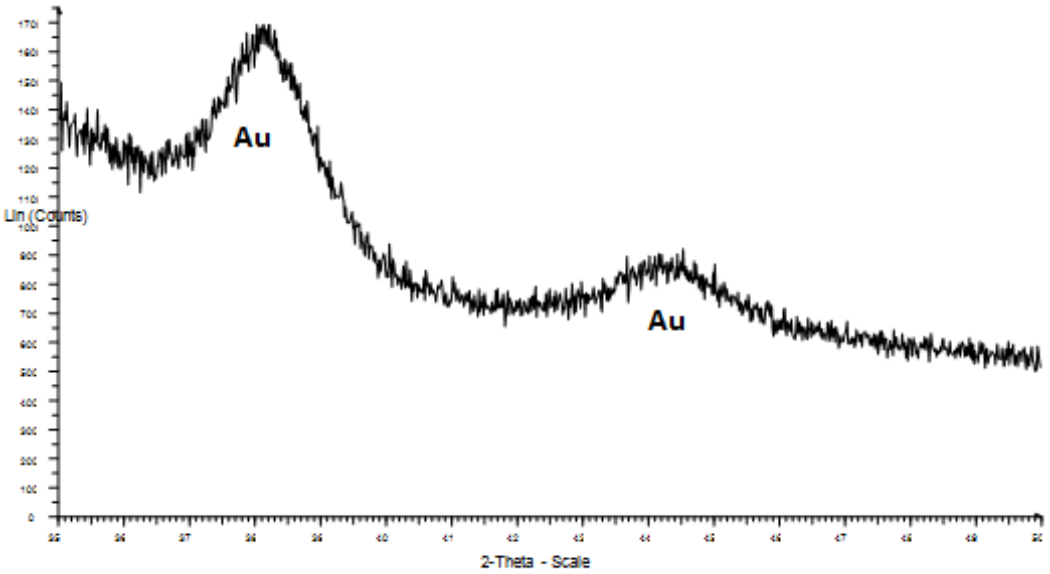


Figure 12.32: 5% Au, 1% Pt, 1.0 M Urea, 0.25 M NH_4OH, pH 7, 200°C, 1hr

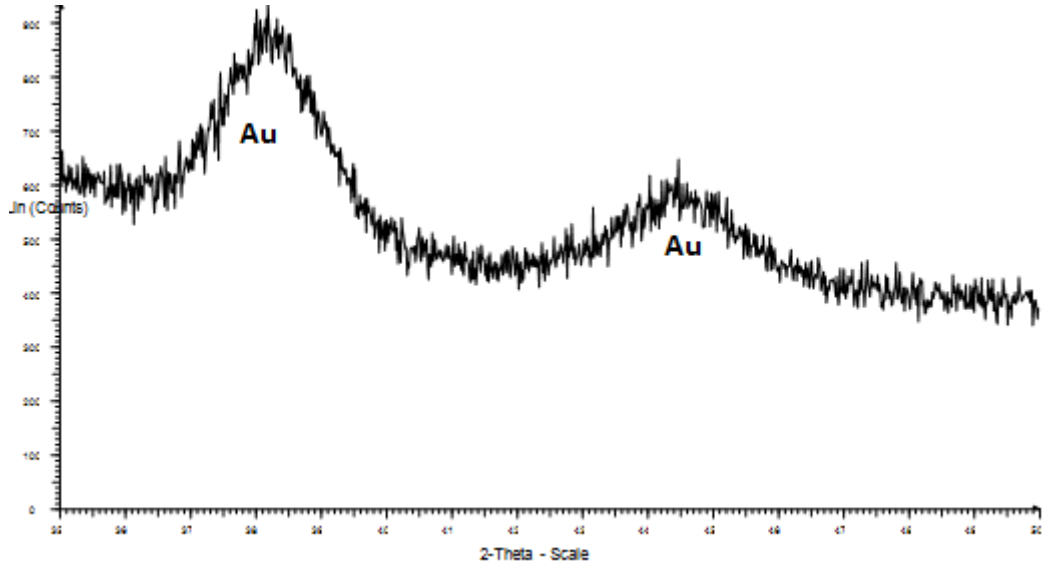


Figure 12.33: 5% Au, 1% Pt, 1.0 M Urea, 0.1 M NH_4OH., ph 7, 300°C, 1hr

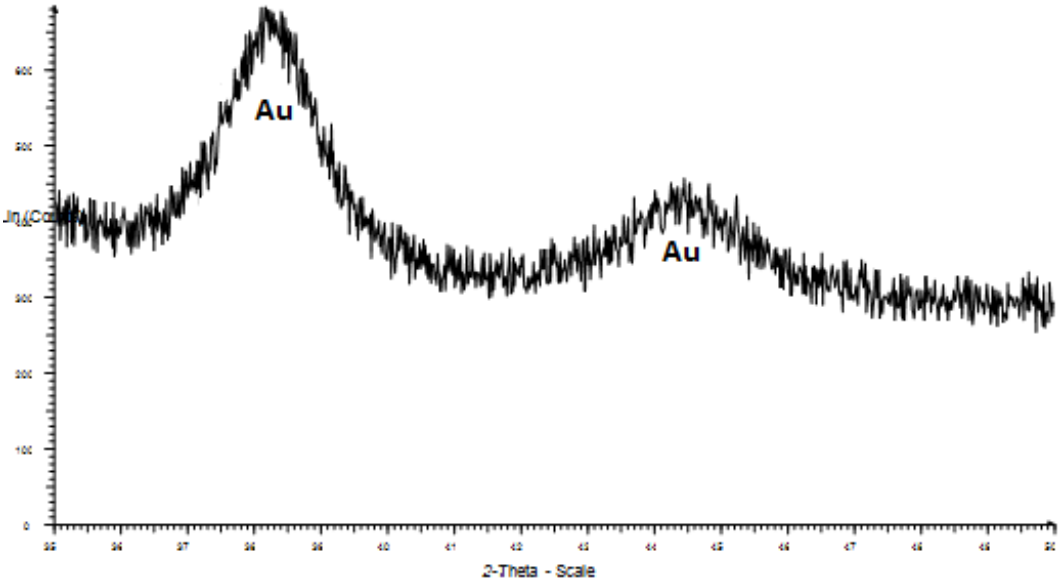


Figure 12.34: 5% Au, 2% Pt, 1.0 M Urea, 0.25 M NH_4OH, pH 7, 200°C, 1hr

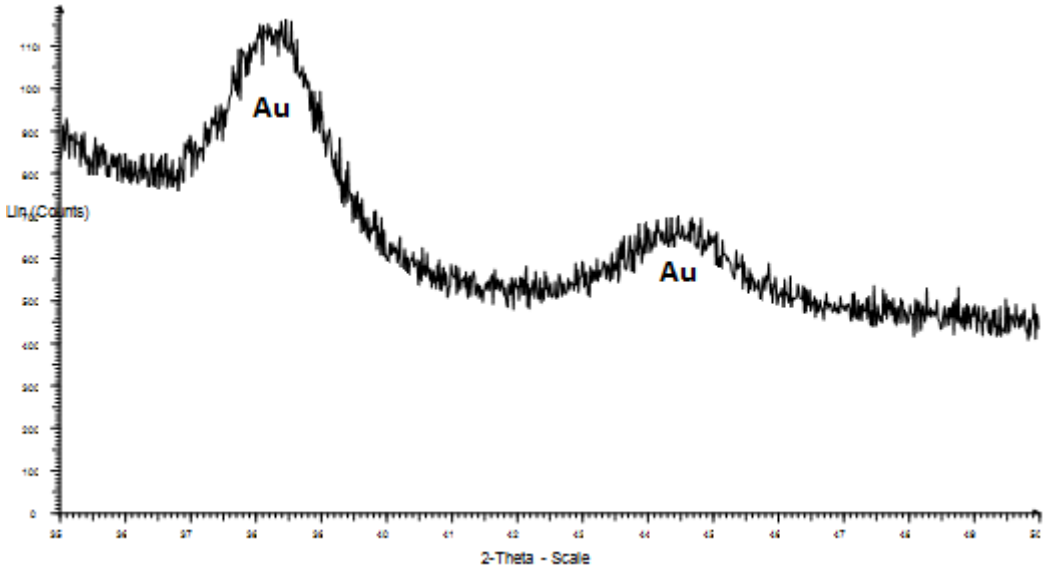


Figure 12.35: 5% Au, 2% Pt, 1.0 M Urea, 0.25 M NH_4OH, pH 7, 300°C, 1hr

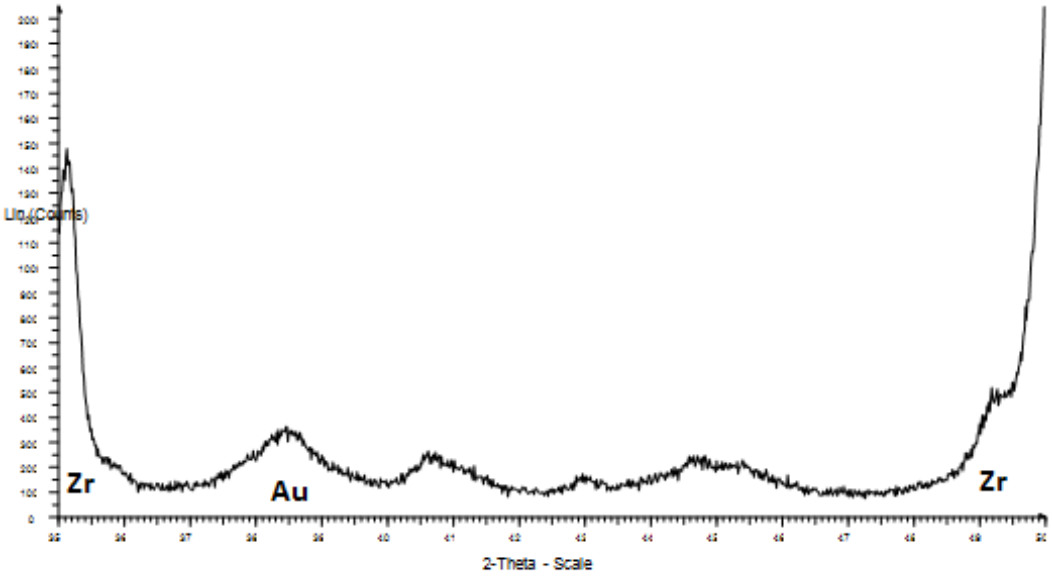


Figure 12.36: 5% Au, 2% Pt, 1.0 M Urea, 0.25 M NH_4OH, pH 7, 200°C, 1hr

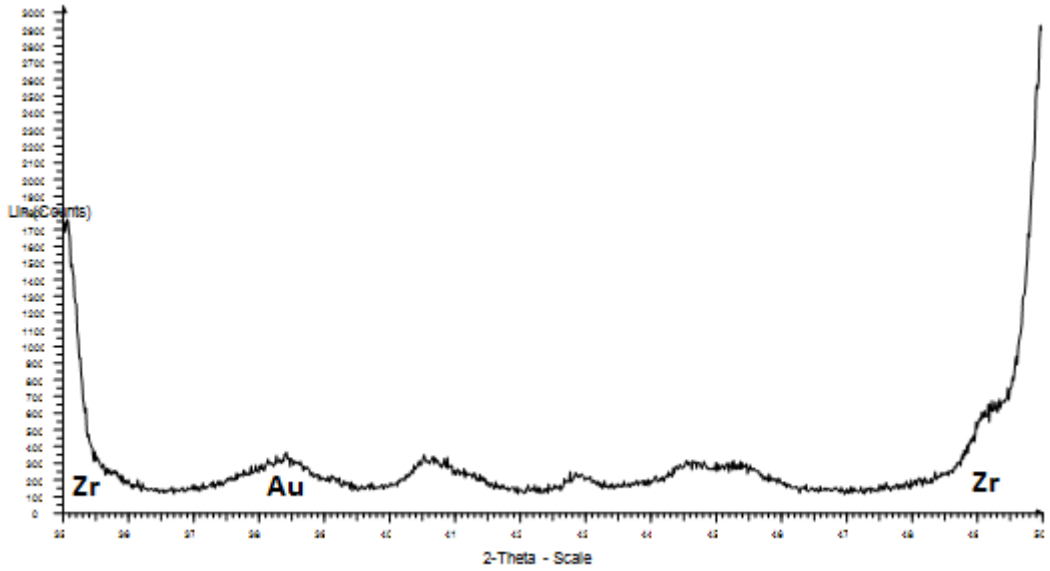


Figure 12.37: 5% Au, 2% Pt, 1.0 M Urea, 0.25 M NH_4OH, pH 7, 300°C, 1hr

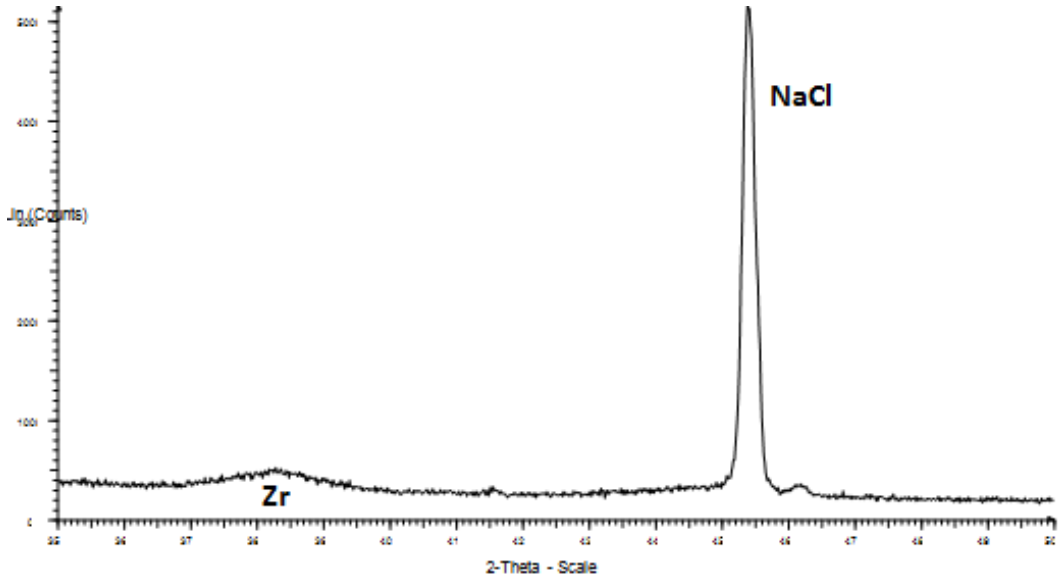


Figure 12.38: 5% Au, 1.0 M Urea, 0.25 M NH_4OH, pH 7, 300°C, std NaCl

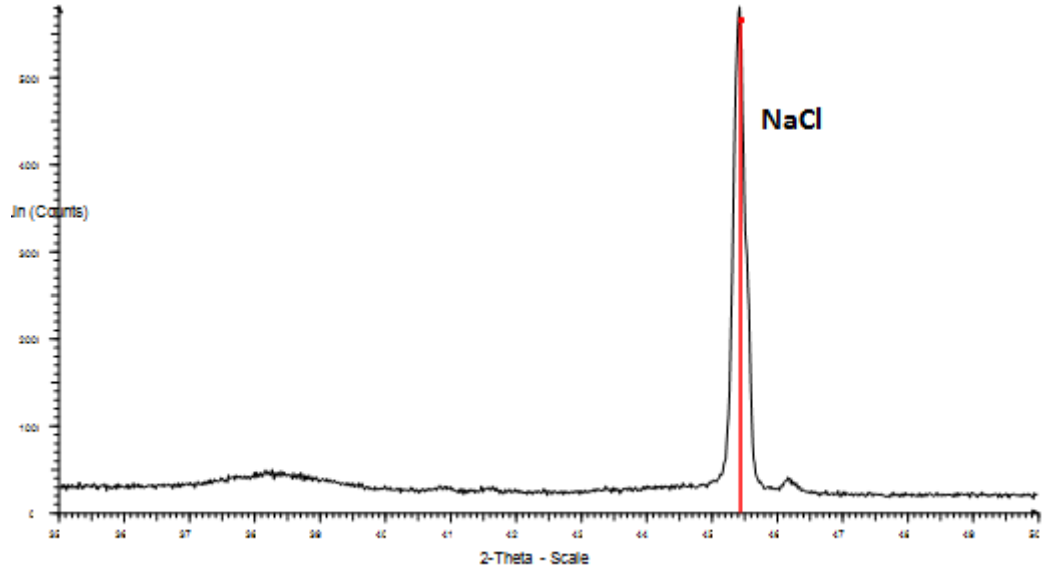


Figure 12.39: 5% Au, 1% Pt, 1.0 M Urea, 0.25 M NH_4OH, pH 7, 300°C, 1hr, std

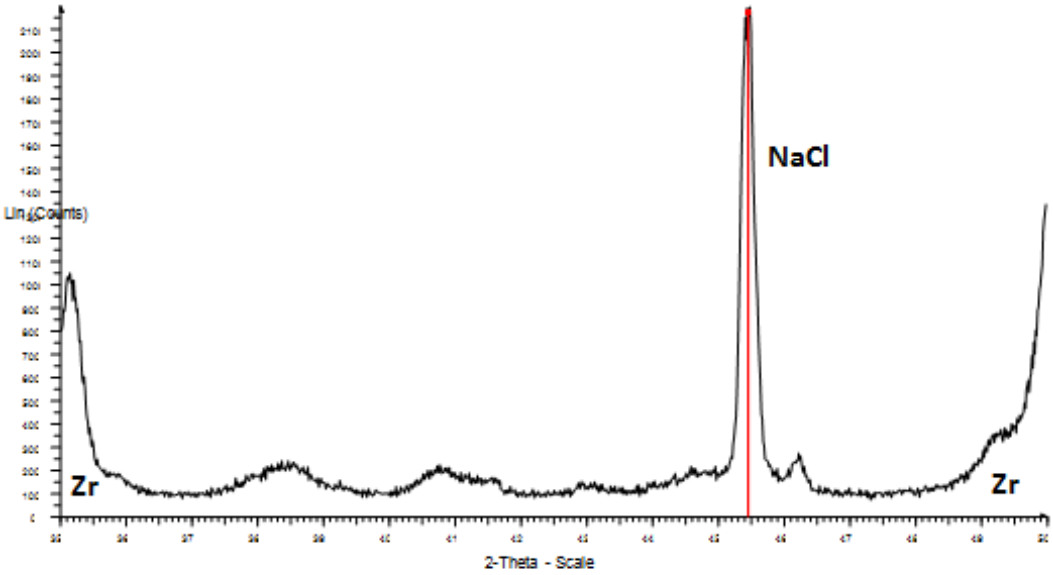


Figure 12.40: 5% Au, 1% Pt, 1.0 M Urea, 0.25M NH_4OH, pH 7, 300°C, 1hr, std

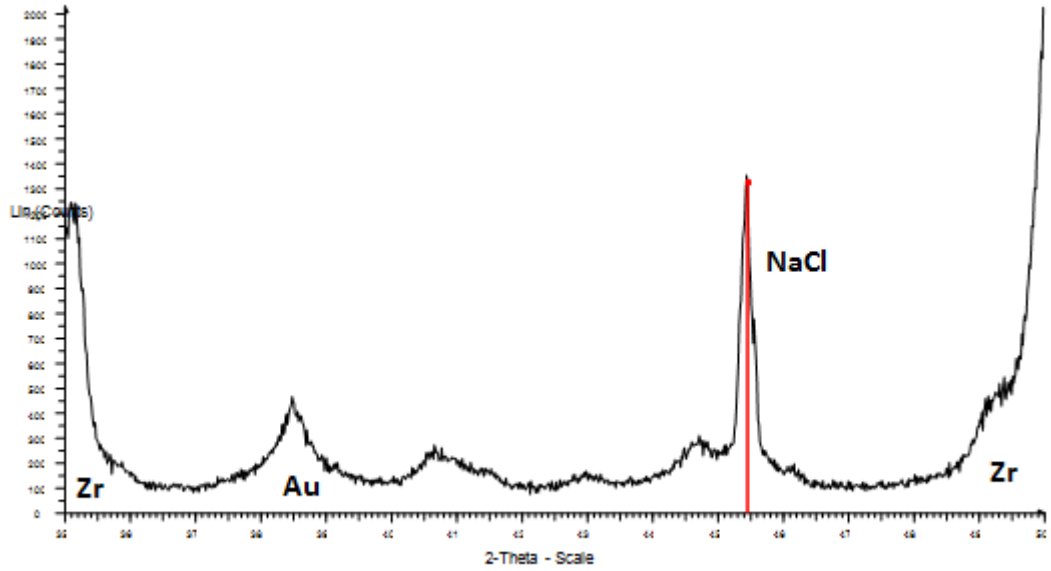


Figure 12.41: 5% Au, 2% Pt, 1.0 M Urea, 0.25 NH_4OH., pH 7, 300°C, 1hr, std

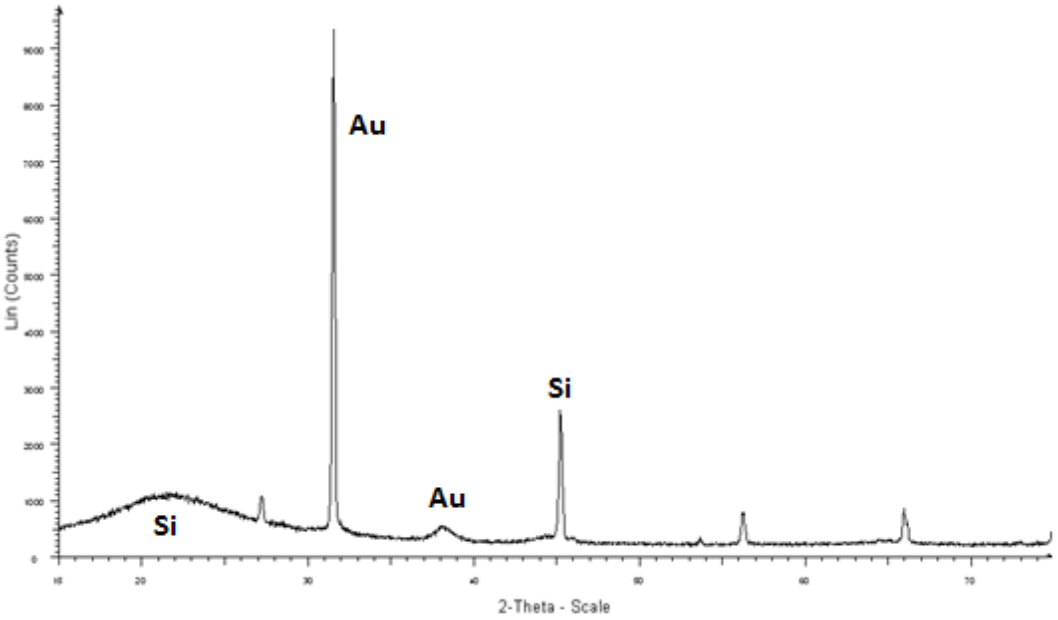


Figure 12.42: 5% Au, 1% Pt, 0.25 M Urea, 0.1 M NH_4OH, pH 7, silica, 400°C, 1hr

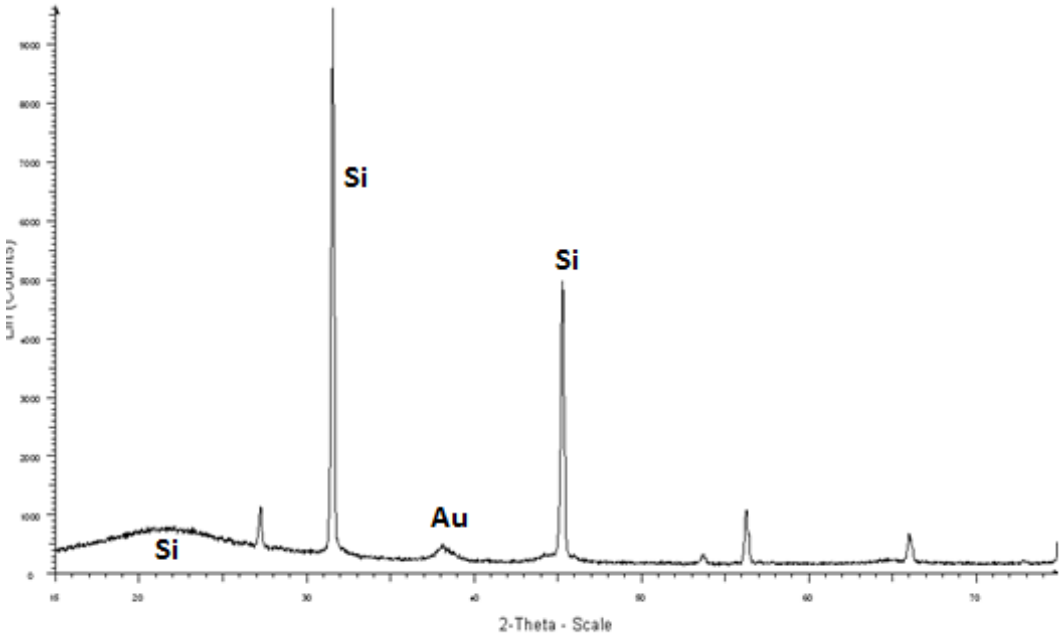


Figure 12.43: 5% Au, 1% Pt, 0.25 M Urea, 0.1 M NH_4OH, pH 7, silica, 400°C, 1hr

BET

Nano anatase as prepared (check for the heated one also!!!) add these in!!!

Nano anatase batch 1

BET Surface Area: 482.3349 ± 7.7741 m^2/g

Slope: 0.008985 ± 0.000145 g/cm^3

STP Y-Intercept: 0.000040 ± 0.000009 g/cm^3 STP

C: 224.79440

Qm: 110.8001 cm^3/g

STP Correlation Coefficient: 0.9996086

Molecular Cross-Sectional Area: 0.1620 nm^2

Nano anantase batch 2

BET Surface Area: 496.9725 ± 6.9871 m^2/g

Slope: 0.008759 ± 0.000165 g/cm^3

STP Y-Intercept: 0.000039 ± 0.000008 g/cm^3 STP

C: 219.85740

Qm: 109.5001 cm^3/g

STP Correlation Coefficient: 0.9997064

Molecular Cross-Sectional Area: 0.1624 nm^2

Nano anatase batch 3

BET Surface Area: 512.6153 ± 7.1527 m^2/g

Slope: 0.008862 ± 0.000176 g/cm^3

STP Y-Intercept: 0.000041 ± 0.000007 g/cm^3 STP

C: 221.72540

Qm: 110.3401 cm^3/g

STP Correlation Coefficient: 0.9997465

Molecular Cross-Sectional Area: 0.1647 nm^2

Heated nano anatase

BET Surface Area: 291.7263 ± 6.7352 m^2/g

Slope: 0.005893 ± 0.000274 g/cm^3

STP Y-Intercept: 0.000028 ± 0.000004 g/cm^3 STP

C: 210.85740

Qm: 82.437 cm^3/g

STP Correlation Coefficient: 0.9997064

Molecular Cross-Sectional Area: 0.1020 nm^2

Nano rutile support.

NRS batch 1.

Surface Area

Single point surface area at P/Po = 0.098547458: 95.3528 m^2/g

BET Surface Area: 101.9050 m^2/g

Pore Volume

Single point adsorption total pore volume of pores less than 144.4069 nm diameter at P/Po = 0.986415754: 0.086586 cm^3/g

Pore Size

Adsorption average pore width (4V/A by BET): 3.39868 nm

BJH Adsorption average pore diameter (4V/A): 4.1278 nm

BJH Desorption average pore diameter (4V/A): 4.1845 nm

NRS batch 2

Surface Area

Single point surface area at P/Po = 0.0982863752: 97.2864 m^2/g

BET Surface Area: 103.1182 m^2/g

Pore Volume

Single point adsorption total pore volume of pores less than 144.4069 nm diameter at P/Po = 0.991728368: 0.088286 cm^3/g

Pore Size

Adsorption average pore width (4V/A by BET): 3.42827 nm

BJH Adsorption average pore diameter (4V/A): 4.23761 nm

BJH Desorption average pore diameter (4V/A): 4.36277 nm

NRS batch 3

Surface Area

Single point surface area at P/Po = 0.091635829: 93.22744 m^2/g

BET Surface Area: 95.3728 m^2/g

Pore Volume

Single point adsorption total pore volume of pores less than 144.4069 nm diameter at P/Po = 0.938728284: 0.08163283 cm^3/g

Pore Size

Adsorption average pore width (4V/A by BET): 3.28425 nm

BJH Adsorption average pore diameter (4V/A): 4.16273 nm

BJH Desorption average pore diameter (4V/A): 4.83647 nm

1% Au on NRS after in-situ PXRD

Single point surface area at P/Po = 0.098274746: 72.951 m^2/g
BET Surface Area: 74.8192 m^2/g

Pore Volume

Single point adsorption total pore volume of pores less than 162.4572 nm diameter at P/Po = 0.9875632762: 0.1031824 cm^3/g

Pore Size

Adsorption average pore width (4V/A by BET): 5.43526 nm

BJH Adsorption average pore diameter (4V/A): 6.72540 nm

BJH Desorption average pore diameter (4V/A): 6.1746 nm

8% Au-NRS catalyst after XRK data collection

Single point surface area at P/Po = 0.098274746: 76.8252 m^2/g
BET Surface Area: 77.4189 m^2/g

Pore Volume

Single point adsorption total pore volume of pores less than 170.4580 nm diameter at P/Po = 0.988522696: 0.122436 cm^3/g

Pore Size

Adsorption average pore width (4V/A by BET): 8.83717 nm

BJH Adsorption average pore diameter (4V/A): 9.8840 nm

BJH Desorption average pore diameter (4V/A): 9.2342 nm

Mintek catalyst.

Single point surface area at P/Po = 0.099293455: 47.7576 m^2/g

BET Surface Area: 48.8834 m^2/g

Pore Volume

Single point adsorption total pore volume of pores less than 92.8199 nm diameter at P/Po = 0.978688000: 0.192806 cm^3/g

Pore Size

Adsorption average pore width (4V/A by BET): 15.77678 nm

BJH Adsorption average pore diameter (4V/A): 17.0736 nm

BJH Desorption average pore diameter (4V/A): 25.5271 nm

Sample 2

Single point surface area at P/Po = 0.0998293312: 46.82 m^2/g

BET Surface Area: 47.3856 m^2/g

Pore Volume

Single point adsorption total pore volume of pores less than 91.1839 nm diameter at P/Po = 0.969638762: 0.191827 cm^3/g

Pore Size

Adsorption average pore width (4V/A by BET): 15.27635 nm

BJH Adsorption average pore diameter (4V/A): 17.3973 nm

BJH Desorption average pore diameter (4V/A): 25.2846 nm